Published in Journals: Batteries, Energies, Sensors and Sustainability

Topic Reprint

Transportation Electrification Key Applications

Battery Storage System, DC/DC Converter, Wireless Charging, Sensors

Edited by
Xiaoyu Li, Jinhao Meng and Xu Liu

mdpi.com/topics

MDPI

Transportation Electrification Key Applications: Battery Storage System, DC/DC Converter, Wireless Charging, Sensors

Transportation Electrification Key Applications: Battery Storage System, DC/DC Converter, Wireless Charging, Sensors

Topic Editors

Xiaoyu Li
Jinhao Meng
Xu Liu

MDPI

Basel • Beijing • Wuhan • Barcelona • Belgrade • Novi Sad • Cluj • Manchester

Topic Editors
Xiaoyu Li
School of Mechanical Engineering
Hebei University Technology
Tianjin
China

Jinhao Meng
School of Electrical Engineering
Xi'an Jiaotong University
Xi'an
China

Xu Liu
State Key Laboratory of Reliability and Intelligence of Electrical Equipment
Hebei University of Technology
Tianjin
China

Editorial Office
MDPI AG
Grosspeteranlage 5
4052 Basel, Switzerland

This is a reprint of the Topic, published open access by the journals *Batteries* (ISSN 2313-0105), *Energies* (ISSN 1996-1073), *Sensors* (ISSN 1424-8220) and *Sustainability* (ISSN 2071-1050), freely accessible at: https://www.mdpi.com/topics/transportation_electrification.

For citation purposes, cite each article independently as indicated on the article page online and as indicated below:

Lastname, A.A.; Lastname, B.B. Article Title. *Journal Name* **Year**, *Volume Number*, Page Range.

ISBN 978-3-7258-4211-7 (Hbk)
ISBN 978-3-7258-4212-4 (PDF)
https://doi.org/10.3390/books978-3-7258-4212-4

Contents

energies

Article

Research and Design of LC Series Resonant Wireless Power Transfer System with Modulation Control Method for Supercapacitor Charging in Linear Motion Systems

Song Xu [1,2], Zhenlin Wang [1], Jingfei Chen [3] and Wei Jiang [2,*]

1 College of Automation, Jiangsu University of Science and Technology, Zhenjiang 212000, China
2 Department of Electrical Engineering, Yangzhou University, Yangzhou 225012, China
3 Haitong Electronic Technology Co., Yangzhou 225100, China
* Correspondence: jiangwei@yzu.edu.cn

Abstract: With the hot topic of "Carbon Neutrality", energy efficiency and saving practices such as reducing fuel consumption, vigorously advocating new energy power and modern rail are now becoming the main research topics of energy conversion technologies. Supercapacitors, with their ability of higher power density, fast charging, and instantaneous high current output, have become an indispensable energy storage element in modern traction systems for modern rail. This proposal introduced wireless power transfer technologies by using LC series resonant technology for charging the supercapacitors. To match the voltage and current level of the supercapacitor, a four-switch buck-boost converter was applied on the secondary side of the load-matching converter. To regulate the wireless transfer power and charging power of the supercapacitor, the active modulation control method was introduced on both the primary and secondary sides of the transfer system. On the primary side, the power is controlled by controlling the current in resonant inductance through the phase shift control method, while on the secondary side, the charging power is controlled by regulating the input voltage of the four-switch buck-boost converter followed by inductance current control. The theoretical analysis under phase shift mode for the primary side and pulse width modulation for a four-switch buck-boost converter with a supercapacitor load (voltage source) were proposed in detail, and the state-space model of the load matching converter was established for controller design to obtain precise voltage and current control. Both open loop and closed loop simulation models were built in the MATLAB/SIMULINK environment, and simulations were carried out to evaluate the system characteristics and control efficiency. The experimental platform was established based on a dsPIC33FJ64GS606 digital controller. Experiments were carried out, and the results successfully verified the effectiveness of the system.

Keywords: modern rail; supercapacitor; LC series resonant; wireless power transfer; load matching converter; modulation control

1. Introduction

Compared with traditional rail, modern rail has been introduced in many cities with the advantages of energy storage, strong adaptability, flexibility, and convenience. Energy storage equipment determines the endurance mileage of modern rail [1,2]. As the most widely used energy storage equipment, battery strings are usually heavy and bulky [3]. To reduce these disadvantages and increase the power receiving ability, using a supercapacitor can be a considerable solution [4]. As the most mature technology of power supply, supplying power by catenary is widely used in modern trams. However, some shortcomings such as contact spark, and wear exist in this power supply mode. To address these issues, the emerging wireless power transfer (WPT) is particularly attractive for modern rail [5–7].

A supercapacitor is widely used as a high-power density energy storage device with the advantages of high current, fast charging and discharging [8], long cycle life [9], high power density [10], high efficiency [11], and environmental protection [12], so the supercapacitors show strong adaptability to the market [13,14]. Supercapacitors have been used as energy storage devices in many high-power applications, such as DC microgrids [15,16] and light rail [17,18]. Supercapacitors perform better than traditional batteries in the field of energy vehicles [19]. Many investigations of supercapacitors have been performed. The different charging strategies for standalone supercapacitors, lithium-ion (Li-ion), and lead-acid batteries were evaluated [20]. The charge redistribution behavior of supercapacitors was analyzed by constant power discharge experiments [21]. A simplified circuit model for supercapacitors based on the voltage-current equation was proposed [22]. In short, although supercapacitors still face some challenges [23], they can be greatly improved in the future [24,25].

For a wireless power transfer (WPT) system applied in modern rail, efficiency and power are two significant factors [26,27]. To increase the efficiency of the system, improving the compensation circuit can achieve optimal control of the equivalent load [28]. To satisfy the requirements of output voltage and current, topology and control strategies are proposed to achieve constant current and voltage [29].

This paper introduces WPT technology into a supercapacitor charging system and proposes an LC resonant WPT system with a modulation control method for supercapacitor charging. An LC series resonant coupling network is applied for power transfer, and a four-switch buck-boost converter is introduced to match the voltage level of the supercapacitor while charging and controlling the charging power. The transfer power is adjusted through both the primary coil RMS current control method and the secondary side voltage-current double-loop control method. The rest of this manuscript is arranged as follows: The structure and topology of the proposed system are introduced in detail in Section 2. Section 3 provides the control system design for primary coil RMS current control and secondary voltage-current control. The simulation and experimental results are presented in Section 4 and Section 5, respectively. The results are compared between simulations and experiments to verify the system characteristics and evaluate the control efficiency. Finally, brief conclusions are made in Section 6.

2. Configuration of the Proposed WPT Charging System

Figure 1 shows the system structure of the proposed wireless power charging system, which mainly consists of six main parts: a DC grid (power source), a high-frequency DC/AC inverter, a resonant coupling tank, a full-bridge AC/DC rectifier, a DC/DC power regulator unit, and supercapacitor (system load). The detailed system topology is presented in Figure 2.

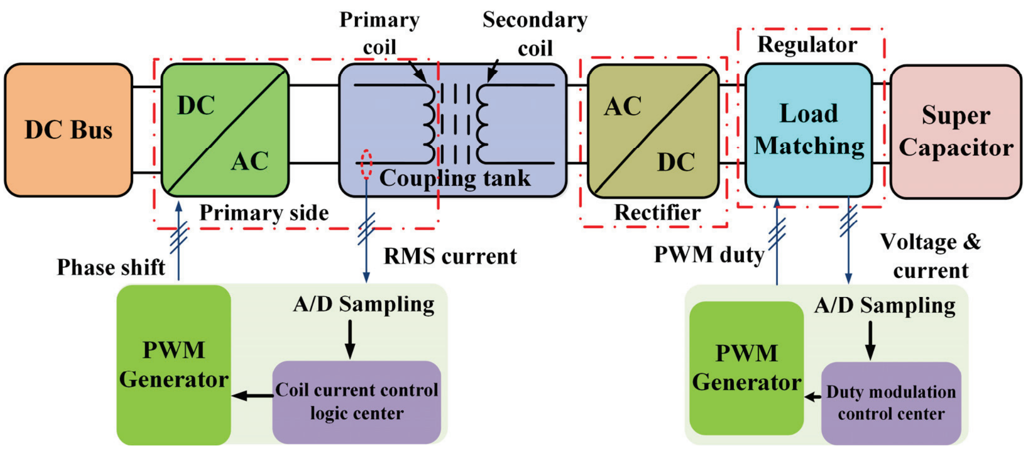

Figure 1. The proposed supercapacitor wireless charging system.

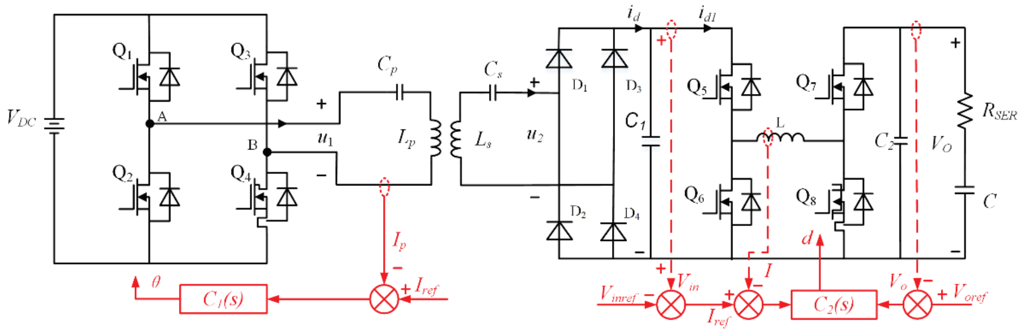

Figure 2. The proposed supercapacitor charging system topology.

As shown in Figure 2, the system can be divided into a primary side and secondary side. On the primary side, the DC grid is simulated by a DC voltage source as the input power of the system, and a full bridge inverter driven by high-frequency PWM transforms the DC voltage to high-frequency AC to supply the LC series resonant coupling tank for power transfer. On the secondary side, the same LC series resonant tank is applied to receive the power transferred from the primary side, and a full bridge rectifier is introduced to convert the received AC voltage to DC voltage. To match the voltage level and control the charging power of the supercapacitor, a DC/DC converter in the form of a four-switch buck-boost converter is applied as a load-matching converter. In this topology, M represents the mutual inductance between the primary and secondary coils. The primary and secondary coil inductances are represented by L_p and L_s, respectively. The resonant capacitors of the primary and secondary coils are expressed by C_p and C_s, respectively.

In this proposal, the modulation control method has been introduced on both the primary side and secondary side. The phase shift control method is applied on the primary side to control the RMS value of the current in L_p, while on the secondary side, the four-switch buck-boost input voltage and inductance current controls are used to control the transfer power.

2.1. Coupling Tank Analysis

For wireless power transfer, the power is transferred from the primary side to the secondary side through inductance coupling, thus the coupling tank plays a significant role in the proposed system. Figure 3 presents the T-type equivalent circuit of the LC resonant coupling tank, where L_p and C_p indicate the primary resonant inductance and capacitor, respectively. L_s and C_s indicate the secondary resonant inductance and capacitor, respectively. U_p is the voltage on the resonant tank, U_s is the output voltage on load R_L, and I_p and I_s represent the input current and output current, respectively. M is the magnetic inductance between the primary coil and the secondary coil.

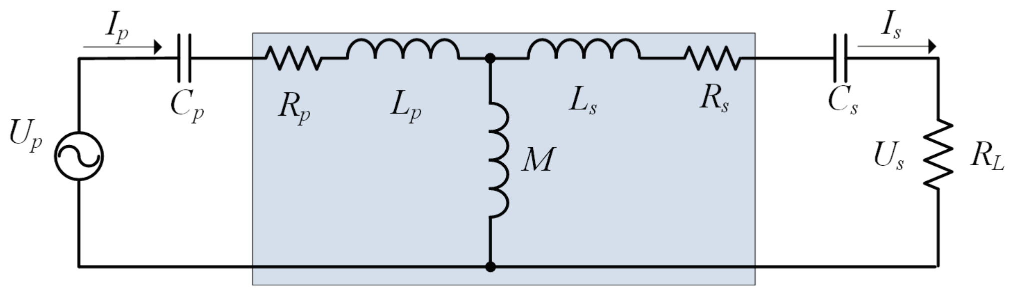

Figure 3. T-type equivalent circuit of LC series resonant coupling tank.

Due to the system working under a resonant state, the energy transfer efficiency (η) can be calculated as Equation (1), where ω_r is the angular speed of the current.

$$\eta = \frac{I_s^2 R_L}{I_p^2 R_p + I_s^2 R_s + I_s^2 R_L} = \frac{R_L}{(R_L + R_s)\left(1 + \frac{R_p(R_s + R_L)}{\omega_r^2 M^2}\right)} \tag{1}$$

The relationship between I_p and I_s is determined by the switching frequency, which should satisfy Equation (2), then I_p and I_s will have the relationship shown in Equation (3).

$$f > \frac{R_p(R_L + R_s)}{M^2} \tag{2}$$

$$\frac{I_\mathrm{p}}{I_s} = \frac{R_\mathrm{s} + R_L}{\omega_0 M} \tag{3}$$

Due to the small internal resistance of the primary coil and secondary coil, the maximum energy transfer efficiency ($\eta_{\max}$) can be approximated as Equation (4).

$$\eta_{\max} = \frac{R_L}{R_\mathrm{s} + R_L} \tag{4}$$

We can conclude that the maximum transfer efficiency is almost 1 and cannot be easily affected by the load R_L.

2.2. Coil Current Constant Characteristics

The proposed WPT system uses a series resonant coupling structure for power transfer, and the current in the coils may have constant characteristics when controlling the input voltage of the four-switch buck-boost conversion constant. The equivalent circuit with a full bridge rectifier and controlled voltage V_{in} is shown in Figure 4. L_p and C_p indicate the primary resonant inductance and capacitor, respectively. L_s and C_s indicate the secondary resonant inductance and capacitor, respectively. $u_p(t)$ is the voltage on the resonant tank, $u_s(t)$ is the input voltage of the rectifier, and $i_p(t)$, $i_s(t)$ represent the input current and output current, respectively. M is the magnetic inductance between the primary coil and the secondary coil. R_L represents the equivalent load.

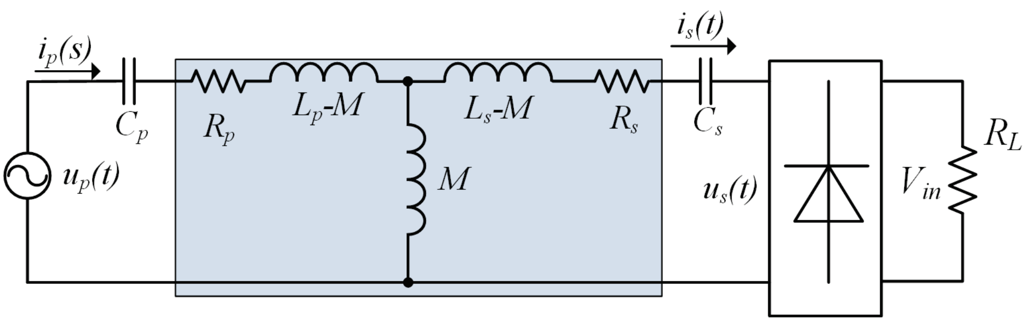

Figure 4. Full system equivalent circuit.

Assuming that the coefficiency between L_p and L_s is k, the DC input voltage is E, the system frequency equals the resonant frequency ω_0, the resonant frequency can be obtained as the equation: $\omega_0 = 2\pi\sqrt{L_p L_s}$. The magnetic inductance between the primary coil and secondary coil can be expressed as Equation (5). K is the coupling factor in the equation.

$$M = K\sqrt{L_p L_s} \tag{5}$$

According to the calculation principle of the full-bridge inverter and rectifier, the voltages $u_p(t)$ and $u_s(t)$ can be obtained as Equations (6) and (7), respectively.

$$u_p(t) = \frac{4E}{\pi}\sin(\omega_0 t) \tag{6}$$

$$u_s(t) = \frac{4V_{in}}{\pi}\sin\left(\omega_0 t + \frac{\pi}{2}\right) \tag{7}$$

Additionally, the voltage can be calculated by Kirchhoff's law, as Equations (8) and (9).

$$i_p(t)\left(j\omega_0 L_p + \frac{1}{j\omega_0 C_p} + R_p\right) - j\omega_0 M i_s(t) = u_p(t) \tag{8}$$

$$i_2(t)\left(j\omega_0 L_2 + \frac{1}{j\omega_0 C_2} + R_2\right) - j\omega_0 M i_1(t) = u_2(t) \tag{9}$$

Due to the system working under a resonant state, the inductor resistance R_p and R_s can be ignored; thus, based on the resonant theory, Equation (10) can be obtained.

$$j\omega_0 L_p + \frac{1}{j\omega_0 C_p} = j\omega_0 L_s + \frac{1}{j\omega_0 C_s} = 0 \tag{10}$$

Substituting Equation (10) into Equations (8) and (9), Equations (11) and (12) can be expressed.

$$j\omega_0 M i_s(t) = -u_p(t) \tag{11}$$

$$j\omega_0 M i_p(t) = -\frac{4V_{in}}{\pi}\sin\left(\omega_0 t + \frac{\pi}{2}\right) \tag{12}$$

By simplifying the above equations, the time domain current in the primary coil and secondary coil can be concluded as Equations (13) and (14), respectively.

$$i_s(t) = -\frac{u_p(t)}{j\omega_0 M} \tag{13}$$

$$i_p(t) = \frac{4V_{in}}{\pi j\omega_0 M}\sin\left(\omega_0 t + \frac{\pi}{2}\right) \tag{14}$$

From the above analysis, it can be concluded that: (1) the primary coil current is only influenced by the controlled input voltage of the four-switch buck-boost converter V_{in}; once V_{in} is controlled, the current will be determined; (2) the secondary coil current is only determined by the input voltage of the inverter (power supply voltage), independent of the load.

3. Control System Design

The control strategies of the proposed system can be divided into two parts: (a) primary coil RMS current control; and (b) secondary power adjustment control. The primary coil RMS current control uses a phase-shift control method to limit the maximum transfer power of the coupling tank, while the secondary power adjustment control applies four-switch buck-boost input voltage control followed by an inductance current control loop to regulate the charging power of the supercapacitor.

3.1. Primary Coil RMS Current Control

On the primary side, the switching frequency of the inverter is set to be the resonant frequency; thus, to limit the maximum transfer power and the power capability of the primary side, the primary coil RMS current control through the phase-shift method needs to be applied. The diagram of the primary coil RMS current control is shown in Figure 5, where a conventional PI controller is applied to control the coil current by adjusting the phase angle θ of the inverter driving signal.

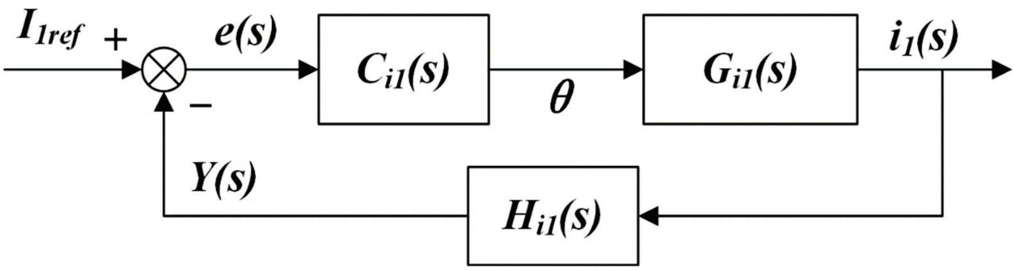

Figure 5. Block diagram of the primary side closed-loop control.

$C_{i1}(s)$ is the conventional PI controller, which generates the phase shift angle for the PWM generator to drive the power stage full-bridge inverter, and $H(s)$ is the feedback current transfer function, which is combined by the RMS current sensor with a low pass filter.

3.2. Secondary Side Power Regulation Control

In this system, a four-switch buck-boost is proposed for dedicated and real-time management of the supercapacitor due to the voltage and current undergoing swings during the charging process. For instance, if a supercapacitor is out of power, its voltage is zero, and then the charging current should be the maximum limit to ensure quick charging. During the charging process, the voltage of the supercapacitor rises, and the current should be minimized to guarantee the trickle charging stage.

The block diagram of secondary power regulation control is presented in Figure 6, and a double loop with an overcharging protection control diagram is proposed. The voltage control loop is an outer loop that is applied to control the input voltage of the four-switch buck-boost load matching converter and generate the inductance current reference value for the inner current loop. The protection loop prevents the supercapacitor from overcharging.

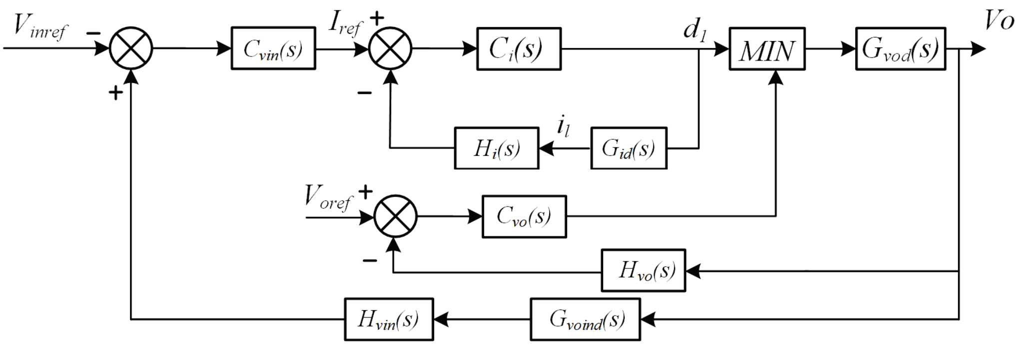

Figure 6. Block diagram of the closed-loop controller.

From the above diagram, $C_{vin}(s)$ is the voltage loop controller, while $C_i(s)$ is the inner current loop controller. Both controllers are conventional PI controllers, formed as Equation (16).

$$C(s) = K_p + \frac{K_i}{s} \tag{15}$$

$C_{vo}(s)$ is the overcharge protection controller, which will work only when the voltage of the supercapacitor is higher than reference V_{oref}, then the duty of PWM will be limited by d_2, otherwise, the PWM duty is controlled by d_1. $G_{vod}(s)$ is the transfer function between the output voltage of the four-switch buck-boost converter and PWM duty, while $G_{vind}(s)$ indicates the relationship between the output voltage and input voltage of the converter, and $G_{id}(s)$ represents the transfer function between the inductance current and PWM duty.

Through the small-signal modeling method, the transfer functions can be obtained as Equations (16)–(18), respectively.

$$G_{vod}(s) = \frac{\widetilde{u}_{out}(s)}{\widetilde{d}(s)} = \frac{U_{in} - L \cdot I_L \cdot s}{L \cdot C \cdot s^2 + \frac{L}{R} \cdot s + (1-D)^2} \tag{16}$$

$$G_{id}(s) = \frac{\widetilde{i}_L(s)}{\widetilde{d}(s)} = \frac{\frac{C \cdot U_{in}}{1-D} \cdot s + \frac{1}{R(1-D)} \cdot U_{in} + (1-D) \cdot I_L}{L \cdot C \cdot s^2 + \frac{L}{R} \cdot s - (1-D)^2} \tag{17}$$

$$G_{voind}(s) = \frac{G_{vind}(s)}{G_{voutd}(s)} = \frac{\frac{\widetilde{u}_{in}(s)}{\widetilde{d}(s)}}{\frac{\widetilde{u}_{out}(s)}{\widetilde{d}(s)}} = \frac{I_L \cdot L \cdot s - U_{in}}{D - D^2} \cdot \frac{L \cdot C \cdot s^2 + \frac{L}{R} \cdot s + (1-D)^2}{U_{\text{in}} - L \cdot I_L \cdot s} \tag{18}$$

4. System Simulation Results

To verify with theoretical analysis of the designed WTP charging system, the simulation model was built up in the MATLAB/SIMULINK environment. The system simulations included two phases. Phase 1 was an open-loop system characteristics scan simulation. Phase 2 was closed-loop simulation to verify the effectiveness of the control system. The simulation model is shown in Figure 7, and Table 1 presents the simulation parameters.

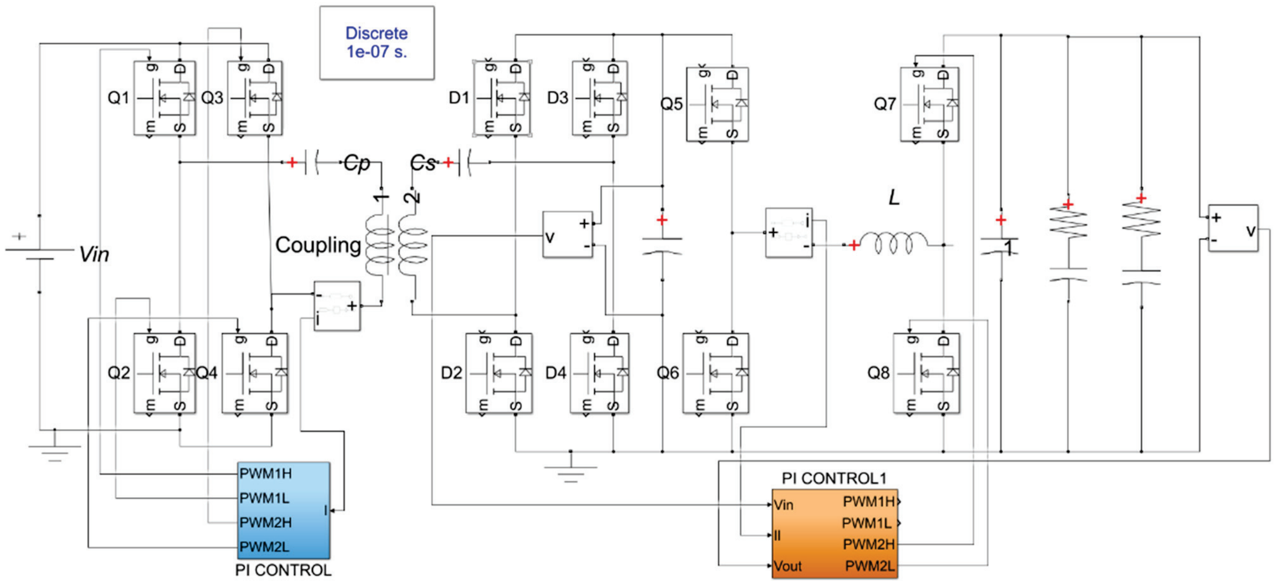

Figure 7. The simulation system.

Table 1. The simulation parameters.

Parameters	Value
Input supply voltage V_{in}	72 V
Inverter switching frequency f_s	85 kHz
Load matching converter switching frequency f_{dc}	40 kHz
Inductance L	220 µH
Primary resonant inductance L_p	500 µH
Primary capacitor C_p	32 nF
Secondary inductance L_s	100 µH
Secondary capacitor C_s	4 µF
Resonant frequency f_r	85 kHz

4.1. Open-Loop System Simulation Results

Open-loop stimulation was focused on the relationship between the primary coil RMS current and phase angle of inverter driving signals, also with a constant four-switch buck-boost input voltage scan. The simulation results are shown in Figure 8.

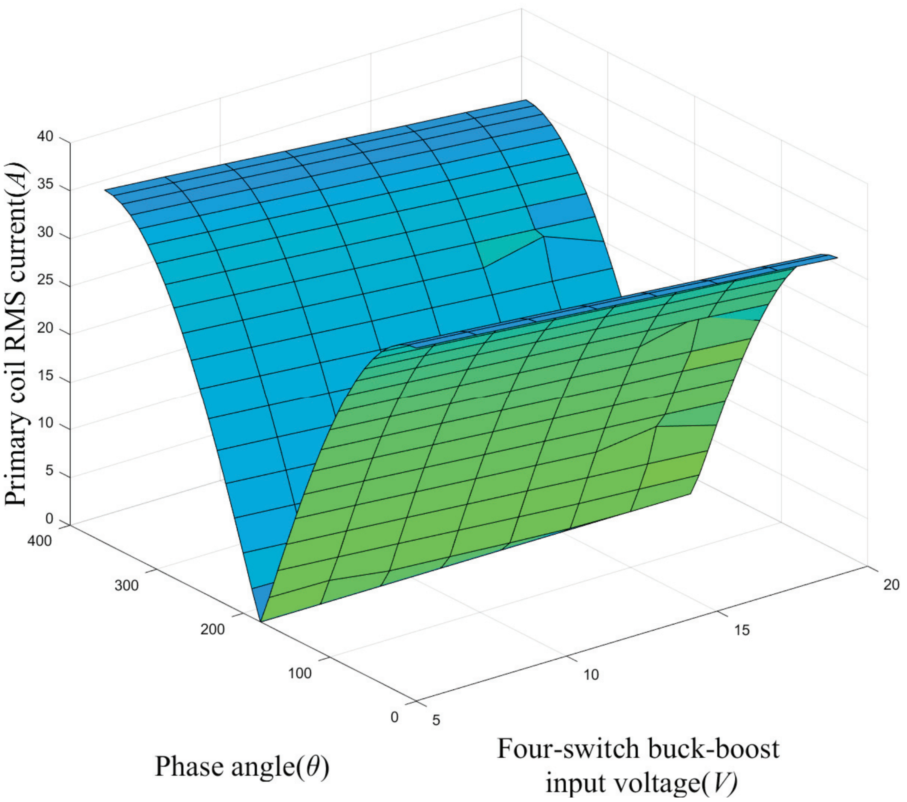

Figure 8. The open-loop characteristics of 3D scanning results.

From the simulation results, it can be concluded that the RMS current in the primary coil decreases while the phase angle increases from 0 to 180 degrees, and in direct proportion to the phase angle θ from 180 to 360 degrees.

In addition, the input voltage of the four-switch buck-boost converter has a weak inverse influence on the RMS current.

4.2. Closed-Loop Simulation Results

The closed-loop simulation was carried out to evaluate the efficiency of the designed control system, which also included two phases. Phase 1 was a constant RMS coil control on the primary side, while Phase 2 was input voltage and inductance current control of the four-switch buck-boost converter on the secondary side.

Figure 9 shows the simulation results of Phase 1. In this simulation, the RMS current reference was 1.4 A, and the controller parameters were K_p = 0.7 and K_I = 400. As shown in the results, the system was working under resonant conditions, and the RMS coil current was successfully controlled.

For the secondary closed-loop simulation, the initial voltage of the supercapacitor group was 20 V, and the capacitance of the supercapacitor was 1 F. The input voltage reference was set as 40 V. The results are shown in Figure 10, and the input voltage and inductance current were precisely controlled.

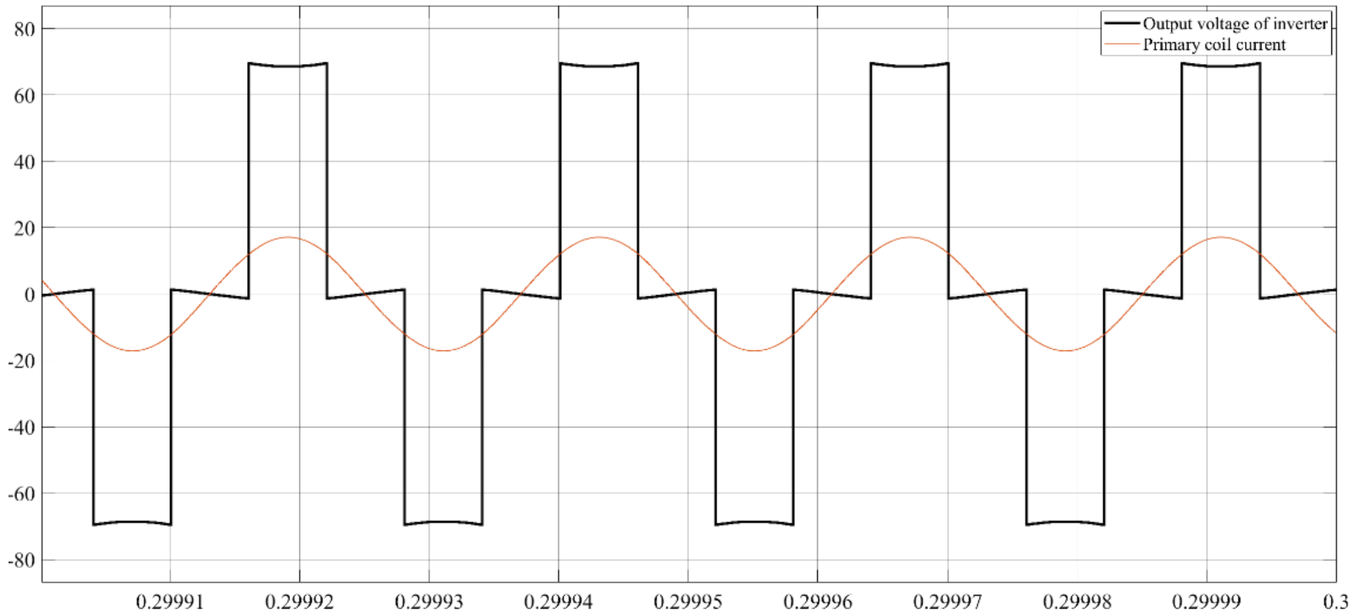

Figure 9. The primary inductor current waveform and inverter output voltage waveform.

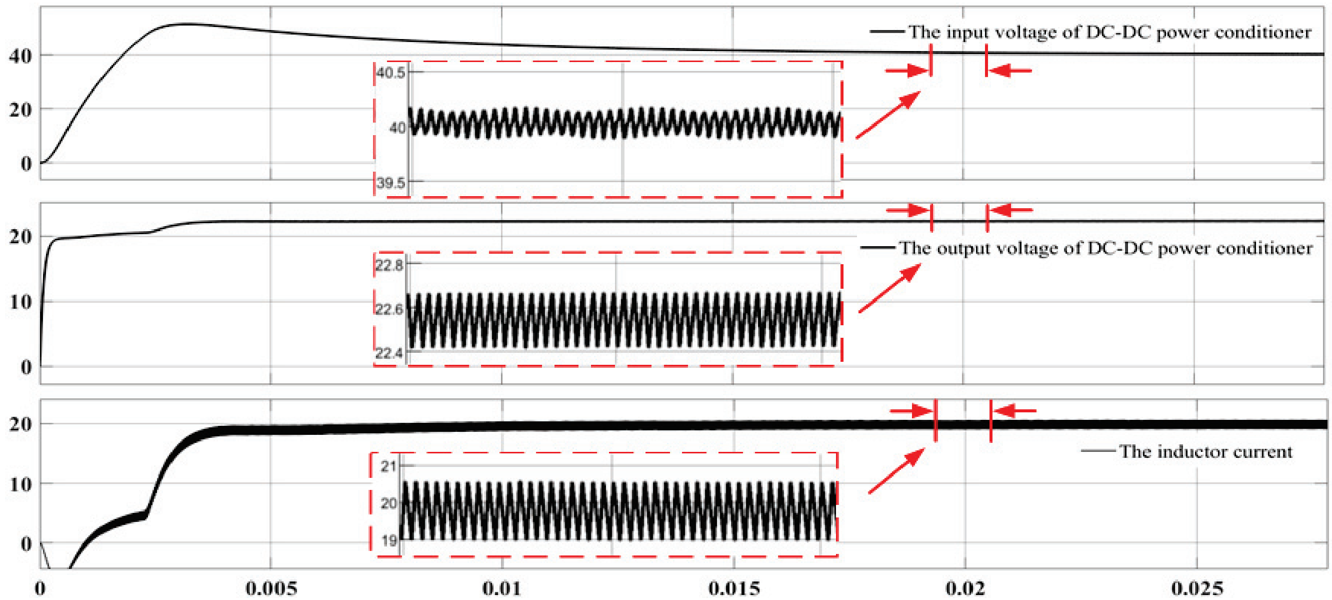

Figure 10. The simulation waveforms of the input voltage, output voltage and inductor current.

Thus, in sum, the control system efficiency was successfully evaluated.

5. Supercapacitor Wireless Charging Experiment

Based on the above theoretical analysis and simulation verification, the experimental platform was constructed as shown in Figure 11 and used a dsPIC33FJ64GS606 digital controller for power stage control. The supercapacitor was combined with two sets of 25 V/15 F with a 72 V DC power generator as the input source. The parameters of the established experimental platform are shown in Table 2.

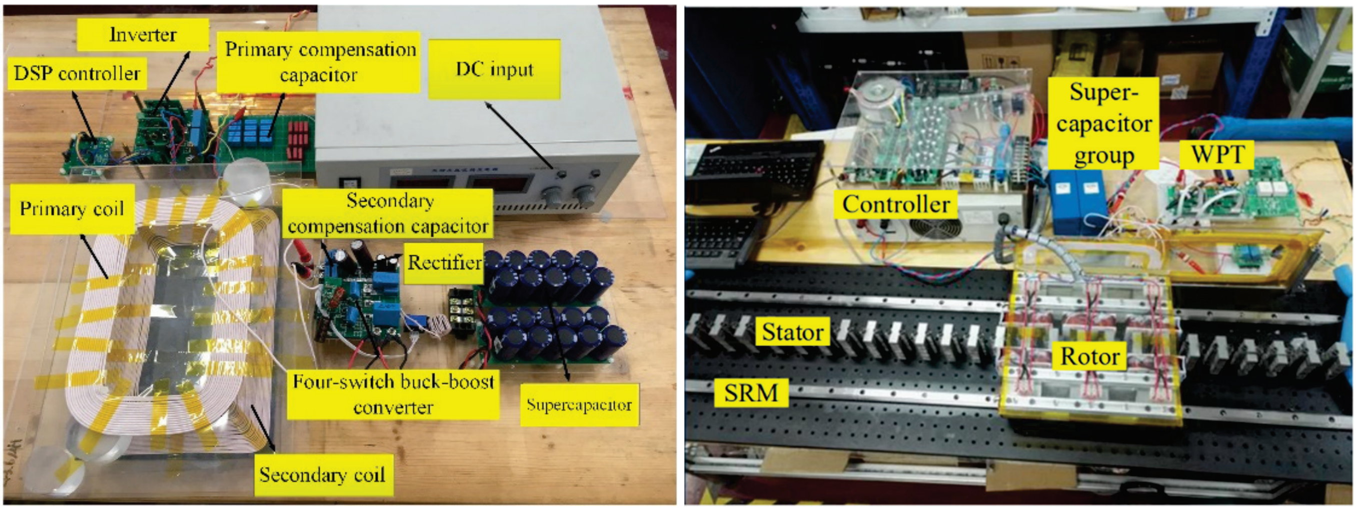

Figure 11. The experimental platform.

Table 2. The environment parameters.

Components	Pattern/Parameter
Digital controller	dsPIC33FJ64GS606
Driving power supplier	KA7805, FSL336
Current sensor	56200C, CHCS-GB5-50A
Primary inductance L_p	500 μH
Primary capacitor C_p	7 nF
Secondary inductance L_s	43.6 μH
Resonant frequency f_r	85.07 kHz
Secondary capacitor C_s	0.1 μF
Supercapacitor	25 V/15 F

5.1. Start-Up Estimation Experiments

Before the power transfer experiments, the startup test of the experimental platform needed to be carried out in two phases. Phase 1: Adjust the inverter switch frequency to ensure that the primary side is working under resonant conditions. Phase 2: Verify that the phase shift on inverter driving signals does not influence the resonant state. Figure 12 and Figure 13 show the experimental results of phase angles θ = 0 and θ = 30 degrees, respectively, under a switching frequency of 85 kHz. There was no phase shift between the primary coil current and the output voltage of the inverter; thus, the system was working under resonance. At the same time, the phase shift angle did not influence the resonant state. The system startup test was successfully verified.

5.2. Primary Coil RMS Current Control Results

As introduced before, the primary side of the proposed system was working under a resonant state, and the coil RMS current was controlled by the phase shift control method. In this experiment, the transfer distance between the two coils was 4 cm, the input voltage was 72 V constant, and the input voltage of the four-switch buck-boost converter was controlled at 35 V constant. By controlling the coil RMS current from 1.2 A to 2.6 A, the results of the transfer power and system efficiency were as shown in Figure 14 and Figure 15, respectively.

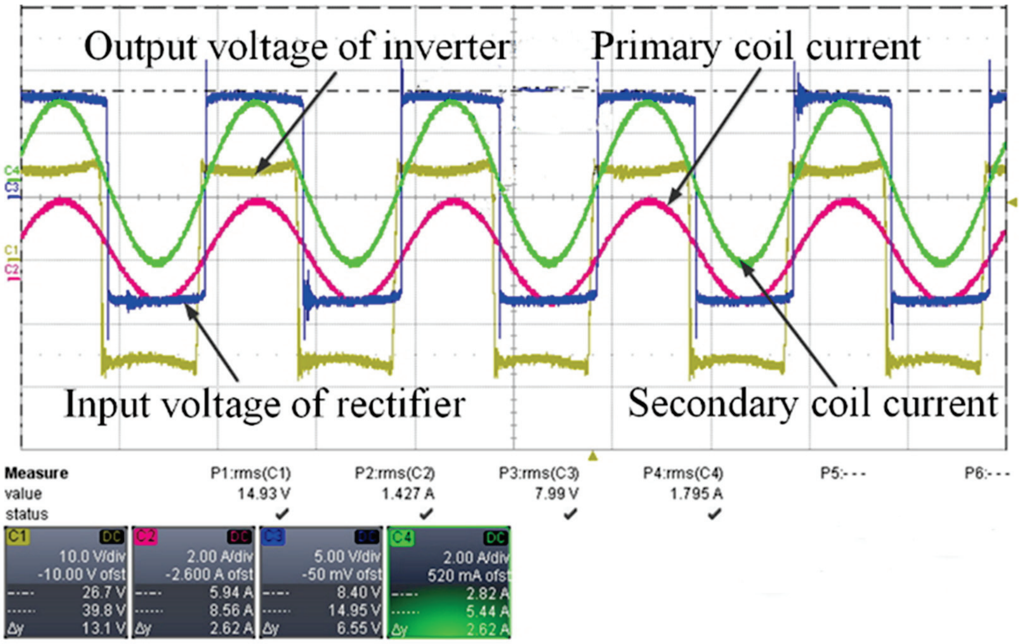

Figure 12. The experimental waveform at resonance.

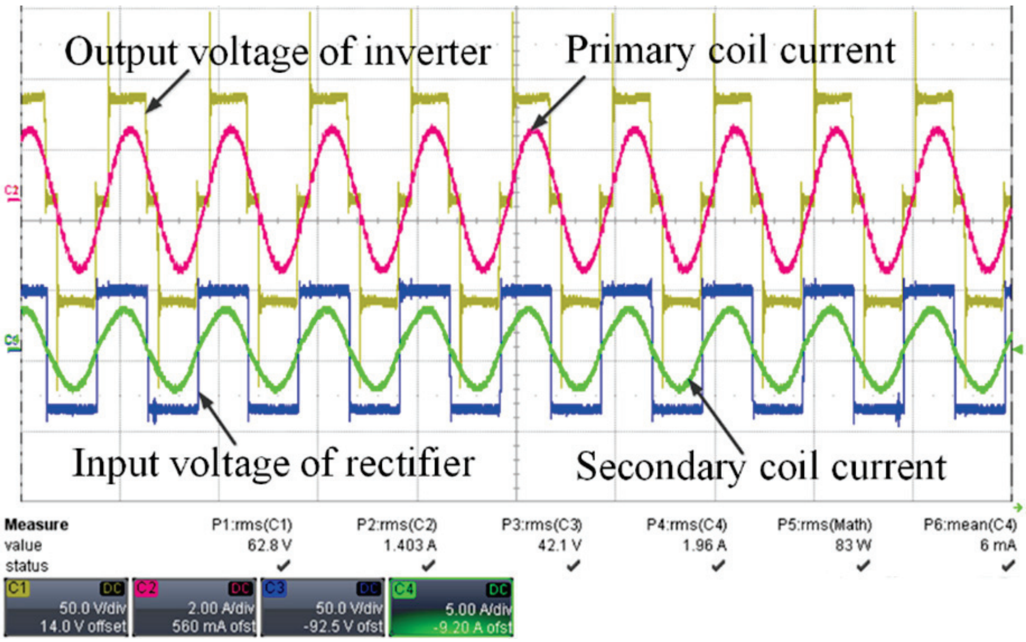

Figure 13. The experimental waveform when the phase shift angle is 30°.

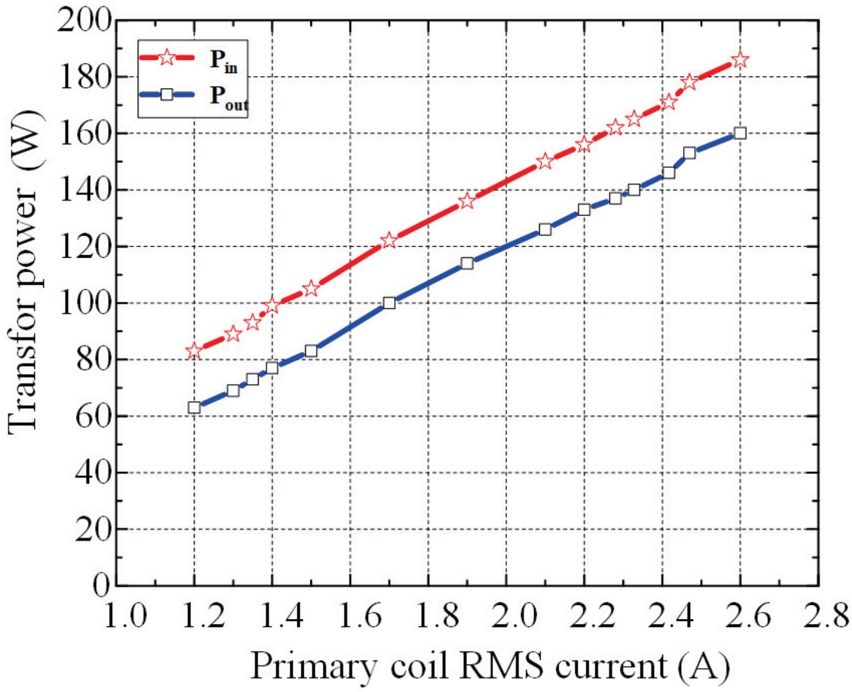

Figure 14. System transfer power vs. primary coil RMS current.

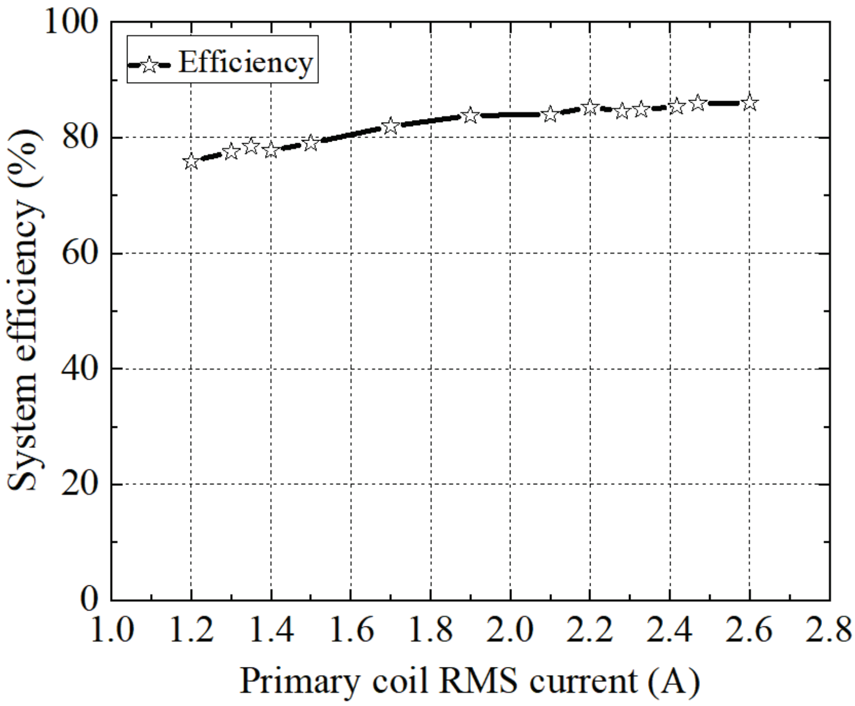

Figure 15. System efficiency vs. primary coil RMS current.

From the results, the input and output power of the proposed system increased with the coil RMS current. Additionally, as the transfer power increased, the transfer efficiency increased slightly, and the RMS current had a positive influence on system efficiency.

5.3. Secondary Side Constant Input Voltage Control Results

This experiment focused on the secondary side control. The experimental conditions were the same as before, and the primary coil RMS current was controlled at 1.4 A constant.

By controlling the input voltage of the four-switch buck-boost converter from 20 V to 48 V, the results were as shown in Figure 16, Figure 17 and Figure 18, respectively.

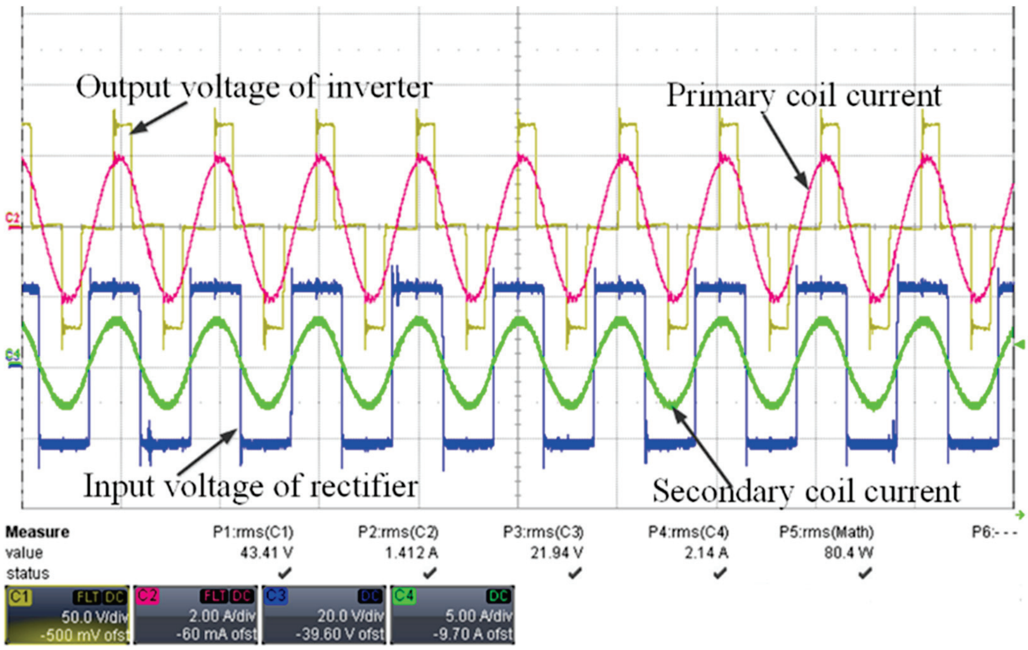

Figure 16. Experimental results with the secondary DC input voltage controlled at 20 V.

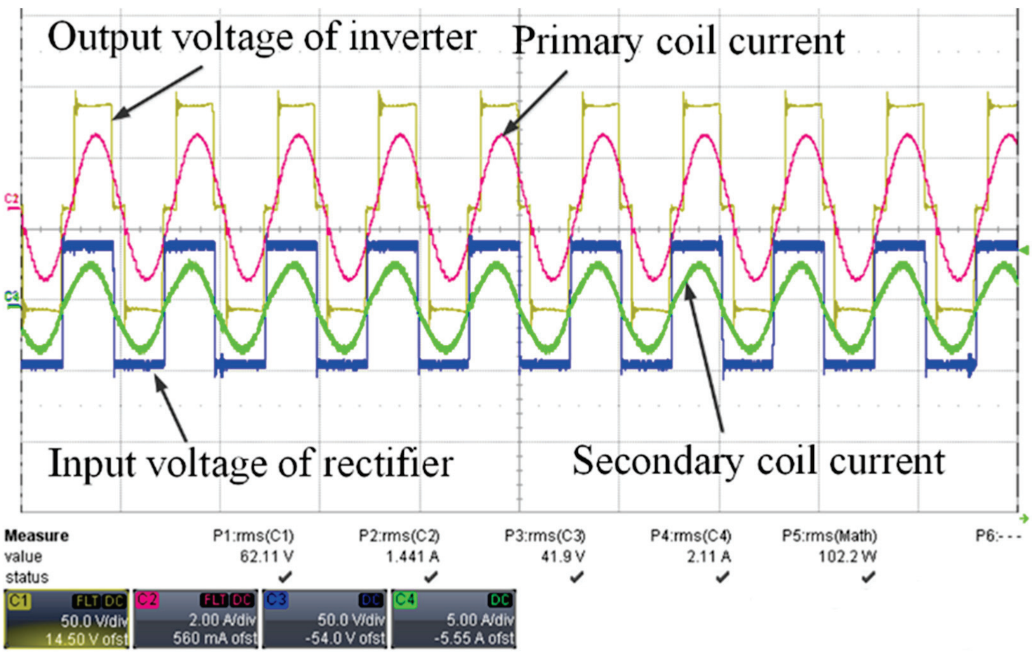

Figure 17. Experimental waveform when the input voltage of the DC-DC power conditioner is 40 V.

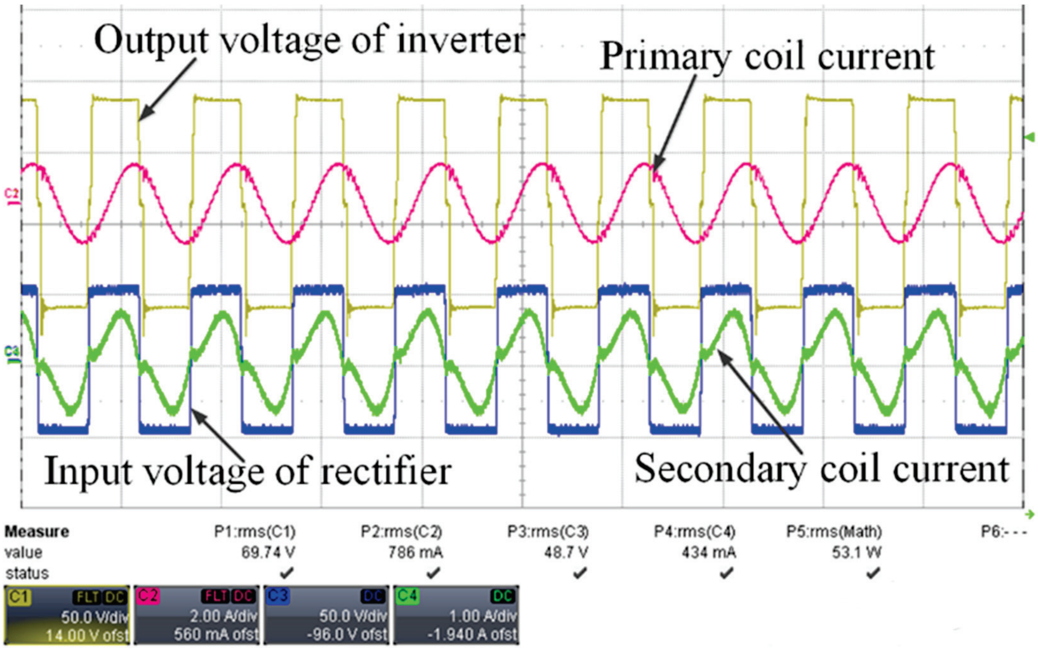

Figure 18. Experimental waveform when the input voltage of the DC-DC power conditioner is 48 V.

Figure 16 shows the experimental results of controlling the input voltage of the four-switch buck-boost converter at 20 V. The phase of the current in the primary coil led to that of the inverter output voltage while the secondary side was working under a resonant state. The output power could be calculated as 47 W with input power obtained as 80.4 W.

The experimental results of controlling the controlling input voltage of the four-switch buck-boost converter at 40 V are shown in Figure 17, where both the primary and secondary resonant tanks were working under a resonant state. The output power could be calculated as 89 W with input power obtained as 102 W.

Figure 18 shows the experimental results of controlling the input voltage of a four-switch buck-boost converter at 48 V. Under this condition, the transfer power was outside the input power capacity of the primary coil RMS current; thus, the primary coil current was out of control, and the system was working under an inductive state. The output power could be calculated as 21.5 W with input power of 53.1 W, and the transfer efficiency dropped sharply.

The voltage scanned experimental results of transfer power and system efficiency are shown in Figure 19 and Figure 20, respectively. From the scanned results, the transfer power could be adjusted by controlling the input voltage of the four-switch buck-boost converter but was limited by the primary coil RMS current. If the required transfer power is outside the limit, the transfer efficiency will drop sharply. Additionally, there is a maximum efficiency under each constant primary coil RMS current; under that point, both the transfer power and efficiency will be optimum.

5.4. System Stability to Changes in the Supercapacitor Voltage Results

Considering the charging characteristics of a supercapacitor, the voltage of the supercapacitor keeps rising during the charging process, so it is necessary to check the system's stability during the charging process.

In this experiment, the voltage on the supercapacitor rose from 10 V to 100 V. Under the same conditions as before, the primary coil RMS current was controlled at 1.4 A, and the input voltage of the four-switch buck-boost converter was controlled at 40 V. The results for the inductor current (charging current) and system efficiency are shown in Figure 21 and Figure 22, respectively.

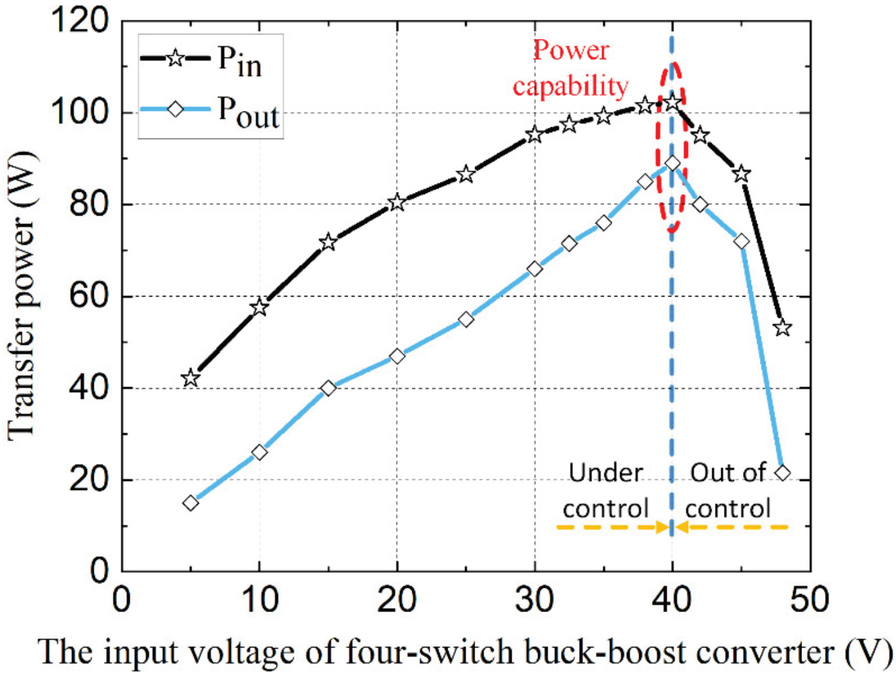

Figure 19. Transfer power vs. input voltage of the four-switch buck-boost converter.

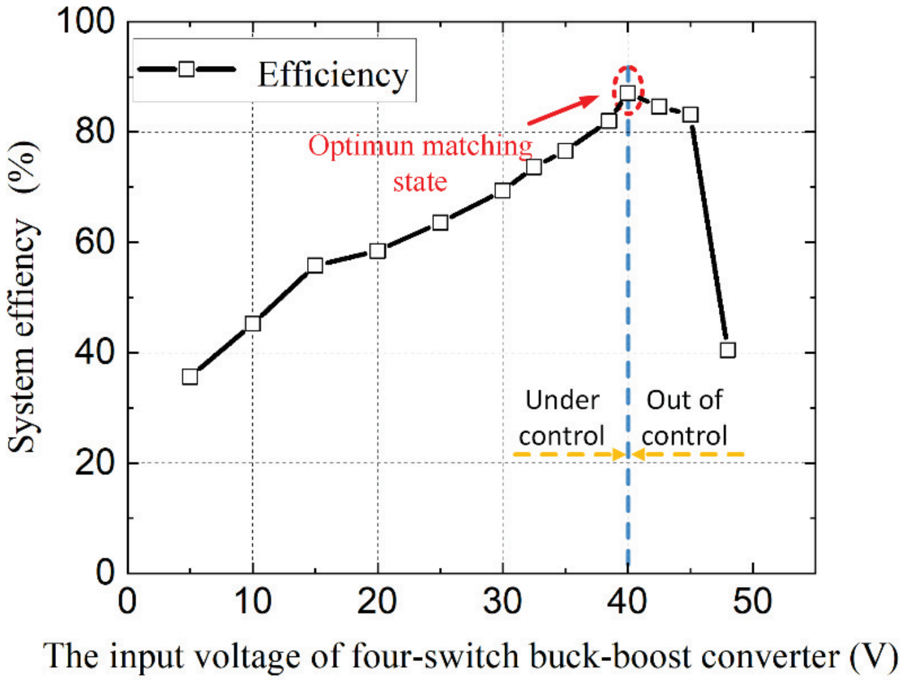

Figure 20. Transfer efficiency vs. input voltage of the four-switch buck-boost converter.

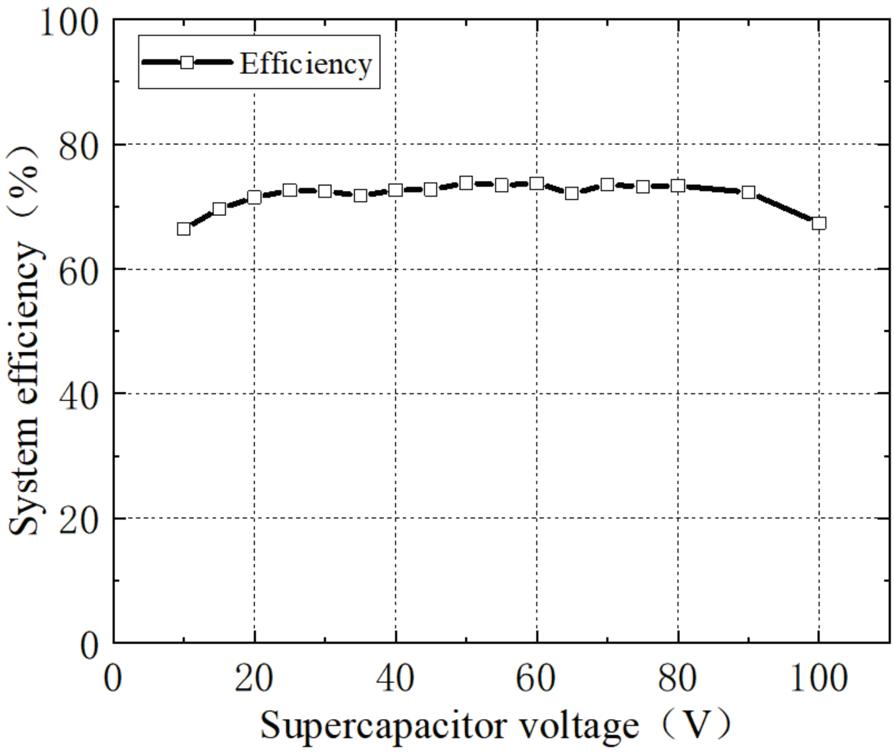

Figure 21. System efficiency vs. supercapacitor voltage during the charging process.

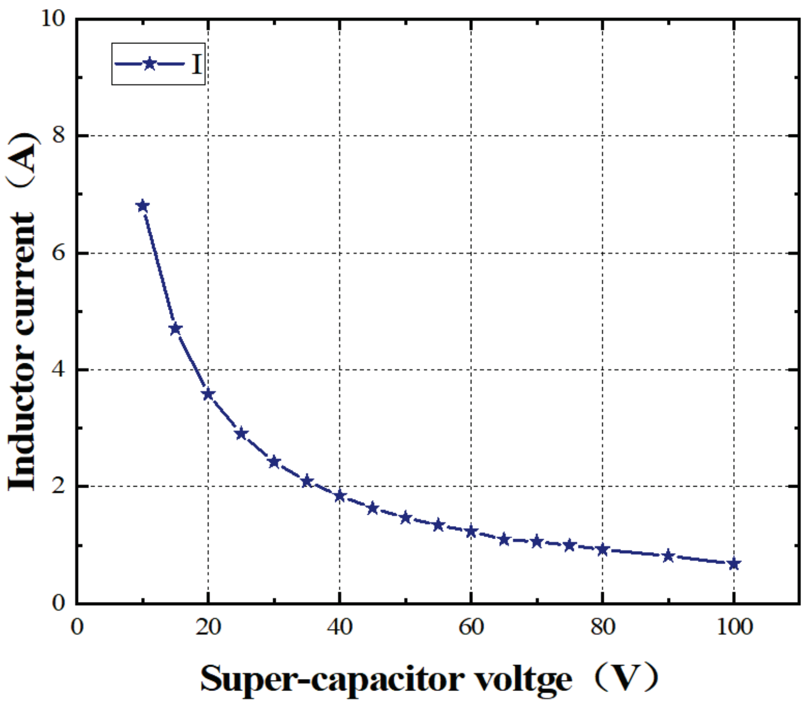

Figure 22. Inductor current vs. supercapacitor voltage during the charging process.

During the charging process, the charging current decreases smoothly while the voltage increases; the most important point is that the system transfer efficiency is not affected by the supercapacitor voltage, and remains almost constant. The waveform of the supercapacitor experimental charging process is shown in Figure 23.

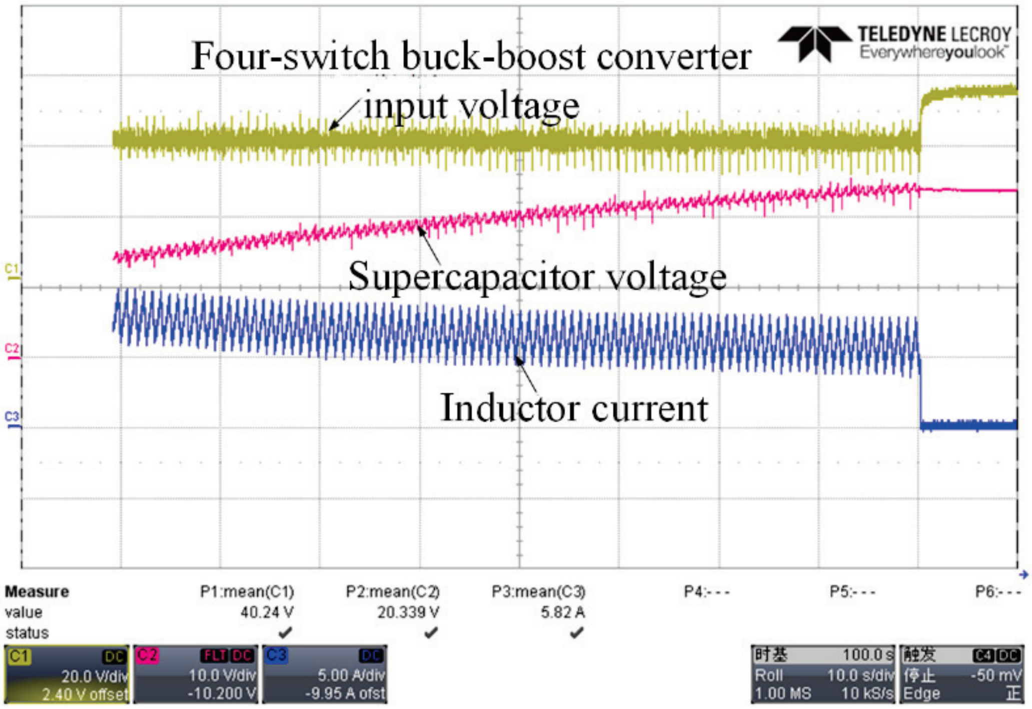

Figure 23. Supercapacitor charging process.

6. Conclusions

In this paper, an LC series resonant WPT system with a modulation control method for supercapacitor charging was proposed. The theoretical analysis of the resonant coupling tank was described in detail with its efficiency and constant current characteristics. A phase shift control method was introduced on the primary side to control the transfer power by controlling the RMS current in the primary coil, while on the secondary side, the received power was controlled by adjusting the input voltage of a four-switch buck-boost load matching converter with a duty cycle modulation control method. The simulation model was established in the MATLAB/SIMULINK environment, and a dsPIC33FJ64GS606-based experimental platform was constructed. Both the simulation and experimental results successfully evaluated the characteristics of the proposed system and verified the control efficiency. Additionally, the system stability during the charging process was successfully confirmed.

Author Contributions: Conceptualization, S.X. and Z.W.; methodology, S.X. and Z.W.; software, S.X. and Z.W.; validation, S.X. and Z.W.; formal analysis, S.X. and Z.W.; investigation, S.X. and Z.W.; resources, S.X. and Z.W.; data curation, S.X. and Z.W.; writing—original draft preparation, S.X. and Z.W.; writing—review and editing, W.J. and J.C.; visualization, S.X.; supervision, S.X. and W.J.; project administration, W.J. and J.C.; funding acquisition, J.C. All authors have read and agreed to the published version of the manuscript.

Funding: This research received no external funding.

Data Availability Statement: Not applicable.

Conflicts of Interest: The authors declare no conflict of interest.

References

1. Wang, S. Research on a New Lithium Battery Applied in Onboard Energy Storage Device of Light Rail Vehicle. In Proceedings of the 2018 2nd IEEE Advanced Information Management, Communicates, Electronic and Automation Control Conference (IMCEC), Xi'an, China, 25–27 May 2018.

2. Castaings, A.; Caron, H.; Kharrat, H.; Ovalle, A.; Vulturescu, B. Energy Storage System based on Supercapacitors for a 750 V DC railway power supply. In Proceedings of the 2018 IEEE International Conference on Electrical Systems for Aircraft, Railway, Ship Propulsion and Road Vehicles & International Transportation Electrification Conference (ESARS-ITEC), Nottingham, UK, 7–9 November 2018; pp. 1–5.
3. Ayad, M.Y.; Becherif, M.; Henni, A.; Aboubou, A.; Wack, M. Sliding mode control and Unit Power Factor applied to embarked supercapacitors for electrical train traction. In Proceedings of the 2010 IEEE International Symposium on Industrial Electronics, Bari, Italy, 4–7 July 2010; pp. 2163–5145.
4. Cheng, L.; Acuna, P.; Wei, S.; Fletcher, J.; Wang, W.; Jiang, J. Fast-Swap Charging: An Improved Operation Mode For Catenary-Free Light Rail Networks. *IEEE Trans. Veh. Technol.* **2018**, *67*, 2912–2920. [CrossRef]
5. Covic, G.A.; Boys, J.T. Modern trends in inductive power transfer for transportation applications. *IEEE J. Emerg. Sel. Top. Power Electron.* **2013**, *1*, 28–41. [CrossRef]
6. Huh, J.; Lee, S.W.; Lee, W.Y.; Cho, G.H. Narrow-width inductive power transfer system for online electrical vehicles. *IEEE Trans. Power Electron.* **2011**, *26*, 3666–3679. [CrossRef]
7. Shin, J.; Shin, S.; Kim, Y.; Ahn, S.; Lee, S.; Jung, G.; Jeon, S.; Cho, D. Design and implementation of shaped magnetic-resonance-based wireless power transfer system for roadway-powered moving electric vehicles. *IEEE Trans. Power Electron.* **2014**, *61*, 1179–1192. [CrossRef]
8. Wang, Y.; Zhang, L.; Hou, H.; Xu, W.; Duan, G.; He, S.; Liu, K.; Jiang, S. Recent progress in carbon-based materials for supercapacitor electrodes: A review. *J. Mater. Sci.* **2021**, *56*, 173–200. [CrossRef]
9. Yin, J.; Zhang, W.; Alhebshi, N.A.; Salah, N.; Alshareef, H.N. Synthesis strategies of porous carbon for supercapacitor applications. *Small Methods* **2020**, *4*, 1900853. [CrossRef]
10. Cheng, F.; Yang, X.; Zhang, S.; Lu, W. Boosting the supercapacitor performances of activated carbon with carbon nanomaterials. *J. Power Sources* **2020**, *450*, 227678. [CrossRef]
11. Saikia, B.K.; Benoy, S.M.; Bora, M.; Tamuly, J.; Pandey, M.; Bhattacharya, D. A brief review on supercapacitor energy storage devices and utilization of natural carbon resources as their electrode materials. *Fuel* **2020**, *282*, 118–196. [CrossRef]
12. Kandasamy, M.; Sahoo, S.; Nayak, S.K.; Chakraborty, B.; Rout, C.S. Recent advances in engineered metal oxide nanostructures for supercapacitor applications: Experimental and theoretical aspects. *J. Mater. Chem. A* **2021**, *9*, 17643–17700. [CrossRef]
13. Yassine, M.; Fabris, D. Performance of Commercially Available Supercapacitors. *Energies* **2017**, *10*, 1340. [CrossRef]
14. Münchgesang, W.; Meisner, P.; Yushin, G. Supercapacitors specialities-Technology review. *AIP Conf. Proc.* **2014**, *1597*, 196–203.
15. Zhu, F.; Yang, Z.; Zhao, Z.; Lin, F. Two-Stage Synthetic Optimization of Supercapacitor-Based Energy Storage Systems, Traction Power Parameters and Train Operation in Urban Rail Transit. *IEEE Trans. Veh. Technol.* **2021**, *70*, 8590–8605. [CrossRef]
16. Fedele, E.; Pasquale, A.D.; Iannuzzi, D.; Pagano, M. Integration of Onboard Batteries and Supercapacitors Based on the Multi-Source Inverter for Light Rail Vehicle. In Proceedings of the 2022 International Power Electronics Conference (IPEC-Himeji 2022—ECCE Asia), Himeji, Japan, 15–19 May 2022; pp. 698–704.
17. Yıldırım, D.; Akşit, M.H.; Yolaçan, C.; Pul, T.; Ermiş, C.; Aghdam, B.H.; Çadırcı, I.; Ermiş, M. Full-Scale Physical Simulator of All SiC Traction Motor Drive With Onboard Supercapacitor ESS for Light-Rail Public Transportation. *IEEE Trans. Ind. Electron.* **2020**, *67*, 6290–6630. [CrossRef]
18. Li, J.; Xin, D.; Wang, H.; Liu, C. Application of Energy Storage System in Rail Transit: A Review. In Proceedings of the 2022 International Conference on Power Energy Systems and Applications (ICoPESA), Virtual Conference, 25–27 February 2022; pp. 539–552.
19. Chu, A.; Braatz, P. Comparison of commercial supercapacitors and high-power lithium-ion batteries for power-assist applications in hybrid electric vehicles: I. Initial characterization. *J. Power Sources* **2002**, *112*, 236–246. [CrossRef]
20. Yasha, P.; Vahidi, A.; Fayazi, S.A. Heuristic versus optimal charging of supercapacitors, lithium-ion, and lead-acid batteries: An efficiency point of view. *IEEE Trans. Control Syst. Technol.* **2018**, *26*, 167–180.
21. Yang, H. Analysis of supercapacitor charge redistribution through constant power experiments. In Proceedings of the 2017 IEEE Power & Energy Society General Meeting, Chicago, IL, USA, 16–20 July 2017; pp. 1–5.
22. Şahİn, M.E.; Blaabjerg, F.; SangwongwanÍch, A. Modelling of supercapacitors based on simplified equivalent circuit. *CPSS TPEA* **2021**, *6*, 31–39. [CrossRef]
23. Guo, W.; Yu, C.; Li, S.; Qiu, J. Toward commercial-level mass-loading electrodes for supercapacitors: Opportunities, challenges and perspectives. *Energy Environ. Sci.* **2021**, *14*, 576–601. [CrossRef]
24. Zhang, S.; Pan, N. Supercapacitors Performance Evaluation. *Adv. Energy Mater.* **2015**, *5*, 1401401. [CrossRef]
25. Zhu, Q.; Zhao, D.; Cheng, M.; Zhou, J.; Owusu, K.A.; Mai, L.; Yu, Y. A new view of supercapacitors: Integrated supercapacitors. *Adv. Energy Mater.* **2019**, *9*, 1901081. [CrossRef]
26. Geng, Y.; Yang, Z.; Lin, F. Design and Control for Catenary Charged Light Rail Vehicle Based on Wireless Power Transfer and Hybrid Energy Storage System. *IEEE Trans. Power Electron.* **2020**, *35*, 7894–7903. [CrossRef]
27. Li, Y.; Mai, R.; Lin, T.; Liu, Y.; Li, Y.; He, Z.; Yu, J. Design and implementation of a novel WPT system for railway applications. In Proceedings of the 2017 IEEE PELS Workshop on Emerging Technologies: Wireless Power Transfer (WoW), Chongqing, China, 20–22 May 2017; pp. 213–221.

28. Song, K.; Zhu, C.; Koh, K.E.; Imura, T.; Hori, Y. Wireless power transfer for running EV powering using multi-parallel segmented rails. In Proceedings of the 2015 IEEE PELS Workshop on Emerging Technologies: Wireless Power (2015 WoW), Daejeon, Korea, 5–6 June 2015; pp. 1–6.
29. Pang, J.; Li, Z.; Xu, C. Design of Automatic Switch of Charging Rail for Electric Vehicle Dynamic Charging System Based on Wireless Power Transmission. In Proceedings of the 2021 IEEE International Conference on Advances in Electrical Engineering and Computer Applications (AEECA), Dalian, China, 27–28 August 2021; pp. 731–737.

sensors

Article

State of Health Estimation Based on the Long Short-Term Memory Network Using Incremental Capacity and Transfer Learning

Lei Yao [1], Jishu Wen [1], Shiming Xu [2], Jie Zheng [2], Junjian Hou [2], Zhanpeng Fang [2] and Yanqiu Xiao [2,*]

[1] Henan Engineering Research Center of New Energy Vehicle Lightweight Design and Manufacturing, Zhengzhou University of Light Industry, Zhengzhou 450001, China

[2] Henan Key Laboratory of Intelligent Manufacturing of Mechanical Equipment, Zhengzhou University of Light Industry, Zhengzhou 450001, China

* Correspondence: xiaoyanqiu@zzuli.edu.cn

Abstract: Battery state of health (SOH) estimating is essential for the safety and preservation of electric vehicles. The degradation mechanism of batteries under different aging conditions has attracted considerable attention in SOH prediction. In this article, the discharge voltage curve early in the cycle is considered to be strongly characteristic during cell aging. Therefore, the battery aging state can be quantitatively characterized by an incremental capacity analysis (ICA) of the voltage distribution. Due to the interference of vibration noise of the test platform, the discrete wavelet transform (DWT) methods are accustomed to soften the premier incremental capacity curves in different hierarchical decompositions. By analyzing the battery aging mechanism, the peak of the curve and its corresponding voltage are used in the characterization of capacity decay by grey relation analysis (GRA) and to optimize the input of the deep learning model, and finally, the double-layer long short-term memory network (LSTM) model is used to train the data. The results demonstrate that the proposed model can predict the SOH of a single battery cycle using only small batch data and the relative error is less than 2%. Further, by freezing the LSTM layer for transfer learning, it can be used for battery health estimation in different loading modes. The results of training and verification show that this method has high accuracy and reliability in SOH estimation.

Keywords: lithium-ion battery; SOH estimation; discrete wavelet transform; grey relation analysis; long-short term memory neural network; transfer learning

1. Introduction

The safety of the lithium-ion battery itself is critical in its practical application. Suppose battery failure occurs in the process of use. In that case, it may lead to performance degradation or loss of the corresponding power equipment or system, which will increase the risk of thermal runaway and even cause personal injury or death [1]. Therefore, as an ideal energy storage device, it is of extensive practical significance to find a method to accurately monitor the SOH of lithium-ion batteries [2]. There are many kinds of research on the life prediction of lithium ions in related fields [3–5]. In terms of research methods, the remaining life prediction methods of lithium-ion batteries can be approximately divided into two categories: model-driven and data-driven methods [6].

The model-based methodology is relatively mature and widely used in engineering practice. The method mainly models the battery according to the elder law and simulates the battery behavior [7–9]. There are several different forms, for instance, the electrochemical impedance spectroscopy model. Wang et al. [10] proposed a model-based estimation method to evaluate the insulation state of the battery pack. Through the principle of electro-engineering, the running state of the battery is simulated to estimate the future running condition of the storm. Galeotti et al. [11] analyzed the electrochemical impedance spectroscopy (EIS) of the battery and found that in continuous use, the ohmic resistance and available capacity increased linearly with the rapid aging of the battery. The stable relationship can be directly used to measure the battery's performance and determine the battery's service life and health status. It is believed that EIS measurement can indirectly obtain charge transfer resistance and directly obtain various measurement parameters such as ohmic resistance, solid electrolyte interface (SEI) resistance, and double-layer capacitance. The parameters can be used to improve the equivalent circuit model of batteries. The accuracy of life prediction is further enhanced. Plett [12] proposed the extended Kalman filter for battery state estimation and proved its accuracy and engineering practicability for quantitative analysis.

Similarly, Yang et al. [13] proposed a battery SOH estimation method based on the adaptive double-extended Kalman filter, which used the double-extended Kalman filter for online estimation and combined the adaptive algorithm and fuzzy controller correct the noise. The dynamic stress test condition experiment verifies it. This method can estimate the battery state. The method-based model is based on the lithium-ion battery degradation and failure mechanism to accomplish the SOH estimation and prediction, although able to represent the aging condition of internal model attenuation rules of critical parameters to achieve the intention of the SOH estimation. Still, with the development of technology, generalization is relatively weak, and prediction and analysis precision also need to be improved.

Compared with the model-based method, the accuracy relies on the accuracy of parameter identification and the complexity of the model, so it is not easy to achieve high reliability and accuracy. With the development of data mining and computing power, the data-driven method has become a hot discussion for more researchers [14–16]—examples include the support vector machine [17], the neural network [18], the extreme learning machine [19], random forest [20], and Gaussian filtering [21].

The data-driven method can process many complex nonlinear system data and has many advantages, such as no need for detailed information on battery characteristics. In addition, some algorithms have a strong generalization and can accurately predict SOH under different working conditions [22]. Wang et al. [23] used a support vector machine to deduce correlation vectors that could be used for training, and combined with the conditional three-parameter model to fit the predicted values of correlation vectors to indicate battery life. Li et al. [24] proposed an online health assessment method for lithium batteries based on the support vector machine (SVM) and particle swarm optimization (PSO), using PSO to optimize the SVM kernel function and combining state of charge (SOC) to estimate SOH. It provides a reference for online battery detection and SOH estimation. Compared with support vector machines, the neural network has a more vital self-learning ability and can obtain higher prediction accuracy [25,26]. For example, the wavelet neural network fully inherits the excellent time-frequency localization characteristics of the wavelet transform. It has the self-learning characteristics of the neural network, so it has nonlinear solid approximation capability [27,28]. Wang et al. [29] proposed a model-free SOH estimation method based on discrete wavelet transform. The method's feasibility was proved by analyzing the output results of different phenomena through a dynamic stress test on the battery. However, the traditional wavelet neural network is trained primarily by the subtraction method, which has the defect of a local optimum. The fusion method can overcome the shortcomings of a single algorithm and give full play to the advantages of multi-algorithm fusion. Jia et al. [30] proposed a multi-scale SOH prediction method, which combined the wavelet neural network and untraced particle filter model and decomposed into low-frequency attenuation trend and high-frequency fluctuation components through discrete wavelet transform. Low-frequency degradation trend data were used to predict the SOH of lithium-ion batteries. Experimental results show that the proposed method still has high accuracy and strong robustness in the early stage of battery life problems. Although the fused neural network method is ideal in battery SOH estimation, the network model needs to be trained under a large amount of data, so extracting high-quality features to make the model have good performance is also a fundamental problem.

The deep learning method does not require a complex feature extraction process and has a strong learning ability and strong generalization of the algorithm [31–33]. As an algorithm structure, it is characterized by multiple parameters and layers, including convolutional neural networks [34], recursive neural networks [35], and other network structures. With the development of 5G technology and computer technology, powerful data computing power can be used to make up for the lack of algorithm complexity, so more deep learning algorithms are used for health state estimation and remaining service life prediction of lithium-ion batteries.

The deep convolutional neural network (DCNN) has stacked the single-layer convolutional neural network many times. By layering layers of hidden layers, the previous layer's output is used as the input of the last layer. This simple model can be used to complete the target learning task and significantly reduce the accuracy error of the calculation results [36]. Su, Laisuo et al. [37] compared the convolutional neural network with the traditional neural network model, used multi-layer convolution to capture the hidden features of lithium-ion batteries from the voltage distribution map, and proved that these hidden features had higher covariance with their cycle life, and the prediction accuracy was also extremely improved. Fan [38] adopted an innovative modeling method; A hybrid algorithm based on a gate-recursive element convolutional neural network was proposed to analyze and study the charging voltage curve of lithium batteries. It provides a novel method for SOH estimation and life prediction. Tracing information from early battery charge measurements, for instance, voltage, current, and temperature, is used to estimate SOH online, Through the verification of two datasets, the effect is also considerable. However, its disadvantages are evident, mainly requiring many training samples and the algorithm's complexity, which requires the system to have a high computing capacity.

However, the aging of the battery is a time series transform process, and historical data are also a considerable feature of information. A recursive neural network (RNN) adopts a feedback mode to return the output parameters to the input and transmit the information back to the network, completing a cycle. Therefore, the network model can remember historical data and apply it to prediction [39]. Nonetheless, when the effective information interval is long, the backpropagation of the RNN will produce the phenomenon of gradient disappearance or explosion. To improve the performance of the model, researchers modify the original neurons and create a more complex classical structure, The long short-term memory recurrent neural network, whose characteristics can be well applied to the estimation and prediction of battery SOH.

Most studies show that one of the current obstacles to lithium battery management systems is a degradation of battery health status, which is mainly reflected in capacity loss [40]. However, the battery's aging does not directly manifest itself in the attenuation of capacity during the early cycle but will affect the voltage curve of the early cycle discharge [41]. Therefore, in order to better improve the SOH prognostics accuracy of lithium-ion batteries, a deep learning method combined with mechanism analysis is proposed to optimize the input of deep learning by mining the early discharge voltage data. The specific prediction flow chart of SOH is shown in Figure 1.

The rest of this article is organized as follows: Section 2 introduces the experimental battery dataset and incremental capacity analysis methods. In Section 3, the structure of the LSTM model was introduced, and the battery health state estimation model was established. Section 4 presents the result of the battery SOH estimation. The conclusion is put in Section 5.

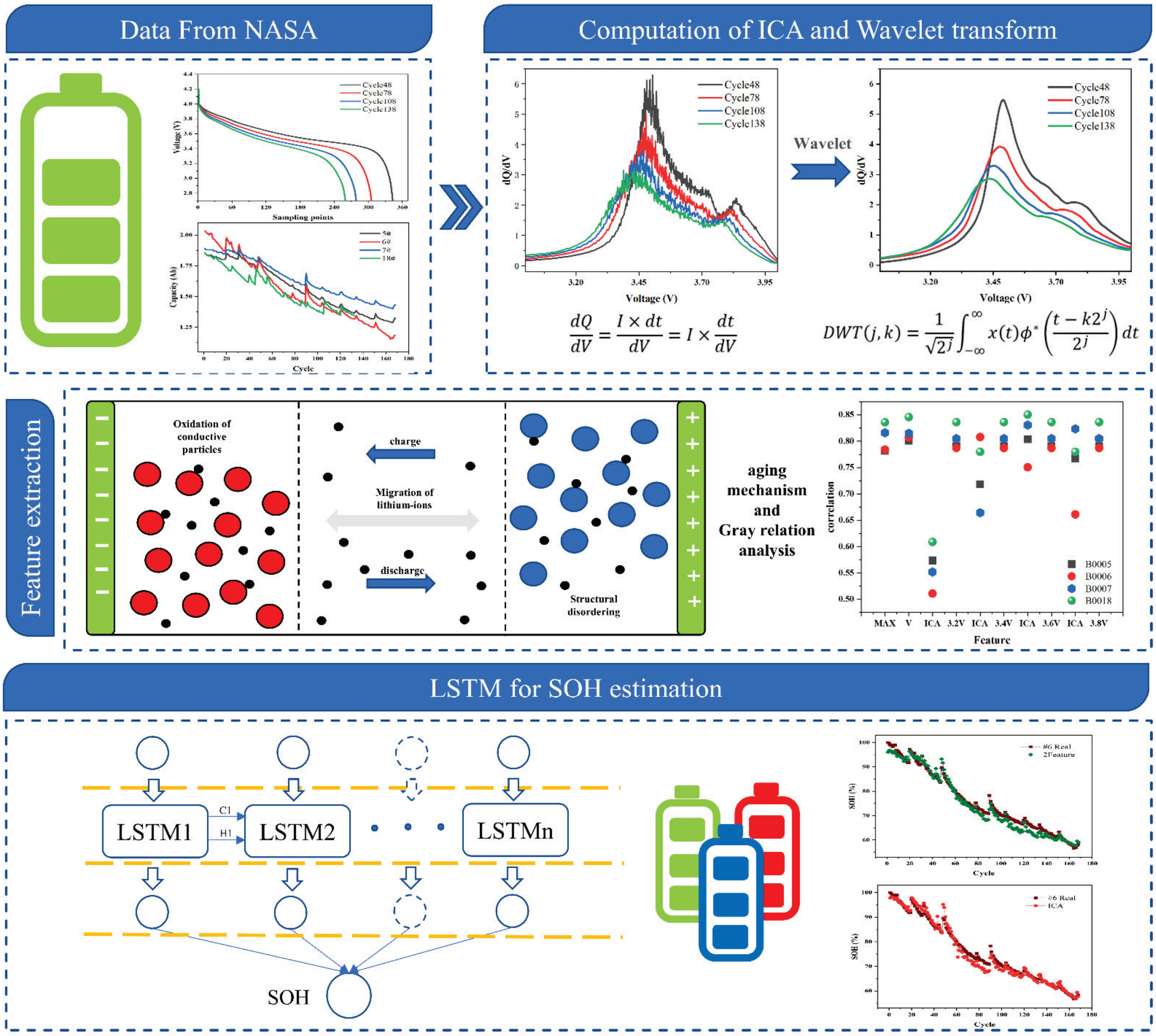

Figure 1. Flow diagram of SOH estimation.

2. Data Preprocessing

This section mainly analyzes the battery aging data from NASA and preprocesses the aging data. At first, the data were cleaned by the kernel smoothing method, and the original incremental capacity value was obtained by calculating the relation between dQ/dV and V. It was found that the influence of noise was inevitable by observing the data. The advanced discrete wavelet transform was used to filter the interference brought by noise and prepared for the subsequent analysis of the aging mechanism.

2.1. Data Acquisition

This article selected datasets from the NASA battery Prediction test platform. Datasets B0005, B0006, B0007, and B0018 were selected to obtain the aging trend of battery life under different conditions. These data are run through four different operation data at room temperature (24 degrees Celsius). Responsible for performing charging in 1.5 A constant current (CC) mode until battery voltage reaches 4.2 V, then continuing in constant voltage (CV) mode until charging current drops to 20 mA. The four batteries are discharged at a constant current 2 A level while waiting for the voltage of 5#, 6#, 7#, and 18# batteries to drop to 2.7, 2.5, 2.2, and 2.5 V, respectively. When the capacity of the battery is lower than 30% of the rated capacity after several cycles, that is, it reaches the end of life, and the experiment stops. These datasets can predict battery SOH. The specific charging and discharging conditions of the four batteries are shown in Table 1. The aging of the battery tends with the number of cycles shown in Figure 2a, Figure 2b indicates the voltage variation of an aging cycle for battery5#.

Table 1. Experiment condition of the battery.

Battery Number	Discharge Current	Voltage Upper	Voltage Lower
B0005	2 A	4.2 V	2.7 V
B0006	2 A	4.2 V	2.5 V
B0007	2 A	4.2 V	2.2 V
B0018	2 A	4.2 V	2.2 V

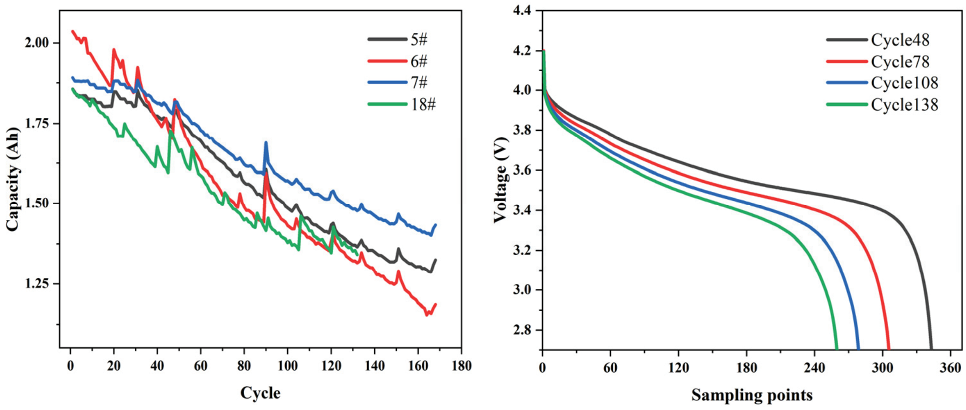

(**a**) (**b**)

Figure 2. Battery aging process and discharge voltage variation: (**a**) capacity attenuation curve; (**b**) voltage variation of the aging cycle schemes follow another format.

As shown in the figure, battery aging does not show capacity attenuation during the early cycle but will affect the early cycle discharge voltage curve. The voltage curve and its derivative are a rich data source, which is very effective in aging diagnosis. The characteristics obtained from the early discharge voltage curve have good predictive performance, even before the decline in battery capacity begins. Therefore, we use the voltage of the discharge cycle to calculate the incremental capacity (IC) curves and extract some features from the IC curve to build a high-precision battery prediction model [38].

2.2. Increment Capacity Curve Analysis

Incremental capacity analysis (ICA) is an important approach to studying the degradation mechanism of material properties of lithium-ion power batteries. The increment capacity curve obtained from the voltage and current data during the charging and discharging process can well reflect the changes in the internal chemical characteristics of lithium-ion power batteries.

In this paper, using the relationship between capacity and voltage in the discharge process to conduct increment capacity analysis, the calculation can be obtained as follows:

$$\frac{dQ}{dV} = \frac{I \times dt}{dV} = I \times \frac{dt}{dV} \tag{1}$$

where Q is the ampere-hour of discharge, and V is the voltage in the discharge stage. Additionally, the constant discharge current is 2 A. The ICA curve is computed by Equation (1). There are many noises in the signal, which brings specific difficulties for subsequent feature extraction work, so we need to use advanced filtering methods to obtain a smoother curve.

The variation trend of the effective signal is generally stable, and the frequency is mainly gathered in the low-frequency band. The noise or useless signal change generally has great uncertainty or fluctuation, and the frequency is primarily in the high-frequency band. So, we will use the method of wavelet noise filtering to process the ICA curve.

The DWT can be obtained by discrete scaling and shift parameters through the Mallat algorithm, which primarily operates a pair of low-pass and high-pass wavelet filters. The signal is reconstructed by the selected decomposition scale and the corresponding wavelet basis function. Finally, the wavelet transform method is used to decompose and reconstruct the signal.

We use discrete wavelet transform to capture nonstationary feature information. When the $\phi(\mathrm{t}) \in L^2(R)$ with zero bases, the DWT can be defined as:

$$DWT(j,k) = \frac{1}{\sqrt{2^j}} \int_{-\infty}^{\infty} x(t)\phi^* \left(\frac{t - k2^j}{2^j} \right) dt \tag{2}$$

where $\phi(t)$ is called the fundamental wavelet and the asterisk indicates the complex conjugate. In Equation (2), there are two parameters of dilation j and translation k. The parameter j impacts the oscillatory frequency and the length of the wavelet. The moved position can be ensured by the parameter k.

The effect of different decomposition levels and different fundamental selections is shown in Figure 3, too many decomposition layers will distort the voltage signal and thus reduce the accuracy. Too few decomposition levels do not do a good job of culling the effects of noise. Horizontal comparison can be seen as the best effect is achieved when the decomposition layers are 6.

There is no theoretical standard for the choice of wavelet basis functions. No wavelet basis function can be optimally denoised for a variety of signals. The Daubechies wavelet family is one of the typical discrete wavelet families and is often used for denoising due to its orthogonality and tight support. As can be seen from the local decomposition diagram, the same 6-layer decomposition, the consistency of fundamental wave selection sym6 is poor, and the db4 total effect is much better by using the Daubechies wavelet family. So by longitudinal comparison, the db4 wavelet basis function is chosen.

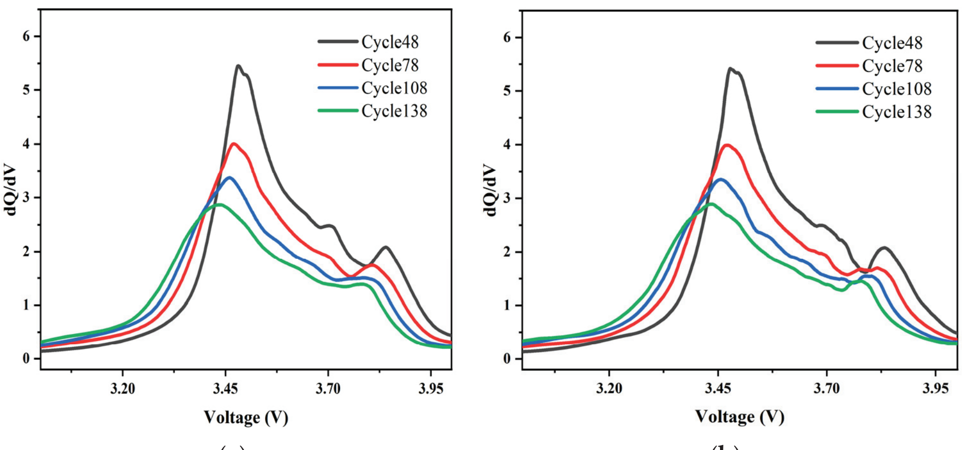

(a) (b)

Figure 3. *Cont.*

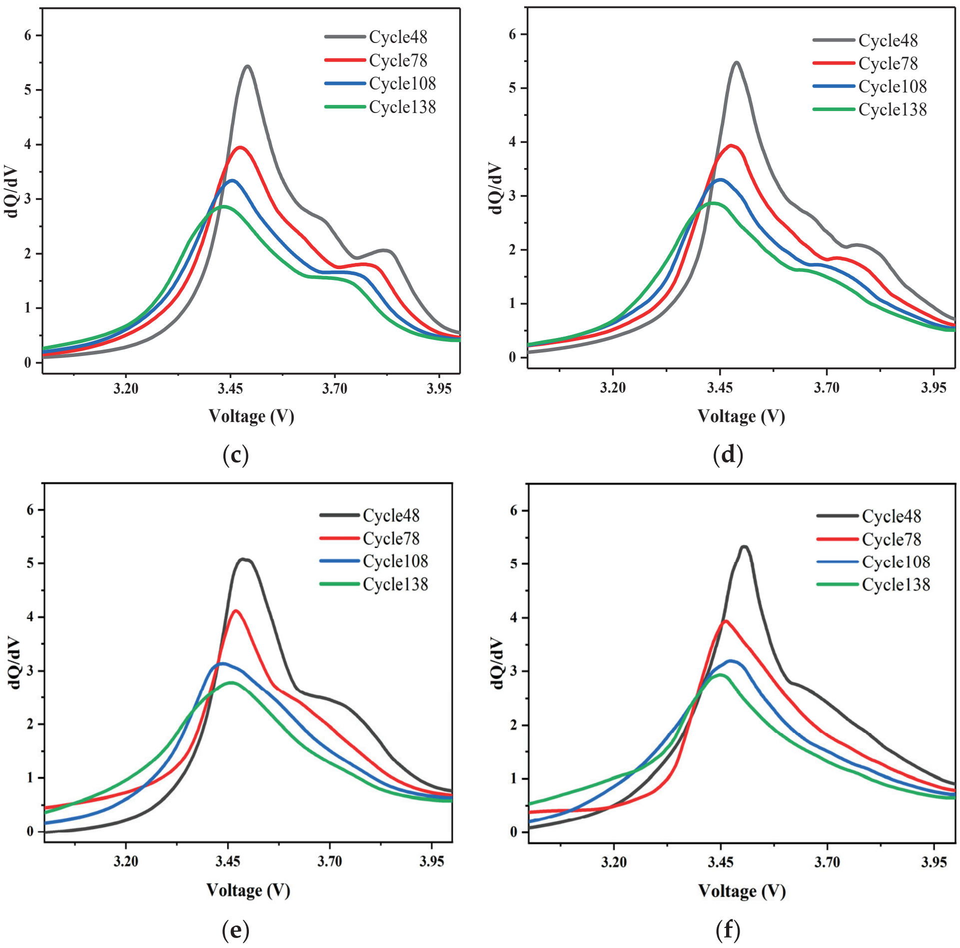

Figure 3. ICA curves after different wavelet filtering. (**a**) Layers:5, wave:sym6. (**b**) Layers:5, wave:db4. (**c**) Layers:6, wave:sym6. (**d**) Layers:6, wave:db4. (**e**) Layers:7, wave:sym6. (**f**) Layers:7, wave:db4.

3. Methodologies

3.1. Grey Relation Analysis

It can be seen in Figure 3 that there is a noticeable peak on the discharge incremental capacity curve, and the district under each peak represents the capacity of the related reaction. The aging mechanism of the battery can be determined by analyzing the change of the increase in each peak with the number of cycles.

As the number of cycles continues to increase, the peak value of the IC curve decreased significantly, indicating that the loss of active material, especially anode material, caused peak degradation. In addition, the change in the peak position means that the battery resistance has also changed. All the peak values of the IC curve move towards low voltage, indicating that the battery resistance is gradually decreasing.

Then, the gray relation analysis method provides a quantitative measurement method for the situation in the development and change of the system and is appropriate for dynamic history analysis. it can judge the correlation between curves by comparing the similarity degree of curve changing trend. Grey relation analysis is a new method to analyze sequence correlation, which can make a good evaluation of the correlation between sequences even in the case of small samples or poor sample information.

The calculation of gray relation analysis are as follows:

(1) Collect the original sequence and select the comparison sequence Xi and reference sequence Y:

$$X_{\mathrm{i}} = \{x_i(k) | k = 1, 2, \cdots, n\} \tag{3}$$

$$Y = \{y(k) | k = 1, 2, \cdots, n\} \tag{4}$$

where n represents the size of the comparison sequence and the reference sequence. "i = 1,2, . . . ,m", m is the number of comparison sequences.

(2) Calculate the correlation coefficient ξ_i *(k)* between x_i *(k)* and y_i *(k)*:

$$\xi_{\mathrm{i}}(k)=\frac{\underset{i}{\min}\underset{k}{\min}|y(k)-x_i\ (k)|+\rho\underset{i}{\max}\underset{k}{\max}|y(k)-x_i\ (k)|}{|y(k)-x_i\ (k)|+\rho\underset{i}{\max}\underset{k}{\max}|y(k)-x_i\ (k)|} \tag{5}$$

$$a=\underset{i}{\min}\underset{k}{\min}|y(k)-x_i\ (k)|,b=\underset{i}{\max}\underset{k}{\max}|y(k)-x_i\ (k)| \tag{6}$$

where $\rho \in [0, 1]$ is the resolution coefficient, the value is usually set to 0.5, a and b are the minimum and maximum polar differences of the reference sequence and the comparison sequence, respectively.

(3) The related degree r_i between reference sequence Y and comparison sequence x_i is calculated:

$$r_{\mathrm{i}}=\frac{1}{n}\sum_{k=1}^{n}\xi_i(k),k=1,2,\cdots,n \tag{7}$$

where $r_i \in [0, 1]$, the closer the correlation degree r_i is to 1, the greater the correlation between X_i and Y.

The feature of peak ICA and its corresponding voltage, ICA value corresponding to 3.2 V, ICA value corresponding to 3.4 V, ICA value corresponding to 3.6 V, and ICA value corresponding to 3.8 V as the input of gray correlation comparison sequence, and capacity as the input of gray correlation reference sequence. The results obtained are shown in Table 2.

Table 2. Grey relation analysis.

Battery Number	Grey Relation Coefficient					
	F1	**F2**	**F3**	**F4**	**F5**	**F6**
5#	0.7815	0.8009	0.5735	0.7184	0.8036	0.7674
6#	0.7842	0.8074	0.5109	0.8081	0.7506	0.6611
7#	0.8161	0.8151	0.5519	0.6642	0.8308	0.8235
18#	0.8361	0.8459	0.6090	0.7801	0.8506	0.7799

F1, F2 is the peak ICA value corresponding to the voltage, and F3–F6 is the ICA value corresponding to the above voltage. Since the voltage does not change, the characteristics corresponding to the fixed voltage are no longer listed.

As dQ/dV-V is a set of correspondence, it can be seen from Table 2 that peak ICA and its corresponding voltage are both high, while other extracted features have high voltage correlation and IC value correlation. To verify the feasibility, the four features with the highest correlation are taken as the first group, and peak ICA is taken as the second group. Peak ICA and its voltage are the third set of characteristic inputs for subsequent models.

3.2. Long Short-Term Memory Modeling

RNN is a network with an inherent loop that processes sequences by iterating through all sequence elements and preserving states containing time-step history feedback.

LSTM is a special RNN that effectively mitigates gradient disappearance and gradient explosion with its' gating mechanism. The internal structure of the general LSTM neural network is shown in Figure 4. The various elements of the LSTM are displayed below.

$$f_t=\sigma\left(W_{xf}x_t+W_{hf}h_{t-1}+b_f\right) \tag{8}$$

$$i_t = \sigma(W_{xi}x_t + W_{hi}h_{t-1} + b_i) \quad (9)$$

$$o_t = \sigma(W_{xo}x_t + W_{ho}h_{t-1} + b_o) \quad (10)$$

$$c_t = f_t \cdot c_{t-1} + i_t \cdot tanh(W_{xc}x_t + W_{hc}h_{t-1} + b_c) \quad (11)$$

$$h_t = o_t \cdot tanh(c_t) \quad (12)$$

where x_t is the input data comprised of increment capacity curve peak and corresponding voltage, subscript t indicates the time step, among them, i, f, and o are three gates, representing input gate, forgetting gate, and output gate, respectively. Long short-term memory can voluntarily add or forget information through the input gate and forget gate, W, b are the weights and biases. The activation function is represented as σ, The sigmoid function is often used to adjust its output value and limit it to values between 0 and 1. When generating candidate memory, the activation function selects tanh to accelerate the convergence of the model. The battery SOH estimation model based on LSTM in this article is based on TensorFlow in Python, which is a commonly used deep learning framework.

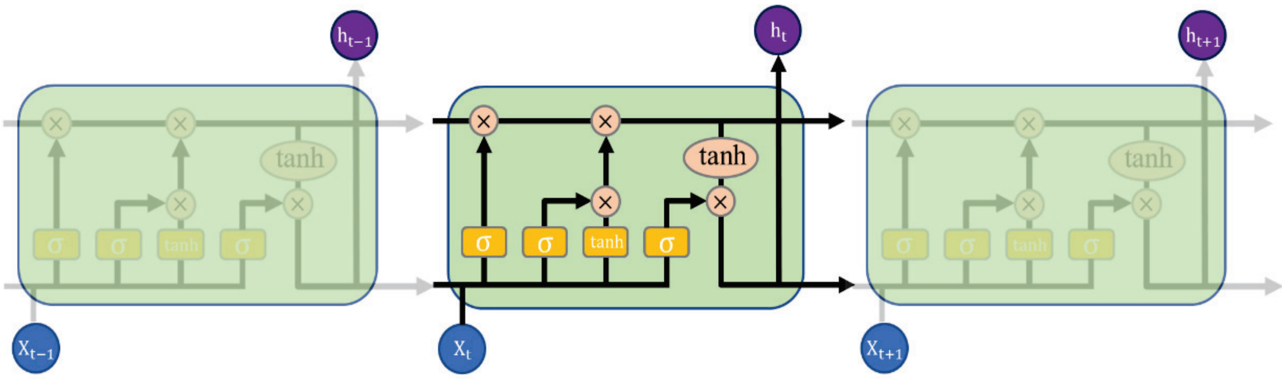

Figure 4. LSTM structure.

4. Results and Discussion

4.1. Model Training Structure

Through the constant adjustment of the model structure, it was found that the number of LSTM layers should not be too high, as the growth in the number of layers will lead to an exponential increase in time and memory overhead, followed by gradient disappearance between layers. When the number of LSTM layers exceeds three or more layers, the gradient disappearing between layers seems very distinct. Because of the time series model, the update iteration of the LSTM layer near the input layer becomes slow. The efficiency of model convergence will also decrease sharply, and it is light to enter the dilemma of local minimum. Therefore, the use of two layers of LSTM in this article maintains a relatively good effect.

Table 3 lists the structure and some of the hyperparameters of the LSTM model. Due to the aging through the mechanism analysis of characteristics and SOH highly correlated, two layers of hidden units, respectively, 75 the establishment of LSTM layer to reach a satisfactory estimation precision, training process, the loss was calculated by the mean absolute error function is more advantageous to regression problems, and use the "Adam" optimizer training network, in order to avoid excessive fitting. Using the Dropout layer, 50% of the training samples are randomly dropped, and root mean square error (RMSE) and mean absolute error (MAE) are used to define the loss function.

Table 3. Hyperparameters setting of LSTM model.

Parameters	Value
Number of units in the LSTM 1	75
Number of units in the LSTM 2	80
Dense	25
Dropout	0.5
Dense	1

4.2. Estimation Results of the Model

First, the prediction model of the single-cell model was established. By observing the capacity attenuation curve and others' analysis of the dataset, we could know that the EOL of the four batteries was all after 100 cycles. Therefore, we took the first 100 cycles as the training set and the remaining cycles as the test set to train single batteries. The predicted curves and loss rates of different characteristics are shown in Figure 5.

Through observation, it was found that the initial capacity of the four batteries is less than the rated capacity, indicating that the battery has aged before the test, so in this article, the capacity of the initial cycle is used as a reference to calculate, through the training of the 5# battery, it is found that the overall loss is less than 3%, so the effect is satisfactory.

There are three groups of different features in the input, the ICA-V prediction effect of this group is the best, and the loss rate is the lowest, although the loss of the three groups was lower than 2.5%. Additionally, it can also obtain good results under the single-peak feature, indicating that the results of gray relation analysis have been proved.

Then, we turn our attention to the 6# battery, it was found that the loss was higher than the other three batteries, and it can be seen through the conversion calibration that the SOH of the battery dropped below 80% during the first 60 cycles alone, indicating that the aging of the 6# battery has been very serious.

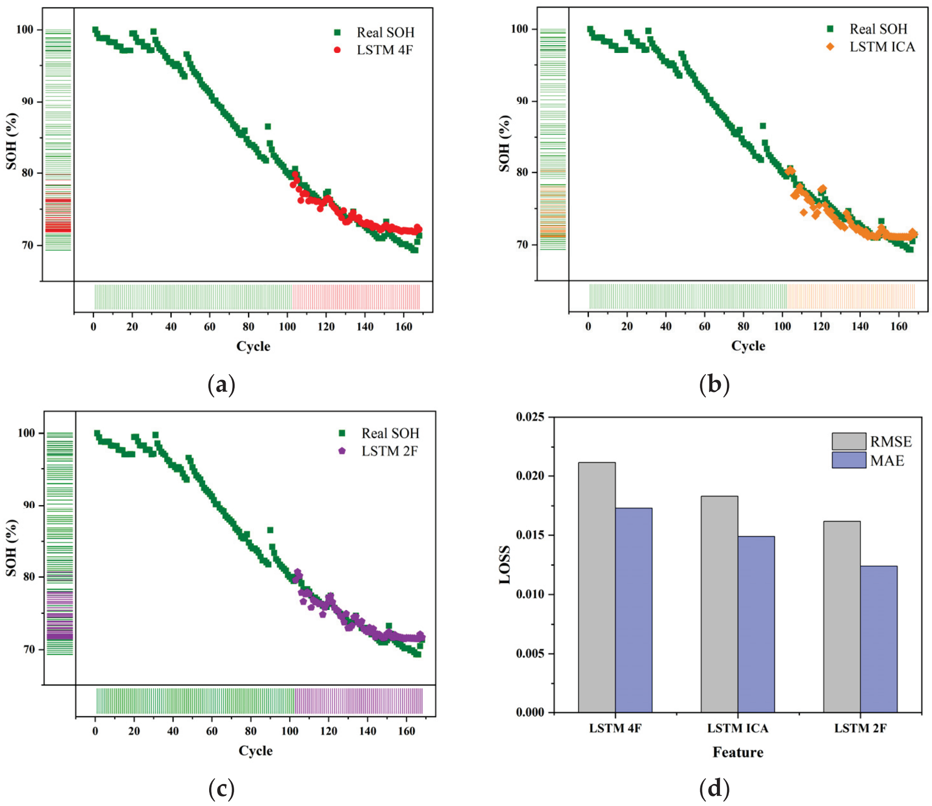

Figure 5. *Cont.*

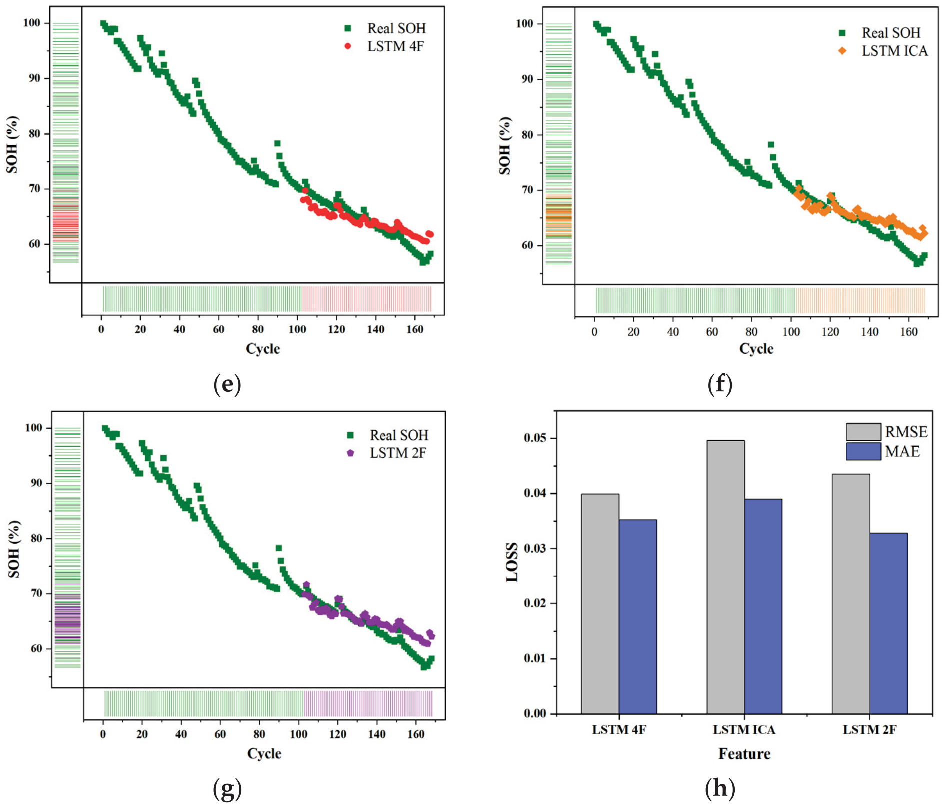

Figure 5. LSTM for 5# and 6# batteries (**a**–**c**). The predicted results of different features for 5#. (**d**) The loss of battery 5# (**e**–**g**). The predicted results of different features for 6# (**h**). The loss of battery 6#.

After adjusting the model structure to a certain extent, the object is converted into the remaining 6#, 7#, and 18# batteries, the loss rate of the test set is all less than 5%, especially on the 5#, 7#,18# battery, the loss rate is less than 2.5%, the predicted results are shown in Figure 6, and the specific verification data are shown in Tables 4 and 5, which further verify the accuracy of the model and determine that the model has a particular generalization ability.

Table 4. The loss rate of 5# and 6#.

		B0005			B0006	
	LSTM 4F	**LSTM ICA**	**LSTM 2F**	**LSTM 4F**	**LSTM ICA**	**LSTM 2F**
RMSE	0.0212	0.0183	0.0162	0.0399	0.0496	0.0435
MAE	0.0173	0.0149	0.0124	0.0352	0.0390	0.0328

Table 5. The loss rate of 7# and 18#.

		B0007			B00018	
	LSTM 4F	**LSTM ICA**	**LSTM 2F**	**LSTM 4F**	**LSTM ICA**	**LSTM 2F**
RMSE	0.0198	0.0185	0.0148	0.0229	0.0168	0.0206
MAE	0.0167	0.0124	0.0111	0.0194	0.0137	0.0174

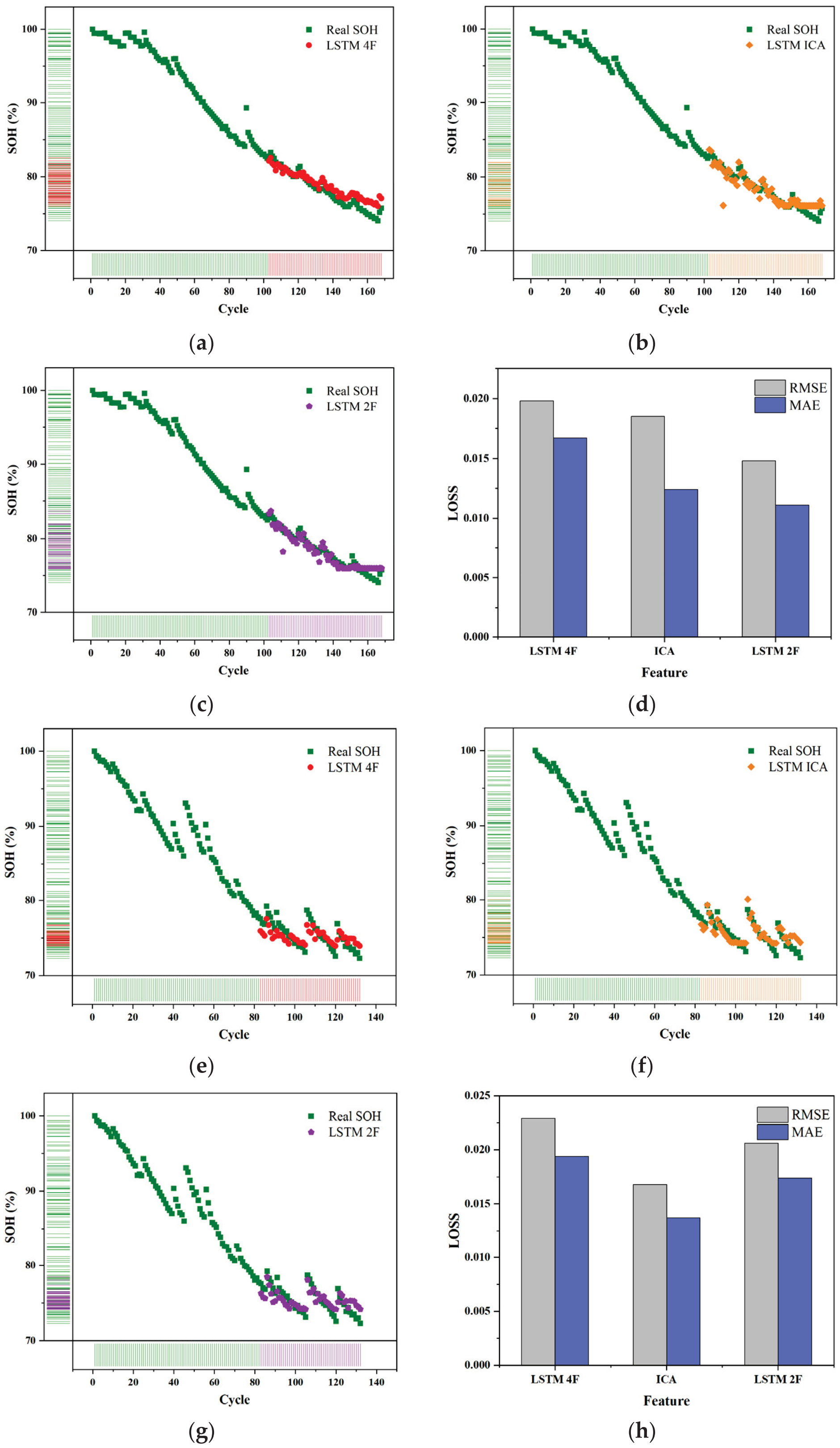

Figure 6. LSTM for 7# and 18# batteries (**a**–**c**). The predicted results of different features for 7# (**d**). The loss of battery 7# (**e**–**g**). The predicted results of different features for 18# (**h**). The loss of battery 18#.

4.3. Estimation Results of the Model

Since the previous prediction of the 6# battery was not as good as the other three batteries, the article then used transfer learning to improve the prediction accuracy of the 6 batteries.

The neural network framework with the same structure as the previous article is built, the first two layers of the LSTM recurrent network are set to the frozen state, the last two layers are assigned to the trainable state, all the aging data of the 5# battery are used as the training set, and the test set is set to the whole sequence of the 6# battery, the prediction effect of the model is shown in Figure 7. It can be seen through the training of this mode, the modified model can predict other batteries similar to the loading mode. Additionally, the average loss rate of different feature inputs has dropped to approximately 3.5%, which verifies the effectiveness of the migration model.

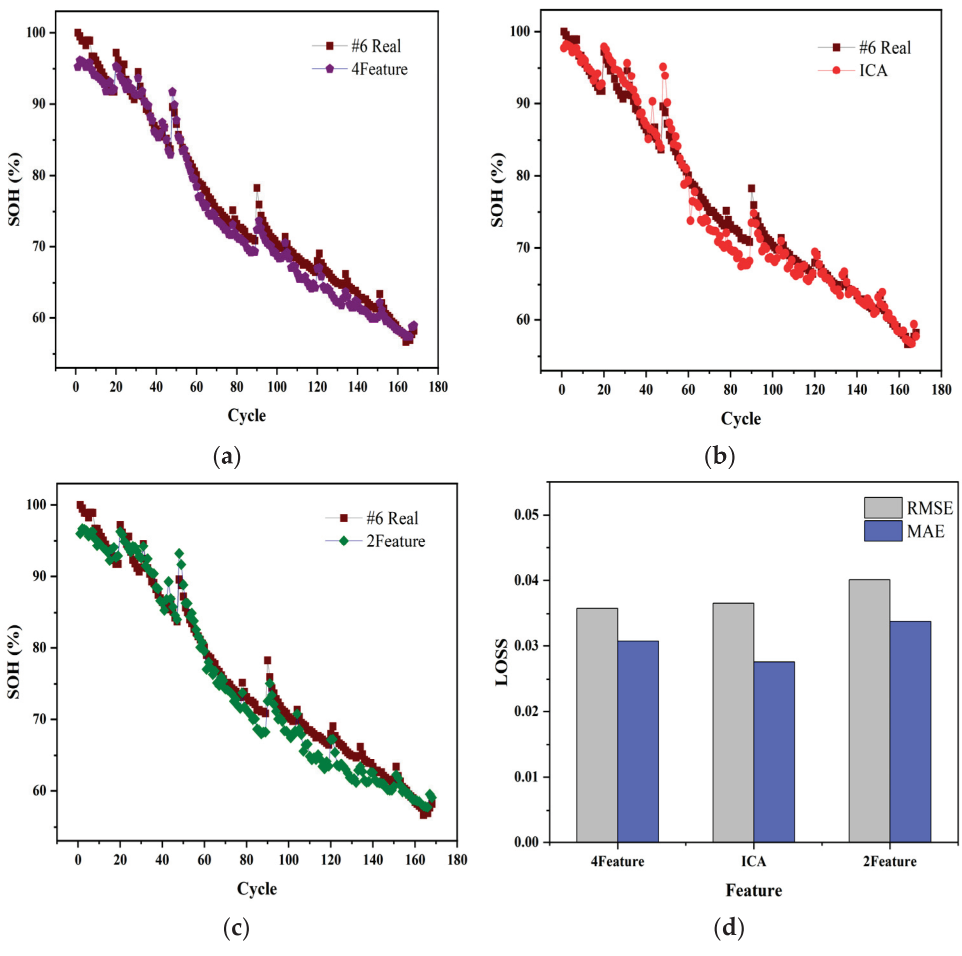

Figure 7. Transform learning for 6# battery (**a**–**c**). The predicted results of different features for 6# (**d**). The loss of battery 6#.

Otherwise, as shown in Figure 8, without changing the model structure, the model was migrated to the Mendeley dataset, and the model accuracy was tested when the first 50%, 60%, 70%, and 80% of the training data were taken from the overall battery data. The results are shown in Table 6, indicating that the modified model can accurately assess the health status of lithium-ion batteries in the Mendeley dataset.

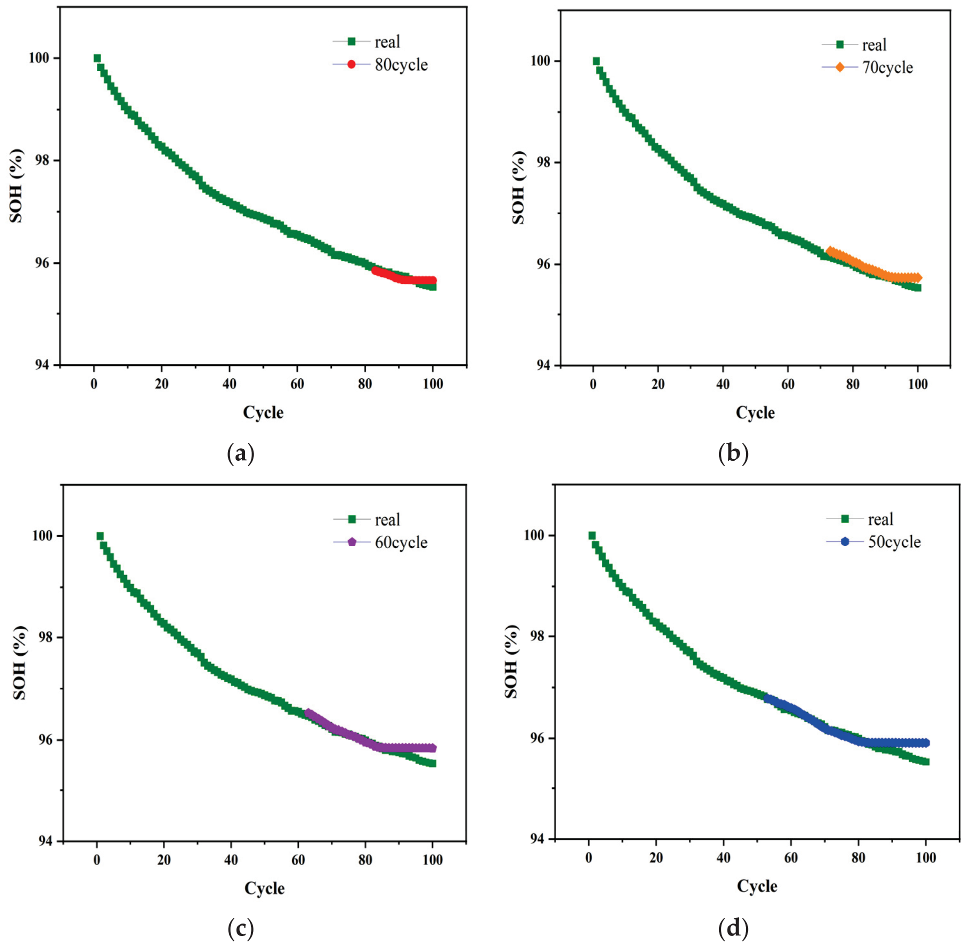

Figure 8. Transfer learning on the Mendeley dataset. (**a**) 80% of the training data. (**b**) 70% of the training data. (**c**) 60% of the training data. (**d**) 50% of the training data.

Table 6. Comparison of prediction results of different training scale models.

Train Scale (%)	RMSE	MAE
80	0.0174	0.0146
70	0.0269	0.0236
60	0.0319	0.0208
50	0.0381	0.0248

5. Conclusions

Accurately predicting and estimating the SOH of the battery system is essential to achieving reliable, efficient, and affordable batteries. The challenge in lithium-ion battery SOH prediction is primarily how to accurately recognize the long-term correlation of hundreds of cycles of batteries based on limited aging data. This paper introduces a SOH prognostic method combining aging mechanism analysis and deep learning. It can still maintain good accuracy in the case of only small batch data. The specific contributions are as follows.

In order to ensure the validity of the data and the accuracy of the subsequent calculation results, kernel smoothing methods are used to remove the outliers when the NASA dataset is preprocessed. Additionally, through the calculation and analysis of the voltage curve, a capacity increment curve that can characterize the aging characteristics of the battery is obtained.

Due to the influence of noise, the observation of signal characteristics is not obvious, and a discrete wavelet transform of decomposition and reconstruction is used to capture the signal characteristics and filter the effects of noise. By analyzing the aging mechanism of the increment capacity curve, a distinct group based on the peak of the curve and the corresponding voltage was extracted. Different from the extraction of other model features, incremental capacity curves with large information features are analyzed and extracted by GRA, combined with a battery aging mechanism to optimize the input of deep learning models. The verification results show that the SOH estimation model has good generalization ability and high prediction accuracy, and the MAE and RMSE of the predicted results are 1.24% and 1.62%, respectively. The error is less than 5% in the subsequent training process of battery 6#. In order to verify the model's mobility, the effect is acceptable by freezing the LSTM layers, slight adjustments to the remaining structure are used for other battery training, and the error is less than 4%.

Owing to the uncertainty of the set weights of deep learning random numbers, the network recommendations compared during the technical evaluation should have a similar number of learnable parameters and use the exact data for training and testing. Otherwise, it is difficult to make general conclusions about the estimated quality. In addition, there are multitudinous environmental factors and the influence of the model itself, such as different loading modes, different working conditions, and ambient temperature. The LSTM network cannot solve difficult parallel computing problems, so the practicability of the model needs to be further considered.

Author Contributions: Conceptualization, L.Y. and J.W.; methodology, J.W. and S.X.; investigation, J.H., J.Z. and Z.F.; writing—original draft preparation, J.W.; writing—review and editing, J.W. and L.Y.; supervision, Y.X. All authors have read and agreed to the published version of the manuscript.

Funding: This research was funded by the Department of Science and Technology of Henan Province, (No: 212102210008 and 222102240116) and Zhengzhou Science and Technology Bureau, (2020CXZX0046).

Institutional Review Board Statement: Not applicable.

Informed Consent Statement: Not applicable.

Data Availability Statement: https://ti.arc.nasa.gov/tech/dash/groups/pcoe/prognostic-data-repository/#battery.

Acknowledgments: The authors are grateful to the Department of Science and Technology of Henan Province, (No: 212102210008 and 222102240116) and Zhengzhou Science and Technology Bureau, (2020CXZX0046).

Conflicts of Interest: The authors declare no conflict of interest.

References

1. Qin, P.; Sun, J.; Yang, X.; Wang, Q. Battery Thermal Management System Based on the Forced-Air Convection: A Review. *eTransportation* **2021**, *7*, 100097. [CrossRef]
2. Lai, X.; Chen, Q.; Tang, X.; Zhou, Y.; Gao, F.; Guo, Y.; Bhagat, R.; Zheng, Y. Critical Review of Life Cycle Assessment of Lithium-Ion Batteries for Electric Vehicles: A Lifespan Perspective. *eTransportation* **2022**, *12*, 100169. [CrossRef]
3. Shang, Y.; Lu, G.; Kang, Y.; Zhou, Z.; Duan, B.; Zhang, C. A Multi-Fault Diagnosis Method Based on Modified Sample Entropy for Lithium-Ion Battery Strings. *J. Power Sources* **2020**, *446*, 227275. [CrossRef]
4. Cacciato, M.; Nobile, G.; Scarcella, G.; Scelba, G. Real-Time Model-Based Estimation of SOC and SOH for Energy Storage Systems. *IEEE Trans. Power Electron.* **2017**, *32*, 794–803. [CrossRef]
5. Mahmoudzadeh Andwari, A.; Pesiridis, A.; Rajoo, S.; Martinez-Botas, R.; Esfahanian, V. A Review of Battery Electric Vehicle Technology and Readiness Levels. *Renew. Sustain. Energy Rev.* **2017**, *78*, 414–430. [CrossRef]
6. Song, Z.; Yang, X.-G.; Yang, N.; Delgado, F.P.; Hofmann, H.; Sun, J. A Study of Cell-to-Cell Variation of Capacity in Parallel-Connected Lithium-Ion Battery Cells. *eTransportation* **2021**, *7*, 100091. [CrossRef]
7. Kim, T.; Qiao, W.; Qu, L. Hysteresis Modeling for Model-Based Condition Monitoring of Lithium-Ion Batteries. In Proceedings of the 2015 IEEE Energy Conversion Congress and Exposition (ECCE), Montreal, QC, Canada, 20–24 September 2015; pp. 5068–5073.
8. Chen, J.-L.; Wang, R.-X. A Modified Model-Based Resistance Estimation of Lithium-Ion Batteries Using Unscented Kalman Filter. In *Wireless and Satellite Systems*; Jia, M., Guo, Q., Meng, W., Eds.; Lecture Notes of the Institute for Computer Sciences, Social Informatics and Telecommunications Engineering; Springer International Publishing: Cham, Switzerland, 2019; Volume 280, pp. 25–40; ISBN 978-3-030-19152-8.

9. Lipu, M.S.H.; Hannan, M.A.; Hussain, A.; Hoque, M.M.; Ker, P.J.; Saad, M.H.M.; Ayob, A. A Review of State of Health and Remaining Useful Life Estimation Methods for Lithium-Ion Battery in Electric Vehicles: Challenges and Recommendations. *J. Clean. Prod.* **2018**, *205*, 115–133. [CrossRef]
10. Wang, Y.; Tian, J.; Chen, Z.; Liu, X. Model Based Insulation Fault Diagnosis for Lithium-Ion Battery Pack in Electric Vehicles. *Measurement* **2019**, *131*, 443–451. [CrossRef]
11. Galeotti, M.; Cinà, L.; Giammanco, C.; Cordiner, S.; Di Carlo, A. Performance Analysis and SOH (State of Health) Evaluation of Lithium Polymer Batteries through Electrochemical Impedance Spectroscopy. *Energy* **2015**, *89*, 678–686. [CrossRef]
12. Plett, G. Extended Kalman Filtering for Battery Management Systems of LiPB-Based HEV Battery PacksPart 1. Background. *J. Power Sources* **2004**, *134*, 252–261. [CrossRef]
13. Yang, K.; Chen, Z.; He, Z.; Wang, Y.; Zhou, Z. Online Estimation of State of Health for the Airborne Li-Ion Battery Using Adaptive DEKF-Based Fuzzy Inference System. *Soft Comput.* **2020**, *24*, 18661–18670. [CrossRef]
14. Yao, L.; Xu, S.; Xiao, Y.; Hou, J.; Gong, X.; Fu, Z.; Tang, A. Fault Identification of Lithium-Ion Battery Pack for Electric Vehicle Based on GA Optimized ELM Neural Network. *IEEE Access* **2022**, *10*, 15007–15022. [CrossRef]
15. Pan, H.; Chen, C.; Gu, M. A State of Health Estimation Method for Lithium-Ion Batteries Based on Improved Particle Filter Considering Capacity Regeneration. *Energies* **2021**, *14*, 5000. [CrossRef]
16. Liu, H.W.; Xu, W.J.; Guo, C. Study on State of Health Estimation Algorithm for Lithium Power Battery Used on Pure Electric Vehicle. *Adv. Mater. Res.* **2012**, *608–609*, 1577–1581. [CrossRef]
17. Xiong, W.; Mo, Y.; Yan, C. Online State-of-Health Estimation for Second-Use Lithium-Ion Batteries Based on Weighted Least Squares Support Vector Machine. *IEEE Access* **2021**, *9*, 1870–1881. [CrossRef]
18. Kim, J.; Chun, H.; Kim, M.; Yu, J.; Kim, K.; Kim, T.; Han, S. Data-Driven State of Health Estimation of Li-Ion Batteries with RPT-Reduced Experimental Data. *IEEE Access* **2019**, *7*, 106987–106997. [CrossRef]
19. Gou, B.; Xu, Y.; Feng, X. An Ensemble Learning-Based Data-Driven Method for Online State-of-Health Estimation of Lithium-Ion Batteries. *IEEE Trans. Transp. Electrif.* **2021**, *7*, 422–436. [CrossRef]
20. Chen, Z.; Sun, M.; Shu, X.; Shen, J.; Xiao, R. On-Board State of Health Estimation for Lithium-Ion Batteries Based on Random Forest. In Proceedings of the 2018 IEEE International Conference on Industrial Technology (ICIT), Lyon, France, 20–22 February 2018; pp. 1754–1759.
21. Liu, D.; Pang, J.; Zhou, J.; Peng, Y.; Pecht, M. Prognostics for State of Health Estimation of Lithium-Ion Batteries Based on Combination Gaussian Process Functional Regression. *Microelectron. Reliab.* **2013**, *53*, 832–839. [CrossRef]
22. Hannan, M.A.; Lipu, M.S.H.; Hussain, A.; Saad, M.H.; Ayob, A. Neural Network Approach for Estimating State of Charge of Lithium-Ion Battery Using Backtracking Search Algorithm. *IEEE Access* **2018**, *6*, 10069–10079. [CrossRef]
23. Wang, D.; Miao, Q.; Pecht, M. Prognostics of Lithium-Ion Batteries Based on Relevance Vectors and a Conditional Three-Parameter Capacity Degradation Model. *J. Power Sources* **2013**, *239*, 253–264. [CrossRef]
24. Li, R.; Li, W.; Zhang, H.; Zhou, Y.; Tian, W. On-Line Estimation Method of Lithium-Ion Battery Health Status Based on PSO-SVM. *Front. Energy Res.* **2021**, *9*, 693249. [CrossRef]
25. Zhang, S.; Zhai, B.; Guo, X.; Wang, K.; Peng, N.; Zhang, X. Synchronous Estimation of State of Health and Remaining Useful Lifetime for Lithium-Ion Battery Using the Incremental Capacity and Artificial Neural Networks. *J. Energy Storage* **2019**, *26*, 100951. [CrossRef]
26. Bo, C.; Zhifeng, B.; Binggang, C. State of Charge Estimation Based on Evolutionary Neural Network. *Energy Convers. Manag.* **2008**, *49*, 2788–2794. [CrossRef]
27. Kim, J.; Cho, B.H. An Innovative Approach for Characteristic Analysis and State-of-Health Diagnosis for a Li-Ion Cell Based on the Discrete Wavelet Transform. *J. Power Sources* **2014**, *260*, 115–130. [CrossRef]
28. Dong, Y.; Fu, Z.; Peng, Y.; Zheng, Y.; Yan, H.; Li, X. Precision Fertilization Method of Field Crops Based on the Wavelet-BP Neural Network in China. *J. Clean. Prod.* **2020**, *246*, 118735. [CrossRef]
29. Wang, Y.; Pan, R.; Yang, D.; Tang, X.; Chen, Z. Remaining Useful Life Prediction of Lithium-Ion Battery Based on Discrete Wavelet Transform. *Energy Procedia* **2017**, *105*, 2053–2058. [CrossRef]
30. Jianfang, J.; Keke, W.; Xiaoqiong, P.; Yuanhao, S.; Jie, W.; Jianchao, Z. Multi-Scale Prediction of RUL and SOH for Lithium-Ion Batteries Based on WNN-UPF Combined Model. *Chin. J. Electron.* **2021**, *30*, 26–35. [CrossRef]
31. Sui, X.; He, S.; Vilsen, S.B.; Meng, J.; Teodorescu, R.; Stroe, D.-I. A Review of Non-Probabilistic Machine Learning-Based State of Health Estimation Techniques for Lithium-Ion Battery. *Appl. Energy* **2021**, *300*, 117346. [CrossRef]
32. Khumprom, P.; Yodo, N. A Data-Driven Predictive Prognostic Model for Lithium-Ion Batteries Based on a Deep Learning Algorithm. *Energies* **2019**, *12*, 660. [CrossRef]
33. Zhang, W.; Li, X.; Li, X. Deep Learning-Based Prognostic Approach for Lithium-Ion Batteries with Adaptive Time-Series Prediction and on-Line Validation. *Measurement* **2020**, *164*, 108052. [CrossRef]
34. Chemali, E.; Kollmeyer, P.J.; Preindl, M.; Fahmy, Y.; Emadi, A. A Convolutional Neural Network Approach for Estimation of Li-Ion Battery State of Health from Charge Profiles. *Energies* **2022**, *15*, 1185. [CrossRef]
35. Jiang, H.; Qin, F.; Cao, J.; Peng, Y.; Shao, Y. Recurrent Neural Network from Adder's Perspective: Carry-Lookahead RNN. *Neural Netw.* **2021**, *144*, 297–306. [CrossRef] [PubMed]

36. Hong, S.; Kang, M.; Jeong, H.; Baek, J. State of Health Estimation for Lithium-Ion Batteries Using Long-Term Recurrent Convolutional Network. In Proceedings of the IECON 2020 The 46th Annual Conference of the IEEE Industrial Electronics Society, Singapore, 18–21 October 2020; pp. 1929–1934.
37. Su, L.; Wu, M.; Li, Z.; Zhang, J. Cycle Life Prediction of Lithium-Ion Batteries Based on Data-Driven Methods. *eTransportation* **2021**, *10*, 100137. [CrossRef]
38. Fan, Y.; Xiao, F.; Li, C.; Yang, G.; Tang, X. A Novel Deep Learning Framework for State of Health Estimation of Lithium-Ion Battery. *J. Energy Storage* **2020**, *32*, 101741. [CrossRef]
39. Mou, L.; Ghamisi, P.; Zhu, X.X. Deep Recurrent Neural Networks for Hyperspectral Image Classification. *IEEE Trans. Geosci. Remote Sens.* **2017**, *55*, 3639–3655. [CrossRef]
40. Tian, J.; Xiong, R.; Shen, W. A Review on State of Health Estimation for Lithium Ion Batteries in Photovoltaic Systems. *eTransportation* **2019**, *2*, 100028. [CrossRef]
41. Deng, Z.; Lin, X.; Cai, J.; Hu, X. Battery Health Estimation with Degradation Pattern Recognition and Transfer Learning. *J. Power Sources* **2022**, *525*, 231027. [CrossRef]

energies

MDPI

Article

Analytical Estimation of Power Losses in a Dual Active Bridge Converter Controlled with a Single-Phase Shift Switching Scheme

Marek Turzyński [1,*], Serafin Bachman [2], Marek Jasiński [2], Szymon Piasecki [2], Marek Ryłko [3], Huang-Jen Chiu [4], Shih-Hao Kuo [4] and Yu-Chen Chang [4]

1 Faculty of Electrical and Control Engineering, Gdansk University of Technology, 80-233 Gdansk, Poland
2 Institute of Control and Industrial Electronics, Warsaw University of Technology, 00-662 Warsaw, Poland
3 SMA Magnetics Sp. z o.o., 32-085 Modlniczka, Poland
4 Department of Electronic and Computer Engineering, National Taiwan University of Science and Technology, Taipei City 106335, Taiwan
* Correspondence: marek.turzynski@pg.edu.pl; Tel.: +48-58-347-16-39

Abstract: Micro-grid solutions around the world rely on the operation of DC/DC power conversion systems. The most commonly used solution for these topologies is the use of a dual active bridge (DAB) converter. Increasing the efficiency and reliability of this system contributes to the improvement in the stability of the entire microgrid. This paper discussed an analytical method of energy efficiency and power loss estimation in a single phase dual active bridge (DAB) converter controlled with a single-phase shift (SPS) modulation scheme for microgrid system stability. The presented approach uses conduction and commutation losses of semiconductors and high frequency transformer. All parameters required for the calculation may be obtained from the manufacturers' datasheets or can be based on a simple measurement. The approach was validated by the comparison of the estimated energy efficiency characteristics with the measured ones for a prototype of a 5 kW single phase DAB converter equipped with silicon carbide metal-oxide semiconductor field-effect transistors (SiC MOSFET).

Keywords: dual active bridge; bidirectional isolated DAB; efficiency; estimation; power loss; analytical calculations; DC/DC converter; SiC MOSFET

1. Introduction

Dual active bridge (DAB) topology is among the most popular DC/DC converters used in electronic power systems. This topology is widely used in DC/DC microgrids as well as mixed networks and owes its popularity to many advanced features such as bidirectional power flow, galvanic isolation, control simplicity, wide range of voltage regulation, and soft switching of semiconductor devices. DAB topology has been applied to solid-state transformers, electromobility, energy storage systems, and DC voltage distribution networks [1,2]. Nowadays, the development of DAB converters is mainly focused on the increase in energy efficiency by using modern power semiconductors (SiC, GaN), where the adaptation of new control strategies enables a reduction in the current stress and the limitation of current RMS values, and a diminishing of DAB transformer power losses [1–6]. Crucially, the application of modern power semiconductor devices enables an increase in the switching frequency up to 1 MHz [7], which results in a higher power density, a reduction in passive components dimensions, and a reduction in the overall converter dimensions.

The problem of energy efficiency evaluation is one of the main aspects of the beginning stage of the design process of a future converter. Importantly, a proper evaluation of power losses allows for a selection of cooling methods and radiator features, which reduce the overall converter dimensions and the total cost. At the early stages of the design process, energy efficiency may be estimated using a simulation tool or via an analytical analysis. Many simulators (e.g., PLECS) offer comprehensive tools for the evaluation of power losses and a thermal analysis using electro-thermal models [8]. This method is easy to use and delivers results with a satisfactory accuracy for the design purpose. However, it requires access to precise models of semiconductors, which not all suppliers offer, because such models are usually shared by manufacturers only for selected types of semiconductors, or the developed models are dedicated to one specific simulator. Crucially, many models of semiconductors presented in the literature cannot be parameterized using the manufacturer's datasheet, hence additional laboratory measurements are required to obtain the model parameters, which is usually time-consuming and increases the total cost [9,10].

Notably, the measurement of some quantities in the DAB converter (e.g., the power loss of a transformer) may be problematic, hence using analytical methods may be a suitable approach to obtaining a power loss distribution.

Another approach uses an analytical analysis based on a set-up of mathematical equations describing the function of the considered converter. It is worth mentioning that the presence of high-frequency currents in a DAB converter AC circuit, or the determination of the switching process mechanism of semiconductors (under soft or hard conditions) in dependence on the converter AC side currents values results in limited usefulness of the analytical methods, which have been derived for classic H-bridge topologies. These approaches are usually described for sinusoidal modulation with a low fundamental current frequency at the inverter AC side [11–13]. Moreover, in some systems, the transistor turn-on losses are neglected [14], or it is assumed that both the turn-on and turn-off processes perform only under hard switching conditions [12]. In available application notes, switching losses under hard conditions are usually calculated using simplified formulas with constant values of time parameters describing the switching processes [4]. Moreover, to simplify the considerations, the impact of transistor gate resistance is often omitted [12,14,15].

In the literature, analytical methods of power loss estimation dedicated to DAB converters have also been proposed.

For example, in [16], an analysis of a power transfer in a single-phase DAB converter was provided. The presented analyses were performed for different cases of input-to-output voltage relations including the influence of the dead time and conduction losses of semiconductor devices. However, the presented analysis was incomplete as it omitted the discussion of the impact of semiconductor switching losses and transformer losses. An interesting approach was presented in [17], where a theoretical analysis of power losses was given, which was used for the optimal design methodology of a single-phase DAB converter. A valuable part of this work is a presentation of an estimation method of capacitors and transformer losses. The obtained results were compared with the results of the simulation and experimental measurements to prove the correctness of the adopted methodology, however, an analysis of the semiconductor switching losses was not included—the authors assumed that all switches were switched under soft conditions. Another solution was presented in [18], where an analysis of the conducted differential mode current harmonic magnitudes and the power factor in a DAB converter was discussed. Importantly, that solution was based on a Fourier series theory, hence its adaptation is more complex and time consuming. This approach may be used for the overall prediction of the DAB operational performance and to optimize and identify the current and voltage ranges. Commutation losses were not considered here either; hence based on the methodology presented in [18], the DAB converter efficiency may only be evaluated in a generic way.

The approach presented in [19] was dedicated to the estimation of semiconductor losses including the impact of dead-time and turn-off process for SiC MOSFET and Si IGBT transistors operating in DAB converters. All of the required parameters may be easily extracted using the manufacturer's datasheet. The used mathematical expressions are not complicated, and method adaptation is not time-consuming. It should be noted that the presented considerations did not take into account the transformer losses, which is a significant disadvantage of the method.

A more advanced approach was described in [20], where the estimation method of semiconductors and transformer losses was proposed. The obtained results were used to improve the overall energy efficiency by modifying and optimizing the DAB converter control strategy. The limitations of the primary approach are the omission of the diodes' reverse recovery process and neglect of the impact of transistor gate resistance on the switching process dynamics.

A comprehensive estimation method of the DAB converter efficiency was proposed in [21]. The transformer losses were predicted using the Steinmetz equation and the semiconductors' conduction and switching losses were also calculated. Additional analyses were performed for hard and soft switching conditions in dependency on the current values in the AC circuit of the DAB converter. The high accuracy of the obtained results and the usefulness of the proposed approach were confirmed by a comparison with the experimental measurement results. However, two different polynomial functions—one for hard switching and one for soft switching—must be used to calculate the semiconductor switching losses. Parameters of these functions were fitted by using least means squares approximation. As a result, the method is complicated and time-consuming.

Based on the presented analysis, it appears that a different approach is necessary. In this paper, a calculation method of power loss and energy efficiency of a one-phase DAB converter composed with SiC-MOSFETs and controlled with single phase shift was proposed. The proposed set of equations, whose coefficients may be easily obtained from the manufacturer's datasheets, describes the commutation and conduction losses of diodes and transistors and the transformer losses were also considered. The correctness of theoretical considerations was verified by comparing the analytical results with the experimental ones, performed on a 5 kW DAB converter prototype.

2. Dual Active Bridge DC/DC Converter

The basic topology of the dual active bridge (DAB) DC/DC converter with a one-phase high frequency transformer is presented in Figure 1a. It consists of two H-bridges coupled by an AC-link formed by a transformer with a turn's ratio $n = N_2/N_1$ and an additional inductor L_d. The DAB converter may be driven using various control methods. Due to its simplicity of implementation, small inertia, and satisfactory dynamic performance, the single phase shift (SPS) switching scheme, where all transistors are switched with a 50% duty cycle ratio and the phase-shift ϕ is used to control the power flow (Figure 1b), was the most common scheme. Nevertheless, using SPS control causes a reduction in the operating range in which semiconductors are switched to soft conditions, especially when the input-to-output voltage ratio is significantly different from 1. Another disadvantage of the application of the SPS modulation scheme is an increase in the rms value of the transformer current at the converter's low output power. As a result, a significant reactive power flow is then observed, which increases the conduction loss and the current stress of transistors and diodes [22,23]. To improve the converter efficiency by reducing the circulating power flow and limiting the current rms value, other control methods, which provide an extra degree of freedom, have been proposed such as extended phase shift (EPS), dual phase shift (DPS), or triple phase shift (TPS) modulation [24,25].

Despite the undeniable advantages of EPS, DPS, and TPS, in comparison with SPS, a practical application of these types of modulation is more complex. These methods significantly complicate the implementations of the modulator, and their efficiency characteristics in relation to the output power, with the change in the voltage ratio, decreases significantly. Hence, in this paper, the authors considered a DAB controlled with a SPS control scheme, however, the proposed approach may be adopted to other modulation types.

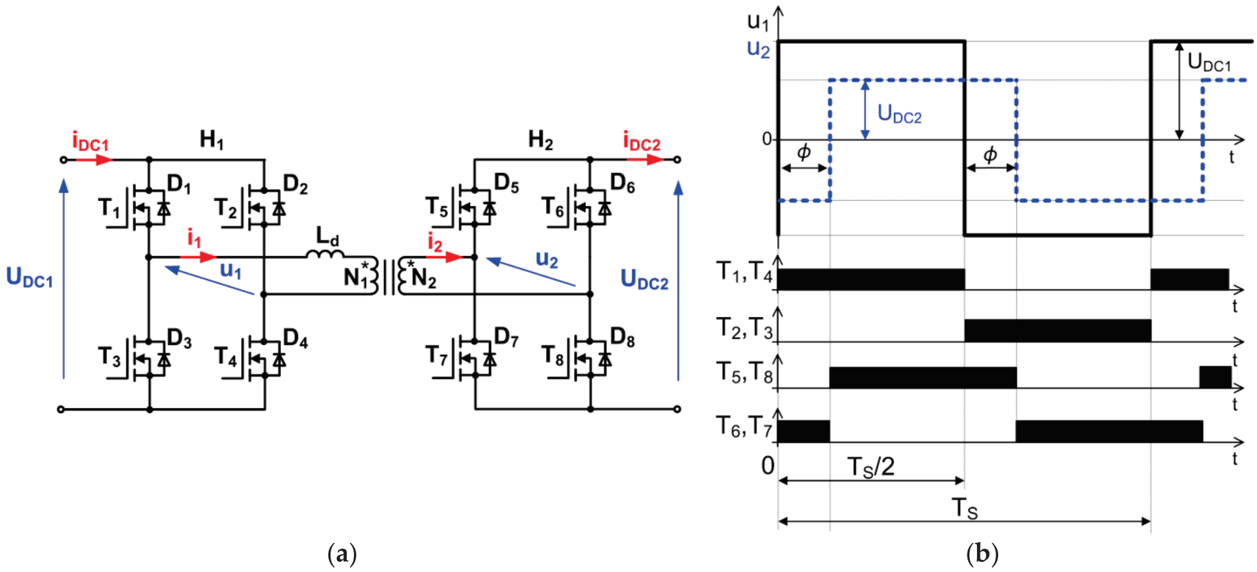

Figure 1. (**a**) Dual active bridge DC/DC converter topology; (**b**) single phase shift modulation scheme.

3. Currents Estimation in a DAB Converter

An equivalent circuit of the single-phase DAB converter (Figure 1a) is presented in Figure 2. A resultant inductance L represents a sum of inductances in the AC-circuit:

$$L = L_d + L_{\delta 1} + L'_{\delta 2}, \tag{1}$$

where:

- L_d—inductance of the additional inductor;
- $L_{\delta 1}$, $L_{\delta 2}{}'$—leakage inductance of each transformer winding converted to the bridge H_1 side: $L_{\delta 2}{}' = L_{\delta 2}/n^2$;
- $L_{\delta 2}$—leakage inductance of transformer winding at the H_2 bridge side; $n = N_2/N_1$—transformer turns ratio.

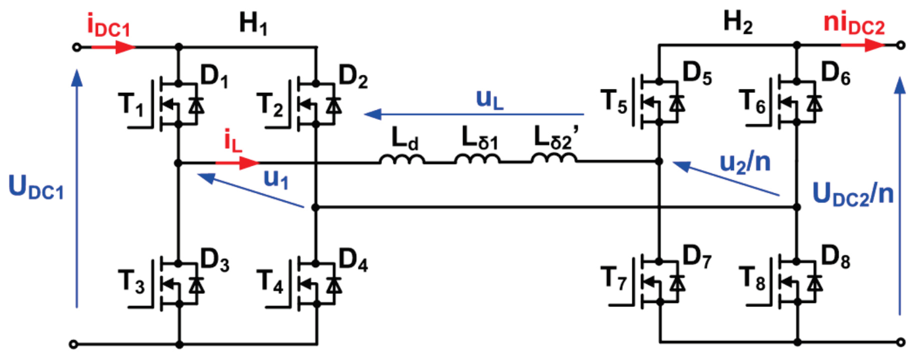

Figure 2. Equivalent circuit of the single-phase DAB converter.

In the presented equivalent scheme, values of the H_2 bridge voltages and currents are also referred to the H_1 bridge side.

In this study, the DAB converter features were considered when the SPS modulation strategy was applied. Each bridge generated a quasi-square wave voltage u_1 and u_2/n with a 50% duty cycle (Figure 3).

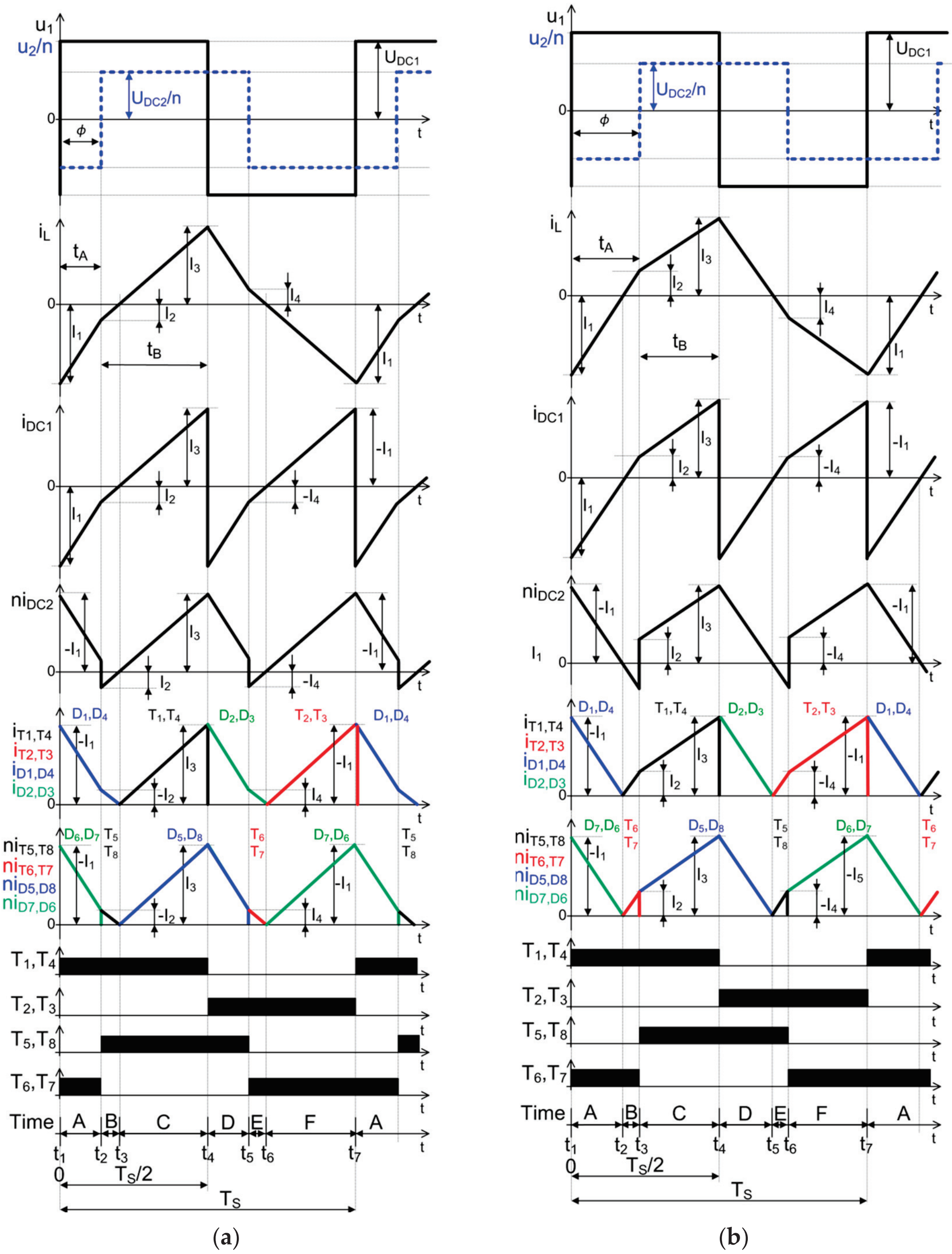

Figure 3. Simplified voltage and current waveforms of DAB converter for $U_{DC1} > U_{DC2}/n$: (**a**) with $I_2 < 0$; (**b**) with $I_2 > 0$.

The value and power flow direction between bridges H_1 and H_2 are controlled by the phase shift ϕ. To simplify the calculations, the impact of the transistors' dead time may be neglected. Similarly, it can be assumed that the values of voltages U_{DC1} and U_{DC2}/n are high enough, which enables the voltage drop to be omitted at the transistors and diodes. In brief, positive values of the phase shift are used when $U_{DC1} > U_{DC2}/n$, however, for a negative value of ϕ, the results may be obtained using a similar approach. In Figure 4, exemplary theoretical waveforms are presented, when $U_{DC1} < U_{DC2}/n$ and $\phi > 0$.

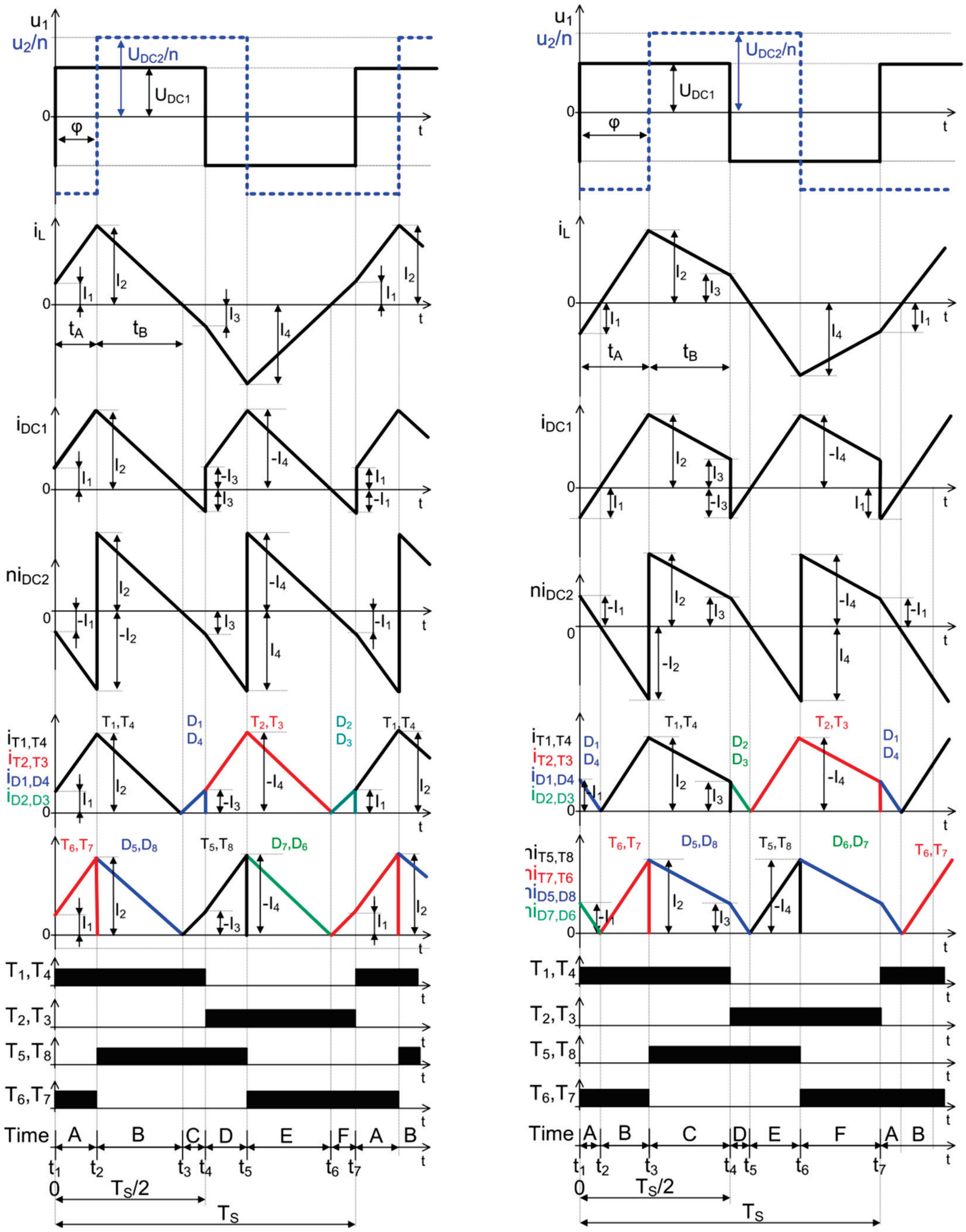

(**a**) (**b**)

Figure 4. Simplified voltage and current waveforms of the DAB converter for $U_{DC1} < U_{DC2}/n$: (**a**) with $I_1 > 0$; (**b**) with $I_1 < 0$.

Based on Figure 3a and an equivalent scheme of the DAB converter (Figure 2), voltage u_L, affecting the inductances in the AC-link, is described by:

- for the time interval t_A:

$$u_{L(A)} = u_1 - \frac{u_2}{n} = U_{DC1} + \frac{U_{DC2}}{n}, \tag{2}$$

- for the time interval t_B:

$$u_{L(B)} = u_1 - \frac{u_2}{n} = U_{DC1} - \frac{U_{DC2}}{n}. \tag{3}$$

Hence, the current i_L in specified time moments is described by:

$$i_L(t_1) = I_1, \tag{4}$$

$$i_L(t_2) = I_2 = I_1 + \frac{u_{L(A)}}{L} t_A \tag{5}$$

and

$$i_L(t_4) = i_L\left(\frac{T_S}{2}\right) = I_3 = I_2 + \frac{u_{L(B)}}{L} t_B = -I_1. \tag{6}$$

Thus, the average values of the input and output currents I_{DC1} and I_{DC2} are given by:

$$I_{DC1(av)} = \frac{2}{T_S}\int_0^{T_S/2} i_{DC1}(t)dt = \frac{1}{T_S}[I_2(t_A + t_B) + I_3(t_B - t_A)], \tag{7}$$

and

$$I_{DC2(av)} = \frac{2}{T_S}\int_0^{T_S/2} i_{DC2}(t)dt = \frac{1}{nT_S}[I_2(t_B - t_A) + I_3(t_A + t_B)]. \tag{8}$$

Because $t_A = T_S/2 - t_B$ and substitutions (2) and (3) to (8), (9) leads to:

$$I_{DC1(av)} = \frac{1}{nT_S}\left[-\frac{2U_{DC2}}{L} {t_B}^2 + \frac{T_S \cdot U_{DC2}}{L} t_B\right], \tag{9}$$

and

$$I_{DC2(av)} = \frac{1}{nT_S}\left[-\frac{2U_{DC1}}{L} {t_B}^2 + \frac{T_S \cdot U_{DC1}}{L} t_B\right]. \tag{10}$$

For known values of $I_{DC1(av)}$ or $I_{DC2(av)}$, n and U_{DC1} or U_{DC2}, the length of the time interval t_B may be easily extracted by solving Equations (9) or (10). Next, the length of interval t_A may be obtained for a specified switching time T_S, which allows for a calculation of the values of current i_L at characteristic moments of the DAB converter operating cycle.

4. Estimation of Transistor and Diode Power Losses

The total power loss P_T of a single transistor operating in a H-bridge is the sum of commutation losses and conduction loss $P_{C(T)}$:

$$P_T = P_{ON(T)} + P_{C(T)} + P_{OFF(T)}, \tag{11}$$

where $P_{ON(T)}$ and $P_{OFF(T)}$ are the turn-on and turn-off switching losses, also called the commutation losses. The total power loss of a single diode P_D may be defined in an analogous way.

Conduction losses result from voltage drops on conducting transistors and diodes. If MOSFET transistors are applied in a converter construction, using a linear approximation of the transistor output characteristic $i_D(u_{DS})$ (Figure 5) allows one to estimate a voltage drop u_{DS} depending on a drain current i_D:

$$u_{DS} = \frac{U_{DS(N)}}{I_{D(N)}} i_D, \tag{12}$$

where $U_{DS(N)}$ and $I_{D(N)}$ are the rated values of the transistor drain-to-source voltage u_{DS} and drain current i_D (given in the manufacturer's datasheet).

Similarly, using a linear approximation of the datasheet diode characteristic $i_{DZ}(u_D)$, the voltage drop u_D caused by a flow of current i_{DZ} may be calculated as:

$$u_D = r_D \cdot i_{DZ} + U_{FO}, \tag{13}$$

where U_{FO} is a diode threshold voltage and r_D is the diode dynamic resistance $r_\mathrm{D} = \Delta u_\mathrm{D}/\Delta i_\mathrm{DZ}$ (Figure 5).

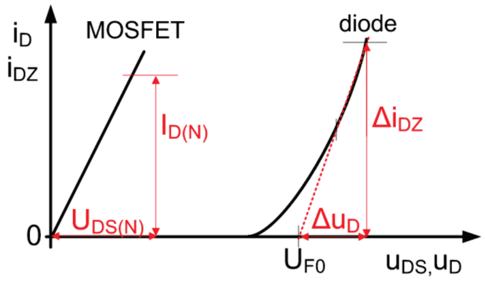

Figure 5. Linearization of the diode and MOSFET steady-state characteristics.

Hence, the conduction power loss of the MOSFET transistor and diode calculated for one switching period T_S are given as follows:

- for MOSFET:

$$P_{C(T)} = \frac{U_{DS(N)}}{I_{D(N)}\,T_S}\int_{t_0}^{t_O+T_S}[i_D(t)]^2dt = \frac{U_{DS(N)}}{I_{D(N)}}\cdot {I_{D(rms)}}^2 \tag{14}$$

- and for the diode:

$$P_{C(D)} = U_{FO}\cdot I_{DZ(av)} + r_D\cdot {I_{DZ(rms)}}^2, \tag{15}$$

where $I_{D(rms)}$ and $I_{DZ(rms)}$ are rms values of transistor and diode currents and $I_{DZ(av)}$ is an average value of a diode current i_{DZ} calculated for one switching period T_S.

Commutation losses result from finite values of the rise and fall times of the transistor voltage and current waveforms during switching processes. Considering the theoretical voltages and current waveforms obtained in a basic switching cell (Figure 6) during the transistor turn-on process under hard conditions, the transistor current i_D reaches the value of the load current I_O before the reduction in the drain-to-source voltage u_{DS} [26] (Figure 7).

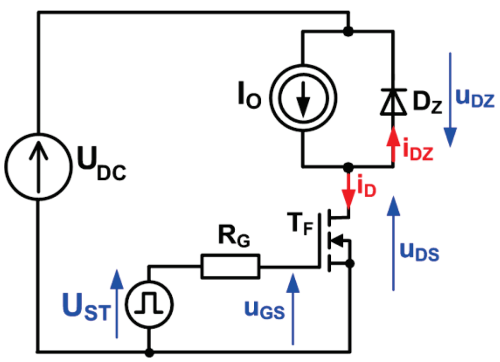

Figure 6. Basic switching cell.

Hence, in the turn-on process of a transistor, two characteristic sub periods may be described. Impacted by the diode D_Z reverse recovery, during the first stage of the turn-on process, the drain current rises to the value, which is a sum of the absolute values of load current I_O and reverse recovery current I_{RM} of diode D_Z (Figure 7b). Considering the waveforms presented in Figure 6, the transistor current i_D derivative with time is expressed by:

$$a_{iD} = \frac{di_D}{dt} = \frac{I_O + |I_{RM}|}{t_{RI}\prime} = \frac{I_O}{t_{RI}}. \tag{16}$$

To estimate the current i_D rise time t_{RI}, a MOSFET gate circuit should be analyzed (Figure 8). During the transistor switching process, which is caused by drive voltage U_{DR} changes, transistor parasitic capacitances C_{GD} and C_{GS} are recharged by the gate current i_G [27]:

$$i_G = C_{GD}\frac{du_{GD}}{dt} + C_{GS}\frac{du_{GS}}{dt}. \tag{17}$$

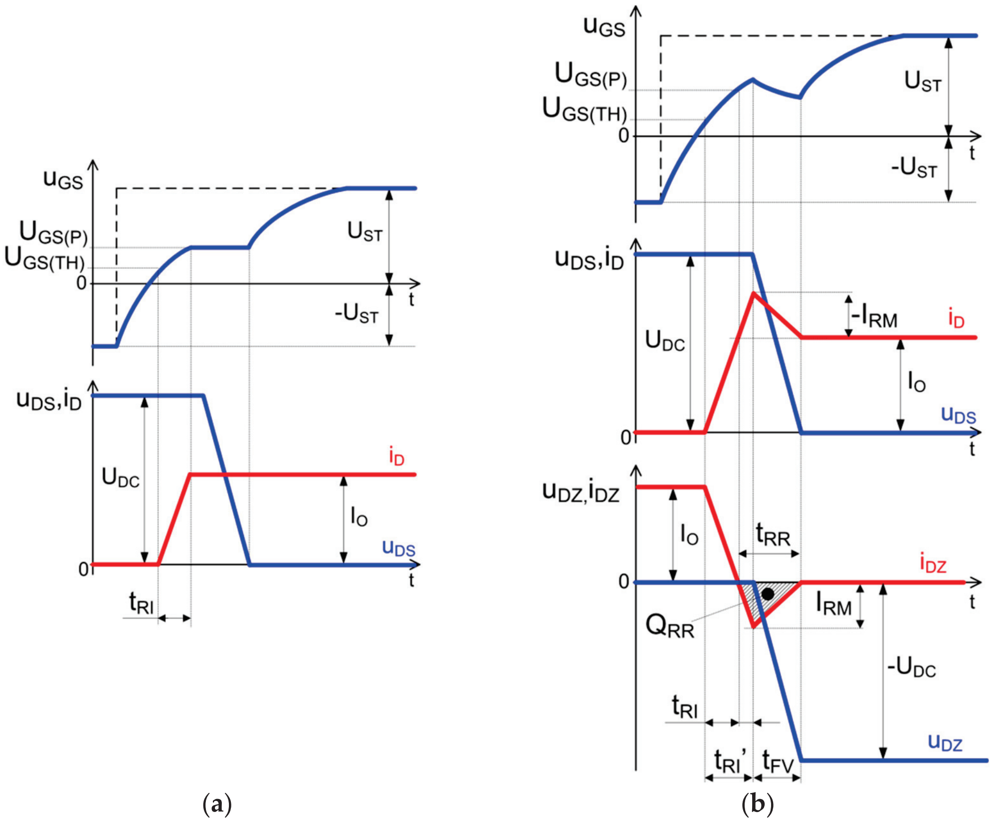

Figure 7. Voltage and current waveforms in a basic switching cell during transistor turn-on process: (**a**) without the diode D_Z reverse recovery; (**b**) with the diode D_Z reverse recovery.

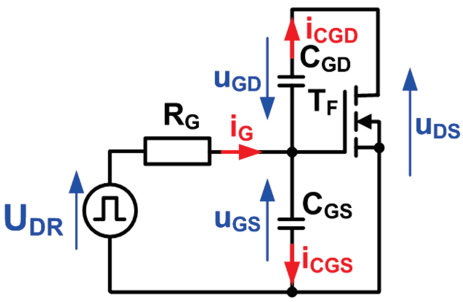

Figure 8. A gate circuit of the MOSFET transistor.

The gate current i_G may also be described by the equation:

$$i_G = \frac{U_{DR} - u_{GS}}{R_G}, \tag{18}$$

where R_G is an external gate resistance. In the manufacturer's datasheet, the values of capacitances C_{GD} and C_{GS} are given as an input capacitance C_{iss} and a reverse transfer capacitance C_{rss} with the following relationships:

$$C_{iss} = C_{GD} + C_{GS} \tag{19}$$

and

$$C_{rss} = C_{GD}. \tag{20}$$

Next, substituting (18)–(20) to Equation (17):

$$\frac{U_{DR}-u_{GS}}{R_G}=C_{rss}\frac{d(u_{GS}-u_{DS})}{dt}+(C_{iss}-C_{rss})\frac{du_{GS}}{dt}, \tag{21}$$

which leads to:

$$\frac{U_{DR}-u_{GS}}{R_G}=C_{iss}\frac{du_{GS}}{dt}-C_{rss}\frac{du_{DS}}{dt}. \tag{22}$$

During the current i_D rise phase of the turn-on process, to simplify the calculations, it can be assumed that the voltage u_{DS} remains constant and its derivative with time equals zero (Figure 7). Hence, Equation (22) may be modified as follows:

$$\frac{U_{DR}-u_{GS}}{R_G}=C_{iss}\frac{du_{GS}}{dt}. \tag{23}$$

Next, transforming Equation (23):

$$dt=\frac{R_G\cdot C_{iss}}{U_{DR}-u_{GS}}du_{GS} \tag{24}$$

the rise time t_{RI} is given by:

$$t_{RI}=\int_{U_{GS(TH)}}^{U_{GS(P)}}\frac{R_G\cdot C_{iss}}{U_{DR}-u_{GS}}du_{GS}=R_GC_{iss}ln\frac{\left|U_{DR}-U_{GS(TH)}\right|}{\left|U_{DR}-U_{GS(P)}\right|}. \tag{25}$$

where $U_{GS(TH)}$ is a MOSFET gate threshold voltage and $U_{GS(P)}$ is a minimal value of the gate-to-source voltage, enabling the conduction of the load current I_O. These values may be obtained from a datasheet transfer characteristic $i_D(u_{GS})$. After the calculation of parameter t_{RI}, the value of derivative di_D/dt may be easily estimated using (16).

To estimate the diode turn-off power loss under hard-switching conditions, a reverse-recovery process must be used. Hence, the values of reverse current I_{RM} and diode reverse recovery time t_{RR} should be evaluated (Figure 7b). To solve this problem, a number of analytical methods using datasheet information have been proposed. For example, in [28], a regression method was proposed to obtain the reverse-recovery parameters during switching intervals, and in [29], a set of equations including, additionally, the impact of parasitic inductances and diode capacitance, was proposed. These methods offer satisfactory accuracy with a maximum error of parameter estimation lower than 10%, however, their application seems to be complex and time consuming. Considering the waveforms presented in Figure 7b, the values of parameters t_{RR}, I_{RM}, and Q_{RR} depend on the load current I_O, diode current derivative with time a_{iDz}, and temperature [30]. In this paper, to be concise, the effect of temperature was omitted. Based on the results of the measurements and the manufacturer's data, the following empirical relations enabling the estimation of t_{RR} and I_{RM} for various values of load current I_O and a_{iDZ} = di_{DZ}/dt were derived:

$$t_{RR}=t_{RR(N)}\left(-0.15\left|\frac{a_{iDz}}{A_{iDz(N)}}\right|+0.2\frac{I_O}{I_{O(N)}}+0.9\right) \tag{26}$$

and:

$$I_{RM}=0.2I_{RM(N)}\left(\frac{I_O}{I_{O(N)}}+1.25\right)\left(\left|\frac{a_{iDz}}{A_{iDz(N)}}\right|+1\right), \tag{27}$$

where:

- a_{iDZ} = di_{DZ}/dt = $-a_{iD}$ (from Equation (16) and Figure 7b);
- $t_{RR(N)}$ is a nominal value of the diode D_Z reverse recovery time measured for the nominal load current $I_{O(N)}$ and nominal derivative with time of the diode current $A_{iDZ(N)}$. These nominal values are usually given in the manufacturer's datasheet.

Thus, the total length of interval t_{RI}' (Figure 7b) is given by:

$$t'_{RI} = t_{RI} + \frac{|I_{RM}|}{a_{iD}}. \tag{28}$$

When the transistor drain current reaches the maximum value, the next phase of the turn-on process begins. Voltage u_{DS} starts to fall and, by the end of interval t_{FV}, the recombination process of the diode charge is finished—voltage u_{DS} is reduced to zero and the diode current is zero (Figure 7b) [12]. Factually, at that moment, the diode current was limited to about 10% of I_{RM} and the voltage u_{DS} was reduced to the value resulting from the voltage drop on the conducting transistor. Hence, the transistor voltage fall time t_{FV} is described by:

$$t_{FV} = t_{RR} - \frac{|I_{RM}|}{a_{iD}}. \tag{29}$$

Considering the waveforms presented in Figure 7b and based on the estimated values of t_{RI}' and t_{FV}, the turn-on power loss of the MOSFET $P_{ON(T)}$ under hard switching conditions is expressed by:

$$P_{ON(T)} = \frac{1}{T_S}\int_0^{t_{FV}+t_{RI}'} u_{DS}(t)\cdot i_D(t)dt. \tag{30}$$

which leads to:

$$P_{ON(T)} = \frac{U_{DC}}{T_S}\left[\frac{t_{RI}'}{2}(I_O + |I_{RM}|) + t_{FV}\left(\frac{I_O}{2} + \frac{|I_{RM}|}{3}\right)\right]. \tag{31}$$

Similarly, the diode reverse recovery power loss is given by:

$$P_{OFF(D)} = \frac{1}{T_S}\int_0^{t_{FV}} u_{DZ}(t)\cdot i_{DZ}(t)dt = \frac{U_{DC}\cdot|I_{RM}|\cdot t_{FV}}{6T_S}. \tag{32}$$

During the MOSFET turn-off process under hard conditions, the transistor u_{DS} voltage reaches the value of the supply voltage U_{DC} before a reduction in the drain current i_D (Figure 9) [26,31]. Analyzing the MOSFET turn-off process (Figure 9), two characteristic phases may be recognized:

- during time interval t_{RV}, voltage u_{DC} rises to U_{DC};
- during time interval t_{FI}, drain current i_D decreases do zero.

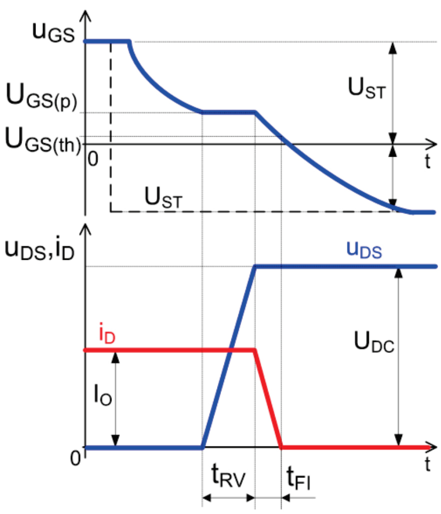

Figure 9. Voltage and current waveforms in a basic switching cell during the transistor turn-off process.

During time interval t_{RV}, assuming the gate-to-source voltage u_{GS} is constant, the transistor is turned off within the flat Miller Plateau Region. Because $u_{GS} = U_{GS(P)}$ and $du_{GS}/dt = 0$, Equation (22) may be simplified:

$$\frac{U_{DR} - U_{GS(P)}}{R_G} = -C_{rss}\frac{du_{DS}}{dt}, \tag{33}$$

which leads to:

$$t_{RV} = \frac{R_G \cdot C_{rss}}{U_{GS(P)} - U_{DR}} \int_0^{U_{DC}} du_{DS} = \frac{R_G \cdot C_{rss} \cdot U_{DC}}{U_{GS(P)} - U_{DR}}. \tag{34}$$

The relation describing a current i_D fall time may also be derived in an analogous way:

$$t_{FI} = \int_{U_{GS(P)}}^{U_{GS(TH)}} \frac{R_G \cdot C_{iss}}{U_{DR} - u_{GS}} du_{GS} = R_G C_{iss} ln \frac{\left|U_{DR} - U_{GS(P)}\right|}{\left|U_{DR} - U_{GS(TH)}\right|}. \tag{35}$$

Thus, MOSFET turn-off power losses are given by:

$$P_{\mathrm{OFF(T)}} = \frac{1}{T_S} \int_0^{t_{RV}+t_{FI}} (u_{\mathrm{DS}}(t) \cdot i_{\mathrm{D}}(t))dt = \frac{U_{\mathrm{DC}} \cdot I_{\mathrm{O}}}{2T_S}(t_{RV} + t_{FI}). \tag{36}$$

For example, from Figure 3, it can be distinguished that transistor pair T_1 and T_4 in bridge H_1 is switched on when diodes D_1 and D_4 conduct, which forms soft switching conditions. Similarly, the turn-on process of transistors T_2 and T_3 also occurs under ZCS (zero current switching) conditions. Hence, it can be assumed that the turn-on power loss for these transistor pairs $P_{ON(T)} = 0$. At moments t_4 and t_7, transistor pairs T_1, T_4 and T_2, T_3 are switched off. In this study, the least favorable operating conditions of semiconductors were assumed, hence, to calculate the power loss $P_{OFF(T)}$ from Equation (36), it was assumed that transistor pairs T_1, T_4 and T_2, T_3 were turned off under hard-switching conditions with a current $i_{T1,T4}(t_4) = i_{T2,T3}(t_7) = -I_1 = I_3$ and supply voltage $U_{DC} = U_{DC1}$. From Figure 3, it can also be distinguished, that if $I_2 < 0$, then transistors T_5, T_8 are switched on and diodes D_6, D_7 are turned off under hard-switching conditions. To calculate transistor T_5 turn-on power losses $P_{ON(T5)}$ and diode D_6 turn-off power losses $P_{OFF(D6)}$, Equations (31) and (32) should then be used for $U_{DC} = U_{DC2}$ and $I_O = I_2/n$. The turn-off process of transistors T_5, T_8 occurs under ZCS conditions, hence, the commutation loss $P_{OFF(T5)}$ equals zero. If $I_2 > 0$, the transistor T_5, T_8 turn-on process ensues when diodes D_1, D_4 conduct, which allows for the development of soft-switching conditions. Nevertheless, the H_2 bridge transistors' turn-off process occurs under hard switching conditions. To calculate the commutation power loss $P_{OFF(T5)}$, Equation (36) may be applied for $U_{DC} = U_{DC2}$ and $I_O = I_2/n$. Notably, that power loss may be calculated only for one transistor and diode for each of bridges H_1 and H_2. Hence, the power loss of transistor T_1 is given by:

$$P_{T1} = P_{C(T1)} + P_{OFF(T1)}, \tag{37}$$

where the transistor T_1 conduction power loss $P_{C(T1)}$ may be calculated from (14):

$$P_{C(T1)} = \frac{U_{DS(N)}}{I_{D(N)}} \cdot {I_{T1(rms)}}^2, \tag{38}$$

and ${I_{T1(rms)}}^2$ is obtained by:

If $I_2 < 0$ (from Figure 3a):

$${I_{T1(rms)}}^2 = \frac{1}{T_S} \int_{t_3}^{t_4} i_L^2(t)dt = \frac{1}{3T_S}\left(\frac{T_S}{2} - t_3\right)I_3^2, \tag{39}$$

and if $I_2 > 0$ (from Figure 3b):

$$I_{T1(rms)}{}^2 = \frac{1}{T_S}\int_{t_2}^{t_4} i_L^2(t)dt = \frac{1}{3T_S}\left[(t_3 - t_2)I_2^2 + \left(\frac{T_S}{2} - t_3\right)\frac{I_3^3 - I_2^3}{I_3 - I_2}\right]. \quad (40)$$

The commutation power loss $P_{OFF(T1)}$ is described in Equation (36). Because diode D_1 is turned off under soft-switching conditions, only a conduction loss (see Equation (15)) may be taken into account:

$$P_{D1} = P_{C(D1)} = U_{FO} \cdot I_{D1(av)} + r_D \cdot I_{D1(rms)}{}^2, \quad (41)$$

where $I_{D1(av)}$ and $I_{D1(rms)}{}^2$ are given as follows:

If $I_2 < 0$ (from Figure 3a):

$$I_{D(av)} = \frac{1}{T_S}\int_0^{t_3}[-i_L(t)]dt = \frac{1}{2T_S}[I_3 t_A - I_2(t_A + t_3 - t_2)], \quad (42)$$

$$I_{D(rms)}{}^2 = \frac{1}{T_S}\int_0^{t_3}[-i_L(t)]^2 dt = \frac{1}{3T_S}\left[\frac{I_1^3 - I_2^3}{I_1 - I_2}t_A + I_2^2(t_3 - t_2)\right]. \quad (43)$$

and if $I_2 > 0$ (from Figure 3b):

$$I_{D(av)} = \frac{1}{T_S}\int_0^{t_2}[-i_L(t)]dt = \frac{1}{2T_S}[I_3(t_2 - t_1)], \quad (44)$$

$$I_{D(rms)}{}^2 = \frac{1}{T_S}\int_0^{t_2}[-i_L(t)]^2 dt = \frac{1}{3T_S}\left[I_3^2(t_2 - t_1)\right]. \quad (45)$$

For the known values I_1, I_2, and I_3, the length of the time intervals $(t_2 - t_1)$, $(t_3 - t_2)$, and $(T_S/2 - t_3)$ for specific values of voltage U_{DC1} and U_{DC2}/n may be obtained from modified Equations (4)–(6).

The total power losses of the H_1 bridge transistors is equal to:

$$P_{TH1} = 4 \cdot P_{T1}, \quad (46)$$

and the total power losses for the bridge H_1 diodes are given by:

$$P_{DH1} = 4 \cdot P_{D1}. \quad (47)$$

Hence, the total power losses of bridge H_1 is equal to:

$$P_{H1} = P_{TH1} + P_{DH1}. \quad (48)$$

The total power losses of all transistors (P_{TH2}) and diodes (P_{DH2}) in a H_2 bridge may be obtained in an analogous way.

5. Transformer Losses

For the analytical evaluation, it was assumed that the transformer total power loss P_{TR} is a sum of the power loss in the core P_{FE}, and the power losses generated in the primary and secondary windings are $P_{CU(prim)}$ and $P_{CU(sec)}$.

$$P_{TR} = P_{FE} + P_{CU(prim)} + P_{CU(sec)}. \quad (49)$$

To calculate the core power loss P_{FE}, a modified Steinmetz's formula may be used, which for rectangular voltages is given as follows [32,33]:

$$P_{FE} = \frac{8}{\pi^2}kf^\alpha B_M^\beta\left(c_0 - c_1 T_C + c_2 T_C^2\right)V_C, \quad (50)$$

- f—inducplified waveforms of voltages;
- B_M—induction peak value [T];
- T_C—core temperature [°C];
- V_{C}—core volume [cm^3].

The coefficients of Equation (50) may be directly obtained from datasheets developed by the core manufacturers.

Considering the scheme presented in Figure 2, an equivalent circuit of the transformer connected in series with an additional choke placed at the primary side is shown in Figure 10. Thus, a magnetizing voltage u_{Lm} affecting the magnetizing inductance L_m is described by:

$$u_{Lm} = \frac{L_{\delta 2}\prime}{L_d + L_{\delta 1} + L_{\delta 2}\prime} u_1 + \frac{L_d + L_{\delta 1}}{L_d + L_{\delta 1} + L_{\delta 2}\prime} \frac{u_2}{n}, \tag{51}$$

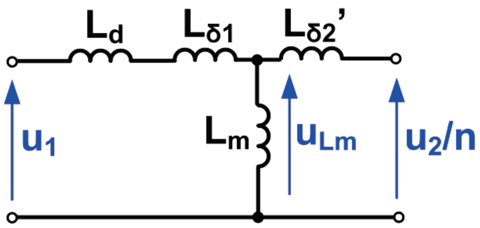

Figure 10. An equivalent circuit of the transformer with an additional choke L_d with values transferred to the DAB H_1 bridge side.

From Figure 2, neglecting a voltage drop on the diodes and transistors and assuming a rectangular shape of the voltage waveforms, the voltages u_1 and u_2/n were equal to, respectively, $\pm U_{DC1}$ and $\pm U_{DC2}/n$. From (51), it may be distinguished that the worst working conditions of core occurred when L_d = 0 and $L_{\delta 2}$ = $L_{\delta 2}'$. Hence, the magnetizing voltage u_{Lm} is then given by:

$$u_{Lm} = \frac{1}{2}\left(u_1 + \frac{u_2}{n}\right), \tag{52}$$

and induction B_M reaches the maximum possible values. Based on waveforms presented in Figure 11, B_M may be described in the following way:

- if $U_{DC1} = U_{DC2}/n$ (Figure 11a):

$$B_M = \frac{\Delta B_1}{2} = \frac{U_{DC1}}{2N_1 S_c} t_B, \tag{53}$$

- if $U_{DC1} > U_{DC2}/n$ (Figure 11b):

$$B_M = \frac{\Delta B_1 + \Delta B_2}{2} = \frac{1}{4N_1 S_c}\left[U_{DC1}\frac{T_S}{2} + \frac{U_{DC2}}{n} t_B\right], \tag{54}$$

- if $U_{DC1} < U_{DC2}/n$ (Figure 11c):

$$B_M = \frac{\Delta B_1 + \Delta B_2}{2} = \frac{1}{4N_1 S_c}\left[U_{DC1} t_B + \frac{U_{DC2}}{n}\frac{T_S}{2}\right], \tag{55}$$

where S_C is a cross-sectional area of the core.

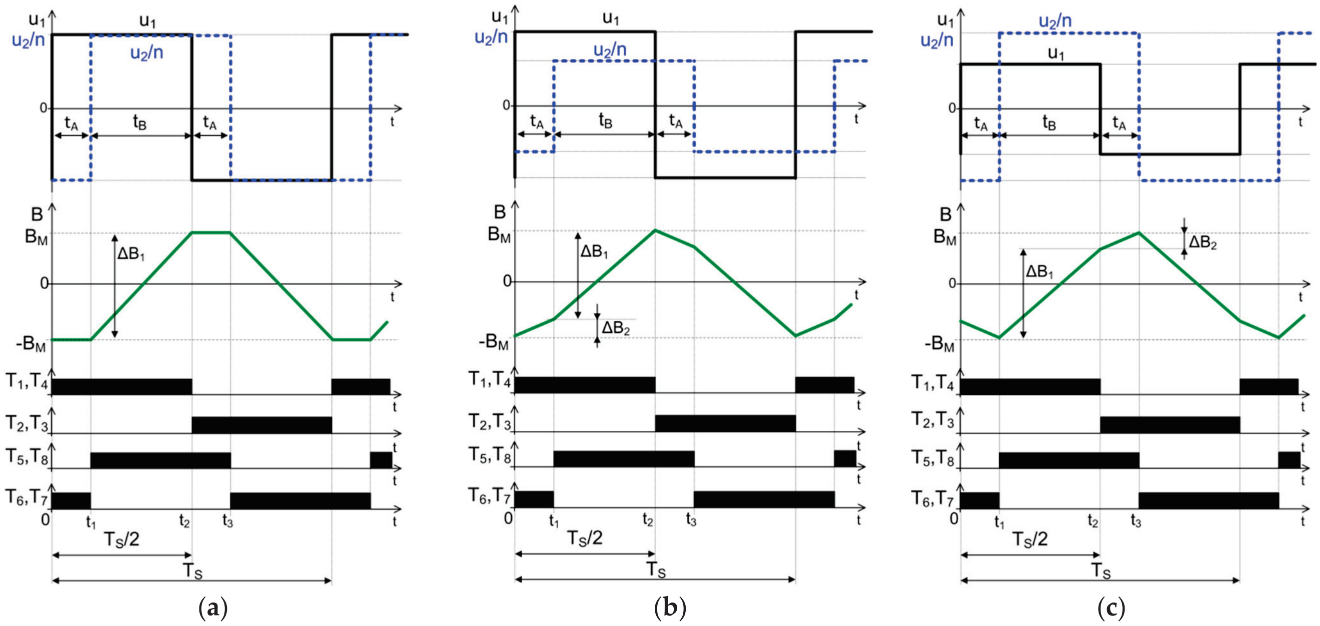

Figure 11. Simplified waveforms of voltages u_1, u_2/n and magnetic induction B for (**a**) $U_{DC1} = U_{DC2}/n$; (**b**) $U_{DC1} > U_{DC2}/n$; (**c**) $U_{DC1} < U_{DC2}/n$.

To simplify the estimation of the transformer windings' power loss P_{CU}, calculations may be performed for the windings' resistance measured for the switching frequency $f_S = 1/T_S$ and the rms value of the windings' currents according to the formula [32]:

$$P_{\mathrm{CU(prim)}} + P_{\mathrm{CU(sec)}} = R_{\mathrm{CU(prim)}} \cdot I^2_{1\mathrm{(rms)}} + R_{\mathrm{CU(sec)}} \cdot I^2_{2\mathrm{(rms)}}, \tag{56}$$

where $R_{CU(prim)}$, $R_{CU(sec)}$ are the resistances of the transformer windings (respectively at the H_1 bridge side and H_2 bridge side) measured for the switching frequency f_S; $I_{1(rms)}$ is the rms value of the transformer current at the bridge H_1 side; $I_{2(rms)}$ is the rms value of the transformer current at the bridge H_2 side given by:

$$I_{2(rms)} = \frac{I_{1(rms)}}{n} = \frac{1}{n}\sqrt{\frac{2}{3T_S}\left[\frac{I_3^3 + I_2^3}{I_3 + I_2}t_A + \frac{I_3^3 - I_2^3}{I_3 - I_2}t_B\right]}. \tag{57}$$

6. Validation

The parameters that are required for DAB converter efficiency calculation using the proposed approach were collated and are explained in Table 1. The described approach was validated by a comparison of the estimated DAB efficiency characteristics with the experimental ones measured for the converter, whose parameters are shown in Table 2. To measure the input P_{IN} and output P_{OUT} power (Figure 12) of the tested DAB converter, a Yokogawa WT5000 precision power analyzer was used. Importantly, the experimental measurements were performed for the DAB converter in a basic configuration without any additional sub-circuits (e.g., start-up resistors were disconnected). Voltages U_{DC1} and U_{DC2} were kept at a constant level U_{DC1} = 670 V and U_{DC2} = 385 V and the output P_{OUT} power was controlled by changes in the load resistance R_L. In the applied laboratory conditions, the maximum output power was limited to 5 kW due to the limitation of the measurement range of the used power analyzer. Waveforms of the current i_1 and voltage u_1 in the AC circuit were measured using a Tektronix DPO3034 oscilloscope equipped with the high-voltage differential probe P5210A and the current probe TCP404XL.

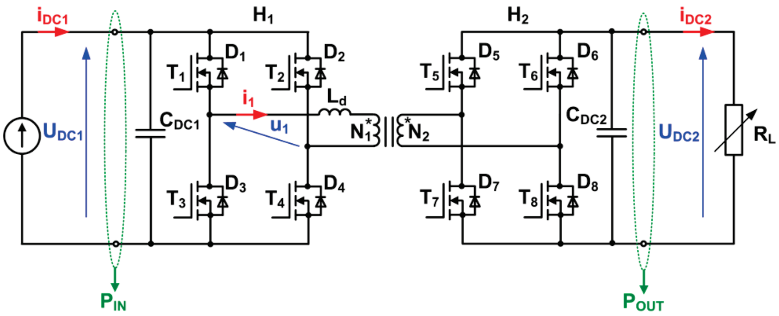

(**a**)

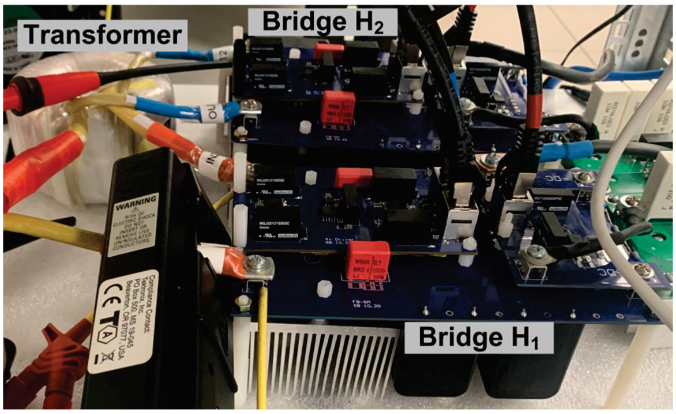

(**b**)

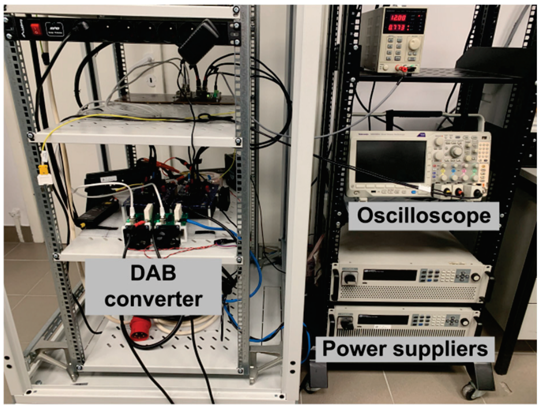

(**c**)

Figure 12. Laboratory setup for the experimental tests: (**a**) Scheme; (**b**) tested DAB converter; (**c**) laboratory stand.

Table 1. The parameters required for the DAB efficiency estimation.

Parameter	Explanation
P_{OUT}	Output power [W]
U_{DC1}	Input voltage [V]
U_{DC2}	Output voltage [V]
$n = N_1/N_2$	Transformer turns ratio
T_S	Switching period [s]
L_d	Inductance of the additional inductor [-]
$L_{\delta 1}$	Leakage inductance of transformer winding at the H_1 bridge side [-]
$L_{\delta 2}$	Leakage inductance of transformer winding at the H_2 bridge side [-]
$U_{DS(N)}$	Rated value of MOSFET drain–to–source voltage [V]
$I_{D(N)}$	Rated value of MOSFET drain current [A]
U_{FO}	Diode threshold voltage [V]
r_D	Diode dynamic resistance [Ω]
C_{iss}	MOSFET input capacitance [F]
C_{rss}	MOSFET reverse transfer capacitance [F]
R_G	MOSFET external gate resistance [Ω]
U_{DR}	MOSFET gate driver voltage [V]
$U_{GS(TH)}$	MOSFET gate threshold voltage [V]
$U_{GS(P)}$	Minimal value of the MOSFET gate-to-source voltage enabling the conduction of load current I_O [V]
$t_{RR(N)}$	Nominal value of the diode D_Z reverse recovery time measured for the nominal load current $I_{O(N)}$ [s]
$A_{iDZ(N)}$	Nominal derivative with time of the diode current during reverse recovery current measurement [A/s]
$I_{RM(N)}$	Diode nominal reverse current measured for $A_{iDZ(N)}$ and $I_{O(N)}$
f	Induction frequency [Hz]
B_M	Induction peak value [T]
T_C	Transformer core temperature [°C]
V_C	V_C—core volume [cm^3]

Table 2. The DAB converter specifications.

Parameter	Specification
Rated output power	5 kW
U_{DC1}	670 V
U_{DC2}	385 V
T_1–T_8, D_1–D_8	F4-23MR12W1M1_B11 (Infineon)
Switching frequency	50 kHz
N_1/N_2	33/18
Transformer	3C95 ferrite core (SMA Magnetics) $O_D = 87/I_D = 5\ 6/H = 50$ mm
L_d	25 µH

At the first step, the accuracy of the input current average value estimation $I_{DC1(av)}$ was evaluated. For the known values of the output power P_{OUT} and voltage U_{DC2}, based on Equations (7)–(10), the average value of the input current was calculated and compared with the experimental results. The maximum noted difference between the estimated and measured values did not exceed 10% and the accuracy increased with the growth in the output power and input current value (Figure 13). Crucially, the proposed analytical approach was simplified, so the impact of some factors (e.g., time dead influence) was not factored in. As a result, the accuracy of the estimation at a lower level of load may be worse.

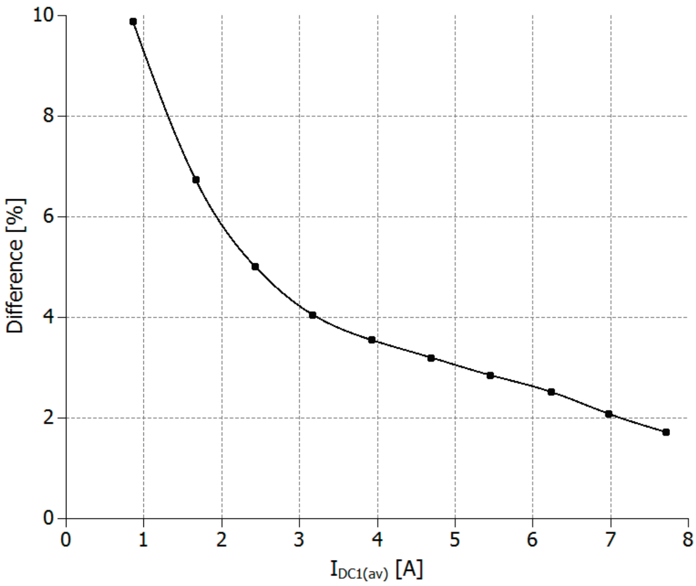

Figure 13. Difference between the measured and estimated average value of the input current i_{DC1}.

A similar conclusion may be drawn for the comparison of the DAB estimated and measured energy efficiency characteristics (Figure 14). The estimated η (P_{OUT}) characteristic followed the shape of the measured one with the highest accuracy noted for the output power exceeding 50% of the maximum out-power. The maximum noted efficiency for the tested DAB converter in a specific range of output power up to 5 kW reached 98%, which was confirmed by both the experimental and analytical results.

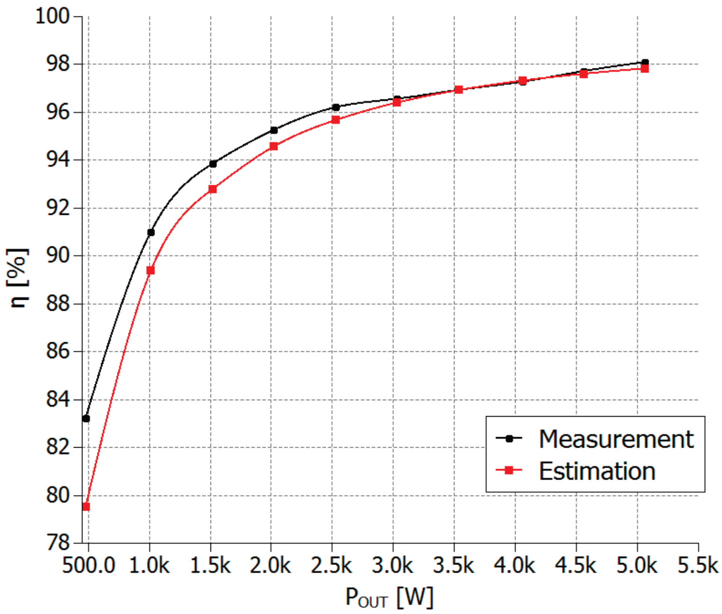

Figure 14. The estimated and measured energy efficiency characteristics of the tested DAB converter.

The application of the proposed analytical method enabled an estimation of the power loss distribution for the main converter components. Based on the estimated characteristics presented in Figure 15, it can be stated that the power losses were mainly generated in bridges H_1 and H_2. Notably, the considered DAB converter operated in conditions that correlated with the theoretical current and voltage waveforms presented in Figure 4a. As a result, transistors T_1–T_4 were turned on under hard-switching conditions with current $I_1 > 0$ and $I_1 = -I_3$. Thus, the commutation power losses in bridge H_1 resulted from the transistor's turn-on process and the reverse recovery process of diodes D_1–D_4. Because value I_1 decreases with the growth of the DAB output power (Figure 16), the commutation losses in bridge H_1 also decrease, so, as a consequence, the bridge H_1 total power loss P_{H1} is reduced.

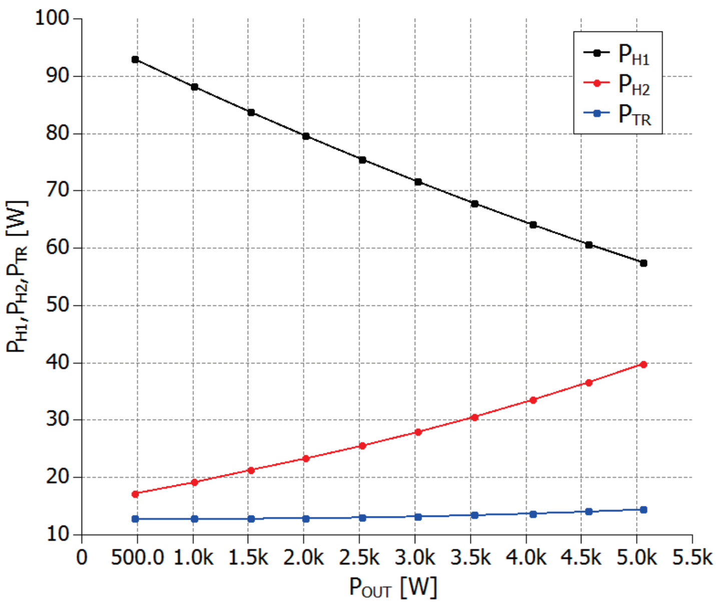

Figure 15. The estimated power loss distribution of the tested DAB converter.

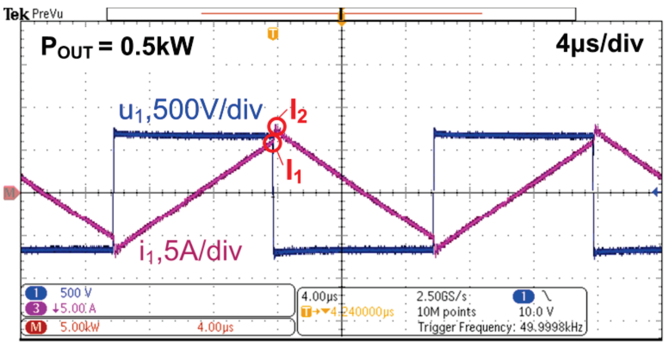

(**a**) (**b**)

Figure 16. Experimental waveforms of the current i_1 and voltage u_1 measured for: (**a**) P_{OUT} = 0.5 kW; (**b**) P_{OUT} = 2 kW.

From Figure 4a, T_5–T_8 were turned off under hard-switching conditions with the current determined by the value of $I_2/n = -I_4/n$. Similarly, since the I_2 value increased with the growth of the out-power P_{OUT} (Figure 16), the transistor's commutation losses increased, so in bridge H_2, the total power loss P_{H2} grew. From Figure 15, the transformer loss P_{TR} obtained using Equation (49) was significantly lower than the losses noted for bridges H_1 and H_2.

Losses generated in each of the bridges H_1 and H_2 were mainly determined by switching losses, however, the share of conduction losses increased with the growth in the DAB converter output power, which resulted from Equations (14) and (15) (Figure 17).

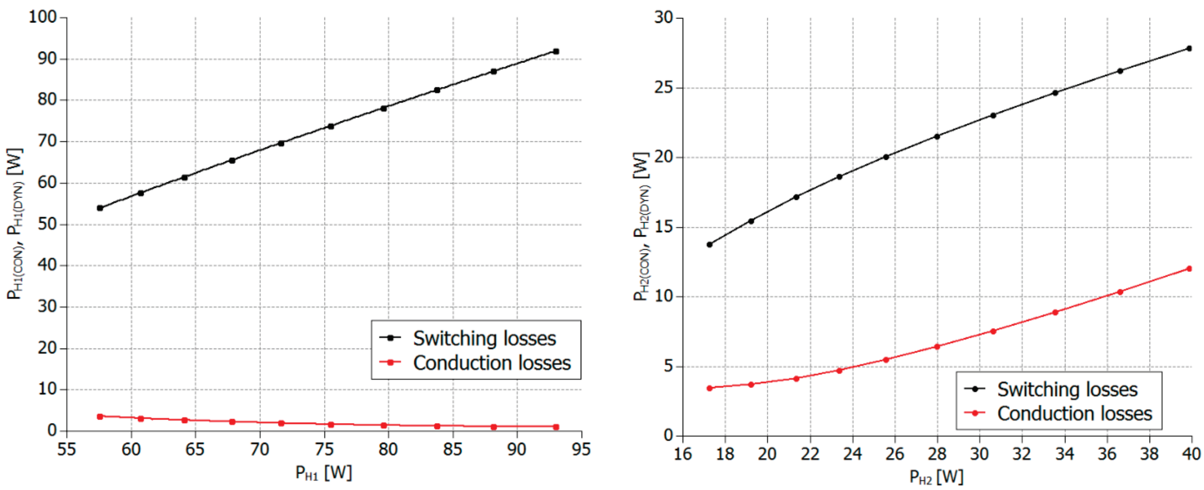

(**a**) (**b**)

Figure 17. Estimated power loss distribution in the considered DAB converter bridges: (**a**) bridge H_1; (**b**) bridge H_2.

Based on the results of the analytical calculation, transformer losses P_{TR} are determined by the loss in the core P_{FE} (Figure 18). In the tested DAB converter, for the specified range of output power up to 5 kW, the value t_B changed within a small range (coefficient $t_B/(0.5T_S)$ does not fall below 0.95), hence, according to Equations (50)–(55), a slight reduction in the core loss P_{FE} was observed. The windings' total power loss P_{CU} depends on the rms value of the primary and secondary windings currents, so it should grow with the increase in the DAB converter output power, which was confirmed by the results of the analytical calculations.

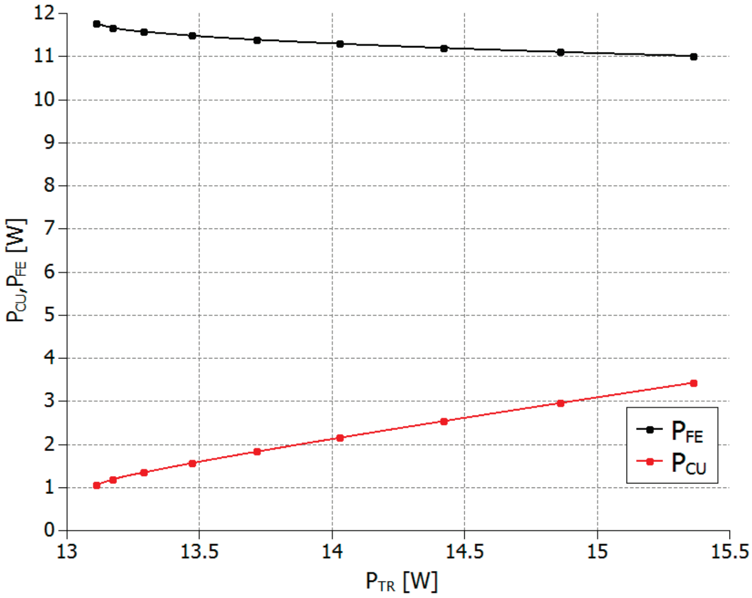

Figure 18. The estimated transformer power loss distribution in the DAB converter.

The presented calculations were also performed for the case when energy was transmitted from bridge H_2 to H_1. In this case, the obtained analytical characteristic $\eta(P_{OUT})$ was also confirmed by the results of the experimental measurements, which validated the adopted approach (Figure 19). Moreover, the results of a detailed analysis of power loss distribution were also convergent with the description above.

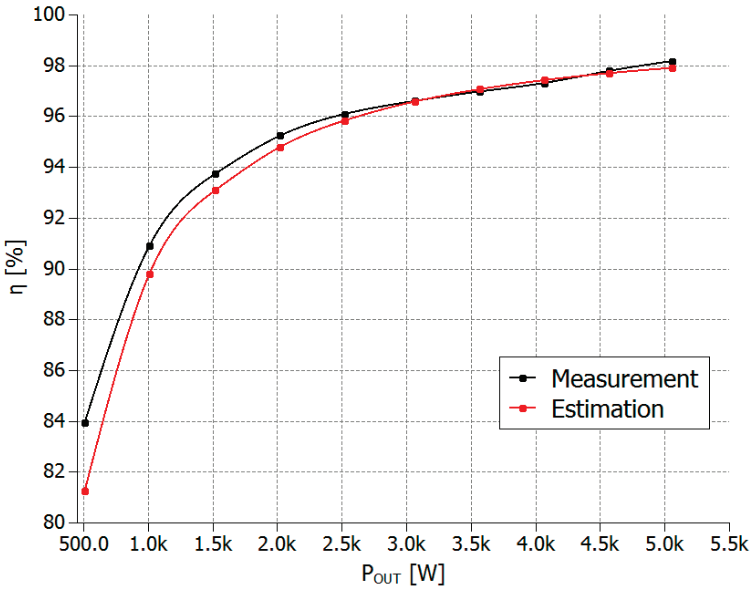

Figure 19. The estimated and measured energy efficiency characteristics of the tested DAB converter for the case when energy is transferred from bridge H_2 to H_1.

Obtained results were compared with ones calculated using the approach proposed in [19]. Adapting this solution is not time-consuming, and all of the required parameters may be obtained based on the manufacturer's datasheet. However, in [19], no methods of transformer loss estimation were proposed, so in both approaches, the same setup of equations based on Steinmetz's formula was used to evaluate the transformer losses. Using both of the compared methods, the obtained efficiency characteristics, calculated for the case when energy was transferred from bridge H_1 to H_2, are presented in Figure 20a. Higher accuracy of the proposed solution was noted, especially for the light load of the converter.

At higher loads, the predominance of the proposed method was also distinguishable. However, the difference between the measured and estimated results using the approach in [19] decreased with the growth in the output power P_{OUT}. One of the main assumptions of the method in [19] is that all transistors are switched-on under soft conditions. It should be noted that considering the assumed direction of energy flow, the transistors in bridge H_1 are turned on under hard-switching conditions. As a result of the transistors' turn-on power losses omission, the total losses of bridge H_1 were underestimated, as presented in Figure 20b. Both compared methods enabled the estimation of the transistors' turn-off losses. However, to simplify the calculations, in the method [19], constant values of the current fall time were assumed. For the converter light load, the obtained power losses of bridge H_2 were comparable. However, the difference between the calculated results slightly increased with the growth in the output power P_{OUT}.

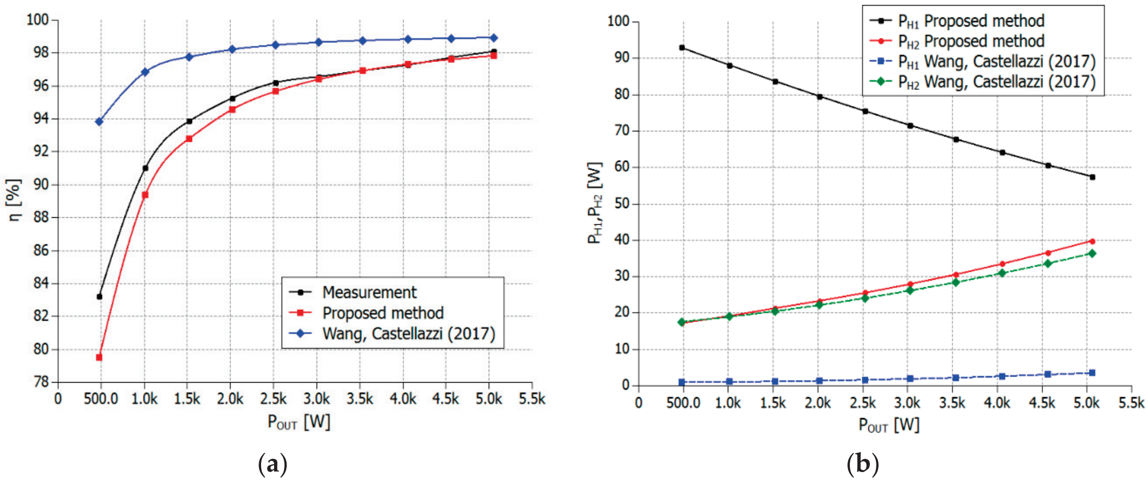

Figure 20. Comparison of the results obtained using the proposed method and approach presented by Wang and Castellazzi in [19]: (**a**) estimated and measured energy efficiency characteristics of the tested DAB converter; (**b**) power loss characteristics of bridges H_1 and H_2.

7. Conclusions

In this paper, an analytical method of power loss estimation in a single-phase DAB converter controlled with a SPS modulation scheme is presented. The obtained results of the calculations were confirmed by the results of the measurements, which proved the correctness of the adopted approach. The method of optimizing the efficiency of the DAB converter proposed and confirmed in the simulation tests can be used in the process of designing converters at the HW level. The proposed method will allow us to complete the calculation of the correct operating point of the system, which will reduce the risk of failure by reducing the operating temperature of the transistors and passive components. Future studies will be focused on the validation of the presented method in a three-phase DAB converter and for DAB converters driven with other switching schemes.

Author Contributions: Conceptualization, M.T., S.B. and M.J.; Methodology, M.T., S.B. and S.P.; Validation, M.T., S.B., M.R. and S.P.; Formal analysis, M.T., M.J. and H.-J.C.; Investigation, M.T., S.B., M.R., M.J. and S.P.; Resources, M.T., S.B., M.R., S.-H.K. and Y.-C.C.; Data curation, M.T., M.J. and H.-J.C.; Writing—original draft preparation, M.T., M.J. and H.-J.C.; Writing—review and editing, M.T., M.J., S.B., S.P., H.-J.C., S.-H.K. and Y.-C.C.; Visualization, M.T. and S.B.; Supervision, M.T. and M.J.; Project administration, M.J and H.-J.C.; Funding acquisition, M.J. All authors have read and agreed to the published version of the manuscript.

Funding: This research was funded by the National Center for Research and Development, and the National Science and Technology Council of Taiwan, Grant NSTC 111-2622-8-011-014-SB within the framework of the project entitled Poland–Taiwan cooperation POLTAJ VII 7th competition Path 1.

Conflicts of Interest: The authors declare no conflict of interest.

References

1. Han, W.; Ma, R.; Liu, Q.; Corradini, L. A conduction losses optimization strategy for DAB converters in wide voltage range. In Proceedings of the IECON 2016-42nd Annual Conference of the IEEE Industrial Electronics Society, Florence, Italy, 23–26 October 2016; pp. 2445–2451. [CrossRef]
2. Zeng, J.; Rao, Y.; Lan, Z.; He, D.; Xiao, F.; Liu, B. Multi-Objective Unified Optimal Control Strategy for DAB Converters with Triple-Phase-Shift Control. *Energies* **2021**, *14*, 6444. [CrossRef]
3. Zhu, M.; Shao, C.; Wang, S.; Hang, L.; He, Y.; Fan, S. System Design of Dual Active Bridge (DAB) Converter Based on GaN HEMT Device. In Proceedings of the 2019 22nd International Conference on Electrical Machines and Systems (ICEMS), Harbin, China, 11–14 August 2019; pp. 1–6. [CrossRef]
4. Xu, X.; Bao, G.; Ma, M.; Wang, Y. Multi-Objective Optimization Phase-Shift Control Strategy for Dual-Active-Bridge Isolated Bidirectional DC-DC Converter. *Inf. MIDEM J. Microelectron. Electron. Compon. Mater.* **2021**, *51*, 179. [CrossRef]
5. Hoang, K.D.; Wang, J. Design optimization of high frequency transformer for dual active bridge DC-DC converter. In Proceedings of the 2012 XXth International Conference on Electrical Machines, Marseille, France, 2–5 September 2012; pp. 2311–2317. [CrossRef]
6. Yao, P.; Jiang, X.; Xue, P.; Li, S.; Lu, S.; Wang, F. Design Optimization of Medium-Frequency Transformer for DAB Converters with DC Bias Capacity. *IEEE J. Emerg. Sel. Top. Power Electron.* **2020**, *9*, 5043–5054. [CrossRef]
7. Xiao, Y.; Zhang, Z.; Andersen, M.A.E.; Sun, K. Impact on ZVS Operation by Splitting Inductance to Both Sides of Transformer for 1-MHz GaN Based DAB Converter. *IEEE Trans. Power Electron.* **2020**, *35*, 11988–12002. [CrossRef]
8. Yan, H.; Zhao, W.; Buticchi, G.; Gerada, C. Active Thermal Control for Modular Power Converters in Multi-Phase Permanent Magnet Synchronous Motor Drive System. *IEEE Access* **2021**, *9*, 7054–7063. [CrossRef]
9. Mukunoki, Y.; Horiguchi, T.; Nakayama, Y.; Nishizawa, A.; Nakamura, Y.; Konno, K.; Kuzumoto, M.; Akagi, H. Modeling of a silicon-carbide MOSFET with focus on internal stray capacitances and inductances, and its verification. In Proceedings of the 2017 IEEE Applied Power Electronics Conference and Exposition (APEC), Tampa, FL, USA, 26–30 March 2017; pp. 2671–2677. [CrossRef]
10. Zhuolin, D.; Dong, Z.; Tao, F.; Xuhui, W. A simple SiC power MOSFET model. In Proceedings of the IECON 2017-43rd Annual Conference of the IEEE Industrial Electronics Society, Beijing, China, 29 October 2017–1 November 2017; pp. 704–708. [CrossRef]
11. Rabkowski, J.; Płatek, T. A study on power losses of the 50 kVA SiC converter including reverse conduction phenomenon. *Bull. Pol. Acad. Sci. Tech. Sci.* **2016**, *64*, 907–914. [CrossRef]
12. Kolar, J.; Zach, F.; Casanellas, F. Losses in PWM inverters using IGBTs. *IEE Proc. Electr. Power Appl.* **1995**, *142*, 285–288. [CrossRef]
13. Meng, Z.; Wang, Y.-F.; Yang, L.; Li, W. Analysis of Power Loss and Improved Simulation Method of a High Frequency Dual-Buck Full-Bridge Inverter. *Energies* **2017**, *10*, 311. [CrossRef]
14. Mestha, L.K.; Evans, P.D. Optimisation of losses in PWM inverters. In Proceedings of the Third International Conference on Power Electronics and Variable-Speed Drives, London, UK, 13–15 July 1988; pp. 394–397.
15. Gopalan, A. Calculating Power Dissipation for a H-Bridge or Half Bridge Driver. 2022. Available online: https://www.ti.com/lit/an/slva504a/slva504a.pdf (accessed on 1 October 2022).
16. Barlik, R.; Nowak, M.; Grzejszczak, P. Power transfer analysis in a single phase dual active bridge. *Bull. Pol. Acad. Sci. Tech. Sci.* **2013**, *61*, 809–828. [CrossRef]
17. Saha, J.; Gorla, N.B.Y.; Subramaniam, A.; Panda, S.K. Analysis of Modulation and Optimal Design Methodology for Half-Bridge Matrix-Based Dual-Active-Bridge (MB-DAB) AC–DC Converter. *IEEE J. Emerg. Sel. Top. Power Electron.* **2021**, *10*, 881–894. [CrossRef]
18. De Freitas Lima, G.; Lembeye, Y.; Ndagijimana, F.; Crebier, J.-C. Modeling of a DAB under phase-shift modulation for design and DM input current filter optimization. In Proceedings of the 2020 22nd European Conference on Power Electronics and Applications (EPE'20 ECCE Europe), Lyon, France, 7–11 September 2020; pp. P.1–P.10. [CrossRef]
19. Wang, Z.; Castellazzi, A. Device loss model of a fully SiC based dual active bridge considering the effect of synchronous rectification and deadtime. In Proceedings of the 2017 IEEE Southern Power Electronics Conference (SPEC), Puerto Varas, Chile, 4–7 December 2017; pp. 1–7. [CrossRef]
20. Jean-Pierre, G.; Altin, N.; El Shafei, A.; Nasiri, A. Overall Efficiency Improvement of a Dual Active Bridge Converter Based on Triple Phase-Shift Control. *Energies* **2022**, *15*, 6933. [CrossRef]
21. Krismer, F.; Kolar, J.W. Accurate Power Loss Model Derivation of a High-Current Dual Active Bridge Converter for an Automotive Application. *IEEE Trans. Ind. Electron.* **2009**, *57*, 881–891. [CrossRef]
22. Das, A.K.; Fernandes, B.G. Fully ZVS, Minimum RMS Current Operation of Isolated Dual Active Bridge DC-DC Converter Employing Dual Phase-Shift Control. In Proceedings of the 2019 21st European Conference on Power Electronics and Applications (EPE '19 ECCE Europe), Genova, Italy, 3–5 September 2019; pp. P.1–P.10. [CrossRef]
23. Calderon, C.; Barrado, A.; Rodriguez, A.; Alou, P.; Lazaro, A.; Fernandez, C.; Zumel, P. General Analysis of Switching Modes in a Dual Active Bridge with Triple Phase Shift Modulation. *Energies* **2018**, *11*, 2419. [CrossRef]
24. Guzmán, P.; Vázquez, N.; Liserre, M.; Orosco, R.; Castillo, S.E.P.; Hernández, C. Two-Stage Modulation Study for DAB Converter. *Electronics* **2021**, *10*, 2561. [CrossRef]

25. Zhang, H.; Isobe, T. An Improved Charge-Based Method Extended to Estimating Appropriate Dead Time for Zero-Voltage-Switching Analysis in Dual-Active-Bridge Converter. *Energies* **2022**, *15*, 671. [CrossRef]
26. Ahmed, R.M.; Todd, R.; Forsyth, A.J. Predicting SiC MOSFET Behavior Under Hard-Switching, Soft-Switching, and False Turn-On Conditions. *IEEE Trans. Ind. Electron.* **2017**, *64*, 9001–9011. [CrossRef]
27. Agrawal, B.; Preindl, M.; Bilgin, B.; Emadi, A. Estimating switching losses for SiC MOSFETs with non-flat miller plateau region. In Proceedings of the 2017 IEEE Applied Power Electronics Conference and Exposition (APEC), Tampa, FL, USA, 26–30 March 2017; pp. 2664–2670. [CrossRef]
28. Naseri, F.; Farjah, E.; Ghanbari, T. KF-based estimation of diode turn-off power loss using datasheet information. *Electron. Lett.* **2019**, *55*, 1082–1084. [CrossRef]
29. Kundu, U.; Sensarma, P. Accurate Estimation of Diode Reverse-Recovery Characteristics from Datasheet Specifications. *IEEE Trans. Power Electron.* **2018**, *33*, 8220–8225. [CrossRef]
30. Jahdi, S.; Alatise, O.; Bonyadi, R.; Alexakis, P.; Fisher, C.A.; Gonzalez, J.A.O.; Ran, L.; Mawby, P. An Analysis of the Switching Performance and Robustness of Power MOSFETs Body Diodes: A Technology Evaluation. *IEEE Trans. Power Electron.* **2014**, *30*, 2383–2394. [CrossRef]
31. Yin, S.; Liu, Y.; Liu, Y.; Tseng, K.J.; Pou, J.; Simanjorang, R. Comparison of SiC Voltage Source Inverters Using Synchronous Rectification and Freewheeling Diode. *IEEE Trans. Ind. Electron.* **2017**, *65*, 1051–1061. [CrossRef]
32. Barlik, R.; Nowak, M.; Grzejszczak, P.; Zdanowski, M. Analytical description of power losses in a transformer operating in the dual active bridge converter. *Bull. Pol. Acad. Sci. Tech. Sci.* **2016**, *64*, 561–574. [CrossRef]
33. Rodriguez-Sotelo, D.; Rodriguez-Licea, M.A.; Araujo-Vargas, I.; Prado-Olivarez, J.; Barranco-Gutiérrez, A.-I.; Perez-Pinal, F.J. Power Losses Models for Magnetic Cores: A Review. *Micromachines* **2022**, *13*, 418. [CrossRef] [PubMed]

energies

Article

A Fault-Tolerant Strategy for Three-Level Flying-Capacitor DC/DC Converter in Spacecraft Power System †

Haijin Li [1,*], Yu Gu [2], Xiaofeng Zhang [1], Zhigang Liu [1], Longlong Zhang [3] and Yi Zeng [1]

1 Beijing Institute of Spacecraft System Engineering, Beijing 100094, China
2 School of Mechanical Engineering and Automation, Harbin Institute of Technology (Shenzhen), Shenzhen 518055, China
3 Department of Electrical Engineering, China University of Petroleum (East China), Qingdao 266580, China
* Correspondence: haijinli@126.com
† This paper is an extended version of our paper published in 2022 IEEE International Power Electronics and Application Conference and Exposition (PEAC), Guangzhou, China, 4–7 November 2022; pp. 1620–1625.

Abstract: With the development of space exploration, high-power and high-voltage power systems are essential for future spacecraft applications. Because of the effects of space radiation such as single event burnout (SEB), the rated voltage of power devices in converters for a spacecraft power system is limited to a level much lower than that for traditional ground applications. Thus, multi-level DC/DC converters are good choices for high-voltage applications in spacecraft. In this paper, a fault-tolerant strategy is proposed for a three-level flying capacitor DC/DC converter to increase the reliability with minimal cost. There is no extra hardware needed for the proposed strategy; the fault tolerance of the converter is only achieved by changing the software control strategy. A stage analysis of the proposed strategy is provided in detail for different fault locations and ratios between the input and output voltage. Finally, a simulation model and prototype are built to verify the effectiveness of the proposed strategy.

Keywords: fault-tolerant strategy; high voltage; three level; flying capacitor; DC/DC converter; spacecraft power system

1. Introduction

The architecture of a high-power spacecraft distributed power system is shown in Figure 1. The spacecraft power system is a typical DC power system [1,2]. It consists of solar arrays, batteries, a fuel cell, flying wheel, power converters, etc. The solar arrays provide the power for the load and charge the battery during the sunlight period of the orbit. Storages such as batteries provide the power for the load during the eclipse period of the orbit. The power converters are used to regulate the DC bus voltage and control the battery charging and discharging. With the development of space exploration, the power capacity of spacecraft has become larger and larger, and the voltage level of the spacecraft power system has become higher and higher. Currently, high voltage and high power are the trends and necessary factors for a spacecraft power system to meet the requirements of future spacecraft, such as high-power SAR satellites, electric propulsion spacecraft, deep space spacecraft, space stations, and space solar energy power stations, etc. [3] The power ratings of these spacecraft will need to be larger than 100 kW, and the voltage level will need to be higher than 1000 V. However, the current power converters cannot meet the requirements of this high-voltage application. The characteristics of the power device in space are obviously different from that on the ground. Due to space radiation effects such as single event burnout, the high-voltage power device is the main limitation for spacecraft power converters. Currently, the available voltage of power devices such as power MOSFETs for spacecraft power converters is lower than 500 V. However, the requirement of the output voltage of converters is much higher than 500 V for future space applications. In order to solve the mismatch between future high-voltage applications and the available low-voltage power devices, the multi-level DC/DC converter is a better solution for these high-voltage applications with the voltage limitation of the power devices. Even though they are not used in traditional spacecraft power systems in which the highest DC bus voltage is 100 V, these converters are widely used in ground high-voltage applications. The voltage stress of the power devices in a multi-level DC/DC converter can clearly be reduced [4–10]. For multi-level DC/DC converters, the number of power devices is relatively larger than the traditional two-level converter. Each failure of the power device may cause the output interruption of the converter, so the reliability of the multi-level DC/DC converter is relatively low without a fault-tolerant strategy [11–16]. In addition, the reliability of the converter is very important for the spacecraft. The failure of the converter will result in huge losses, especially for an unmanned spacecraft. Thus, the fault-tolerant strategy is very important for the multi-level converter in a spacecraft power system. Fault-tolerant schemes of multi-level DC/DC converters have been proposed by researchers [14–20]. The redundant subsystem, units, circuits, or devices have been added to multi-level converters to improve their reliability [14,15,17,18]. The fuse is a common component that is used to isolate the short-circuit fault parts of the converter. The main disadvantage of the fuses is that the blowing time of a fuse is difficult to control. Moreover, the use of a fuse will increase the parasitic inductance of the commutation loops of the converter, and larger parasitic inductance causes a higher voltage stress, which reduces the reliability of power devices [19,20]. Additional hardware is needed for these former methods. However, the additional hardware increases the mass of the converter, which results in an obviously higher cost of the launch. For space application, the limitation of the mass of converters is extremely strict. A three-level flying capacitor DC/DC converter is the typical multi-level DC/DC converter. A fault-tolerant control strategy for three-level flying capacitor DC/DC converters is proposed in this paper. The reliability of the three-level DC/DC converter is improved with minimal cost. The fault tolerance of the converter is achieved by only changing the software strategy, and no extra hardware is needed. The concept of the fault-tolerant strategy can also be applied in other multi-level converters.

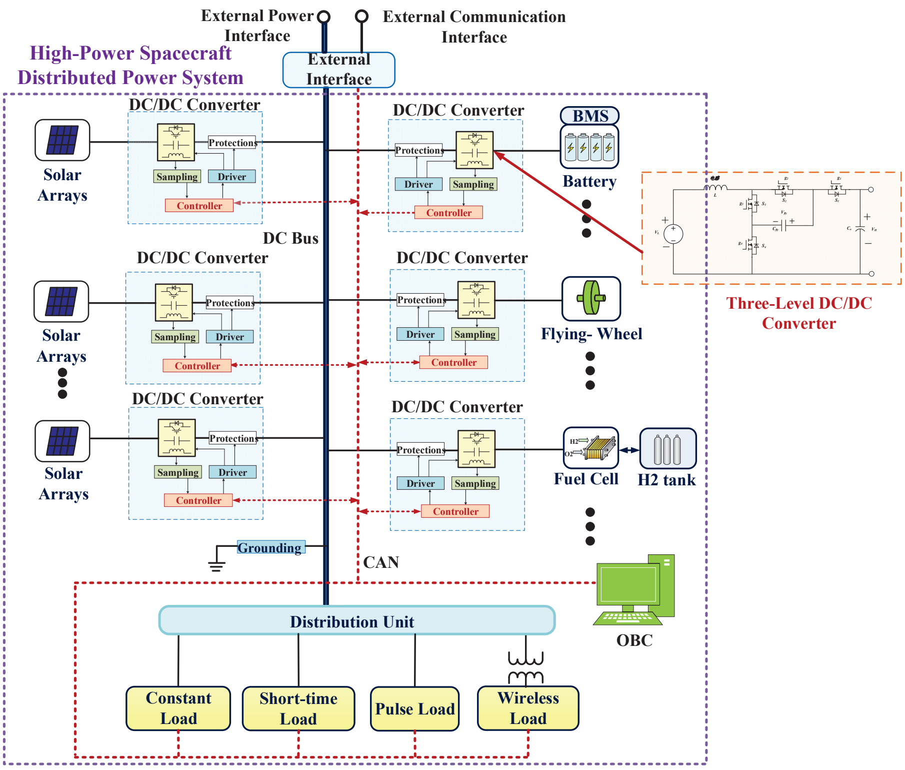

Figure 1. Typical high-power spacecraft distributed power system with DC/DC converters.

In Section 2, the control scheme of the fault-tolerant strategy for a three-level flying capacitor DC/DC converter is introduced. In Section 3, the stage analysis of the converter under short-circuit fault conditions is given in detail. In Section 4, the proposed strategy under different conditions is verified by experiments and simulations. Finally, the conclusions are summarized.

2. Control Scheme of Fault-Tolerant Strategy for Three-Level Flying Capacitor DC/DC Converter

In order to achieve the fault-tolerant operation of the three-level flying capacitor DC/DC converter after a short-circuit fault of the power devices, a seamless transfer control from three-level mode to two-level mode is designed. Before the fault, the converter operates in three-level mode, and after the fault, the converter operates in two-level mode. The control scheme of the proposed fault-tolerant strategy for a three-level flying capacitor DC/DC converter is shown in Figure 2.

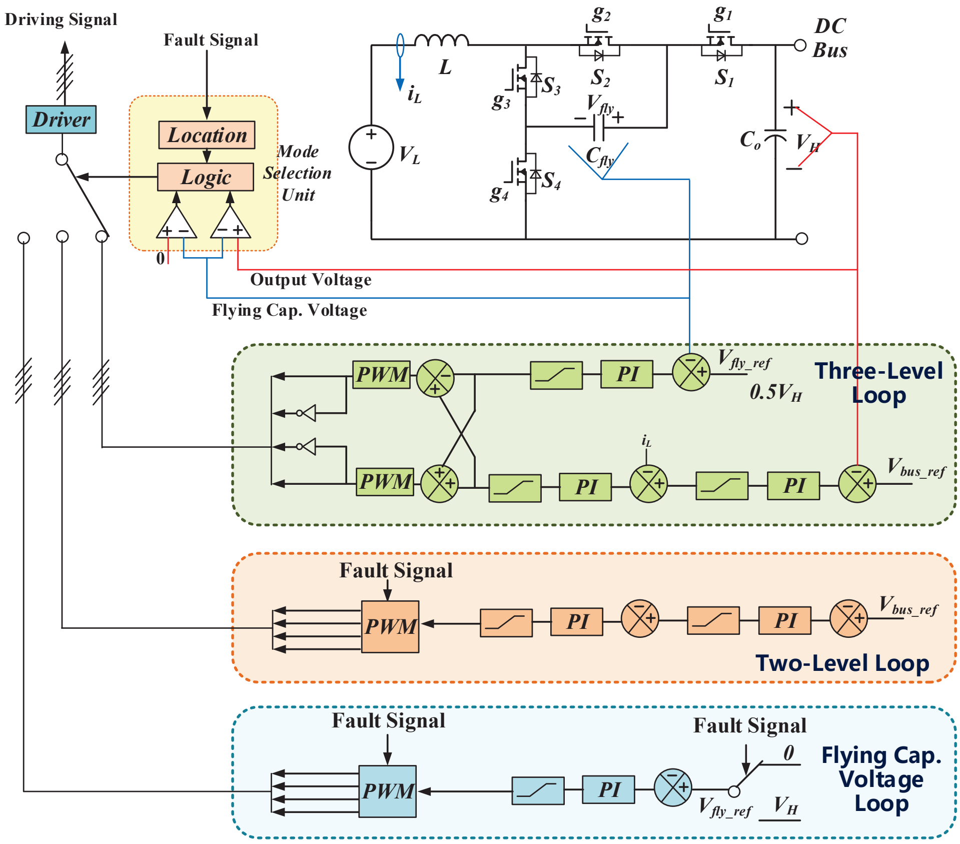

Figure 2. Control scheme of the fault-tolerant strategy for flying capacitor DC/DC converter.

The fault-tolerant strategy consists of three loops, including a three-level voltage regulation loop, a flying capacitor voltage loop, and a two-level voltage regulation loop. When the power devices of the converter are normal, the output voltage and flying capacitor voltage are regulated by a three-level voltage regulation loop. Output voltage and flying capacitor voltage are two control targets for the three-level voltage regulation loop. The reference of flying capacitor voltage is half of the reference of the output voltage of the converter. When a short-circuit fault of the power device occurs, the converter is regulated by the flying capacitor voltage loop after the short-circuit fault of the power device is detected. If a short-circuit fault of inner switch S_2 or S_3 occurs, the voltage reference of the flying capacitor changes from half of the output voltage to zero. The normal inner power devices are opened immediately, and the driver signals of the normal inner switches are set as low. If a short-circuit fault of outer switch S_1 or S_4 occurs, the reference of the flying capacitor voltage changes from half of the output voltage to the output voltage, and the driver signals of the normal outer switches are set as high. When the voltage of the flying capacitor reaches the reference value, the converter changes its mode to the two-level mode. If the inner switch is at fault, the driver of the other inner switch is set as high in the two-level mode. The driver signals of the two outer switches operate in the complementary state. If the outer switch is at fault, the driver of the other outer switch is set as high. The driver signals of the two inner switches operate in the complementary state.

3. Analysis of Operation Modes for the Converter under Short-Circuit Fault Conditions

According to the analysis of the flying capacitor three-level DC/DC converter, the operation stages of the converter are different between the situation in which the ratio of the input and output voltage is smaller than 0.5 ($V_L < 0.5\ V_H$) and the situation in which the ratio is larger than 0.5 ($V_L > 0.5\ V_H$).

The diagram in Figure 3 shows the key quantity for the situation in which the short-circuit fault occurs in switch S_3 when the ratio of the input and output voltage is smaller than 0.5 ($V_L < 0.5\ V_H$). When the short-circuit fault of switch S_3 is detected by the detection circuit, the converter is regulated from the three-level mode to the flying capacitor voltage control mode. The reference of the flying capacitor voltage decreases from half of the output voltage V_H to zero. The voltage of the flying capacitor is changed by the flying capacitor voltage loop from half of the output voltage to zero during this stage. After the voltage of the flying capacitor is detected to have reached zero, the converter finishes the flying capacitor voltage control mode and begins to operate in two-level mode.

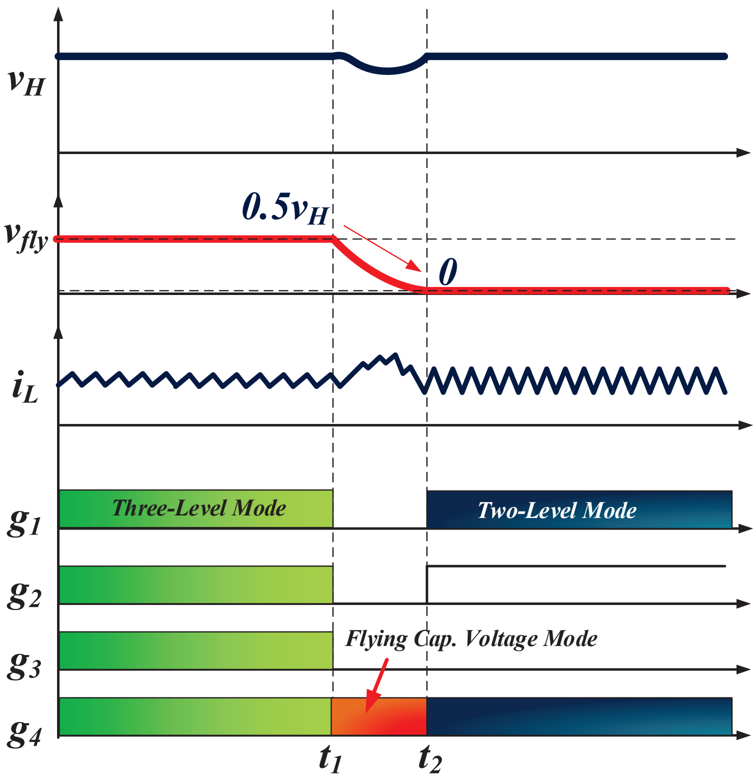

Figure 3. The diagram of the key quantity under the situation in which short-circuit fault occurs in switch S_3.

The analysis of operation stages under this fault situation is shown in Figure 4. The g_1, g_2, g_3, and g_4 are gate drivers of switches S_1, S_2, S_3, and S_4, respectively. When $V_L < 0.5\ V_H$, the duty cycle of inner switches g_3 and g_4 is larger than 0.5. The three-level mode is the pre-fault mode. The stages of the three-level mode are shown in Figure 5. There are four stages in the three-level mode. In the three-level mode, the driver signal of g_1 and g_4 are complementary, and the driver signal of g_2 and g_3 are complementary.

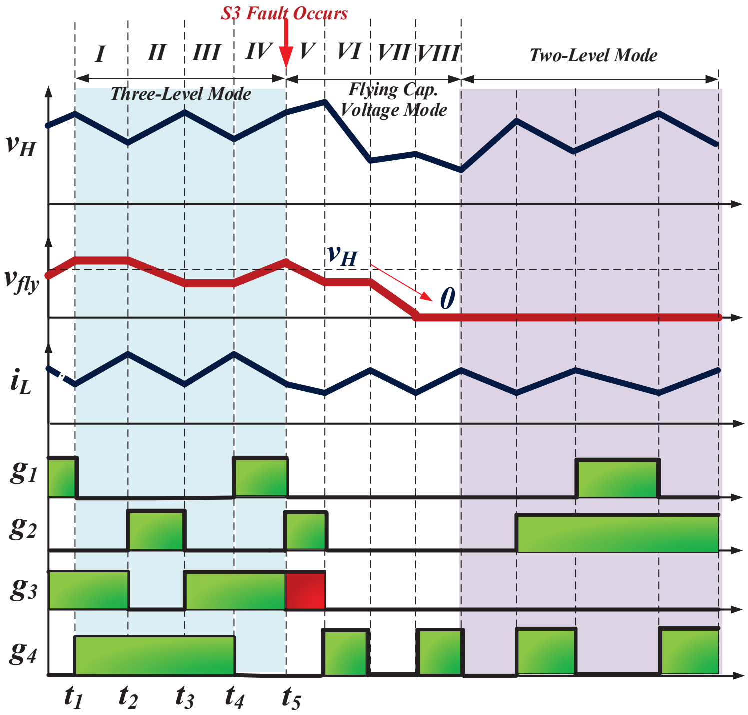

Figure 4. Stages analysis when short-circuit fault occurs in S_3 ($V_L < 0.5\ V_H$).

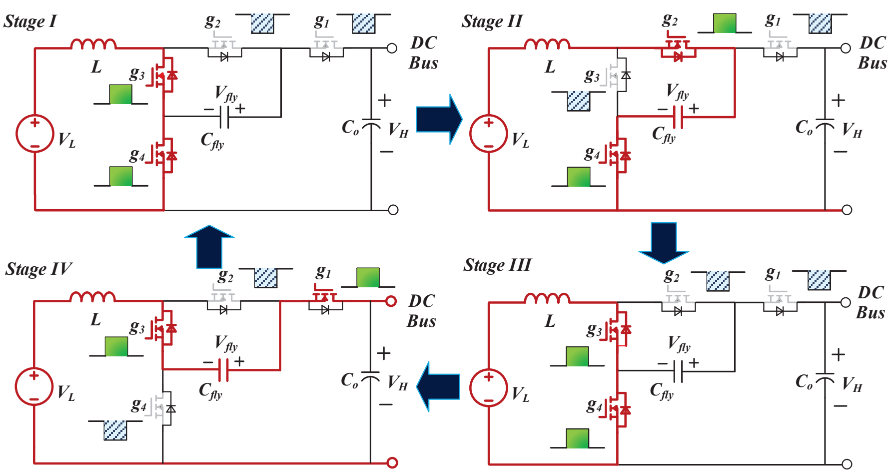

Figure 5. Stages of the three-level mode when $V_L < 0.5\ V_H$.

The stages during the flying capacitor voltage control mode are shown in Figure 6. There are also three stages after the short-circuit fault occurs. In Stage V, S_3 is short-circuited and S_2 turns on, then the flying capacitor is short-circuited. There is a large current spike occurring in S_2, so the fault is detected. After the fault is detected, the converter operates in Stage VI and VIII; in these two stages, g_4 is in the PWM state, and the values of g_1, g_2, and g_3 are 0 when the short-circuit fault occurs in S_3. Similarly, g_1 is in the PWM state, and the values of g_2, g_3, and g_4 are 0 when the short-circuit fault occurs in switch S_2. The two-level mode is the post-fault mode. In the two-level mode, the driver signal of g_1 and g_4 are complementary, and g_2 is set as 1 when the short-circuit fault occurs in switch S_3. Similarly, g_3 is set as 1 when S_2 is where the fault occurs.

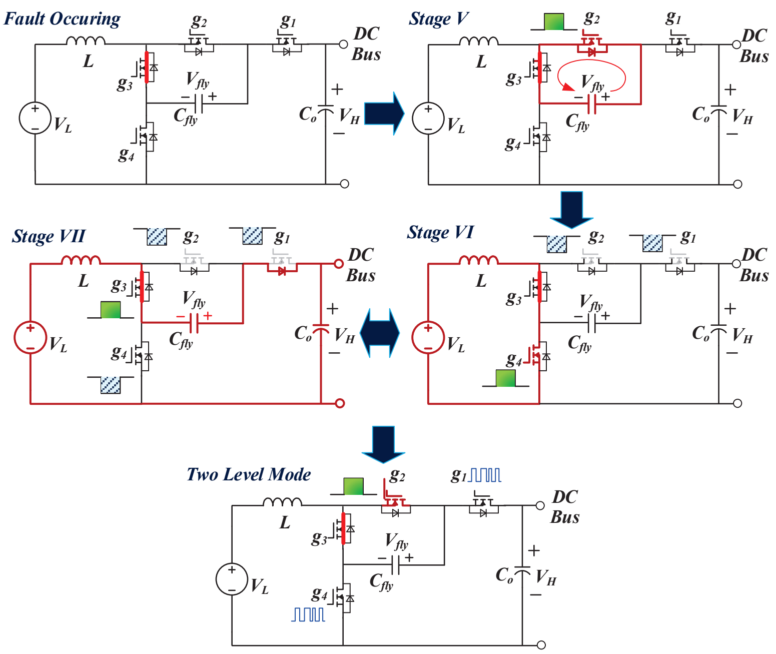

Figure 6. Stages of capacitor voltage control mode after short-circuit fault occurs in S_3.

The diagram in Figure 7 shows the key quantities under the situation in which the short-circuit fault occurs in the outer switch S_4 when V_L is lower than 0.5 V_H. Before the fault occurs, the converter operates in three-level mode. When the short-circuit fault of the switch S_4 is detected, the converter begins to operate in flying capacitor voltage control mode. The flying capacitor voltage is regulated gradually from half of the output voltage to output voltage. When the flying capacitor voltage reaches the output voltage, the converter turns to operate in two-level mode.

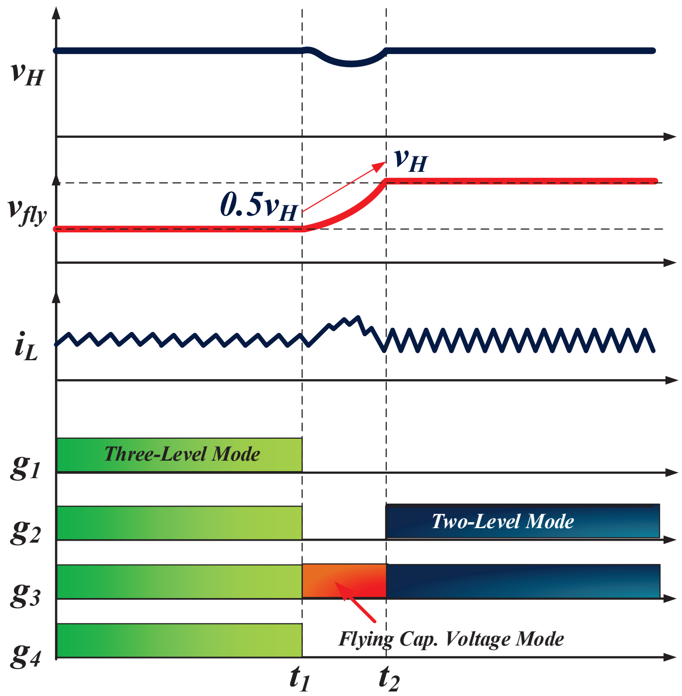

Figure 7. The diagram of the key quantity under the situation in which short-circuit fault occurs in switch S_4.

The stage analysis in this situation is shown in Figure 8. The stages of the three-level mode are the same as those in which the short-circuit fault of S_3 occurs. The stages of the flying capacitor voltage control mode after a short-circuit fault are shown in Figure 9. There are three stages after the short-circuit fault occurs in the outer switches. In Stage V of the flying capacitor voltage mode, g_4 is short-circuited and g_1 turns on; then the output capacitor is connected directly with the flying capacitor. Due to the existence of the voltage difference between the output voltage and the flying capacitor voltage, there is a current spike occurring in S_1, and the fault can be detected. After Stage V, the converter operates in Stages VI and VII. In these two stages, g_3 is in the PWM state, and g_1, g_2, and g_4 are 0 when the short-circuit fault occurs in S_4. Similarly, g_2 is in the PWM state, and g_1, g_3, and g_4 are 0 when the short-circuit fault occurs in S_1. In the two-level mode, the driver signal of g_2 and g_3 are complementary, and g_1 is set as 1 when the fault occurs in S_4. Similarly, g_4 is set as 1 when the fault occurs in S_1.

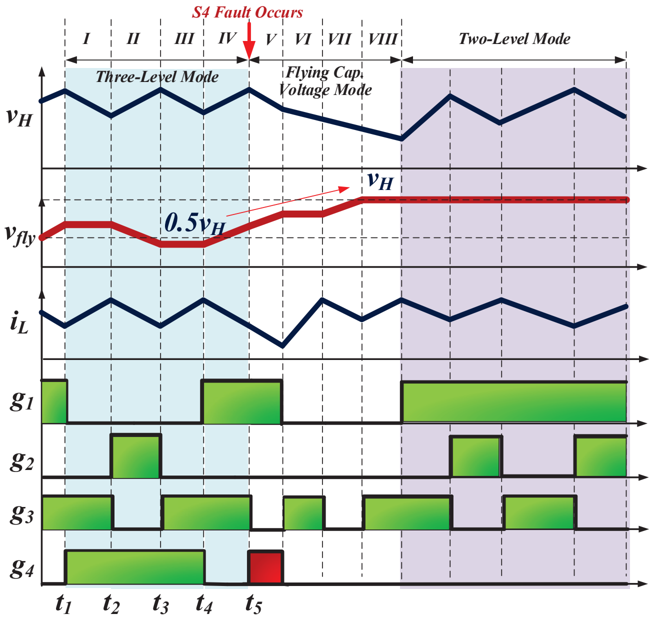

Figure 8. Stage analysis ($V_L < 0.5\ V_H$).

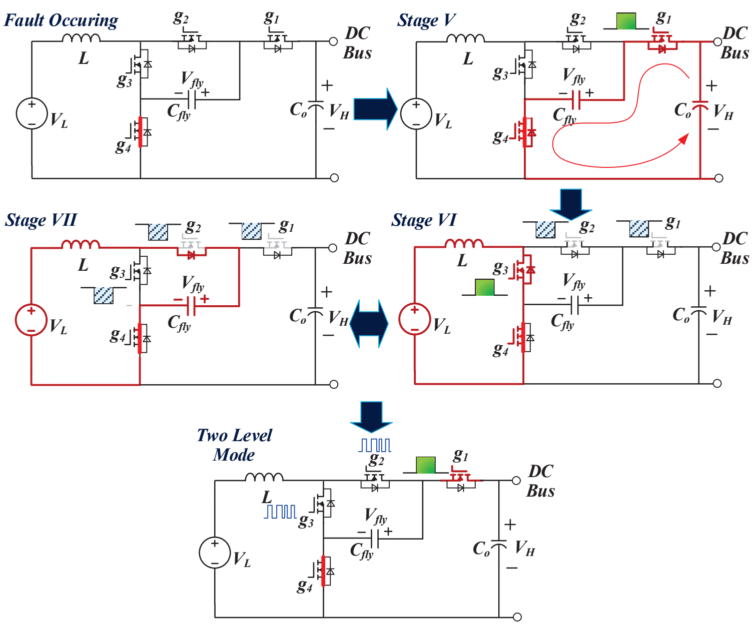

Figure 9. Stages of S_4 short-circuited.

Then the situation when V_L is higher than 0.5 V_H is analyzed in detail. The stage analysis is shown in Figure 10 for when S_3 is short-circuited in this situation. This situation is different from the situation when V_L is lower than 0.5 V_H. The duty cycle of g_3 and g_4 is less than 0.5.

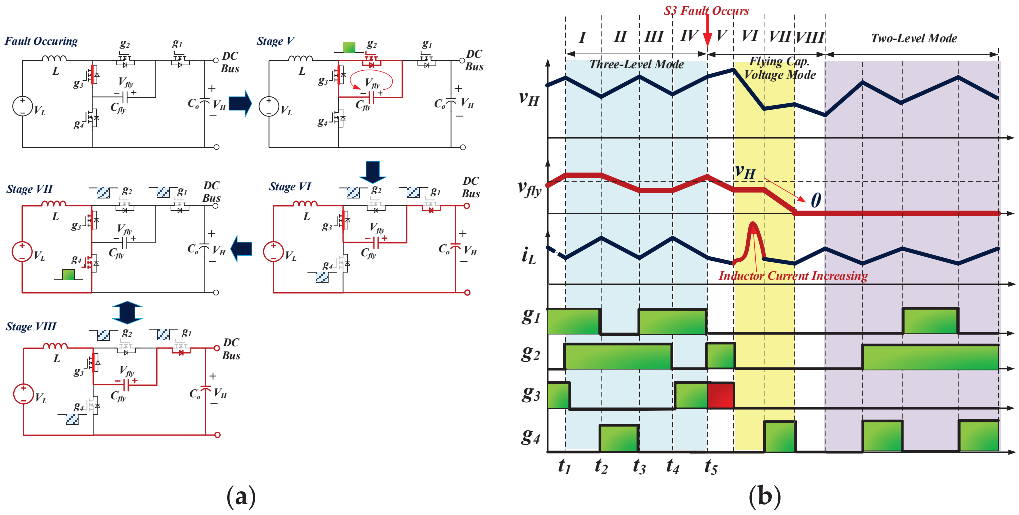

Figure 10. Short-circuit fault analysis (V_L > 0.5 V_H). (**a**) The stages when S_3 is short-circuited; (**b**) stage analysis.

When the short-circuit fault of S_3 is detected, the converter is regulated by the flying capacitor voltage control loop. Then S_4 is opened. Because V_L > 0.5 V_H and the initial value of v_{fly} is half of v_H, inequality (1) can be derived at the beginning of the fault. The voltage difference between the inductor is always positive. It should be noticed that if inequality (2) holds, the current of the inductor will continue to increase during Stage VI. When v_{fly} is lower than $(v_H - v_L)$, the converter operates in Stages VII and VIII. When the flying capacitor voltage reaches 0, the converter turns into the two-level mode, and the S_2 is closed.

$$v_L > v_H - v_{fly} \ \ (v_L > 0.5v_H, V_{fly} = 0.5v_H) \tag{1}$$

$$v_{fly} > v_H - v_L \tag{2}$$

The proper inductance value of the inductor L should be designed, and additional an over-current protection method should be considered. The flying capacitor voltage and inductor current can be calculated by (3). The current spike analysis in this situation when S_3 is short-circuited is shown in Figure 11.

$$\begin{cases} v_{fly}(\mathrm{t}) = \frac{I_L\sqrt{LC}}{\mathrm{C}}\sin(\frac{1}{\sqrt{LC}}\mathrm{t}) + (V_{fly} - V_H + V_L)\cos(\frac{1}{\sqrt{LC}}\mathrm{t}) + (V_H - V_L) \\ i_L(\mathrm{t}) = I_L\cos(\frac{1}{\sqrt{LC}}\mathrm{t}) - \frac{(V_{fly} - V_H + V_L)C}{\sqrt{LC}}\sin(\frac{1}{\sqrt{LC}}\mathrm{t}) \end{cases} \tag{3}$$

where v_{fly} is the flying capacitor voltage, V_H is the output voltage, V_L is the input voltage, L is the inductance of the input inductor, C is the capacitance of the flying capacitor, i_L is the current value of the inductor, and I_L is the initial value of the inductor current. If the output voltage is 100 V, the input voltage is 80 V, the inductor is 1 mH, and the initial current of the inductor is 10 A, then it can be calculated that the maximum inductor current is 17.2 A. The maximum current under different levels of inductance when S_3 is short-circuited is shown in Figure 12.

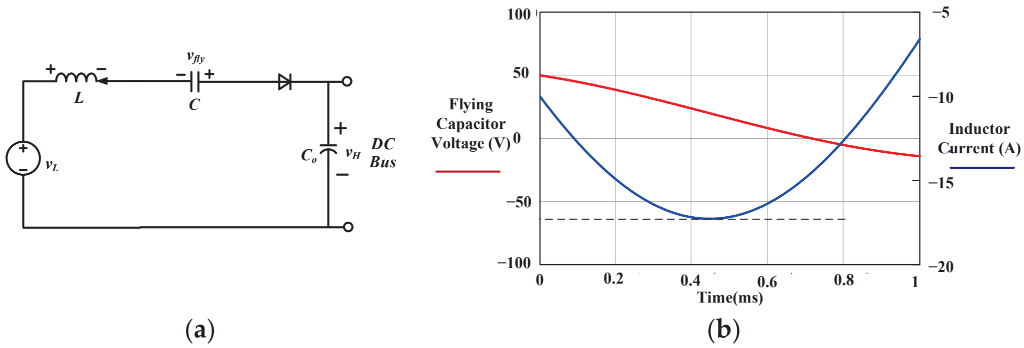

Figure 11. The analysis of the stages under S_3 fault. (**a**) Equivalent circuit; (**b**) the simulation curve (V_L 80 V, V_H 100 V, initial value of I_L-10 A).

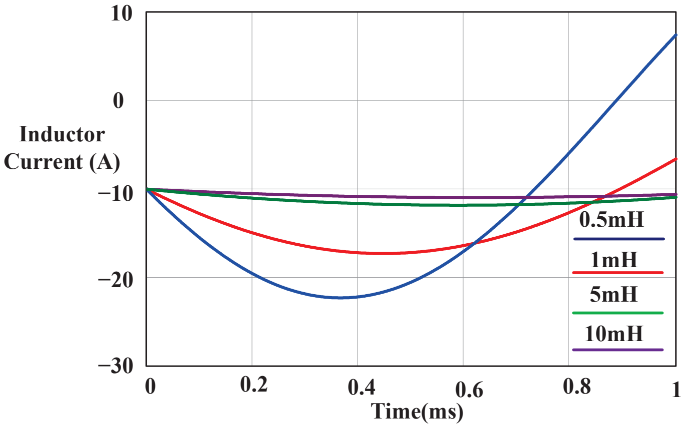

Figure 12. Maximum current under different levels of inductance when S_3 is short-circuited.

The current spike analysis when S_4 is short-circuited is shown in Figure 13. When the short-circuit fault of S_4 is detected, S_3 is turned off. Because v_L is larger than 0.5 V_H and the initial value of V_{fly} is half of V_H, inequality (4) can be derived at the beginning of the fault. The voltage difference between the inductor is always positive. It should be noticed that if inequality (5) holds, the current of the inductor will continue to increase during Stage VI. When v_{fly} is higher than 0.5 V_H, the converter operates in Stages VII and VIII.

$$v_L > v_{fly} \;\; (v_L > 0.5v_H, V_{fly} = 0.5v_H) \tag{4}$$

$$v_{fly} < 0.5v_H \tag{5}$$

When the voltage of the flying capacitor voltage reaches V_H, S_1 is turned off. The proper inductance should also be designed carefully. The flying capacitor voltage and inductor current can be calculated by (4). The current spike analysis is given in Figure 14. If we take the same parameters as the situation when S3 is faulty, the maximum inductor current is 17.2 A. The maximum current under different levels of inductance when S_4 is short-circuited is shown in Figure 15.

$$\begin{cases} v_{fly}(\mathrm{t}) = \frac{I_L\sqrt{LC}}{C}\sin(\frac{1}{\sqrt{LC}}\mathrm{t}) + (V_{fly} - V_L)\cos(\frac{1}{\sqrt{LC}}\mathrm{t}) + (V_L) \\ i_L(\mathrm{t}) = I_L\cos(\frac{1}{\sqrt{LC}}\mathrm{t}) - \frac{(V_{fly}-V_L)C}{\sqrt{LC}}\sin(\frac{1}{\sqrt{LC}}\mathrm{t}) \end{cases} \tag{6}$$

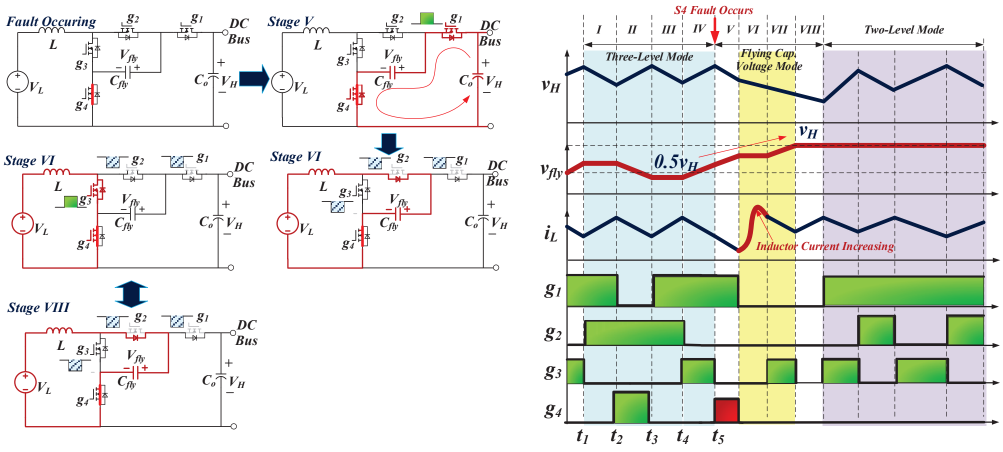

Figure 13. Short-circuit fault analysis (V_L > 0.5 V_H). (**a**) The stages when S_4 is short-circuited; (**b**) stage analysis.

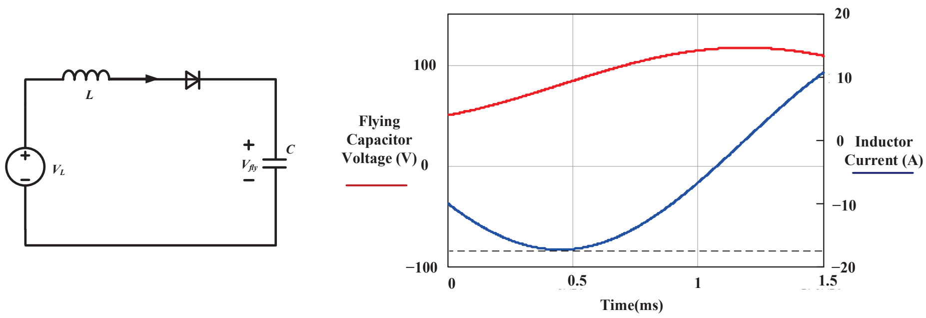

Figure 14. The analysis of the stages under S_4 fault. (**a**) Equivalent circuit; (**b**) the simulation curve (V_L 80 V, V_H 100 V, initial value of I_L 10 A).

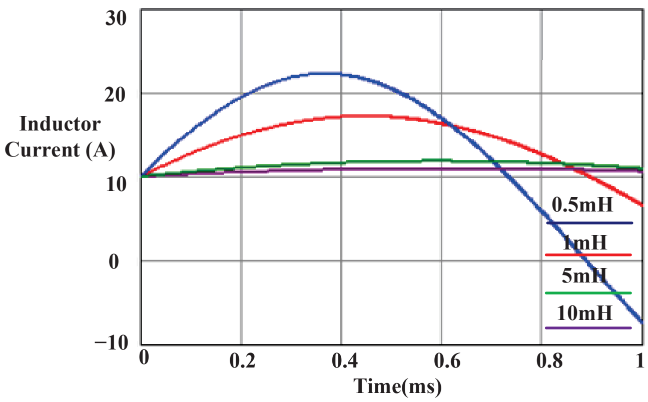

Figure 15. Maximum current under different levels of inductance when S_4 is short-circuited.

The parameters of the flying capacitor DC/DC converter can be calculated as below. According to the stage analysis of the circuit, the inductance of the input inductor is derived by (7), the capacitance of the flying capacitor is derived by (8), and the capacitance of the output capacitor is derived by (9).

$$L_{IN} = \begin{cases} \frac{(\frac{U_o}{2} - U_{IN})(1-D)}{\delta_I I_{in} \cdot f_s} & (D > 0.5) \\ \frac{(U_{IN} - \frac{U_o}{2}) \cdot D}{\delta_I I_{in} \cdot f_s} & (D < 0.5) \end{cases} \tag{7}$$

$$C_{fly} = \begin{cases} \frac{I_{IN}(1-D)}{\frac{\delta_f U_o}{2} \cdot f_s} & (D > 0.5) \\ \frac{I_{IN} D}{\frac{\delta_f U_o}{2} \cdot f_s} & (D < 0.5) \end{cases} \tag{8}$$

$$C_o = \frac{I_o}{\delta_o U_o \cdot f_s} \tag{9}$$

where the output voltage U_o is 100 V, the input voltage U_{IN} is 30~80 V, the switching frequency f_s is 10,000 Hz, the duty cycle D is 0.2~0.7, the input current I_{IN} is 33 A, the output current Io is 10 A, the ripple ratio of the input current δ_I is 0.02, the ripple ratio of the flying capacitor voltage δ_f is 0.1, and the ripple ratio of the output capacitor voltage δ_o is 0.01. Then the inductor is 0.9 mH, the flying capacitor is 200 μF, and the output capacitor is 1 mF. With the consideration of the current spike analysis after a short-circuit fault in the simulation, the inductance of the inductor is chosen as 1 mH, and the capacitances of the flying capacitor and the output capacitor are chosen as 200 μF and 1 mF, respectively.

4. Simulation and Experiment Verifications of the Fault-Tolerant Strategy

In order to verify the proposed fault-tolerant strategy, the simulation model of the flying capacitor three-level DC/DC converter based on PSIM was built. In the model, the rated power of the flying capacitor three-level converter is 1 kW. The output voltage of the converter is 100 V. The two types of input voltage are considered, including 30 V (V_L<0.5 V_H) and 80 V (V_L > 0.5 V_H). The inductance of the inductor is 1 mH. The capacitance of the flying capacitor is 200 uF, and the capacitance of the output capacitor is 1 mF. The parameters of the simulation are shown in Table 1.

Table 1. The parameters of the different simulation cases.

Item	Case I (Figure 16) Value	Case II (Figure 17) Value	Case III (Figure 18) Value	Case IV (Figure 19) Value
Input voltage	30 V	30 V	80 V	80 V
Output DC bus voltage	100 V	100 V	100 V	100 V
Input inductor	1 mH	1 mH	1 mH	1 mH
Flying capacitor	200 μF	200 μF	200 μF	200 μF
Output bus capacitor	1 mF	1 mF	1 mF	1 mF
Load power	100 W/1000 W	100 W/1000 W	100 W/1000 W	100 W/1000 W
Fault location	Inner switch S_3	Outer switch S_4	Inner switch S_3	Outer switch S_4

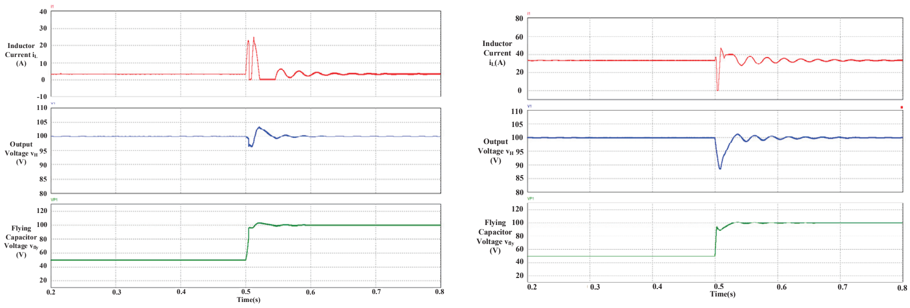

(**a**) (**b**)

Figure 16. The waveforms of S_4 short-circuit fault (V_L < 0.5 V_H). (**a**) Light load 100 W; (**b**) heavy load 1000 W.

The simulation waveforms when a short-circuit fault occurs in outer switch S_4 under two load conditions are shown in Figure 16. It can be seen that the output voltage of the converter is uninterruptible when a short-circuit fault of S_4 occurs. The mode transfer after the fault is seamless.

The simulation results when the input voltage is lower than half of the output voltage are shown in Figure 17. The waveforms when a short-circuit fault occurs in inner switch

S_3 under different load conditions are shown in Figure 17a,b. The two load conditions are 100 W for a light load and 1000 W for a heavy load. It can be seen that the output voltage of the converter is uninterruptible after the S_3 fault occurs. The spike of the current and voltage is in the normal range during the mode transition after the fault.

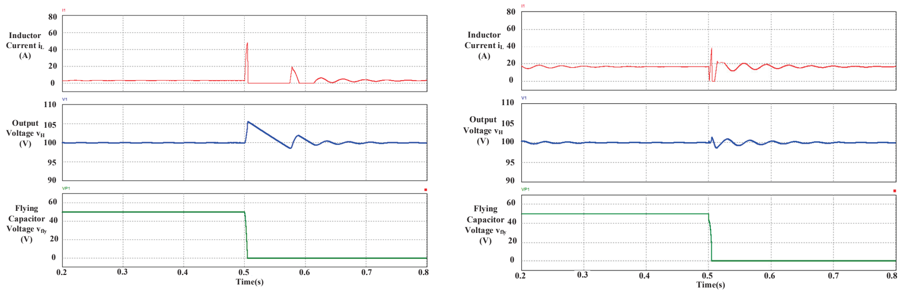

(**a**) (**b**)

Figure 17. The waveforms of S_3 short-circuit fault (V_L < 0.5 V_H). (**a**) Light load 100 W; (**b**) heavy load 1000 W.

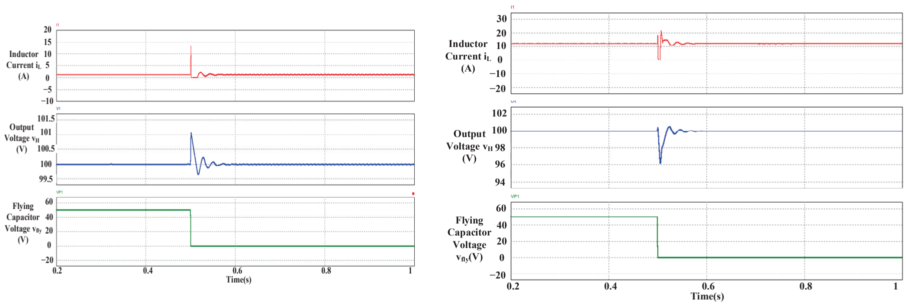

(**a**) (**b**)

Figure 18. The waveforms of S_3 short-circuit fault (V_L > 0.5 V_H). (**a**) Light load 100 W; (**b**) heavy load 1000 W.

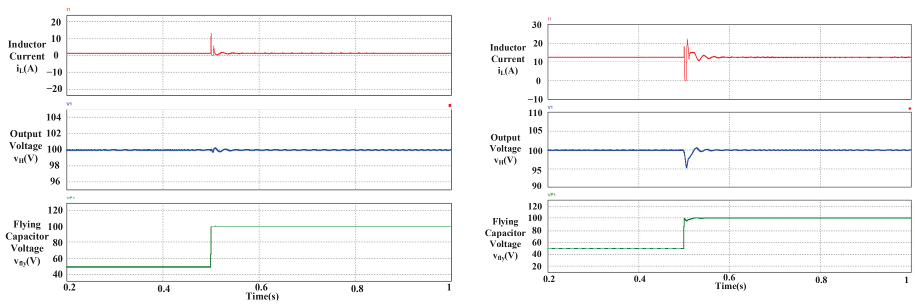

(**a**) (**b**)

Figure 19. The waveforms of S_4 short-circuit fault (V_L > 0.5 V_H). (**a**) Light load 100 W; (**b**) heavy load 1000 W.

The simulation results when the input voltage is higher than half of the output voltage are shown in Figures 18 and 19. The waveforms when a short-circuit fault occurs in S_3 under two different load conditions including a light load and a heavy load are shown in Figure 18a,b, and the waveforms when a short-circuit fault occurs in S_4 under two different load conditions are shown in Figure 19a,b. It can also be seen that the output voltage is uninterruptible when two types of faults occur. The spike and surge of the current and voltage are also in the normal range.

The prototype of the three-level flying capacitor DC/DC converter is built to verify the fault-tolerant strategy. The parameters of the prototype are shown in Table 2.

Table 2. The parameters of the prototype of flying capacitor DC/DC converter.

Item	Value
Input voltage	10 V
Output DC bus voltage	32 V
Input inductor	100 µH
Flying capacitor	20 µF
Output bus capacitor	470 µF

The waveform when the short-circuit fault of S3 occurs is shown in Figure 20a. CH1 is the output voltage of the converter. CH2 is the flying capacitor voltage. CH3 is the trigger signal. CH4 is the driver signal of the power switch S3. The waveform of the three-level mode before the fault occurs is shown in Figure 20b. The waveform during the fault is shown in Figure 20c. It can be seen that the output voltage is uninterruptible and the flying capacitor voltage is regulated from 16 V to 0. The waveform of the two-level mode after the fault occurs is shown in Figure 20d. The waveform when the short-circuit fault of S4 occurs is shown in Figure 21a. The waveform before an S4 fault is shown in Figure 21b. The waveform during the fault is shown in Figure 21c. It can be seen that the output voltage is uninterruptible and the flying capacitor voltage is regulated from 16 V to 32 V. After the S4 fault, the waveform is shown in Figure 21d.

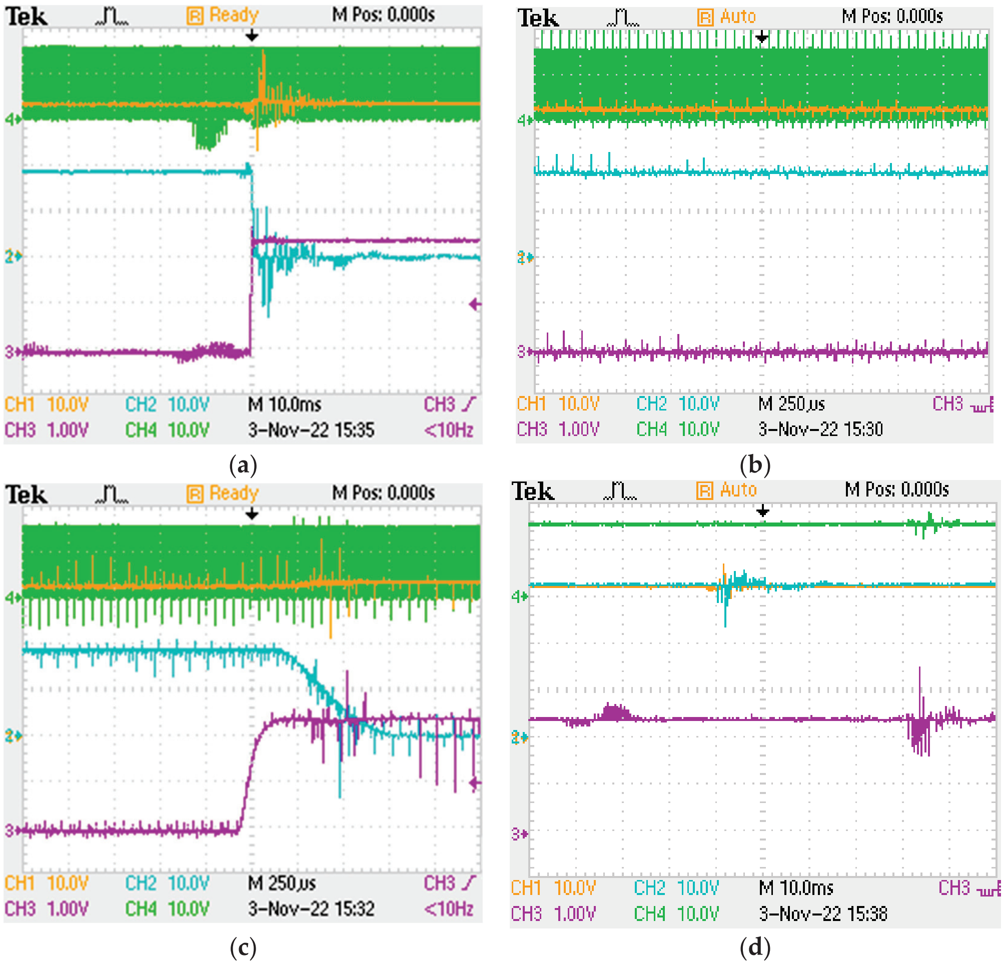

Figure 20. The experimental waveforms of S_3 short-circuit fault. (**a**) Overall stages; (**b**) the waveform of three-level mode before S_3 fault; (**c**) the waveform of S_3 short-circuit fault during fault; (**d**) the waveform of two-level mode after S_3 fault.

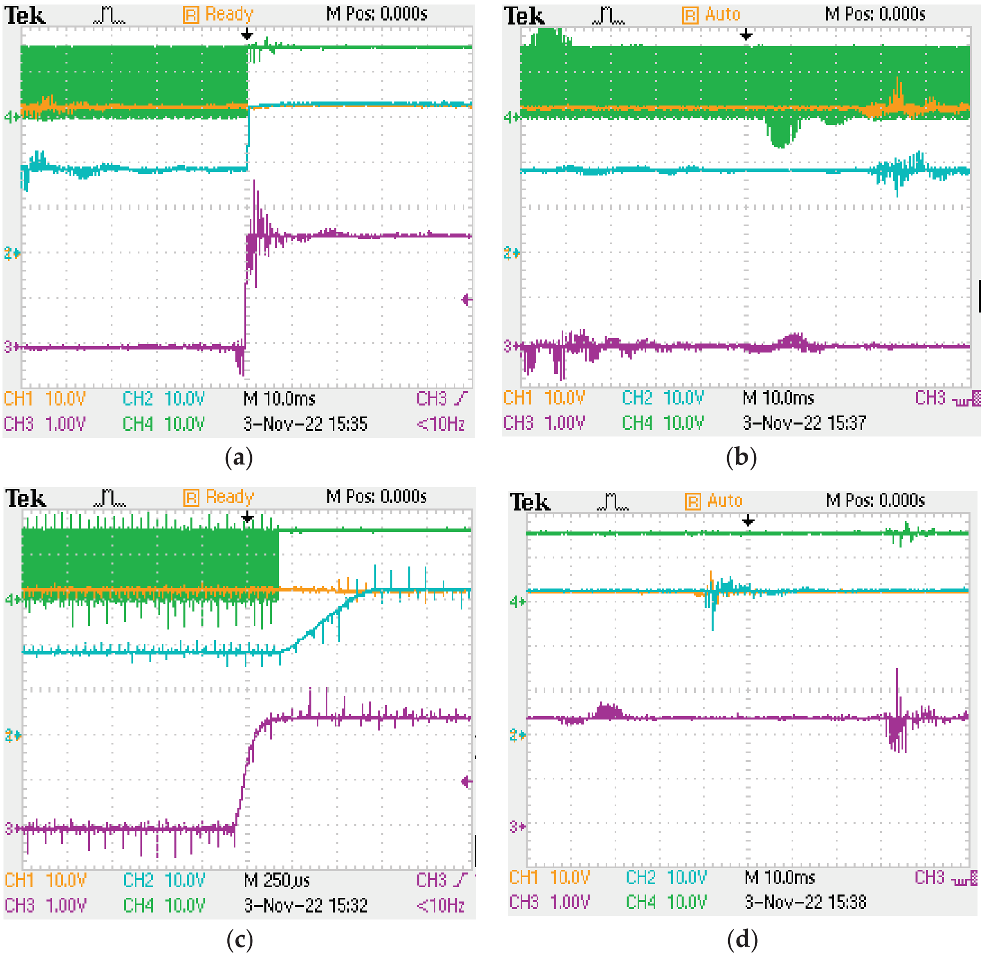

Figure 21. The experimental waveforms of S_4 short-circuit fault. (**a**) Overall stages; (**b**) the waveform of three-level mode before S_4 fault; (**c**) the waveform of S_4 short-circuit fault during fault; (**d**) the waveform of two-level mode after S_4 fault.

5. Conclusions

In order to improve the reliability of converters for the interface of the PV, battery, or other sources in spacecraft power systems for future high-voltage application, the fault-tolerant strategy of a three-level flying capacitor DC/DC converter is proposed in this paper. If a short-circuit fault occurs in the power devices, the converter can provide uninterruptible power for the load. It can turn from the three-level mode to the two-level mode, and during the mode transition, the voltage of the flying capacitor is regulated to the different target value based on the different fault locations. There is no extra hardware needed for this proposed strategy; the fault tolerance of the converter is only achieved by changing the software control strategy, and the reliability of the converter is improved with minimal cost. The stage analysis of the three-level converter is provided in detail. Different ratios between the input and output voltage and different fault locations are considered. Finally, a simulation model and prototype of the converter with the fault-tolerant strategy are built to verify the proposed strategy. The results show the fault tolerance operation of the converter is achieved after a short-circuit fault occurs.

Author Contributions: Conceptualization, H.L.; methodology, H.L., X.Z., Z.L. and Y.Z.; validation, H.L., Y.G. and L.Z. All authors have read and agreed to the published version of the manuscript.

Funding: This work is supported by the National Natural Science Foundation of China (52007007).

Institutional Review Board Statement: Not applicable.

Informed Consent Statement: Not applicable.

Data Availability Statement: Not applicable.

Conflicts of Interest: The authors declare no conflict of interest.

References

1. Zhang, X.; Li, H. Design of Software Defined Spacecraft Distributed Power Supply System. *Spacecr. Eng.* **2020**, *29*, 51–58.
2. Zhang, M.; Liu, Y.; Li, H.; Zhang, W.; Zhang, X.; Xia, N.; Zhu, L.; Mu, H.; Liu, Z. Design of 100kW Distributed Reconfigurable Electrical Power System for Spacecraft. *Spacecr. Eng.* **2021**, *30*, 86–94.
3. Bekemans, M.; Bronchart, F.; Scalais, T.; Franke, A. Configurable High Voltage Power Supply for Full Electric Propulsion Spacecraft. In Proceedings of the 2019 European Space Power Conference (ESPC 2019), Juan-les-Pins, France, 30 September–4 October 2019. [CrossRef]
4. Dusmez, S.; Hasanzadeh, A.; Khaligh, A. Comparative Analysis of Bidirectional Three-Level DC–DC Converter for Automotive Applications. *IEEE Trans. Ind. Electron.* **2014**, *62*, 3305–3315. [CrossRef]
5. Ruan, X.; Li, B.; Chen, Q.; Tan, S.-C.; Tse, C.K. Fundamental considerations of three-level DC–DC converters: Topologies, analyses, and control. *IEEE Trans. Circuits Syst. I Regul. Pap.* **2008**, *55*, 3733–3743. [CrossRef]
6. Kesarwani, K.; Stauth, J.T. Resonant and multi-mode operation of flying capacitor multi-level DC-DC converters. In Proceedings of the 2015 IEEE 16th Workshop on Control and Modeling for Power Electronics (COMPEL), Vancouver, BC, Canada, 12–15 July 2015; pp. 1–8.
7. Tesaki, K.; Ishida, Y.; Hagiwara, M. Control and Experimental Verification of a Bidirectional Non-isolated DC-DC Converter Based on Three-level Flying-Capacitor Converters. *IEEJ J. Ind. Appl.* **2021**, *10*, 114–123. [CrossRef]
8. Cuzner, R.M.; Bendre, A.R.; Faill, P.J.; Semenov, B. Implementation of a non-isolated three level DC/DC converter suitable for high power systems. In Proceedings of the 2007 IEEE Industry Applications Annual Meeting, New Orleans, LA, USA, 23–27 September 2007; pp. 2001–2008.
9. Choi, M.; Jeong, D.K. Design of High Step-Down Ratio Isolated Three-Level Half-Bridge DC–DC Converter With Balanced Voltage on Flying Capacitor. *IEEE Trans. Power Electron.* **2022**, *37*, 10213–10225. [CrossRef]
10. Zhong, Z.; Chen, Y.; Zhang, P.; Kang, Y. A cost-effective circuit for three-level flying-capacitor buck converter combining the soft-start, flying capacitor pre-charging and snubber functions. In Proceedings of the 2014 IEEE Energy Conversion Congress and Exposition (ECCE), Pittsburgh, PA, USA, 14–18 September 2014; pp. 3658–3663. [CrossRef]
11. Zhang, W.; Xu, D.; Enjeti, P.N.; Li, H.; Hawke, J.T.; Krishnamoorthy, H.S. Survey on Fault-Tolerant Techniques for Power Electronic Converters. *IEEE Trans. Power Electron.* **2014**, *29*, 6319–6331. [CrossRef]
12. Kumar, G.K.; Elangovan, D. Review on fault-diagnosis and fault-tolerance for DC–DC converters. *IET Power Electron.* **2020**, *13*, 1–13. [CrossRef]
13. Bento, F.; Cardoso, A.J.M. A comprehensive survey on fault diagnosis and fault tolerance of DC-DC converters. *Chin. J. Electr. Eng.* **2018**, *4*, 1–12. [CrossRef]
14. Gleissner, M.; Bakran, M.M. Design and control of fault-tolerant nonisolated multiphase multilevel DC–DC converters for automotive power systems. *IEEE Trans. Ind. Appl.* **2015**, *52*, 1785–1795.
15. Pazouki, E.; Sozer, Y.; De Abreu-Garcia, J.A. Fault Diagnosis and Fault-Tolerant Control Operation of Nonisolated DC–DC Converters. *IEEE Trans. Ind. Appl.* **2017**, *54*, 310–320. [CrossRef]
16. Wang, H.; Li, H.; Yan, C.; Xu, D. A Short-Circuit Fault-Tolerant Strategy for Three-Phase Four-Wire Flying Capacitor Three-Level Inverters. In Proceedings of the 2019 IEEE 10th International Symposium on Power Electronics for Distributed Generation Systems (PEDG), Xi'an, China, 3–6 June 2019; pp. 781–786. [CrossRef]
17. Xu, S.; Zhang, J.; Hang, J. Investigation of a Fault-Tolerant Three-Level T-Type Inverter System. *IEEE Trans. Ind. Appl.* **2017**, *53*, 4613–4623. [CrossRef]
18. Sheng, H.; Wang, F.; Tipton, C.W., IV. A fault detection and protection scheme for three-level DC–DC converters based on monitoring flying capacitor voltage. *IEEE Trans. Power Electron.* **2011**, *27*, 685–697. [CrossRef]
19. Choi, U.M.; Blaabjerg, F.; Lee, K.B. Study and Handling "Methods of Power IGBT Module Failures in Power Electronic Converter Systems. *IEEE Trans. Power Electron.* **2015**, *30*, 2517–2533. [CrossRef]
20. Soon, J.L.; Lu, D.D.C. Design of fuse–MOSFET pair for fault-tolerant DC/DC converters. *IEEE Trans. Power Electron.* **2016**, *31*, 6069–6074. [CrossRef]

energies

MDPI

Article

Analysis of Losses in Two Different Control Approaches for S-S Wireless Power Transfer Systems for Electric Vehicle

Abhay Kumar [1,*], Manuele Bertoluzzo [1,*], Rupesh Kumar Jha [2] and Amritansh Sagar [1]

1 Department of Industrial Engineering, University of Padova, 35131 Padua, Italy
2 Tata Consultancy Services, Bangalore 560066, India
* Correspondence: abhay.kumar@studenti.unipd.it (A.K.); manuele.bertoluzzo@unipd.it (M.B.)

Abstract: This paper presents the study and detailed analysis of converter losses at different stages together with the series-series (S-S) compensating coils in wireless power transfer (WPT) systems, via two distinct approaches to control the power converters. The two approaches towards wireless DC–DC power flow control are termed as the Single Active High-Frequency Wireless Power Transfer (SAHFWPT) system and the Dual Active High-Frequency Wireless Power Transfer (DAHFWPT) system. The operation of converters in SAHFWPT and DAHFWPT are controlled by the extended phase shift (EPS) and dual phase shift method respectively. The general schematic of the SAHFWPT system consists of an active bridge and a passive bridge, while the schematic of the DAHFWPT system consists of both active bridges. The efficiency evolutions of ideal SAHFWPT and DAHFWPT are far away from the real ones. Moreover, this article analyzes the operation and losses of the uni-directional power flow of the WPT system, i.e., from the DC bus in the primary side to the battery load in the secondary side. The loss estimation includes high-frequency switching losses, conduction losses, hard turn on and turn off coil losses, etc. Moreover, the efficiency of the WPT system depends on operation of the converter. A 50 W–3600 W Power range system at a resonant frequency of 85 kHz is implemented in MATLAB/SIMULATION to demonstrate the validity of the proposed method.

Keywords: single active bridge; dual active bridge; wireless power transfer; DC–DC converter; converter loss; electrical vehicle

1. Introduction

The typical wireless power transfer (WPT) systems have several ranges in terms of power ratings, from a few watts to kilowatts, depending on the applications, such as portable electrical devices, medical devices (Pacemaker), mechanical instruments, and transportation (electrical vehicles (EVs)) in [1,2].

In the current scenario, the energy storage system (ESS) plays an important role during the different trend of power demand as explained in [3]. As intensity of renewable energy (RE) is not constant throughout a day, the ESS plays a crucial role in the area of storage excess energy that can be generated by the RE sources [4], and that can be used to power the various loads such as a household load, industrial load, street load, etc. when we are not able to use the RE sources. The wireless DC–DC converters are becoming more pervasive due to the fact that they are compact in size, isolated power flow between the resonating coils, and have excellent efficiency. In earlier studies, there have been a lot of isolated DC–DC power converters, such as single active bridge (SAB), dual active bridge (DAB), phase shift full bridge (PSFB), and so on for high-frequency applications mentioned in [5–8].

Figure 1 shows the generalized schematic of the wireless DC–DC converter that can be used for both Single Active High-Frequency Wireless Power Transfer (SAHFWPT) and Dual Active High-Frequency Wireless Power Transfer (DAHFWPT). During the operation of the SAHFWPT system, the primary side converter operates as an active converter, i.e., high-frequency inverter, and the secondary side converter operates as a passive converter through the diode, i.e., uncontrolled rectifier. The control approach of the primary H-bridge converter takes place by the internal phase shift control method as describe in [9–11]. In the operation of DAHFWPT system, the primary and secondary sides H-bridge converters are operating as active bridges, but their operation is different, i.e., the primary works as the high-frequency inverter and the secondary works as the controlled rectifier [12]. Moreover, the control of the primary and secondary H-bridge converters was also takes place by the internal phase shift control method. However, in both the SAHFWPT and DAHFWPT converters, power transfer takes place via external phase shift of converter from the source voltage V_S to the load which can be considered equivalent load resistance R_B in place of the battery. As the H-bridge works at high frequency, the passive components (i.e., S-S coupling coil, source filters, and load filters) compatibly reduce in size so that the SAHFWPT and DAHFWPT system stand out due to the high values for the power density as well as specific power in [13–16].

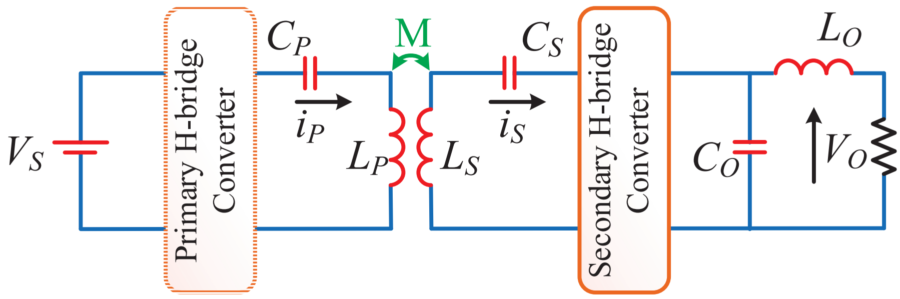

Figure 1. Schematic of wireless DC–DC converter.

As previously stated, the SAHFWPT and the DAHFWPT converters can be used in applications requiring both uni-directional and Bi-directional power flow, such as electric vehicles, household appliances, mobile phones, medical devices, and other fields [17]. The schematics for SAHFWPT and DAHFWPT in Figure 1 include two H-Bridge, besides the two H-bridges, with following elements: (1) the coupling coils L_P and L_S as well as the series resonating capacitors C_P and C_S, which keep coil current sinusoidal even when the voltage across the series compensated coil in a quasi-square or square wave; the mutual inductance M between the primary and secondary coils; (2) the capacitor C_O, which filters out ripple of the voltage V_O; (3) the inductor L_O, which can filter out the ripple of current that passes through R_B; (4) and the resistance R_B represents the battery's equivalent resistance [18–24].

The most effective optimization models are those that are based on the nonlinear equivalent model of the magnetic equivalent coupler of the WPT converters. This model considers the losses that are incurred as a result of the nonlinear operation of the converters, which include the conduction losses in MOSFETs, diodes, and body diodes, the hard-switching loss of the switches, and the reverse recovery loss of diodes. The gap between standard loss models and experimental measurements is well-known in [6]. Table 1 provides a comparison overview between a SAHFWPT and a DAHFWPT in terms of control method, losses, and selection of extra DC–DC converter. It is ideal to build a DAHFWPT battery charger with no additional DC–DC converter. Soft switching of the inverter and active rectifier circuits takes place with the help of zero voltage switching (ZVS) and zero current switching (ZCS), resulting in low circulating reactive power when the external phase shift of the converters is equal to $3\pi/2$, and optimized overall loss is described in [14]. Depending on their application, four distinct switching modes (single phase shift (SPS) [25], extended phase shift (EPS), dual phase shift (DPS) [26], and triple phase shift (TPS) [6] may be used to optimize converters losses. Whereas, SAHFWPT is ideal to build a battery charger with an additional DC–DC converter, while SAHFWPT has no circulating current as the external phase shift angle is fixed at $3\pi/2$, soft switching of the inverter and passive rectifier by the help of zero voltage switching (ZVS) and zero current switching (ZCS) are mention in [27], and overall loss optimization. Depending on their use, two distinct switching options are available, such as SPS and EPS. The S-S coil losses are included in both systems, but these losses are not same as they are dependent on the current and design parameters of the coil.

Table 1. A comparison is made between a SAHFWPT and a DAHFWPT.

Feature		SAHFWPT			DAHFWPT		
Reference		[3]	[5]	[6–9]	[3]	[5]	[6–9]
Switching control	SPS	×	√	√	×	√	√
	EPS	√	√	√	×	√	√
	DPS	×	×	×	√	√	√
	TPS	×	×	×	×	√	√
Additional chopper		√	√	√	×	×	×
Hard switching of MOSFET		×	×	√	×	×	√
Circulating current		×	×	×	×	√	√
S-S coil loss		√	√	√	√	√	√
Overall loss analysis		×	×	√	×	×	√

Many of the articles discuss the switching operation, power flow operation, and different approaches to control of the SAHFWPT and DAHFWPT converters for EV. The comparative study of power loss of converters and coils during operation of the SAHFWPT and DAHFWPT converters is discussed in this article. Apart from that, the purpose of this paper is to study the effects on the overall efficiency of the WPT of the two different control methods, i.e., EPS and DPS of the H-bridge converter for SAHFWPT and DAHFWPT, respectively. Further, we performed a comparative analysis of the power range of WPT, while keeping the battery voltage constant. For this study, we fixed the internal phase angle of the primary and secondary H-bridge, the angles to be equal in the operation of DAHFWPT, and we are aware that the secondary of SAHFWPT works as the uncontrolled rectifier. So, to maintain the same power drawn from the source as DAHFWPT, we must only change the internal phase shift angle of the primary H-bridge.

Here is how the rest of the article is put together: In Section 2, we provide a quick overview of the SAHFWPT and DAHFWPT, as well as how the switching of converter takes place at 85 kHz based on the SAE J2954 standard. Besides that, there is a comparison of secondary power. In Section 3, we briefly discuss the loss study at different stages of the converters. In Section 4, we compare the efficiency of the coupling coil of both systems. In Section 5 we report the result, the SAHFWPT and DAHFWPT are tested based on their total loss, and their maximum rated input power for a given power, the behavior of the current, and voltage in the primary and secondary the system efficiency. The paper concludes in Section 6.

2. Methods of Operation of SAHFWPT and DAHFWPT

2.1. Circuit Schematic

The schematics of the SAHFWPT and DAHFWPT converters are shown in Figure 2a,b. The SAHFWPT and DAHFWPT are separated into primary and secondary sections. The primary active H-bridge is designed as the high-frequency primary converter (HFPC), which is powered by the DC source voltages V_{DCP_S} and V_{DCP_D} for both the SAHFWPT and the DAHFWPT, respectively. HFPC work as a high-frequency phase shift inverter, generating high-frequency quasi-square wave output voltages v_{HFPC_S} and v_{HFPC_D}. The output current i_{P_S} and i_{P_D} are sinusoidal due to the resonating effect of the coil. Moreover, output voltage waveform level depends on switching control method, as mentioned in

Table 1. The output voltage levels of HFPC by SPS and EPS switching are two and three, whereas in the control operation the HFSC have an output voltage level of two in SAHFWPT and DAHFWPT. Aside from these two switching methods, the DPS and TPS are only useful for DAHFWPT. Since the SAHFWPT secondary is uncontrolled and the resulting voltage is always two levels. The HFPC consists of four MOSFETs ($T_5 - T_8$). Furthermore, if we look at the HFPC schematic in Figure 2a,b, we can observe the antiparallel body diodes ($D_5 - D_8$) of MOSFETs, that can be operated when the circulating current flow takes place. The coupled coils create the connection between the primary and secondary converter by wireless means. The secondary H-bridges is referred as the high-frequency secondary rectifier (HFSR) or high-frequency secondary converter (HFSC) according to their passive or active operations, respectively. The voltage v_{HFSR_S} and v_{HFSC_D} induced in the secondary coil due to variation in current i_{P_S} and i_{P_D} in the primary coil, according to the Faraday law of induction, secondary voltage serves as the input voltage source of the HFSR and HFSC and the current i_{S_S} and i_{S_D} flow through the secondary coil. The output voltage V_{O_S} and V_{O_D} of the HFSR and HFSC are applied across the equivalent load, which includes the low pass filter $L_O C_O$ and R_B equivalent battery resistance, where C_O can be used to smooth or remove the ripple of voltage V_{O_S} and V_{O_D}, and L_O can be used to smooth or remove ripple of current I_{O_S} and I_{O_D}. The output voltages V_{O_S} and V_{O_D}, as well as the currents I_{O_S} and I_{O_D}, are kept at the desire levels for charging the battery by the phase-shifted regulation of the HFPC and HFSC. The HFSR and HFSC are fabricated of four high-frequency diodes ($D_9 - D_{12}$) and MOSFETs ($T_9 - T_{12}$) with the relevant antiparallel body diodes ($D_9 - D_{12}$), respectively. The primary side's input filter is a C_I filter, which is not seen in Figure 2a,b.

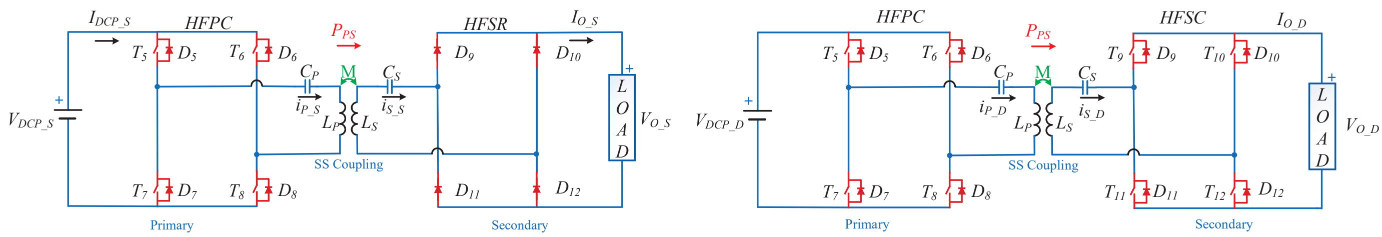

(**a**) (**b**)

Figure 2. Schematic of WPT converter with equivalent load (**a**) SAHFWPT (**b**) DAHFWPT.

The switching frequency of the SAHFWPT and DAHFWPT converters are in the range of 79–90 kHz. The operating frequency was fixed at 85 kHz and the resonant circuits are tuned to this frequency as in [9,10]. This frequency is selected as per the J2954 standard of the society of automotive engineering (SAE) about charging of electric vehicle through WPT. The design of self-inductor L_P, L_S and capacitors C_P, C_S of the series-series resonating coil are usually at resonating frequency ω_r i.e,

$$\omega_r = \frac{1}{\sqrt{L_P C_P}} = \frac{1}{\sqrt{L_S C_S}} \tag{1}$$

2.2. Operation and Analysis

Figure 3a,b depict the switching operation of the SAHFWPT and DAHFWPT converters at resonance frequency. The EPS and DPS switching mechanisms are used to control the converters of SAHFWPT and DAHFWPT, respectively. The plot is divided in three parts: (1) gate signals of the HFPC on the upper section of the plot, (2) waveforms of current and voltage of HFPC together with the conduction intervals of its switches, (3) and waveforms of current and voltage for HFSR together with the conduction intervals of its switches in the case of SAHFWPT (Figure 3a) and gate signals. For correlation between both the wave forms, the gate signals in the upper section are assumed same for both SAHFWPT and DAHFWPT, the HFPC switching operation takes place by the internal phase shift angle between its two legs. The middle part of Figure 3a,b, depicts the direction of current flow through the HFPC's. During the positive half cycle of the current, three different switching periods can be recognized, namely (1) interval 1: (0 to $\Phi - \alpha/2$), (2) interval 2: ($\Phi - \alpha/2$ to $\Phi + \alpha/2$), and (3) interval 3: ($\Phi + \alpha/2$ to π). While the currents i_{P_S} and i_{P_D} circulate in the MOSFETs and body diode, the circulating current does not flow across the source voltage V_{DCP_S} and V_{DCP_D}, respectively. Indeed, the output voltage of HFPC is zero, i.e., $v_{HFPC\_S} = v_{HFPC\_D} = 0$, in the intervals 1 and 3. Switches (T8, D7), and (T5, D6) are in conduction state, as the energy stored in the reactive element such as L_P and C_P forces the current to circulate in intervals 1 and 3. Aside from that, the amplitudes of v_{HFPC_S} and v_{HFPC_D} in interval 2 are identical to V_{DCP_S} and V_{DCP_D}. The wave forms clearly show that the output voltages v_{HFPC_S} and v_{HFPC_D} square, as well as the currents current i_{P_S} and i_{P_D} sinosuidal, are in the same phase and have half-wave symmetry, due to the resonating behavior of the coil. As per the Faraday law induction, EMF is induced in the secondary coil due to flux linkage between the primary and secondary. The average power P_{PS} flow from primary to secondary due to induced voltage in the secondary, which can serve as voltage source for the SAHFWPT and DAHFWPT secondary.

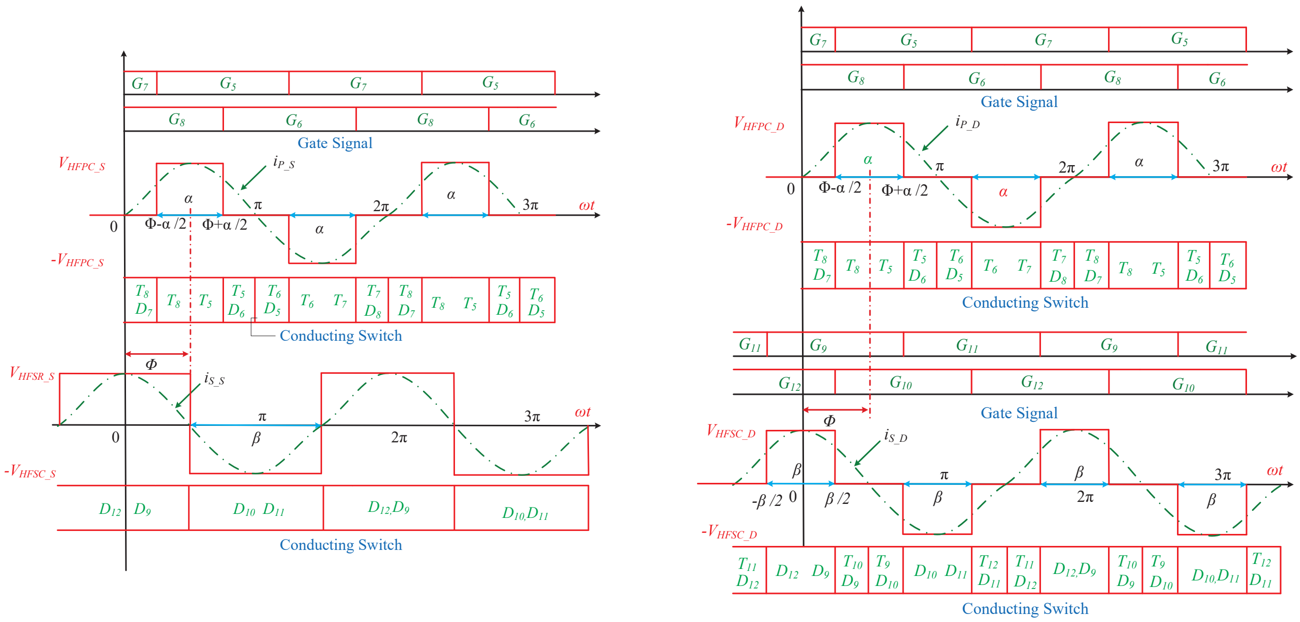

(**a**) (**b**)

Figure 3. Control signal and operating waveform of WPT (**a**) SAHFWPT (**b**) DAHFWPT.

HFSR and HFSC converters are passive and active in behavior, respectively. As shown in the lower part of the waveform in Figure 3a, HFSR conducts for a full cycle, i.e., (D_{12}, D_9) conducts during the positive half cycle and (D_{10}, D_{11}) conducts during the negative half cycle. As a matter of fact, the HFSR input voltage v_{HFSR_S} and current i_{S_S} are square and sin wave, respectively, thanks to the resonating behavior of the coil. On the contrary, the active rectifier HFSC operation during the positive half cycle is divided into three intervals: (1) interval 1: $-\pi/2$ to $-\beta/2$; (2) interval 2: $-\beta/2$ to $\beta/2$; and (3) interval 3: $\beta/2$ to $\pi/2$). In the intervals 1 and 3, the output voltage of HFSC is zero, i.e., $v_{HFSC\_D} = 0$, while the current i_{S_D} flows in the MOSFETs and body diodes of HFSC and do not reach the load. The switches (T_{11}, D_{12}) and (T_{10}, D_9) are in conduction state during the intervals 1 and 3 respectively. The circulation of current occurs due to the energy stored in the reactive elements such as C_S and L_S. Apart from this, the amplitudes of v_{HFSR_S} and v_{HFSC_D} are equal to V_{O_S} and V_{O_D} in the interval 2. From the shape of the wave form, it was easy to see that the output voltages v_{HFSR_S} and v_{HFSC_D} square and the currents i_{S_S} and

i_{S_D} sinusoidal have the same phase and are half-wave symmetric, due to the resonating behavior of the coil.

The output voltages V_{O_S}, V_{O_D} and currents i_{S_S}, i_{S_D} of the HFSR, and HFSC are almost constant due to filtering effect of L_O and C_O. The external phase shift angle for primary and secondary converter is fixed at Φ in the case of SAHFWPT and DAHFWPT.

The equivalent circuit of SAHFWPT and DAHFWPT with S-S coupling is shown in Figure 4. As per Figure 3 the operation begins at time t = 0, and the internal phase shift angles of HFPC and HFSC are α and β, respectively (whereas in the case of SAHFWPT, β = π is fixed). The external phase shift angle Φ varying in the range [0 2π] during the operation of DAHFWPT (whereas Φ = 3π/2 is fixed in the case of SAHFWPT). The voltages v_{HFPC} and v_{HFSC} are expressed as a Fourier series as follows:

$$v_{HFPC}(t) = v_{HFPC\_M} \sum_{n=1,\,3,\ldots}^{\infty} \frac{1}{n} \sin(\omega_r t) \sin\left(\frac{n\alpha}{2}\right) \quad (2)$$

$$v_{HFSC}(t) = v_{HFSC\_M} \sum_{n=1,\,3,\ldots}^{\infty} \frac{1}{n} \sin(\omega_r t + \Phi) \sin\left(\frac{n\beta}{2}\right) \quad (3)$$

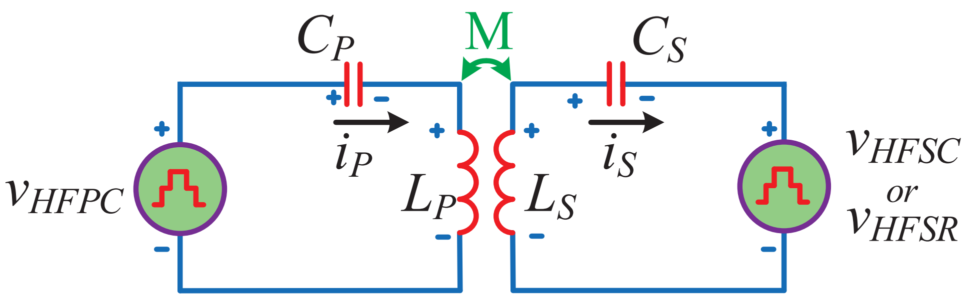

Figure 4. Equivalent circuit of the SAHFWPT and DAHFWPT with S-S coupling.

The maximum values of amplitudes for the first harmonic components of the voltages of the HFPC and HFSC of DAHFWPT are represented by v_{HFPC_M} and v_{HFSC_M}, respectively. Take into consideration that the external phase shift angle Φ ranges in the interval [0, 2π] for the Bi-directional operation DAHFWPT, whilst for the uni-directional operation, such as power flow exclusively from primary to secondary, the external phase shift angle Φ spans the interval [π, 2π]. However, for maximum power transfer it is Φ = 3π/2. Apart from Φ = 3π/2 value, the power transfer is not maximal due to the reactive current being not in the phase with the HFPC output and HFSC input voltage. This leads the circulating current flowing through the converter and coil.

Since the HFSR is a passive converter, the following conditions hold β = π and Φ = 3π/2, and from (3) the input voltage for the HFSR is expressed as:

$$v_{HFSR}(t) = v_{HFSR\_M} \sum_{n=1,\,3,\ldots}^{\infty} \frac{1}{n} \sin(\omega_r t + \Phi) \quad (4)$$

The harmonic and maximum harmonic input voltage of HFSR of SAHFWPT are represented by v_{HFSR} and v_{HFSR_M}. From Equation (2) it is clear that primary voltage v_{HFPC} relation is same for SAHFWPT and DAHFWPT. So from Figures 3 and 4 $v_{HFPC\_S} = v_{HFPC\_D} = v_{HFPC}$. Indeed the secondary voltage relation is not same, from the Figures 3 and 4, $v_{HFSR\_S} = v_{HFSR}$ and $v_{HFSC\_D} = v_{HFSC}$, respectively.

Applying Kirchhoff's voltage law in Figure 4, we obtain

$$v_{HFPC}(t) = R_P i_P(t) + L_P \frac{di_P(t)}{dt} + v_{P_C}(t) + v_P(t) \quad (5)$$

$$v_{HFSC}(t) = -R_S i_S(t) + +L_S \frac{di_s(t)}{dt} + v_{s_C}(t) + v_S(t) \quad (6)$$

where R_P and R_S internal resistance, L_P and L_s self-impedance of coil, $v_{P_C}(t)$ and $v_{S_C}(t)$ voltage drop across capacitor, $i_P(t)$ and $i_S(t)$ current flow from the S-S coil, $v_P(t)$ = M$\frac{di_S(t)}{dt}$ and $v_S(t)$ = $-$M$\frac{di_P(t)}{dt}$ are the induced voltage of primary and secondary S-S coils, respectively, M is the mutual inductance.

At the resonance frequency, the instantaneous power absorbed by the inductor L_P, L_S is equal to the instantaneous power delivered by the capacitor C_P, C_S. The net power delivered and absorbed by the capacitor and inductor is zero in the primary and secondary S-S coils, respectively. The impedance of the S-S coils is minimum at the resonating condition. Indeed, primary and secondary coil impedances are minimum; therefore, they represent the internal resistance of the S-S coil, i.e., R_P, R_S. Therefore, Equations (5) and (6) are re-arranged at resonating frequency as

$$i_P(t) = \frac{v_{HFPC}(t) - v_P(t)}{R_P}$$

$$i_S(t) = \frac{-v_{HFSC}(t) + v_S(t)}{R_S} \quad (7)$$

The voltage and current relationship at fundamental resonance frequency are represented in (8) to (11) for the DAHFWPT, similarly it is represented in (12) to (15) for SAHFWPT, by using approximation ωM $>>$ R_S and $(\omega M)^2$ $>>$ $R_P R_S$ for high Q-factor coil [6]. The expressions DAHFWPT and SAHFWPT are represented at fundamental harmonic approximation of the sinusoidal component in Tables 2 and 3 [20,22], respectively.

Table 2. DAHFWPT current voltage expressions at fundamental harmonic.

$v_{HFPC\_1}(t) = v_{HFPC\_1\_M}\sin\left(\frac{\alpha}{2}\right)\sin(\omega_r t)$	(8)	$v_{HFSC\_1}(t) = v_{HFSC\_1\_M}\sin\left(\frac{\beta}{2}\right)\sin(\omega_r t + \Phi)$	(9)
$i_{P\_D\_1}(t) = \frac{v_{HFSC\_1\_M}}{M\omega_r}\sin\left(\frac{\beta}{2}\right)\cos(\omega_r t + \Phi)$	(10)	$i_{s\_1}(t) = \frac{-v_{HFPC\_1\_M}}{M\omega_r}\sin\left(\frac{\alpha}{2}\right)\cos(\omega_r t)$	(11)

Table 3. SAHFWPT current voltage expressions at fundamental harmonic.

$v_{HFPC\_1}(t) = v_{HFPC\_1\_M}\sin\left(\frac{\alpha}{2}\right)\sin(\omega_r t)$	(12)	$v_{HFSR\_1}(t) = v_{HFSR\_1\_M}\sin(\omega_r t + \Phi)$	(13)
$i_{P\_S\_1}(t) = \frac{v_{HFSR\_1\_M}}{M\omega_r}\cos(\omega_r t + \Phi)$	(14)	$i_{s\_1}(t) = \frac{-v_{HFPC\_1\_M}}{M\omega_r}\sin\left(\frac{\alpha}{2}\right)\cos(\omega_r t)$	(15)

$v_{HFPC\_1\_M}$, $v_{HFSC\_1\_M}$ and v_{HFPC_1}, v_{HFSC_1} are the fundamental maximum amplitude and fundamental voltage of HFPC and HFSC, respectively. The secondary fundamental currents i_{s_1}, represented in Equations (11) and (15) for DAHFWPT and SAHFWPT, are the same as they only depend on α. Moreover, the primary fundamental current $i_{P\_D\_1}$ of DAHFWPT depends on β, while the primary fundamental current $i_{P\_S\_1}$ of SAHFWPT is constant, as β is fixed at π.

The uni-directional power flow was considered only in the case of battery charging, and the rated source voltages V_{DCP_S} = V_{DCP_D} = 386 V are constant for SAHFWPT and DAHFWPT; as mentioned in Table 4 the battery voltage is also same, i.e., V_{O_S} = V_{O_D} = 120 V. The secondary absolute lossless power for SAHFWPT and DAHFWPT can be express in (16) and (17) by using the (9), (11), (13), and (15)

$$P_{SAHFWPT\_S} = \frac{-v_{HFPC\_1\_M} v_{HFSC\_1\_M}\sin\left(\frac{\alpha}{2}\right)\sin(\Phi)}{2\omega M} \quad (16)$$

$$P_{DAHFWPT\_S} = \frac{-v_{HFPC\_1\_M} v_{HFSC\_1\_M}\sin\left(\frac{\alpha}{2}\right)\sin\left(\frac{\beta}{2}\right)\sin(\Phi)}{2\omega M} \quad (17)$$

where $v_{HFPC\_1\_M} = \frac{4V_{DCP\_S}}{\pi}$ and $v_{HFSR\_1\_M} = \frac{4V_O}{\pi}$ are the maximum voltage at the primary and secondary coil. From the Equations (16) and (17), the secondary power can be regulated using the internal phase shift angles α = β ∈ [0, 2π], and external phase shift angle Φ ∈ [π, 2π], while in Equation (16) β = π and Φ = 3π/2. the secondary power of SAHFWPT and DAHFWPT can be related by Equation (18):

$$P_{DAHFWPT\_S} = \sin\left(\frac{\beta}{2}\right) P_{SAHFWPT\_S} \tag{18}$$

Table 4. Simulation parameter for EV.

Parameters	Symbols	Values
Source Rated Voltage	V_{DCP_S}, V_{DCP_D}	384 V
Battery Rated voltage	V_{O_S}, V_{O_D}	120 V
Resonating frequency	f_r	85 kHz
MOSFETs	$T_5 - T_{12}$	SiHG33N60EF
Self-Inductance	$L_P L_S$	220 µH
Compensation Capacitors	$C_P C_S$	15.9 nF
S-S coil Resistance	$R_P R_S$	0.5 Ω
Mutual-Inductance	M	22.5 µH

Figure 5 shows the comparison of power curve between DAHFWPT and SAHFWPT of secondary power, w.r.t α, where α is in radian. The power $P_{DAHFWPT\_S}$ plotted with the red line, and $P_{SAHFWPT\_S}$ plotted with the blue line are directly related with sin(α/2) as mentioned in (18), when we fixed Φ = 3π/2 for maximum power transfer condition. From the power curve, it can be proven that the power of DAHFWPT and SAHFWPT are same at α = 3.14, i.e., π. Apart from that, DAHFWPT power sinusoidal decreases and it is always less than the SAHFWPT power that decreases almost linearly. It is observed in Figure 5 that SAHFWPT and DAHFWPT have similar instantaneous power, the internal phase shift angle of secondary power of DAHFWPT is always bigger than secondary power of SAHFWPT.

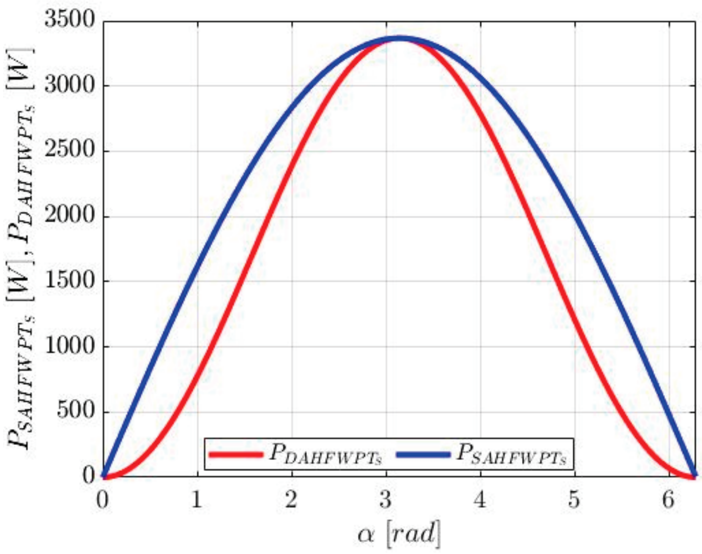

Figure 5. Secondary of the S-S coupling coil power relation of SAHFWPT and DAHFWPT w.r.t. α.

3. Methods of Loss Analysis of SAHFWPT and DAHFWPT

The operation of SAHFWPT and DAHFWPT are approximately same. The only difference is in the operation of the secondary side converter. The secondary HFSR of SAHFWPT is the passive converter, while the secondary HFSC of DAHFWPT is the active converter. Because HFSR and HFSC work in different ways, they are operating in the soft switching mode and the hard switching mode, respectively. Indeed, the switching losses of switches for the HFSR and HFSC are lower and higher, respectively. However, each diode of the HFSR are conducted for a π phase interval, whereas the conducting phase interval of the HFSC switches depending on β which one varies in the range of [0, 2π] so that the conduction period of HFSC switches may be π or the lesser than π period. The conduction loss of MOSFETs and body diodes depends on the amount of current flowing in the converter. As the secondary converter operation of the SAHFWPT and DAHFWPT are not the same, the power drawn from the source towards the rated load is different. Furthermore, conduction losses are only equal at the α = β = π. Apart from this loss, the few losses that depend on the converters are due to the gate charge, body diode conduction, output capacitor, body diode recovery, hard turn on, and hard turn off. In this section the comparative loss in the S-S coil is elaborated by using simulation parameter that listed in Table 4 whilst the losses in the filter capacitor and inductor are neglected.

3.1. S-S Coil Loss

Referring to the equivalent circuit shown in Figure 4, the resistive loss of the S-S coupling coil [10] can be expressed as:

$$P_{S-S\_coil\_SAHFWPT\_loss} = i^2_{P\_S\_1\_rms} R_P + i^2_{S\_1\_rms} R_S \tag{19}$$

$$P_{S-S\_coil\_DAHFWPT\_loss} = i^2_{P\_D\_1\_rms} R_P + i^2_{S\_1\_rms} R_S \tag{20}$$

where $i_{P\_S\_1\_rms}$, $i_{P\_D\_1\_rms}$, and $i_{S\_1\_rms}$ are the rms values of $i_{P\_S\_1}$, $i_{P\_D\_1}$, and i_{S_1}, respectively. R_P and R_S are the primary and secondary coil resistance. Using (10), (14) and any one from (11) and (15), we obtain

$$i_{P\_S\_1\_rms} = \frac{v_{HFSR\_1\_M}}{\sqrt{2} M \omega_r} \tag{21}$$

$$i_{P\_D\_1\_rms} = \frac{v_{HFSC\_1\_M}}{\sqrt{2} M \omega_r} \sin\left(\frac{\beta}{2}\right) \tag{22}$$

$$i_{S\_1\_rms} = \frac{v_{HFPC\_1\_M}}{\sqrt{2} M \omega_r} \sin\left(\frac{\alpha}{2}\right) \tag{23}$$

The efficiency of the S-S coupling coil of SAHFWPT and DAHFWPT can be expressed by using (16), (17), (19), and (20) as

$$\eta_{S-S\_coil\_SAHFWPT} = \frac{P_{SAHFWPT\_S}}{P_{SAHFWPT\_S} + P_{S-S\_coil\_SAHFWPT\_loss}} \tag{24}$$

$$\eta_{S-S\_coil\_DAHFWPT} = \frac{P_{DAHFWPT\_S}}{P_{DAHFWPT\_S} + P_{S-S\_coil\_DAHFWPT\_loss}} \tag{25}$$

$$\eta_{S-S\_coil\_SAHFWPT} = \frac{\eta_{S-S\_coil\_DAHFWPT}(A + B + C)\sin\frac{\alpha}{2}}{A\sin\frac{\alpha}{2} + B + C\sin^2\frac{\alpha}{2}} \tag{26}$$

Equation (26) represents the relation between $\eta_{S-S\_coil\_SAHFWPT}$ and $\eta_{S-S\_coil\_DAHFWPT}$ and can be derive by using (16), (17), (19), (20), (24), and (25) and setting

$$\begin{gathered} A = \frac{v_{HFPC\_1\_M} v_{HFSR\_1\_M}}{2M\omega_r} \\ B = \frac{\mathrm{R} v^2{}_{HFSR\_1\_M}}{2M^2 \omega^2{}_r} \\ C = \frac{\mathrm{R} v^2{}_{HFPC\_1\_M}}{2M^2 \omega^2{}_r} \\ R = R_R = R_S \\ \alpha = \beta \end{gathered} \tag{27}$$

Figure 6 shows the comparison of the S-S coil efficiency curves of SAHFWPT and DAHFWPT w.r.t α. They are computed by (24) and (25), using the parameters listed in Table 4 taken from an experimental setup. The efficiency plot of $\eta_{S-S\_coil\_SAHFWPT}$ is drawn in a solid blue line, while the plot of $\eta_{S-S\_coil\_DAHFWPT}$ is drawn in solid red line. At $\alpha = \pi$ the efficiency is equal in both systems. The efficiency of both systems are approximately same in the range of 2 rads to 4 rads. Further with movement left from 2 rads and right from 4 rads and up to approximate 0.3 rads and 6 rads, the efficiency of the SAHFWPT is higher than the DAHFWPT. Equation (26) complies with the graph plotted in Figure 6.

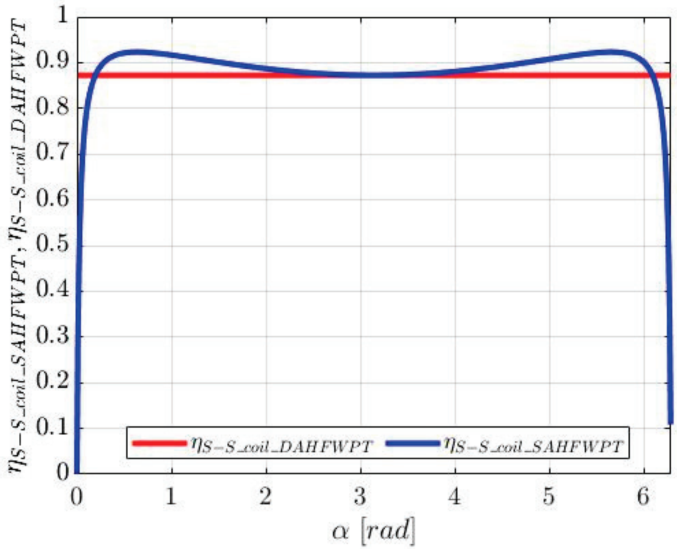

Figure 6. S-S coupling coil efficiency of SAHFWPT and DAHFWPT w.r.t. α.

3.2. Loss of HFSR, HFSC and HFPC

According to the Figure 2a,b, the secondary and primary converters of SAHFWPT and DAHFWPT are denoted as HFSR, HFSC, and HFPC. Two MOSFETs SiHG33N60EF are turned on at a same instant of time in the HFSC and HFPC converter during the active mode. Furthermore, the diodes are used for the passive mode of the HFSR. As the converters have a different operating principle, their losses are not equal.

3.2.1. Conduction Loss of MOSFET and Diodes

The conduction loss depends on amount of current flowing through the converter switches during in operating state, i.e., $i_{s\_1\_\mathrm{rms}}$, $i_{P\_s\_1\_\mathrm{rms}}$, and $i_{P\_D\_1\_\mathrm{rms}}$. The current $i_{s\_1\_\mathrm{rms}}$ depends on α, but α is not the same in both the HFSR and HFSC converters for the same instantaneous power. As shown in Figure 5, the current flowing through HFSR is less than the current following through the HFSC apart from $\alpha = \pi$. The current $i_{P\_s\_1\_\mathrm{rms}}$ is constant at 8.99 A whilst $i_{P\_D\_1\_\mathrm{rms}}$ varies depending on β, and is always lower than or equal to 8.99 A. The conduction losses of the diodes, body diodes, and MOSFETs are $P_{HFSR\_Cond\_loss}$, $P_{HFSC\_Cond\_loss}$, $P_{HFPC\_Cond\_S\_loss}$, and $P_{HFPC\_Cond\_D\_loss}$ and are represented in Equations (28)–(31), respectively [11] as

$$P_{HFSR\_Cond\_loss} = 2i_{S\_1\_rms}^2 R_{SD\_on} + 2V_{SD}\left|i_{S\_1\_avg}\right| \quad (28)$$

$$P_{HFSC\_Cond\_loss} = 2i_{S\_1\_rms}^2 R_{SD\_on} + 2V_{SD}\left|i_{S\_1\_avg}\right| \quad (29)$$

$$P_{HFPC\_Cond\_S\_loss} = 2i_{P\_S\_1\_rms}^2 R_{SD\_on} \quad (30)$$

$$P_{HFPC\_Cond\_D\_loss} = 2i_{P\_D\_1\_rms}^2 R_{SD\_on} \quad (31)$$

where $i_{P\_D\_1\_avg}$ and $i_{S\_1\_avg}$ are the average currents flowing in the diodes of the HFPC and HFSR in half of the switching period. From the data sheet of SiHG33N60EF, R_{SD_on} results in about 0.085 Ω and the diode forward voltage V_{SD} is about 0.9 V.

3.2.2. Hard Turn on and off Loss

The switching loss of diodes of MOSFETs for HFSR are zero, as diodes turn on and turn off at zero current, as shown in Figure 3a. However, in the HFSC the body diodes D_9 and D_{12} have hard turn on and turn off at $\frac{-\beta}{2}$ and $\frac{\beta}{2}$ as shown in Figure 3b. The power $P_{HFSC\_on\_\_off\_loss}$ corresponds to the switching loss of switches for the HFSC and is given by (32) in [12,13], the power $P_{HFPC\_on\_\_off\_S\_loss}$, and $P_{HFPC\_on\_\_off\_D\_loss}$ are the switching loss of switches for the HFPC for SAHFWPT and DAHFWPT, respectively, and they are provided by (33) and (34), respectively as

$$P_{HFSC\_on\_\_off\_loss} = \frac{1}{2} f_r V_{O\_D} I_{on} t_{on} + \frac{1}{2} f_r V_{O\_D} I_{off} t_{off} \tag{32}$$

$$P_{HFPC\_on\_\_off\_S\_loss} = \frac{1}{2} f_r V_{DCP\_S} I_{on} t_{on} + \frac{1}{2} f_r V_{DCP\_S} I_{off} t_{off} \tag{33}$$

$$P_{HFPC\_on\_\_off\_D\_loss} = \frac{1}{2} f_r V_{DCP\_D} I_{on} t_{on} + \frac{1}{2} f_r V_{DCP\_D} I_{off} t_{off} \tag{34}$$

From the data sheet of SiHG33N60EF, t_{on} and t_{off} are 28ns and 161ns, respectively. I_{on} and I_{off} are on the and off current of $i_{S\_1\_rms}$ at $\frac{-\beta}{2}$ and $\frac{\beta}{2}$ in the HFSC shown in Figure 3b. I_{on} and I_{off} are the on and off current of $i_{P\_S\_1\_rms}$; I_{on} and I_{off} are on and off current of $i_{P\_D\_1\_rms}$ current at $\Phi - \frac{\alpha}{2}$ and $\Phi + \frac{\alpha}{2}$ in the HFPC for the SAHFWPT and DAHFWPT shown in Figure 3a,b, respectively.

3.2.3. Other Switching Losses in the MOSFET

Apart from the above losses of the MOSFET, the overall switching loss estimation depends on some other losses. Such as, output capacitance C_{OSS} and body diode reverse recovery losses. When MOSFETs turn off, the energy stored in the C_{OSS} discharges through the body diode and originates the turn on loss provided in [22]. The P_{Coss_loss} in C_{OSS} is expressed in Equation (35) as

$$P_{Coss\_loss} = \frac{1}{2} f_r C_{oss} V_{DS}^2 \tag{35}$$

From the data sheet of SiHG33N60EF $C_{oss} = 154\ pF$, the switching frequency is same as resonating frequency $f_r = 85$ kHz and the drain to source voltage V_{DS} is the same as the voltage applied across the converter.

The body diode reverse recovery takes place [10], therefore the diode turns off while carrying a positive forward current due to the large reverse time t_{rr}. The relation for body diode reverse recovery loss P_{body_loss} is as follows

$$P_{body\_loss} = f_r Q_{rr} V_{off} \tag{36}$$

where V_{off} is the forward voltage drop of the diode during the conduction. $Q_{rr} = 2\mu C$ is the reverse recovery charge.

4. Efficiency of SAHFWPT and DAHFWPT

The efficiency is the ratio of the output power to the input power of any system. The general expression for efficiency is

$$\eta = \frac{P_O}{P_{in}} \tag{37}$$

whereas $P_{in} = P_O + P_{loss}$ with P_{loss} denoting the overall losses of the system, P_{in} represents the input power and P_O represents the output power. Equation (37) express the overall efficiency of the system. However, overall efficiency expression for SAHFWPT and DAHFWPT follow Equation (37). and are represented as $\eta_{SAHFWPT}$ and $\eta_{DAHFWPT}$ and formulated in Equations (38) and (39), respectively.

$$\eta_{SAHFWPT} = \frac{P_B}{P_B + P_{SAHFWPT\_loss}} \tag{38}$$

$$\eta_{DAHFWPT} = \frac{P_B}{P_B + P_{DAHFWPT\_loss}} \tag{39}$$

where P_B represents the power at the battery end. $P_{SAHFWPT\_loss}$ and $P_{DAHFWPT\_loss}$ represent the overall loss of the SAHFWPT and DAHFWPT, respectively. They can be subdivided into the contributions provided by

$$P_{SAHFWPT\_loss} = P_{S-S\_coil\_SAHFWPT\_loss} + P_{HFSR\_Cond\_loss} + P_{HFPC\_Cond\_S\_loss} + P_{Coss\_loss} + P_{body\_loss} + P_{HFPC\_on\_\_off\_S\_loss} \tag{40}$$

$$P_{DAHFWPT\_loss} = P_{S-S\_coil\_DAHFWPT\_loss} + P_{HFSC\_Cond\_loss} + P_{HFPC\_Cond\_D\_loss} + P_{Coss\_loss} + P_{body\_loss} + P_{HFPC\_on\_\_off\_D\_loss} + P_{HFSC\_on\_\_off\_loss} \tag{41}$$

The Equations (40) and (41) represent the overall loss of the WPT system. That includes coil loss, conduction loss of switch, output capacitor of MOSFET discharging time loss, diode, body diode reverse recovery loss, and converter on and off losses are included for both the SAHFWPT and DAHFWPT system.

5. Simulation Results

The SAHFWPT and DAHFWPT in Figure 2a,b were simulated in MATLAB with the parameters specified in Table 4. This section presents the discussion about the overall losses and the efficiency of the system, described by the loss characteristics and efficiency curve. Voltage and current plots in Figure 7a refer to SAHFWPT, the solid blue line represent the output voltage of HFPC and the input voltage of HFSR in steady state and the corresponding currents using the solid red lines. Voltage and current plots in Figure 7b refer to DAHFWPS, the solid blue line the output voltage of HFPC and input voltage of HFSC in steady state, and the corresponding currents using the solid red lines. For a clear viewing of the current, the primary current and the secondary current are multiplied by the factors 20 and 3, respectively. Due to resonating behavior of the S-S coupling coil, the currents of primary and secondary coils are sinusoidal in nature and the voltage are a quasi-square wave. The input power ratings are 1252 W and 472 W at $\alpha = 0.73$ for SAHFWPT and DAHFWPT, respectively.

The first column of Table 5 contains the different value of α. For the analysis, we consider α equal to β as a reference value. The second column reports the input power, the third column contains the overall loss of the system, the fourth column contains the overall loss in percentage. Columns two, three, and four are further subdivided into SAHFWPT and DAHFWPT. From the analytical data reported in Table 5, the percentage losses of SAHFWPT decrease as α decreases, but near to zero value of α, percentage losses increase. On the contrary, in the case of DAHFWPT, losses percentage is almost constant as α decreases but, as it happens with SAHFWPT, near to the zero value of α loss percentage increases and losses in DAHFWPT are higher than losses in SAHFWPT. However, the instantaneous input power of SAHFWPT and DAHFWPT at $\alpha = 0.33$ are 604 W and 102 W. These results are obtained at $\Phi = 3\pi/2$.

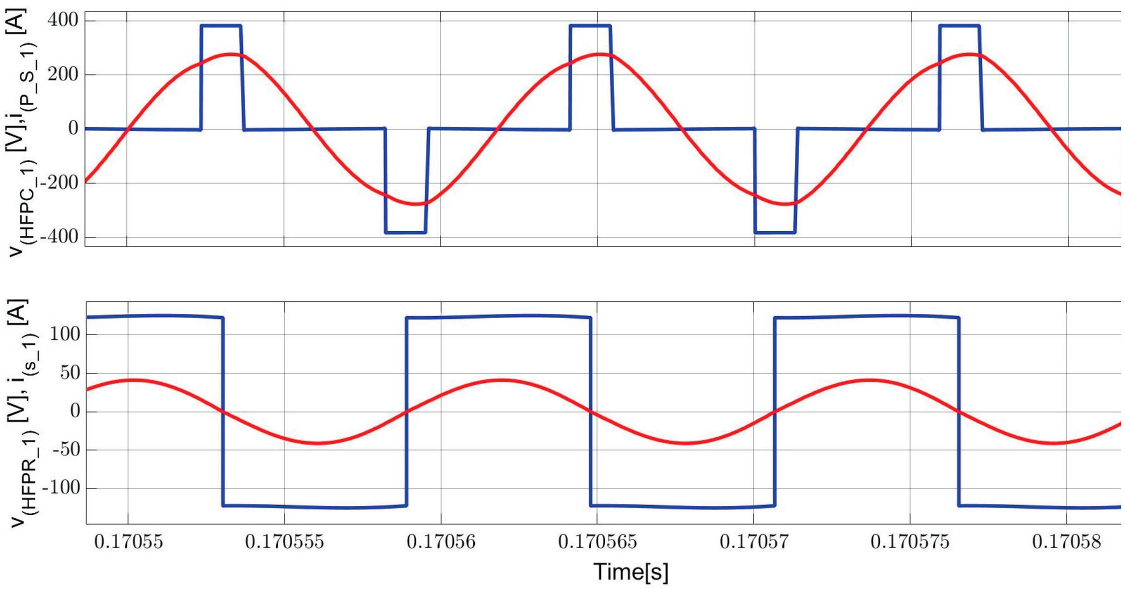

(**a**)

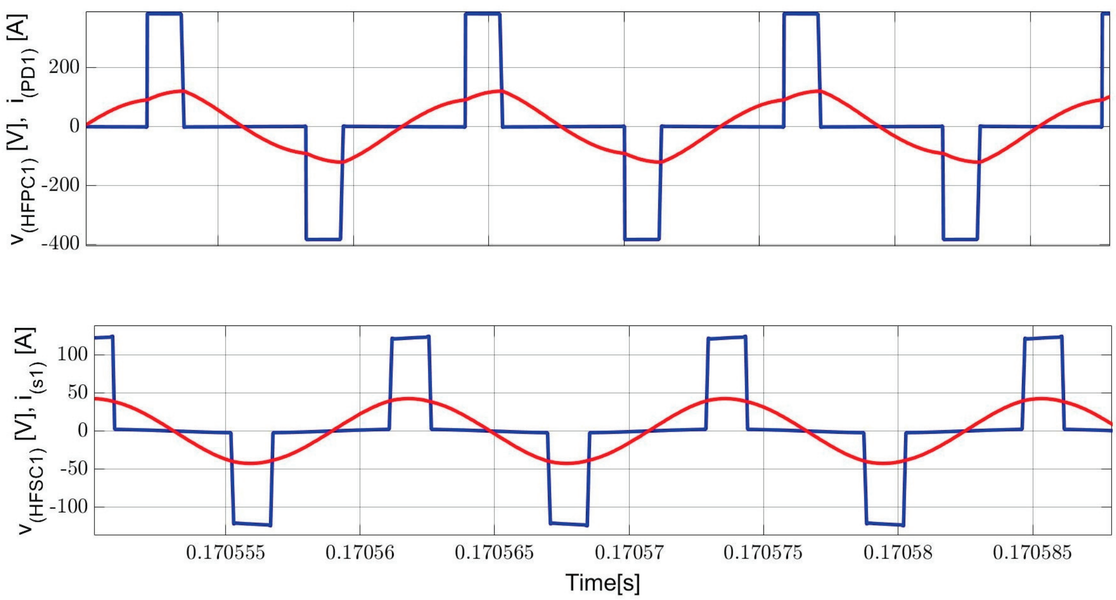

(**b**)

Figure 7. Current (red) and voltage (blue) wave input of primary coil and output of the secondary coil of (**a**) SAHFWPT (**b**) and DAHFWPT.

Table 5. Overall loss analytical data for SAHFWPT and DAHFWPT at Φ = 3π/2 and α = β.

α	Input Power		Loss into the System		% Loss into the System	
	SAHFWPT	**DAHFWPT**	**SAHFWPT**	**DAHFWPT**	**SAHFWPT**	**DAHFWPT**
3.12	3605	3605	586	586	16.25	16.25
2.16	3146	2807	469	453	14.97	16.15
1.82	2795	2252	388	361	13.87	16.05
1.44	2312	1574	290	250	12.54	15.88
1.14	1881	1057	217	165	11.51	15.65
0.73	1245	467	136	71	10.94	15.23
0.33	605	102	99	23	16.34	22.43

Figure 8a,b show the steady state input power and the loss curves of the SAHFWPT in solid blue line and DAHFWPT in solid red line. The input power of the system is in the range of 0 to 3600 W. As per Equation (18), SAHFWPT input power is always greater than DAHFWPT at equal α apart from $\alpha = \pi$. Both input power and loss curve are symmetric with respect to $\alpha = 3.14$. From the loss curve, it is visible that the losses in SAHFWPT are always greater than losses in DAHFWPT. Consequently, for the same instantaneous input power in both systems, the losses are not same. For example, at the input power equal to 2004 W indicated by data tip at $\alpha = 1.68$ and $\alpha = 5.06$, the losses are 320 W and 236 W for the DAHFWPT and the SAHFWPT, respectively. From the above discussion and Table 5 data, it is proven that the losses of SAHFWPT are less than or equal to the DAHFWPT.

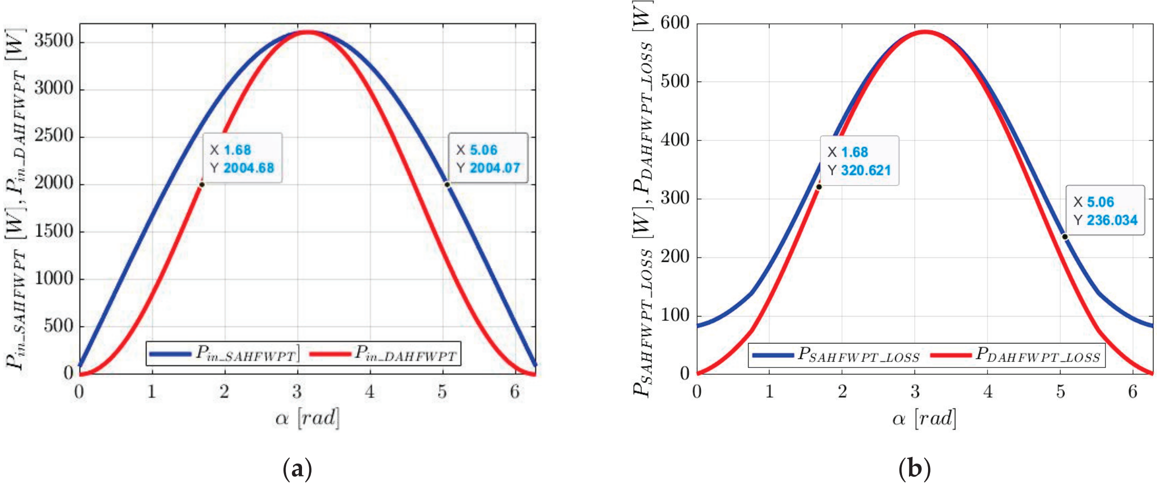

Figure 8. (**a**) Input power (**b**) overall losses of the system w.r.t. α.

Figure 9a presents efficiency plots, i.e., $\eta_{SAHFWPT}$ in solid blue line and $\eta_{DAHFWPT}$ in solid red line as a function of the internal phase shift angle α, obtained from (38) and (39) for the SAHFWPT and DAHFWPT, respectively. Both the maximum efficiencies of the SAHFWPT and DAHFWPT, i.e., 89.2% and 84.9%, are reached at $\alpha = 0.73$, respectively. The efficiencies $\eta_{SAHFWPT}$ and $\eta_{DAHFWPT}$ have two picks at $\alpha = 0.73$ and 5.55. For α in the ranges from 0.73 to 2.3 and from 3.98 to 5.55 the efficiency $\eta_{SAHFWPT}$ is always greater than $\eta_{DAHFWPT}$. Moreover, in these range of $\eta_{DAHFWPT}$ the results nearly constant. For α ranging in the interval from 2.3 to 3.98, the efficiency $\eta_{SAHFWPT}$ is almost equal to $\eta_{DAHFWPT}$.

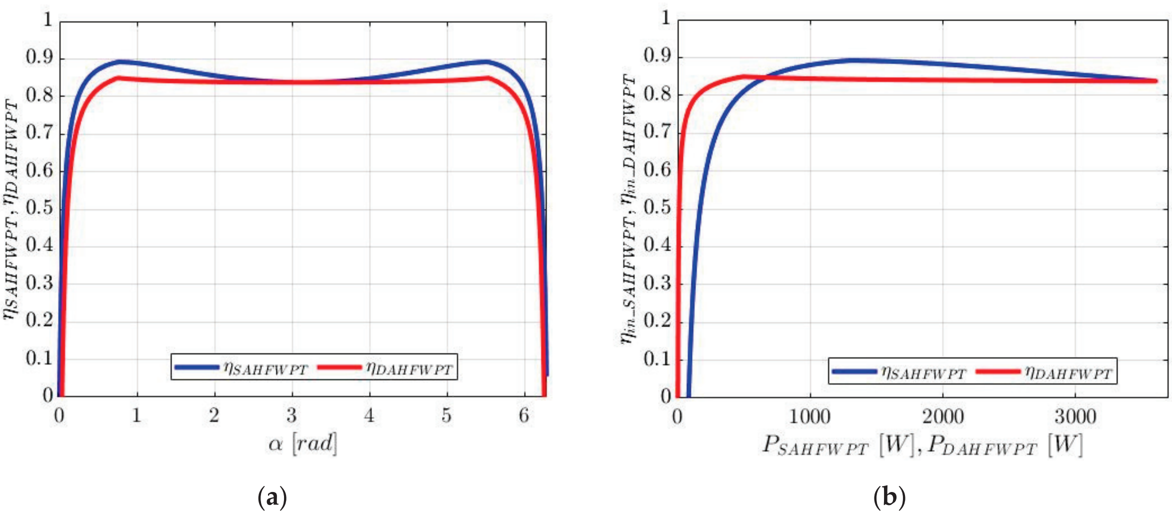

Figure 9. Efficiency of WPT system (**a**) w.r.t. α (**b**) w.r.t. $P_{SAHFWPT}$ *and* $P_{DAHFWPT}$.

Figure 9b reports the efficiency plots as a function of the input power $P_{SAHFWPT}$ and $P_{DAHFWPT}$, obtained from (38) and (39), respectively. The maximum efficiencies of 89.2% and 84.9% of SAHFWPT and DAHFWPT are reached at $P_{SAHFWPT} = 1325$ W and $P_{DAHFWPT} = 491$ W, respectively. It is visible that the operating conditions of the SAHFWPT and DAHFWPT can be divided into two zones. When power $P_{SAHFWPT}$ is in the interval [648 W 3606 W], efficiency $\eta_{SAHFWPT}$ is greater than efficiency $\eta_{DAHFWPT}$. However, for the input power $P_{DAHFWPT}$ less than 648 W, the efficiency $\eta_{DAHFWPT}$ is greater than the efficiency $\eta_{SAHFWPT}$.

At the end of the study and their losses comparison of SAHFWPT and DAHFWPT, we are able to decide the superiority of the DC–DC converters, in terms of efficiency and input power. As per the above discussion, the efficiency performance of the SAHFWPT is greater than that of DAHFWPT in the medium power range. Indeed, at medium power the efficiency of the SAHFWPT is 4.3% more than the efficiency of the DAHFWPT. Whilst for the low power range the efficiency of the SAHFWPT is approximately 12% less than the efficiency of the DAHFWPT.

6. Conclusions

This article presents a step-by-step comparison study of the losses at different stages of converters and S-S coupling coils together with the control approaches of primary and secondary converters of the SAHFWPT and DAHFWPT, respectively, at a domestic load, i.e., domestic load input power up to 3600 W. This includes the uni-directional power flow estimation at each stage of the WPT system, such as the HFPC, primary coil, secondary coil, HFSC, and HFSR. The power assessment includes the estimation of system losses considering the switches losses, conduction losses, hard turn on and off losses, and S-S coil losses, etc. These estimations of the power are performed according to the SAE J2954 and the domestic grid power. To analyze the comparative performance of SAHFWPT and DAHFWPT, the two different converters control approaches, i.e., EPS and DPS methods took place by varying the internal and external phase shift angle. This was further verified through MATLAB, and the respective power loss and efficiency plots were drawn. Following from the simulation result discussion reported in Section 5 about the loss and efficiency of the SAHFWPT and the DAHFWPT, the efficiency of the SAHFWPT converter was found always superior at the medium power level of domestic use, i.e., 89.2%. Indeed, it has approximately 4% higher efficiency. Whereas in the lower and higher power ranges, the DAHFWPT is more efficient than the SAHFWPT with this method of control.

The literature has reported about the use of the SAHFWPT and DAHFWPT system to control the battery current during charging. Indeed, charging through the SAHFWPT needs one more DC–DC converter to control the battery charging. Nevertheless, since the efficiency of SAHFWPT is higher than that of DAHFWPT in medium power range of domestic use, we have a new result: if we are able to design the secondary DC–DC converter (i.e., chopper) having approximately 98% efficiency, then the SAHFWPT is superior in terms of efficiency at medium power of domestic use.

Author Contributions: Conceptualization, A.K. and M.B.; methodology A.K. and M.B.; software, A.K., M.B. and R.K.J.; validation, A.K.; formal analysis, A.K.; investigation, A.K.; resources A.K., M.B., R.K.J. and A.S.; data curation, A.K., M.B., R.K.J. and A.S.; writing-original draft preparation, A.K., M.B., R.K.J. and AS.; writing-review and editing, A.K., M.B., R.K.J. and A.S.; visualization, A.K., M.B., R.K.J. and A.S.; supervision, A.K. and M.B. All authors have read and agreed to the published version of the manuscript.

Funding: This research received no external funding.

Data Availability Statement: Most of the data and the results are reported in the paper. Additional data can be requested from the corresponding author.

Conflicts of Interest: The authors declare no conflict of interest.

Nomenclature

SAHFWPT	Single Active High-Frequency wireless power transfer
DAHFWPT	Dual Active High-Frequency wireless power transfer
SPS	Single Phase Shift
EPS	Extended Phase Shift
DPS	Dual Phase Shift
TPS	Triple Phase shift
EV	Electrical Vehicle
RE	Renewable Energy
ESS	Energy Storage System
SAB	Single Active Bridge
DAB	Dual Active Bridge
PSFB	Phase Shift Full Bridge
DC	Direct Current
V_S	Source Voltage
R_B	Battery Equivalent Resistance
C_O	Output low pass filter capacitor
L_O	Output low pass filter inductor
ZVS	Zero Voltage Switching
ZCS	Zero Current Switching
HFPC	High-frequency Primary Converter
HFSC	High-frequency Secondary Converter
HFSR	High-frequency Secondary Rectifier
V_{DCP_S}, V_{DCP_D}	DC voltage source of SAHFWPT and DAHFWPT
v_{HFPC_S}, v_{HFPC_D}	Output voltage of HFPC of SAHFWPT and DAHFWPT
i_{P_S}, i_{P_D}	Output current of HFPC of SAHFWPT and DAHFWPT
v_{HFSR_S}, v_{HFSC_S}	Input voltage of HFSR and HFSC of SAHFWPT and DAHFWPT
i_{S_S}, i_{S_D}	Input current of HFSR and HFSC of SAHFWPT and DAHFWPT
V_{O_S},V_{O_D}	Output voltage of HFSR and HFSC of SAHFWPT and DAHFWPT
ω_r	Resonant Frequency
Φ	External Phase shift angle
α	Internal phase shift angle of HFPC
β	Internal phase shift angle of HFSC
v_{HFPC_M}, v_{HFSC_M}	Peak amplitude of output and input voltage of HFPC and HFSC of DAHFWPT
v_{HFSR_M}	Peak amplitude of input voltage of HFSR of SAHFWPT
C_P, C_S	Primary and secondary resonant capacitor
L_P, L_S	Primary and secondary coil self-inductance
R_P, R_S	Primary and secondary coil resistance
Z_P,Z_S	Impedance of primary and secondary coil
M	Coils mutual inductance
v_P,v_S	Primary and secondary coil induce voltage
i_P, i_S	Primary and secondary coil circulating current
P_{PS}	Average power flow from primary to secondary
v_{HFPC_1}, v_{HFSC_1}	Fundamental Output and Input voltage of HFPC and HFSC of DAHFWPT
v_{HFSR_1}	Fundamental of Input voltage of HFSR of SAHFWPT
$i_{P\_D\_1}$, $i_{P\_S\_1}$	Fundamental primary coil current of DAHFWPT and SAHFWPT
i_{s_1}	Fundamental secondary coil current of DAHFWPT and SAHFWPT
$P_{DAHFWPT\_S}$, $P_{SAHFWPT\_S}$	Secondary Power of DAHFWPT and SAHFWPT
$P_{S-S\_coil\_DAHFWPT\_loss}$, $P_{S-S\_coil\_SAHFWPT\_loss}$	Coil Loss of DAHFWPT and SAHFWPT
$\eta_{S-S\_coil\_DAHFWPT}$, $\eta_{S-S\_coil\_SAHFWPT}$	Efficiency of coil of DAHFWPT and SAHFWPT
$P_{HFPC\_Cond\_S\_loss}$, $P_{HFSR\_Cond\_loss}$	Conduction loss of HFPC and HFSR of SAHFWPT
$P_{HFPC\_Cond\_D\_loss}$, $P_{HFSC\_Cond\_loss}$	Conduction loss of HFPC and HFSC of DAHFWPT
$P_{HFSC\_on\_\_off\_loss}$	Switching loss of switches for HFSC
$P_{HFPC\_on\_\_off\_D\_loss}$, $P_{HFPC\_on\_\_off\_S\_loss}$	Switching loss of switches for HFPC of DAHFWPT and SAHFWPT
P_{Coss_loss}	Output capacitor loss of MOSFET
P_{body_loss}	Body diode reverse recovery loss
η	Efficiency

P_O	Output Power
P_{in}	Input Power
P_{loss}	Power Loss
P_B	Power of Battery
$P_{SAHFWPT\_loss}$	Overall loss Power of SAHFWPT
$P_{DAHFWPT\_loss}$	Overall loss Power of DAHFWPT
$\eta_{SAHFWPT}$	Efficiency of SAHFWPT
$\eta_{DAHFWPT}$	Efficiency of DAHFWPT
WPT	Wireless Power Transfer

References

1. Chen, T.; Zhang, X.-P.; Wang, J.; Li, J.; Wu, C.; Hu, M.; Bian, H. A Review on Electric Vehicle Charging Infrastructure Development in the UK. *J. Mod. Power Syst. Clean Energy* **2020**, *8*, 193–205. [CrossRef]
2. Far, M.F.; Paakkinen, M.; Cremers, P. A Framework for Charging Standardisation of Electric Buses in Europe. In Proceedings of the IEEE Vehicle Power and Propulsion Conference (VPPC), Gijon, Spain, 18 November–16 December 2020; pp. 1–4.
3. Bertoluzzo, M.; Giacomuzzi, S.; Kumar, A. Design of a Bidirectional Wireless Power Transfer System for Vehicle-to-Home Applications. *Vehicles* **2021**, *3*, 406–425. [CrossRef]
4. Fontana, C.; Forato, M.; Bertoluzzo, M.; Buja, G. Design characteristics of SAB and DAB converters. In Proceedings of the Intl Aegean Conference on Electrical Machines & Power Electronics (ACEMP) Intl Conference on Optimization of Electrical & Electronic Equipment (OPTIM) & Intl Symposium on Advanced Electromechanical Motion Systems (ELECTROMOTION), Side, Turkey, 2–4 September 2015; pp. 661–668.
5. Jha, R.; Forato, M.; Prakash, S.; Dashora, H.; Buja, G. An Analysis-Supported Design of a Single Active Bridge (SAB) Converter. *Energies* **2022**, *15*, 666. [CrossRef]
6. Zhao, B.; Song, Q.; Liu, W.; Sun, Y. Overview of Dual-Active-Bridge Isolated Bidirectional DC–DC Converter for High-Frequency-Link Power-Conversion System. *IEEE Trans. Power Electron.* **2014**, *29*, 4091–4106. [CrossRef]
7. Xu, F.; Wong, S.C.; Tse, C.K. Overall Loss Compensation and Optimization Control in Single-Stage Inductive Power Transfer Converter Delivering Constant Power. *IEEE Trans. Power Electron.* **2022**, *37*, 1146–1158. [CrossRef]
8. Di Capua, G.; Femia, N.; Petrone, G.; Lisi, G.; Du, D.; Subramonian, R. Rajaram Subramonian. Power and efficiency analysis of high-frequency Wireless Power Transfer Systems. *Int. J. Electr. Power Energy Syst.* **2017**, *84*, 124–134. [CrossRef]
9. *J2954: Wireless Power Transfer for Light-Duty Plug-In/Electric Vehicles and Alignment Methodology*; SAE International: Warrendale, PA, USA, 2020.
10. Gonzalez-Gonzalez, J.M.; Trivino-Cabrera, A.; Aguado, J.A. Assessment of the Power Losses in a SAE J2954-Compliant Wireless Charger. *IEEE Access* **2022**, *10*, 54474–54483. [CrossRef]
11. Ravikiran, V.; Keshri, R.; Rathore, A.; Chakraborty, C. Loss Analysis of Resonant Inductive Power Transfer System for Wireless Charging of e-Rickshaw. In Proceedings of the IEEE 28th International Symposium on Industrial Electronics (ISIE), Vancouver, BC, Canada, 12–14 June 2019; pp. 2559–2564.
12. Di Capua, G.; Femia, N.; Lisi, G. Impact of losses and mismatches on power and efficiency of Wireless Power Transfer Systems with controlled secondary-side rectifier. *Integration* **2016**, *55*, 384–392. [CrossRef]
13. Acquaviva, A.; Rodionov, A.; Kersten, A.; Thiringer, T.; Liu, Y. Analytical Conduction Loss Calculation of a MOSFET Three-Phase Inverter Accounting for the Reverse Conduction and the Blanking Time. *IEEE Trans. Ind. Electron.* **2021**, *68*, 6682–6691. [CrossRef]
14. Kalra, G.R.; Pearce, M.G.S.; Kim, S.; Thrimawithana, D.J.; Covic, G.A. A Power Loss Measurement Technique for Inductive Power Transfer Magnetic Couplers. *IEEE J. Emerg. Sel. Topics Ind. Electron.* **2020**, *1*, 113–122. [CrossRef]
15. Carretero, C. Coupling Power Losses in Inductive Power Transfer Systems with Litz-Wire Coils. *IEEE Trans. Ind. Electron.* **2017**, *64*, 4474–4482. [CrossRef]
16. Rossmanith, H.; Doebroenti, M.; Albach, M.; Exner, D. Measurement and Characterization of High Frequency Losses in Nonideal Litz Wires. *IEEE Trans. Power Electron.* **2011**, *26*, 3386–3394. [CrossRef]
17. Ren, Y.; Xu, M.; Zhou, J.; Lee, F. Analytical loss model of power MOSFET. *IEEE Trans. Power Electron.* **2006**, *21*, 310–319.
18. Huang, Z.; Lam, C.S.; Mak, P.I.; Martins, R.S.; Wong, S.C.; Tse, C.K. A Single-Stage Inductive-Power-Transfer Converter for Constant-Power and Maximum-Efficiency Battery Charging. *IEEE Trans. on Power Electron.* **2020**, *35*, 8973–8984. [CrossRef]
19. Fu, M.; Tang, Z.; Liu, M.; Ma, C.; Zhu, X. Full-bridge rectifier input reactance compensation in Megahertz wireless power transfer systems. In Proceedings of the IEEE PELS Workshop on Emerging Technologies: Wireless Power, Daejeon, Republic of Korea, 5–6 June 2015; pp. 1–5.
20. Enssle, A.; Parspour, N. Power Loss Shifted Design of Inductive Energy Transfer Systems. *IEEE Open J. Power Electron.* **2020**, *1*, 113–123. [CrossRef]
21. Shiba, K.; Morimasa, A.; Hirano, H. Design and Development of Low-Loss Transformer for Powering Small Implantable Medical Devices. *IEEE Trans. Biomed. Circuits Syst.* **2010**, *4*, 77–85. [CrossRef] [PubMed]
22. Di Capua, G.; Sánchez, J.A.; Cabrera, A.T.; Cabrera, D.F.; Femia, N.; Petrone, G.; Spagnuolo, G. A losses-based analysis for electric vehicle wireless chargers. In Proceedings of the International Conference on Synthesis, Modeling, Analysis and Simulation Methods and Applications to Circuit Design (SMACD), Istanbul, Turkey, 7–9 September 2015; pp. 1–4.

23. Sagar, A.; Kumar, A.; Bertoluzzo, M.; Jha, R.K. Analysis and Design of a Two-winding Wireless Power Transfer System with Higher System Efficiency and Maximum Load Power. In Proceedings of the IECON 2022—48th Annual Conference of the IEEE Industrial Electronics Society, Brussels, Belgium, 17–20 October 2022; pp. 1–6.
24. Van Mulders, J.; Delabie, D.; Lecluyse, C.; Buyle, C.; Callebaut, G.; Van der Perre, L.; De Strycker, L. Wireless Power Transfer: Systems, Circuits, Standards, and Use Cases. *Sensors* **2022**, *22*, 5573. [CrossRef] [PubMed]
25. Turzyński, M.; Bachman, S.; Jasiński, M.; Piasecki, S.; Ryłko, M.; Chiu, H.-J.; Kuo, S.-H.; Chang, Y.-C. Analytical Estimation of Power Losses in a Dual Active Bridge Converter Controlled with a Single-Phase Shift Switching Scheme. *Energies* **2022**, *15*, 8262. [CrossRef]
26. Oggier, G.G.; García, G.O.; Oliva, A.R. Switching Control Strategy to Minimize Dual Active Bridge Converter Losses. *IEEE Trans. Power Electron.* **2009**, *24*, 1826–1838. [CrossRef]
27. Bai, H.; Mi, C. Eliminate Reactive Power and Increase System Efficiency of Isolated Bidirectional Dual-Active-Bridge DC–DC Converters Using Novel Dual-Phase-Shift Control. *IEEE Trans. Power Electron.* **2008**, *23*, 2905–2914. [CrossRef]

batteries

MDPI

Article

Optimal Utilization of Charging Resources of Fast Charging Station with Opportunistic Electric Vehicle Users

Konara Mudiyanselage Sandun Y. Konara *, Mohan Lal Kolhe *, Nils Ulltveit-Moe and Indika A. M. Balapuwaduge

Faculty of Engineering and Science, University of Agder, P.O. Box 422, 4604 Kristiansand, Norway
* Correspondence: konara@uia.no (K.M.S.Y.K.); mohan.l.kolhe@uia.no (M.L.K.)

Abstract: The key challenge with the rapid proliferation of electric vehicles (EVs) is to optimally manage the available energy charging resources at EV fast-charging stations (FCSs). Furthermore, the rapid deployment of fast-charging stations provides a viable solution to the potential driving range anxiety and charging autonomy. Costly grid reinforcements due to extra load caused by fast charging can be omitted using a dedicated energy storage and/or renewable energy system at the FCS. The energy supply and fixed number of EV supply equipment (EVSE) are considered as the limited charging resources of FCS. Amidst various uncertainties associated with the EV charging process, how to optimally utilize limited charging resources with opportunistic ultra-fast charging EV users (UEVs) is studied in this work. This work proposes resource allocation and charging coordination strategies that facilitate UEVs to dynamically exploit these limited charging resources with defined liabilities when pre-scheduled users (SEVs) do not occupy them to utilize limited charging resources maximally. Moreover, the proposed dynamic charging coordination strategies are analyzed with a Monte Carlo simulation (MCS). The presented numerical results reveal that the major drawbacks of under-utilization of limited charging resources by SEVs can be significantly improved through dynamic charging resource allocation and coordination along with UEVs. With the proposed charging coordination strategies in this study, the maximum charging resource utilization of considered FCS with 10 EVSE has been improved to 90%, which bounds to 78% only with SEVs.

Keywords: electric vehicles; DC fast charging; fast-charging station; performance assessment of EV charging; hierarchical charging control

1. Introduction

The proliferation of electric vehicles (EVs) does have enough potential to significantly reduce environmental and health-related issues caused by vehicular contaminant emissions. The rapid adoption of EVs on roads contributes to the United Nations' sustainable development goals (SDGs) in terms of mobility to achieve an affordable, reliable, and sustainable mode of transportation [1]. Electric transportation provides feasible solutions to the high reliance on fossil fuels and the volatility of their prices, in addition to environmental and health concerns associated with fossil-fuel based transportation [2].

The required number of EVs on the road needed to accomplish net-zero emission targets defined by the International Energy Agency (IEA) remain enormous, as the current EV market share is significantly lower than what is required [3,4]. In this context, high vehicle cost, long charging time, range anxiety, and charging autonomy pose major challenges to promoting EVs. Although high EV battery capacity assures a high driving range, it increases weight as well as represents a high share of EV price [5,6]. Moreover, currently, EV batteries are emerging with high energy and power densities in addition to long-life time due to perceptible advancements in lithium-ion battery technology over the last decade. Therefore, high energy and power-dense batteries and modern energy conversion technologies enable EV manufacturers to produce high-capacity EVs with fast charging capabilities [7–10].

Currently, EV and/or EV supply equipment (EVSE) manufacturers produce DC off-board chargers that can potentially provide high power ratings ranging from 50 kW to 400 kW [11]. Therefore, DC fast-charging stations (FCSs) can be deployed widely to overcome the challenges that are barriers to promoting EVs. Sparsely deployed FCSs may promote wholesale market adoption of lightweight EVs, as they can have similar refueling experience to gasoline counterparts [12].

Although the sparse deployment of FCSs would alleviate charging and range concerns of long trips without requiring costly high-capacity EVs, high penetration of FCSs poses substantial impacts on the power grid in terms of network capacity, power system stability, and power quality. When FCS demand grows, rapid voltage changes and voltage flicker take place at the distribution grid. An FCS is a significant harmonic emission source to the grid that results in both voltage and current harmonic distortion. As EVSE are power electronic-based systems, an FCS causes super harmonic distortion in the power grid [13]. Therefore, increasing penetration of FCSs into the distribution grid requires costly grid reinforcements or reconstructions to avoid issues related to power quality, network capacity, and energy market operation [13,14]. However, these costly grid reinforcements and reconstructions can be mitigated by embedding a renewable energy system (RES) or energy storage (ES) into the FCS while employing a coordinated charging scheme [15–17]. Therefore, the contract demand, RES, or ES can be considered as the energy supply of the FCS that should ensures uninterruptible supply. To avoid grid stresses, the power supply of the FCS should strictly adhere to grid constraints while maximally utilizing the local energy supply.

Usually battery technology limits the maximum charging power. The material used for the battery electrodes affects the energy and power density of a lithium-ion battery. Moreover, the maximum charging power of a battery depends on the thermal performance of the cell, and the cooling arrangement in both the cell and pack level has a great impact on a battery's maximum charging power [18–21]. The majority of commercial EV models are equipped with battery packs with a size ranging from 10 kWh to 100 kWh, along with specific charging constraints. Therefore, this wide range of charging demand has to be taken into consideration when developing charging coordination and scheduling schemes. To cope with the wide range of charging demand, the ICE61851 [22] and ICE62196 [23] standards contemplate a wide range of DC-fast chargers capable of providing fast and ultra-fast charging.

As far as commercially available EV models are concerned, it takes several minutes to a few hours for rechargem depending on the EV capacity, charging constraints of the EV batteries, the current state of charge (SoC), and EV user preferences. Therefore, it necessitates a charging scheduling scheme specially for time-consuming charging processes to optimize the charging process while adhering to a set of constraints enforced by the power grid and energy market. Different objectives related to the EV charging process at the FCS can be considered to formulate the optimization problem for EV charging. In this context, extensive research studies have been devoted to schedule EVs and coordinate the charging process at a CS over a planning horizon by considering various objectives such as economic aspects, operational aspects, service quality aspects, etc. Those research efforts focused on managing the EV fleet at FCSs can be basically split into two categories: (1) off-line or online/time-advance or real-time strategies; (2) static or mobility-aware strategies. Furthermore, most of the charging scheduling schemes presented in the literature employ a hierarchical architecture that allows tackling different objectives/aspects at different hierarchical layers [24]. Most of the presented deterministic charging scheduling optimization problems assume that the input data for the problem are accurately known in advance [24–26].

Although an offline strategy obtains the optimum charging schedule, due to various uncertainties associated with EV charging, illustrated in Figure 1, the expected revenue might not be accomplished in real-time operation, and the obtained solution would not be a feasible or practical one. In order to cope with these uncertainties, authors have incorporated several techniques to optimally schedule EVs at the CS with this hierarchical approach. In some cases (e.g., [27,28]), intermediate or upper layers schedule charging processes with a static approach as an offline schedule, and the CS execute this schedule in real-time using a straight-forward heuristic algorithm with less computational overhead to cope with the dynamic environment.

In some other set of studies presented (e.g., [29,30]), the proposed static algorithm is executed iteratively to deal with the stochastic nature of the EV charging process. To minimize the revenue loss due to cancellations of scheduled charging processes and unexpected departures, authors in [31] proposed multi-aggregator collaborative scheduling. As the EV demand can be shared among multiple aggregators in these strategies, the peak load caused by the high penetration of EVs can be smoothed at the power grid level.

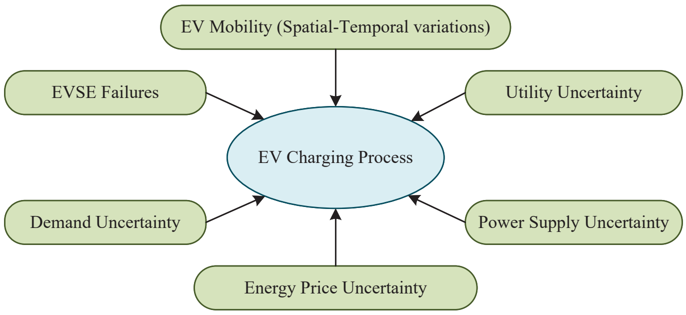

Figure 1. Uncertain aspects for EV charging process [24].

This research focuses more on the benefits of the CS (aggregator) rather than the distinct charging demands of heterogeneous EV users. In these studies, attention was given to admitted EVs at the CS. Research into charging management of plugged-in EVs can be useful from the aggregator and grid stability perspectives, but to counterbalance customer/EV user satisfaction, it is important to consider the quality of service related to EV charging in terms of EV blockage, preemptage, reliability, availability, etc. More importantly, optimal utilization of the FCS capacity with limited energy resources is an open research hotshot. Nevertheless, the proposed strategies would have been more realistic, feasible, and practical if a limited number of chargers/EVSE had been considered in the aforementioned research.

These research studies [32,33] proposed their charging scheduling strategies by considering limited charging resources. However, they have employed only the charging station capacity in their analysis but not the limited number of chargers/ EVSE. In a more realistic charging coordination scheme, the number of chargers/ EVSE and their individual capacity put another constraint on the charging coordination. However, limited charging resources including both energy resources and chargers/EVSE might not be optimally utilized by the registered/scheduled EV users due to various uncertainties, shown in Figure 1, in dynamic conditions. Moreover, scheduling the charging processes with only a few minutes of duration (long-trip drivers or ultra-fast charging users) might not be realistic. Although substantial research efforts have been devoted to optimal scheduling of EVs at a CS, how to effectively exploit unused limited charging resources allocated for scheduled users (SEVs) to further enhance resource utilization is not adequately analyzed to the best of the authors' knowledge.

Therefore, we propose event-based dynamic charging resource allocation and charging coordination strategies so that opportunistic ultra-fast charging users (UEVs) are allowed with different access privileges to exploit unused limited charging resources when registered SEVs are not very active within the FCS. In this work, we employ Monte Carlo simulation approach to assess the performance of the FCS in terms of charging resource utilization, charging completion, and quality of service aspects.

The novel technical contributions from this work can be summarized as follows:

1. Dynamic charging resource coordination strategies are proposed so that UEVs can exploit unused limited charging resources to enhance the charging resource utilization at the FCS while assuring high-quality service for both types of users.
2. Resource allocation and charging coordination is performed in a manner that the system changes its state when an event occurs and it remains until the next event occurs. This alleviates more practical issues of frequent on–off or modulating charging coordination strategies.
3. Performance evaluation parameters are defined and analyzed in a generic nature to evaluate the quality of service (QoS) of charging processes of SEVs and UEVs.

The subsequent sections of this paper are organized as follows. Section 2 describes the proposed dynamic charging resource coordination strategies. In Section 3, Monte Carlo simulation-based performance assessment framework associated with proposed charging coordination strategies is elaborated in Section 3.2, followed by Section 3.3 that explains the FCS centric performance assessment framework. Section 4 discusses obtained results from the developed MCS for selected scenarios. Finally, Section 5 concludes the innovative findings while highlighting further work related to this effort.

2. Dynamic Charging Coordination Strategies

An FCS is built with a limited number of off-board chargers/EVSE and energy supply units with limited capacity. Therefore, a commercial FCS intends to maximize the profit by scheduling EVs optimally with the effective use of available limited resources. However, due to various uncertainties associated with the scheduled charging process, charging resources may not be optimally utilized even though the EV schedule obtains the maximized profit with SEVs. In order to get the advantage of very short charging time associated with ultra-fast charging technology, this work intends to evaluate the overall performance of an FCS that serves both SEVs and opportunistic ultra-fast charging EV users (UEVs), as illustrated in Figure 2.

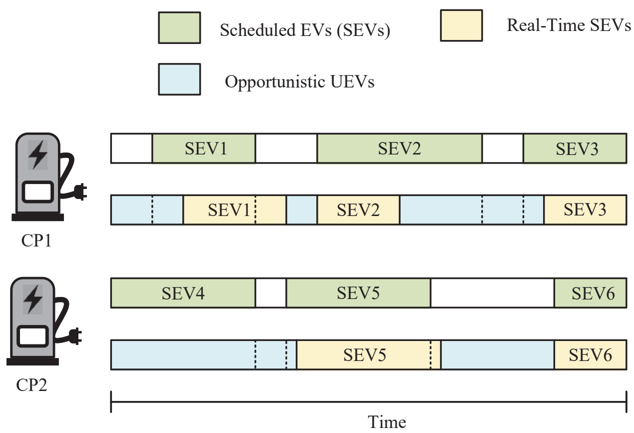

Figure 2. Utilization of charging resources by UEVs.

When we consider the operation of FCS, there are basically two types of EV users, as tabulated in Table 1: (1) SEVs and (2) UEVs with distinct privileges and constraints in accessing the FCS.

Table 1. Access privileges and constraints of EV users.

SEVs	UEVs
• Access according to a prior agreement	• Access opportunistically
• Charged at specified charge rate P_s; $P_s \in [P_s^{min}, P_s^{max}]$	• Charged at specified higher charge rate $P_u = nP_s; (n \in \mathbb{Z}^+)$, $P_u \in [P_u^{min}, P_u^{max}]$
• Charger is guaranteed during scheduled time	• Charger is assigned if charging resources are available only
• Not subject to blockages	• Subject to blockages
• Charging process regularly finishes	• Charging process is liable to be preempted before regularly finishes
• Expect uninterruptible EV charging	• Expect to charge as quickly as possible

The prime objective of FCS is to provide uninterruptible EV charging to SEVs who have prior agreements with the FCS. The operating model of the considered FCS is illustrated in Figure 3.

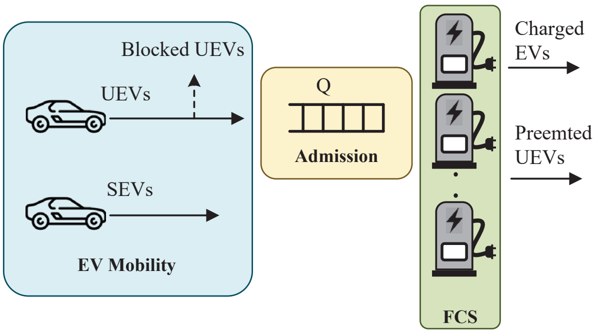

Figure 3. Proposed operation mechanism of the FCS [34–36].

In this work, we have considered an already deployed FCS with M; $(M \in \mathbb{Z}^+)$ number of off-board chargers (OBCs), and it is assumed that the charging power of each charger can be adjustable. A queue space (Q) with q number of queue points (QPs) is allocated so that newly arrived UEVs are queued if charging resources are not available. In the meantime, FCS admits opportunistic UEVs to compensate for under-utilization of limited charging resources. SEVs are charged at a specified charge rate of $P_s; P_s \in [P_s^{min}, P_s^{max}]$. Consequently, the capacity of FCS is limited to MP_s^{max} throughout the operating horizon. Therefore, depending on the availability of charging resources, UEVs can be charged at high charge rate. Based on the day-to-day life activities of EV users and the charging constraints of EV batteries, some EV users may need undisturbed and prioritized EV charging (i.e., SEVs). At the same time, some other EV users just want to enhance their cruise range by refilling their high-capacity EV batteries up to the maximum possible level quickly during their journey. Consequently, they can be considered as UEVs. Therefore, FCSs should have a charging pricing mechanism for SEVs and OEVs based on charging priorities. Moreover, EVs capable of ultra-fast charging with high charging power rates can request to be an UEV so that they can charge their EVs with an economical pricing scheme. In this work, we assume that the charging rate of UEVs is nP_s and the value n is selected such that nP_s is less than the maximum capacity of an OBC (P_c^{max}). Therefore, it is considered that $P_c^{max} = nP_s^{max}$.

Although the OBC capacity is nP_s^{max}, we consider that the initial capacity of the FCS is MP_s^{max}. In this work, we intend to analyze the possibility of enhancing capacity utilization with the help of heterogeneous EV users. However, with regard to M OBCs, the maximum capacity of FCS is nMP_s^{max}. Depending on the progressing charging demand, the capacity of the FCS can be scaled up to nMP_s^{max} from MP_s^{max}.

3. Methods

This work intends to develop a Monte Carlo simulation-based performance assessment framework to analyze proposed charging resource coordination strategies.

When we consider the whole charging management at the FCS, there are two stages: (1) scheduling SEVs in a optimal way to maximize the profit; (2) admitting UEVs as secondary users to further enhance the utilization of limited charging resources. In this work, we focus on the impact of opportunistic users over SEVs and themselves. Monte Carlo simulation is used to analyze system dynamics and uncertainties associated with the EV charging process.

3.1. Stochastic EV Mobility Model

Monte Carlo simulation is developed to analyze proposed charging coordination strategies. Therefore, the following assumptions are made to develop this MCS model.

- The arrivals of SEVs and UEVs are Poisson processes with mean arrival rates of λ_s and λ_u, respectively (λ denotes the average number of charging requests made by the respective category of EVs per unit time).
- All OBCs are homogeneous and the charging time of a OBC is exponentially distributed with the service rate of μ_c (μ_c rate denotes the average number of charged EVs per OBC per unit time).
- Admission delays associated with EVs at the FCS are negligible as compared to charging times.

The EV mobility model is developed as a continuous-time discrete-space stochastic model. The arrival rate and service rate are considered as time-dependent data to cater system dynamics. Let T be the planning horizon and thus, we consider δt intervals over T. Consequently, the planning horizon can be denoted as $(0, \delta t, 2\delta t, \ldots, t, t+\delta t, t+2\delta t, \ldots, T)$. It is considered that the number of arrivals within time interval t follows a Poisson distribution under the following conditions. If the average arrival rate of EVs is λ_t ($\lambda_t > 0$) over the $[t,\ t+\delta t]$, the probability of one arrival of EV during $[t,\ t+\delta t]$ is $\lambda_t t + O(\delta t)$; $O(\delta t)$: order of δt. The probability of more than one arrival of EVs during $[t,\ t+\delta t]$ is $O(\delta t)$. The occurrence of EV arrivals in non-overlapping intervals are mutually independent. Then, the number of EV arrivals $(N_t,\ t \geq 0)$ occurring during $[t,\ \delta t]$ can be modeled as a Poisson process with parameter λ_t as expressed in (1) [34–36].

$$P\{N_t\} = \frac{\exp(\lambda_t)(\lambda_t)^{N_t}}{N_t!} \tag{1}$$

3.2. Dynamic Charging Coordination Model

To develop the MCS model with proposed event-based dynamic charging coordination strategies, the following events are considered: SEV or UEV arrivals at FCS and SEV or UEV departures from FCS. Each plugged-in EV and each queued EV are sequentially indexed and placed in dynamic arrays $\left(\boldsymbol{A}^{\boldsymbol{ev}}_{\boldsymbol{j_{ev}(t)\times l}};\ j_{ev}(t) \leq M\right)$ and $\left(\boldsymbol{A}^{\boldsymbol{q}}_{\boldsymbol{j_q(t)\times l}};\ j_q(t) \leq Q\right)$, respectively, to analyze system dynamics. Let t^a_k, t^p_k, t^c_k, t^r_k, α_k, and β_k be the arrival time, plugged-in time, required charging time, remaining charging time, EV user type, and index of the kth $(k \in\ \mathbb{Z}^+)$ plugged-in EV, an element of $\boldsymbol{A}^{\boldsymbol{ev}}_{\boldsymbol{j_{ev}(t_k)}}$ associated with the kth SEV or UEV arrival at time t_k can be expressed as (2). Similarly, an $\boldsymbol{A}^{\boldsymbol{ev}}_{\boldsymbol{j_{ev}(\tau_m)}}$ element is derived for an SEV or UEV departure at time τ_m. If t_c follows the exponential distribution, it is expressed in (3).

$$\boldsymbol{A}^{\boldsymbol{ev}}_{\boldsymbol{j_{ev}(t_k)}} = \left\{t^a_k,\ t^p_k,\ t^c_k,\ t^r_k,\ \alpha_k,\ \beta_k\right\} \tag{2}$$

$$P(t_c, \mu_c) = \frac{1}{\mu_c}\exp\left(\frac{-t_c}{\mu_c}\right) \tag{3}$$

The MCS model keeps its current state in terms of allocated resources, the number of plugged-in EVs, and their charging power unchanged until the next event occurs.

Information pertaining to all possible events is kept in matrix $\boldsymbol{A}^{ev}_{\boldsymbol{M}\times\boldsymbol{l}\times\boldsymbol{T}}$. Therefore, $\boldsymbol{A}^{ev}$ that accounts for all possible x events taken place at $t_1, t_2, \ldots, t_x$ within 0 to T can be expressed as (4). Similarly, all the information of queued EVs at each event is kept in $\boldsymbol{A}^{q}$ expressed in (5).

$$\boldsymbol{A}^{ev} = \left[\boldsymbol{A}^{ev}_{j_{ev}(t_1)},\ \boldsymbol{A}^{ev}_{j_{ev}(t_2)},\ \ldots\ ,\boldsymbol{A}^{ev}_{j_{ev}(t_k)},\ \boldsymbol{A}^{ev}_{j_{ev}(t_{k+1})},\ \ldots\ ,\boldsymbol{A}^{ev}_{j_{ev}(t_x)},\ \right] \tag{4}$$

$$\boldsymbol{A}^{q} = \left[\boldsymbol{A}^{q}_{j_q(t_1)},\ \boldsymbol{A}^{q}_{j_q(t_2)},\ \ldots\ ,\boldsymbol{A}^{q}_{j_q(t_k)},\ \boldsymbol{A}^{q}_{j_q(t_{k+1})},\ \ldots\ ,\boldsymbol{A}^{q}_{j_q(t_x)},\ \right] \tag{5}$$

The FCS is obliged to admit SEVs if they arrive within the scheduled time period. For charging resource allocation, M number of OBCs and a queue with Q number of queuing points (QPs) $(M, Q \in \mathbb{Z}^+)$ are considered. The queue is reserved only for UEVs at the arrival if charging resources are not adequate to admit them. To update system matrix A^{ev} and A^q, the following events are considered.

Arrival of SEVs at FCS: Charging resource allocation for SEVs is illustrated in Algorithm 1. When an SEV arrives at the FCS at time t_k, if there is at least one idle CP, it is plugged into the FCS without disturbing any ongoing UEV charging process. Otherwise, one charging process of UEV has to be preempted to admit the newly arrived SEV, as they are liable to do so.

Algorithm 1: Pseudo code (PC) for updating $A^{ev}_{j_{ev}(t_k)}$ at SEV arrivals.

Input : $j_s(t_k)$: Number of plugged-in SEVs at time t_k
Input : $j_u(t_k)$: Number of plugged-in UEVs at time t_k
Input : $j_{sa}(t_k)$: Total number of arrived SEVs at time t_k
Input : $j_{ev}(t_k)$: Total number of plugged-in EVs by time t_k
Output: $A^{ev}_{j_{ev}(t_k)}$: Plugged-in EVs matrix at time t_k
Output: $A^{q}_{j_q(t_k)}$: Queued EVs matrix at time t_k

if $j_s(t_k) + nj_u(t_k) < M$ **then**
  $j_s(t_{k+1}) = j_s(t_k) + 1,\ j_u(t_{k+1}) = j_u(t_k)$
  $j_{sa}(t_{k+1}) = j_{sa}(t_k) + 1,\ j_{ev}(t_{k+1}) = j_{ev}(t_k) + 1$
  SEV is plugged-into an idle OBC.
  $\boldsymbol{A}^{ev}_{\boldsymbol{j_{ev}(t_{k+1})}}(i; \alpha_k \sim idle) = \left\{t^a_{k+1},\ t^p_{k+1},\ t^c_{k+1},\ t^r_{k+1},\ \alpha_{k+1},\ \beta_{k+1}\right\}$
else if $j_s(t_k) + nj_u(t_k) == M$ *AND* $j_u(t) > 0$ **then**
  $j_s(t_{k+1}) = j_s(t_k) + 1,\ j_u(t_{k+1}) = j_u(t_k) - 1$
  $j_{sa}(t_{k+1}) = j_{sa}(t_k) + 1,\ j_{ev}(t_{k+1}) = j_{ev}(t_k)$
  SEV is plugged-into the vacated OBC by UEV.
  $\boldsymbol{A}^{ev}_{\boldsymbol{j_{ev}(t_{k+1})}}(i; \alpha_k \sim uev) = \left\{t^a_{k+1},\ t^p_{k+1},\ t^c_{k+1},\ t^r_{k+1},\ \alpha_{k+1},\ \beta_{k+1}\right\}$
else
  Block the SEV
end

Departure of SEVs from FCS: Algorithm 2 explains how charging resources are coordinated upon a departure of SEV at time t_k. Once an SEVs' charging process regularly finishes, it departs the FCS, resulting in an idle OBC. For this OBC, the chance is given to queued UEVs if any. Otherwise, the OBC will be idle.

Algorithm 2: PC for updating $A^{ev}_{j_{ev}(t_k)}$ and $A^{q}_{j_q(t_k)}$ at SEV departures.

Input : $j_s(t_k)$: Number of plugged-in SEVs at time t_k
Input : $j_u(t_k)$: Number of plugged-in UEVs at time t_m
Input : $j_q(t_k)$: Total number of queued UEVs at time t_k
Input : $j_{ev}(t_k)$: Total number of plugged-in EVs at time t_k
Input : $A^{q}_{j_q(t_k)}$: Queued EVs matrix at time t_k
Output: $A^{ev}_{j_{ev}(t_k)}$: Plugged-in EVs matrix at time t_k

$j_s(t_{k+1}) = j_s(t_k) - 1$
if $\left(0 < j_q(t_k) \leq Q\right)$ *AND* $(M - (j_s(t_{k+1}) + nj_u(t_k)) \geq n)$ **then**
  $j_u(t_{k+1}) = j_u(t_k) + 1$
  $j_q(t_{k+1}) = j_q(t_k) - 1,\ j_{ev}(t_{k+1}) = j_{ev}(t_k)$
  Queued UEV is plugged-in.
  $\boldsymbol{A}^{ev}_{j_{ev}(t_{k+1})}(i; t^r_k == 0) = \boldsymbol{A}^{q}_{j_q(t_k)}(1)$
else
  $j_s(t_{k+1}) = j_s(t_k) - 1,\ j_u(t_{k+1}) = j_u(t_k)$
  $j_q(t_{k+1}) = j_q(t_k),\ j_{ev}(t_{k+1}) = j_{ev}(t_k) - 1$
  OBC is idle.
  $\boldsymbol{A}^{ev}_{j_{ev}(t_{k+1})}(i; t^r_k == 0) = \mathbf{0}$
end

Arrival of UEVs at FCS: The FCS accepts UEVs if SEVs do not occupy all the OBCs. The charging process of plugged-in UEVs are not preempted upon the arrival of a new UEV. When a new UEV arrives at the FCS, it is plugged in if at least an OBC and enough energy resources are available to provide a charge rate of P^{max}_u. Otherwise, the UEV is blocked. Charging resource allocation for newly arrived UEVs is illustrated in Algorithm 3.

Algorithm 3: PC for updating $A^{ev}_{j_{ev}(t_k)}$ and $A^{q}_{j_q(t_k)}$ at UEV arrivals.

Input : $j_s(t_k)$: Number of plugged-in SEVs at time t_k
Input : $j_u(t_k)$: Number of plugged-in UEVs at time t_k
Input : $j_{ua}(t_k)$: Total number of arrived SEVs at time t_k
Input : $j_{ev}(t_k)$: Total number of plugged-in EVs by time t_k
Output: $A^{ev}_{j_{ev}(t_k)}$: Plugged-in EVs matrix at time t_k
Output: $A^{q}_{j_q(t_k)}$: Queued EVs matrix at time t_k

if $M - (j_s(t_k) + nj_u(t_k)) \geq n$ **then**
  $j_s(t_{k+1}) = j_s(t_k),\ j_u(t_{k+1}) = j_u(t_k) + 1$
  $j_{ua}(t_{k+1}) = j_{ua}(t_k) + 1,\ j_{ev}(t_{k+1}) = j_{ev}(t_k) + 1$
  UEV is plugged-into an idle OBC.
  $\boldsymbol{A}^{ev}_{j_{ev}(t_{k+1})}(i; \alpha_k \sim idle) = \left\{t^a_{k+1},\ t^p_{k+1},\ t^c_{k+1},\ t^r_{k+1},\ \alpha_{k+1},\ \beta_{k+1}\right\}$
else if $j_q(t_k) < Q$ **then**
  $j_s(t_{k+1}) = j_s(t_k),\ j_u(t_{k+1}) = j_u(t_k) + 1$
  $j_{sa}(t_{k+1}) = j_{sa}(t_k) + 1,\ j_{ev}(t_{k+1}) = j_{ev}(t_k)$
  UEV is queued.
  $\boldsymbol{A}^{q}_{j_q(t_{k+1})}(i; \alpha_k \sim vacant) = \left\{t^a_{k+1},\ t^p_{k+1},\ t^c_{k+1},\ t^r_{k+1},\ \alpha_{k+1},\ \beta_{k+1}\right\}$
else
  Block the SEV
end

Departure of UEVs from FCS: Unlike for SEVs, an UEV departure leaves one OBC and energy resources associated with n OBCs. The idle OBC(s) that appeared in the FCS due to the departure of a UEV will be offered to EVs waiting in the queue. If the queue is empty, then the vacant BCS(s) become idle. The charging resource coordination upon a UEV departure is performed according to Algorithm 4.

Algorithm 4: PC for updating $A^{ev}_{j_{ev}(t_k)}$ and $A^{q}_{j_q(t_k)}$ at UEV departures.

Input : $j_s(t_k)$: Number of plugged-in SEVs at time t_k
Input : $j_u(t_k)$: Number of plugged-in UEVs at time t_k
Input : $j_q(t_k)$: Total number of queued UEVs at time t_k
Input : $j_{ev}(t_k)$: Total number of plugged-in EVs at time t_k
Input : $A^{q}_{j_q(t_k)}$: Queued EVs matrix at time t_k
Output: $A^{ev}_{j_{ev}(t_k)}$: Plugged-in EVs matrix at time t_k

if $\left(0 < j_q(t_k) \leq Q\right)$ **then**
    $j_s(t_{k+1}) = j_s(t_k),\ j_u(t_{k+1}) = j_u(t_k)$
    $j_q(t_{k+1}) = j_q(t_k) - 1,\ j_{ev}(t_{k+1}) = j_{ev}(t_k)$
    Queued UEV is plugged-in.
    $\boldsymbol{A^{ev}_{j_{ev}(t_{k+1})}}(i; t^r_k == 0) = \boldsymbol{A^{q}_{j_q(t_k)}}(1)$
else
    $j_s(t_{k+1}) = j_s(t_k),\ j_u(t_{k+1}) = j_u(t_k) - 1$
    $j_q(t_{k+1}) = j_q(t_k),\ j_{ev}(t_{k+1}) = j_{ev}(t_k) - 1$
    OBC is idle.
    $\boldsymbol{A^{ev}_{j_{ev}(t_{k+1})}}(i; t^r_k == 0) = \boldsymbol{0}$
end

3.3. FCS Centric Performance Evaluation Parameters

At an FCS, the optimum resource allocation for EVs is very indispensable for sustainable operation. When there are two EV categories, it is necessary to analyze the blockages and waiting of inferior users.

However, high charging resource utilization may affect the charging completion rates of both plugged-in SEVs and UEVs. Upon the arrival of SEVs, some charging processes of UEVs might be preempted. Analyzing all these aspects is very essential for the FCS to provide high-quality service to EV users. In this work, we develop an MCS model with proposed resource allocation and charging coordination strategies as an event-driven model and simulate for a large time horizon until the model comes to its equilibrium. From the system matrices $(\boldsymbol{A^{ev}},\ \boldsymbol{A^{q}})$, we have analyzed the performance of developed strategies in terms of charging resource utilization and charging service quality.

3.3.1. Blocking Probability of UEVs $(P_{b,uev})$

Although the FCS accepts UEVs to enhance the utilization of limited charging resources, there may be occasions where a charging request from a UEV has to be dropped due to limited or unavailable charging resources. Therefore, upon arrival of a UEV at the FCS, there is a probability that the charging request is denied. This EV blockage is a crucial factor to be analyzed from a service quality perspective. A charging request from an UEV is denied when the following conditions are met at the same time: (1) all OBCs are occupied; (2) energy resources are not adequate to admit the new UEV; (3) the allocated space for the queue is full. The blocking probability of UEVs can be obtained with (6).

$$P_{b,uev} = \frac{j_{ua}(t_x) - \sum_{\substack{k=1,\\ j_u(t_k) > j_u(t_{k-1})}}^{x} [j_u(t_k) - j_u(t_{k-1})]}{j_{ua}(t_x)} \quad ; \ \forall \boldsymbol{A}^{ev}_{j_{ev}(t_k)|t\in[0\ T]} \tag{6}$$

3.3.2. Preempting Probability of UEVs $(P_{p,uev})$

According to the defined admission control and charging coordination strategies, the charging process of UEVs are liable to be preempted if charging resources are not adequate to admit SEVs. This action is defined as the preempting of UEVs. Therefore, the probability at which an ongoing charging process of a UEV is forcibly terminated before being regularly finished is termed as the preempting probability of UEVs. If there are limitations for certain user types to utilize limited charging resources, the charging quality of such users is a crucial factor to be analyzed for long-term benefits. By considering derived system matrix $(\boldsymbol{A}^{ev})$, $P_{p,uev}$ can be derived as expressed in (7).

$$P_{p,uev} = \frac{\sum_{\substack{k=1, \\ j_s(t_k)>j_s(t_{k-1}),\ j_u(t_k)<j_u(t_{k-1})}}^{x} [j_u(t_{k-1}) - j_u(t_k)]}{\sum_{\substack{k=1, \\ j_u(t_k)>j_u(t_{k-1})}}^{x} [j_u(t_k) - j_u(t_{k-1})]} \quad ;\ \forall \boldsymbol{A}^{ev}_{j_{ev}(t_k)|t\in[0\ T]} \tag{7}$$

3.3.3. Mean Charging Time at the FCS $(\bar{t}_c)$

Amidst busy schedules, users prefer to get their EVs recharged as fast as possible, hence, the total time spent at the FCS is going to be a crucial measure for evaluating the service quality provided by the FCS. Total time of charging is not only essential for operation management but also for finding the optimum location and the size of the FCS within a certain area/region. Specifically, analyzing the mean time spent by an opportunistic UEV at the FCS is indispensable for assuring quality service for secondary users. The total time spent by SEVs at FCS is nothing but the required charging time to attain the requested SoC. However, as some of UEVs have to wait at the queue and terminate their charging process forcibly before being regularly finished, this $\bar{t}_c$ provides very essential QoS measurement for opportunistic users. Mean charging time of SEVs can be obtained from $(\boldsymbol{A}^{ev})$ as expressed in (8).

$$\bar{t}_{c,sev} = \frac{\sum_{\substack{k=1, \\ \beta_k\neq\beta_{k-1},\ \alpha_i\sim sev}}^{x} \sum_{i=1,}^{j_{ev}(t_k)} t_i^c}{\sum_{\substack{k=1, \\ j_u(t_k)==j_u(t_{k-1}),\ j_s(t_k)<j_s(t_{k-1})}}^{x} [j_s(t_{k-1}) - j_s(t_k)]} \quad ;\ \forall \boldsymbol{A}^{ev}_{j_{ev}(t_k)|t\in[0\ T]} \tag{8}$$

$$\bar{t}_{c,uev} = \frac{\sum_{\substack{k=1, \\ \beta_k\neq\beta_{k-1},\ \alpha_i\sim uev,\ t_i^r==0}}^{x} \sum_{i=1,}^{j_{ev}(t_k)} t_i^c}{\sum_{\substack{k=1, \\ j_s(t_k)==j_s(t_{k-1}),\ j_u(t_k)<j_u(t_{k-1})}}^{x} [j_u(t_{k-1}) - j_u(t_k)]} \quad ;\ \forall \boldsymbol{A}^{ev}_{j_{ev}(t_k)|t\in[0\ T]} \tag{9}$$

In order to analyze the total time spent by UEVs at the FCS, we consider both mean charging time $(\bar{t}_c)$ and mean waiting time $(\bar{t}_q)$ at the queue. Therefore, the total waiting time of UEVs over total queued UEVs gives the mean waiting time of UEVs $(\bar{t}_{q,uev})$ as expressed in (10).

$$\bar{t}_{q,uev} = \frac{\sum_{\substack{k=1, \\ \beta_k\neq\beta_{k-1},\ \alpha_i\sim uev}}^{x} \sum_{i=1,}^{j_{ev}(t_k)} t_i^a - t_i^p \quad ;\ \forall \boldsymbol{A}^{ev}_{j_{ev}(t_k)|t\in[0\ T]}}{\sum_{\substack{k=1, \\ j_u(t_k)>j_u(t_{k-1})}}^{x} [j_u(t_k) - j_u(t_{k-1})] \quad ;\ \forall \boldsymbol{A}^{q}_{j_q(t_k)|t\in[0\ T]}} \tag{10}$$

The total mean time spent by an EV user type (SEV or UEV) can be found by calculating the summation of $(\bar{t}_c)$ and $(\bar{t}_q)$.

3.3.4. Mean Charging Completion Rate $(\dot{c})$

Mean charging completion rate $(\dot{c})$ of a particular EV user type implies the corresponding number of charging processes that finish regularly attaining the requested SoC within unit time. As we have employed secondary users over scheduled or registered users in the proposed strategies, it is very essential to evaluate the impact on one another in the charging process. Therefore, $\dot{c}_{sev}$ and $\dot{c}_{uev}$ are expressed in (11) and (12), respectively.

$$\dot{c}_{sev} = \frac{\sum_{k=2,}^{x}[j_s(t_{k-1})-j_s(t_k)]/T}{j_u(t_k)==j_u(t_{k-1}),\ j_s(t_k)<j_s(t_{k-1})};\ \forall \boldsymbol{A}^{ev}_{j_{ev}(t_k)|t\in[0\ T]} \tag{11}$$

$$\dot{c}_{uev} = \frac{\sum_{k=2,}^{x}[j_u(t_{k-1})-j_u(t_k)]/T}{j_s(t_k)==j_s(t_{k-1}),\ j_u(t_k)<j_u(t_{k-1})};\ \forall \boldsymbol{A}^{ev}_{j_{ev}(t_k)|t\in[0\ T]} \tag{12}$$

3.3.5. Charging Resource Utilization of the FCS (U)

The main objective of this work is to further maximize the utilization of limited charging resources with opportunistic UEVs providing a compensation to under-utilization of limited charging resources due to various uncertainties associated with EV charging process. Therefore, charging resource utilization is an important parameter to present the overall performance of the FCSs' operation. In this work, as we have considered the total capacity of the FCS along with the number of OBCs instead of employing a separate demand limit. The charging resource utilization (U) is defined as the steady state value of utilized OBCs over the total number of OBCs. Therefore, U can be expressed as in (13).

$$U = \sum_{k=1}^{x}[j_s(t_k) + nj_u(t_k)]/Mx;\ \forall \boldsymbol{A}^{ev}_{j_{ev}(t_k)|t\in[0\ T]} \tag{13}$$

The presented MCS based analytical model assesses the performance of proposed dynamic charging resource coordination strategies for selected categories of EV users depending on their charging priorities.

4. Results and Discussion

How to compensate under-utilization of limited charging resources of an FCS due to uncertainties associated with the SEV charging process is analyzed in this work. This section elaborates on the behavior of FCS for a variation of EV arrivals. In this section, we have incorporated derived performance assessment parameters in Section 3.3 to evaluate the ability of developed charging resource coordination strategies in enhancing the charging resource utilization while providing a satisfactory service quality for EV users. In the considered scenario, the FCS is equipped with 10 CPs (i.e, $M = 10$) that can adjust the charging power within a specified range in steps. The MCS parameter n is set to 2.

4.1. Charging Resource Utilization

We intend to analyze how UEVs can enhance the utilization of limited charging resources by quickly exploiting charging resources when SEVs do not occupy them. In this analysis, we consider the variation of charging resource utilization with and without UEVs.

Therefore, we have considered three cases where λ_u is set to $18\ \mathrm{h}^{-1}$, $24\ \mathrm{h}^{-1}$, and $30\ \mathrm{h}^{-1}$ while λ_s varies from 0 to $60\ \mathrm{h}^{-1}$. The variation of U against λ_s is shown in Figure 4. Figure 4 depicts that unexploited charging resources by SEVs can be effectively utilized with UEVs. It is evident that proposed strategies have improved the U with opportunistic UEVs. Limited charging resources are not optimally utilized at higher values of λ_s due to high blockages of EVs. For the considered case in Figure 4, U cannot be enhanced beyond 78%. However, by allowing opportunistic UEVs to exploit unused charging resources to attain high power charging, U has been improved up to 90%.

Figure 5 plots the variation of U against λ_s and λ_u. From Figure 5, it can be seen that U cannot be improved more than 78% with SEVs, even at high arrival rates. However, by letting UEVs exploit available charging resources when SEVs are not very active within the FCS, limited charging resources can be maximally (92%) utilized. Even for lower values of λ_s, U is significantly enhanced with opportunistic UEVs. The plots of U against λ_s and λ_u shows continuous ascent with positive slope due to high blockages of EVs and preemptions of UEVs at high arrival rates.

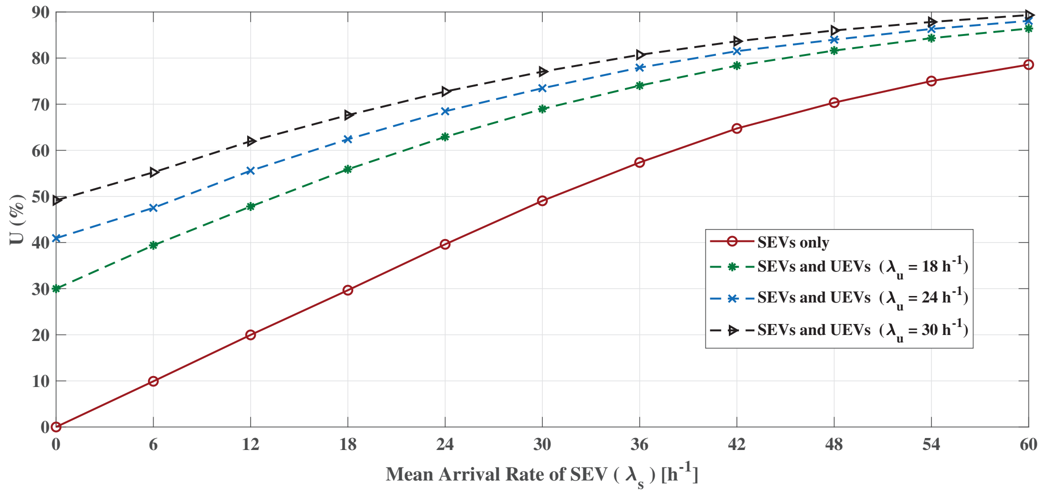

Figure 4. Charging resource utilization with λ_s.

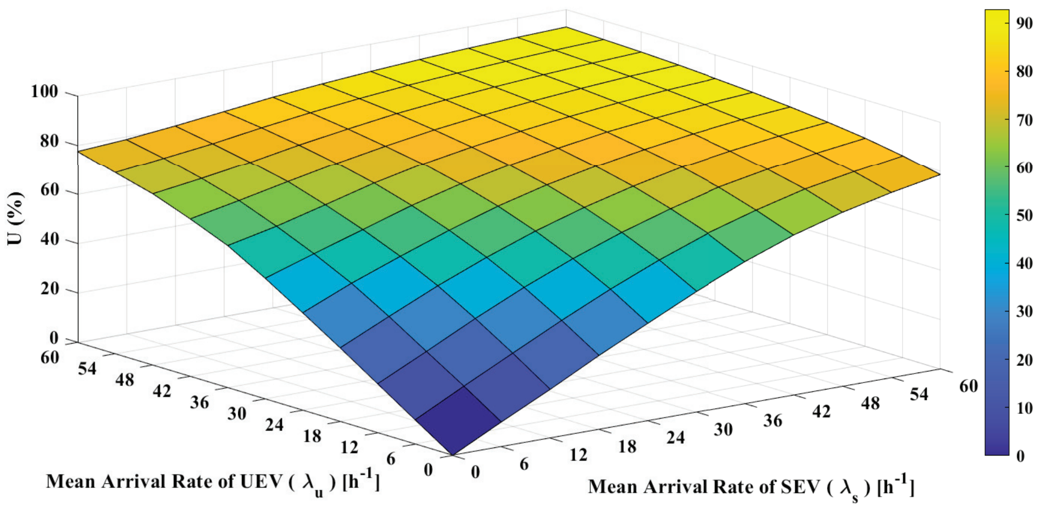

Figure 5. Charging resource utilization with λ_s and λ_u.

4.2. Mean Charging Completion Rate

To analyze the impact of opportunistic UEVs on the charging process of SEVs, the mean charging completion rate of the particular EV user type is used. The mean charging completion rate $(\dot{c})$ implies the number of completed charging processes of the considered EV user category within a unit of time. Assuring a high quality service for SEVs is dispensable as they have prior agreements for an uninterruptible charging process. Derived expressions for the mean charging completion rates of SEVs $(\dot{c}_{sev})$ and UEVs $(\dot{c}_{uev})$ (Equations (11) and (12)) are considered for the analysis in this subsection. Figure 6a,b illustrate the variation of mean completion rates of SEVs and UEVs as a function of λ_s and λ_u, respectively. The increment of SEV arrivals at the FCS deteriorates the mean charging completion rate of UEVs, but the reverse does not happen. The value of $\dot{c}_{sev}$ shows continuous ascent against λ_s with positively decreasing slope due to possible blockages of SEVs at high arrival rates. More importantly, resource coordination strategy with aggregation shows better performance in terms of the charging completion of SEVs. In order to analyze the mutual impact of EV charging completion, we have plotted $\dot{c}$ against both λ_s and λ_u within a range starting from 0 to 60 h^{-1}. As Figure 6a depicts, an increment of λ_u does not make any impact on SEVs. Nevertheless, although $\dot{c}_{uev}$ shows a continuous ascent with λ_u, the rate of change of the increment gradually decreases when λ_s is increased.

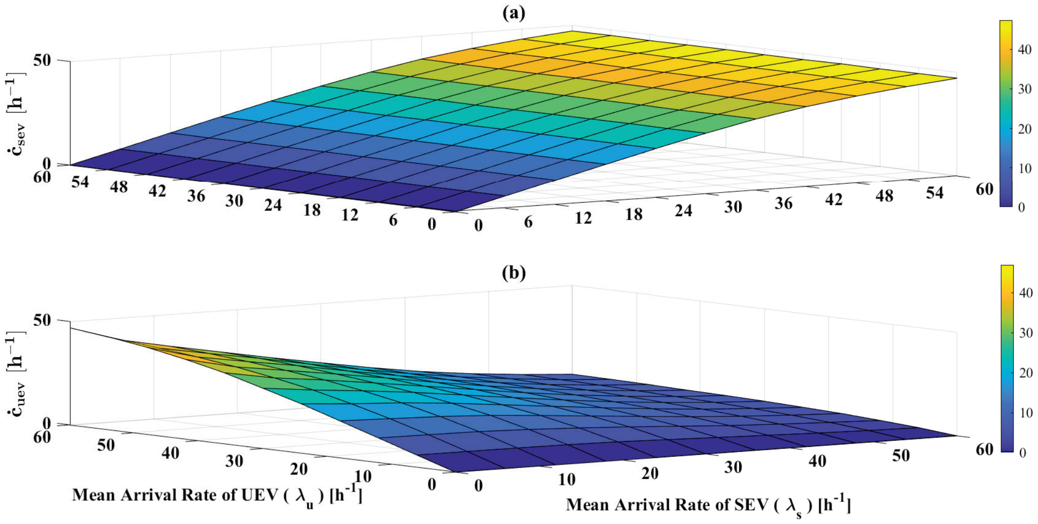

Figure 6. Mean charging completion rate of EVs with λ_s and λ_u.

4.3. Blocking and Preempting Probability of UEVs

When there are different user categories with defined privileges, assessing user satisfaction in terms of accessing and utilizing limited charging resources is vital. Especially, as UEVs are liable to have their charging process terminated forcibly if charging resources are not adequate to admit the newly arrived SEV, evaluating the likelihood of such preemptages is indispensable for long-term operation of the FCS. Therefore, we have analyzed the blocking and preempting probabilities. Figure 7a,b depict the variation of blocking and preempting probabilities of UEVs as a function of both λ_s and λ_u. From Figure 7, we can observe that both blocking and preempting probabilities of UEVs show continuous ascent with λ_s. It can be seen that the blockage and preemptage of UEVs become significant when SEVs are more active. In the considered scenario (Figure 7), for the available EV charging resources, the blocking probability gradually increases to 0.6 when λ_s increases from 0 to 60 h^{-1}.

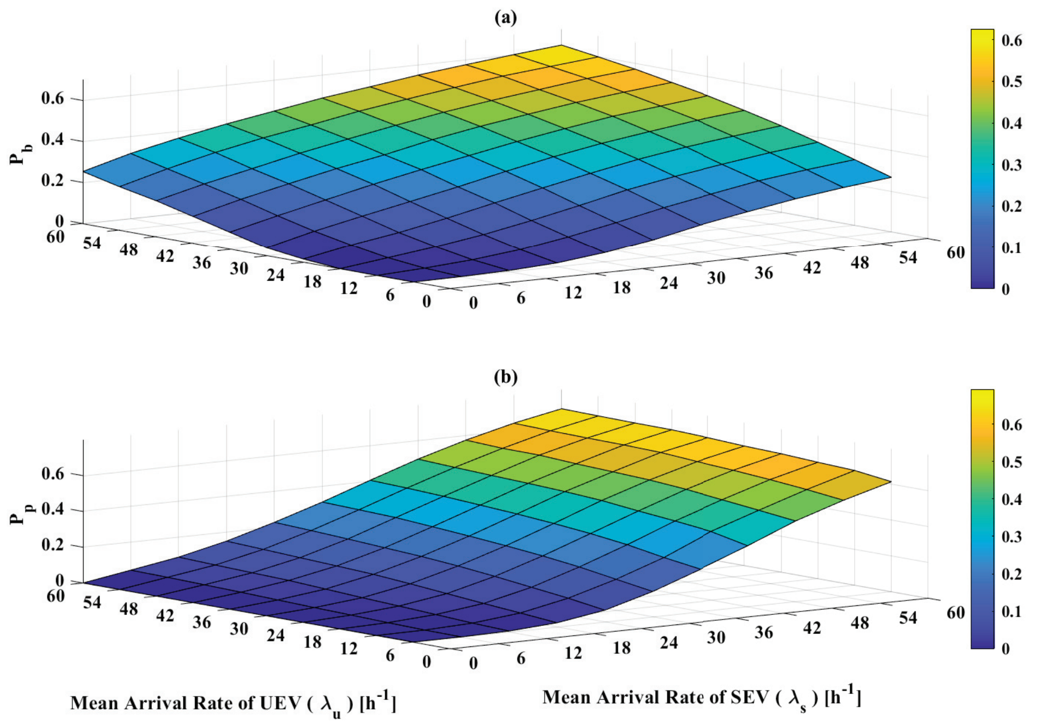

Figure 7. (**a**) Blocking and (**b**) preempting probability of UEVs with λ_s and λ_u.

Nevertheless, we can observe that blockage of UEVs is influenced by themselves. Moreover, at the same arrival rate of SEVs, preempting probability is also around 0.6, which is a bit higher value from a service quality point of view. To provide satisfactory service to UEVs, the FCS would schedule SEVs so that it does not exceed the mean arrival rate 30 h^{-1} for a considered time horizon.

All these parameters should be taken into account to evaluate the FCS centric performance.

5. Conclusions

In this paper, we have analyzed how opportunistic ultra-fast charging EV users can be incorporated to further enhance the utilization of limited charging resources. The proposed strategy enables UEVs to exploit unused charging resources by scheduled EV users at FCS to enhance charging resource utilization. Developed event-based dynamic charging resource allocation and coordination strategies are analyzed with Monte Carlo simulation. The presented results show a coordination strategy to optimally utilize the limited charging resources of FCS with opportunistic EV users considering uncertainties associated with EV charging process. In this work, the presented results prove that the developed charging resource coordination strategy significantly improves the charging resource utilization of the FCS at any arrival rate of SEVs. At higher arrival rates of EVs, FCS accomplishes more than 90% of resource utilization, which is bounded to 78% only with SEVs.

Along with the proposed strategies, we have derived a framework of a generic nature using MCS to assess the FCS-centric performance in terms of charging resource utilization, charging completion rates of EV users, blocking probability, preempting probability, waiting time, charging time, etc. This FCS-centric performance assessment framework can be incorporated at the planing and deployment stages to find the optimum siting and sizing of FCSs. At the operating stage of an FCS, the developed framework can be used to ensure a high-quality service to both SEVs and UEVs, as it provides a quantitative overview of the whole charging process within and outside the FCS in long-term operation. The proposed work will be extended for analysis with charging resource aggregation and different UEV categories. Charging coordination strategies will be further improved to reduce preempting probability of UEVs with mobile chargers. Utilization of mobile chargers will be further analyzed to enhance the charging reliability of EVs.

Author Contributions: K.M.S.Y.K.: conceptualization, methodology, software, formal analysis, validation, writing—original draft preparation; M.L.K.: supervision, conceptualization, methodology, formal analysis; N.U.-M.: co-supervision, conceptualization, methodology; I.A.M.B.: software, formal analysis. All authors have read and agreed to the published version of the manuscript.

Funding: This research received no external funding.

Institutional Review Board Statement: This study did not require ethical approval.

Informed Consent Statement: Not applicable.

Data Availability Statement: Not applicable.

Conflicts of Interest: The authors declare no conflict of interest.

References

1. Transforming Our World: The 2030 Agenda for Sustainable Development. 2021. Available online: https://sdgs.un.org/2030agenda (accessed on 18 July 2022).
2. Shang, Y.; Shang, Y.; Yu, H.; Shao, Z.; Jian, L. Achieving Efficient and Adaptable Dispatching for Vehicle-to-Grid Using Distributed Edge Computing and Attention-Based LSTM. *IEEE Trans. Industr. Inform.* **2020**, *18*, 6915–6926. [CrossRef]
3. Global EV Outlook 2021, IEA, Paris. 2021. Available online: www.iea.org/reports/global-ev-outlook-2021 (accessed on 18 July 2022).
4. Muneer, T.; Kolhe, M.; Doyle, A. *Electric Vehicles: Prospects and Challenges*; Elsevier: Amsterdam, The Netherlands, 2017.

5. Aretxabaleta, I.; De Alegría, I.M.; Andreu, J.; Kortabarria, I.; Robles, E. High-Voltage Stations for Electric Vehicle Fast-Charging: Trends, Standards, Charging Modes and Comparison of Unity Power-Factor Rectifiers. *IEEE Access* **2021**, *9*, 102177–102194. [CrossRef]
6. Philippot, M.; Alvarez, G.; Ayerbe, E.; Van Mierlo, J.; Messagie, M. Eco-Efficiency of a Lithium-Ion Battery for Electric Vehicles: Influence of Manufacturing Country and Commodity Prices on GHG Emissions and Costs. *Batteries* **2019**, *5*, 23. [CrossRef]
7. Hannan, M.A.; Hoque, M.M.; Hussain, A.; Yusof, Y.; Ker, P.J. State-of-the-art and energy management system of lithium-ion batteries in electric vehicle applications: Issues and recommendations. *IEEE Access* **2018**, *6*, 19362–19378. [CrossRef]
8. Das, U.K.; Shrivastava, P.; Tey, K.S.; Idris, M.Y.I.B.; Mekhilef, S.; Jamei, E.; Seyedmahmoudian, M.; Stojcevski, A. Advancement of lithium-ion battery cells voltage equalization techniques: A review. *Renew. Sustain. Energy Rev.* **2020**, *134*, 110227. [CrossRef]
9. Cano, Z.P.; Banham, D.; Ye, S.; Hintennach, A.; Lu, J.; Fowler, M.; Chen, Z. Batteries and fuel cells for emerging electric vehicle markets. *Nat. Energy* **2018**, *3*, 279–289. [CrossRef]
10. Chen, Q.; Lai, X.; Gu, H.; Tang, X.; Gao, F.; Han, X.; Zheng, Y. Investigating carbon footprint and carbon reduction potential using a cradle-to-cradle LCA approach on lithium-ion batteries for electric vehicles in China. *J. Clean. Prod.* **2022**, *369*, 133342. [CrossRef]
11. Tu, H.; Feng, H.; Srdic, S.; Lukic, S. Extreme Fast Charging of Electric Vehicles: A Technology Overview. *IEEE Trans. Transp. Electrif.* **2019**, *5*, 861–878. [CrossRef]
12. Gan, X.; Zhang, H.; Hang, G.; Qin, Z.; Jin, H. Fast-Charging Station Deployment Considering Elastic Demand. *IEEE Trans. Transp. Electrif.* **2020**, *6*, 158–169. [CrossRef]
13. Wang, L.; Qin, Z.; Slangen, T.; Bauer, P.; Van Wijk, T. Grid Impact of Electric Vehicle Fast Charging Stations: Trends, Standards, Issues and Mitigation Measures - An Overview. *IEEE Open J. Power Electron.* **2021**, *2*, 56–74. [CrossRef]
14. Shang, Y.; Liu, M.; Shao, Z.; Jian, L. Internet of smart charging points with photovoltaic Integration: A high-efficiency scheme enabling optimal dispatching between electric vehicles and power grids. *Appl. Energy* **2020**, *278*, 115640. [CrossRef]
15. Rafi, M.A.H.; Bauman, J. A Comprehensive Review of DC Fast-Charging Stations With Energy Storage: Architectures, Power Converters, and Analysis. *IEEE Trans. Transp. Electrif.* **2021**, *7*, 245–368. [CrossRef]
16. Konara, K.M.S.Y.; Kolhe, M.L.; Sharma, A. Power Dispatching Techniques as a Finite State Machine for a Standalone Photovoltaic System with a Hybrid Energy Storage. *AIMS Energy* **2020**, *8*, 214–230. [CrossRef]
17. Konara, K.M.S.Y.; Kolhe, M.L.; Sharma, A. Power Flow Management Controller within a Grid Connected Photovoltaic Based Active Generator as a Finite State Machine using Hierarchical Approach with Droop Characteristics. *Renew. Energy* **2020**, *155*, 1021–1031. [CrossRef]
18. Yan, G.; Liu, D.; Li, J.; Mu, G. A cost accounting method of the Li-ion battery energy storage system for frequency regulation considering the effect of life degradation. *Prot. Control. Mod. Power Syst.* **2018**, *3*, 1–9. [CrossRef]
19. Scarabaggio, P.; Carli, R.; Cavone, G.; Dotoli, M. Smart Control Strategies for Primary Frequency Regulation through Electric Vehicles: A Battery Degradation Perspective. *Energies* **2020**, *13*, 4586. [CrossRef]
20. Lai, X.; Yuan, M.; Tang, X.; Yao, Y.; Weng, J.; Gao, F.; Ma, W.; Zheng, Y. Co-Estimation of State-of-Charge and State-of-Health for Lithium-Ion Batteries Considering Temperature and Ageing. *Energies* **2022**, *15*, 7416. [CrossRef]
21. Tang, X.; Zhou, Y.; Gao, F.; Lai, X. Joint estimation of state-of-charge and state-of-health for all cells in the battery pack using "leader-follower" strategy. *eTransportation* **2023**, *15* 100213. [CrossRef]
22. *IEC 61851*; Electric Vehicle Conductive Charging System. International Electrotechnical Commission (IEC): Geneva, Switzerland, 2017.
23. *IEC 62196*; Plugs, Socket-Outlets, Vehicle Connectors and Vehicle Inlets—Conductive Charging of Electric Vehicles. International Electrotechnical Commission (IEC): Geneva, Switzerland, 2014.
24. Nimalsiri, N.I.; Mediwaththe, C.P.; Ratnam, E.L.; Shaw, M.; Smith, D.B.; Halgamuge, S.K. A Survey of Algorithms for Distributed Charging Control of Electric Vehicles in Smart Grid. *IEEE Trans. Intell. Transp. Syst.* **2019**, *21*, 4497–4515. [CrossRef]
25. Zheng, Y.; Niu, S.; Shang, Y.; Shao, Z.; Jian, L. Integrating plug-in electric vehicles into power grids: A comprehensive review on power interaction mode, scheduling methodology and mathematical foundation. *Renew. Sust. Energ. Rev.* **2019**, *112*, 424–439. [CrossRef]
26. Mukherjee, J.C.; Gupta, A. Review of Charge Scheduling of Electric Vehicles in Smart Grid. *IEEE Syst. J.* **2015**, *9*, 1541–1553. [CrossRef]
27. Xu, Z.; Su, W.; Hu, Z.; Song, Y.; Zhang, H. A Hierarchical Framework for Coordinated Charging of Plug-In Electric Vehicles in China. *IEEE Trans. Smart Grid* **2016**, *7*, 428–438. [CrossRef]
28. Qi, W.; Xu, Z.; Shen, Z.-J.M.; Hu, Z.; Song, Y. Hierarchical coordinated control of plug-in electric vehicles charging in multifamily dwellings. *IEEE Trans. Smart Grid* **2014**, *5*, 1465–1474. [CrossRef]
29. Vandael, S.; Claessens, B.; Hommelberg, M.; Holvoet, T.; Deconinck, G. A Scalable Three-Step Approach for Demand Side Management of Plug-in Hybrid Vehicles. *IEEE Trans. Smart Grid* **2013**, *4*, 720–728. [CrossRef]
30. Molderink, A.; Bakker, V.; Bosman, M.G.C.; Hurink, J.L.; Smit, G.J.M. Management and control of domestic smart grid technology. *IEEE Trans. Smart Grid* **2010**, *1*, 109–119. [CrossRef]
31. Mukherjee, J.C.; Gupta, A. Distributed charge scheduling of plug-in electric vehicles using inter-aggregator collaboration. *IEEE Trans. Smart Grid* **2017**, *8*, 331–341. [CrossRef]

32. Ghosh, A.; Aggarwal, V. Control of Charging of Electric Vehicles Through Menu-Based Pricing. *IEEE Trans. Smart Grid* **2018**, *4*, 5918–5929. [CrossRef]
33. Alinia, B.; Hajiesmaili, M.H.; Crespi, N. Online EV Charging Scheduling With On-Arrival Commitment. *IEEE Trans. Intell. Transp. Syst.* **2019**, *21*, 4524–4537. [CrossRef]
34. Konara, K.M.S.Y.; Kolhe, M.L. Priority Based Coordinated Electric Vehicle Charging System for Heterogeneous Traffic. In Proceedings of the 5th International Conference on Smart and Sustainable Technologies (SpliTech), Split, Croatia, 23–26 September 2020.
35. Konara, K.M.S.Y.; Kolhe, M.L. Queue Based Dynamic Charging Resource Allocation and Coordination for Heterogeneous Traffic in an Electrical Vehicle Charging Station. *Energy Sources Part A Recover. Util. Environ. Eff.* **2021**, 1–18.. [CrossRef]
36. Konara, K.M.S.Y.; Kolhe, M.L. Charging Coordination of Opportunistic EV Users at Fast Charging Station with Adaptive Charging. In Proceedings of the IEEE Transportation Electrification Conference (ITEC-India), New Delhi, India, 16–19 December 2021; pp. 1–6.

energies

Article

Performance Comparison of Pure Electric Vehicles with Two-Speed Transmission and Adaptive Gear Shifting Strategy Design

Bolin He [1], Yong Chen [1,*], Qiang Wei [2], Cong Wang [3], Changyin Wei [1] and Xiaoyu Li [1,*]

1 Tianjin Key Laboratory of New Energy Automobile Power Transmission and Safety Technology, School of Mechanical Engineering, Hebei University of Technology, Tianjin 300130, China; 202111201017@stu.hebut.edu.cn (B.H.)
2 Key Laboratory of Hebei Province on Scale-Span Intelligent Equipment Technology, School of Mechanical Engineering, Hebei University of Technology, Tianjin 300401, China
3 School of Vehicle and Mobility, Tsinghua University, Beijing 100190, China
* Correspondence: chenyong@gxu.edu.cn (Y.C.); lixiaoyu@hebut.edu.cn (X.L.)

Abstract: The two-speed automatic transmission can adjust the drive motor speed of electric vehicles and expand their output torque range. This study proposes a rule-based partitioned gear-shifting strategy for pure electric vehicles equipped with a two-speed dual-clutch transmission, combining economic and dynamic shifting strategies to ensure low energy consumption and strong power. Specifically, fuzzy logic is applied to adaptively modify the partition shifting strategy online, to reduce invalid gearshifts, increase the service life of the transmission, and improve driving comfort. Finally, we compare the economic performance and dynamic performance of pure electric vehicles equipped with a two-speed dual-clutch transmission and a single-speed final drive. The results show that the vehicle equipped with the two-speed dual-clutch transmission has better economic and dynamic performance. In addition, its maximum climbing ability was verified by rig testing. These results prove that the two-speed dual-clutch automatic transmission and the gear-shifting strategy proposed in this study can comprehensively improve the performance of pure electric vehicles.

Keywords: two-speed automatic transmission; pure electric vehicle; gear-shifting strategy; economic performance; dynamic performance

1. Introduction

Currently, energy and pollution problems are becoming increasingly serious worldwide [1]. As a representative solution for clean energy vehicles, the promotion of pure electric vehicles is considered an important way to alleviate fossil fuel consumption and environmental pollution problems [2–4]. For a long time, the research hotspot of pure electric vehicles, especially passenger vehicles, has mostly focused on batteries, motors, and configurations [5–7]. Meanwhile, the automatic transmission is a very important part of traditional vehicles and hybrid vehicles [8], but it is often neglected in pure electric vehicles. Although pure electric vehicles have made great contributions to energy conservation and emission reduction, from the perspective of the energy industry chain, the electrical energy required for the charging of pure electric vehicles still consumes a lot of fuel and causes huge pollution [9]. Therefore, it is necessary to continuously improve the economic performance of pure electric vehicles, while ensuring dynamic performance. An automatic transmission can adjust the motor speed by shifting gears to ensure that the motor works more efficiently [10]. Moreover, with an automatic transmission, a vehicle's requirements for motor performance and battery capacity will be reduced, thus saving more resources, reducing pollution, and reducing vehicle manufacturing costs.

Compared with multi-speed transmissions two-speed transmissions are adopted more widely in the field of pure electric vehicles due to their better performance and simpler structure. The commonly used forms of automatic transmissions are dual clutch automatic transmissions (DCTs), automatic manual transmissions (AMTs), and planetary automatic transmissions (ATs). ATs have a more complex structure, higher costs, and lower transmission efficiency than AMTs and DCTs; AMTs and DCTs have excellent dynamic performance, high transmission efficiency, and low manufacturing costs [11,12]. However, AMTs need to cut off the power transmission between the power source and the gears during the shifting process and then switch the gears; thus, there is a power interruption during the shifting process, which will reduce driving comfort [13]. Therefore, DCTs are the preferred transmission mode for pure electric vehicles.

The gear-shifting strategy is very important for transmission-equipped vehicles, and the formulation of the shifting strategy greatly affects the dynamic and economic performance of vehicles. Previous studies are mainly divided into dynamic shifting strategies, economic shifting strategies, and comprehensive shifting strategies. Zhu et al. proposed a dynamic shifting strategy and an economic shifting strategy based on a multi-speed automatic transmission for pure electric vehicles and proved that the two strategies can improve the dynamic and economic efficiency of vehicles [14]. He et al. developed an effective energy management strategy for a two-speed dual-motor transmission pure electric vehicle using an MPC-based longitudinal dynamics model. The offline global optimization method was used to optimize the gear-shifting strategy and the torque distribution [15]. Gao et al. designed the ratio of the two-speed I-AMT and optimized the shifting process, and their research proved that the two-speed I-AMT can improve economy and power [16]. Jeoung et al. applied a greedy algorithm based on speed prediction to find the optimal gear-shift point for the transmission [17]. Lin et al. used dynamic programming and the k-means algorithm to design and compare the hybrid shifting strategy of the multi-speed AMT of urban buses [18]. Shen et al. proposed a dynamic-programming-based hybrid vehicle shifting strategy and optimized the shifting strategy based on the typical Chinese urban driving cycle [19]. Jain designed the electric vehicle transmission shifting strategy with a genetic algorithm and optimized the shifting strategy with the non-dominated sorting genetic algorithm (NSGA-II) [20]. Liu et al. proposed an optimal shifting strategy of the two-speed automatic transmission for electric vehicles based on a multi-objective cuckoo algorithm, considering braking energy recovery efficiency and driving comfort [21]. The dynamic shifting strategy aims to provide the maximum power for the vehicle, while the economic shifting strategy aims to ensure the best energy-saving performance of the vehicle. The comprehensive shifting strategy strives to select a balance point between the dynamic performance and the economic performance through the optimization algorithm, so that the formulated shifting strategy can take into account these two performances [22]. Therefore, optimization-based comprehensive strategies are now more widely adopted.

However, the economic performance and the dynamic performance of a vehicle are usually contradictory [23], causing the equilibrium point found by the optimization algorithm to hurt both dynamic performance and economic performance. This paper adopts a new concept and proposes a partition gear-shifting strategy. In cases where economic performance needs to be more considered (such as urban driving, low-speed driving, and frequent start-stop road sections), the economic gear-shifting strategy is adopted. In contrast, in cases where dynamic performance needs to be more considered (such as in high-speed driving road sections), the dynamic gear-shifting strategy is adopted. In addition, fuzzy logic is introduced to adjust the shifting strategy online to reduce unnecessary shifting, thus obtaining better driving comfort and improving the service life of the transmission. It should also be noted that drivers can also adjust the shift strategy manually, according to their actual situations.

Most of the existing research focuses on formulating gear-shifting strategies for pure electric vehicle transmissions or optimizing transmission parameters. Some researchers have studied the effects of different power systems, different configurations, and other factors on the performance of new energy vehicles through comparative methods. Granovskii et al. compared traditional vehicles, hybrid electric vehicles, pure electric vehicles, and fuel-cell vehicles from the perspectives of economics and environmental pollution [24]. Li et al. compared the economic performance of modular dual-motor electric vehicles and single-motor electric vehicles [25]. Ragheb et al. compared the climbing ability of fuel-cell hybrid vehicles with internal combustion engine vehicles [26]. Wu et al. proposed a dual-motor electric vehicle model with two configurations of planetary gear and parallel gear and compared it with the traditional single-motor electric vehicle from the perspective of economy [27]. Spanoudakis et al. studied the effect of transmission on electric vehicle energy consumption through experiments [28].

To determine the influence of two-speed automatic transmission on the performance of pure electric vehicles and to explore the possibility of widespread application of two-speed transmissions, this research established two identical pure electric vehicle models, without a transmission system. Then, we compared the economic and dynamic performances of a pure electric vehicle with a two-speed dual-clutch transmission and a vehicle equipped with a single-speed final drive only. Finally, the climbing ability of the pure electric vehicle with the two-speed transmission was verified through rig testing.

There are three perspectives on the possible contributions of this research:

(1) A partition gear-shifting strategy combining the economic and dynamic performances of pure electric vehicle two-speed transmission was designed, and fuzzy logic was utilized to adjust the partition shifting strategy online.
(2) Via comparison, the influence of the two-speed transmission on the economic and dynamic performances of the pure electric vehicle was revealed.
(3) A few contributions to the application of automatic transmission in the field of passenger pure electric vehicles are provided.

The remainder of this paper is structured as follows: the battery model, the motor model, the two-speed dual-clutch transmission model, and the longitudinal dynamics model of vehicles are discussed in Section 2. In Section 3, the design of a partitioned gear-shifting strategy is discussed, fuzzy logic is introduced to adjust the shifting strategy online, and the effect of the online adjustment is verified. In Section 4, the two configurations of pure electric vehicles are compared in terms of economic performance and dynamic performance, and the simulation results are analyzed. The research contents of this paper are summarized in Section 5.

2. Powertrain Structure and System Modeling

In this paper, the research target was to investigate the effect of a two-speed transmission on the performance of pure electric vehicles. The configurations of a pure electric vehicle equipped with a two-speed dry dual-clutch transmission (EVT) and an electric vehicle without transmission (EV) are shown in Figure 1a,b, respectively. The components of the EVT included a motor, a converter, a battery pack, a two-speed dry dual-clutch automatic transmission (2DCT), a final drive, and a differential. Except for the transmission, the other components of the EV were the same as those of the EVT. The major parameters of the two electric vehicle structures are presented in Table 1, including the essential parameters of the primary components and the vehicle body. To investigate and compare the performance of two electric vehicles, the vehicles and the major components of the powertrain system needed to be modeled.

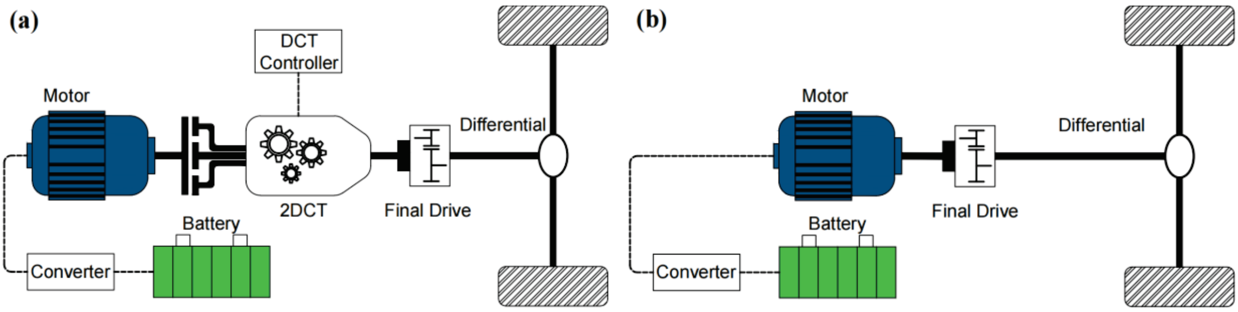

Figure 1. Configurations of EVT and EV: (**a**) EVT; (**b**) EV.

Table 1. The parameters of EVT and EV.

Item	Parameter	Unit	Value
Vehicle	Vehicle mass (EVT)	kg	1758
	Vehicle mass (EV)	kg	1730
	Rolling resistance coefficient		0.0083
	Rotating mass conversion factor		1.08
	Air resistance coefficient		0.28
	Vehicle frontal area	m^2	2.1
	Dynamic radius of the wheel	m	0.31
Battery	Rated capacity	Ah	88.24
	Battery voltage	V	340
Motor	Peak power	kw	110
	Peak speed	r/min	12,000
	Peak torque	Nm	230
Transmission	First gear ratio		3
	Second gear ratio		1.19
Final Drive	Final drive ratio (EVT)		3.91
	Final drive ratio (EV)		8.28

2.1. Battery Modeling

To facilitate the investigation, a simplified internal resistance model was adopted for the battery, ignoring the effect of temperature on the electrical performance of the battery [29]. The equivalent electric circuit for the battery is shown in Figure 2. The internal resistance characteristic curves and the open-circuit voltage curves are shown in Figure 3a,b, respectively. The output voltage V_{out} is [30]:

$$V_{out} = V_{oc} - I_{bat} \cdot R_{int} \tag{1}$$

where V_{oc} refers to the open circuit voltage, I_{bat} denotes the battery's output current, and R_{int} represents the internal resistance.

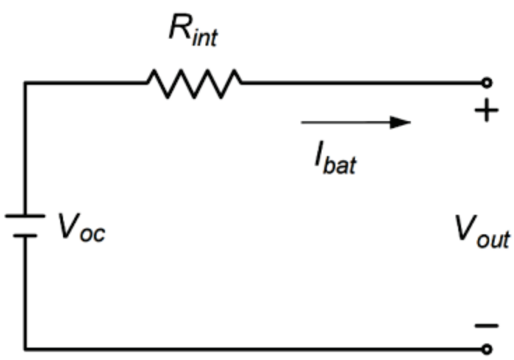

Figure 2. Equivalent circuit of the battery.

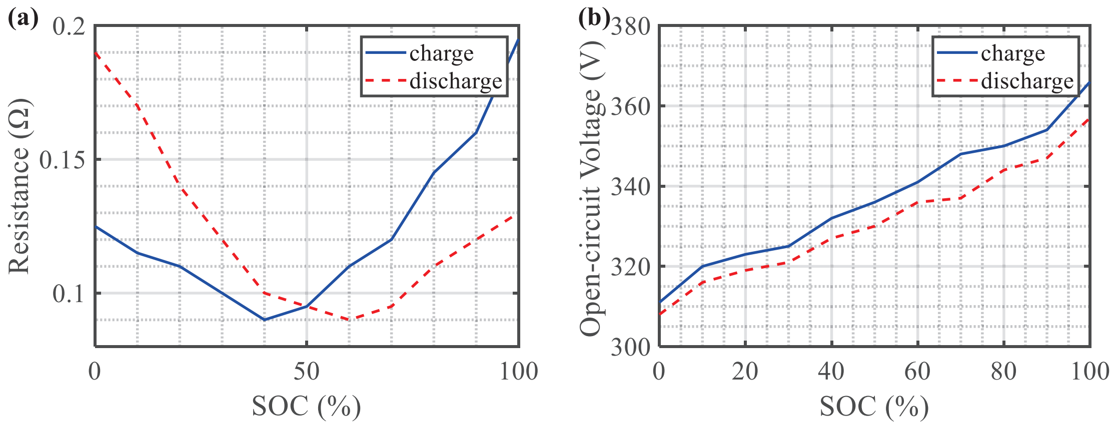

Figure 3. (**a**) Internal resistance of the battery; (**b**) open circuit of the voltage of the battery.

The battery's open circuit voltage and equivalent internal resistance have a mapping relationship with the state of charge (*SOC*) of the battery when the battery is discharged or charged. The changes in battery currents under the two states can be expressed as:

$$I_{bat} = \begin{cases} \frac{P_d}{V_{out}} \\ \frac{P_c}{V_{out}} \end{cases} \tag{2}$$

where P_d is the discharge power of the battery and P_c is the charge power of the battery. The table lookup relationship between P_d, P_c, and battery *SOC* is shown in Figure 3a,b, respectively. Furthermore, the following relationship can be obtained by substituting Equation (1) into Equation (2):

$$I_{bat} = \frac{V_{out} - \left({V_{out}}^2 - 4R_{int}P\right)^{0.5}}{4R_{int}} \tag{3}$$

where P represents the discharge and charging current of the battery. A simplified but reliable *SOC* estimation based on the ampere integration method was adopted.

$$SOC = SOC_{int} - \frac{1}{C_0}\int_0^t I_{bat}dt \tag{4}$$

where SOC_{int} is the initial *SOC* and C_0 is the battery capacity.

2.2. Electric Motor Model

The motor model was established according to its torque characteristics, and the efficiency map. Under the driving mode, the output torque was produced according to the demanding torque and the motor efficiency, then transmitted to the automatic transmission. When the motor was operating under the generator mode, a part of the braking energy was recovered and stored in the battery according to the motor's efficiency [31]. The output power in driving mode P_m is:

$$P_m = P_{req}\eta_m = T_m n_m \tag{5}$$

$$\eta_m = f(T_m, n_m) \tag{6}$$

The power in generator mode P_g is:

$$P_g = \frac{P_{req}}{\eta_m} = T_m n_m \tag{7}$$

where η_m denotes the electric motor efficiency, T_m and n_m refer to the torque and speed of the motor, respectively, P_{req} refers to the required power, and P_m and P_g represent the output power of the motor, respectively. The motor selected a permanent magnet synchronous motor (PMSM), and the efficiency of the motor is shown in Figure 4.

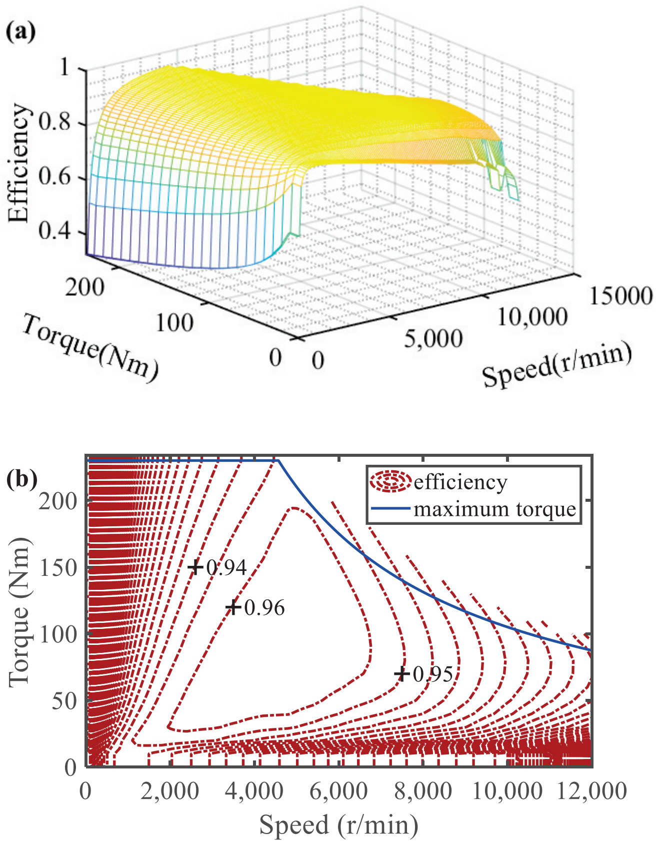

Figure 4. Motor efficiency map: (**a**) 3-D efficiency map; (**b**) Contour efficiency map.

2.3. Transmission Model

In this study, the research object was a two-speed dry dual-clutch automatic transmission (2DCT). The transmission was completely self-developed. The first gear transmission ratio i_1, the second gear transmission ratio i_2, the key parameters of the vehicle are shown in Table 1, the Structure of 2DCT is shown in Figure 5.

The 2DCT includes two operating states under different driving situationsa a gear-switching state and a normal combination state. When the transmission is shifting gears, the two clutches work together. The dynamic balance equation from the motor output shaft to the clutch active friction plate is [32]:

$$J_m\omega'_m = T_m - b_m\omega_m - T_{c1} - T_{c2} \quad (8)$$

where J_m denotes the rotational inertia of the motor output shaft and clutch drive shaft; ω_m means the angular speed of the output shaft of the motor; b_m is the rotational damping coefficient of the motor output shaft; and T_{c1} and T_{c2} represent the torque transferred by clutch C_1 and C_2, respectively.

$$\begin{cases} J_{c1}\omega'_{c1} = T_{c1} - b_{c1}\omega_{c1} - T_1 \\ J_{c2}\omega'_{c2} = T_{c2} - b_{c2}\omega_{c2} - T_2 \end{cases} \quad (9)$$

where J_{c1}, J_{c2} represent the rotational inertia of the driven part of C_1 and C_2, respectively; ω_{c1}, ω_{c2} are the angular velocities of C_1 and C_2, respectively; b_{c1}, b_{c2} are the rotational damping coefficients of driven shafts of C_1 and C_2, respectively; and T_1, T_2 are the output torque of the clutch driven shafts, respectively. The clutch output torque is:

$$T_{cn} = \frac{2}{3} sgn(\Delta\omega) \mu NRF_n \tag{10}$$

$$sgn(\Delta\omega) = \begin{cases} 1 & \omega_m - \omega_{cn} > 0 \\ 0 & \omega_m - \omega_{cn} = 0 \\ -1 & \omega_m - \omega_{cn} < 0 \end{cases} \tag{11}$$

where n takes 1, 2; R is the clutch equivalence radius; N is the number of clutch working surfaces; F_n is the pressure applied to the clutch; and μ is the friction coefficient of the clutch friction plate. The dynamic balance equation of the clutch output is:

$$T_0 = i_0(i_1 T_1 + i_2 T_2) \tag{12}$$

where T_0 indicates the output torque of transmission.

To drive the vehicle, the output torque of the transmission is delivered to the tires through the drive shaft; the dynamic balance equation at the drive shaft is:

$$J_w \omega'_w = T_w - b_w \omega_w - T_f \tag{13}$$

where J_w is the rotational inertia of the drive shaft section, ω_w is the rotational damping coefficient of the drive shaft section, and T_f is the total resistance torque applied to the wheel.

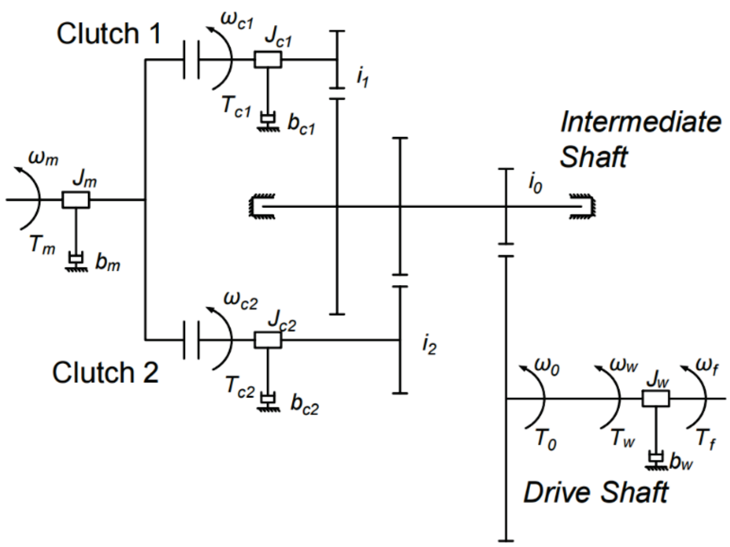

Figure 5. 2DCT transmission structure schematic diagram.

2.4. Longitudinal Dynamics Model of Vehicle

The longitudinal dynamics model of vehicles can be described as [33]:

$$\frac{T_{rq} i_n i_0 \eta_t}{r} = mgf cos\alpha + mgsin\alpha + \frac{C_d A}{21.15} v^2 + \delta m \frac{dv}{dt} \tag{14}$$

where T_{rq} is the driving torque demand, η_t is the efficiency of transmission, m is the mass of the vehicle, g is the gravity acceleration, f is the coefficient of rolling resistance, α is the angle of the road slope, A is the frontal area of the vehicle, v is the velocity of the vehicle, C_d is the drag coefficient, and δ is the coefficient of rotational mass conversion.

$$\delta = 1 + \frac{\sum J_w}{mr^2} + \frac{J_f {i_n}^2 {i_0}^2 \eta_t}{mr^2} \tag{15}$$

where J_w is the rotational inertia of the wheel and J_f is the moment of inertia of the flywheel.

3. Gear-Shifting Strategy

The rule-based gear-shifting strategy is divided into an economic strategy and a dynamic strategy, etc. A rule-based shifting strategy usually considers a certain type of performance only; although it is unable to cover all targets, it can maximize one single performance with more reliability. The economic shifting strategy selects gears that enable the motor to work more efficiently. The dynamic shifting strategy selects gears with higher acceleration to ensure a greater acceleration. In this paper, a partitioned shifting strategy was adopted, combining the economic strategy with the dynamic strategy. While a vehicle is driving at low and medium speeds (below 80 km/h), in the case of urban roads and rural roads, the economic shifting strategy is adopted to ensure that the vehicle is more energy efficient. During a high-speed range (speeds over 80 km/h), for example on highways and expressways, the dynamic shifting strategy is applied to make sure the vehicle has strong power. The VCU will select the shifting strategy according to the average driving speed at the last minute. When the average speed is less than 80 km/h, the economic shifting strategy will be selected; otherwise, the dynamic shifting strategy will be selected. In addition, drivers can change the strategy manually, according to their actual situations and requirements.

3.1. Economic Gear-Shifting Strategy

The principle of the economic shifting strategy is to select the intersection of motor efficiency curves at different gears as the optimal shifting point under the certain accelerator pedal opening degree. The curves of motor efficiency at different accelerator pedal openings can be obtained according to vehicle speed.

$$\eta_m = f\left(T_m, \frac{i_n i_0 v}{0.377r}\right) \tag{16}$$

In this study, 20%, 40%, 60%, 80%, and 100% accelerator pedal openings were selected to design the efficiency curves. The motor efficiency curves at different accelerator pedal openings and the economic shifting curves are shown in Figure 6a,b, respectively.

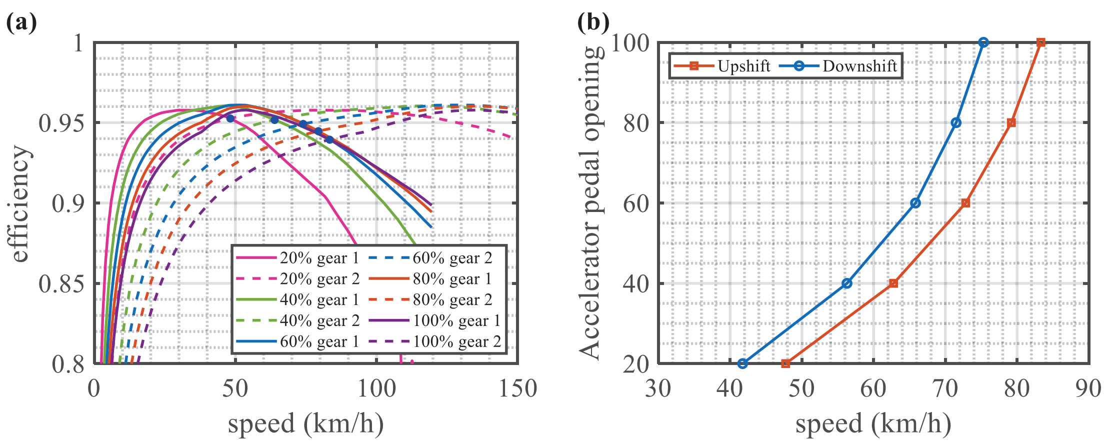

Figure 6. Economic shifting strategy: (**a**) motor efficiency curves; (**b**) economic shift curves.

The economic shifting curve obtained by the above method is the upshift curve. The downshift curve is usually chosen to be another curve when the shifting speed is lower than the upshift curve. In this paper, a divergent shift rule was used to determine the economic downshift curve. This meant that the magnitude of the downshift speed delay increased with the increase of the accelerator pedal opening.

With the pedal opening decrease, the speed delay of downshifting becomes smaller, which leads to shifting easily into higher gears, thereby ensuring less energy consumption. When the pedal opening increases, the speed delay of downshifting becomes larger, which is beneficial in reducing invalid shifts.

3.2. Dynamic Gear-Shifting Strategy

The principle of the dynamic shifting strategy is to select the intersection of the vehicle acceleration curves at different gears as the optimal shifting point under the certain accelerator pedal opening degree. The curves of vehicle acceleration at different accelerator pedal openings can be obtained according to vehicle speed and Equation (17) [34].

$$a = \frac{1}{\delta m}\left(\frac{T_{rq} i_n i_0 \eta_t}{r} - mgf cos\alpha - mgsin\alpha - \frac{C_d A v^2}{21.15}\right) \tag{17}$$

Accelerator pedal openings of 20%, 40%, 60%, 80%, and 100% were selected to design the acceleration shifting curves. The vehicle acceleration curves at different accelerator pedal openings and the dynamic shifting curves are shown in Figure 7a,b, respectively.

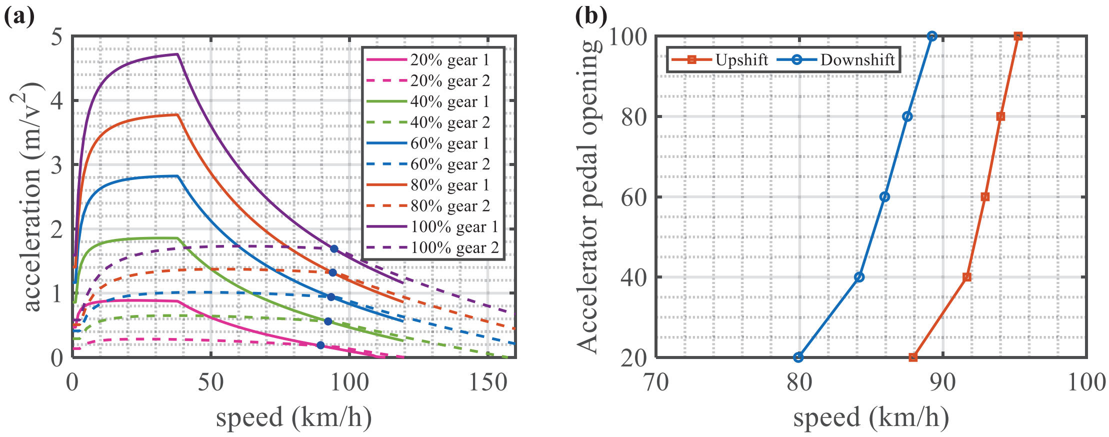

Figure 7. Dynamic shifting strategy: (**a**) vehicle acceleration curves; (**b**) dynamic shift curves.

The dynamic shifting curve obtained by the above method is the upshift curve. The downshift curve was also chosen to be another curve when the shifting speed was lower than the upshift curve. In this paper, a convergent shift rule was used to determine the dynamic downshift curve. This meant that the magnitude of the downshift speed delay decreased with the increase in the accelerator pedal opening.

With the pedal opening increase, the speed delay of downshifting becomes smaller, which leads to shifting easily into lower gears, thus ensuring better dynamic performance. When the pedal opening decreases, the speed delay becomes larger, which is favorable in reducing invalid shifts.

3.3. Gear-Shifting Strategy Online Modification

Due to the characteristics of pure electric vehicles, the motor speed is usually high during gear-shifting, which leads to greater abrasion of the dual-clutch transmission. If there is frequent and meaningless shifting, the service life of the transmission will be seriously diminished, and the jerk of shifting will also diminish driving comfort, which hinders the widespread application of the dual-clutch transmission on pure electric vehicles. This study proposes an adjustment strategy based on fuzzy logic by introducing a third shift parameter considering the dynamic characteristics of the vehicle and making online modifications to the original partitioned shifting strategy to alleviate this problem.

The partitioned shifting strategy can meet the requirements of saving energy in low-speed driving conditions and ensuring dynamic performance in a high-speed situation.

However, the strategy is based on the steady-state characteristics of the motor, ignoring the dynamic characteristics of the vehicle while it is moving. The accelerator pedal opening and the speed of the vehicle are utilized as the shifting control parameters. The speed reflects the state of the vehicle's movement, and the opening of the accelerator pedal reflects the driver's driving state.

Vehicle acceleration was introduced as the third variable for the economic shifting strategy, together with the vehicle speed and the accelerator pedal opening as the input of the fuzzy logic. Acceleration was chosen because, while adopting an economic shifting strategy, the power should be guaranteed as much as possible. The vehicle acceleration as a dynamic parameter reflects the driver's intention, which can be taken into account to adjust the shifting strategy. The adjustment amount of the shifting curves is considered an output variable. The online adjustment of the shifting curve enables the strategy to integrate the driver's intention, which makes the strategy more reasonable, thereby reducing the number of invalid gearshifts. The vehicle speed, the accelerator pedal opening, and the vehicle acceleration were in the range of 0 to 80, 0 to 1, and −5 to 5, respectively. The range of the output was −8 to 8. In the fuzzy rules of the economic shifting strategy, the membership functions of the input and output variables are as shown in Figure 8.

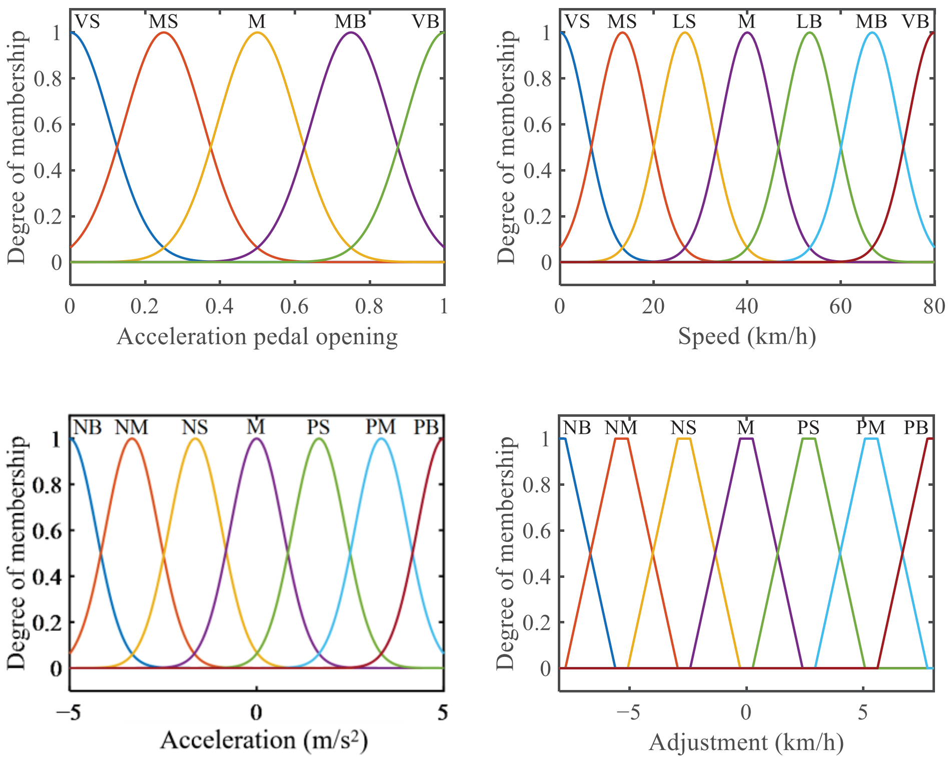

Figure 8. Membership functions of the input and output variables in fuzzy rules of economic shifting strategy.

According to the characteristics of the input variables, fuzzy rules were established according to each variable, and a total of 84 rules were formulated based on engineering experience. The characteristic maps of fuzzy logic are shown in Figure 9a,b, respectively. The principle of fuzzy rules design is that the higher the speed of the vehicle, the greater the adjustment; the higher the absolute value of vehicle acceleration, the larger the absolute value of adjustment; the larger the opening of the accelerator pedal, the smaller the adjustment; when the acceleration is positive, the amount of adjustment is negative; when the acceleration is negative, the amount of adjustment is positive. The strategy was modified online, depending on the output variables of the fuzzy logic.

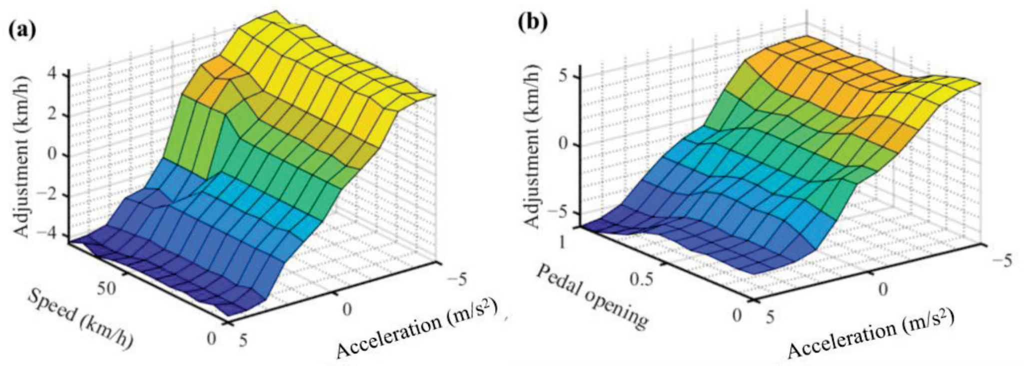

Figure 9. Characteristic maps of fuzzy logic in economic shifting strategy: (**a**) Fuzzy logic for speed, acceleration and adjustment; (**b**) Fuzzy logic for pedal opening, acceleration and adjustment.

The change rate of the accelerator pedal opening was introduced as the third variable for the dynamic shifting strategy, together with the vehicle speed and the accelerator pedal opening as the input of the fuzzy logic. The change rate of the accelerator pedal was chosen because the driver's desire for acceleration should be considered more deeply when the dynamic shifting strategy is adopted. As a dynamic parameter, the accelerator pedal change rate can more accurately reflect the driver's intention, which can be taken into account to adjust the gear-shifting strategy. The adjustment amount of the shifting curves was considered an output variable. The online adjustment of the shifting curve enabled the strategy to be more in line with the driver's intention, which made the strategy more reasonable, thereby reducing the number of invalid gearshifts. The vehicle speed, the accelerator pedal opening, and the accelerator pedal opening change rate are in the range of 80 to 120, 0 to 1, and −70 to 70, respectively. The range of the output variable is −8 to 8. In the fuzzy rules of dynamic shifting strategy, the membership functions of the variables are as shown in Figure 10.

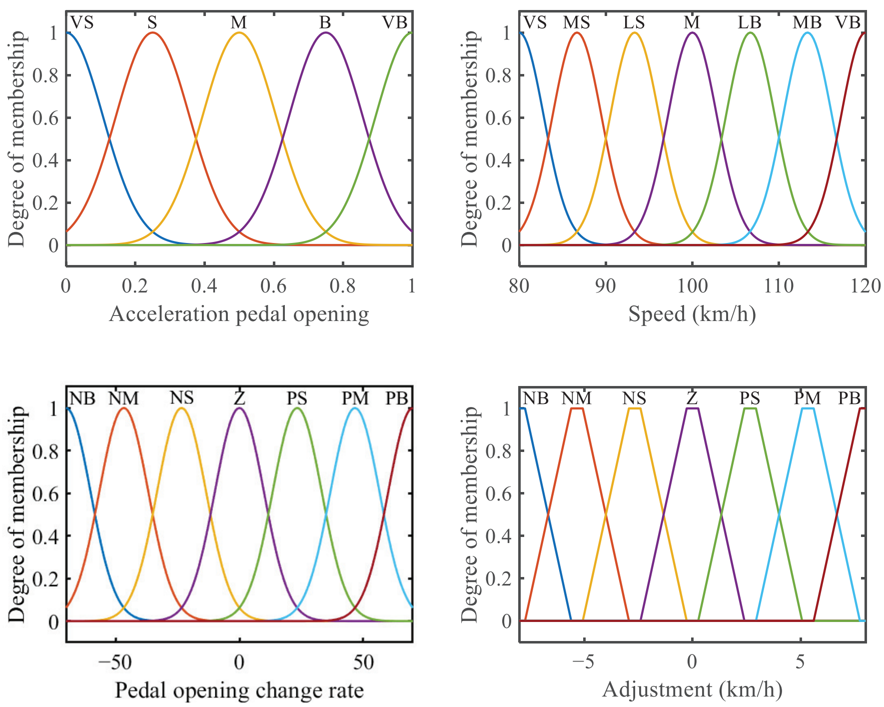

Figure 10. Membership functions of the input and output variables in fuzzy rules of dynamic shifting strategy.

There were also 84 rules for the fuzzy logic of dynamic shifting strategy; the characteristic maps of fuzzy logic are shown in Figure 11a,b, respectively. The principle of fuzzy rules design is that the higher the speed of the vehicle, the greater the adjustment; the higher the absolute value of the change rate of accelerator pedal opening, the larger the absolute value of adjustment; the larger the opening of the accelerator pedal, the smaller the adjustment; when the accelerator pedal opening change rate is positive, the amount of speed adjustment is negative; and when the change rate is negative, the amount of speed adjustment is positive. When fuzzy logic strategy is integrated in the TCU controller, the overall control system framework is as shown in Figure 12.

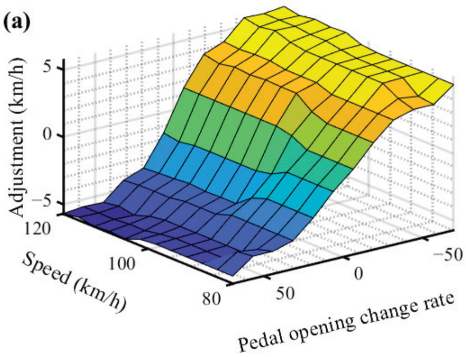

Figure 11. Characteristic maps of fuzzy logic in dynamic shifting strategy: (**a**) Fuzzy logic for speed, pedal change rate and adjustment; (**b**) Fuzzy logic for pedal opening, pedal change rate and adjustment.

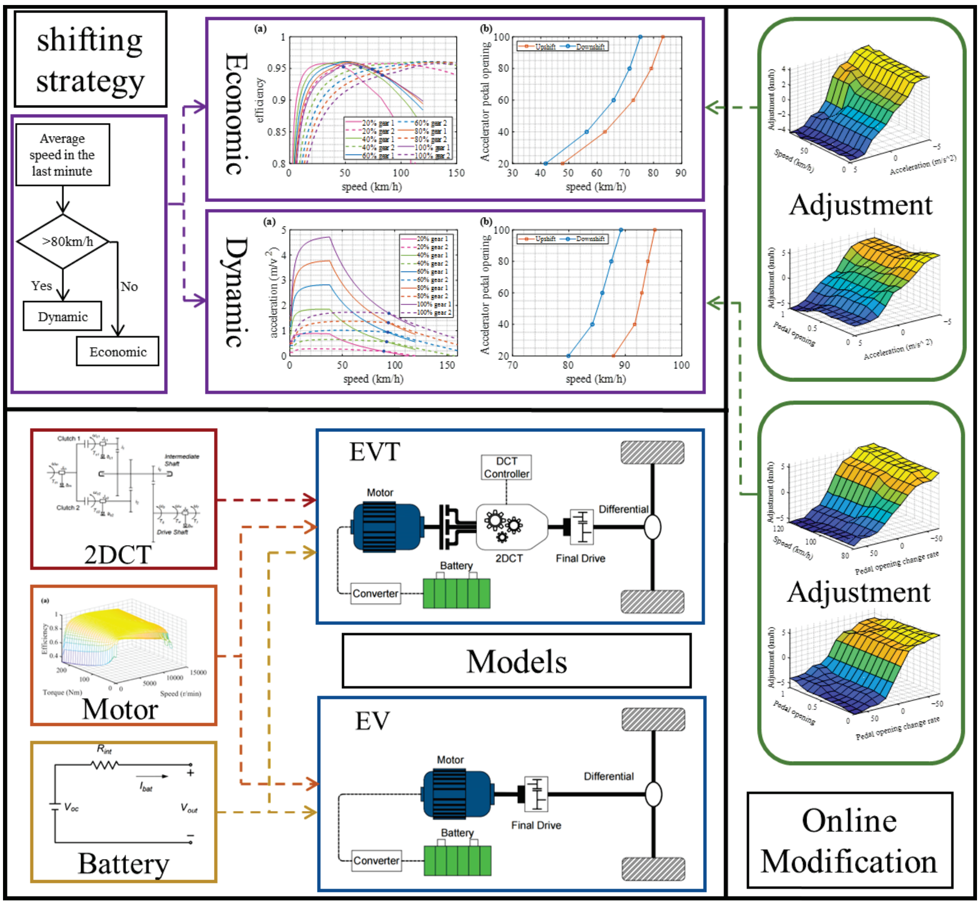

Figure 12. Control system framework.

In this study, NEDC, UDDS, and WLTC driving cycles were adopted to verify the online modification effect of the fuzzy logic on the shifting strategy. The three driving cycles and vehicle speed tracking are shown in Figure 13a,c,e, respectively. As can be seen from the figures, the vehicle speed was tracked well. The gearshifts before and after the online modification under these three driving cycles are shown in Figure 13b,d,f, respectively.

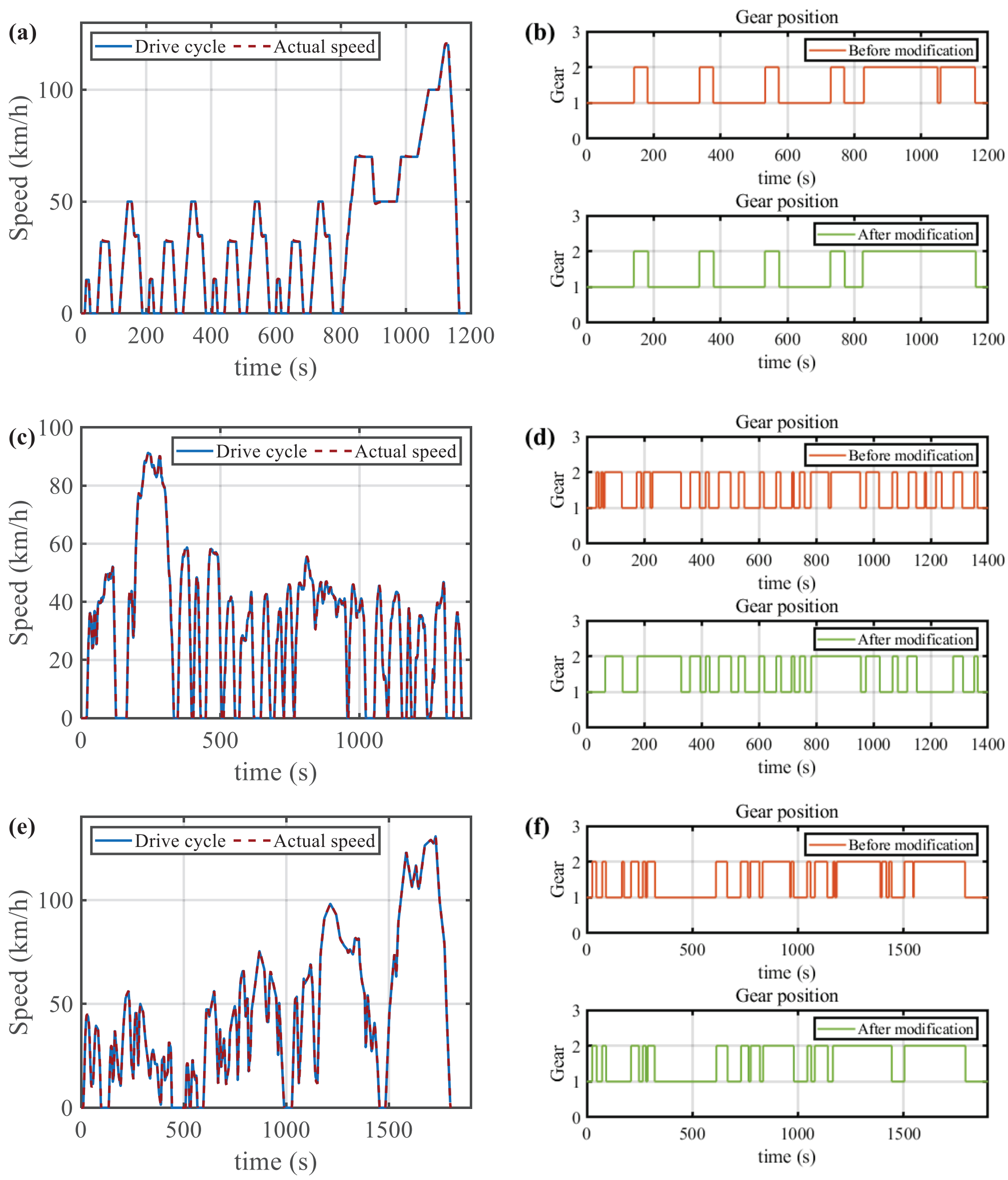

Figure 13. Vehicle speed tracking and gearshifts trajectories: (**a**) NEDC driving cycle; (**b**) Gear position; (**c**) UDDS driving cycle; (**d**) Gear position; (**e**) WLTC driving cycle; (**f**) Gear position.

As shown in Figure 13b, under the NEDC driving cycle, the 2DCT was shifted 12 times before the online modification; after the modification, the number of gearshifts dropped to 10. We eliminated one upshift and one downshift that had very short intervals. As shown in Figure 13d, in the UDDS driving cycle, the gearshift times of the 2DCT before and after the online modification were 46 and 32, respectively, which were reduced by 14 times. It should be noted that before the online modification, the vehicle experienced frequent invalid gearshifts around 50 s and around 200 s, which will damage the clutches, reduce their working life, and affect driving comfort. Fortunately, this phenomenon was significantly reduced after modification. In addition, at other stages during the entire driving cycle, the modification strategy worked, reducing some of the invalid gearshifts.

As shown in Figure 13f, under the WLTC driving cycle, the gearshift times of the 2DCT before and after the online modification were 38 and 26, respectively, which were reduced 12 times. It is worth noting that among the 12 reduced shifts, 10 were invalid frequent shifts, at about 960 s, 1165 s, 1400 s, 1550 s, etc. Overall, the fuzzy logic online modification had good performance and could correct the deficiencies of the previous shifting strategy.

4. Comparison and Verification

4.1. Comparison of Vehicle Economic Performance

Motor efficiency is critical to economic performance. The three driving cycles, NEDC, UDDS, and WLTC, were applied for the EVT and its gear-shifting strategy to verify the motor efficiency. The motor efficiency curves of the three driving cycles are shown in Figure 14a–c, respectively.

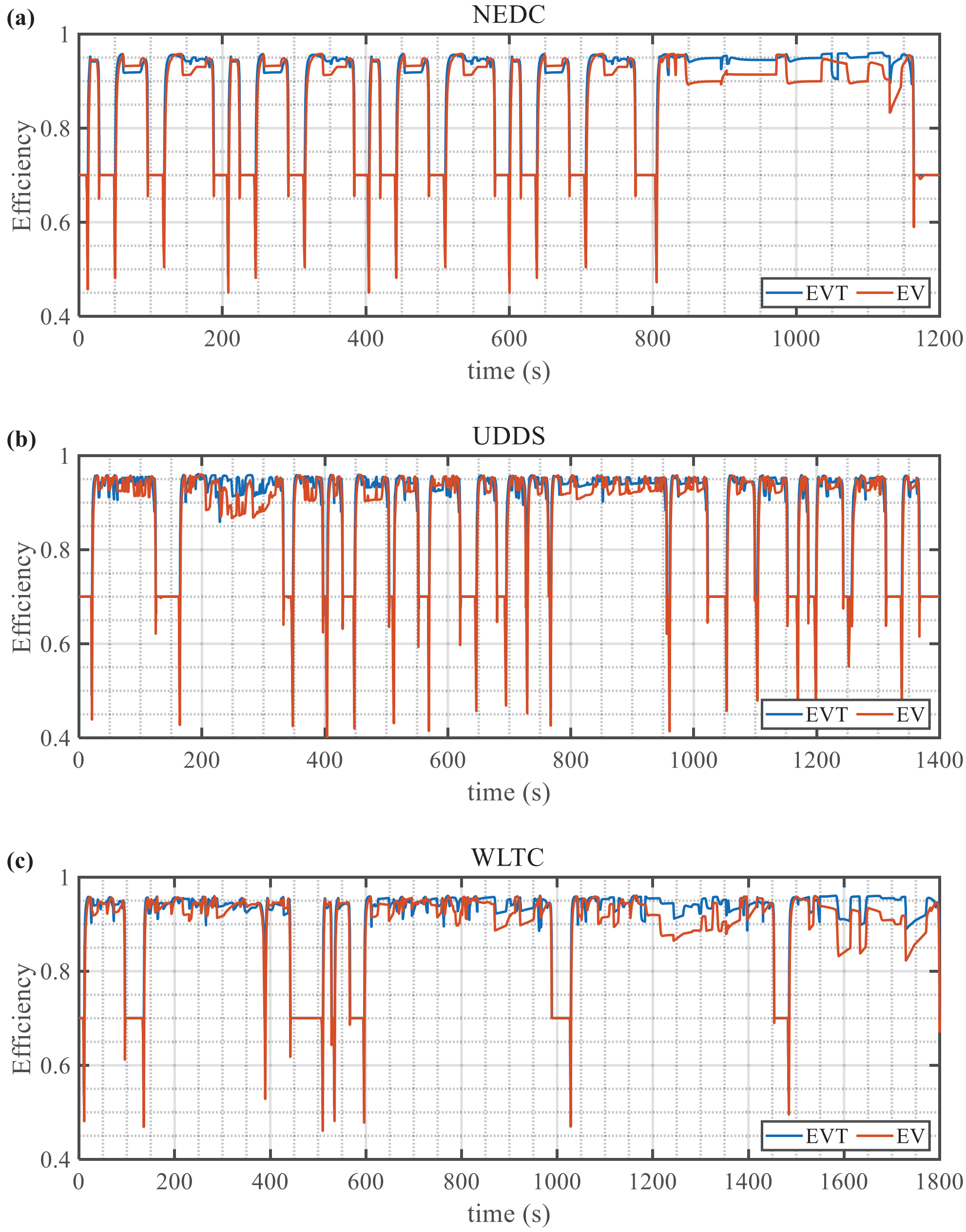

Figure 14. Motor efficiency in three driving cycles: (**a**) Efficiency under NEDC driving cycle; (**b**) Efficiency under UDDS driving cycle; (**c**) Efficiency under WLTC driving cycle.

As shown in Figure 14a, in the NEDC driving cycle, the motor efficiency of the EVT was higher than that of the EV most of the time, especially when the vehicle was driven in the high-speed driving phase. According to the shifting strategy, the 2DCT shifted to the second gear state in this phase, and obviously, the working efficiency of the EVT motor was significantly higher than that of the EV in this phase.

As shown in Figure 14b, in the UDDS driving cycle, the motor working efficiency of the EVT was higher than that of the EV in most cases, but the gap was not huge. However, in some relatively high-speed periods, such as 220 s to 340 s, the motor efficiency of the EVT was much higher than that of the EV, because the 2DCT was in second gear state during these periods.

As shown in Figure 14c, under the WLTC driving cycle, the motor efficiencies of the EVT and the EV were not much different in the low-speed period. With increases in the vehicle speed, the motor efficiency of the EVT was slightly higher than that of the EV in the medium speed periods, such as 840 s to 960 s, because the 2DCT switched between first and second gear more frequently during this period. In the high-speed period, since the 2DCT often stays in the second gear state, the motor efficiency of the EVT was significantly higher than that of the EV. These phenomena show that the 2DCT can enhance the efficiency of the motor.

The battery SOC curves of two types of vehicles in the NEDC, UDDS, and WLTC driving cycles are shown in Figure 15a–c, respectively. The braking recovery energy curves are shown in Figure 16a–c, respectively. The final values of the SOC and the braking energy recovery are shown in Table 2. The braking energy was recovered according to a fixed proportion; 30% of the total braking energy was recovered.

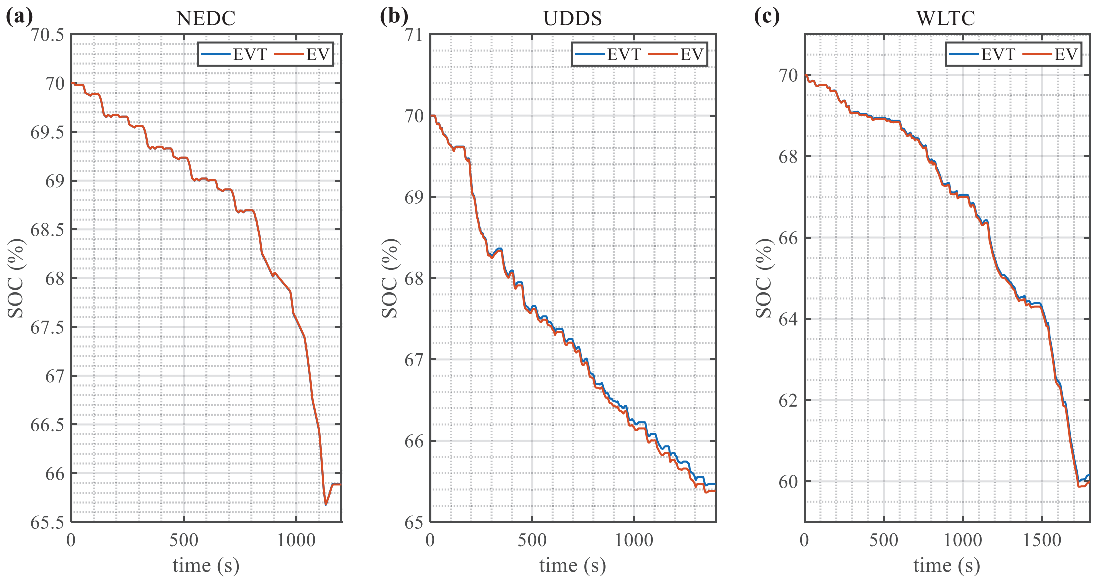

Figure 15. Battery SOC curves in three driving cycles: (**a**) NEDC driving cycle; (**b**) UDDS driving cycle; (**c**) WLTC driving cycle.

Table 2. The final value of battery SOC and braking energy recovery.

Drive Cycle	Vehicle Type	Final SOC (%)	Braking Recovery Energy (kJ)
NEDC	EVT	65.89	578.69
	EV	65.88	572.64
UDDS	EVT	65.47	908.43
	EV	65.38	844.60
WLTC	EVT	60.16	1131.90
	EV	59.97	957.15

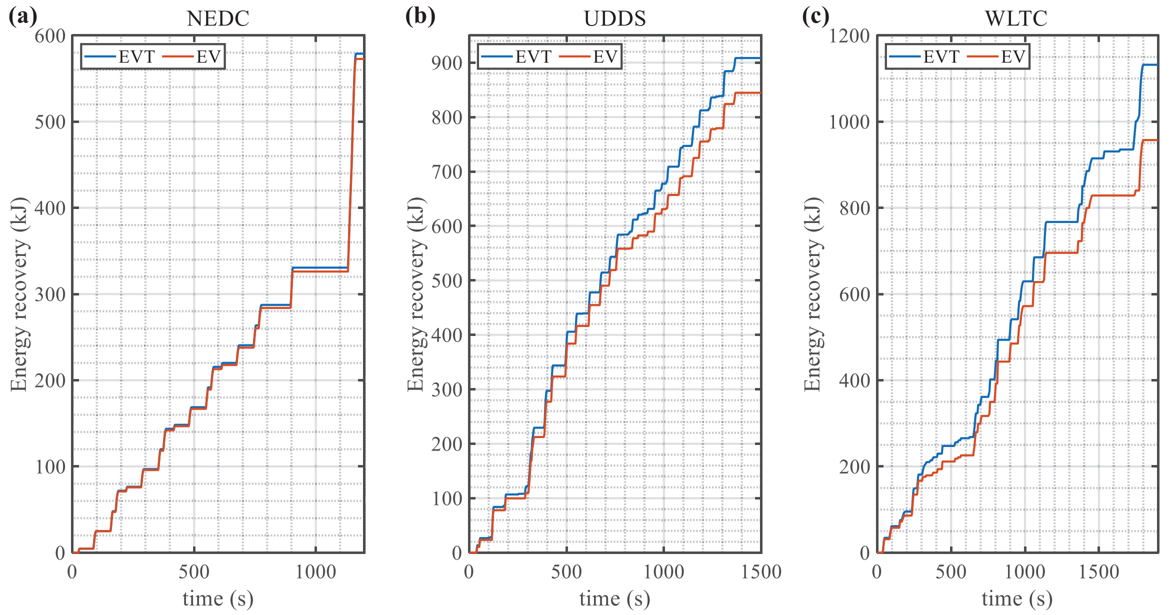

Figure 16. Braking recovery energy curves in three driving cycles: (**a**) NEDC driving cycle; (**b**) UDDS driving cycle; (**c**) WLTC driving cycle.

As shown in Figures 15a and 16a, the SOC curve of the EVT was not much different than that of the EV under the NEDC driving cycle; the braking recovery energy of the EVT was 6.05 kJ higher than that of the EV. According to Figures 15b and 16b, in the UDDS driving cycle, the SOC curve of the EVT declined more slowly than that of the EV, and the final value improved by 0.09%; the braking recovery energy of the EVT increased by 7.6%. These changes were due to the UDDS driving cycle being more complicated and having more braking periods. With the driving time increases, the gap between the SOC curves and the gap between the braking recovery energy curves both increased, which meant that the longer the driving distance, the more energy the EVT saved. As shown in Figures 15c and 16c, under the WLTC driving cycle, the SOC curve of the EVT declined more slowly than that of the EV; the final values have improved by 0.19%, and the braking recovery energy of the EVT increased by 18.25%. This was because the 2DCT was in the second gear state during the high-speed period, which reduced the motor speed so that the motor could work in a more efficient range whether it was driving or braking. Like the UDDS, with the increase in driving time, the gap between the SOC curves and between the braking recovery energy curves increased.

In summary, the EVT is superior to the EV in terms of economic performance, and the 2DCT made a significant contribution to this superiority. Moreover, for the EVT, the energy-saving control strategy can be more optimized, which also provides a greater potential for energy-saving.

4.2. Comparison of Vehicle Dynamic Performance

Considering the acceleration time, the climbing ability, and the maximum speed, the dynamic performances of the EVT and the EV were compared and analyzed. Acceleration time reflects the acceleration ability of the vehicle and is one of the most critical indicators of vehicle dynamic performance. The acceleration times from 0 to 100 km/h and 0 to 50 km/h for the EVT and the EV on a flat road with a slope of 0% are shown in Figure 17a,b, respectively. The acceleration times in the 4% road slope are shown in Figure 17c,d, and the acceleration times in the 6% road slope are shown in Figure 17e,f.

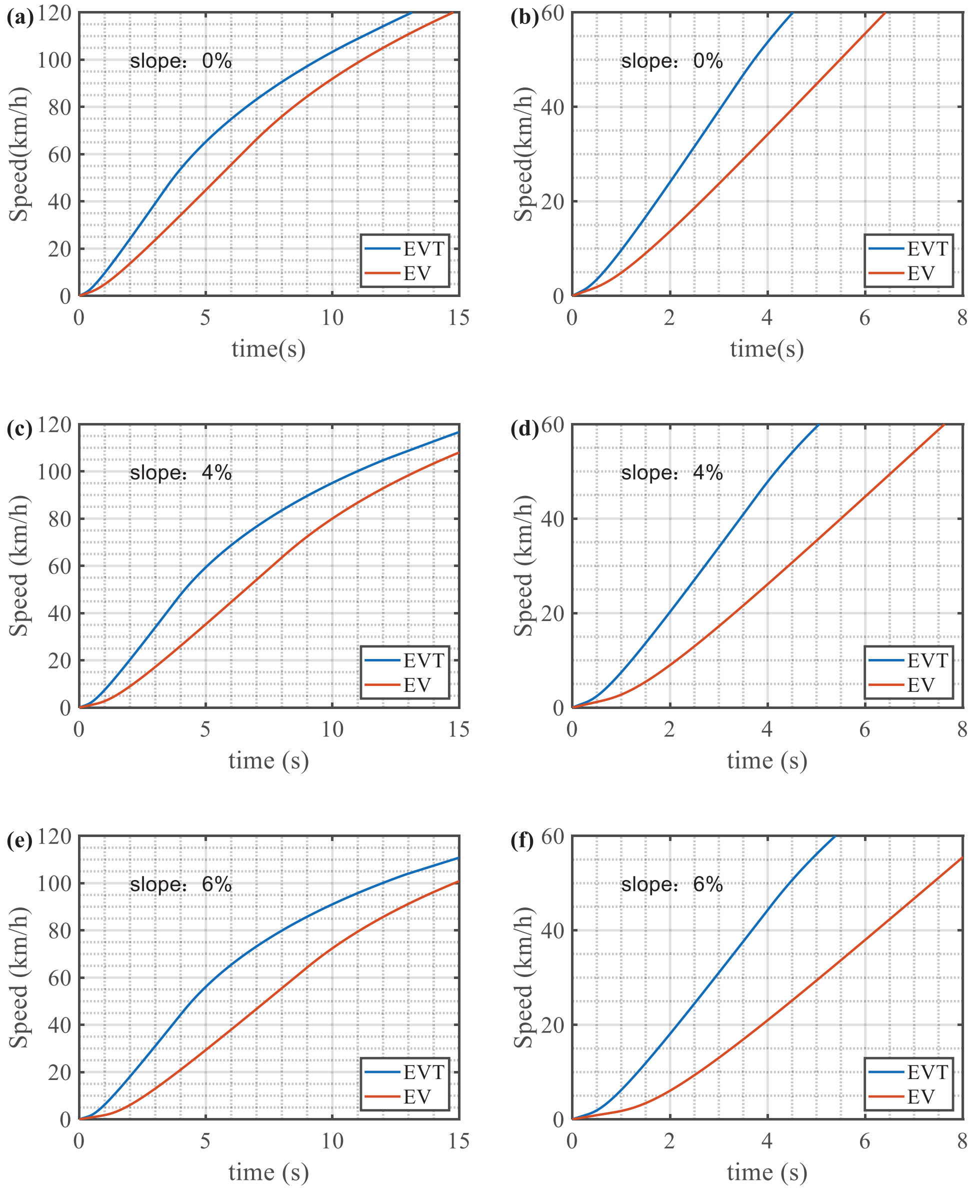

Figure 17. Acceleration time at different road slopes: (**a**) Acceleration time from 0 to 100 km/h at 0% slope; (**b**) Acceleration time from 0 to 50 km/h at 0% slope; (**c**) Acceleration time from 0 to 100 km/h at 4% slope; (**d**) Acceleration time from 0 to 50 km/h at 4% slope; (**e**) Acceleration time from 0 to 100 km/h at 6% slope; (**f**) Acceleration time from 0 to 50 km/h at 6% slope.

The acceleration times of the EVT and the EV are shown in Table 3.

Table 3. Acceleration times of EVT and EV.

Slope	Vehicle Type	0~100 km/h (s)	0~50 km/h (s)
0%	EVT	9.45	3.72
	EV	11.19	5.48
4%	EVT	10.97	4.17
	EV	13.32	6.57
6%	EVT	11.98	4.45
	EV	14.81	7.37

Compared with the EV, the 0–100 km/h acceleration time of the EVT increased by 15.55% and the 0–50 km/h acceleration time increased by 32.29% on the level road. The 0–100 km/h acceleration time of the EVT increased by 17.64% and the 0–50 km/h acceleration time increased by 36.53% at the 4% road slope. At the 6% road slope, the 0–100 km/h acceleration time of the EVT increased by 19.11% and the 0–50 km/h acceleration time increased by 39.62%. In summary, the acceleration ability of the EVT was greatly improved, especially at 0–50 km/h. Specifically, it improved even more in climbing situations, and as the road slope increased, the improvement was more obvious. The maximum vehicle speeds of the EVT and the EV on the level roads and the maximum climbing slopes at a speed of 30 km/h, respectively, are shown in Table 4.

Table 4. Maximum climbing slopes and vehicle speeds of EVT and EV.

Vehicle Type	Max Slope	Max Speed
EVT	36%	228 km/h
EV	25%	169 km/h

The maximum climbing slope of the EVT increased by 32.4% compared to the EV at a 30 km/h vehicle speed. The theoretical maximum speed of the EVT improved by 34%, compared to that of the EV. The above changes show that equipping with the 2DCT significantly improved the dynamic performance of pure electric vehicles.

4.3. Rig Testing

To prove the accuracy of the model and simulation, a test rig was used to verify the climbing ability of the EVT. The test rig consisted of a power supply, a motor, a transmission, wheels, flywheels, MCU, TCU, a magnetic powder brake, a host computer, etc. The structure of the test rig is shown in Figures 18 and 19. The resistance of the vehicle when it was running is shown in Equation (18) and Equation (19), respectively.

$$F_z = F_f + F_g + F_a + F_i \tag{18}$$

$$\begin{cases} F_f = mgf cos\alpha \\ F_g = mgsin\alpha \\ F_a = \frac{C_d A}{21.15} v^2 \\ F_i = \delta m \frac{dv}{dt} \end{cases} \tag{19}$$

where F_z, F_f, F_g, F_a, and F_i are the driving resistance, the rolling resistance, the slope resistance, the air resistance, and the acceleration resistance, respectively.

When the vehicle drove on a level road at a speed of 30 km/h, the driving resistance was 168 N and the torque on the wheels was 52 Nm. When the road slope became 36%, the driving resistance of the vehicle was 5994.9 N and the torque on the wheels was 1858.4 Nm.

The reference speed and the actual speed are shown in Figure 20a. The reference speed gradually increased from 0 to 30 km/h, reaching 30 km/h at 187 s. The test rig accelerated during the period from 0 to 187 s and the actual speed reached 30 km/h at 187 s. The torque curve of the magnetic powder brake is shown in Figure 20b. To simulate the resistance at 30 km/h, the braking torque of the magnetic powder brake was 52 Nm during the period from 0 to 200 s. Then, it increased during the period from 200 to 491 s and reached 1858.4 Nm at 491 s. From this moment, the test rig started to simulate the resistance of driving on a 36% slope road at a speed of 30 km/h. As can be seen from Figure 20, the test rig could drive normally.

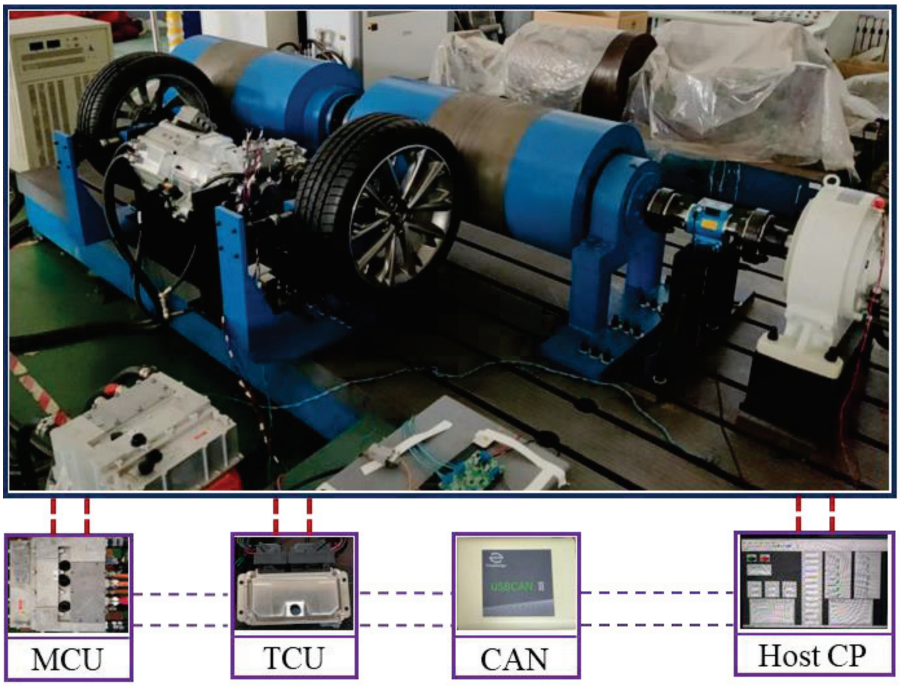

Figure 18. Testing rig.

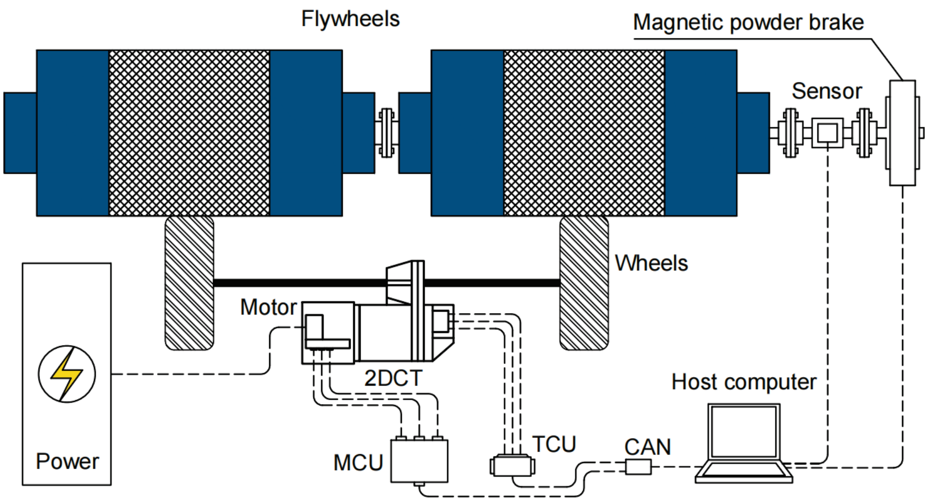

Figure 19. Testing rig composition frame.

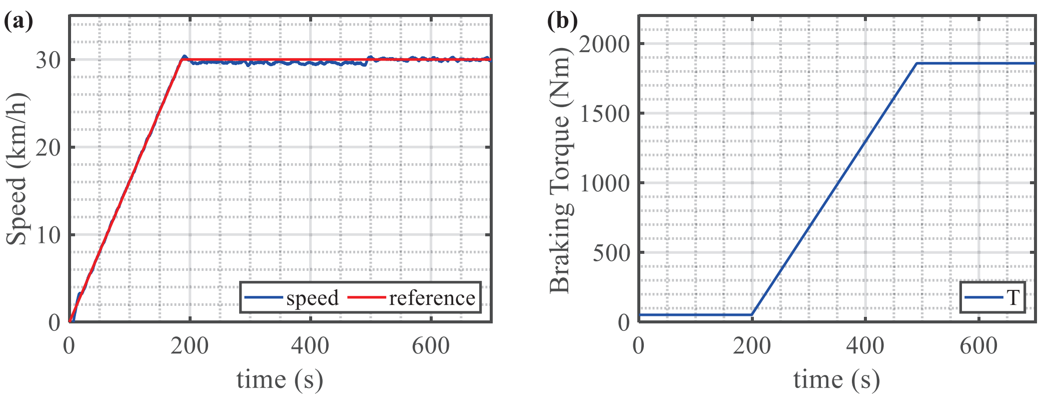

Figure 20. Test conditions and results: (**a**) Vehicle speed tracking; (**b**) Brake torque trajectory.

5. Conclusions

In this paper, an EV equipped with a two-speed DCT was used as the research target to study the effect of the 2DCT on the performance of electric vehicles. A rule-based partitioned gear-shifting strategy was designed, which combined the economic shifting strategy with the dynamic shifting strategy. Fuzzy logic was introduced to modify the gear-shifting strategy online and was proven to be effective in reducing unnecessary shifts, thereby increasing driving comfort and transmission working life. The model of the EVT and the EV were established based on Matlab/Simulink. The motor working efficiency, the battery SOC curve, and the braking energy recovery were compared under three driving cycles of NEDC, UDDS and WLTC. The EVT outperformed the EV in all of these aspects. According to the research results, in a vehicle equipped with a two-speed transmission, the rotation speed of the motor can be adjusted by shifting gears, allowing the motor to work more effectively in both drive mode and brake recovery mode; thus, the EVT can achieve better economic performance. In addition, when the vehicle is running at a relatively low speed, the two-speed transmission stays in first gear with a larger ratio, which provides the vehicle with greater torque; therefore, the EVT has greater acceleration and climbing ability than the EV. When the vehicle speed is high, the transmission stays in second gear with a smaller ratio, which leads the vehicle to be able to reach a higher speed than that of the EV. With the support of the two-speed transmission, the EVT has better dynamic performance. Finally, the maximum climbing capacity of the EVT was verified by the rig test.

In the future, the effect of various shifting strategies on vehicle performance will be investigated. The impact of shifting jerk on driving comfort during high-speed shifts will also be investigated to further explore the value of two-speed transmissions for widespread use in EVs. In addition, the braking energy recovery strategy will be studied.

Author Contributions: Methodology, B.H.; software, B.H. and C.W. (Changyin Wei); validation, B.H. and Y.C.; formal analysis, X.L. and C.W. (Cong Wang); investigation, Q.W.; resources, Y.C.; data curation, B.H.; writing—original draft preparation, B.H. and X.L.; writing—review and editing, B.H. and X.L.; supervision, Y.C. All authors have read and agreed to the published version of the manuscript.

Funding: This research was funded by Hebei Province full-time introduction of high-end talent projects (NO. 20181228).

Conflicts of Interest: The authors declare no conflict of interest.

References

1. Wei, C.Y.; Sun, X.X.; Chen, Y.; Zang, L.B.; Bai, S.J. Comparison of architecture and adaptive energy management strategy for plug-in hybrid electric logistics vehicle. *Energy* **2021**, *230*, 14. [CrossRef]
2. Nguyen, C.T.; Walker, P.D.; Zhang, N. Shifting strategy and energy management of a two-motor drive powertrain for extended-range electric buses. *Mech. Mach. Theory* **2020**, *153*, 17. [CrossRef]
3. Itani, K.; De Bernardinis, A.; Khatir, Z.; Jammal, A.; Oueidat, M. Regenerative Braking Modeling, Control, and Simulation of a Hybrid Energy Storage System for an Electric Vehicle in Extreme Conditions. *IEEE Trans. Transp. Electrif.* **2016**, *2*, 465–479. [CrossRef]
4. Cai, W.; Wu, X.; Zhou, M.; Liang, Y.; Wang, Y. Review and Development of Electric Motor Systems and Electric Powertrains for New Energy Vehicles. *Automot. Innov.* **2021**, *4*, 3–22. [CrossRef]
5. Sun, X.D.; Shi, Z.; Lei, G.; Guo, Y.G.; Zhu, J.G. Analysis and Design Optimization of a Permanent Magnet Synchronous Motor for a Campus Patrol Electric Vehicle. *IEEE Trans. Veh. Technol.* **2019**, *68*, 10535–10544. [CrossRef]
6. Saw, L.H.; Ye, Y.H.; Tay, A.A.O. Integration issues of lithium-ion battery into electric vehicles battery pack. *J. Clean Prod.* **2016**, *113*, 1032–1045. [CrossRef]
7. Lin, Q.F.; Niu, S.X.; Cai, F.B.; Fu, W.N.; Shang, L.K. Design and Optimization of a Novel Dual-PM Machine for Electric Vehicle Applications. *IEEE Trans. Veh. Technol.* **2020**, *69*, 14391–14400. [CrossRef]
8. You, Y.; Sun, D.Y.; Qin, D.T. Shift strategy of a new continuously variable transmission based wheel loader. *Mech. Mach. Theory* **2018**, *130*, 313–329. [CrossRef]
9. Puricelli, S.; Cardellini, G.; Casadei, S.; Faedo, D.; van den Oever, A.E.M.; Grosso, M. A review on biofuels for light-duty vehicles in Europe. *Renew. Sust. Energ. Rev.* **2021**, *137*, 19. [CrossRef]

10. Hu, J.J.; Ran, H.L.; Pang, T.; Zhang, Y. Parameter design and performance analysis of shift actuator for a two-speed automatic mechanical transmission for pure electric vehicles. *Adv. Mech. Eng.* **2016**, *8*, 15. [CrossRef]
11. Liang, J.; Walker, P.D.; Ruan, J.; Yang, H.T.; Wu, J.L.; Zhang, N. Gearshift and brake distribution control for regenerative braking in electric vehicles with dual clutch transmission. *Mech. Mach. Theory* **2019**, *133*, 1–22. [CrossRef]
12. Hu, M.H.; Chen, L.; Wang, D.Y.; Xu, Z.F.; Xu, P.; Qin, D.T.; Zhou, A.J. Modeling and characteristic study of the shifting engagement process in stepped transmission. *Mech. Mach. Theory* **2020**, *151*, 12. [CrossRef]
13. Qin, D.T.; Yao, M.Y.; Chen, S.J.; Lyu, S.K. Shifting Process Control for Two-Speed Automated Mechanical Transmission of Pure Electric Vehicles. *Int. J. Precis. Eng. Manuf.* **2016**, *17*, 623–629. [CrossRef]
14. Zhu, B.; Zhang, N.; Walker, P.; Zhou, X.X.; Zhan, W.Z.; Wei, Y.Y.; Ke, N.J. Gear shift schedule design for multi-speed pure electric vehicles. *Proc. Inst. Mech. Eng. Part D J. Automob. Eng.* **2015**, *229*, 70–82. [CrossRef]
15. He, H.W.; Han, M.; Liu, W.; Cao, J.F.; Shi, M.; Zhou, N.N. MPC-based longitudinal control strategy considering energy consumption for a dual-motor electric vehicle. *Energy* **2022**, *253*, 16. [CrossRef]
16. Gao, B.Z.; Liang, Q.; Xiang, Y.; Guo, L.L.; Chen, H. Gear ratio optimization and shift control of 2-speed I-AMT in electric vehicle. *Mech. Syst. Signal Proc.* **2015**, *50-51*, 615–631. [CrossRef]
17. Jeoung, D.; Min, K.H.; Sunwoo, M. Automatic Transmission Shift Strategy Based on Greedy Algorithm Using Predicted Velocity. *Int. J. Automot. Technol.* **2020**, *21*, 159–168. [CrossRef]
18. Lin, C.; Zhao, M.J.; Pan, H.; Yi, J. Blending gear shift strategy design and comparison study for a battery electric city bus with AMT. *Energy* **2019**, *185*, 1–14. [CrossRef]
19. Shen, W.C.; Yu, H.L.; Hu, Y.H.; Xi, J.Q. Optimization of Shift Schedule for Hybrid Electric Vehicle with Automated Manual Transmission. *Energies* **2016**, *9*, 220. [CrossRef]
20. Saini, V.; Singh, S.; Nv, S.; Jain, H. Genetic Algorithm Based Gear Shift Optimization for Electric Vehicles. *SAE Int. J. Altern. Powertrains* **2016**, *5*, 348–356. [CrossRef]
21. Liu, Y.G.; Gao, D.K.; Zhai, K.N.; Huang, Q.; Chen, Z.; Zhang, Y. Coordinated control strategy for braking and shifting for electric vehicle with two-speed automatic transmission. *eTransportation* **2022**, *13*, 16. [CrossRef]
22. Nguyen, C.T.; Walker, P.D.; Zhang, N. Optimization and coordinated control of gear shift and mode transition for a dual-motor electric vehicle. *Mech. Syst. Signal Proc.* **2021**, *158*, 18. [CrossRef]
23. Xu, X.; Liang, J.; Hao, Q.; Dong, P.; Wang, S.; Guo, W.; Liu, Y.; Lu, Z.; Geng, J.; Yan, B. A Novel Electric Dual Motor Transmission for Heavy Commercial Vehicles. *Automot. Innov.* **2021**, *4*, 34–43. [CrossRef]
24. Granovskii, M.; Dincer, I.; Rosen, M.A. Economic and environmental comparison of conventional, hybrid, electric and hydrogen fuel cell vehicles. *J. Power Sources* **2006**, *159*, 1186–1193. [CrossRef]
25. Li, K.B.; Bouscayrol, A.; Han, S.L.; Cui, S.M. Comparisons of Electric Vehicles Using Modular Cascade Machines System and Classical Single Drive Electric Machine. *IEEE Trans. Veh. Technol.* **2018**, *67*, 354–361. [CrossRef]
26. Ragheb, H.; Aydin, M.; El-Gindy, M.; Kishawy, H.A. Comparison of gradability performance of fuel cell hybrid electric and internal-combustion engine vehicles. *J. Power Sources* **2013**, *221*, 447–454. [CrossRef]
27. Wu, J.L.; Liang, J.J.Y.; Ruan, J.G.; Zhang, N.; Walker, P.D. Efficiency comparison of electric vehicles powertrains with dual motor and single motor input. *Mech. Mach. Theory* **2018**, *128*, 569–585. [CrossRef]
28. Spanoudakis, P.; Tsourveloudis, N.C.; Doitsidis, L.; Karapidakis, E.S. Experimental Research of Transmissions on Electric Vehicles' Energy Consumption. *Energies* **2019**, *12*, 388. [CrossRef]
29. Li, X.Y.; Yuan, C.G.; Wang, Z.P.; He, J.T.; Yu, S.K. Lithium battery state-of-health estimation and remaining useful lifetime prediction based on non-parametric aging model and particle filter algorithm. *eTransportation* **2022**, *11*, 11. [CrossRef]
30. Li, X.Y.; Yuan, C.G.; Wang, Z.P.; Xie, J.L. A data-fusion framework for lithium battery health condition Estimation Based on differential thermal voltammetry. *Energy* **2022**, *239*, 13. [CrossRef]
31. Li, L.; Li, X.J.; Wang, X.Y.; Song, J.; He, K.; Li, C.F. Analysis of downshift's improvement to energy efficiency of an electric vehicle during regenerative braking. *Appl. Energy* **2016**, *176*, 125–137. [CrossRef]
32. Kim, S.; Oh, J.; Choi, S. Gear shift control of a dual-clutch transmission using optimal control allocation. *Mech. Mach. Theory* **2017**, *113*, 109–125. [CrossRef]
33. Xu, C.; Geyer, S.; Fathy, H.K. Formulation and Comparison of Two Real-Time Predictive Gear Shift Algorithms for Connected/Automated Heavy-Duty Vehicles. *IEEE Trans. Veh. Technol.* **2019**, *68*, 7498–7510. [CrossRef]
34. Huang, R.C.; He, H.W.; Zhao, X.Y.; Wang, Y.L.; Li, M.L. Battery health-aware and naturalistic data-driven energy management for hybrid electric bus based on TD3 deep reinforcement learning algorithm. *Appl. Energy* **2022**, *321*, 15. [CrossRef]

sensors

MDPI

Article

Theoretical and Experimental Investigations on High-Precision Micro-Low-Gravity Simulation Technology for Lunar Mobile Vehicle

Weijie Hou [1,2], Yongbo Hao [3], Chang Wang [2], Lei Chen [4], Guangping Li [2], Baoshan Zhao [2], Hao Wang [2], Qingqing Wei [4], Shuo Xu [2], Kai Feng [1] and Libin Zang [2,5,*]

1 College of Mechanical and Vehicle Engineering, Hunan University, Changsha 410082, China
2 Tianjin Key Laboratory of Microgravity and Hypogravity Environment Simulation Technology, Tianjin Institute of Aerospace Mechanical and Electrical Equipment, Tianjin 300301, China
3 Beijing Institute of Control Engineering, Beijing 100190, China
4 Beijing Key Laboratory of Intelligent Space Robotic Systems Technology and Applications, Beijing Institute of Spacecraft System Engineering, Beijing 100094, China
5 School of Mechanical Engineering, Tianjin University, Tianjin 300350, China
* Correspondence: zanglibin906@163.com

Abstract: With the development of space technology, the functions of lunar vehicles are constantly enriched, and the structure is constantly complicated, which puts forward more stringent requirements for its ground micro-low-gravity simulation test technology. This paper puts forward a high-precision and high-dynamic landing buffer test method based on the principle of magnetic quasi-zero stiffness. Firstly, the micro-low-gravity simulation system for the lunar vehicle was designed. The dynamic model of the system and a position control method based on fuzzy PID parameter tuning were established. Then, the dynamic characteristics of the system were analyzed through joint simulation. At last, a prototype of the lunar vehicle's vertical constant force support system was built, and a micro-low-gravity landing buffer test was carried out. The results show that the simulation results were in good agreement with the test results. The sensitivity of the system was better than 0.1%, and the constant force deviation was 0.1% under landing impact conditions. The new method and idea are put forward to improve the micro-low-gravity simulation technology of lunar vehicles.

Keywords: magnetic quasi-zero stiffness; lander; lunar vehicle; dynamics; micro-low-gravity simulation

1. Introduction

Future manned and unmanned lunar base exploration missions put forward clear requirements for a multi-functional intelligent flying mobile vehicle carrier platform with assembly, exploration, and low-altitude flight capabilities [1]. Therefore, the new lunar vehicle (Figure 1) needs to break through key technologies, such as all-terrain active adaptation to the mobile mechanism, the planning and control of compound mobile mechanisms, and GNC (Guidance Navigation Control) flying at ultra-low altitudes to realize high-precision soft landing in complex terrain, to adapt to the harsh environment on the polar surface, and to take off repeatedly from the lunar surface [2].

The gravity field environment between the moon and the earth is very different [3]. Thus, the lunar vehicle carrier platform has more special characteristics compared with ground vehicles. It must pass mechanical properties and mobility performance tests such as landing buffer, passing performance, stability performance, obstacle-crossing performance, turning performance, and driving smoothness [4]. In the research field of micro-low-gravity simulation tests of planetary vehicles, researchers from the United States, Russian Federation, and China have made many attempts and explorations. The low-gravity experimental system of NASA (National Aeronautics and Space Administration) manned planetary vehicles is an active system [5,6]. A mechanism similar to the crown block is used to realize the following movement in a large range, and the two-dimensional servo platform is used to realize the accurate following movement in a small range. The active tracking constant tension suspension scheme was also adopted in the ground experiment of a Russian planetary vehicle [7]. The force balance method was mainly used in the ground test of China Chang'E Series detectors, which puts forward the unloading form based on a single sling [8]. In the buffer landing test of the Chang'E-III, the multi-rigid-body low-gravity simulation and simulation accuracy made new progress [9]. In the infield test of the lunar vehicle, methods such as adding a counterweight on the rocker's arm and adjusting the suspension spring stress point were adopted [10]. As a result, the force between each wheel of the patrol car and the ground is the same as that on the lunar surface in various working conditions such as plane driving, climbing, and obstacle crossing. However, the shaking interference of the suspension rope system, especially when the vertical direction is under high dynamic conditions, has a great influence on the dynamic characteristics of the vehicle due to the large unloading error of the constant-force suspension. It has a significant impact on test accuracy under high-speed and high dynamic conditions. Therefore, under high dynamic conditions, high-precision constant force unloading is still a difficult problem in the micro-low-gravity simulation field at home and abroad [11,12]. The quasi-zero stiffness system is a kind of mechanism with high static stiffness and low dynamic stiffness characteristics. The characteristics of quasi-zero stiffness with high carrying capacity and low dynamic stiffness can be obtained through a specially designed mechanism in a certain stroke [13], which can solve the problem that the high stiffness of ordinary elastic element affects the accuracy of tension output. Carrella [14] proposed a method to obtain the quasi-zero stiffness mechanism in parallel with three springs. Tang [15] used the method of parallel positive and negative stiffness to obtain the improved quasi-zero stiffness mechanism in a three-spring parallel. Niu [16] proposed a tandem-tensioning constant torque mechanism to replace the buffer spring, which improved the mechanism significantly, increased the system bandwidth, and achieved an enhanced dynamic constant-force performance. Thus, the application of quasi-zero stiffness system in the field of gravity compensation provides a good solution. Whereas, in the mechanical contact quasi-zero stiffness system, there is inevitably friction between contact pairs [17]. For these reasons, the magnetic quasi-zero stiffness has the characteristics of no friction, large load, and fast dynamic response [18–20], which provides a new idea for the constant supporting force with a heavy load, long stroke, and high precision in the vertical direction.

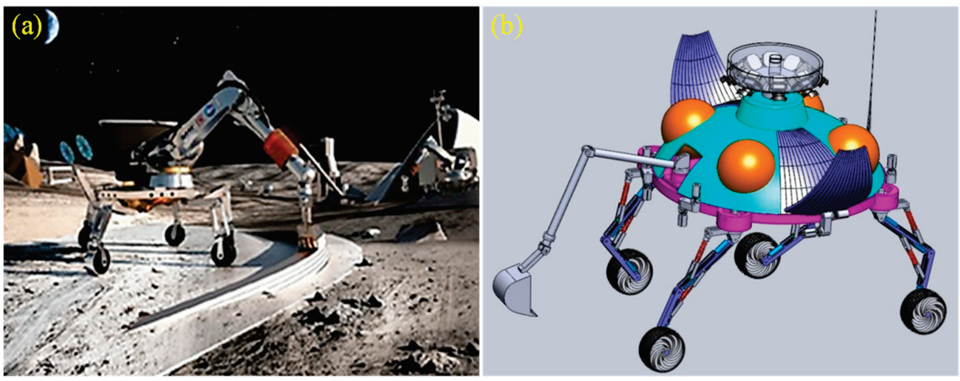

Figure 1. The lunar vehicle. (**a**) physical diagram, (**b**) three-dimensional model diagram.

In view of the test requirements of the future flying mobile vehicle platform, how to further improve the simulation accuracy of vehicle dynamics and improve the unloading accuracy when the vehicle moves rapidly has become a key issue. Therefore, this paper focuses on the high dynamic constant force unloading technology in the vertical direction. In this paper, a new three-dimensional high-precision and micro-low gravity simulation test system based on magnetic quasi-zero stiffness was designed. A position control method based on fuzzy PID (Proportion Integration Differentiation) parameter tuning was proposed, and a gravity balance system with high precision, large range, and fast response was realized. The performance of the prototype was tested and analyzed by simulation and experiment, which can provide a useful attempt for the test of intelligent flying mobile vehicle carrier platforms in a manned/unmanned lunar base in the future.

The structure of this paper is as follows: the theoretical model of the micro-low-gravity simulation system for a lunar vehicle and the research methods are shown in Section 2. Section 3 formulates the prototype of the vertical constant force mechanism and the evaluation experiment. Section 4 focuses on the analysis and discussion of the landing buffer simulation experimental results. The conclusion is given in Section 5.

2. Theoretical Model and Methods

2.1. Design of Micro-Low-Gravity Simulation System for Lunar Vehicle

The schematic architecture of the lunar vehicle micro-low-gravity simulation test system is shown in Figure 2a,b. The micro-low-gravity simulation system can realize the high-precision simulation of the lunar vehicle landing process (Figure 2c) and the self-adaptive height adjustment during the horizontal movement with the lunar vehicle (Figure 2d). During the micro-low-gravity simulation test, a three-free air floating ball bearing is used to adjust the attitude of the lunar vehicle to achieve horizontal balance. In order to ensure that the force between the wheel and the ground is the same as the lunar surface in various working conditions, such as plane driving, climbing, and obstacle crossing during the landing buffer and patrol, a magnetic quasi-zero stiffness mechanism and a stroke amplification mechanism are introduced to realize vertical unloading.

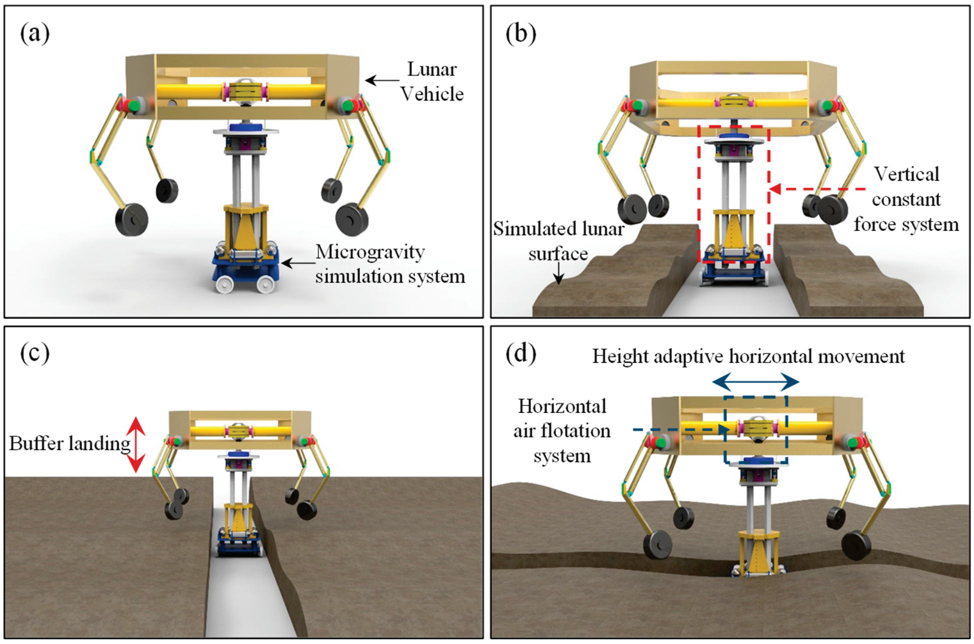

Figure 2. Three-dimensional schematic diagram of micro-low-gravity simulation system structure. (**a**) system architecture, (**b**) lunar vehicle infield test, (**c**) buffer landing simulation, (**d**) horizontal movement simulation.

2.2. Principle of Magnetic Quasi-Zero Stiffness

The magnetic quasi-zero stiffness (M-QZS) mechanism is based on the "repulsion" magnetic negative stiffness principle of permanent magnets and is formed by connecting the main bearing positive stiffness subunit and the magnetic negative stiffness subunit in parallel [21]. Figure 3 shows the principle of magnetic quasi-zero stiffness unit. As the main bearing unit, the positive stiffness mechanical spring bears the static load. The relation of the quasi-zero stiffness system is shown as Formula (1).

$$\begin{cases} k_1 > 0 \\ k_2 < 0 \\ k = k_1 + k_2 \approx 0 \end{cases} \tag{1}$$

where k_1 is the stiffness of the mechanical spring, k_2 is the stiffness of the magnetic spring, and k is the stiffness of the system.

When the mechanism is in a balanced state, as is shown in Figure 3a, the supporting force provided by the positive stiffness spring is equal to the gravity generated by the static load, which satisfies the following formula.

$$F_1 = mg \tag{2}$$

where F_1 is the main load-bearing positive stiffness subunit force, as is shown in Figure 3, m is the mass of the load, and g is the acceleration of gravity on the Earth.

When the downward external force F_i is applied to the static load, as is shown in Figure 3b, the main load-bearing positive stiffness subunit force F_1 increases upward, and the output force F_2 generated by the negative stiffness magnetic spring increases downward. For this reason, the mechanical stiffness and magnetic stiffness are satisfying Equation (2) within a certain range of motion. Then,

$$F_1' = mg + F_2 \tag{3}$$

At the same time, the friction resistance can be neglected because of the air-floating guidance. Therefore, non-contact magnetic zero stiffness overcomes the mechanical friction defect of the mechanical negative stiffness spring and has the advantages of compact structure and adjustable stiffness.

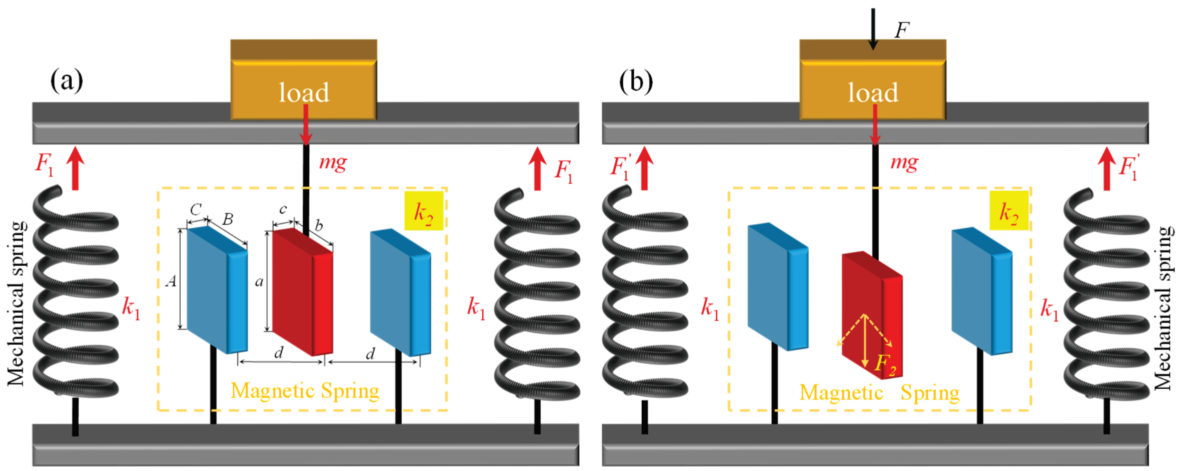

Figure 3. Principle of magnetic quasi-zero stiffness. (**a**) ateady state, (**b**) applying external load.

According to the model of magnetic charge [20,22], the stiffness of the magnetic spring can be obtained by Equation (4).

$$K_S = \frac{JJ'}{2\pi\mu_0} \sum_{i=0}^{1} \sum_{j=0}^{1} \sum_{k=0}^{1} \sum_{l=0}^{1} \sum_{p=0}^{1} \sum_{q=0}^{1} (-1)^{i+j+k+l+p+q} \varphi(L_{ij}, M_{kl}, N_{pq}, r) \tag{4}$$

with

$$\varphi(L_{ij}, M_{kl}, N_{pq}, r) = r + M_{kl} \ln(r - M_{kl}) \tag{5}$$

The variables can be calculated according to Equation (6).

$$\begin{cases} L_{ij} = \Delta x + (-1)^j A/2 - (-1)^i a/2 \\ M_{kl} = (-1)^l B/2 - (-1)^k b/2 \\ N_{pq} = d + (-1)^q C/2 - (-1)^p c/2 \\ r = \sqrt{L_{ij}^2 + M_{kl}^2 + N_{pq}^2} \end{cases} \tag{6}$$

where J and $J\prime$ are the magnetic polarization intensity vector, and the magnetic springs design parameters A, B, C, a, b, c, and d were shown in Figure 3. Δx is the deformation of the supporting unit, which can be calculated by $\Delta x = x_{ve} - x_{sy}$ as shown in Figure 4.

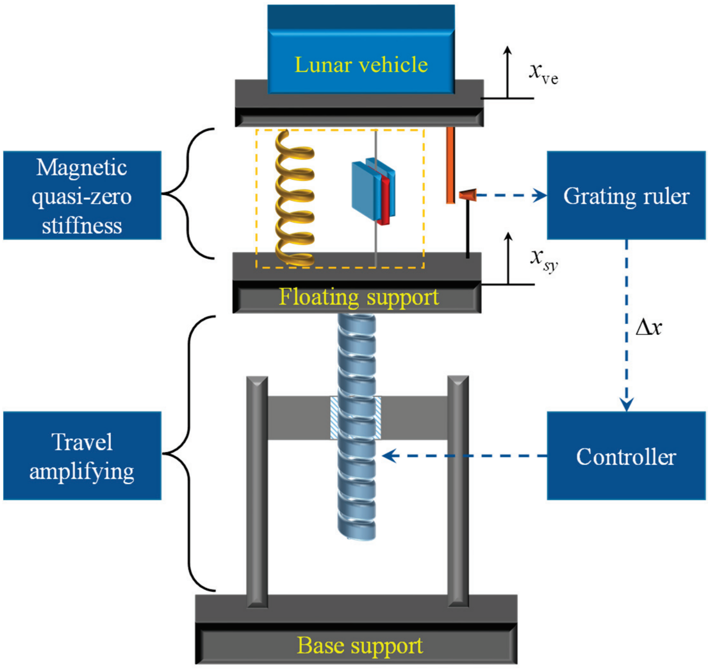

Figure 4. Schematic diagram of the lunar vehicle test system.

2.3. M-QZS Vertical Constant Force System

2.3.1. Dynamic Model

Figure 4 shows the schematic diagram of the M-QZS vertical constant force support system for the lunar vehicle gravity compensation. The magnetic quasi-zero stiffness mechanism is connected in series with the stroke amplification mechanism, in which the M-QZS can output constant force in a small stroke range, and the floating support is actively controlled by the servo system to amplify the constant force stroke.

When the lunar vehicle is in the lunar and earth field environment, the vertical dynamic can be formulated as Equations (7) and (8), respectively.

$$m_{ve}\ddot{x} = F_e - m_{ve}g_{lu} \tag{7}$$

$$m_{ve}\ddot{x} = F_e - m_{ve}g \tag{8}$$

where, m_{ve} is the mass of the lunar vehicle, F_e is the external force on the spacecraft, g_{lu} is the lunar gravity, and g is the Earth's gravity; therefore, $g_{lu} = g/6$.

Therefore, when the lunar vehicle is simulated on the ground in the gravity field of the earth, it is necessary to provide a compensation force to offset part of the gravity generated by the Earth. Regardless of the transmission mass and the damping of the air, the dynamic model of the lunar vehicle is formulated as follows

$$m_{ve}\ddot{x} = F_e - (m_{ve}g - F_{com}) \quad (9)$$

where, F_{com} is the compensation force.

The dynamic characteristics of the vertical constant force support system in the vertical direction meet the following conditions.

$$\begin{cases} m_{ve}\ddot{x}_{ve} = F_e - m_{ve}g + F_0 + F_\Delta \\ m_{sy}\ddot{x}_{sy} = F_{sy} + F_{dsy} - m_{sy}g - F_0 - F_\Delta \end{cases} \quad (10)$$

where F_0 is the ideal value of the system supporting force.

The dynamic model of simulated load is shown in Formula (11) under the real zero-gravity environment.

$$F_e = m_{ve}\ddot{x} + c(\dot{x}_{ve} - \dot{x}_{sy}) + k(x_{ve} - x_{sy}) \quad (11)$$

where, x_{ve} is the vertical displacement of the lunar vehicle, and x_{sy} is the displacement of the servo system.

Since there is no influence of contact friction, the change of supporting force of the constant force system can be determined by Formula (12).

$$F_\Delta = k(x_{ve} - x_{sy}) + c(\dot{x}_{ve} - \dot{x}_{sy}) \quad (12)$$

In the analysis, the constitutive model of the M-QZS is simplified as a parallel combination of a constant force and a nonlinear spring, and the constant force is equal to the gravity of the simulated load carried by the M-QZS. By measuring the stiffness–displacement data of the M-QZS under a static load, the stiffness–displacement curve is drawn in Figure 5. The stiffness K displacement equation of the M-QZS is fitted by the least square method as shown in Formula (13). It can be seen from Figure 5 that the stiffness of the zero stiffness mechanism is lower than 8 N/mm within the range of ±3 mm, and the stiffness of the system increases obviously with the increase in compression.

$$r = 0.6715x^3 - 2.405x^2 + 1.787x + 6.712 \quad (13)$$

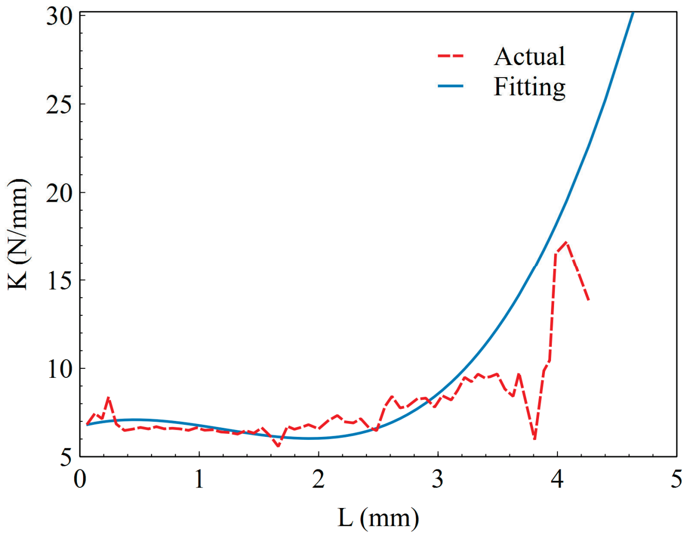

Figure 5. Stiffness–displacement curve of magnetic zero stiffness mechanism.

2.3.2. Control System Design and Active Control Strategy

In the closed-loop control constant force system, the control strategy of the force closed loop or the force potential coupling is usually adopted. That is, the force and position sensor is used to directly measure the force signal or simultaneously detect the force signal and displacement signal. However, the sensitivity of the force sensor is inversely proportional to its range, that is, as the range increases, the sensitivity decreases [23]. With the accuracy of 0.5% of the high dynamic force sensor, when the pressure reaches 5000 N, the measurement error of the force sensor will reach more than 25 N. Thus, the error is hard to ignore. On the other hand, due to the sudden change of input force signal in the process of lunar vehicle landing buffer, the rapidity of the active following control of the stroke amplification mechanism is extremely demanding. Therefore, the closed-loop control of the position information was adopted in this system instead of the traditional closed-loop control of the force information.

A position control method based on fuzzy PID parameter tuning was proposed for the system. Figure 6 shows the block diagram of the micro-low-gravity simulation test system control strategy. In this system, the M-QZS is connected in series with the stroke amplification mechanism. Due to the M-QZS keeping a low stiffness in a certain range while carrying heavy loads, the relative displacement difference between the simulated load and the floating support is directly measured with a high-precision grating ruler. The Δx is used as feedback to participate in the control closed loop of the stroke amplifying mechanism. $G_C(s)$ is the transfer function of the controller, and $G_D(s)$ is the transfer function of the stroke amplifying mechanism, as can be seen from Figure 6. When Δx approaches zero, that is, x_{ve} is equal to x_{sy}, this can ensure that the constant force system can truly simulate the micro-low-gravity environment. At the same time, because the sudden change of force will not affect the displacement instantly, the change in high-frequency force is responded to by the M-QZS, which greatly reduces the speed requirement of the stroke amplification mechanism.

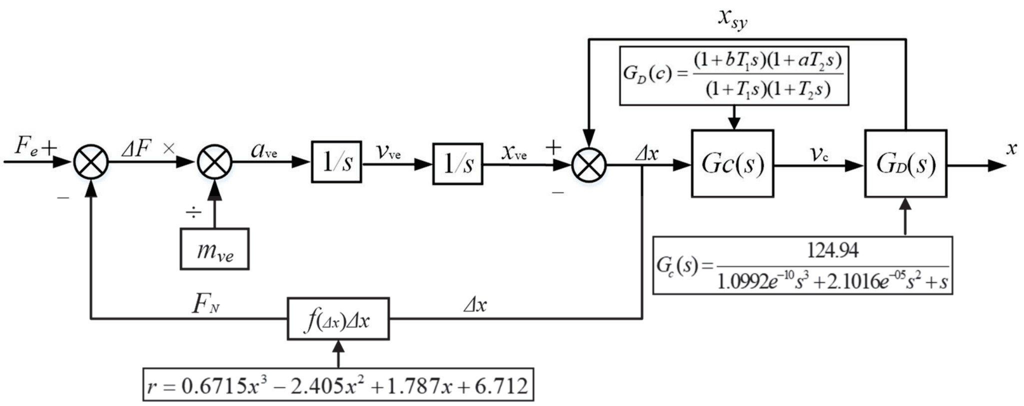

Figure 6. Active control strategy block diagram.

The constant force controller adopts a fuzzy self-adaptive tuning PID control algorithm, as shown in Figure 7. The controller takes the position error as input, and uses fuzzy to modify PID parameters online. A multi-input and multi-output fuzzy controller were adopted to fuzzify the position signal of the system and input it to the controller. We set the fuzzy sets of variables Δx, ΔF, and the control quantities ΔKp, ΔKi, and ΔKd in the operation of the simulation system as NB (negative big), NM (negative middle), NS (negative small), ZE (zero), PS (positive small), PM (middle) and PB (fair).

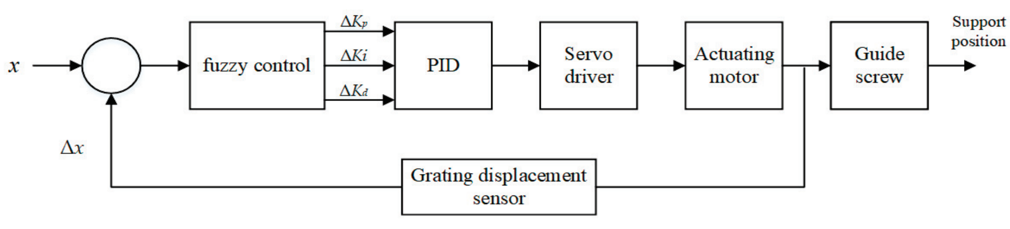

Figure 7. Constant force control principle based on fuzzy PID.

2.4. Dynamic Simulation of Micro-Low-Gravity Simulation System

The three-dimensional solid model of the M-QZS vertical constant force support system was established by Solidworks, and then the system model was imported into SimMechanics to obtain the inertia and mass parameters of each component. Then, define the motion constraint relationship between each component of the system. According to the measured displacement–stiffness data of the zero-stiffness mechanism, the spring damping model of the magnetic zero-stiffness mechanism was established in SimMechanics. The mechanical simulation model of the system was completed, and the input parameters of the simulation test are shown in Table 1.

Table 1. The input parameters for simulation test.

Parameters	Value
external force (N)	0.98
mass of lunar vehicle (kg)	94.5
falling height (mm)	170

3. Design and Performance Evaluation Experiment

3.1. System Architecture

3.1.1. Structure Composition

As is shown in Figure 8, the prototype of the vertical constant force mechanism in the micro-low-gravity simulation system of lunar vehicles was mainly composed of four parts: the M-QZS constant force support system, the simulated landing surface, the stroke amplification mechanism, a grating ruler, and an integrated control system. The air bearing was used in the M-QZS, which makes the negative stiffness rotor move frictionless in the vertical direction. The stroke amplification mechanism was composed of a polished lead screw guide rail, and, at the same time, a guide rod was installed on the landing surface. The above design ensured the vertical movement during the simulated buffer test.

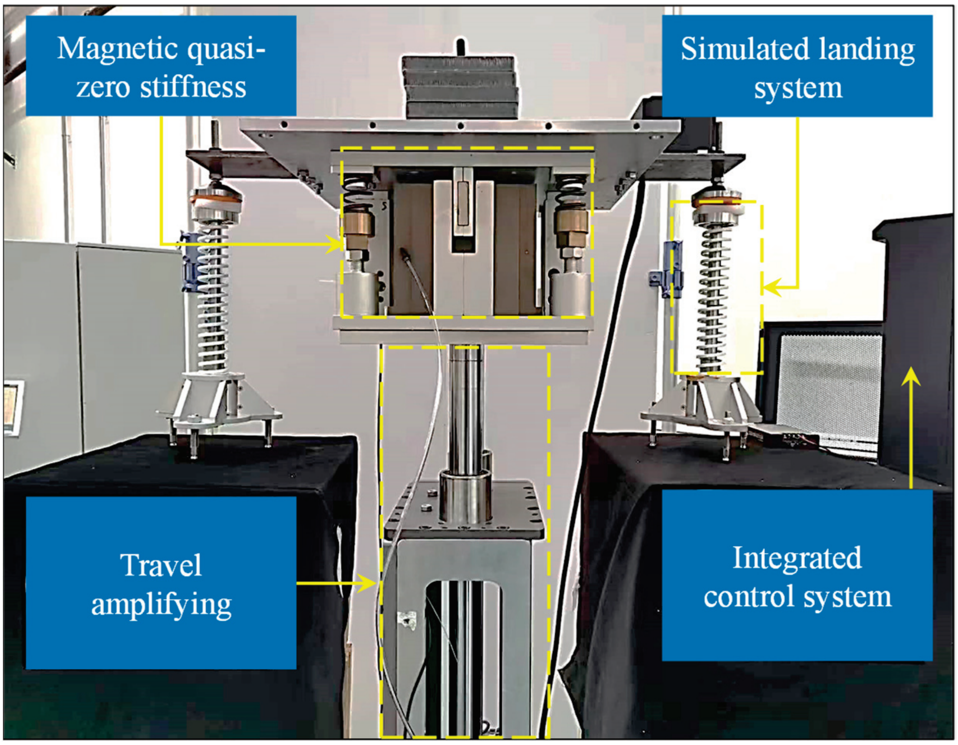

Figure 8. Prototype of landing buffer simulation test system for lunar vehicle.

The stroke amplifying mechanism was mainly composed of a servo motor, a timing belt, a turn screw, and a linear guide rod. The motor SGD7S-550A made by Yaskawa Electric was selected as the severing motor, with detailed parameters shown in Table 2. The transmission ratio of the synchronous belt was 1:1. The maximum vertical movement speed of the stroke amplifying mechanism was 1250 mm/s, and the positioning accuracy and repeated positioning accuracy of the mechanism were better than 1 µm. The grating ruler (VIA-0100, MicroE Systems Co. Ltd., Natick, MA, USA), which has a resolution of 0.1 µm, was utilized to measure the deformation of constant force system. A spring with vertical guidance was installed on the landing surface, which was used to simulate the rebound phenomenon of the lunar vehicle in the landing process.

Table 2. The parameters of the stroke amplifying mechanism.

Parts	Parameters	Value
Servo motor	Power (kW) Torque (Nm) rated speed (rpm)	7.5 48 1500
Turn-screw	Stroke (mm) Lead (mm)	480 50

3.1.2. Integrated Control System

The integrated control system transformed the windows system into a hard real-time system by installing the RTX (Real Time eXecutive) real-time system on the Windows 7 system (32-bit and 2016 version). Among them, a MFC man–machine interface ran on the Windows system, and the servo control program ran on the RTX system in real time. The clock resolution of the RTX can reach 100 nanoseconds, and the minimum timer period can be 1000, 500, 200, and 100 microseconds, thus ensuring the high-speed operation of the servo algorithm. There are four cores in the CPU. When installing the RTX system, two cores were assigned to the RTX system and two cores to windows system. The minimum real-time cycle unit of the RTX system was 10 microseconds. In this study, the running cycle of the RTX system was set to 1 ms, which meets the requirements of the control system. The human–machine interface is shown in Figure 9.

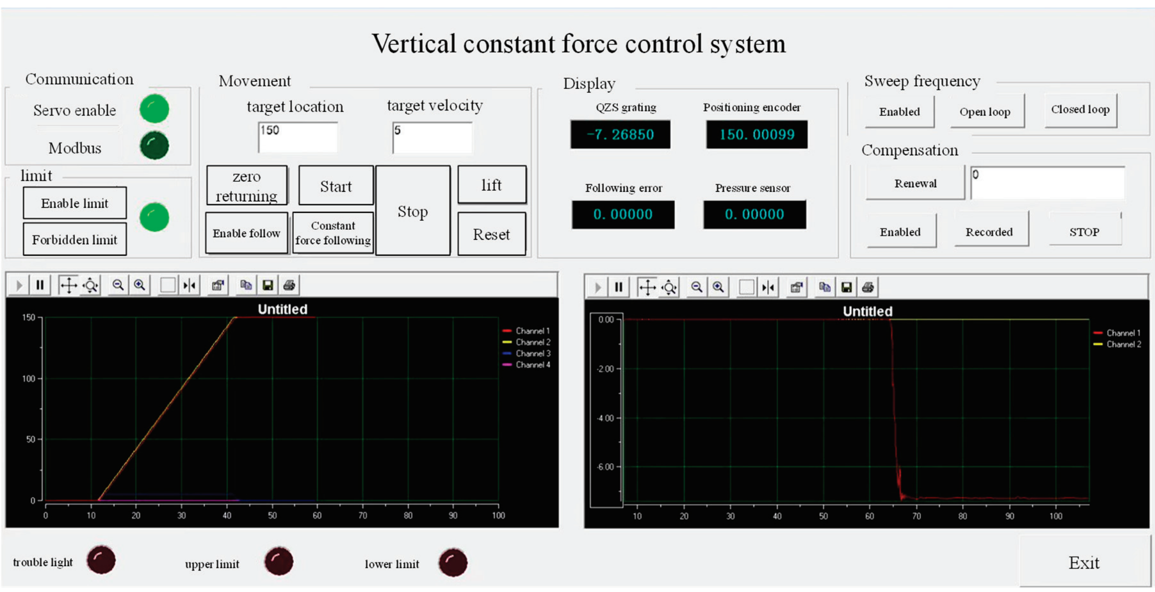

Figure 9. Man–machine interface of M-QZS vertical constant force.

3.2. Test Method

The working conditions of the lunar vehicle landing buffer simulation test in the micro-low-gravity environment are shown in Table 3. The mass of the lunar vehicle was 94.5 kg. The constant force on the test object was provided by a weight to simulate the dynamics of the lunar vehicle in the micro-low-gravity environment. In order to realize the simulation of different acceleration conditions from zero gravity to microgravity, the external force of 0.98~196 N was selected, which can be equivalent to the theoretical gravity acceleration of 0.00106~0.17 g. When the external force was 196 N, the equivalent gravity acceleration was about 1/6 g, which is the working condition of lunar gravity acceleration. The mass of the weights was 0.1 kg, 1 kg, 10 kg, and 20 kg, which simulate the constant force of 0.98 N, 9.8 N, 98 N, and 196 N, respectively. The travel amplifying mechanism was raised to 170 mm from the landing surface, and the system was in a balanced state at this time. The acceleration value was calculated by Formula (14).

$$a_{ve} = \frac{m_e g}{m_{ve} + m_e} \tag{14}$$

where m_e is the mass of the weight.

Table 3. The input parameters of landing buffer test.

Parameters	Value
mass of the weight (kg)	0.1 1 10 20
mass of the lunar vehicle (kg)	94.5
falling height (mm)	170

During the experiment, the integrated control system ran with a servo cycle of 1 ms. The grating with a resolution of 0.001 mm was used to measure the relative displacement difference, which is the input of the control algorithm of the stroke amplification mechanism. The acceleration of the test object landing process was collected in real time through the high-precision inertial navigation unit, the model of which was IMU330A, which had an acceleration resolution of 0.07 mg. The displacement of the stroke amplification mechanism during the whole falling process was measured through the rotary encoder provided by the servo motor, which had a displacement measurement resolution of 0.006 mm.

4. Results and Discussion

4.1. Simulation Results

Figure 10 shows the simulation results based om the working conditions in Table 1. It can be seen from Figure 10a,b that, during the falling process, the simulated load was uniformly accelerated, and the displacement curve was parabolic. As can be seen from Figure 10c, the deformation displacement Δx was 0.06 mm in the falling process. According to Equation (12), the constant force deviation was 0.04 N, as is shown in Figure 10d. The constant force accuracy was 0.04% in the uniform acceleration stage and 0.08% in the collision landing stage, which shows that the control strategy could achieve high constant force accuracy in the simulation stage and meet the requirements of subsequent tests.

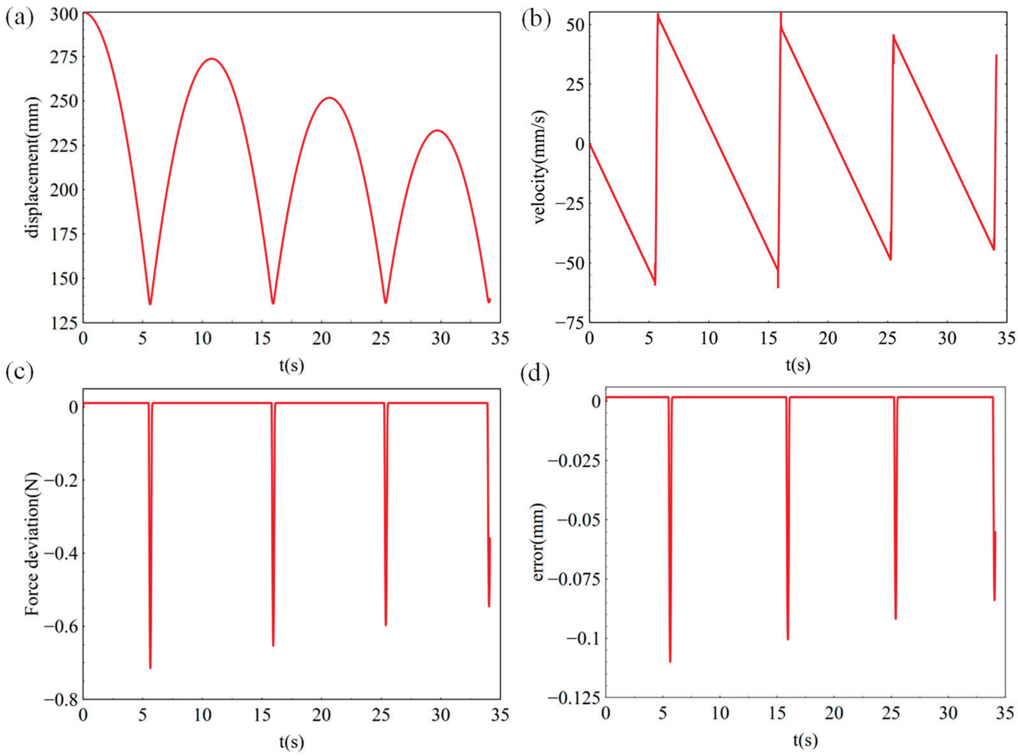

Figure 10. Simulation results of the landing buffer tests with input force of 0.98 N. (**a**) re-displacement curve, (**b**) velocity curve, (**c**) force deviation, (**d**) following error.

4.2. Experimental Results

Figures 11–13 show the results of the landing buffer test with 0.98 N, 9.8 N, 98 N, and 196 N equivalent external force, respectively. It can be seen obviously from the displacement and velocity curve in Figure 11 that the simulation object moved smoothly in different external force. Within a few tens of seconds, the simulator repeatedly rebounded to the ground. In the fall time of 20~60 s, the simulator bounced off the ground several times under different external forces. From the test results of the acceleration curve in Figure 13d, it can be seen that the acceleration of the simulator was about 0.17 g in a steady state when it fell, which is the exact equivalent of the gravity acceleration in lunar conditions. The test system reproduced the phenomenon that the lunar vehicle bounces when it falls in the micro-low-gravity simulation environment.

As is shown in Figure 12a–d, the max velocity of the simulation object was 57.37 mm/s, 152.53 mm/s, 551.67 mm/s, and 647.81 mm/s with 0.98 N, 9.8 N, 98 N, and 196 N equivalent external force, respectively. With the increase in the weight, the speed and acceleration of the test object increased. Figure 13a–d show the acceleration results of the test object with different equivalent external forces. It can be seen that the acceleration curve fluctuated in a small range around the theoretical acceleration value of the experimental object, which is a blue dotted line in the figure, during the falling process.

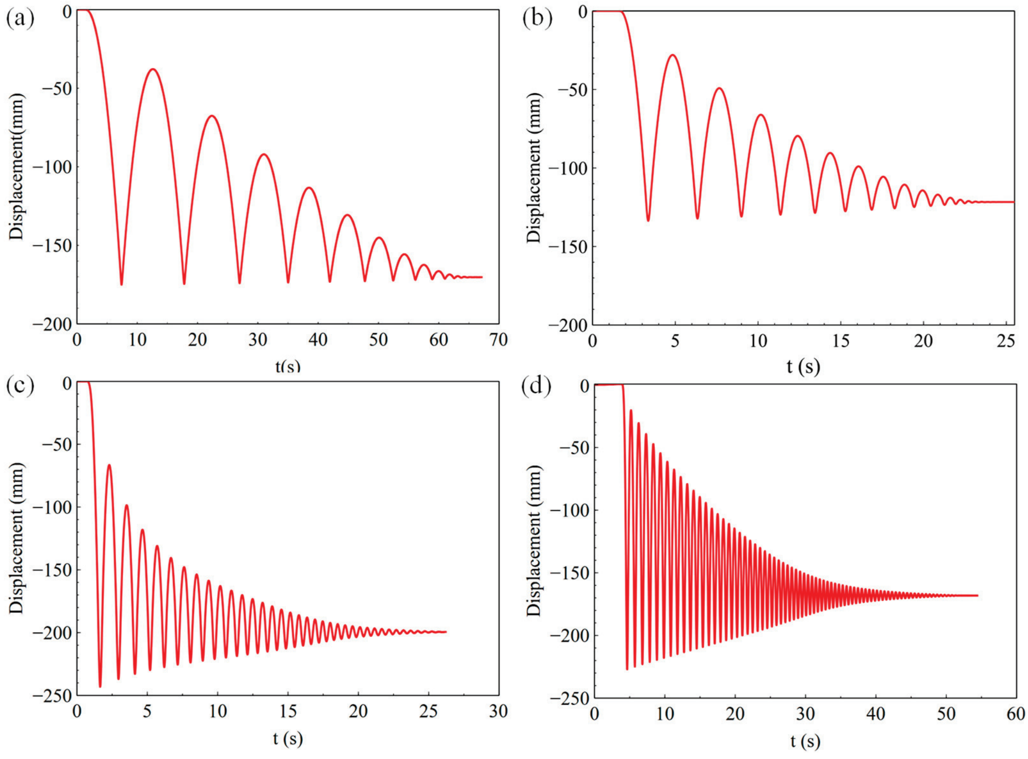

Figure 11. Displacement of the landing buffer tests with external force of (**a**) 0.98 N, (**b**) 9.8 N, (**c**) 98 N, (**d**) 196 N.

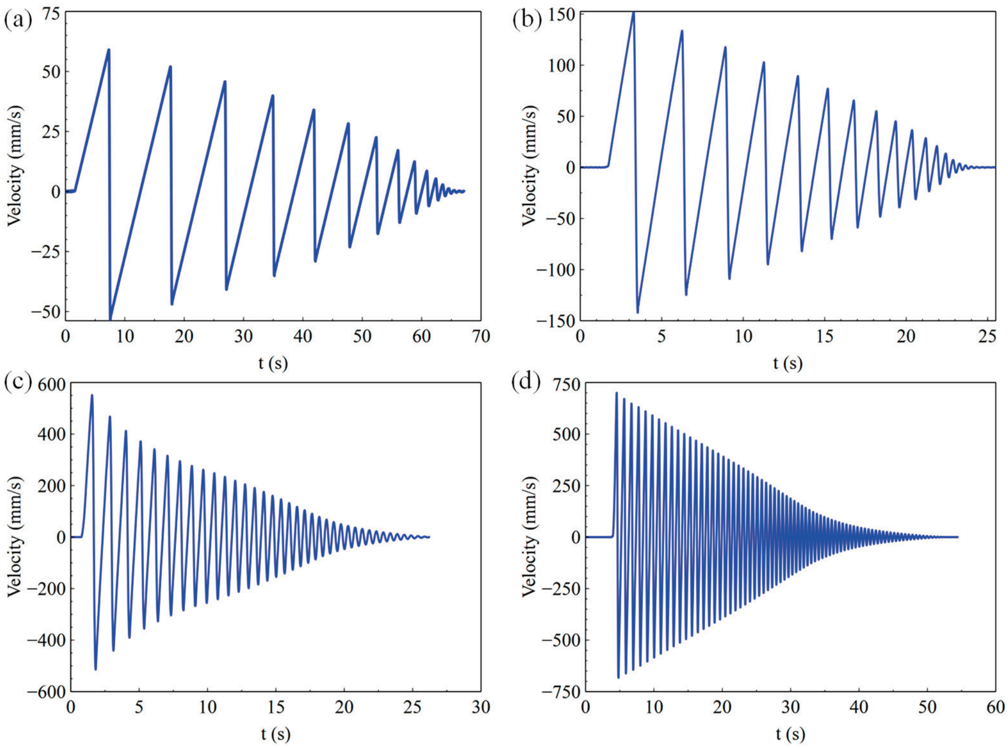

Figure 12. Velocity of the landing buffer tests with external force of (**a**) 0.98 N, (**b**) 9.8 N, (**c**) 96 N, (**d**) 196 N.

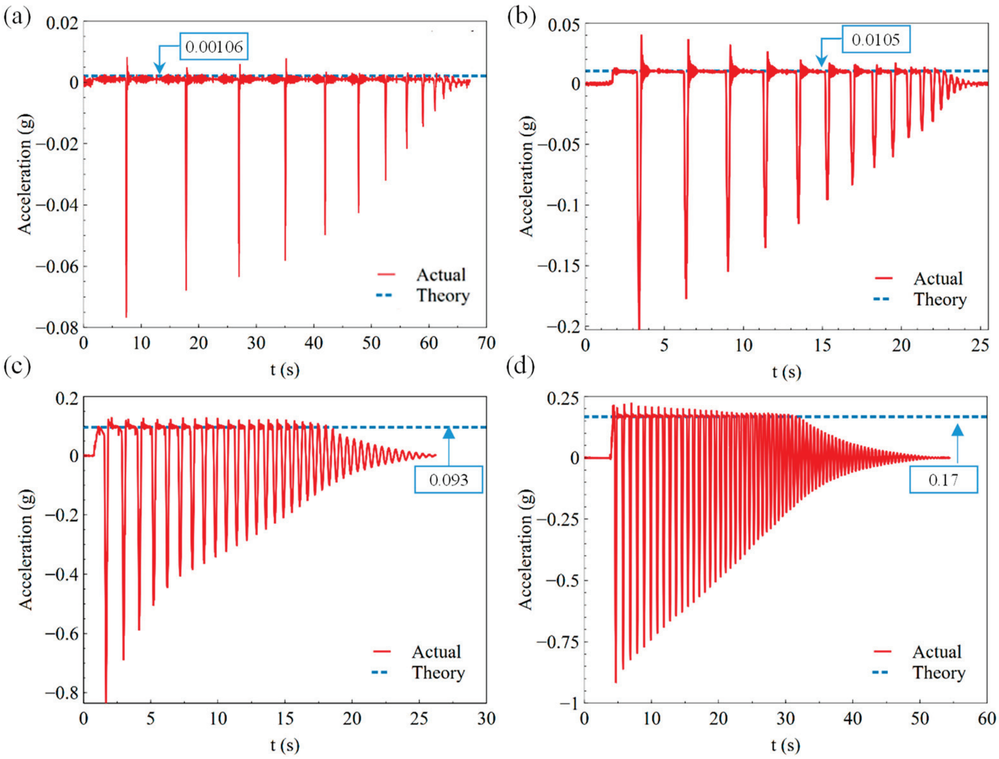

Figure 13. Acceleration of the landing buffer tests with external force of (**a**) 0.98 N, (**b**) 9.8 N, (**c**) 96 N, (**d**) 196 N.

4.3. Discussion

The key parameter pairs of simulation and test are shown in Table 4. As can be seen from the simulation and test results, the coincidence degree between the falling acceleration and the maximum speed parameter of the simulation and the test was more than 90%. The coincidence degree of the first rebound period of the simulation and the test was 98.2%, and the coincidence degree of the first rebound peak was 99%, which well represents the consistency between the simulation and the test. It can be shown that the simulation system could accurately verify the accuracy of the control model.

Table 4. Comparison of simulation and test results with external force of 0.98 N.

Falling Parameters	Simulation	Experimental
Acceleration (g)	0.001058	0.00106 ± 0.001
Max velocity (mm/s)	58.504	59.37
First rebound period (s)	10.59	10.39
First rebound amplitude (mm)	264.73	262.15

In order to further analyze the constant force accuracy of the vertical constant force support system under different equivalent external forces, the constant force deviation curve under four working conditions was compared, as is shown in Figure 14. For the test object of 956 N, the system could accurately identify the external force of 0.98 N, and the constant force deviation was only 0.04 N. With the equivalent lunar gravity acceleration, that is, the external force was 196 N, the constant force deviation was 1.9 N. The constant force error was less than 0.1%. These results proved that the gravity compensation method based on magnetic quasi-zero stiffness and the designed prototype was very sensitive to small forces. Compared with the unloading accuracy of the traditional mechanical constant system and cylinder constant force system, the unloading accuracy of the M-QZS constant force system reached 0.1%, which is higher than the mechanical constant force unloading accuracy of 0.5% [24,25] and the cylinder constant force unloading accuracy of 0.2% [26].

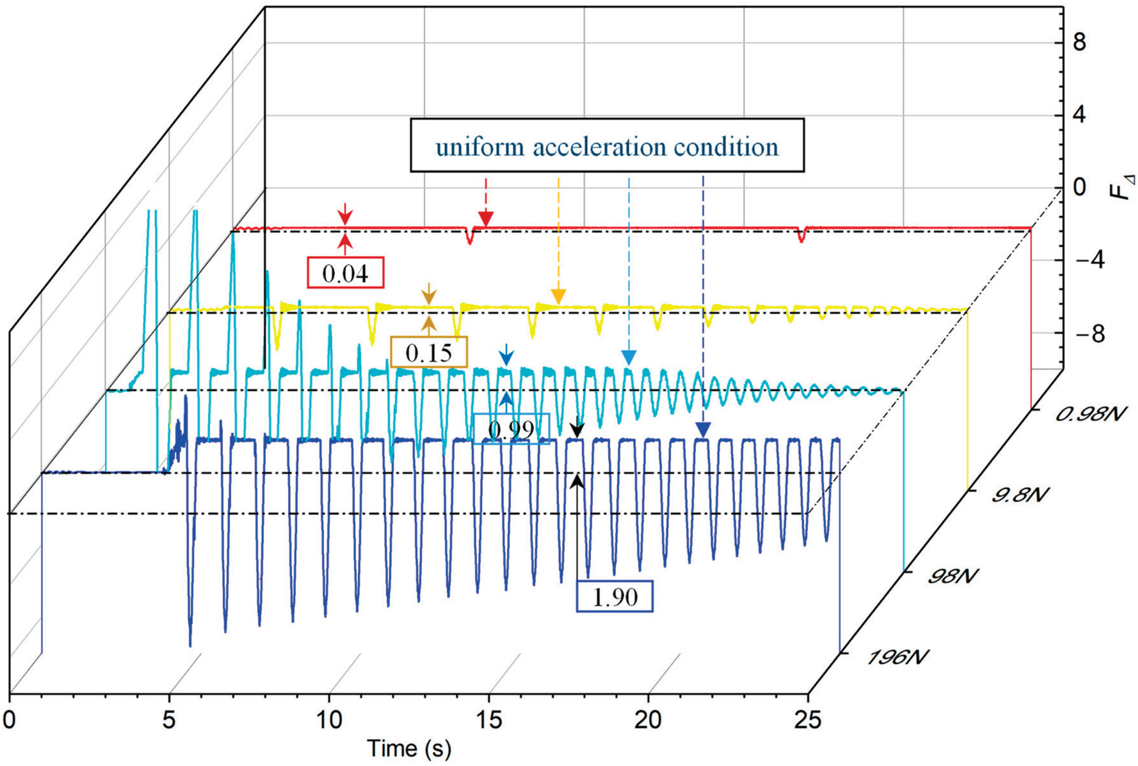

Figure 14. Constant force deviation of the landing buffer tests with external force of 0.98 N, 9.8 N, 96 N, 196 N.

What's more, it can be also found that, with the increase in external force, the deviation of constant force increased slightly. The main reason is that the deformation of the M-QZS system and the dynamic response speed increased with the increase in external force. Therefore, it is necessary to further improve the response accuracy of the servo following system under heavy load. The experiment of this study was carried out in normal temperature and atmospheric environment, and the influence of wind resistance was ignored. For future spacecraft with large volumes and high dynamic motion, it is also necessary to consider the unloading behavior under vacuum conditions when the air resistance is difficult to ignore.

5. Conclusions

In this paper, a high-dynamic and long-range constant force supporting system based on magnetic quasi-zero stiffness for lunar vehicles was designed. The results include the following:

1. The non-contact/frictionless M-QZS mechanism was combined with the stroke amplification structure, which realized high-precision and high-dynamic constant force maintenance in the vertical direction. It provided a new method for the micro-low-gravity simulation test of lunar vehicles on the ground.
2. A position control method based on fuzzy PID parameter tuning was proposed, and the dynamic characteristics of the system were simulated and analyzed using joint simulation technology, which verified the feasibility and accuracy of the control model.
3. The prototype of the micro-low-gravity simulation test system for the lunar vehicle was built, and landing buffer tests under different external forces were carried out. The results show that the system had good stability and high accuracy under different external loads. The force sensitivity was better than 0.1%, and the constant force error was less than 0.1%. The test object bounced up many times during the landing buffer test, which successfully reproduced the phenomenon of the lunar vehicle touchdown rebound during landing in a slight micro-low-gravity environment.

4. Later, the research on vertical adaptive adjustment during horizontal movement of the lunar vehicle will be carried out. The performance of the test system to maintain vertical constant force accuracy will be further verified when the lunar vehicle walks on the undulating road surface in the next step.

Author Contributions: Conceptualization, L.Z. and W.H.; methodology, H.W. and C.W.; software, C.W.; validation, C.W., G.L. and L.C.; formal analysis, W.H.; investigation, L.Z.; resources, Y.H.; data curation, C.W.; writing—original draft preparation, H.W.; writing—review and editing, L.Z.; visualization, Q.W.; supervision, B.Z. and K.F.; project administration, L.Z. and Y.H.; funding acquisition, S.X. All authors have read and agreed to the published version of the manuscript.

Funding: This research was funded by the China Aerospace Science and Technology Corporation Application Innovation Plan, grant number 6230114002.

Institutional Review Board Statement: Not applicable.

Informed Consent Statement: Not applicable.

Data Availability Statement: Not applicable.

Conflicts of Interest: The authors declare no conflict of interest.

References

1. Lund, T. Lunar roving vehicle and exploration of the moon. In *Early Exploration of the Moon: Ranger to Apollo, Luna to Lunniy Korabl*; Springer: Berlin/Heidelberg, Germany, 2018; pp. 303–324.
2. Wysor, R. Preliminary design study of a lunar gravity simulator. In Proceedings of the National Symposium on Saturn V/Apollo and Beyond, Huntsville, AL, USA, 11–14 June 1967.
3. Hirt, C.; Kuhn, M. Convergence and divergence in spherical harmonic series of the gravitational field generated by high-resolution planetary topography-A case study for the Moon. *J. Geophys. Res. Planets* **2017**, *122*, 1727–1746. [CrossRef]
4. Liu, Z. *Single-Cable Gravity Compensation for Planetary Rovers and Experimental Researches*; Harbin Institute of Technology: Harbin, China, 2013.
5. Silva, A.F.B.; Santos, A.V.; Meggiolaro, M.A.; Neto, M.S. A rough terrain traction control technique for all-wheel-drive mobile robots. *J. Braz. Soc. Mech. Sci. Eng.* **2010**, *32*, 489–501. [CrossRef]
6. Han, O.; Kienholz, D.; Janzen, P.; Kidney, S. Gravity-off-loading system for large-displacement ground testing of spacecraft mechanisms. In Proceedings of the 40th Aerospace Mechanisms Symposium, Mountain View, CA, USA, 12 May 2010.
7. Kemurdjian, A.; Khakhanov, U. Development of simulation means for a gravity forces. In *Robotics 2000*; American Society Civil Engineers: Virginia, VA, USA, 2000; pp. 220–225.
8. Liu, Z.; Gao, H.; Deng, Z. Design of the Low Gravity Simulation System for Planetary Rovers. *Robot* **2013**, *35*, 750–756. [CrossRef]
9. Li, S.; Jiang, X.; Tao, T. Guidance summary and assessment of the Chang'e-3 powered descent and landing. *J. Spacecr. Rocket.* **2016**, *53*, 258–277. [CrossRef]
10. Sun, Z.Z.; Zhang, H.; Jia, Y.; Xueying, W.U.; Shen, Z.R.; Ren, D.P.; Dang, Z.L.; Wang, C.; Zheng, G.U.; Chen, B.C. Ground validation technologies for Chang'E-3 lunar spacecraft. *Sci. Sin.* **2014**, *44*, 369.
11. Hockman, B.J.; Frick, A.; Reid, R.G.; Nesnas, I.A.; Pavone, M. Design, control, and experimentation of internally-actuated rovers for the exploration of low-gravity planetary bodies. *J. Field Robot.* **2017**, *34*, 5–24. [CrossRef]
12. Ren, D.; Li, J.; Zhang, Z.; Du, Y.; Huang, H.; Shu, Y.; Peng, J.; Ruan, J.; Zhang, W.; Zhang, G. Ground-test validation technologies for Chang'e-5 lunar probe. *Sci. Sin. Technol.* **2021**, *51*, 778–787. [CrossRef]
13. Guo, L.; Wang, X.; Fan, R.L.; Bi, F. Review on Development of High-Static–Low-Dynamic-Stiffness Seat Cushion Mattress for Vibration Control of Seating Suspension System. *Appl. Sci.* **2020**, *10*, 2887. [CrossRef]
14. Carrella, A.; Brennan, M.; Waters, T. Static analysis of a passive vibration isolator with quasi-zero-stiffness characteristic. *J. Sound Vib.* **2007**, *301*, 678–689. [CrossRef]
15. Tang, R.; Huang, H.; Huang, Z. Design and experiment of a suspension device based on quasi-zero-stiffness technology for microgravity simulation. *Spacecarft Environ. Eng.* **2017**, *34*, 222–228.
16. Niu, F.; Liu, Z.; Gao, H.; Yu, H.; Li, N.; Deng, Z. An enhanced cascade constant-force system based on an improved low-stiffness mechanism. *Mech. Mach. Theory* **2022**, *167*, 104544. [CrossRef]
17. Zang, L.; Zhong, Q.; Chen, Y.; Hou, W.; Zhao, B.; Wu, Y. Effect of coating thickness on tribological properties of manganese phosphate conversion coating in different motion conditions. *Tribol. Int.* **2022**, *176*, 107894. [CrossRef]
18. Zhou, R.; Zhou, Y.; Chen, X.; Hou, W.; Wang, C.; Wang, H.; Jiang, W. Gravity compensation method via magnetic quasi-zero stiffness combined with a quasi-zero deformation control strategy. *Sci. China Technol. Sci.* **2022**, *65*, 1738–1748. [CrossRef]
19. Robertson, W.S.; Kidner, M.; Cazzolato, B.S.; Zander, A.C. Theoretical design parameters for a quasi-zero stiffness magnetic spring for vibration isolation. *J. Sound Vib.* **2009**, *326*, 88–103. [CrossRef]

20. Wu, J.; Zeng, L.; Han, B.; Zhou, Y.; Luo, X.; Li, X.; Chen, X.; Jiang, W. Analysis and design of a novel arrayed magnetic spring with high negative stiffness for low-frequency vibration isolation. *Int. J. Mech. Sci.* **2022**, *216*, 106980. [CrossRef]
21. Wu, W.; Chen, X.; Shan, Y. Analysis and experiment of a vibration isolator using a novel magnetic spring with negative stiffness. *J. Sound Vib.* **2014**, *333*, 2958–2970. [CrossRef]
22. Allag, H.; Yonnet, J.-P. 3-D analytical calculation of the torque and force exerted between two cuboidal magnets. *IEEE Trans. Magn.* **2009**, *45*, 3969–3972. [CrossRef]
23. Abushagur, A.A.; Arsad, N.; Reaz, M.I.; Bakar, A.A. Advances in bio-tactile sensors for minimally invasive surgery using the fibre Bragg grating force sensor technique: A survey. *Sensors* **2014**, *14*, 6633–6665. [CrossRef] [PubMed]
24. Valle, P. Reduced gravity testing of robots (and humans) using the active response gravity offload system. In Proceedings of the International Conference on Intelligent Robots and Systems, Vancouver, BC, Canada, 24–28 September 2017.
25. Zhang, H. *Control Method Research Based on Suspended Low-Gravity Environment Simulation*; Harbin Institute of Technology: Harbin, China, 2021.
26. Li, H. *Research of Zero Gravity Multidimensional Unfolding Test Apparatus*; Zhejiang University of Technology: Hangzhou, China, 2015.

batteries

MDPI

Article

An Optimized Random Forest Regression Model for Li-Ion Battery Prognostics and Health Management

Geng Wang [1], Zhiqiang Lyu [2] and Xiaoyu Li [3,*]

1 State Key Laboratory of Structural Analysis, Optimization and CAE Software for Industrial Equipment, Dalian University of Technology, Dalian 116024, China; dlutwg@mail.dlut.edu.cn
2 School of Internet, Anhui University, Hefei 230039, China; lyuzhiqiang@ahu.edu.cn
3 School of Mechanical Engineering, Hebei University of Technology, Tianjin 300130, China
* Correspondence: lixiaoyu@hebut.edu.cn

Abstract: This study proposes an optimized random forest regression model to achieve online battery prognostics and health management. To estimate the battery state of health (SOH), two aging features (AFs) are extracted based on the incremental capacity curve (ICC) to quantify capacity degradation, further analyzed through Pearson's correlation coefficient. To further predict the remaining useful life (RUL), the online AFs are extrapolated to predict the degradation trends through the closed-loop least square method. To capture the underlying relationship between AFs and capacity, a random forest regression model is developed; meanwhile, the hyperparameters are determined using Bayesian optimization (BO) to enhance the learning and generalization ability. The method of co-simulation using MATLAB and LabVIEW is introduced to develop a battery management system (BMS) for online verification of the proposed method. Based on the open-access battery aging datasets, the results for the mean error of estimated SOH is 1.8152% and the predicted RUL is 32 cycles, which is better than some common methods.

Keywords: lithium-ion battery; prognostics and health management; state of health; remaining useful life; random forest regression model; Bayesian optimization

1. Introduction

With the emergence of the energy crisis and environmental pollution, low-emission and fuel-efficient vehicles relying mainly on electric vehicles (EVs) have been widely focused on and applied in recent years [1,2]. The lithium-ion battery has become the predominant battery in EVs, owing to its high energy density and cycle life, low self-discharge performance, and eco-friendliness [3,4]. As a typical electrochemical energy storage device, the side reactions inside batteries result in a decrease in the cell performance after the continuous charging−discharging cycles. Such a decline in batteries in EVs results in range reduction and even safety accidents (https://unece.org/transport/documents/2022/04/standards/un-gtr-no22-vehicle-battery-durability-electrified-vehicles [5] (accessed on 20 May 2023)). Thus, EVs involve prognostics and health management (PHM) to evaluate the battery aging levels [6,7].

Two critical challenges confronted in battery PHM are the estimation of state of health (SOH) and the prediction of remaining useful life (RUL). The definition of SOH is the ratio between the current capacity and rated capacity [8,9], while RUL is the cycle number when SOH reaches the presupposed level [10]. Therefore, the two key parameters can be regarded as the battery aging state from different time-scale perspectives, respectively. The safety and reliability of battery systems can be improved with accurate SOH and RUL. In addition, SOH and RUL are a kind of internal characteristic that cannot directly be measured; therefore, some techniques are employed to evaluate the battery aging state.

1.1. Review of the Methods for SOH

By reviewing the literature, existing techniques can be divided into direct measurement, model-based, and data-driven methods.

1.1.1. Direct Measurement

Direct measurement implies measuring the capacity or resistance to calculate battery SOH. For instance, the coulomb counting method is typically used to measure battery capacity for SOH. However, the coulomb counting method requires a time-consuming charging−discharging process, and deep charging damages the battery lifespan to some extent [11]. Another technology is to measure the internal resistance through special equipment such as internal resistance test devices or electrochemical impedance spectroscopy (EIS) [12]. Direct measurement has the highest accuracy; however, it has limited application scenarios. Therefore, direct measurement is more functional for calibrating things requiring online estimation in electric vehicles.

1.1.2. Model-Based Methods

This type of method monitors battery degradation through a battery model and adaptive filter methods. The electrochemical model (EM) is a type of first-principle model used to describe the battery dynamic performance through some partial differential equations [13,14]. Based on the pseudo-2D and single-particle models, Bi et al. [15] developed a composite model where four sensitive parameters are selected and tracked through the particle filter (PF). Allam et al. [16] established a temperature-dependent single-particle model, and then an adaptive interconnected observer is employed for state estimation and aging-sensitive transport parameter identification. Despite the simplification of the model, EM still has a high computation complexity. Therefore, the equivalent circuit model (ECM) is relatively more popular because of its simple structure and low computational complexity [17]. Using the Thevenin model, Zou et al. [18] fused the capacity variable into the state-space model for state of charge (SOC) estimation, after which the Extended Kalman filter (EKF) is employed to achieve combined SOH and SOC estimation. Furthermore, Lyu et al. [19] developed a linear aging model to illustrate and expand the underlying relationship between the model parameters and battery capacity. ECM is a dynamic model to describe the dynamic performance of batteries on a relatively short time scale; however, it is weak in the description of aging on a long-time scale. Therefore, battery models play a major role in the accuracy and robustness of model-based methods.

1.1.3. Data-Driven Methods

In recent years, machine learning has received widespread attention and application. Data-driven methods utilize machine learning methods such as neural networks, deep learning, and Gaussian process regression to describe battery degradation [20]. Hamar et al. [21] developed a neural network as the comparison of the semi-empirical holistic model based on aging datasets from EVs. Pradyumna et al. [22] used a convolutional neural network (CNN) to train the battery aging model based on the EIS test for accurate capacity estimation. Zhang et al. [23] developed a novel deep-learning approach for lithium-ion batteries. Pan et al. [24] extracted the health indicators from the smoothed incremental capacity curve (ICC); furthermore, an improved GPR is applied to estimate battery capacity. Wu et al. [25] selected aging features (AFs) from the multi-source charging data, and a GA-based support vector regression is utilized for SOH estimation. The data-driven methods are a type of model-free method to achieve online SOH estimation. As a result, great sample data are necessary to train a “black box” with excellent nonlinear mapping and generalization ability.

1.2. Review of the Methods for RUL

Compared with SOH estimation, RUL cannot be measured using one or a few tests directly. Thus, the methods for RUL prediction can only be categorized into two groups: model-based and data-driven methods.

1.2.1. Model-Based Methods

The model tends to be an empirical model in RUL prediction, such as an exponential model, instead of a dynamic model. For instance, Zhang et al. [11] developed a double-exponential model to predict RUL by tracking and extrapolating battery capacity degradation through PF. Based on the same exponential model, Duong et al. [26] introduced the Heuristic Kalman algorithm to address the sample degeneracy of PF for RUL prediction. Wei et al. [27] established a support-vector-regression (SVR)-based aging model based on a lumped parameter battery model; furthermore, PF is used to predict the capacity degradation. Downey et al. [28] proposed a half-cell model for degradation parameter extraction and fitted a mathematical model to predict RUL. Liu et al. [29] used the parameters of a simplified electrochemical model (SEM) as the state variables, and then PF is used to achieve high-quality capacity extrapolation. Denoising and tracking are two advantages of model-based RUL prediction; however, the empirical model cannot acclimatize to different application scenarios.

1.2.2. Data-Driven Methods

Data-driven methods are used to predict RUL through some machine learning methods [30]. Afshari et al. [31] defined 19 features using the differential voltage and differential capacity curves, and sparse Bayesian learning is employed for early RUL prediction. Feng et al. [32] fitted the surface temperature in a specified time range through an exponential model, and the change rate for the temperature is the AFs for predictive modelling of capacity through the relevance vector machine (RVM). Relative to a single machine learning method, some hybrid methods have been developed to assimilate the strong points of different methods for better learning ability. Using AFs from the charging process, Yao et al. [33] established an RVM model to depict the correlation between AFs and capacity, followed by constructing an extreme learning machine (ELM) for predicting battery capacity based on AFs. Meanwhile, the parameters of ELM and RVM are optimized by particle swarm optimization (PSO). With adequate historical battery data, data-driven methods offer an excellent solution to predict RUL.

1.3. Contribution of the Paper

According to the anterior analysis, SOH estimation and RUL prediction require an accurate and robust battery aging model to quantify battery degradation. Either way, to establish such a battery aging model, some issues need to be addressed: (1) how to link up the online measurement information with the battery aging effectively and (2) how to extrapolate the trend of battery aging using measurable information.

In this study, to solve the difficult problems for online SOH estimation and RUL prediction, the contribution rests on three areas: (1) two online AFs are extracted to quantify the battery capacity based on the partial charging process; (2) combined with the counted cycle and linear regression, a close-loop framework to extrapolate the AFs is established; (3) an optimized random forest (RF) regression model is developed to capture the underlying mapping relationship between the AFs and capacity, then online SOH estimation and RUL prediction are achieved.

2. Aging Features for SOH and RUL

Battery SOH and RUL are two main indicators that reflect the battery aging level from the perspective of capacity and cycle, respectively, as follows:

$$\begin{cases} \text{SOH} = \frac{C_i}{C} \times 100\% \\ \text{RUL} = Cycle_{\text{total}} - Cycle_i \end{cases} \tag{1}$$

where the numerator and denominator C represent the current and rated capacity, respectively. *Cycle* represents the number of cycles, and the subscript i and total represent the ith cycle and the total cycles, respectively. A full charging−discharging process is defined as a cycle. The failure threshold is set as 80% of the rated capacity.

2.1. Battery Aging Datasets and Aging Features

The open-access datasets provided by the Center for Advanced Life Cycle Engineering (CALCE) were utilized. In the selected datasets, four prismatic battery cells (labeled CS 35, 36, 37, and 38) with a rated capacity of 1.1 Ah were tested. The detailed description of the testing can be found in [34]. It should be noted that the four batteries were tested with the same conditions; however, the final performances were different owing to the inevitable inconsistency.

In [35], incremental capacity analysis (ICA) has been proven to be an effective technology to investigate battery aging. Under a constant-current charging state, the voltage plateau can be transformed into a recognizable peak in the incremental capacity curve (ICC) according to Equation (1).

$$ICC = \frac{dQ}{dV} = I \times \frac{dt}{dV} = I \times 1\frac{dV}{dt} \tag{2}$$

where Q is the charging capacity, which is the time t integral of current I. V is the terminal voltage. Therefore, ICC can be further obtained based on the online measuring information.

According to the current research [34,35], the voltage range of 3.8–4.2 V is an important range to evaluate battery degradation. Herein, 3.8–4.1 V is selected to calculate the ICC for further battery aging assessment. However, the sampling noise inevitably has a significant influence on the differential calculation. LOWESS is a non-parametric regression technique that uses a weighted average of nearby data points to estimate a smooth curve. It is particularly useful when dealing with noisy or non-linear data, as it can capture complex relationships between variables. Therefore, the LOWESS method was employed to smooth the noised ICC to eliminate or reduce threats of noise through the sliding window mechanism and linear least squares. Meanwhile, the Gaussian smoothing and movmean smoothing were used as the control groups to evaluate the smoothing performance. The smoothing results are shown in Figure 1.

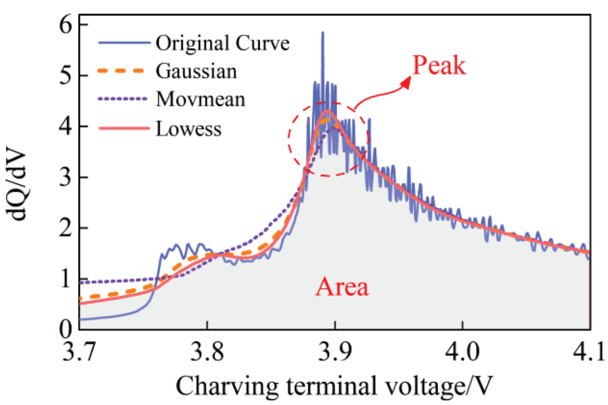

Figure 1. The smoothing results of ICC.

As shown in Figure 1, the smoothed ICC by LOWESS can identify the profile of ICC relative to the original ICC, including the peak of the incremental capacity curve (PICC) and the area under the ICC (named charged capacity of equal voltage (CCEV)). In contrast, Gaussian smoothing and movmean smoothing methods are both linear filters that smooth out fluctuations in the data by averaging the nearby values. While they are useful for removing noise and identifying trends, they may not accurately capture the underlying relationships between variables. Therefore, LOWESS can achieve high fidelity denoising of the noised ICC.

Furthermore, the ageing data of battery CS 38 were utilized to illustrate the evolutions of ICCs, as shown in Figure 2, the smoothed ICC by LOWESS can identify the profile of ICC relative to the original IC. The results indicate that ICCs exhibit a downward drift with an increase in the number of cycles. The PICC in the ICC possesses unique features in terms of shape, intensity, and position, providing insights into the electrochemical process in LIBs. Previous literature suggests that the degradation of PICC observed in the charging data may be attributed to the loss of active materials. As the cycle increases, the active materials become unavailable for lithium insertion, leading to internal changes that significantly impact the PICC. Additionally, such degradation mechanisms increase the battery resistance. Overall, ICCs serve as an effective means to describe battery capacity degradation during ageing. Therefore, the PICC and CCEV of the ICC can be extracted as AFs to evaluate the battery aging level.

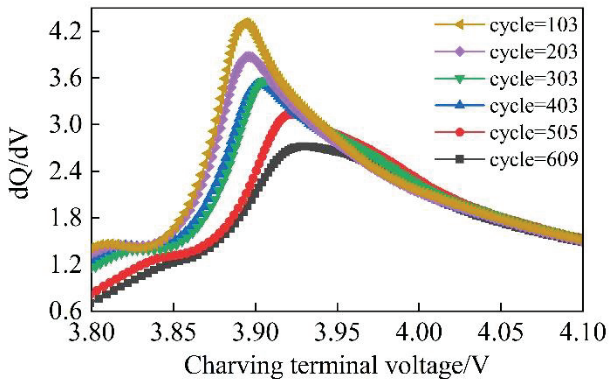

Figure 2. The smoothing results of ICC.

The Pearson's correlation coefficients R_p between the AFs and capacity are calculated by Pearson correlation analysis according to Equation (2), to evaluate the effectiveness of extracted Afs, and the results are shown Figure 3.

$$R_\mathrm{p} = \frac{\sum (X - \overline{X})(Y - \overline{Y})}{\sqrt{\sum (X - \overline{X})^2}\sqrt{\sum (Y - \overline{Y})^2}} \tag{3}$$

where $\overline{X}$ and $\overline{Y}$ are the mean values of the AFs X and Y capacity, respectively.

Based on Figure 3, it is significant for AFS to describe battery capacity degradation. Typically, a coefficient greater than 0.8 is considered strong, while a coefficient less than 0.5 is regarded as weak. In this case, the minimum value of R_p obtained is 0.9604, indicating a strong correlation between the AFs and capacity degradation. Moreover, most of the R_p values are approximately 0.98, further reinforcing the existence of a strong correlation between these variables. Additionally, the high correlation coefficients (>0.98) obtained between the ageing features suggest a strong coupling relationship between them. These results provide valuable insights into the understanding of battery ageing mechanisms and could have implications for the development of effective battery management strategies. Based on the ICC-based AFs, SOH estimation can be further carried out.

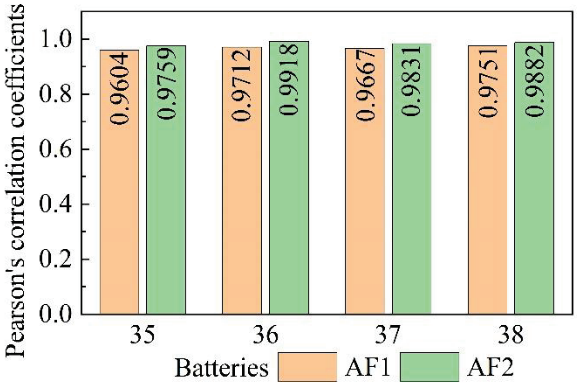

Figure 3. The smoothing results of ICC.

2.2. The Extrapolation of the Aging Features

For RUL prediction, the future aging trends need to be extrapolated standing on the historical measurable or estimated information. The modelling based on estimated information would introduce the predicted errors again, which leads to an inaccurate prediction of RUL. Herein, we try to model the measure AFs for extrapolation and RUL prediction.

The two AFs can be regarded as the monotone series, respectively; meanwhile, the cycle can be regarded as the time series. Thus, the monotonicity of AFs can be utilized to model and predict the growing trend. For this purpose, Pearson's correlation coefficients are used to evaluate the relationship between the AFs and the cycle, and the results are illustrated in Figure 4.

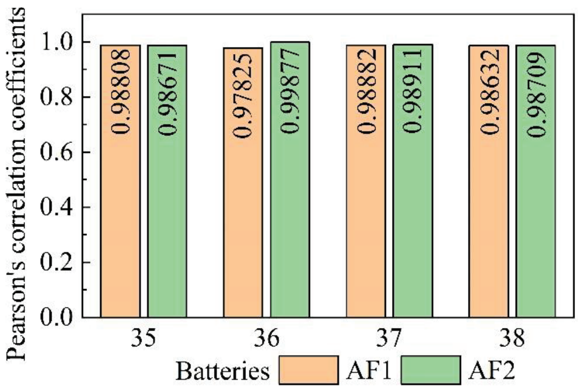

Figure 4. Pearson's correlation coefficients.

Pearson's correlation coefficient is a statistical measure that can quantify the degree of correlation between variables. The coefficients range from −1 to +1, and a greater coefficient implies a stronger correlation while the sign ± indicates the positive and negative correlation [36]. As shown in Figure 4, the coefficients are greater than 0.97. Such results suggest that there are strong linear relationships between the two AFs and cycles. In other words, linear fitting can be employed to model the trends between the AFs and cycle:

$$\begin{cases} PICC_i = f(cycle_i) \\ CCEV_i = g(cycle_i) \end{cases} \tag{4}$$

where f and g represent the two independent linear mappings. Herein, the least square method is utilized to determine the linear mapping based on the known data. However, the amount of online data increase gradually with battery age. The latest data need to be incorporated with the known data to establish linear mapping. Therefore, the mechanism of metabolism is introduced. The process of remodeling for AFs is shown in Figure 5:

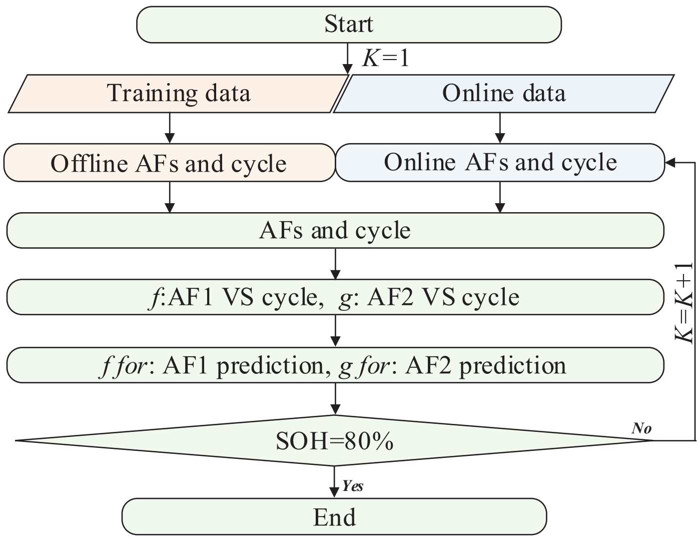

Figure 5. The modelling of metabolism.

As shown in Figure 5, the modelling can be implemented as follows:

(1) Based on the offline training data, the AFs and cycle are extracted as the dependent variable and independent variable, respectively. Then, the least square method is employed to model the relationships between cycle and AFs; furthermore, the parameterized mapping f and g are obtained.

(2) For a new battery, the cycle is defined as a sequence of real numbers that starts at 1. Then, the defined cycle is fed into the parameterized mapping f and g, the outputs of f and g are the two predicted AFs.

(3) When the battery is used, the measurable AFs and cycles are obtained. Combining the measurable data with the offline training data based on the metabolism, the new data are established. Then, the new data are employed to parameterize the f, g. With the continuous charging and discharging of the battery, the measurable AFs and cycles are used to reconstruct the modelling data continually.

Based on the predicted AFs, the further trend of battery degradation can be captured for RUL prediction.

3. Methodologies

As mentioned previously, AFs can be utilized to evaluate the current aging state and predict future degradation trends. How to establish a model for capturing the underlying relationship between AFs and capacity is an important factor in SOH estimation and RUL prediction. Herein, RF is employed to deal with this dilemma.

3.1. Random Forest Regression Optimization Model

RF is a typical bagging-based ensemble learning method that combines multiple randomized decision trees and averages their outputs [37]. Through resampling the original data using the Bootstrap sampling method, a new training set is constructed to build a classification tree or regression tree for each new sample set using the CART method, as well as to provide the final prediction results according to the results of all of the decision trees. Compared with other machine learning algorithms, such as back propagation neural networks (BPNN) and SVR, RF exhibit superior scalability in processing large-scale high-dimensional data with fewer optimization parameters. Additionally, RF's built-in estimation methods enhance the generalization ability of the prediction models, making it a more advantageous approach in machine learning. A schematic representation of the RF is depicted in Figure 6.

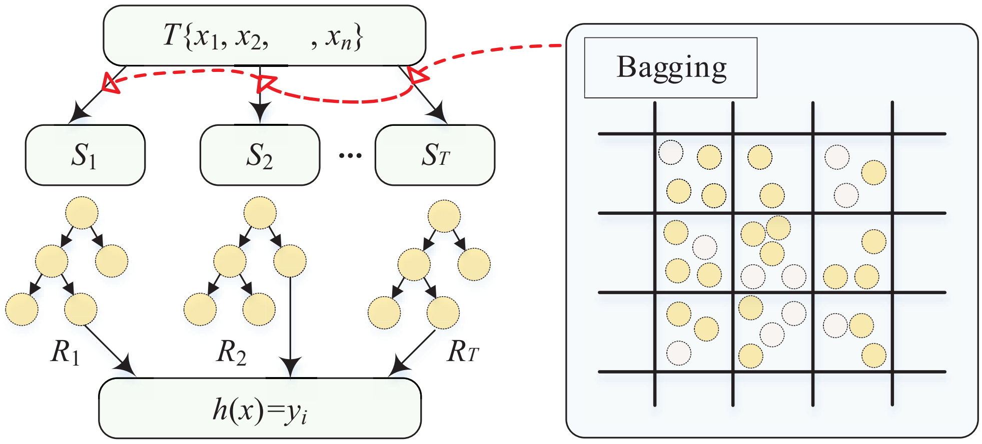

Figure 6. The schematic diagram of the RF.

As shown in Figure 6, the implementation steps of planning for RF are as follows:

(1) Bootstrap is employed to resample the origin data, and then T sample sets for training are obtained and labeled $\{S_1, S_1, \cdots S_T\}$.

(2) The newly resampled training set is utilized to build the corresponding regression tree model $R_1, R_1, \cdots R_T$. Prior to attribute selection for each internal node, T attributes are randomly sampled from M attributes, and the optimal splitting method among these attributes is employed to partition each node. The CART algorithm is utilized as the splitting method. It should be noted that, unlike the decision tree algorithm, there is no need to prune the CART. Finally, an RF model $y = h(x)$ is determined.

(3) For unknown test samples, each regression tree can be used to calculate, and the corresponding predicted value of each regression tree can be obtained $\{R_1(X), R_1(X), \cdots R_T(X)\}$.

(4) The predicted values obtained from each individual regression tree are averaged and utilized as the final prediction outcome of the random forest model.

The new training set will not encompass all the data from the original training set because of Bootstrap. The excluded dataset is referred to as an out-of-bag (*OOB*) sample. Usually, a selection of two-thirds of the original training set samples is utilized to construct the regression function. The remaining data constitute the *OOB* sample, which is the new test set. The remaining data from the *OOB* sample are the new test set. Each time a regression tree is constructed using the new training set, the performance of the regression tree is evaluated by utilizing the *OOB* sample as a built-in cross-validation process. Thanks to this, the RF algorithm is capable of computing unbiased generalization errors without relying on unbiased estimation of such errors. The algorithm can also calculate unbiased estimates of generalization errors without using external data subsets. In addition, this built-in cross-validation feature enhances the ability to generalize RF algorithms using independent test data. In addition, this built-in cross-validation feature enhances the ability to generalize RF algorithms using independent test data. The error of *OOB* is calculated as follows:

$$\mathrm{MSE} \approx \mathrm{MSE}^{OOB} = \frac{\sum_{i=1}^{s} [\hat{y}(\mathbf{X}_i) - y_i]^2}{s} \tag{5}$$

where $\hat{y}(X_i)$ and $y(X_i)$ are the predicted and true values of X_i, respectively, and s is the number of *OOB* samples.

Two of the most important hyperparameters in RF are necessary to determine the following: (1) The complexity (depth) of the trees in the forest. Deep trees tend to overfit, but shallow trees tend to underfit. (2) When growing the trees, the number of predictors to sample at each node. How to determine the hyperparameters plays a vital role in the prediction accuracy of RF to choose the best model.

3.2. Bayesian Optimization

An optimization algorithm assumes that the objective function is known to obtain the derivative and that the objective function is convex. Nonetheless, for some problems, in the parameter adjustment process, the objective function may not have a convex form, requiring heavy calculations and poor results. To solve such a problem, BO is developed. The core idea of BO is to leverage prior knowledge for approximating the posterior distribution of an unknown objective function, and subsequently selecting the next sampling hyperparameter combination based on this distribution [38]. To approach the objective function as closely as possible, the Bayesian algorithm adopts a proxy model, and the Gaussian process (GP) is often used to establish such a proxy model. With the GP algorithm, prior functions are defined that can be used to incorporate prior information about the objective function (smoothness, for example). BO is composed of two parts: a Bayesian statistical model is employed to represent the objective function, and an acquisition function is utilized to determine where to sample next. After conducting the initial space-filling experiment design, which typically involves selecting points uniformly at random to evaluate the target; these points are then iteratively utilized to allocate the remaining budget for N function evaluations. A typical pseudo-code of BO is shown in Algorithm 1:

Algorithm 1: Bayesian optimization

for n=1, 2, . . . , **do**
select new x_{n+1} by optimizing acquisition function α
$x_{n+1} = \arg\max_{x} \alpha(x; D_n)$
query objective function to obtain y_{n+1}
augment data $D_{n+1} = \{D_n, (x_{n+1}, y_{n+1})\}$
update statistical model
end **for**

Based on BO, two optimal hyperparameters can be obtained; furthermore, an optimized RF can be trained to possess excellent abilities for learning and generalization. Then, the optimized RF can be utilized to capture the underlying correlation between AFs and capacity.

3.3. The Flowchart for SOH and RUL

According to the optimized RF model, a framework is established for estimating battery SOH and predicting RUL, as illustrated in Figure 7.

According to Figure 7, the process of SOH estimation and RUL prediction are described as follows:

(1) Online AFs extraction and prediction: (1) Based on the charging process, the online AFs are extracted to quantify the battery capacity degradation indirectly. Meanwhile, the correlation analysis is implemented to judge the effectiveness. (2) The historical and online AFs are modelled to predict the trends of AFs through extrapolation.

(2) Optimized random forest regression model: (1) According to the offline datasets, the original datasets are divided into a training set and testing set. (2) BO is employed to determine the optimal hyperparameters of RF based on the offline datasets. (3) The optimal hyperparameter is applied to RF, and an optimized RF model is trained.

(3) Model evaluation: (1) The online extracted AFs are fed into the optimized RF model to estimate battery capacity and calculate SOH. (2) The predicted AFs are simultaneously fed into the optimized RF model to predict the battery capacity and RUL.

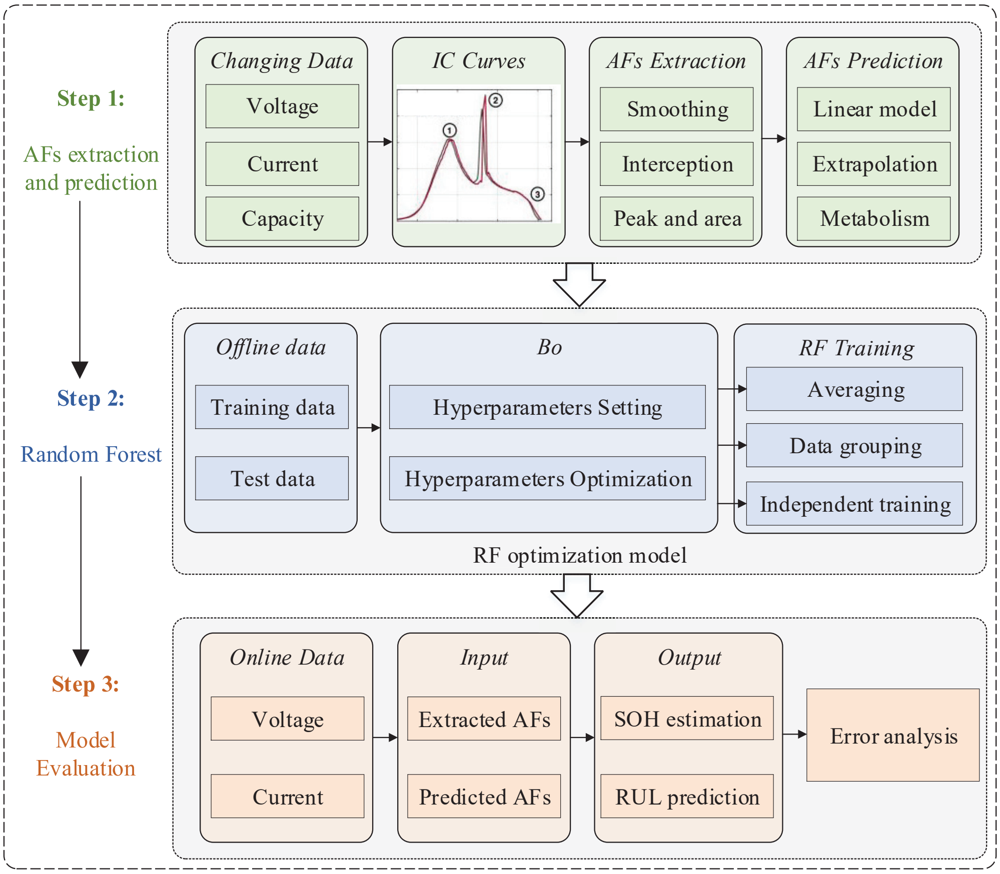

Figure 7. The framework for battery SOH estimation and RUL prediction.

Furthermore, the embedded development of the flowchart for BMS is implemented based on hybrid programming through MATLAB and LabVIEW. MATLAB is regarded as the data processing center, while LabVIEW is used to acquire data and develop the human machine interface (HMI). In other words, MATLAB treats the online measurement information, trains the optimized RF model, and then estimates SOH and predicts RUL. The online information and the output are displayed on HMI by LabVIEW; meanwhile, the results are stored locally along with metadata. The interface of BMS is shown in Figure 8.

In Figure 8, BMS can be implemented through the following steps:

(1) Offline data acquisition: The charging and discharging of the battery are implemented through the Arbin battery test system.

(2) Online AFs extraction and prediction: Based on the online measurements, the online AFs are extracted, and then the future trends of AFs are predicted based on the online measurements and historical AFs.

(3) Online implementation: According to RF and BO, an optimal RF model is trained to capture the correlation between AFs and capacity. Furthermore, the RF model is embedded into LabVIEW for achieving online SOH estimation and RUL prediction based on the extracted AFs and predicted AFs. The results are shown in HMI and saved locally.

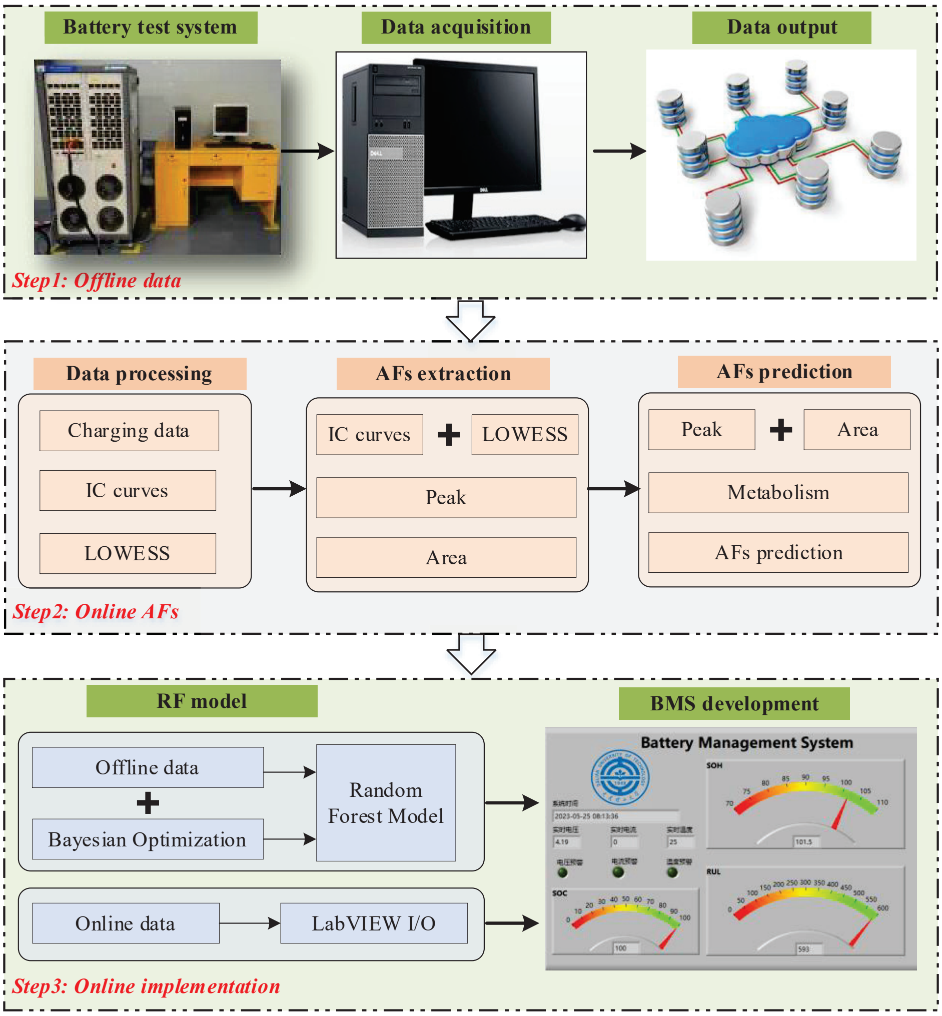

Figure 8. BMS for online battery SOH estimation and RUL prediction.

4. Results and Discussion

For the four batteries, batteries CS 36 and 38 are as the training datasets to obtain the optimized RF model for BMS development, while batteries CS 35 and 37 are as the test datasets for the validation of online SOH estimation and RUL prediction. Based on the developed BMS, the signal collection is implemented through the file I/O interface, and then the stored results of SOH estimation and RUL prediction for BMS are analyzed.

4.1. SOH Estimation

Taking the cycle number as the X axis, the SOH as the left Y axis, and the SOH error as the right Y axis, draw the curves of the measured and estimated SOH, shown in Figure 9, based on the results of SOH estimation.

Furthermore, the estimation error is analyzed from the different error evaluation indicators, encompassing the maximum absolute error (MAE) and root mean square error (RMSE), as illustrated in Equation (6):

$$\begin{cases} MAE = \max(|y - \hat{y}|) \\ RMSE = \sqrt{\frac{1}{n}\Sigma_1^n |y - \hat{y}|^2} \end{cases} \quad (6)$$

where y and $\hat{y}$ are the true and estimated values, respectively; n is the number of the sequence; and i is the index of the sequence.

The result of the statistics is shown in Table 1.

Table 1. Error analysis of SOH estimation.

Index	MAE (%)	RMSE
CS 35	1.0379	0.4185
CS 37	2.5925	1.0976
Mean	1.8152	0.7581

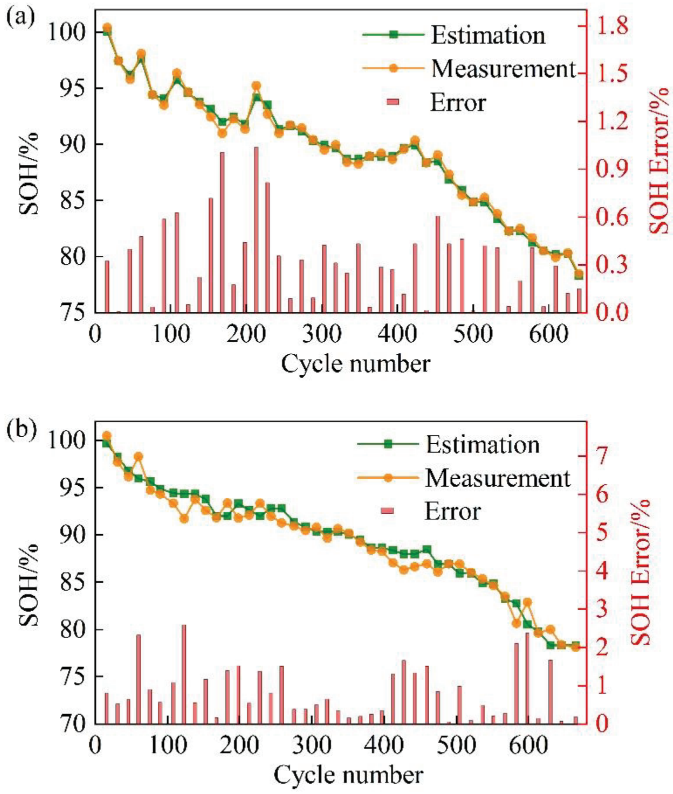

Figure 9. BMS for online battery SOH estimation and SOH prediction: (**a**) CS35 and (**b**) CS37.

Based on Figure 9 and Table 1, the following can be drawn:

(1) As the cycle increases, the battery SOH has a nonlinear decreasing tendency. In addition, the local battery capacity regeneration phenomenon plays a vital role in battery capacity degradation. The phenomenon brings great difficulty to accurate capacity tracking.

(2) The optimized RF model is capable of achieving precise battery SOH estimation. The estimated SOH has a high degree of coincidence with the measured SOH. However, the degree of deviation in the local capacity regeneration stage is greater than in the global degradation stage.

(3) From the perspective of SOH estimation error, the maximum MAE and RMSE for the two batteries are 2.5925 and 1.0976, respectively. In addition, the mean MAE and EMSE are 1.8152 and 0.7581, respectively, the mean MAE and RMSE suggest that the developed BMS can achieve accurate SOH estimation.

4.2. RUL Prediction

Similarly, taking the cycle number as the X axis, the RUL as the left Y axis, and the RUL error as the right Y axis, the curves of the measured and estimated SOH are drawn as shown in Figure 10 based on the results of RUL estimation.

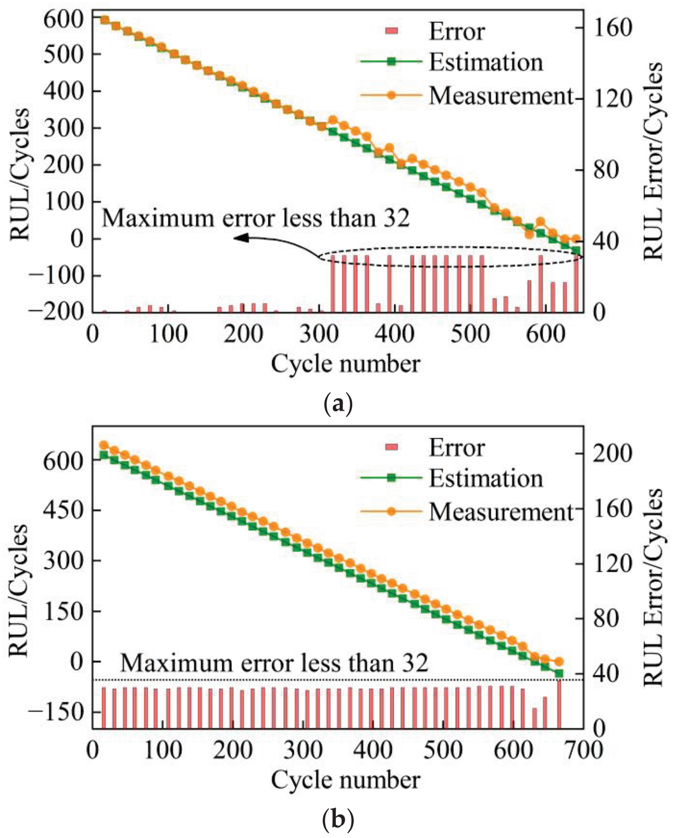

Figure 10. BMS for online battery RUL estimation and RUL prediction: (**a**) CS35 and (**b**) CS37.

Furthermore, the estimation error is analyzed from the different error evaluation indicators, consisting of MAE and RMSE. The results of the statistics are shown in Table 2.

Table 2. Error analysis of RUL prediction.

Index	MAE (Cycle)	RMSE
CS 35	32	20.3961
CS 37	32	29.3198
Mean	32	24.8580

Based on Figure 10 and Table 2, the following can be drawn:

(1) As the cycle increases, RUL continues to gradually decline. Combined with the definition of RUL, there is a significant negative linear correlation between the number of cycles and the measured RUL.

(2) The predicted RUL can track the measured RUL, and the predicted curves vibrate around the true RUL. In addition, the differences between the measured and predicted RUL remain basically unchanged during the full life cycle. According to the predicted RUL, the developed BMS can achieve continuous RUL prediction.

(3) In the whole prediction process, the maximum MAE and RMSE for the two batteries are 32 and 29.3198 cycles. Furthermore, the mean MAE and RMSE are 32 and 24.8580 cycles, respectively. Comparatively speaking, the developed BMS can predict the RUL with a high accuracy continuously.

4.3. Discussion

For providing a fair performance comparison, different methods are implemented for SOH estimation and RUL prediction with the same framework; herein, the traditional BP neural network (BPNN) with a single hidden layer, 20 nodes, and a Sigmoid activation function [39]; SVM with a radial basis kernel function [35]; and RF without optimization are selected. Meanwhile, the means of evaluation indexes for the two batteries are calculated, and the results are shown in Table 3.

Table 3. Error comparison analysis.

Batteries	Index	Mean MAE	Mean RMSE
BPNN	SOH estimation	2.6138	1.0838
	RUL prediction	33.5	28.2835
SVM	SOH estimation	3.1786	1.3333
	RUL prediction	33.5	33.5
RF	SOH estimation	2.7293	1.1627
	RUL prediction	33.5	30.6125

According to the results shown in Table 3, the mean MAEs of SOH estimation for the three methods are 2.6138, 3.1786, and 2.7293, and the mean RMSEs are 1.0838, 1.3333, and 1.1627; for RUL prediction, the mean MAEs are about 33.5, while the mean RMSEs are 28.2835, 33.5, and 30.6125. Relatively speaking, BPNN has the best performance for the SOH estimation and RUL prediction in the three methods; however, the results are still worse than the proposed optimization model. Especially, RF without optimization cannot determine the appropriate hyperparameters; thus, the estimation or prediction performance is lower than the RF optimization model.

To sum up, the excellent SOH estimation and RUL prediction suggest that the developed optimized RF model and BMS can achieve the effective online application of PHM. As the main components of the framework, the embedded method for BMS plays a crucial role.

(1) The bagging is employed in RF to avoid the correlation among multiple decision trees. Furthermore, the diversity of the trees can be improved by constructing different subsets of training data. Therefore, the RF model becomes more robust to slight variations in input data due to greater stability by utilizing bagging; also, bagging reduces noise through generating non-correlated trees using different training samples.

(2) It is necessary for the RF model to only tune two hyperparameters. Herein, BO is effective at addressing optimization problems where the objective function is unknown or a black-box function. BO amalgamates the function's prior distribution with the sample information (evidence) to derive the function's posterior property, and subsequently employs this information to ascertain the optimal position of the said function based on predetermined criteria. Therefore, in a small number of samples, BO can achieve high accuracy in a short time.

(3) The development of co-simulation using LabVIEW and MATLAB for verification of the optimized RF model is carried out. Based on BMS, the co-simulation technology brings about a new idea to implement the simulation of the hardware in the loop.

5. Conclusions

In this study, an optimized RF model is developed for online SOH estimation and RUL prediction, as follows:

(1) Based on the partial charging data, two ICC-based AFs are extracted. In addition, the AFs are proven to have a strong correlation with battery capacity and quantify the battery capacity degradation.

(2) An RF model is developed to capture the underlying relationship between battery capacity and AFs. Meanwhile, BO is employed to determine the hyperparameters of the RF model, in order to obtain an optimized RF model.

(3) The developed RF optimization model is deployed through co-simulation using LabVIEW and MATLAB for online SOH estimation and RUL prediction. The aging datasets are employed to validate the effectiveness of the proposed method with an average SOH

estimation error of less than 1.8152% and an average RUL prediction error of less than 32 cycles.

This work does not take into account the influence of the different temperature and the failure thresholds. In future work, we will pay more attention to the temperature and threshold variations. On the other hand, the digitally controlled power supply embedded in the RF optimization model will be used to develop an estimator in the charger for online estimation of battery in-loop capacity under more uncontrolled environmental factors. Meanwhile, the echelon utilization of the retired EVs needs to be researched.

Author Contributions: G.W. conceived the idea of SOH estimation, led and supervised the project, and participated in paper writing and revision. Z.L. and X.L. supervised and led the project. All of the authors have revised the manuscript and agreed with its content. All authors have read and agreed to the published version of the manuscript.

Funding: This research was funded by the doctoral research project of Anhui University.

Data Availability Statement: The data presented in this study are openly available in https://calce.umd.edu/battery-data (accessed on 20 May 2023).

Conflicts of Interest: The authors declare no conflict of interest.

Nomenclature

EV	Electric vehicle
PHM	Prognostics and health management
SOH	State of health
RUL	Remaining useful life
EM	Electrochemical model
ECM	Equivalent circuit model
PF	Particle filter
SOC	State of charge
EKF	Extended Kalman filter
AF	Aging feature
BO	Bayesian optimization
BMS	Battery management system
RF	Random forest
SVR	Support vector regression
EIS	Electrochemical impedance spectroscopy
RVM	Relevance vector machine
ELM	Extreme learning machine
ICC	Incremental capacity curve
ICA	Incremental capacity analysis
PSO	Particle swarm optimization
LOWESS	Locally weighted scatterplot smoothing
PICC	Peak of the incremental capacity curve
CCEV	Charged capacity of equal voltage
BPNN	Back propagation neural networks

References

1. Li, X.; Yuan, C.; Wang, Z.; He, J.; Yu, S. Lithium battery state-of-health estimation and remaining useful lifetime prediction based on non-parametric aging model and particle filter algorithm. *eTransportation* **2022**, *11*, 100156. [CrossRef]
2. Yu, Q.; Huang, Y.; Tang, A.; Wang, C.; Shen, W. Ocv-soc-temperature relationship construction and state of charge estimation for a series—parallel lithium-ion battery pack. *IEEE Trans. Intell. Transp. Syst.* **2023**, *24*, 6362–6371. [CrossRef]
3. Guo, Y.; Yang, D.; Zhao, K.; Wang, K. State of health estimation for lithium-ion battery based on bi-directional long short-term memory neural network and attention mechanism. *Energy Rep.* **2022**, *8*, 208–215. [CrossRef]
4. Yu, Q.; Liu, Y.; Long, S.; Jin, X.; Li, J.; Shen, W. A branch current estimation and correction method for a parallel connected battery system based on dual bp neural networks. *Green Energy Intell. Transp.* **2022**, *1*, 100029. [CrossRef]
5. Lin, D.; Zhang, X.; Wang, L.; Zhao, B. State of health estimation of lithium-ion batteries based on a novel indirect health indicator. *Energy Rep.* **2022**, *8*, 606–613. [CrossRef]

6. Wang, C.; Yu, C.; Guo, W.; Wang, Z.; Tan, J. Identification of typical sub-health state of traction battery based on a data-driven approach. *Batteries* **2022**, *8*, 65. [CrossRef]
7. Zhao, J.; Burke, A.F. Electric vehicle batteries: Status and perspectives of data-driven diagnosis and prognosis. *Batteries* **2022**, *8*, 142. [CrossRef]
8. Wang, H.; Li, J.; Liu, X.; Rao, J.; Fan, Y.; Tan, X. Online state of health estimation for lithium-ion batteries based on a dual self-attention multivariate time series prediction network. *Energy Rep.* **2022**, *8*, 8953–8964. [CrossRef]
9. Wang, Z.; Feng, G.; Zhen, D.; Gu, F.; Ball, A. A review on online state of charge and state of health estimation for lithium-ion batteries in electric vehicles. *Energy Rep.* **2021**, *7*, 5141–5161. [CrossRef]
10. Wang, S.; Jin, S.; Bai, D.; Fan, Y.; Shi, H.; Fernandez, C. A critical review of improved deep learning methods for the remaining useful life prediction of lithium-ion batteries. *Energy Rep.* **2021**, *7*, 5562–5574. [CrossRef]
11. Hu, X.; Jiang, J.; Cao, D.; Egardt, B. Battery health prognosis for electric vehicles using sample entropy and sparse bayesian predictive modeling. *IEEE Trans. Ind. Electron.* **2016**, *63*, 2645–2656. [CrossRef]
12. Kuipers, M.; Schröer, P.; Nemeth, T.; Zappen, H.; Blömeke, A.; Sauer, D.U. An algorithm for an online electrochemical impedance spectroscopy and battery parameter estimation: Development, verification and validation. *J. Energy Storage* **2020**, *30*, 101517. [CrossRef]
13. Li, J.; Adewuyi, K.; Lotfi, N.; Landers, R.G.; Park, J. A single particle model with chemical/mechanical degradation physics for lithium ion battery state of health (soh) estimation. *Appl. Energy* **2018**, *212*, 1178–1190. [CrossRef]
14. Du, X.; Meng, J.; Zhang, Y.; Huang, X.; Wang, S.; Liu, P.; Liu, T. An information appraisal procedure: Endows reliable online parameter identification to lithium-ion battery model. *IEEE Trans. Ind. Electron.* **2022**, *69*, 5889–5899. [CrossRef]
15. Bi, Y.; Yin, Y.; Choe, S. Online state of health and aging parameter estimation using a physics-based life model with a particle filter. *J. Power Sources* **2020**, *476*, 228655. [CrossRef]
16. Allam, A.; Onori, S. Online capacity estimation for lithium-ion battery cells via an electrochemical model-based adaptive interconnected observer. *IEEE Trans. Control Syst. Technol.* **2021**, *29*, 1636–1651. [CrossRef]
17. Yu, Q.; Dai, L.; Xiong, R.; Chen, Z.; Zhang, X.; Shen, W. Current sensor fault diagnosis method based on an improved equivalent circuit battery model. *Appl. Energy* **2022**, *310*, 118588. [CrossRef]
18. Zou, Y.; Hu, X.; Ma, H.; Li, S.E. Combined state of charge and state of health estimation over lithium-ion battery cell cycle lifespan for electric vehicles. *J. Power Sources* **2015**, *273*, 793–803. [CrossRef]
19. Lyu, Z.; Gao, R. A model-based and data-driven joint method for state-of-health estimation of lithium-ion battery in electric vehicles. *Int. J. Energy Res.* **2019**, *43*, 7956–7969. [CrossRef]
20. Vanem, E.; Salucci, C.B.; Bakdi, A.; Alnes, Ø.Å.S. Data-driven state of health modelling—A review of state of the art and reflections on applications for maritime battery systems. *J. Energy Storage* **2021**, *43*, 103158. [CrossRef]
21. Hamar, J.C.; Erhard, S.V.; Canesso, A.; Kohlschmidt, J.; Olivain, N.; Jossen, A. State-of-health estimation using a neural network trained on vehicle data. *J. Power Sources* **2021**, *512*, 230493. [CrossRef]
22. Pradyumna, T.K.; Cho, K.; Kim, M.; Choi, W. Capacity estimation of lithium-ion batteries using convolutional neural network and impedance spectra. *J. Power Electron.* **2022**, *22*, 850–858. [CrossRef]
23. Zhang, W.; Li, X.; Li, X. Deep learning-based prognostic approach for lithium-ion batteries with adaptive time-series prediction and on-line validation. *Measurement* **2020**, *164*, 108052. [CrossRef]
24. Pan, W.; Luo, X.; Zhu, M.; Ye, J.; Gong, L.; Qu, H. A health indicator extraction and optimization for capacity estimation of li-ion battery using incremental capacity curves. *J. Energy Storage* **2021**, *42*, 103072. [CrossRef]
25. Wu, J.; Fang, L.; Meng, J.; Lin, M.; Dong, G. Optimized multi-source fusion based state of health estimation for lithium-ion battery in fast charge applications. *IEEE Trans. Energy Convers.* **2022**, *37*, 1489–1498. [CrossRef]
26. Duong, P.L.T.; Raghavan, N. Heuristic kalman optimized particle filter for remaining useful life prediction of lithium-ion battery. *Microelectron. Reliab.* **2018**, *81*, 232–243. [CrossRef]
27. Wei, J.; Dong, G.; Chen, Z. Remaining useful life prediction and state of health diagnosis for lithium-ion batteries using particle filter and support vector regression. *IEEE Trans. Ind. Electron.* **2018**, *65*, 5634–5643. [CrossRef]
28. Downey, A.; Lui, Y.; Hu, C.; Laflamme, S.; Hu, S. Physics-based prognostics of lithium-ion battery using non-linear least squares with dynamic bounds. *Reliab. Eng. Syst. Saf.* **2019**, *182*, 1–12. [CrossRef]
29. Liu, Q.; Zhang, J.; Li, K.; Lv, C. The remaining useful life prediction by using electrochemical model in the particle filter framework for lithium-ion batteries. *IEEE Access* **2020**, *8*, 126661–126670. [CrossRef]
30. Hu, X.; Xu, L.; Lin, X.; Pecht, M. Battery lifetime prognostics. *Joule* **2020**, *4*, 310–346. [CrossRef]
31. Afshari, S.S.; Cui, S.; Xu, X.; Liang, X. Remaining useful life early prediction of batteries based on the differential voltage and differential capacity curves. *IEEE Trans. Instrum. Meas.* **2022**, *71*, 6500709. [CrossRef]
32. Feng, H.; Song, D. A health indicator extraction based on surface temperature for lithium-ion batteries remaining useful life prediction. *J. Energy Storage* **2021**, *34*, 102118. [CrossRef]
33. Yao, F.; He, W.; Wu, Y.; Ding, F.; Meng, D. Remaining useful life prediction of lithium-ion batteries using a hybrid model. *Energy* **2022**, *248*, 123622. [CrossRef]
34. Lyu, Z.; Gao, R.; Li, X. A partial charging curve-based data-fusion-model method for capacity estimation of li-ion battery. *J. Power Sources* **2021**, *483*, 229131. [CrossRef]

35. Li, X.; Yuan, C.; Wang, Z. State of health estimation for li-ion battery via partial incremental capacity analysis based on support vector regression. *Energy* **2020**, *203*, 117852. [CrossRef]
36. Lyu, Z.; Wang, G.; Gao, R. Synchronous state of health estimation and remaining useful lifetime prediction of li-ion battery through optimized relevance vector machine framework. *Energy* **2022**, *251*, 123852.
37. Li, Y.; Zou, C.; Berecibar, M.; Nanini-Maury, E.; Chan, J.C.W.; van den Bossche, P.; Van Mierlo, J.; Omar, N. Random forest regression for online capacity estimation of lithium-ion batteries. *Appl. Energy* **2018**, *232*, 197–210. [CrossRef]
38. Wu, J.; Chen, X.; Zhang, H.; Xiong, L.; Lei, H.; Deng, S. Hyperparameter optimization for machine learning models based on bayesian optimizationb. *J. Electron. Sci. Technol.* **2019**, *17*, 26–40.
39. Lin, H.; Kang, L.; Xie, D.; Linghu, J.; Li, J. Online state-of-health estimation of lithium-ion battery based on incremental capacity curve and bp neural network. *Batteries* **2022**, *8*, 29. [CrossRef]

sensors

MDPI

Article

Uncertainty of Standardized Track Insulation Measurement Methods for Stray Current Assessment

Sahil Bhagat [1], Jacopo Bongiorno [2] and Andrea Mariscotti [1,*]

[1] DITEN, University of Genova, 16145 Genova, Italy; 5025527@studenti.unige.it
[2] RINA Services S.p.A., 16138 Genoa, Italy; jacopo.bongiorno@rina.org
* Correspondence: andrea.mariscotti@unige.it

Abstract: Stray current is a relevant phenomenon in particular for DC electrified transportation systems, affecting track and infrastructure within the right of way and other structures and installations nearby. It worsens with time and the level of protection depends on timely maintenance, as well as correct design choices. The assessment of track insulation is the starting point for both stray current monitoring systems and at commissioning or upon major changes. Standardized methods (ref. EN 50122-2 or IEC 62128-2) have been almost unchanged in the last 20 years but suffer from accuracy issues and variability due to parameters and conditions not under the operator's control. The uncertainty of test methods is increasingly important now that contractual specifications require a high level of insulation for new systems. A critical discussion and analysis of the sources of variability and practical constraints is proposed, followed by an evaluation of uncertainty, with the objective not only to assess the accuracy of the provided results, but also to foster research on innovative, more flexible and accurate methods.

Keywords: DC power systems; guideway electric transportation systems; stray current; test methods; uncertainty

1. Introduction

All electrified transportation systems (ETSs) of the guideway type are affected by return current leakage from the guiding track into the soil, coupling to structures nearby. Examples of victims are sleepers and the track bed [1–3], platform screen doors and other metallic parts at platforms [4], viaducts, bridges and building foundations [5,6], pipelines and reservoirs [7–9], etc., as well as corrosion of power earthing systems and saturation of transformers [10–12].

In general, the effect of current flow through the interface of a metal with an electrolyte solution (such as the soil itself, or cement for concrete structures) causes corrosion, affecting the solidity and durability of said structures. The first victims are the sleepers and rail fasteners [13–15]: in the case of a local insulation loss, they may become a hotspot, with a significant increase in current density, although the overall track leakage may be acceptable over a longer length.

For this reason, preferred verification methods should be able to operate on a local basis, that is, for short enough track sections, providing a valuable indication for rapid visual inspection and repair. However, they should also be easily applicable to longer stretches, favoring rapid diagnosis of a long line, at least as a periodic preliminary check.

Track current insulation phenomena, apart from the spatial dimension, develop through time, with testing, monitoring and evolution of insulation degradation having different time scales:

- from seconds to minutes, if applying test signals in off-service conditions: time intervals of seconds are necessary for the polarization of electrolytes in the test circuit to take place, after which, test quantities can be measured with care to reject external noise with sufficiently long observation times;

- from hours to weeks, if using track electric quantities during train service:
- from days to years, considering the normal evolution of track insulation degradation, with aging of insulating materials, pollution of surfaces, stagnation of water, etc.

The relevance of stray current assessment, in general, is proven by the consequences of corrosion: weakening of structures within the right of way and nearby, impairment of track stability, spillage and breakage of pipes and reservoirs, more onerous repairs and corrective maintenance rather than normal preventive operation.

A significant modeling and simulation effort has developed through the years in order to understand the coupling mechanisms and to globally address the problem with suitable design choices and provisions [16–20]. Prevention and compensation of stray current is, in fact, taking place by means of various systems: optimization of traditional track and transit systems [21,22], passive stray current collection systems [23], traditional track voltage limitation [4,24], active track potential control and redistribution of traction current [25,26].

Stray current monitoring systems are gaining popularity [27] as they provide feedback on the health status of an important asset, although the interpretation of collected data and identification of necessary actions with the right timing are still complex problems that are unsolved [28].

The measurement of voltage and current quantities at track, substation negative and stray current collection is as accurate as the combination of probes used and the sampling channels. However, stray current evaluation using such approaches necessitates initial tuning (and, possibly, periodic verification) that depends on the assessment of current track insulation: sources of variability beyond instrumental uncertainty, including site conditions, are, thus, considered in this work, focusing on standardized methods.

In particular, the humidity conditions and the wet status of the track are not explicitly indicated nor discussed in the standards. A large deal of track insulation variation can be ascribed to the water percentage: a water film on the surface of the track and fastener insulating elements can compromise the otherwise good insulation level provided by the volumic insulation resistance of polymeric materials. For an increased amount of water, to the extent of completely wet fasteners and rail base, any insulating provision is compromised and the measured performance is that of electric conduction through water. For example, a 6.6 mS/km track wetted by water jet increased its conductance 15 times, returning to an intermediate value five times larger than the dry reference value after 30 min on a dry day at 28 °C.

Track insulation measurement is guided by the standard EN 50122-2 [29] (equivalent to the IEC 62128-2 that is still in its 2013 version [30]) that distinguishes three methods:

- method A.2, track insulation with civil structure: the important point that makes this less invasive compared to method A.3 is that the running rails are continuous and do not need to be sectioned; however, the test setup is more complex, with more measured quantities involved and an overall worse accuracy. The evaluation of uncertainty and optimal test conditions is discussed in Section 2;
- method A.3, track insulation without civil structure: the presence or absence of the civil structure is not the relevant point here, as the running rails must be sectioned to the desired length, either by cutting them or exploiting the presence of insulating rail joints; this is a more accurate method and should be preferred whenever possible, especially for high track insulation values;
- method A.4, lateral voltage gradient method in open area sites: this method measures the voltage gradient in the soil caused by running trains, with the field laterally extending from the tracks at two points at different distances; it is suitable for large open areas, but necessitates access to soil as homogeneous as possible and may, thus, be disturbed by buried structures and installations, such as in an urban context.

With contractual specifications requiring track insulation levels of the order of 100 Ωkm or better, the uncertainty of measurement methods is negatively affected at such low track leakage current levels, as we will see in the following, with some methods performing better than others.

Apart from the metrological aspects, such as variability and uncertainty, the three methods have different impact and cost in terms of organization and preparation, including the necessary operations to set up the test and to bring back the system in the original conditions. These, in fact, are the real cost-driving factors and, in general, methods that can be overlapped to the track without affecting its structural integrity should be preferred (in our case, methods A.2 and A.4). In addition, the overall time duration to fit within the engineering hours and the compatibility with commercial traffic for systems already in operation are two other relevant aspects: method A.2, of course, cannot be used in the current implementation in the presence of trains, and method A.3 is absolutely not compatible with train runs, whereas method A.4 exploits the normal line traffic as the test signal (and provides track voltage information as well).

The purpose of this work is to analyze and discuss three methods for track insulation assessment that are reported in the Annex A (informative) of the EN 50122-2 standard [29,31]. Their description has been unchanged for more than 20 years and the test experience of several years, including discussions during test campaigns, has uncovered various points that are vague, insufficiently detailed, and, in some cases, have had a significant impact on the quality of the results and their uncertainty.

Sections 2–4 consider the three methods separately, discussing the setup and equations, providing practical considerations and identifying relevant factors, and then proceeding to the estimation of variability and uncertainty. Each section provides numerical examples and analyzes experimental data from past test campaigns. The outcomes are then summarized and discussed by comparing the three methods in the conclusions in Section 5.

2. Method A.2: Continuous Track, Line Closed to Traffic

2.1. Method Description and Setup

The method basically achieves the estimation of the leaking current in the track section under measurement (from now on, simply "track section") by subtracting the rail current flowing outside the track section (indicated by $I_{r,\mathrm{F1}}$, $I_{r,\mathrm{F3}}$ for the leftmost position and $I_{r,\mathrm{G1}}$, $I_{r,\mathrm{G3}}$ for the rightmost position) from the applied source current I_s. The setup, annotated with the relevant electrical quantities, is shown in Figure 1.

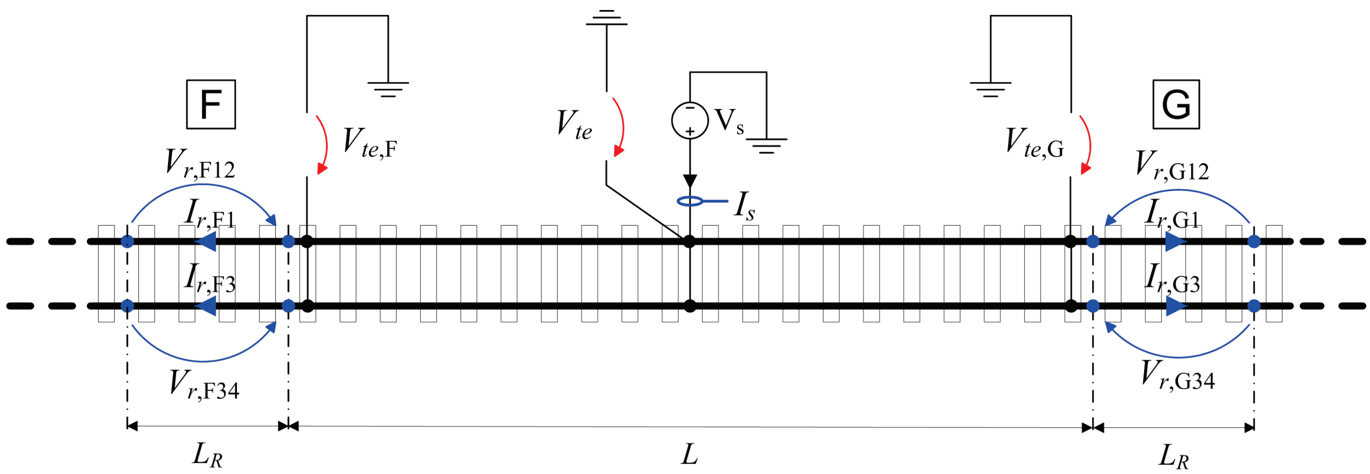

Figure 1. Sketch of the method A.2 setup for a track insulation measurement: the current measuring circuits in blue, the voltage measuring circuits in red.

The I_s intensity depends on the used voltage level V_s and the overall resistance-to-earth of the entire system, that is, of the tracks that can be considered electrically continuous from the point of injection of the test current. It is evident, then, that the I_s current does not change with the location and injection point. In addition, a very well-insulated system will sink a low test current anyway. The use of higher test voltages of course increases the test current intensity, but this is usually not performed only for this purpose, but rather to provide a test level that is much larger than the internal voltage barriers due to oxidized surfaces and electrolytes, ruling them out as a major source of error. To this end, polarity reversal may be used, canceling to some extent such offset voltages. A 50 V test is a common choice, as it does not pose serious problems of electrical safety.

The current flowing along the rails in the measured track section causes a voltage drop (indicated as $V_{r,\mathrm{F12}}$, $V_{r,\mathrm{F34}}$,$V_{r,\mathrm{G12}}$, $V_{r,\mathrm{G34}}$ in Figure 1) that, for moderate current intensity, is negligible, but in a general perspective should be included.

The rail current leaving the track section is measured either by direct measurement or by means of the voltage drop on the rails themselves (as suggested by EN 50122-2). The former approach is hindered by the lack of such large openable DC current sensors (Rogowski coils work in AC). The latter approach is commonly used and relies on the measurement of a small voltage drop of the order of some mV. The voltage drops $V_{r,\mathrm{F12}}$, $V_{r,\mathrm{F34}}$, $V_{r,\mathrm{G12}}$, $V_{r,\mathrm{G34}}$ are given by the local rail resistance $R_{r,\mathrm{F1}}$, $R_{r,\mathrm{F3}}$, $R_{r,\mathrm{G1}}$, $R_{r,\mathrm{G3}}$ multiplied by the flowing current, so that the latter can be estimated by measuring or assuming the rail resistance values.

$$I_{r,\mathrm{F1}} = \frac{V_{r,\mathrm{F12}}}{R_{r,\mathrm{F1}}} \qquad I_{r,\mathrm{F3}} = \frac{V_{r,\mathrm{F34}}}{R_{r,\mathrm{F3}}} \qquad I_{r,\mathrm{G1}} = \frac{V_{r,\mathrm{G12}}}{R_{r,\mathrm{G1}}} \qquad I_{r,\mathrm{G3}} = \frac{V_{r,\mathrm{G34}}}{R_{r,\mathrm{G3}}} \tag{1}$$

The precaution advised is not to include welded points or fish plates (bypassing an insulating rail joint, IRJ) in the rail segment that is used to measure each respective voltage drop. As indicated by EN 50122-2, such welding points could add up to 5% of the longitudinal rail resistance, impacting on accuracy. In addition, the rail length L_R, across which the voltage drop is measured, is prescribed to be 10 m [29]. When the intensity of the test current I_s is not large (for example, due to an overall well-insulated system) and the voltage drop signal intensity is not sufficient, a doubled length brought to 20 m is a sensible compromise to increase it. In general, the rail resistance is taken from datasheets or measured at the location where tests are carried out, and the resulting per-unit rail resistance value R_r is unique for all four voltage drop measuring points.

$$R_{r,\mathrm{F1}} = R_r L_R \qquad R_{r,\mathrm{F3}} = R_r L_R \qquad R_{r,\mathrm{G1}} = R_r L_R \qquad R_{r,\mathrm{G3}} = R_r L_R \tag{2}$$

For DC and very low frequency, the relevant rail resistance is the DC value, that can be assumed, in general, to be between about 33 mΩ/km to 40 mΩ/km, as documented in [32]. The most commonly used rails for, e.g., metro applications, are of the UIC 54 and UIC 60 types, with different hardness levels, providing resistance of the order of 36 mΩ/km and 33 mΩ/km, respectively. It is apparent that, with a rail current flowing outside the test section of, e.g., 10 A, the expected voltage drop is 3.6 mV and 3.3 mV, respectively, over a 10 m voltage drop measuring rail segment.

The final complete formula for determination of the track-to-earth resistance R_{te} is given by

$$R_{te,\mathrm{A2}} = \frac{(\delta V_{te} + \delta V_{te,\mathrm{F}} + \delta V_{te,\mathrm{G}})/3}{I_s - (I_{r,\mathrm{F1}} + I_{r,\mathrm{F3}} + I_{r,\mathrm{G1}} + I_{r,\mathrm{G3}})} \tag{3}$$

where δ voltage quantities are understood as the difference between the on and off condition value, for example, $\delta V_{te,\mathrm{F}} = V_{te,\mathrm{F}}(\mathrm{on}) - V_{te,\mathrm{F}}(\mathrm{off})$. Multiplication by L expressed in km gives the per-unit insulation resistance to compare with the limits.

It is observed that EN 50122-2 [29] reports this formula incorrectly, as the shown test setup is for the whole track (so, for estimate of the track-to-earth insulation), but the current quantities are only two, taken for one rail only.

2.2. Practical Factors

Voltage drop readings are generally affected by a significant common-mode disturbance (any time the signal is read by a non-insulated voltage probe), as well as the pre-existing flowing current, e.g., at the utility frequency (50 Hz) or fluctuating at low frequency. The reason is the unavoidable influence of external sources, in particular, if the system is already energized and operating, so that substations during engineering hours still have the negative connected to the track. The unavoidable difference in the potential of the utility earth at different locations causes a current flow along the tracks.

In addition, the rail current marked in Figure 1 is, ideally, the one flowing along the short rail section of length d that provides the indirect voltage drop measurement. In reality, the current entering such a section flows along the rails and leaks transversely at the same time, for which, the larger the d, the larger the difference between these two current values entering and exiting the measurement section. The measurement error can be minimized by assigning to each $I_{r,X}$ the average value within the section as the voltage drop measurement implies, and, thus, using an effective length of the section under measurement equal to $L + d$, rather than L.

The use of rail current probes would solve the problem of the small longitudinal voltage drop across the rails and would provide a floating signal that rejects the common-mode rail potential. Possible probes include Hall effect and fluxgate probes that are large enough to embrace the rail section or Rogowski coil, provided that the test is carried out with a low-frequency AC signal, but not a pure DC component.

In addition, if carrying out the test with a DC source, offsets are quite relevant, being of the same order of magnitude as the expected voltage drop (see the previously estimated 3.3 mV to 3.6 mV).

A general optimized arrangement for the classical setup (using voltage probes, as shown in Figure 1) requires a short-circuit connection (cross bond) between rails, creating a reference node at the remote (A or B) location to which both voltage drop readings are referred (shown in Figure 2).

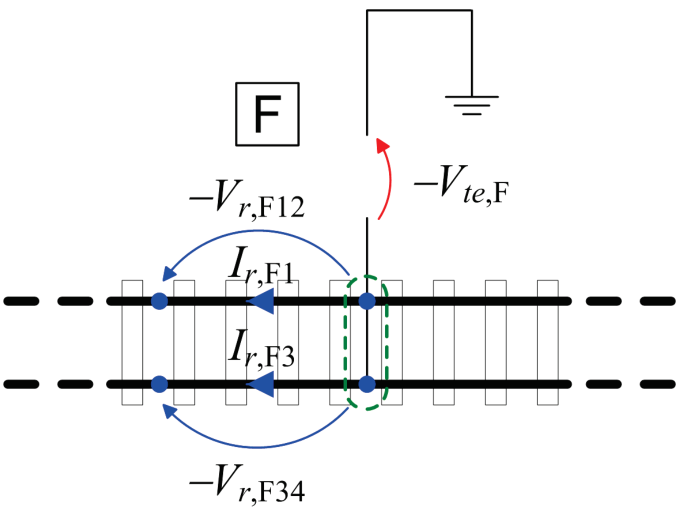

Figure 2. Modification in method A.2 to the rail voltage drop measuring terminals and to the track-to-earth voltage measuring terminal in order to obtain a unique potential reference node (circled in green) and avoid ground loops.

Galvanic isolation and rejection of the common mode can also be achieved using differential voltage probes that, however, introduce a signal reduction (such as a 1:10 factor) and additional noise (being active devices). The use of rail current probes instead would solve the problem *tout court* providing a cleaner floating signal: Hall-effect or fluxgate probes of this size do not exist to the authors' knowledge, so that a Rogowski coil should be used that requires AC test signals. Some Rogowski models have, in reality, a frequency response extended down to a few Hz and good droop capability, so that an alternating DC voltage could be exploited.

Using instead a real AC signal (such as that provided by an amplifier) makes the method more complex (signal generator and amplifier to add), but provides a clean current measurement. It is only a formal issue, accepting that the track insulation resistance values measured with a pure DC current or a low-frequency AC signal are comparable. To this end, two points need to be checked regarding the equivalent circuit of a running rail.

- The longitudinal impedance of a running rail is comprised of an internal inductance term and an AC resistance term, both accounting for AC effects, such as the skin effect and hysteresis, and related losses [33,34]; values for low current (<50 A) amount to about 0.8 μH/m and 100 μΩ/m, with the former contributing less than 25 μΩ/m of the inductive reactance at 50 Hz.
- The stray capacitance of a running rail amounts to less than 10 nF/m (obtained by multiplying by 2 the values shown in [35]), providing more than 300 kΩ of capacitive reactance, easily shunted by the transversal track insulation term considered here.

We may conclude that the equivalent circuit of a running rail in AC at low frequency does not differ from that at DC for the purpose of determining the track-to-earth insulation resistance, with the exception that the longitudinal resistance (and impedance) are larger and cannot be used any longer reliably for the determination of the flowing current. The measurement of the flowing rail current could then be achieved by using Rogowski coils that ensure a complete rejection of common-mode signals and a more favorable signal-to-noise ratio. Another method of rail current measurement that allows train circulation, and can be a semi-permanent installation, is by means of close-up sensors, based on the inductive effect [36], with arrays of such elementary sensors for better reconstruction [37], or alternative methods, such as the Hall or magneto-resistive effect [38].

The locations A and B and the central point of injection of the test signal could be separated by a hundred meters, as well as 1 km or so, so that connecting all channels to a single data acquisition system is a problem, not only for the length of the necessary cables, but for the consequential noise pickup of such cables. Separate measuring stations are preferred, necessitating, as a matter of fact, more personnel and instrumentation.

2.3. Variability and Uncertainty Analysis

Variability is considered by listing the external factors that have a significant influence on the results and that should be accounted for in the uncertainty analysis. The identification of such factors and their spread is, thus, a necessary initial step for the uncertainty analysis that focuses on (3).

The rail current $I_{r,X}$ (with "X" standing for F1, F3, G1, or G3) is estimated by measuring the rail voltage drop over the rail section of length L_R and applying (1). The uncertainty is then

$$u\{I_{r,X}\} = \sqrt{(u\{V_{r,X}\})^2 + (u\{R_{r,X}\})^2} \tag{4}$$

where the uncertainty of the voltage reading $u\{V_{r,X}\}$ is derived directly by the employed instrumentation, and that of the rail resistance $u\{R_{r,X}\}$ is related to its variability, and to the availability of measured values for the specific system and track section, or the use of tabular data.

For $u\{V_{r,X}\}$, it is observed that the reading scale is quite low, of the order of a few mV, whereas the track voltage readings are in the more favorable range of tens of V. The measuring multimeter/data logger must be carefully selected as apparently good items of equipment might have quite different performance in the mV range. An overview is provided in Table 1.

From the uncertainty estimates above, it is clear that extreme care must be adopted for the voltage drop measurement and suitable instrumentation must be selected. Medium-performance portable multimeters, such as Fluke 117, are clearly inadequate, and a high-performance multimeter, such as the H29S, barely achieves the minimum necessary performance (about 8% of uncertainty budgeted for the rail current measurements and the remaining 6% for the three track voltage $V_{te,X}$ measurements and the test current I_s measurement). Specialized portable data acquisition systems, such as Minilog2, achieve a satisfactory target performance of about 1%, whereas generic ones (e.g., the National Instruments card) achieve the same performance as a high-performance multimeter.

Table 1. Examples of uncertainty values of various instruments for mV range readings.

Brand/Model	Uncert. Expression	$u\{V_{rX}\}$ @ 1 mV	$u\{V_{rX}\}$ @ 3 mV
Weilekes Elektronik MiniLog2	0.5% + 10 μV	1.5%	0.83%
National Instruments USB 6210	0.05% FS + 12 μV	8.9%	3.0%
Gossen Metrawatt H29S	0.02% + 0.01% FS + 5 cts.	0.02% + 0.01% 300 mV + (2 × 300 mV/30,000)/1 mV = 0.02% + 3% + 2% = 5.02%	0.02% + 0.01% 300 mV + (2 × 300 mV/30,000)/3 mV = 0.02% + 3% + 0.66% = 3.68%
Fluke 117	0.5% + 2 cts.	0.5% + (2 × 600 mV/6000)/1 mV = 20.5%	0.5% + (2 × 600 mV/6000)/3 mV = 7.17%

The uncertainty of the rail resistance values is not influenced by the instrumental uncertainty of the rail resistance measurement, but by the variability between rails of the same section and, in general, of different sections (from different production batches or different manufacturers). The problem is discussed in [32], where various examples of experimentally determined values are provided as well.

The expression at the denominator of (3), where the current leaking within the track section is determined by the difference of the injected test current I_s and the "escaping" rail currents (flowing outside the section), is inherently exposed to measurement errors, especially for well-insulated tracks. Let us assume that we test with a test voltage $V_s = 50\,\text{V}$, resulting in a test current $I_s = 10\,\text{A}$, a track section of 100 m of a well-insulated system, such as one with 100 Ωkm insulation, resulting in $R_{te} = 1\,\text{k}\Omega$ for the measured section. The expected leaking current is approximately given by $I_l^* = V_s/R_{te} \approx 50\,\text{mA}$. The four escaping currents ($I_{r,\text{F1}}$,$I_{r,\text{F3}}$, $I_{r,\text{G1}}$, $I_{r,\text{G3}}$) must, thus, give about 9.95 A in total, so about 2.5 A each, or, in the extreme case of a measurement taken near the beginning of the line, two rail currents will be at about 5 A and the other two approximately zero. A 1% uncertainty for each of these currents will cause a measurement error $\varepsilon_{Ir,X} \approx 50\,\text{mA}$, that is exactly in the range of the target value of the leaking current. It is easy to see that a 200% measurement error can be reached under the reasonable assumption of random combination of the four error terms compared to I_l^*. The method, thus, provides acceptable accuracy only if:

- a long track section is tested: a 10-times longer track (1 km) will provide a 10-times larger I_l^* and the resulting errors will, this time, be about 20% (large, but acceptable);
- a track with poor insulation is tested: similarly, an insulation level of only 10 Ωkm will provide a similar distribution of the errors, so a 10-times larger I_l^* will again reach an uncertainty of the order of 20%.

The uncertainty of (3) can be estimated by formally calculating the propagation of uncertainty for each of the relevant quantities. The four rail current terms at the denominator and the three track voltage terms at the numerator have identical effects and may be calculated only once.

The current terms at the denominator form a difference that is handled by using the absolute and not the relative error, so that they are not ready to be expressed in terms of uncertainty. For a difference $C = A - B$, the following expression holds $\text{var}[C] = \text{var}[A] + \text{var}[B]$. It is easy to see that A indicates I_s and B indicates $(I_{r,\text{F1}} + I_{r,\text{F3}} + I_{r,\text{G1}} + I_{r,\text{G3}})$, and their difference may be indicated for simplicity as δI. These expressions, however, can be manipulated based on the assumption that the result is small, as I_s and $(I_{r,\text{F1}} + I_{r,\text{F3}} + I_{r,\text{G1}} + I_{r,\text{G3}})$ are almost equal (quite true for a well-insulated system): the difference is, thus, expressed as a small multiplying coefficient k of the half sum, or of either of the two terms with an acceptable degree of approximation.

$$C = A - B = k(A + B)/2 \approx kB \tag{5}$$

where the rightmost equality is justified by the fact that the uncertainty of the measured $(I_{r,\mathrm{F1}} + I_{r,\mathrm{F3}} + I_{r,\mathrm{G1}} + I_{r,\mathrm{G3}})$ is much larger than that of I_s when the used methods are the rail voltage drop and current clamp (or shunt), respectively.

In practice, with a test current $I_S = 20\,\mathrm{A}$ and a test voltage $V_S = 50\,\mathrm{V}$, a track with a good insulation level of 100 Ωkm would have leakage of only $I_l = V_S/200\,\Omega = 50\,\mathrm{mA}$ for a 200 m-long track section. The value of k would then be $k = I_l/I_S = 0.25\%$, smaller or comparable to the accuracy of the used instrumentation, as estimated in Table 1. A longer test section, e.g., 1 km, would provide $k = 1.25\%$.

The three voltage terms at the numerator follow a similar rule, that is, the summation is managed by using the absolute error, or, in other words, the dispersion or variance, and not its relative (or normalized) version. Assuming that they are measured with the same instrumentation (such as an identical multimeter or different channels of the same data acquisition system), their variances are identical, so that the resulting variance of the average $V_{te,\mathrm{avg}}$ is one third of them: $\mathrm{var}[V_{te,\mathrm{avg}}] = \mathrm{var}[V_{te,\mathrm{X}}]/3$.

It is possible, thus, to estimate the uncertainty considering (3) as a pure ratio, having introduced the factor k:

$$\mathrm{var}[R_{te,\mathrm{A2}}] \approx \sqrt{\left(\frac{\partial R_{te,\mathrm{A2}}}{\partial V_{te,\mathrm{avg}}}\right)^2 \mathrm{var}[V_{te,\mathrm{avg}}] + \left(\frac{\partial R_{te,A2}}{\partial \delta I}\right)^2 \mathrm{var}[\delta I]} \tag{6}$$

The two terms then correspond to:

$$\frac{\partial R_{te,\mathrm{A2}}}{\partial V_{te,\mathrm{avg}}} = \frac{1}{\delta I} = \frac{R_{te,\mathrm{A2}}}{V_{te,\mathrm{avg}}} \qquad \frac{\partial R_{te,\mathrm{A2}}}{\partial \delta I} = -\frac{V_{te,\mathrm{avg}}}{(\delta I)^2} = \frac{R_{te,\mathrm{A2}}}{\delta I} \tag{7}$$

The uncertainty of $R_{te,\mathrm{A2}}$ is then given by

$$u\{R_{te,\mathrm{A2}}\} \approx \sqrt{\left(u\{V_{te,\mathrm{avg}}\}\right)^2 + \left(u\{\delta I\}\right)^2} = \sqrt{\left(u\{V_{te,\mathrm{avg}}\}\right)^2 + \left(k/2\,u\{I_{r,\mathrm{X}}\}\right)^2} \tag{8}$$

The reciprocal of the factor k is the amplification effect observed above for the resulting uncertainty.

3. Method A.3: Sectioned Track, Line Closed to Traffic

3.1. Method Description and Setup

This method requires the interruption of the longitudinal electrical conductivity of the rails at the two points that define the measured track section of length $L_{t,A3}$. Then, measuring the electrical insulation between a rail segment and the earth is a straightforward volt-amperometric measurement: a voltage V_s is applied between the rail and the earth at one of its ends. The measurement of the flowing current I_s must be accompanied by the measurement of the rail-to-earth voltage, not only at some intermediate preferred position $V_{te,\mathrm{A3}}(\mathrm{P})$ (EN 50122-2 indicates a minimum distance of 50 m from the injection point, but not a maximum one), but also at the opposite end, in order to estimate the voltage drop along the rail or track $V_{te,\mathrm{A3}}(\mathrm{Q})$. The difference between the two voltages is required by EN 50122-2 [29] to be less than 10%, but nothing is said on how to remediate in cases where this requirement is not fulfilled. The effect on the resulting track insulation is discussed below in Section 3.2.

The method could be applied to a single rail or a whole track. The latter is a necessity in the presence of frequent rail-to-rail bonds, including coupling bonds for track circuits that at DC are short-circuit connections as well. The setup is shown in Figure 3 for the measurement of the whole track.

EN 50122-2 proposes a simple relationship, such as

$$R_{te,\mathrm{A3}} = \frac{V_{te,\mathrm{A3}}(\mathrm{P})}{I_s} \tag{9}$$

where L is expressed in km. Again, multiplication by L expressed in km gives the per-unit insulation resistance to compare with the limits.

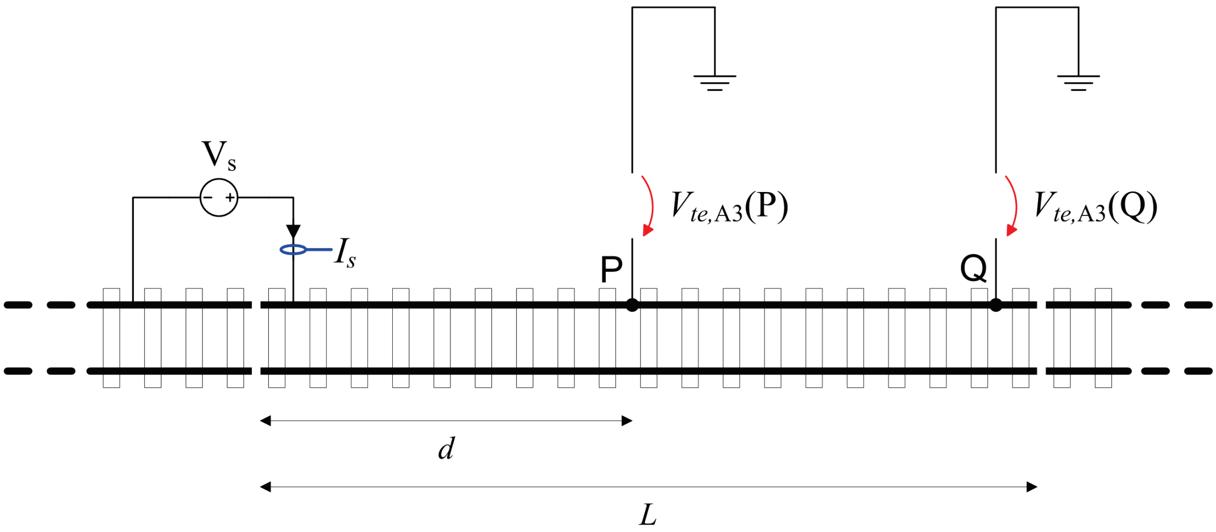

Figure 3. Sketch of the method A.3 setup for a rail insulation measurement: the current measuring circuits in blue, the voltage measuring circuits in red.

This method is more accurate than method A.2, with a minimum number of quantities involved and no need to estimate the current flowing in each rail. Assuming again a test voltage up to 50 V, for rail segments of some hundreds of meters, the flowing test current ranges from some mA up to a fraction of A for the most common track insulation values and can be conveniently measured with an amperometer (multimeter). The method is exposed to some variability as a consequence of variable or not well-specified parameters (earthing resistance of the test supply, distance d of the intermediate voltmetric terminal, overall length of the track section L) that are reviewed in Section 3.3 based on results in [39–41].

3.2. Practical Factors

The earthing of the power supply providing the test voltage V_s and the earth reference for the voltmetric terminals at P and Q can be implemented in various ways based on practical convenience:

- an earth electrode may be used driven into the soil at a convenient distance from the tested track (EN 50122-2 requires 30 m minimum); the reason for such distance is avoiding distortion of the electric field in the soil; the earthing resistance is quite limited anyway, for which, even in good soil, values lower than about 50 Ω are difficult to achieve, so that this earthing system is suitable for the voltmetric terminals, but not for the test supply;
- using the remaining part of the system before the injection point, earthing the test supply with a resistance R_0 usually of some Ω; with systems of limited length or still under construction, instead, R_0 reaches too high values; the influence of this parameter was evaluated in [39] and is considered later in Section 3.3;
- earthed parts, such as cable trays, sharing the earthing resistance of the power distribution system, usually of the order of 1 Ω or less, can be used for both purposes (earthing the power supply and providing a reference for voltmetric measurements);
- the concrete structure supporting the track, if provided with reinforcement, cannot be used, being too close to the track under test.

Since, in many cases, the electrical isolation of the track section is achieved by pre-existing IRJs, choosing a too short section length (with a larger insulation resistance value) exposes the results to the influence of the far-from-ideal isolating performance of the IRJ. For example, a well-insulated system with $R_{te} = 100\,\Omega\text{km}$ amounts to $1\,\text{k}\Omega$ for a section length of 100 m; the measurement could be compromised by an IRJ with insulating resistance of the order of $10\,\text{k}\Omega$ (still barely acceptable in terms of the standard).

3.3. Variability and Uncertainty Analysis

This method, as the most accurate, was assessed for its variability in [39–41].

The test should be performed by measuring V_{te} in on and off conditions, so compensating for pre-existing potentials. It was observed in [39] that practical measurements show a significant rapid decay of the potential during depolarization and that a lack of synchronization of a few seconds could cause a significant error. In fact, EN 50122-2 does not clarify the procedure to adopt to take the off-condition reading: for insulating the rail joint efficiency only, it specifies "directly after the switching off"; however, this does not clarify if we are speaking of a fraction of a second or some seconds. The off potential is supposed to be subtracted from the on reading, aiming at compensating extraneous voltages, but the rapid decay (with a steep slope) implies a significant error for timing errors in the first second or so. A better technique is that of polarity reversal that compensates for offset voltages and other bias voltages.

The effect of rail resistance was also considered on the two terminal voltages $V_{te,\text{A3}}(\text{P})$ and $V_{te,\text{A3}}(\text{Q})$, and on the estimated track insulation. Considering the value of I_s, as determined approximately by $I_s = V_s / R_{te,\text{A3}}$, a worst-case scenario of maximum voltage (50 V) and lowest track insulation ($2\,\Omega/\text{km}$) would bring this to $I_s = 25\,\text{A}/\text{km}$. Recalling the track resistance of the order of $16.5\,\text{m}\Omega/\text{km}$ to $18\,\text{m}\Omega/\text{km}$, this causes a maximum longitudinal voltage drop of $0.45\,\text{V}/\text{km}$, that is less than 1% of the applied voltage. The requirement is, thus, always fulfilled.

The influence of the rail resistance was quantified in [39] by simulation, using an equivalent circuit. The variability in the track-to-earth conductance G_{re} is shown in Figure 4 for a reference case $G^*_{re} = 10\,\text{mS}/\text{km}$, corresponding to $100\,\Omega\text{km}$. The effect of rail resistance and the consequential longitudinal voltage drop is stronger for longer track sections, as expected, as the overall rail resistance is larger and, at the same time, the shunt resistance to earth is smaller. For a track length up to 1 km, the influence of the rail resistance is below 0.5% and can be made smaller by bringing the voltage terminal towards the middle of the section, rather than closer to the injection point.

After the variability sources related to the parameters and setup have been assessed, the uncertainty *per se* of (9) is evaluated straightforwardly by propagation of the uncertainty from the measured quantities for a simple V/I resistance estimate.

$$u\{R_{te,\text{A3}}\} = \sqrt{(u\{V_{te,\text{A3}}(\text{P})\})^2 + (u\{I_s\})^2} \tag{10}$$

The expression indicates a direct dependence on the uncertainty of the voltage and current measurements that are both carried out in ideal conditions, that is, for a conveniently large value, the former, and, with a clamp (or shunt), the latter. Total instrumental uncertainty values as low as 0.5% can be easily attained; overall uncertainty may be estimated to be as low as 1% including variability, as in Figure 4, excluding the problem related to the off-potential. For the off-potential, careful selection of timing is important as the off-potential is not only taken for a large reading as track voltage, but also for the low-value readings of the rail voltage drop where even small errors are relevant (although depolarization in such readings should not take place, but fluctuation does).

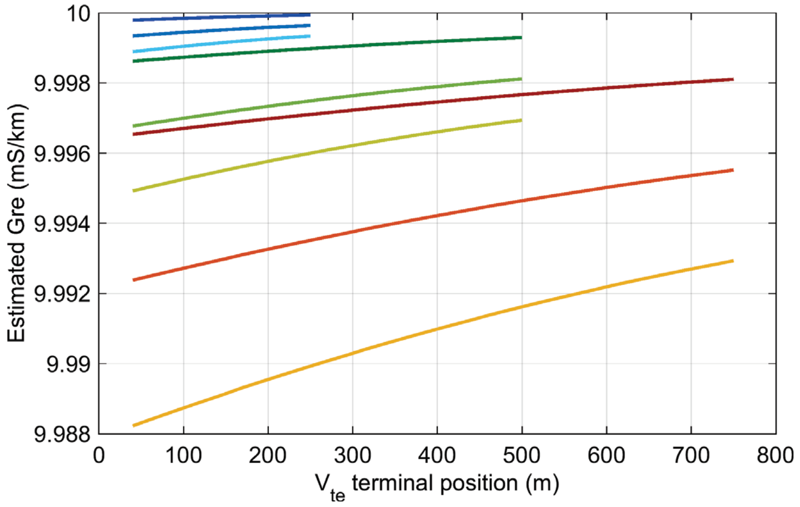

Figure 4. Track insulation G_{re} for different rail resistance values $R_r = 20\,\text{m}\Omega/\text{km}$, $40\,\text{m}\Omega/\text{km}$, $60\,\text{m}\Omega/\text{km}$ (shown from dark to light color) vs. voltmetric terminal position P (varying between 50 m and $L_t/2$ from the injection point). Track section of variable length $L_t = 500\,\text{m}$ (blue), $L_t = 1000\,\text{m}$ (green) and $L_t = 1500\,\text{m}$ (red). Earthing resistance at the injection point $R_0 = 5\,\Omega$. Reference ideal value of rail insulation $G^*_{re} = 10\,\text{mS/km}$.

4. Method A.4: Lateral Potential Gradient in Normal Service

This method exploits the running trains as a source of track potential fluctuations by which to estimate the track-to-earth insulation. The track is in normal condition and does not need any special arrangement; the potential is measured by connecting one conductor not interfering with the dynamic train gabarit (so, with no impact on traffic and safety).

4.1. Method Description and Setup

This method is well-suited for open areas where the track runs at grade without continuous civil structures to use as a potential reference, as may occur in urban and suburban at-grade line sections.

In this case a remote potential reference is taken by means of a vertical electrode driven in the soil and the measurement of the current dispersion and consequential field gradient in the soil is local, not distributed along the track section as we have considered so far for the two previous methods.

The method is described in Figure 5 that provides a sketch of the setup and the most relevant quantities. The setup focuses on a transversal section of the line assumed to be of negligible longitudinal size, but minor contributions from adjacent track sections cannot be ruled out. EN 50122-2 and the technical literature do not provide any indications on this to the authors' knowledge.

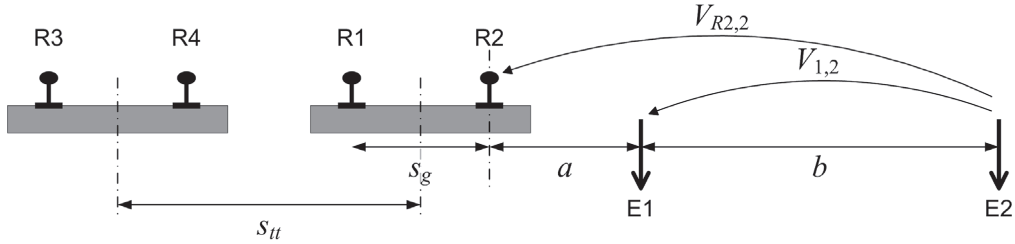

Figure 5. Sketch of the method A.4 setup for a track insulation measurement, showing the double track and the two electrodes (E1 and E2) and related geometrical quantities.

The two rails of an assumed single-track layout are separated by the quantity s (with good approximation corresponding to the track gauge, that is, in reality, measured between the internal edges of the rail heads); the two external electrodes E1 and E2 are located in natural soil at distances a and $a + b$ from the nearest rail, with b being the separation of the two electrodes.

The basic equation for the determination of the track-to-earth conductance G_{TE} is based on the assumption of an inverse dependency with distance for the electric field in the soil.

$$G_{\mathrm{TE,A4}} = \frac{m_{sr}\,\pi\,1000}{\rho[\log(b + 0.5s) - \log(a + 0.5s)]} \tag{11}$$

where m_{sr} is called the "stray current transfer ratio", the factor "1000" adjusts for expressing the conductance per km, and ρ is the soil resistivity expressed in Ωm (discussed below in Section 4.2). The quantity s takes the value of s_g for single-track cases and s_{tt} for double-track cases.

The 2010 version of EN 50122-2 [31] reported two different formulations for the cases of single- and double-track layout, as shown in (12) and (13), respectively, using the notation $G_{\mathrm{TE,A4,1}}$ and $G_{\mathrm{TE,A4,2}}$. The quantities s_g and s_{tt} stand for the track gauge and the inter-track separation (measured from the track axes), respectively. The new 2021 version [29] uses only one Equation (11) and does not make such a distinction, stating simply that, for the single-track case, the quantity $s = s_g$, and, for the double-track case, the overall conductance must be divided by 2, and that the quantity s becomes the inter-track-axes distance s_{tt}.

$$G_{\mathrm{TE,A4,1}} = \frac{m_{sr}\,\pi\,2000}{\rho\left[\log\left(b(b + s_g)\right) - \log\left(a(a + s_g)\right)\right]} \tag{12}$$

$$G_{\mathrm{TE,A4,2}} = \frac{m_{sr}\,\pi\,1000}{\rho\left[\log\left((b + 0.5s_g)(b + 0.5s_g + s_{tt})\right) - \log\left((a + 0.5s_g)(a + 0.5s_g + s_{tt})\right)\right]} \tag{13}$$

The numerical difference between this different formulation of the two versions of the standard is considered below in Section 4.3.

The quantity m_{sr} is stated in the standard to be determined as the linear regression of the "rail potential gradient", as if there is a derivative operation involved. In reality, this point is not explained well, with confusion between small letters and big letters for the same quantities and the introduction of a "delta" symbol that is not then supported by any equation nor appears in the figures.

Simply, m_{sr} is the angular coefficient of the linear regression of the collected rail potentials $V_{R2,2}$ vs. the inter-electrode potentials $V_{1,2}$, using electrode E2 as reference.

The estimate must be carried out with a significant number of well-distributed samples, to avoid ill-conditioning of the linear regression estimate: in other words, a short time record with all potential readings having similar values causes indeterminacy, whereas a longer record with several train passages creates an elongated cloud of points that provides a more robust estimate.

4.2. Practical Factors

This method is suitable for at grade scenarios, in particular, in suburban contexts, but requires free space laterally to the track of minimum 80 m (as per the recent 2022 version of EN 50122-2, but only 30 m in the older 2010 version that was more manageable).

In addition, access to natural soil near the track to place the first electrode is also necessary. This distance a has no minimum specification, but the standard warns that such electrodes should be far away from pits and other metallic parts near the track that could distort the field; practically speaking, as tramway and light railway tracks often run in parallel to suburban roads, such a distance is limited to a few meters maximum or, skipping the road width, is of the order of 5 m to 10 m.

The typical context, however, includes a problem of coordination with road traffic and interference with private property (e.g., accessible soil may be located in private gardens or access granted passing through private property). The method is minimally invasive, in that it requires digging a vertical electrode of small dimensions (e.g., 0.5 m) and passing of a couple of electric wires of small cross-section (e.g., 1.5 mm^2 for mechanical robustness).

Practical constraints as well, such as the presence of a road, a park area with asphalt, or a building, may prevent access to natural soil, and, thus, require deviation from the preferred reference values for a and b, so that knowledge of the tolerances and sensitivity of results to such changes is needed. This is verified in Section 4.3.

Soil resistivity values must be determined by a separate measurement using a four-electrode method [42]. The problems related to this quantity are many:

- accessibility of the area to place the test electrodes in a line, as prescribed by the Wenner method (four electrodes in a line, with external ones for the test current I_t and the inner ones for the voltage reading V_t, spaced by s); the resulting apparent soil resistivity value can be calculated from the resistance reading $R = V_t/I_t$ as $\rho = 2\pi sR$; the resistivity value refers to the depth s, so that, to double the probed depth, the electrodes span is doubled as well;
- often, the Schlumberger method is used instead, because it requires the movement of two electrodes only, keeping the inner ones for voltage more compact; keeping their separation s and calling p the separation between each external one and the nearest voltage electrode (with $p > 2s$), the resistivity may be estimated again from the calculated resistance value as $\rho = \pi p(p+s)/sR$ and the depth is $p + s/2$, deeper than the previous one; in other words, for a given target depth, the Schlumberger method is more compact and faster;
- specifically focusing on the track geometry and roads nearby, keeping s of the order of 1 m to 2 m, the separation p may increase to what is allowed by the areas nearby (e.g., 5 m to 20 m); the depth values to focus on are in this range and they should be supported by a careful analysis of the resistivity values behavior to determine abnormal distributions and lack of homogeneity;
- it is, in fact, observed that interference by other metallic/conductive buried structures is almost certain in an urban/suburban context and larger volumes of soil (going deeper) help to average the contributions.

4.3. Variability and Uncertainty Analysis

The variability and uncertainty issues of the method are considered from three standpoints:

- first, a practical example of an extensive test campaign carried out along a tramway line is considered in order to focus on data dispersion, determination of the linear regression slope m_{sr}, etc.; the results are reported in the next Section 4.4 for consistency with previous sections;
- then, formulations are analyzed for sensitivity to the parameters and to robustness to extreme situations caused by practical issues, such as issues in placing electrodes;
- last, propagation of uncertainty is calculated using the given formulations, having already evaluated the behavior for uncommon values of parameters.

The determination of m_{sr} is quite robust to outliers and even to a small fraction of corrupted data, provided that the recording is long enough to have a statistically significant set of good cases representing the typical dynamics of the system. As a rule of thumb, we have, in the past, used multiples of the headway time that each correspondto single tram/train passages. Deviations are possible, but, for the purpose of the determination of m_{sr}, they are not relevant, unless where two trams/trains pass in front of the electrodes almost at the same time. In this case, repeated occurrences are necessary so that the recording lengths of some hours are suitable. In the examples shown in the next section, the number of samples was cut to two hours. The sampling time is not of such importance, and the 2 Hz sampling time suggested by EN 50122-2 for stray current monitoring could be used.

EN 50122-2 has changed the two separate formulas of the 2010 version, adopting a unique formulation for both single- and double-track configurations, as introduced in

Section 4.1. Figure 6 reports a comparison between formulas for single- and a double-track configurations, having fixed the inter-track separation $s_{tt} = s_g + 2\,\mathrm{m}$, with $s_g = 1.5\,\mathrm{m}$.

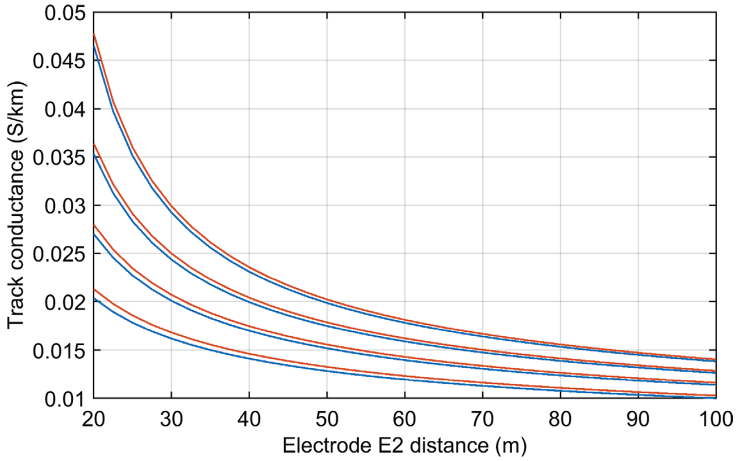

(**a**)

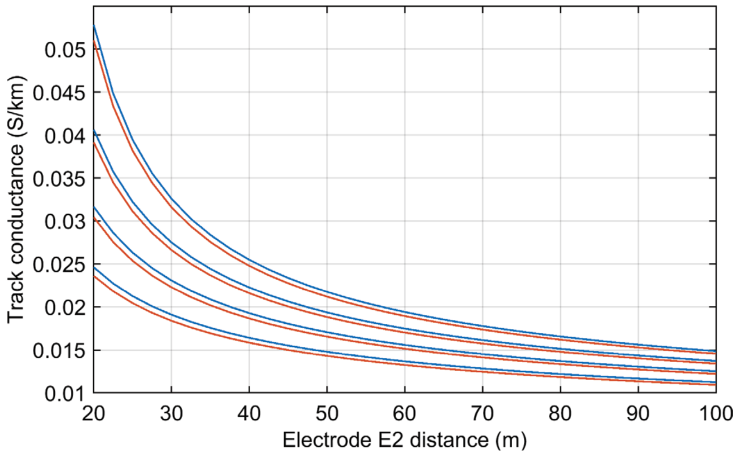

(**b**)

Figure 6. Comparison of method A4 formulas of track-to-earth conductance given in EN 50122-2 versions 2010 (blue) and 2022 (light brown): (**a**) single-track case, (**b**) double-track case. The reference parameters are: $\rho = 50\,\Omega\mathrm{m}$, $m_{sr} = 0.001$, $s_g = 1.5\,\mathrm{m}$ and $s_{tt} = s_g + 2\,\mathrm{m}$. The difference between curves is of the order of 10% to 18% for the various a values.

Considering (11), the propagation of uncertainty is operated using partial derivatives, but focusing on the quantities that are subject to the largest uncertainty (m_{sr} and ρ) as the geometrical quantities a, b and s can be measured with high accuracy. Their uncertainty, in fact, is much less than 1% as a and b have errors lower than 1 cm over several meters and s is almost "exact" for mechanical and safety reasons (the rail gauge is periodically checked to be 1.435 m between the internal edges; the inter-track gap is also stable and constant as the track was positioned with accuracy of the order of mm).

$$\mathrm{var}[G_{TE}] \approx \sqrt{\left(\frac{\partial G_{TE}}{\partial m_{sr}}\right)^2 \mathrm{var}[m_{sr}] + \left(\frac{\partial G_{TE}}{\partial \rho}\right)^2 \mathrm{var}[\rho]} \tag{14}$$

The two terms then correspond to:

$$\frac{\partial G_{TE}}{\partial m_{sr}} = \frac{\pi\, 1000}{\rho[\log(b+0.5s) - \log(a+0.5s)]} = \frac{G_{TE}}{m_{sr}} \tag{15}$$

$$\frac{\partial G_{TE}}{\partial \rho} = -\frac{m_{sr}\,\pi\,1000}{[\log(b+0.5s)-\log(a+0.5s)]}\,\frac{1}{\rho^2} = \frac{G_{TE}}{\rho} \tag{16}$$

The uncertainty after normalization by G_{TE}^2 is then, as expected,

$$u\{G_{TE}\} \approx \sqrt{(u\{m_{sr}\})^2 + (u\{\rho\})^2} \tag{17}$$

Evaluating the basic uncertainty of the two quantities m_{sr} and ρ is a complex task:

- For m_{sr}, it is a matter of propagating the uncertainty of $V_{R2,2}$ and $V_{1,2}$ through the least mean square (LMS) regression, as performed in [43] for the determination of stray capacitance (as the intercept and not the slope, as in the present case).
- For ρ, it is not a matter of uncertainty alone: the measurement itself is carried out by automatic volt-amperometric measurements at undisturbed frequencies, and the calibration with reference resistors indicates an instrumental uncertainty of the order of 1% to 2%, depending on the resistance values. The variability in the soil resistivity instead should be accounted for depending on the location, depth and environmental/seasonal conditions. The latter may be ruled out if the soil resistivity is measured immediately before (or after) the track measurements. The former can be accounted for by repeated measurements and then taking a weighted average as the ρ value and their dispersion as a Type A estimate of their uncertainty.

4.4. Application to a Tramway System

Method A.4 has been successfully applied to a new freshly commissioned tramway for urban sections with embedded rail that were, nevertheless, characterized by a large amount of green areas nearby (and access to natural soil). Other sections near the end of the line were instead tested during construction with method A.3, as the running rails were still not welded at several points. For the last portion of the line near the port with no access to public soil, the method A.2 was used instead over short time intervals during the day with suspension of the trial service.

Method A.4 brought with it information on track voltage values as added value. The results shown in Figure 7 report the voltages of the track and electrode E1 with respect to electrode E2 on the left and the estimated angular coefficient (stray current ratio m_{sr}) by linear regression on the right, providing a graphical representation of the dispersion of the data points. The orange line is the LMS regression line whose angular coefficient corresponds to m_{sr}: the plot of the three locations at the same vertical scale (although the $V_{R2,2}$ potential was much different), aids appreciation of the change in slope between locations due to the different values of a and b, reflecting the practical constraints of soil accessibility.

Table 2 then reports the numeric values of the estimated track conductance G_{TE} and coefficient m_{sr}, together with the parameters of the geometry (namely, the electrode positions) and soil resistivity.

The resulting G_{TE} values are quite compact, with a 4:1 proportion between the two extreme values; for an embedded track in north European climate conditions, they are quite satisfactory, being an order of magnitude below the EN 50122-2 limit of 2 S/km (embedded tramway track).

Table 2. Worked out method A4 on three locations of the same tramway system: geometry parameters and main results.

Location	ρ (Ω m)	a (m)	b (m)	s_g (m)	s_{tt} (m)	m_{sr}	G_{TE} (S km)
1	17.1	11.1	37.8	1.5	6.7	0.000605	0.0436
2	19.8	14.2	46.2	1.5	3.7	0.0026	0.1525
3	38.6	8.6	45.7	1.5	3.9	0.0038	0.0949

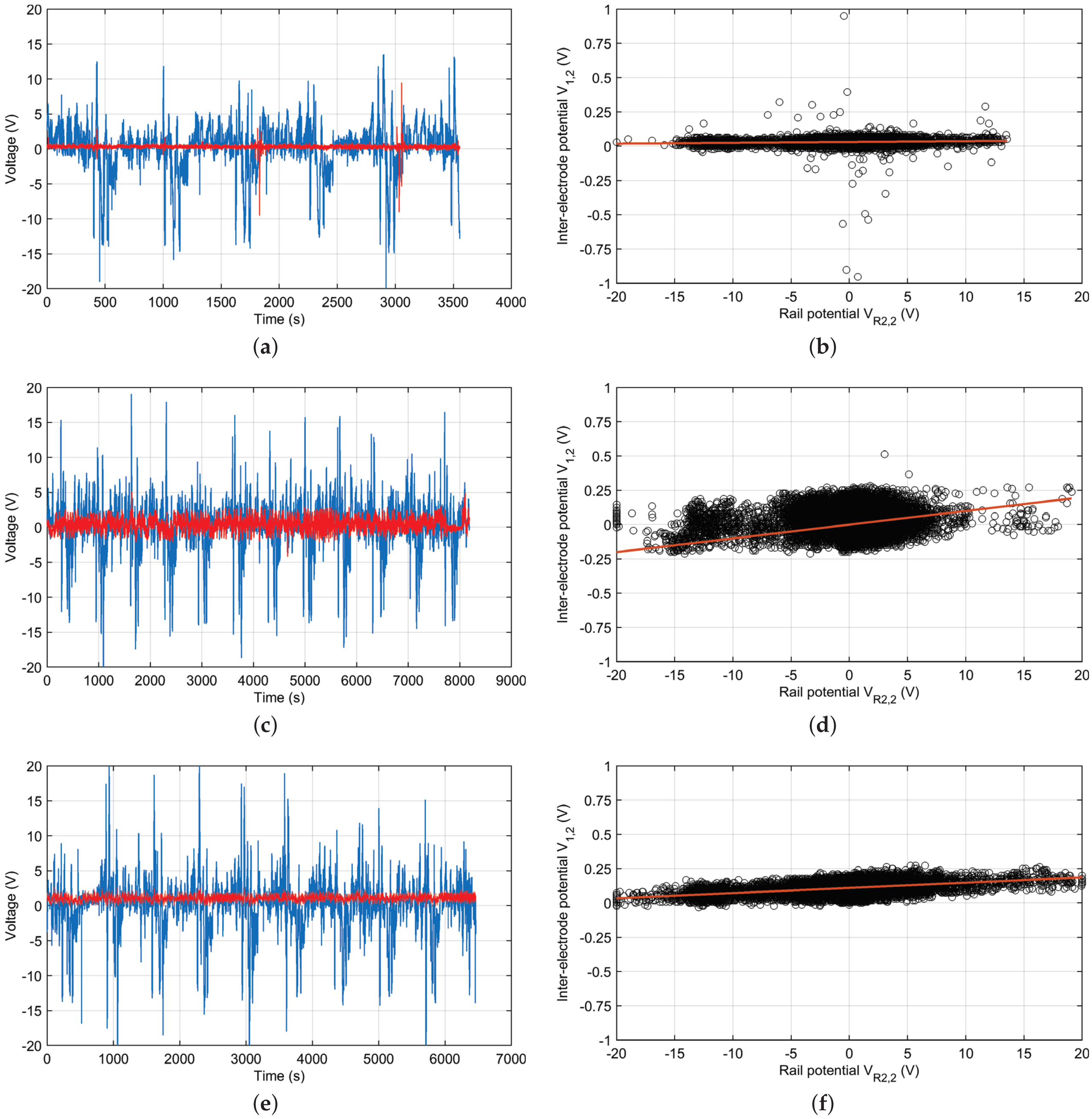

Figure 7. Results of method A.4 measurements for three positions along a tramway route in an urban context: (**a**,**c**,**e**) voltages of the track and electrode E1 with respect to electrode E2, in blue and red respectively; (**b**,**d**,**f**) estimated angular coefficient (stray current ratio m_{sr}) by linear regression (black circles are original samples, the orange line is the resulting linear regression).

5. Discussion and Conclusions

This work has considered the three methods for track insulation measurement, standardized by EN 50122-2 (or IEC 62128-2). Each method has advantages and disadvantages from a system-level perspective: method A.3 requiring the electrical interruption of the running rails, in contrast to method A.2; in addition, method A.4 not only uses the track unaltered, but exploits the normal traffic as a driving signal, and is, thus, compatible with commercial service hours, in contrast to methods A.2 and A.3 that necessitate a free line and, thus, are applicable during construction or engineering hours.

In further detail, each method is based on a certain number of electrical quantities and is characterized by some level of complexity. Method A.3 is the least complex, related directly to the definition of track insulation resistance, and involves a simple volt-amperometric measurement of the track-to-earth resistance, measuring the track (or rail) voltage at an intermediate point at some distance away from the point of application of the test voltage. The uncertainty is minimal (one voltage and one current measurement), but there exists a, albeit small, variability vs. the earthing resistance of the test supply and vs. the positioning of the voltage terminal. The other two methods are, however, less invasive, not necessitating the physical sectioning of the running rails and, for method A.4, being compatible with normal traffic.

An acceptable uncertainty for track insulation assessment is never clearly made explicit in the standards and contractual specifications. Considering all the sources of variability and instrumental uncertainty, a 10% to 20% standard uncertainty level may be acceptable.

The variability and uncertainty of the methods cannot be thought of as separate, as many parameters that implicitly or explicitly are part of the track insulation equation are determined with high uncertainty (e.g., soil resistivity), are subject to change (e.g., with temperature, on a seasonal basis, etc.), or are not sufficiently constrained and depend somewhat on the operator's choice (position of the voltage terminal, distance of the electrodes from the track, etc.). In other words, instrumental uncertainty is often a factor of lesser importance, except when the rail current is determined by voltage drop measurements (that is, the most uncertain measurement method). In this case, it was shown in Table 1 that multimeters, in general, may perform poorly if not specifically designed for such a task, e.g., mV scale reading. The accuracy of method A.2, that relies heavily on two or four rail current measurements, is, thus, significantly affected: the track length is, thus, subject to an additional constraint of minimum length to allow for a current leakage estimate with sufficient accuracy (a); such minimum length is discussed and found to be in the range of some hundreds m to 1 km, depending on the track insulation level.

Having assessed the metrological characteristics of such methods, together with other characteristics (such as the impact on system operation and the complexity of the setup), the conclusion is that methods that do not require rail sectioning should be preferred, despite their lower accuracy (including variability and uncertainty). So, research effort should be in the direction of improving repeatability and uncertainty, and, in particular, the development of methods with better spatial resolution: method A.2, in fact, is subject to the identified minimum track length requirement to preserve a minimum acceptable uncertainty level, whereas method A.4 has no clear relationship with the portion of track included in the so-determined track insulation value.

Another specific research direction is the improvement of rail current measurement, avoiding the use of the rail voltage drop, providing an immediate benefit for method A.2 in terms of uncertainty: current sensors able to measure rail current are, unfortunately, of the AC type (such as Rogowski coils and close-up magnetic sensors), so that a study should be carried out of the equivalence of DC and AC measurements, with the aim of track insulation determination for stray current assessment.

Finally, method A.4 is very promising for measurements on existing systems under normal traffic conditions (so, under real exploitation conditions) and should be further investigated in terms of the effect of the influence of buried conductive parts and the behavior of the electric field in the soil with respect to soil inhomogeneity, and, as a consequence, the required resolution and extent of soil resistivity mapping.

Author Contributions: Conceptualization, J.B. and A.M.; methodology, S.B. and J.B.; software, S.B. and J.B.; formal analysis, A.M.; writing—original draft preparation, A.M.; writing—review and editing, S.B., J.B. and A.M.; supervision, A.M. All authors have read and agreed to the published version of the manuscript.

Funding: This research received no external funding.

Institutional Review Board Statement: Not applicable.

Informed Consent Statement: Not applicable.

Data Availability Statement: The data presented in this study are available on request from the corresponding author. The data are not publicly available due to confidentiality of method A.4 tests carried out in a specific project.

Conflicts of Interest: The authors declare no conflict of interest.

References

1. Vranešić, K.; Lakušić, S.; Serdar, M. Corrosion and stray currents at urban track infrastructure. *J. Croat. Assoc. Civ. Eng.* **2020**, *72*, 593–606. [CrossRef]
2. Xu, W.; Zhang, B.; Deng, Y.; Wang, Z.; Jiang, Q.; Yang, L.; Zhang, J. Corrosion of rail tracks and their protection. *Corros. Rev.* **2020**, *39*, 1–13. [CrossRef]
3. Vranešić, K.; Lakušić, S.; Serdar, M. Influence of Stray Current on Fastening System Components in Urban Railway Tracks. *Appl. Sci.* **2023**, *13*, 5757. [CrossRef]
4. Mariscotti, A. Electrical Safety and Stray Current Protection With Platform Screen Doors in DC Rapid Transit. *IEEE Trans. Transp. Electrif.* **2021**, *7*, 1724–1732. [CrossRef]
5. Jin, H.; Yu, S. Effect of DC stray current on rebar corrosion in cracked segment of shield tunnel. *Constr. Build. Mater.* **2021**, *272*, 121646. [CrossRef]
6. Ai, H.; Li, G.; Wang, B.; Panesar, D.K.; He, X. Degradation mechanism of cement-based materials under the effects of stray current, chloride and sulfate. *Eng. Fail. Anal.* **2022**, *142*, 106746. [CrossRef]
7. Qian, S.; Cheng, Y.F. Accelerated corrosion of pipeline steel and reduced cathodic protection effectiveness under direct current interference. *Constr. Build. Mater.* **2017**, *148*, 675–685. [CrossRef]
8. Mujezinović, A.; Martinez, S.; Kekez, K. Estimating harmful effect of dynamic stray currents on pipeline by simultaneous multiparametric field measurements, continuous wavelet cross-correlation analysis, and frequency plots. *Mater. Corros.* **2018**, *70*, 357–365. [CrossRef]
9. Szymenderski, J.; Machczyński, W.; Budnik, K. Modeling Effects of Stochastic Stray Currents from D.C. Traction on Corrosion Hazard of Buried Pipelines. *Energies* **2019**, *12*, 4570. [CrossRef]
10. Yu, K.; Ni, Y.; Zeng, X.; Peng, P.; Fan, X.; Leng, Y. Modeling and Analysis of Transformer DC Bias Current Caused by Metro Stray Current. *IEEJ Trans. Electr. Electron. Eng.* **2020**, *15*, 1507–1519. [CrossRef]
11. Du, L.; Chang, S.; Wang, S. The Research on DC Loop of Regional Power Grid Caused by the Operation of the Subway. *Electronics* **2020**, *9*, 613. [CrossRef]
12. Li, C.; Du, Q.; Guo, Y.; Liu, Y.; Yang, F.; Chen, L.; Zhang, X.; Huang, G.; Gao, G.; Wu, G. Modeling of Stray Currents From Metro Intruding Into Power System Considering the Complex Geological Conditions in Modern Megacities. *IEEE Trans. Transp. Electrif.* **2023**, *9*, 1653–1663. [CrossRef]
13. Isozaki, H.; Oosawa, J.; Kawano, Y.; Hirasawa, R.; Kubota, S.; Konishi, S. Measures Against Electrolytic Rail Corrosion in Tokyo Metro Subway Tunnels. *Procedia Eng.* **2016**, *165*, 583–592. [CrossRef]
14. Vranešić, K.; Serdar, M.; Lakušić, S.; Kolář, V.; Mariscotti, A. Dynamic Stray Current Measuring Methods in Urban Areas. *Balt. J. Road Bridge Eng.* **2022**, *17*, 146–170. [CrossRef]
15. Regula, M.; Siranec, M.; Otcenasova, A.; Hoger, M. Possibilities of the stray current measurement and corrosive risk evaluation. *Electr. Eng.* **2022**, *104*, 2497–2513. [CrossRef]
16. Fichera, F.; Mariscotti, A.; Ogunsola, A. Evaluating stray current from DC electrified transit systems with lumped parameter and multi-layer soil models. In Proceedings of the Eurocon 2013, Zagreb, Croatia, 1–4 July 2013 ; IEEE: Piscataway, NJ, USA, 2013. [CrossRef]
17. Wang, C.; Li, W.; Wang, Y.; Xu, S.; Li, K. Evaluation Model for the Scope of DC Interference Generated by Stray Currents in Light Rail Systems. *Energies* **2019**, *12*, 746. [CrossRef]
18. Bhagat, S.; Yang, X.; Wang, M.; Mariscotti, A. Review and Evaluation of Stray Current Mitigation for Urban Rail Transit. *Diangong Jishu Xuebao/Trans. China Electrotech. Soc.* **2021**, *36*, 4851—4863. [CrossRef]
19. Zhou, Q.; Lin, S.; Lin, X.; Wang, A. A Uniform Model for Stray Current of Long-Line DC Metro Systems. *IEEE Trans. Transp. Electrif.* **2022**, *8*, 2915–2927. [CrossRef]
20. Du, G.; Zheng, Z.; Li, Q.; Xu, F.; Zhang, T.; Zhang, D.; Zhang, X.; Huang, W. Multi-state unified calculation model of rail potential and stray current in DC railway systems. *IET Electr. Syst. Transp.* **2023**, *13*, e12070. [CrossRef]
21. Bahra, K.; Catlow, R.E. Control of Stray Currents for DC Traction Systems. In Proceedings of the International Conference on Electric Railways in a United Europe, Amsterdam, The Netherlands, 27–30 March 1995; pp. 136–142.
22. Liu, W.; Li, T.; Jie, Z.; Weiguo, P.; Yichen, Y. Evaluation of the Effect of Stray Current Collection System in DC-Electrified Railway System. *IEEE Trans. Veh. Technol.* **2021**, *70*, 6542–6553. [CrossRef]
23. Juybari, E.Z.; Keypour, R.; Niasati, M. Voltage distribution indices method to analyse the performance of various structures of stray current collectors in direct current transit lines. *IET Electr. Syst. Transp.* **2021**, *11*, 322–332. [CrossRef]
24. Kampeerawat, W.; Jongudomkarn, J.; Kirawanich, P.; Sumpavakup, C. Effect of Voltage Limiting Device Operation on Rail Potential and Stray Current in DC Railway Systems. *GMSARN Int. J.* **2023**, *17*, 213–219.

25. Gu, J.; Yang, X.; Zheng, T.Q.; Xia, X.; Zhao, Z.; Chen, M. Rail Potential and Stray Current Mitigation for Urban Rail Transit With Multiple Trains Under Multiple Conditions. *IEEE Trans. Transp. Electrif.* **2022**, *8*, 1684–1694. [CrossRef]
26. Wei, L.; Jie, Z.; Tian, L.; Siwen, L.; Long, Y. The Influence of Drainage Device on Stray Current Distribution in DC Traction Power Supply System. *Trans. China Electrotech. Soc.* **2022**, *37*, 4565–4574. [CrossRef]
27. Peng, P.; Zeng, X.; Leng, Y.; Yu, K.; Ni, Y. A New On-line Monitoring Method for Stray Current of DC Metro System. *IEEJ Trans. Electr. Electron. Eng.* **2020**, *15*, 1482–1492. [CrossRef]
28. Mariscotti, A. Stray Current Protection and Monitoring Systems: Characteristic Quantities, Assessment of Performance and Verification. *Sensors* **2020**, *20*, 6610. [CrossRef]
29. *EN 50122-2:2022*; Railway Applications—Fixed Installations—Electrical Safety, Earthing and the Return Circuit. Part 2: Provisions against the Effects of Stray Currents Caused by DC Traction Systems. CENELEC: Brussels, Belgium, 2022.
30. *IEC 62128-2*; Railway Applications—Fixed Installations—Electrical Safety, Earthing and the Return Circuit. Part 2: Provisions against the Effects of Stray Currents Caused by DC Traction Systems. IEC: Geneva, Switzerland, 2013.
31. *EN 50122-2:2010*; Railway Applications—Fixed Installations—Electrical Safety, Earthing and the Return Circuit. Part 2: Provisions against the Effects of Stray Currents Caused by DC Traction Systems. CENELEC: Brussels, Belgium, 2010.
32. Mariscotti, A. Impact of rail impedance intrinsic variability on railway system operation, EMC and safety. *Int. J. Electr. Comput. Eng. (IJECE)* **2021**, *11*, 17. [CrossRef]
33. Mariscotti, A.; Pozzobon, P. Measurement of the internal impedance of traction rails at 50 Hz. *IEEE Trans. Instrum. Meas.* **2000**, *49*, 294–299. [CrossRef]
34. Mariscotti, A.; Pozzobon, P. Resistance and Internal Inductance of Traction Rails at Power Frequency: A Survey. *IEEE Trans. Veh. Technol.* **2004**, *53*, 1069–1075. [CrossRef]
35. Mariscotti, A.; Pozzobon, P. Determination of the Electrical Parameters of Railway Traction Lines: Calculation, Measurement, and Reference Data. *IEEE Trans. Power Deliv.* **2004**, *19*, 1538–1546. [CrossRef]
36. Mariscotti, A. Rail Current Measurement With Noninvasive Large Dynamic Probe. *IEEE Trans. Instrum. Meas.* **2009**, *58*, 1610–1616. [CrossRef]
37. Rienzo, L.D.; Li, D.; Pignari, S.A.; Fedeli, E. Array of rectilinear solenoids for rail current measurement. In Proceedings of the International Symposium on Electromagnetic Compatibility-EMC EUROPE, Rome, Italy, 17–21 September 2012; IEEE: Piscataway, NJ, USA, 2012. [CrossRef]
38. Xu, X.; Chen, H.; Liu, T.; Zhu, M.; Wang, J. On-Line Detection of Railway Power Frequency Current Based on Tunnel Magnetoresistance. *IEEE Trans. Instrum. Meas.* **2023**, *72*, 1–9. [CrossRef]
39. Bongiorno, J.; Mariscotti, A. Accuracy of railway track conductance and joint efficiency measurement methods. *ACTA IMEKO* **2015**, *4*, 82. [CrossRef]
40. Bongiorno, J.; Gianoglio, C. Experimental variability of track to ground conductance measurements. *J. Phys. Conf. Ser.* **2018**, *1065*, 052015. [CrossRef]
41. Bongiorno, J.; Mariscotti, A. Variability of measured railway track conductance due to test set-up. *ACTA IMEKO* **2019**, *7*, 21. [CrossRef]
42. *IEEE Std. 81-2012*; IEEE Guide for Measuring Earth Resistivity, Ground Impedance, and Earth Surface Potentials of a Grounding System. IEEE: Piscataway, NJ, USA, 2012.
43. Mariscotti, A. Measuring the Stray Capacitance of Solenoids with a Transmitting and a Receiving Coil. *Metrol. Meas. Syst.* **2011**, *18*, 47–56. [CrossRef]

sustainability

MDPI

Article

A Data-Driven Comprehensive Battery SOH Evaluation and Prediction Method Based on Improved CRITIC-GRA and Att-BiGRU

Peng Liu [1], Cheng Liu [1], Zhenpo Wang [1], Qiushi Wang [1,*], Jinlei Han [2] and Yapeng Zhou [3]

[1] National Engineering Research Center of Electric Vehicles, School of Mechanical Engineering, Beijing Institute of Technology, Beijing 100081, China; bitliupeng@bit.edu.cn (P.L.); liucheng981127@163.com (C.L.)
[2] Fawer Smarter Energy Technology Company Limited, Jilin 130062, China; hanjinlei@fawer.com.cn
[3] China Merchants Testing Vehicle Technology Research Institute Co., Ltd., Chongqing 401329, China; peng66886688@163.com
* Correspondence: wangqiushi@bit.edu.cn

Abstract: The state-of-health (SOH) of lithium-ion batteries has a significant impact on the safety and reliability of electric vehicles. However, existing research on battery SOH estimation mainly relies on laboratory battery data and does not take into account the multi-faceted nature of battery aging, which limits the comprehensive and effective evaluation and prediction of battery health in real-world applications. To address these limitations, this study utilizes real electric vehicle operational data to propose a comprehensive battery health evaluation indicator and a deep learning predictive model. In this study, the battery capacity, ohmic resistance, and maximum output power were initially extracted as individual health indicators from actual vehicle operation data. Subsequently, a methodology that combines the improved criteria importance through inter-criteria correlation (CRITIC) weighting method with the grey relational analysis (GRA) method is employed to construct the comprehensive battery health evaluation indicator. Finally, a prediction model based on the attention mechanism and the bidirectional gated recurrent unit (Att-BiGRU) is proposed to forecast the comprehensive evaluation indicator. Experimental results using real-world vehicle data demonstrate that the proposed comprehensive health indicator can provide a thorough representation of the battery health state. Furthermore, the Att-BiGRU prediction model outperforms traditional machine learning models in terms of prediction accuracy.

Keywords: lithium-ion batteries; health estimation; comprehensive evaluation; deep learning

1. Introduction

In response to global climate change, the energy crisis, and the pursuit of low-carbon goals, the development of electric vehicles has become an inevitable trend in the global automotive industry [1–4]. With the advent of vehicle electrification, the driving range and safety of electric vehicles have become major concerns. Lithium-ion batteries (LIBs), responsible for energy storage and supply, are core components of electric vehicles, and their performance and health state have significant impacts on the reliability and safety of electric vehicles [5–7]. Although LIBs have long lifespans, they experience varying degrees of aging and degradation with increasing usage time and cycles [8–10]. Therefore, accurately assessing and predicting the state-of-health (SOH) of batteries has become a research hotspot.

Currently, the SOH of LIBs is mainly represented by single features, which can be classified into capacity-based methods, internal resistance-based methods, and power-based methods [11]. The capacity-based method represents SOH by the ratio of the current capacity to the initial capacity of the battery. The internal resistance-based method reflects battery health by measuring the growth rate of the battery's ohmic resistance. The power-based method characterizes battery health by assessing the power state during charge and discharge at specific state-of-charge (SOC) levels [12,13].

Methods for estimating battery SOH can be categorized into experimental methods, model-based methods, and data-driven methods [14,15]. Experimental methods involve testing batteries under controlled laboratory conditions, but they have limitations such as long testing cycles and differences between laboratory conditions and real-world operating conditions, making them unsuitable for online estimation of SOH in real-world vehicle applications [16]. Model-based methods rely on mathematical models, electrochemical models, or equivalent circuit models to simulate the dynamic response characteristics of batteries and identify battery parameters for health estimation [17–19]. However, model-based methods struggle to accurately simulate the internal working characteristics of batteries, which limits their accuracy and practicality for real-world battery systems. In contrast, data-driven methods extract battery health feature parameters directly from large amounts of data without the need for a detailed understanding of battery chemistry. These methods then establish a mapping relationship between the extracted features and SOH through model training to achieve health state estimation [20,21]. For instance, Lin et al. constructed an SOH estimator using an explainable boosting machine based on the Oxford dataset by extracting features such as internal resistance and thermal–electric coupling [22]. Xiong et al. proposed a feature extraction method that combines multiple algorithms to extract the most relevant features from different voltage ranges using laboratory battery aging data, and a machine learning algorithm was used to estimate SOH [23]. Tian et al. proposed an SOH prediction model based on an end-to-end deep convolutional neural network, which used short-time charging features extracted from small windows and directly mapped battery capacity [24]. These data-driven methods have shown promising prediction performance for battery SOH.

However, several challenges still exist for battery SOH evaluation and prediction for real-world electric vehicles. First, battery ageing is a comprehensive process with manifestations in many aspects, existing SOH representation methods for batteries that consider only a single factor fail to comprehensively evaluate the various aspects of battery performance, which do not meet the practical requirements of electric vehicle applications. Furthermore, there are no effective weighing methods proposed for battery multi-parameter health indicator evaluation, which is imperative for scoring the overall battery performance and remaining value. Lastly, most of these methods are established under well-controlled laboratory conditions that are quite different from the time-varying EV operating conditions, which raises concerns about their performance for real-world battery SOH estimation.

To address the above issues, this paper proposes a comprehensive evaluation and prediction method for battery health based on real-world vehicle data. The main contributions of the paper are as follows:

(1) Based on the characteristics of real-world EV data, basic health indicators including capacity, ohmic resistance, and maximum output power are extracted using specific methods suitable for EV application scenarios.
(2) An improved criteria importance through the inter-criteria correlation (CRITIC) weighting method is introduced in order to obtain objective weights for three typical battery health indicators. These weights are then combined with the grey relational analysis (GRA) method to construct a comprehensive evaluation indicator for battery health.
(3) Leveraging the advantages of bidirectional gated recurrent unit (BiGRU) and attention mechanism, an Att-BiGRU deep learning model is developed to predict the comprehensive health state of batteries.

The overall research framework of this paper is shown in Figure 1. The remainder of this paper is organized as follows: Section 2 describes the data used in this study and the methods for extracting health indicators. Section 3 presents the calculation method for the comprehensive battery health indicator and introduces the developed Att-BiGRU prediction model. Section 4 validates the effectiveness and accuracy of the proposed methods. Finally, Section 5 concludes the paper.

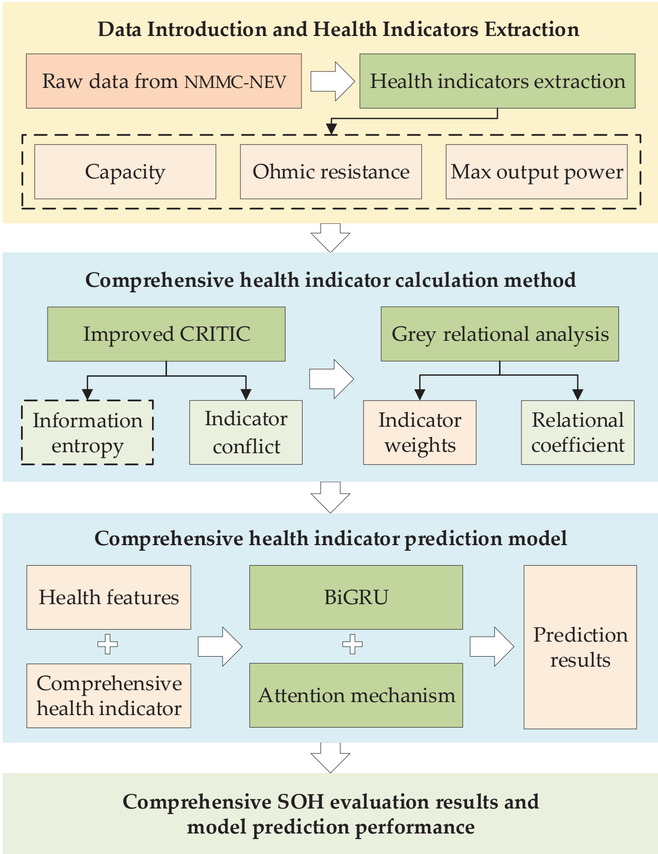

Figure 1. The overall research framework of the study.

2. Data Introduction and Health Indicators Extraction

2.1. Data Introduction

The data used in this study are collected from the open lab of the National Monitoring and Management Center for New Energy Vehicles (NMMC-NEV), which records the actual operating data of over 10 million new energy vehicles. The platform provides real-time data including time, vehicle speed, cumulative mileage, total voltage, total current, SOC, temperature, and other variables. The sampling frequency of these data is 0.1 Hz, which can accurately reflect the vehicle and battery states.

Due to their regular driving patterns and long travel distances, electric buses are suitable for analyzing battery health. Therefore, this study selects multiple electric buses of a certain model from the NMMC-NEV, with each bus having an accumulated mileage exceeding 150,000 km. The specifications of the selected vehicles are presented in Table 1. The selected vehicles were put into operation in Guangdong and Liaoning provinces in May 2017. To ensure the amount of data, the actual operating data of the selected vehicles from May 2017 to May 2021 are used to conduct a comprehensive health evaluation and prediction study in this article. Data preprocessing methods such as data smoothing, and data interpolating are implemented to clean the dataset, which is a crucial preliminary for ensuring the quality of the dataset.

Table 1. The specifications of the selected vehicles.

Parameter	Value
Cathode material	$LiFePO_4$
Battery capacity	240 Ah
Driving range	300 km
Motor power	100 kW
Curb weight	8500 kg

2.2. Extraction of Health Representation Indicators

Through the analysis in Section 1, we know that capacity, internal resistance, and power are commonly used battery health evaluation indicators in previous studies. Therefore, in this section, we select these three single indicators as the basic indicators for comprehensive battery health evaluation. The specific extraction methods of different indicators are as follows.

2.2.1. Capacity

In the actual operation of electric vehicles, it is rare to have complete charge and discharge cycles, making it difficult to calculate the actual capacity of the battery. To ensure an adequate sample size and the effectiveness of capacity analysis, this study characterizes the battery's capacity degradation by calculating the regional charging capacity within a certain SOC interval, as described in [25]. As shown in Figure 2, the fitted curve indicates that the regional capacity of the battery gradually decreases with increasing cumulative mileage, indicating a decline in the actual capacity of the battery. Additionally, capacity is an important performance parameter of batteries that directly affects the driving range of electric vehicles. Therefore, capacity can be used as an indicator to evaluate the health state of batteries.

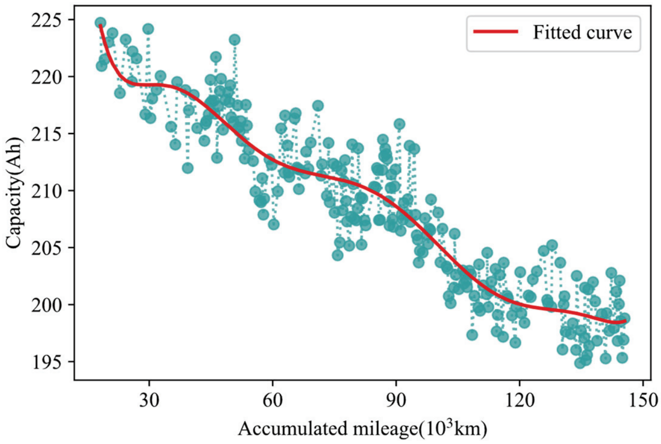

Figure 2. The battery capacity degrades with increasing accumulated mileage.

2.2.2. Ohmic Resistance

Due to the unavailability of direct access to the battery's ohmic resistance from the large data platform, this study employs a first-order equivalent circuit model to identify the ohmic resistance. The identification results are shown in Figure 3. It can be observed that the ohmic resistance of the battery exhibits periodic variations with increasing cumulative mileage, showing an overall increasing trend. Additionally, the ohmic resistance is significantly influenced by temperature, with higher resistance values observed in the low-temperature range compared to the high-temperature range. After fitting the ohmic resistance at 27 °C and 37 °C, it is found that the resistance growth rate is higher in the low-temperature range. Therefore, the ohmic resistance demonstrates periodic changes with the aging of batteries and can be used as an indicator to evaluate the health state of batteries.

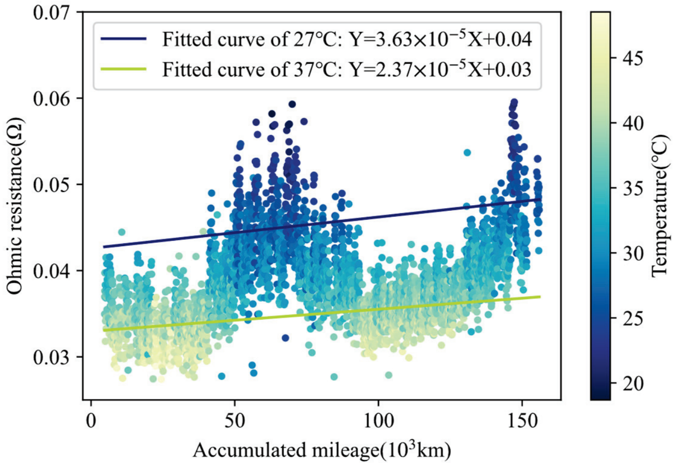

Figure 3. The ohmic resistance of the battery exhibits changes with increasing accumulated mileage.

2.2.3. Maximum Output Power

Since it is not feasible to directly conduct maximum output power tests on operating vehicles, this study calculates the maximum output power within each driving segment based on the power definition. Then, the average of the maximum output power of each driving segment within each 1000-km interval is calculated as the maximum output power of the battery over a long-time duration. Figure 4 illustrates that the maximum output power of the selected electric buses decreases most significantly at high temperatures with increasing cumulative mileage, exhibiting an overall declining trend. Additionally, the power output of the battery has an impact on the vehicle's driving performance. Therefore, the maximum power output can be used as an evaluation indicator for the health state of the battery.

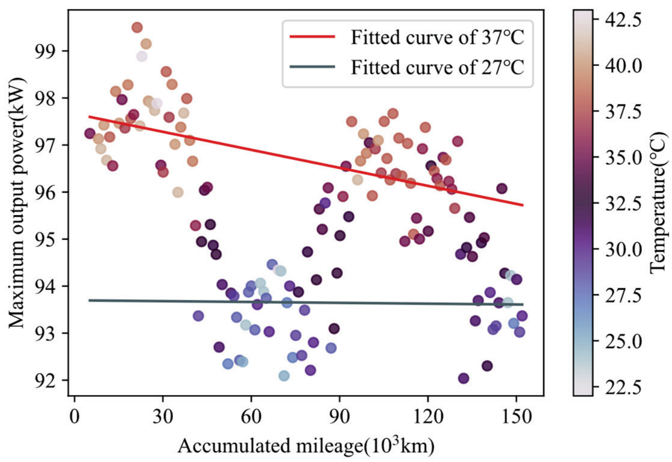

Figure 4. The maximum output power of the battery decreases with increasing accumulated mileage.

3. Methods

3.1. Comprehensive Battery Health Indicator Based on Improved CRITIC and GRA

3.1.1. Improved CRITIC Weighting Method

The CRITIC method is an objective weighting approach that simultaneously considers the impact of data variability within indicators and the interrelationships among indicators. Specifically, it employs two key concepts to determine weights: the contrast intensity and the conflicting character of the evaluation criteria [26]. First, if an indicator exhibits significant differences in values across various samples, it possesses a higher contrast intensity, resulting in a larger weight. Second, if an indicator shows stronger correlations with other indicators, it has less conflict with them, resulting in a smaller weight. Generally, standard deviation is used to measure the contrast intensity, while correlation coefficients are employed to assess the conflict among indicators.

Due to the limitations of standard deviation in fully capturing the information within a single indicator, as it mainly measures the dispersion and fluctuation of data, this study proposes a modified method using information entropy instead of standard deviation to represent the comparative strength of data within each indicator. Information entropy can provide a more comprehensive quantification of the information content within each indicator, allowing for a more accurate evaluation of the comparative strength of indicators [27].

The improved CRITIC weighting method consists of the following steps:

1. Data normalization

In this paper, different sequences of battery health indicators during total life cycles are normalized in two cases. For indicators such as capacity and maximum output power that decrease gradually with battery aging, the following formula is used for normalization:

$$x_{ij}^* = \frac{x_{ij} - \min_i\{x_{ij}\}}{\max_i\{x_{ij}\} - \min_i\{x_{ij}\}}, \tag{1}$$

where i is the number of life cycles and j is the number of health indicators.

For indicators such as ohmic internal resistance, which increases gradually with battery aging, the following formula is used:

$$x_{ij}^* = \frac{\max_i\{x_{ij}\} - x_{ij}}{\max_i\{x_{ij}\} - \min_i\{x_{ij}\}}. \tag{2}$$

2. Calculate the comparative strength of indicators based on information entropy

First, the entropy value of each metric is calculated as shown in the following equation:

$$h_j = -\frac{1}{\ln m}\sum_{i=1}^{m} p_{ij}\ln(p_{ij}), \tag{3}$$

where

$$p_{ij} = \frac{x_{ij}^*}{\sum_{i=1}^{m} x_{ij}^*}. \tag{4}$$

The more information the data contains, the lower the entropy. Therefore, in the improved CRITIC weighting method, the comparative strength can be represented as

$$H_j = 1 - h_j. \tag{5}$$

3. Calculate the conflict between indicators

A stronger correlation between a single indicator and the other indicators indicates a higher degree of duplicated information and a lower level of conflict. Therefore, the quantification formula for conflict is as follows:

$$R_j = \sum_{k=1}^{n}\left(1 - r_{jk}\right), \tag{6}$$

where r_{jk} is the correlation between the jth indicator and the other indicators.

4. Calculate the weights for each indicator

Firstly, we calculate the amount of comprehensive information for each indicator using

$$C_j = H_j \times R_j. \tag{7}$$

Then, the weights of the indicators are calculated in the following equation:

$$w_j = \frac{C_j}{\sum\limits_{i=1}^{n} C_j}. \tag{8}$$

3.1.2. GRA Comprehensive Evaluation Method

GRA is a comprehensive evaluation method used for multi-criteria decision analysis. It leverages the principle of correlation, measuring the degree of similarity between a reference sequence and a comparison sequence [28]. By quantifying the grey relational coefficient, GRA provides a numerical indicator of the relationship strength between variables.

The GRA method mainly consists of the following steps:

1. Construct the evaluation matrix

In this study, three health evaluation indicators were selected. Here, we have constructed a scoring matrix for these different evaluation indicators at varying accumulated mileage points. This matrix is subjected to the same data normalization method as used in the improved CRITIC. The resulting normalized scoring matrix is presented below:

$$\mathbf{Z} = \begin{bmatrix} z_{11} & z_{12} & z_{13} \\ z_{21} & z_{22} & z_{23} \\ \vdots & \vdots & \vdots \\ z_{m1} & z_{m2} & z_{m3} \end{bmatrix}, \tag{9}$$

where each column represents a health evaluation indicator, and each row represents the values of all indicators at different cumulative mileage.

2. Determine the reference sequence

The reference sequence is derived from the normalized matrix, which is generally the optimal value of each column. Following the application of indicator normalization, this paper selects the maximum values from each column as the reference sequence.

The formula for the positive ideal solution is expressed as follows:

$$\mathbf{Z}_0 = (z_1, z_2, z_3), \tag{10}$$

where

$$z_j = \max\{z_{1j}, z_{2j}, \ldots, z_{mj}\}. \tag{11}$$

3. Calculate the grey relational coefficient

The gray correlation coefficient is used to determine the closeness of each comparison sequence to the reference sequence. The specific formula is defined as

$$\gamma\left(z_{1j}, z_{ij}\right) = \frac{\min\limits_{i}\min\limits_{j}\Delta_{ij} + \rho\max\limits_{i}\max\limits_{j}\Delta_{ij}}{\Delta_{ij} + \rho\max\limits_{i}\max\limits_{j}\Delta_{ij}}, \tag{12}$$

where ρ is the distinguishing coefficient, and $\Delta_{ij} = \left|z_{1j} - z_{ij}\right|$ is the difference matrix.

4. Calculate the grey relational grade

The gray relational grade (GRG) is used to measure the similarity between different comparison sequences and the reference sequence. Different health indicators have different contributions to the comprehensive evaluation results. Therefore, this paper integrates the weight of the health indicator into the CRG; that is, it uses the weighted CRG to determine the comprehensive battery SOH. The calculation method of the weighted CRG is as follows:

$$r_i = \sum_{j=1}^{n} w_j \gamma\left(z_{1j}, z_{ij}\right), \tag{13}$$

where w_j represents the weight of each health indicator, which can be obtained using the improved CRITIC weighting method proposed in this study.

3.1.3. The Improved CRITIC-GRA Method

To achieve a more objective and comprehensive battery SOH evaluation, this section combines the improved CRITIC weighting method and the GRA method to propose a comprehensive battery health evaluation indicator that considers multiple single battery health indicators.

First, an evaluation indicator matrix is constructed based on the extracted single battery health indicator data; then, the improved CRITIC weighting method is used to calculate the objective weights of different battery health indicators and the indicator weight matrix is constructed; then, the GRA is used to calculate the gray correlation coefficients of different health indicators under different degradation conditions and construct the gray correlation coefficient matrix; finally, the objective weights of different indicators are integrated into the quantification of gray correlation degrees; that is, the gray correlation coefficient matrix is multiplied by the objective weight matrix of single health indicators to obtain the final comprehensive evaluation indicator. The calculation formula of the battery health comprehensive evaluation indicator proposed in this section is as follows:

$$\mathbf{Co\_SOH} = \mathbf{\Gamma} \times \mathbf{W^T} = \begin{bmatrix} \gamma_{11} & \gamma_{12} & \gamma_{13} \\ \gamma_{21} & \gamma_{22} & \gamma_{23} \\ \vdots & \vdots & \vdots \\ \gamma_{m1} & \gamma_{m2} & \gamma_{m3} \end{bmatrix} \times \begin{bmatrix} w_1 \\ w_2 \\ w_3 \end{bmatrix}, \tag{14}$$

where $\mathbf{\Gamma}$ is the gray correlation coefficient matrix and $\mathbf{W^T}$ is the objective weight matrix.

3.2. Battery Comprehensive Health Prediction Model Based on Att-BiGRU

3.2.1. Feature Extraction for Model Input

The input features of the model play a crucial role in influencing the prediction performance. Initially, during the process of health indicator extraction, it was observed that there exists a strong correlation between cumulative mileage and battery health indicators. Furthermore, temperature also directly affects certain indicators. Therefore, this study directly extracted two health features, cumulative mileage and temperature, from the raw data variables. Moreover, research suggests that SOC and charging current are vital factors impacting battery health. To comprehensively exploit real-world vehicle data and ensure accurate predictions by the model, this study further computes and extracts 8 health features from the charging segments, focusing on SOC, voltage, and current.

Consequently, a total of 10 health features were obtained, as presented in Table 2, thereby accounting for the multifaceted aspects of battery health evaluation.

Table 2. Extracted health features.

Number	Feature	Number	Feature
F1	Accumulated mileage	F6	Charging start voltage
F2	Temperature	F7	Charging end voltage
F3	Charging start SOC	F8	Charging voltage difference
F4	Charging end SOC	F9	Maximum charging current
F5	Charging SOC difference	F10	Average charging current

3.2.2. Att-BiGRU

The gated recurrent unit (GRU) is an improved version of recurrent neural networks (RNNs). GRU introduces two gating mechanisms, namely, the reset gate and the update gate, to regulate the flow of information within the hidden state. This design mitigates the challenges of gradient vanishing or exploding encountered by l RNNs during long-term memory and backpropagation. The fundamental computational unit of GRU is outlined in Figure 5.

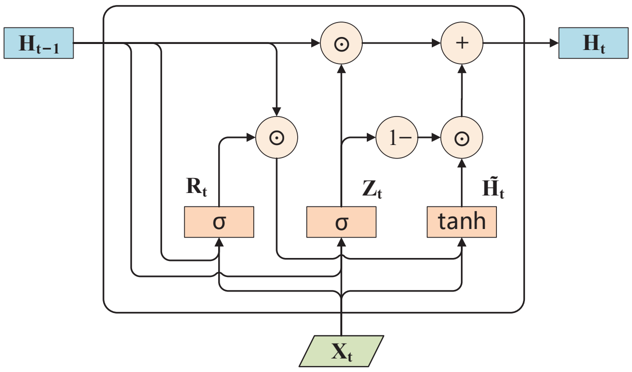

Figure 5. The fundamental computational unit of GRU.

The BiGRU model is a bidirectional recurrent neural network consisting of both forward and backward GRU layers. The forward GRU layer processes input sequences in chronological order, while the backward GRU layer processes input sequences in reverse chronological order. At time step "t", the hidden state of the BiGRU is obtained by concatenating the forward and backward hidden states. This approach enables the model to simultaneously incorporate past and future information, facilitating a more effective modeling of inter-sequence dependencies.

The attention mechanism is a widely employed technique in tasks such as natural language processing and machine translation, aiming to model the varying degrees of focus on different segments within sequences. Traditional sequence models employ fixed-weight parameters to process each element within a sequence. However, this fixed-weight approach may fall short of effectively capturing vital contextual information for longer sequences or intricate semantic relationships. In contrast, the attention mechanism employs dynamic weights that allow the model to adaptively allocate more attention to crucial segments, depending on the task's requirements.

While BiGRU offers some improvement in addressing the issue of long-distance dependencies in RNNs, its information retention capability still remains limited. This study introduces a fusion model of the BiGRU and the attention mechanism, aiming to address these limitations. The proposed approach involves employing the attention mechanism to dynamically weight the hidden states of BiGRU at each step, thereby directing attention towards hidden states that hold greater significance for predictive outcomes. The Att-BiGRU model inherits the advantages of BiGRU while simultaneously mitigating the loss of node information during the prediction process for long sequences.

The constructed Att-BiGRU prediction model in this study is illustrated in Figure 6.

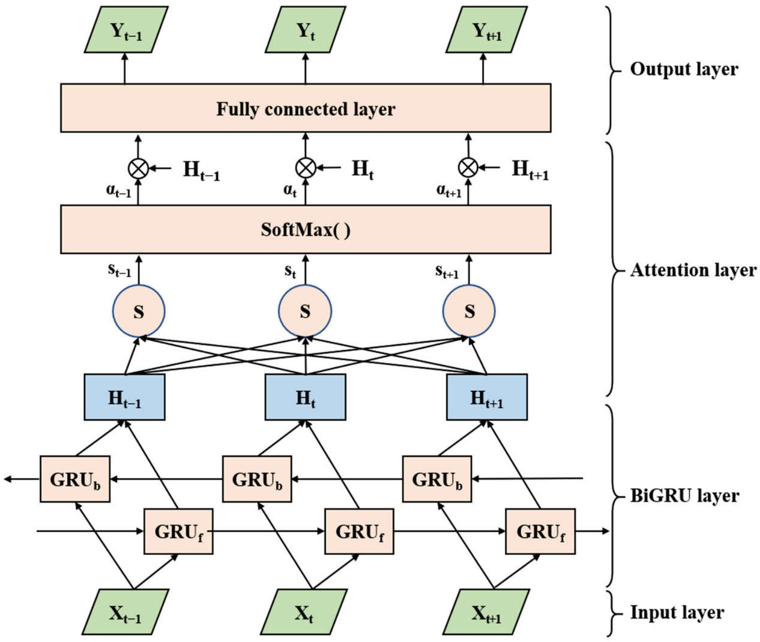

Figure 6. The structure of Att-BiGRU.

4. Results and Discussion

All the results in this section are obtained based on a personal computer equipped with an AMD Ryzen 7 4800U CPU, an AMD Radeon Graphics, and 16 GB RAM (Santa Clara, CA, USA). The deep learning models run on the PyTorch framework based on Python 3.8.

4.1. Results of Comprehensive Battery Health Evaluation

In this section, we select four electric buses of the same model in actual operation to conduct verification and discussion of the proposed method. Vehicle A and Vehicle B operate in Shenyang with an average temperature of 10.1 °C, while Vehicle C and Vehicle D operate in Guangzhou with an average temperature of 21.9 °C.

First, we used the method in Section 2.2 to extract health indicator data for the four vehicles. Then, based on the extracted battery health indicator data, the improved CRITIC weighting method was employed to ascertain the weights of each indicator, as presented in Table 3. The weights shed light on the relative importance of different health indicators for each bus. For Vehicle A and Vehicle B, the internal resistance carries the highest weight at 0.41 and 0.48, which could potentially be attributed to the lower average temperature in the city where they operate. This lower temperature might lead to a faster increase in internal resistance due to battery aging. For Vehicle C and Vehicle D, the capacity indicator holds the highest weight at 0.53 and 0.54. However, it does not exhibit overwhelming dominance when compared to the other two indicators. In conclusion, these weight distributions underscore the limitation of relying solely on a single health indicator to depict the battery's health state, as it might present an overly narrow perspective.

Table 3. The weights of each indicator.

Vehicle	Capacity	Resistance	Power
A	0.38	0.41	0.21
B	0.34	0.48	0.18
C	0.53	0.21	0.26
D	0.54	0.24	0.22

Subsequently, the GRA method was employed to calculate the comprehensive battery health indicators for both buses. In Figure 7, the curve labeled "SOH" represents the battery SOH based on capacity and the "Co_SOH" represents the comprehensive health indicator, while the "D-value" represents the difference between them. It can be observed that for all four vehicles, the values of comprehensive health indicators obtained in this study differ from the capacity-based SOH by approximately ±4%. For Vehicle A, prior to reaching 90,000 km, the Co_SOH is slightly higher than the SOH. Afterwards, the Co_SOH experiences an accelerated decline, becoming lower than the SOH, and the difference between them gradually increases. Similarly, for Vehicle B, up to 70,000 km, the Co_SOH and SOH are relatively close, with Co_SOH being slightly lower than SOH. Afterwards, Co_SOH experiences an accelerated decline, and the difference between them gradually increases. The changing trends in Co_SOH for Vehicle A and Vehicle B are indeed primarily related to the higher weight assigned to ohmic resistance compared to capacity in the evaluation process. In contrast, Vehicles C and D exhibit similar patterns, where Co_SOH is slightly higher than SOH, and the difference accumulates as the mileage increases. This is primarily due to the lower weight assigned to ohmic resistance and maximum output power compared to capacity in the evaluation process. Conclusively, the proposed comprehensive health indicator in this study provides a more comprehensive representation of the battery health state, effectively capturing various degradation aspects.

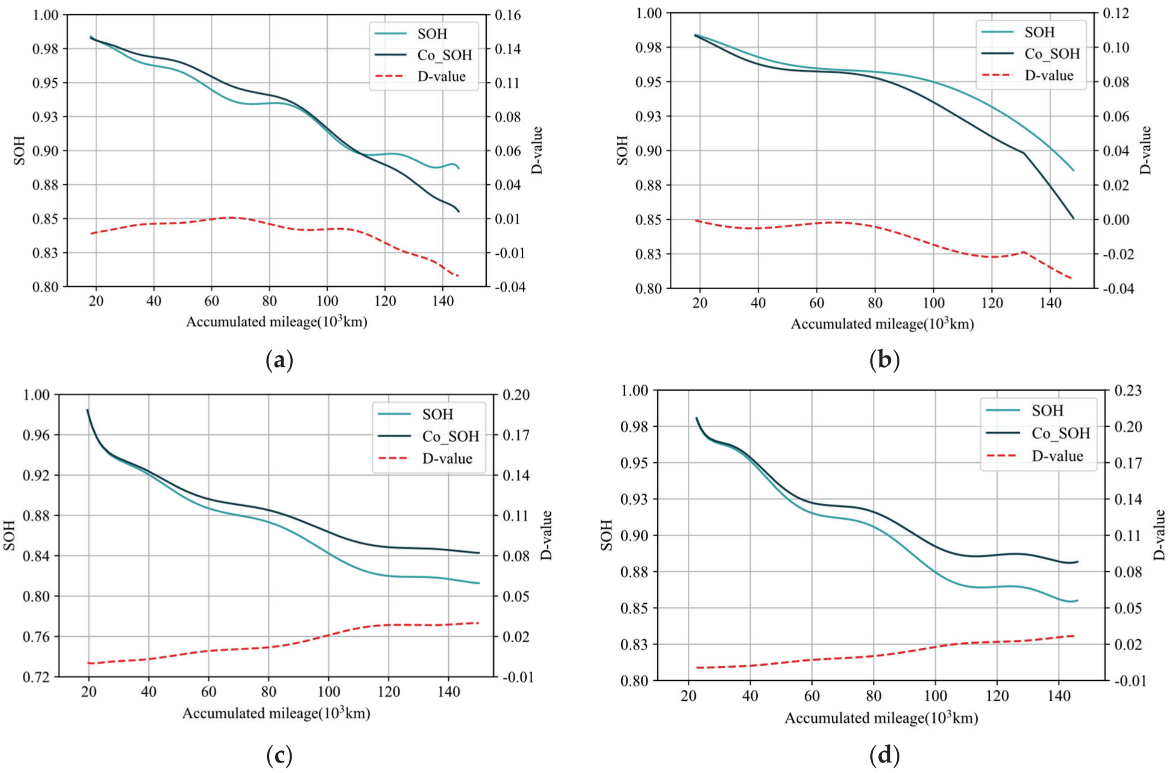

Figure 7. Comprehensive indicator of battery health: (**a**) Vehicle A; (**b**) Vehicle B; (**c**) Vehicle C; (**d**) Vehicle D.

4.2. Prediction of Comprehensive Health Indicator

In this study, the prediction of the comprehensive battery health indicator is treated as a time series forecasting task. The prediction utilizes data considered as time series data, where each row represents a time frame. Therefore, in this section, according to the order of accumulated mileage from small to large, the 10 health features initially selected in Section 3.2 are used as input features, and the comprehensive health indicator obtained in Section 3.1 is used as a label to construct the data set used in the Att-BiGRU model. The first 70% of the dataset is the training set, and the last 30% is the test set.

In order to ensure prediction accuracy and improve prediction speed, this section conducts a correlation analysis on the initially selected 10 health features in this study. Features with an absolute value of correlation coefficient greater than 0.5 with the comprehensive health indicator of the battery are selected as input features for the prediction model. Taking Vehicle A as an example, the correlation of each feature with the comprehensive health indicator is shown in Figure 8.

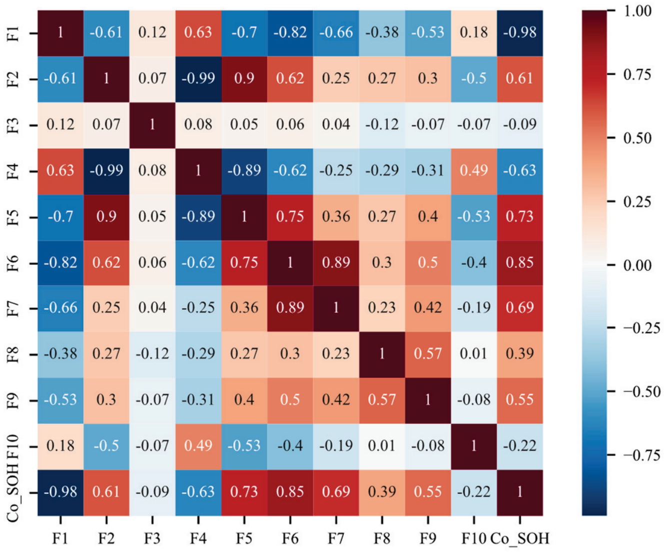

Figure 8. Correlation of each feature with the comprehensive health indicator.

Here, the time step of the Att-BiGRU model is set to 1; that is, the data of the previous segment is used to predict the comprehensive health of the current segment. To assess the prediction performance of the Att-BiGRU model, a comparative analysis is conducted against XGBoost, GRU, and BiGRU models. The predicted values are presented in Figure 9, and the prediction performance is summarized in Table 4.

From Figure 9, it is evident that for all vehicles, the Att-BiGRU model exhibits a commendable ability to fit the original comprehensive health indicator values. In contrast to the classic ensemble learning approach, XGBoost, the predictive curves of Att-BiGRU, GRU, and BiGRU models display reduced volatility, closely aligning with the true values.

As presented in Table 4, across the prediction of different vehicle data, the Att-BiGRU model outperforms other models in terms of root mean square error (RMSE), mean absolute error (MAE) and R^2. With the largest RMSE and MAE, XGBoost consistently demonstrates the least accuracy among the models. Deep learning methods such as GRU, BiGRU, and especially Att-BiGRU exhibit a marked improvement in predictive accuracy compared to XGBoost. While BiGRU offers a slight advantage over GRU, the enhancement is moderate. Incorporating the attention mechanism into BiGRU significantly enhances predictive accuracy and reduces prediction errors. For Vehicle A, Att-BiGRU yields an RMSE of 0.056, representing a 32% reduction compared to BiGRU. Furthermore, Att-BiGRU's MAE of 0.048 is 29% lower than BiGRU. For Vehicle B, the RMSE of Att-BiGRU is 0.071, which is 28% lower than BiGRU. In addition, Att-BiGRU's MAE of 0.063 is 26% lower than BiGRU. For Vehicle C, the RMSE of Att-BiGRU is 0.070, which is 27% lower than BiGRU. In addition, Att-BiGRU's MAE of 0.045 is 35% lower than BiGRU. Similarly, for Vehicle D, Att-BiGRU achieves an RMSE of 0.032, 29% lower than BiGRU and an MAE of 0.025, indicating a 32% improvement over BiGRU. In addition, Att-BiGRU achieves the largest R^2 values among all models in all four vehicles, reaching more than 0.956, which means that the prediction results fit the real curve well. Especially compared with XGBoost, the R^2 value has been improved by 6% on average. Hence, the employed Att-BiGRU model for comprehensive battery health indicator prediction proves to be highly effective.

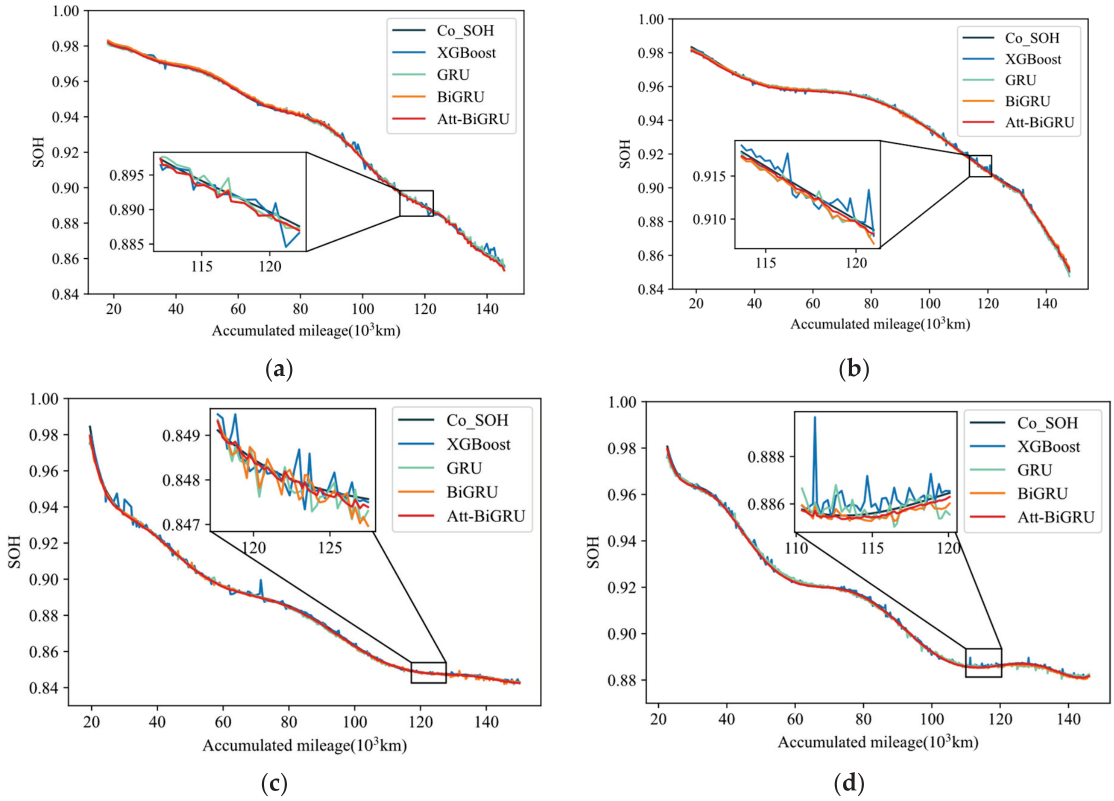

Figure 9. Prediction results of Att-BiGRU model: (**a**) Vehicle A; (**b**) Vehicle B; (**c**) Vehicle C; (**d**) Vehicle D.

Table 4. Prediction performance of the comprehensive health indicator across different models.

Model	A			B			C			D		
	RMSE	MAE	R^2	RMSE	MAE	R^2	RMSE	MAE	R^2	RMSE	MAE	R^2
XGB	0.132	0.097	0.924	0.205	0.150	0.910	0.214	0.128	0.908	0.116	0.081	0.927
GRU	0.094	0.072	0.942	0.107	0.088	0.928	0.106	0.081	0.933	0.087	0.067	0.945
BiGRU	0.082	0.068	0.951	0.098	0.085	0.937	0.096	0.069	0.949	0.045	0.037	0.972
Att-BiGRU	0.056	0.048	0.973	0.071	0.063	0.956	0.070	0.045	0.971	0.032	0.025	0.985

5. Conclusions

In order to address the limitation of the single indicator in battery health evaluation, this paper proposes a comprehensive evaluation and prediction method considering multiple health indicators based on real-world vehicle data. Initially, common battery health evaluation indicators are extracted, and their evolution characteristics with battery aging are analyzed. Objective weights for each evaluation indicator are determined using the improved CRITIC weighting method, followed by the derivation of a comprehensive health indicator through the integration of GRA algorithm. Subsequently, the Att-BiGRU model is employed to predict the proposed comprehensive health indicator. Comparative analyses are conducted against other predictive models. The introduced comprehensive health indicator offers a more holistic evaluation of battery health state and demonstrates good interpretability. The predictive model utilizing Att-BiGRU for the comprehensive health indicator attains a low RMSE of only 0.032 and a MAE of 0.025, both outperforming algorithms such as XGBoost, GRU, and BiGRU in terms of prediction accuracy. In conclusion, this study makes valuable contributions by offering a multi-faceted battery health evaluation framework and an accurate predictive model, ultimately contributing to a more comprehensive understanding of battery health state evaluation.

In future research, we will extract more health state evaluation indicators based on actual vehicle operating data to further improve the comprehensiveness of the battery health comprehensive evaluation indicator proposed in this article. In addition, in the future, we will further improve the practicality of the method proposed in this article and try to carry out real vehicle deployment.

Author Contributions: Conceptualization, P.L. and C.L.; methodology, C.L.; software, C.L.; validation, C.L.; formal analysis, P.L. and Q.W.; investigation, C.L.; resources, P.L., Z.W., J.H. and Y.Z.; data curation, C.L.; writing—original draft preparation, C.L.; writing—review and editing, Q.W.; visualization, C.L.; supervision, P.L.; project administration, P.L. and Q.W.; funding acquisition, P.L., Z.W., J.H. and Y.Z. All authors have read and agreed to the published version of the manuscript.

Funding: This research was funded by the Jilin Scientific and Technological Development Program (No. 20220301019GX) and the Chongqing Doctoral Through-Train Research Project (No. sl202100000050).

Institutional Review Board Statement: Not applicable.

Informed Consent Statement: Not applicable.

Data Availability Statement: Data sharing is not applicable to this article.

Conflicts of Interest: The authors declare no conflict of interest.

References

1. Su, C.-W.; Yuan, X.; Tao, R.; Umar, M. Can new energy vehicles help to achieve carbon neutrality targets? *J. Environ. Manag.* **2021**, *297*, 113348. [CrossRef]
2. Li, T.; Ma, L.; Liu, Z.; Yi, C.; Liang, K. Dual carbon goal-based quadrilateral evolutionary game: Study on the new energy vehicle industry in China. *Int. J. Environ. Res. Public Health* **2023**, *20*, 3217. [CrossRef]
3. Hou, F.; Chen, X.; Chen, X.; Yang, F.; Ma, Z.; Zhang, S.; Liu, C.; Zhao, Y.; Guo, F. Comprehensive analysis method of determining global long-term GHG mitigation potential of passenger battery electric vehicles. *J. Clean. Prod.* **2021**, *289*, 125137. [CrossRef]
4. Yuan, X.; Cai, Y. Forecasting the development trend of low emission vehicle technologies: Based on patent data. *Technol. Forecast. Soc. Chang.* **2021**, *166*, 120651. [CrossRef]
5. Lai, X.; Chen, Q.; Tang, X.; Zhou, Y.; Gao, F.; Guo, Y.; Bhagat, R.; Zheng, Y. Critical review of life cycle assessment of lithium-ion batteries for electric vehicles: A lifespan perspective. *eTransportation* **2022**, *12*, 100169. [CrossRef]
6. Lipu, M.H.; Hannan, M.; Karim, T.F.; Hussain, A.; Saad, M.H.M.; Ayob, A.; Miah, M.S.; Mahlia, T.I. Intelligent algorithms and control strategies for battery management system in electric vehicles: Progress, challenges and future outlook. *J. Clean. Prod.* **2021**, *292*, 126044. [CrossRef]
7. Liu, Y.; He, Y.; Bian, H.; Guo, W.; Zhang, X. A review of lithium-ion battery state of charge estimation based on deep learning: Directions for improvement and future trends. *J. Energy Storage* **2022**, *52*, 104664. [CrossRef]
8. Han, X.; Lu, L.; Zheng, Y.; Feng, X.; Li, Z.; Li, J.; Ouyang, M. A review on the key issues of the lithium ion battery degradation among the whole life cycle. *eTransportation* **2019**, *1*, 100005. [CrossRef]
9. Capkova, D.; Knap, V.; Fedorkova, A.S.; Stroe, D.-I. Investigation of the temperature and DOD effect on the performance-degradation behavior of lithium–sulfur pouch cells during calendar aging. *Appl. Energy* **2023**, *332*, 120543. [CrossRef]
10. Olabi, A.; Wilberforce, T.; Sayed, E.T.; Abo-Khalil, A.G.; Maghrabie, H.M.; Elsaid, K.; Abdelkareem, M.A. Battery energy storage systems and SWOT (strengths, weakness, opportunities, and threats) analysis of batteries in power transmission. *Energy* **2022**, *254*, 123987. [CrossRef]
11. Yang, S.; Zhang, C.; Jiang, J.; Zhang, W.; Zhang, L.; Wang, Y. Review on state-of-health of lithium-ion batteries: Characterizations, estimations and applications. *J. Clean. Prod.* **2021**, *314*, 128015. [CrossRef]
12. Farmann, A.; Sauer, D.U. A comprehensive review of on-board State-of-Available-Power prediction techniques for lithium-ion batteries in electric vehicles. *J. Power Sources* **2016**, *329*, 123–137. [CrossRef]
13. Barai, A.; Uddin, K.; Widanage, W.D.; McGordon, A.; Jennings, P. A study of the influence of measurement timescale on internal resistance characterisation methodologies for lithium-ion cells. *Sci. Rep.* **2018**, *8*, 21. [CrossRef] [PubMed]
14. Pradhan, S.K.; Chakraborty, B. Battery management strategies: An essential review for battery state of health monitoring techniques. *J. Energy Storage* **2022**, *51*, 104427. [CrossRef]
15. Ge, M.-F.; Liu, Y.; Jiang, X.; Liu, J. A review on state of health estimations and remaining useful life prognostics of lithium-ion batteries. *Measurement* **2021**, *174*, 109057. [CrossRef]
16. Xiong, R.; Li, L.; Tian, J. Towards a smarter battery management system: A critical review on battery state of health monitoring methods. *J. Power Sources* **2018**, *405*, 18–29. [CrossRef]
17. Xu, Z.; Wang, J.; Lund, P.D.; Zhang, Y. Co-estimating the state of charge and health of lithium batteries through combining a minimalist electrochemical model and an equivalent circuit model. *Energy* **2022**, *240*, 122815. [CrossRef]
18. Liu, F.; Shao, C.; Su, W.; Liu, Y. Online joint estimator of key states for battery based on a new equivalent circuit model. *J. Energy Storage* **2022**, *52*, 104780. [CrossRef]

19. Zhang, M.; Liu, Y.; Li, D.; Cui, X.; Wang, L.; Li, L.; Wang, K. Electrochemical impedance spectroscopy: A new chapter in the fast and accurate estimation of the state of health for lithium-ion batteries. *Energies* **2023**, *16*, 1599. [CrossRef]
20. Zhang, M.; Yang, D.; Du, J.; Sun, H.; Li, L.; Wang, L.; Wang, K. A review of SOH prediction of Li-ion batteries based on data-driven algorithms. *Energies* **2023**, *16*, 3167. [CrossRef]
21. Ng, M.-F.; Zhao, J.; Yan, Q.; Conduit, G.J.; Seh, Z.W. Predicting the state of charge and health of batteries using data-driven machine learning. *Nat. Mach. Intell.* **2020**, *2*, 161–170. [CrossRef]
22. Lin, M.; Yan, C.; Wang, W.; Dong, G.; Meng, J.; Wu, J. A data-driven approach for estimating state-of-health of lithium-ion batteries considering internal resistance. *Energy* **2023**, *277*, 127675. [CrossRef]
23. Xiong, R.; Sun, Y.; Wang, C.; Tian, J.; Chen, X.; Li, H.; Zhang, Q. A data-driven method for extracting aging features to accurately predict the battery health. *Energy Storage Mater.* **2023**, *57*, 460–470. [CrossRef]
24. Tian, J.; Xiong, R.; Shen, W.; Lu, J.; Sun, F. Flexible battery state of health and state of charge estimation using partial charging data and deep learning. *Energy Storage Mater.* **2022**, *51*, 372–381. [CrossRef]
25. Einhorn, M.; Conte, F.V.; Kral, C.; Fleig, J. A method for online capacity estimation of lithium-ion battery cells using the state of charge and the transferred charge. *IEEE Trans. Ind. Appl.* **2011**, *48*, 736–741. [CrossRef]
26. Diakoulaki, D.; Mavrotas, G.; Papayannakis, L. Determining objective weights in multiple criteria problems: The critic method. *Comput. Oper. Res.* **1995**, *22*, 763–770. [CrossRef]
27. Chen, P. Effects of the entropy weight on TOPSIS. *Expert Syst. Appl.* **2021**, *168*, 114186. [CrossRef]
28. Julong, D. Introduction to grey system theory. *J. Grey Syst.* **1989**, *1*, 1–24.

sensors

MDPI

Article

Bidirectional Six-Pack SiC Boost–Buck Converter Using Droop Control in DC Nano-Grid

Yeonwoo Kim [1] and Sewan Choi [2,*]

[1] Department of Automotive Parts, Busan Machinery Research Center, Korea Institute of Machinery & Materials, Busan 46744, Republic of Korea; woo@kimm.re.kr

[2] Department of Electrical & Information Engineering, Seoul National University of Science and Technology, Seoul 01811, Republic of Korea

* Correspondence: schoi@seoultech.ac.kr

Abstract: This paper proposes a bidirectional boost–buck converter employing a six-pack SiC intelligent power module using droop control in DC nano-grids. The topology is constructed as a cascaded structure of an interleaved boost converter and buck converter. A six-pack SiC intelligent power module (IPM), which is suitable for the proposed cascaded structure, is adopted for high efficiency and compactness. A hybrid control scheme, in which holding a particular switch always results in a turn-off or turn-on state according to the boost mode and the buck mode, is employed to reduce the switching losses. By applying the hybrid control scheme, the number of switching operations of the switches can be minimized. Since switchover of the current controller is not required, smooth transition is enabled not only from the buck mode to the boost mode but also vice versa. As a parallel control, a secondary control is employed with DC droop control, which has a trade-off relationship between voltage sag and current sharing. It is possible to enhance the accuracy of current sharing while effectively regulating the DC link voltage without voltage sag. This is verified experimentally using two modules as laboratory prototypes, of which the power rating is 20 kW each.

Keywords: DC nano-grid; droop control; bidirectional boost–buck converter; six-pack SiC-IPM; ESS

1. Introduction

With the increasing demand for distributed power generation systems and energy storage systems (ESS) in remote islands and mountainous areas, research on small-scale power grids has been actively underway [1–10]. Nano-grids also fall into the category of small-scale power grids; their rated power is 1 MW or less, which is lower than that of micro-grids [11,12]. DC nano-grids do not experience issues related to stability, frequency, synchronization, and reactive power, unlike AC nano-grids. DC nano-grids are also advantageous in that they allow DC power generation systems, such as solar photovoltaic (PV) systems and fuel cells, to feed DC loads without secondary power conversion [13,14]. Figure 1 presents the overall structure of a DC nano-grid system composed of ESS, PV systems, uninterruptible power supplies (UPS), electric vehicles (EV), and DC loads. In general, when the grid voltage is three-phase 380 V, the DC link voltage ranges from 750 V to 800 V. DC–DC converters are designed to cover a wide range of voltages in order to allow the use of various types of batteries, which can be employed in ESS or EV. Moreover, bidirectional converters have a very important role in DC nano-grids. The representative topology of a bidirectional converter is DAB, and research on bidirectional converters, such as the various control methods of DAB and variants of DAB hardware, is being actively conducted [15–20]. However, in order to apply the various batteries used in ESS and EV to DC nano-grids, a buck–boost-type topology is needed, rather than a buck-type or boost-type topology. This is due to it being used to cope with cases where the battery voltage is higher or lower than the DC link voltage when the DC link voltage is fixed. Furthermore, it is worth noting that DC–DC converters are required to be able to step up and step down the voltage during both the charging and discharging of batteries [21,22]. Converters, which allow for bidirectional power flow and are able to step up and step -down the voltage while charging and discharging, include the synchronous rectification buck–boost converter, the Ćuk converter, and the SEPIC converter. However, these converters have a disadvantage; the voltage rating of their switch corresponds to the sum of input and output voltages, thereby it is very high [23–29].

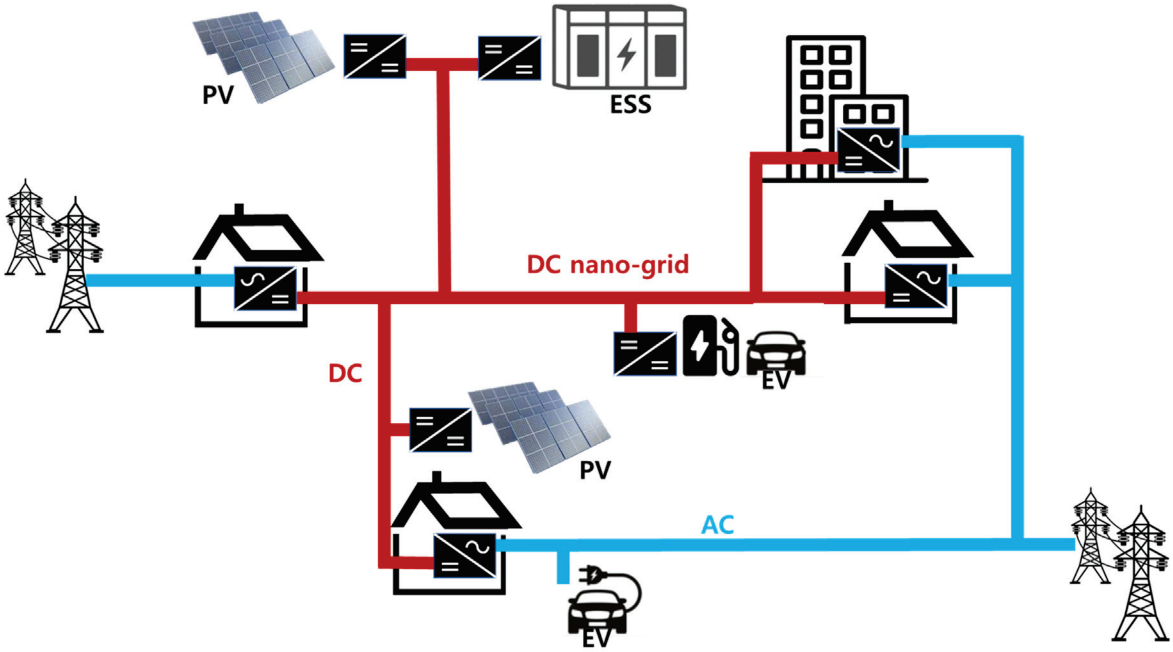

Figure 1. Structure of DC nano-grid system.

In contrast, a cascaded converter is not only capable of bidirectional operations and stepping up and stepping down the voltage during charging and discharging but the voltage rating of its switch is also low. Therefore, cascade-type converters for voltage stepping up/down are suitable for applying the various batteries used in ESS or EV to the DC nano-grid. Cascaded converters can be classified into cascaded buck–boost converters and cascaded boost–buck converters according to the combination order. In general, an interleaving method is applied to decrease the current rating of the switch, which makes switch selection easier and reduces the volume of passive devices. The conventional cascaded buck–boost converter is interleaved, and its topology is presented in Figure 2a. In general, modular switching devices are preferred to obtain converters with a higher efficiency and a more compact structure. Thus, six-pack intelligent power modules (IPM) are often employed. However, IPM cannot be used in an optimum manner in a cascaded buck–boost converter, because the number of MOSFETs are mismatched. The converter requires both the input and output stages to have the same number of phases for interleaving. Even though the interleaving cascaded buck–boost converter transforms asymmetrically, as shown in Figure 2b,c, the IPM is not used optimally, since high-side MOSFET (Q_1, Q_3, Q_5) drains are disconnected partially. In Figure 2b, the drains of Q_1 and Q_3 are disconnected, and the drains of Q_3 and Q_5 are disconnected in Figure 2c. In order to use the six-pack IPM optimally, high-side MOSFET drains should be connected to each other.

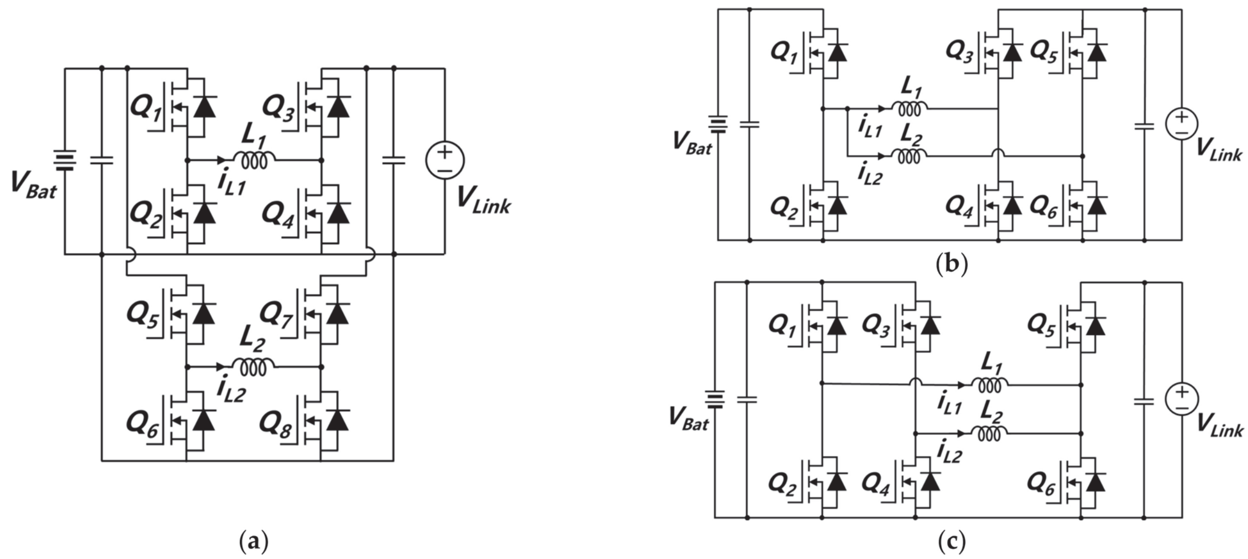

Figure 2. Interleaving cascaded buck–boost converter: (**a**) Symmetrical structure, (**b**,**c**) Asymmetrical structure.

Meanwhile, in DC nano-grids, converters are often modularized for various reasons, for example, better capacity scalability, easier system maintenance, and improved reliability [30,31]. Modular converters require parallel operation control methods for accurate current sharing. Among the parallel operation techniques, droop control is advantageous in that it requires no communication between modules to achieve load sharing and can be installed wherever necessary regardless of site conditions [32,33]. However, load sharing between modules may be inaccurately conducted due to differences in the line impedances connecting the converter to the load, thereby leading to voltage sag [34–36].

This paper proposes a high-efficiency bidirectional modular converter with a wide voltage range capable of the stepping up and stepping down the voltage. The converter modules are connected in parallel for current sharing, and each module is constructed to have a cascaded structure comprising a two-phase interleaved boost converter and a single-phase buck converter. In order to make the converter higher in efficiency and more compact in structure, modular devices are preferred. Among them, a six-pack SiC-based IPM is optimally employed through the proposed topology configuration. In addition, a hybrid switching control scheme, in which a particular switch always held in a turn-off or turn-on state according to the boost mode and buck mode is applied to minimize the number of switching operations, thereby reducing switching losses. Each converter module is controlled using an algorithm, for which the switchover of the current controller is not required. This enables the smooth transfer from the buck mode to the boost mode and vice versa. Furthermore, the application of parallel control, combined with the DC droop control and secondary control algorithms, is found to increase the accuracy of current sharing while enhancing the ability of the system to compensate for voltage sag.

Sections 2 and 3 of this paper are described as the structure and configuration of the proposed DC nano-grid system and the bidirectional converter, respectively. In Section 4, a description of parallel operation control is provided. The experimental results are presented and discussed in Section 5, and the performance of two 20 kW prototypes are experimentally verified.

2. DC Nano-Grid System

The design specifications of the DC nano-grid system proposed in this paper are summarized in Table 1.

Table 1. Specification of the DC nano-grid system.

	Parameter	Value
PV	Voltage range Input power	225–830 V 120 kW
Battery	Voltage range Input power	225–830 V 80 kW
DC-DC Converter	Output power DC-link voltage Nominal DC-link voltage Efficiency Charging method	20 kW 700–750 V 750 V 98.5% (@20 kW) CC, CP, and CV

Figure 3 illustrates the power flow of the overall system, which is composed of ESS, PV generators, grid, and loads. For the current sharing of the 80 kW ESS, four 20 kW bidirectional converters are connected in parallel. Figure 3a shows the case where the grid is connected properly. In this case, the AC–DC converter controls the DC link voltage. When the amount of load exceeds the amount of power generated by the PV system, the DC–DC converter of the ESS feeds the load through constant power (CP) control. In contrast, when the amount of load is smaller than the amount of power generated by the PV system, the DC–DC converter charges the battery through constant current–constant voltage (CC–CV) control. Figure 3b shows the case wherein the electrical power goes out unexpectedly. This causes the grid to be shut down. In this case, the converter of the ESS controls the DC link voltage. In order to increase the performance of current sharing between the converter modules while improving the system's ability to compensate for the DC link voltage sag, DC droop control and secondary control algorithms are applied. When the amount of load is larger than the amount of PV power generation, the converters discharge the battery, and when the amount of load is smaller than the amount of PV power generation, the converters then charge the battery.

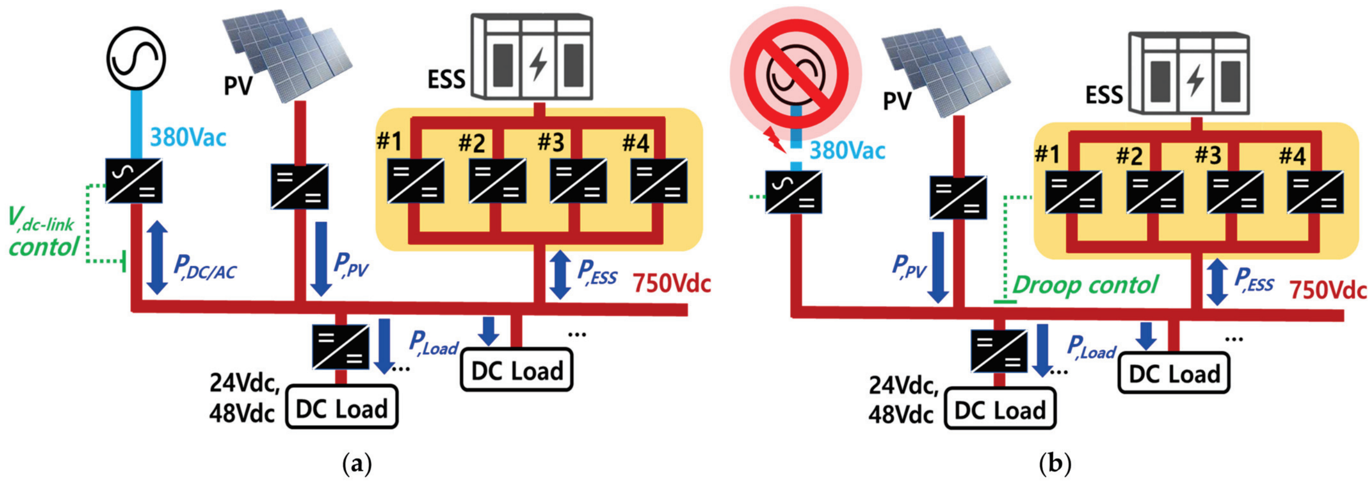

Figure 3. Islanding test scheme in dc nano-grid system: (**a**) Case of the grid connected, (**b**) Case of islanding.

3. Proposed Bidirectional Converter

3.1. Topology Selection

The DC link voltage is 750 V, while the battery voltage ranges from 225 to 830 V; hence, the DC–DC converter is required to not only allow for bidirectional power flow but also to buck and boost the voltage. Among converters capable of stepping up/stepping down the voltage in bidirectional power flow are cascaded converters. Cascaded converters can be classified into cascaded buck–boost converters and cascaded boost–buck converters depending on the combination order. The cascaded buck–boost converter has a cascaded structure of a buck converter in the first stage and a boost converter in the second stage. In contrast, the cascaded boost–buck converter has a cascaded structure of a boost converter in the first stage and a buck converter in the second stage [37–39]. Among them, the cascaded buck–boost converter additionally requires a filter due to its larger battery current ripple [40–42]. Moreover, when the cascaded buck–boost converter is interleaved and employs a six-pack IPM, the IPM cannot be used in an optimum manner. This is because the number of MOSFETs is mismatched. The converter requires both the input and output stages to have the same number of phases for interleaving. Even though the interleaving cascaded buck–boost converter transforms asymmetrically, the IPM is not used optimally. This is because high-side drains are disconnected partially. In order to use the six-pack IPM optimally, high-side MOSFET drains should be connected to each other. In contrast, the cascaded boost–buck converter has a smaller current ripple compared to the cascaded buck–boost converter, since input and output inductors act as filter. When interleaving is applied, the cascaded boost–buck converter, which is symmetrical in structure, cannot use the IPM optimally, because the number of MOSFETs is mismatched. However, the cascaded boost–buck converter, which is asymmetrical in structure, allows different numbers of phases for the input and output stages. Therefore, it is possible to optimally use a commercial six-pack IPM. Figure 4 shows the proposed bidirectional DC–DC converter with a cascaded structure comprising a two-phase interleaved boost converter and a single-phase buck converter.

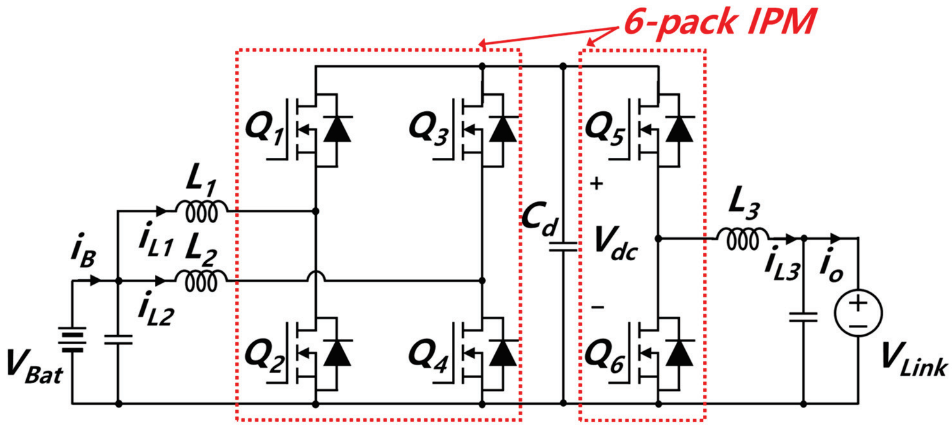

Figure 4. Proposed bi-directional boost-buck converter.

Figure 5 shows a commercial SiC-based six-pack IPM composed of a SiC MOSFET. The IPM and its schematic diagram are presented as Figure 5a,b, respectively. The SiC MOSFET has good characteristics of switching and conducting. SiC has a lower drift layer resistance internally than Si-based switches and does not need to inject minority carriers to lower the on-resistance per unit area; high-speed switching is possible. Moreover, SiC has a higher doping concentration than Si-based switches, so it is possible to achieve low on-resistance [43–45]. PMF75-120-S002 (MITSUBISHI Electric Co. Ltd., Tokyo, Japan) is applied. The IPM is embedded with gate drivers and protection circuits; it also contains a relatively small number of parasitic components. The rated voltage is 1200 V, and the rated current is 75 A. The maximum current in the switch of the proposed converter is 63 A in the boost mode and 34 A in the buck mode. In other words, the converter proposed for using the IPM is suitable.

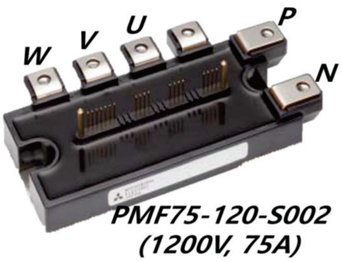

(a)

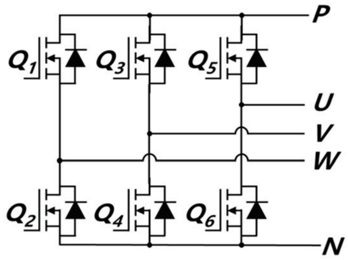

(b)

Figure 5. SiC-IPM: (**a**) IPM, (**b**) IPM Schematic diagram.

In order to compare switch losses under the same conditions, the cascaded buck–boost converter's topology is modified asymmetrically, as shown in Figure 2c, and is compared with the proposed converter. The reason for choosing the topology as shown in Figure 2c, instead of the topology shown in Figure 2a,b, is that conduction loss is lowest among the three cases and the number of switches is lower than that in the symmetrical structure. Hybrid switching is known to minimize the number of switching operations according to the boost mode and buck mode, thereby reducing switching losses and achieving high efficiency. With hybrid switching applied to the topologies of Figure 2c and the proposed converter, Figure 2c and the proposed converter are compared with regard to the maximum voltage and current of the switch, parameters of inductors and capacitors, and also to the necessity of an additional filter as shown in Table 2. The total number of switches is the same, but the number of inductors and capacitors is greater in the proposed topology than in Figure 2c's topology. In general, passive devices account for a large portion of the overall volume of the converter. Given that the proposed topology has a small battery current ripple and does noy require the addition of a filter, the proposed topology is similar to the topology shown in Figure 2c in terms of volume.

Table 2. Comparison of topology.

Parameter		Figure 2c	Proposed
Switch	$V_{\text{peak}}, I_{\text{peak}}$ (No. of switches)	830 V, 63 A (2) 830 V, 20 A (2) 750 V, 63 A (2)	750 V, 63 A (2) 830 V, 63 A (2) 830 V, 34 A (2)
	Total number	6	6
Capacitor	I_{rms} (No. of switches)	27 uF, 27 A, (1) 125 uF, 2.2 A, (1)	27 uF, 2.2 A, (2) 125 uF, 27 A, (1)
Inductor	I_{rms} (No. of switches)	600 uH, 56 A, (2)	600 uH, 56 A, (2) 600 uH, 33 A, (1)
Necessity of additional filter on input and output		Yes	No

Figure 6 shows a comparison of estimated power losses resulting from the switches using Equations (1) and (2) [46,47] when hybrid switching is applied to both topologies.

$$P_{switching} = [0.5I_D V_{DS} f_{sw}(t_{on} + t_{off})] + [0.5C_{oss} V_{DS}^2 f_{sw}] \tag{1}$$

$$P_{conduction} = I_{rms}^2 R_{DS(on)} \tag{2}$$

Figure 6. Comparison of calculated loss: (**a**) Conduction loss, (**b**) Switching loss.

The conduction losses of the two topologies are compared in Figure 6a. The proposed topology shows a smaller conduction loss due to a lower switch current. As shown in Figure 6b, there is no significant difference in the switching loss because hybrid switching is equally applied to both topologies.

3.2. Hybrid Switching Technique

In the proposed converter, switches in each leg operate in a complementary manner. Instead of operating all six switches each time, the proposed converter allows switches to operate through hybrid switching, as shown in Figure 7. Main duties D_1 ~D_3 are matched with main switches Q_2, Q_4, and Q_5, respectively. With the battery as an input and the DC link as an output, in the boost mode, switches from Q_1 to Q_4 execute switching operations, Q_5 remains turned on, and Q_6 remains turned off, as shown in Figure 7a. During boost mode, the voltage of the capacitor V_{dc}, of which the middle position of the topology, is equivalent to the DC link voltage. In the buck mode, as shown in Figure 7b, switches Q_5 and Q_6 perform switching operations, Q_1 and Q_3 remain turned on, and Q_2 and Q_4, remain turned off. During buck mode, the voltage of capacitor V_{dc} is equivalent to the battery voltage. In contrast, with the DC link as an input and the battery as an output, the switching patterns are reversed. In other words, switching operation in the boost mode proceeds as shown in Figure 7b, and switching operation in the buck mode proceeds as shown in Figure 7a. This paper discusses the proposed topology and control scheme, based on batteries as input and DC links as output.

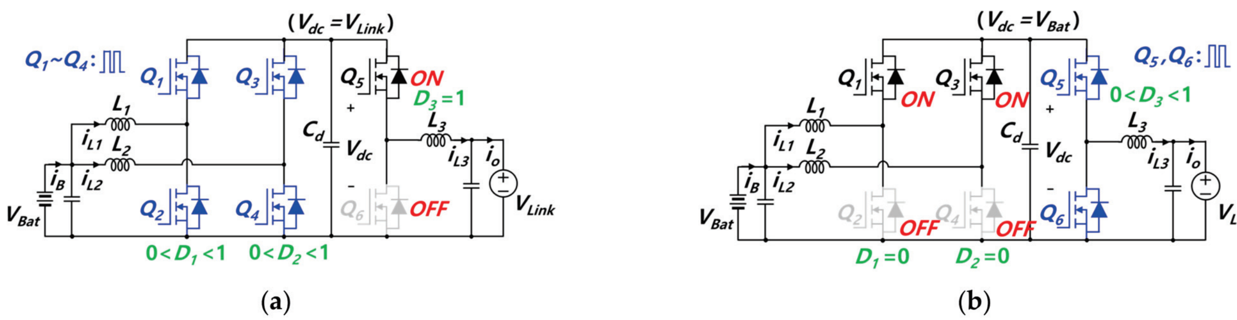

Figure 7. Operation mode for hybrid switching: (**a**) Boost mode, (**b**) Buck mode.

Hybrid switching is applied to the proposed bidirectional converter to minimize the number of switching operations according to the buck mode and boost mode. Thereby, switching losses are reduced. Furthermore, the converter would constitute a two-stage converter with a slow output response if all six switches operated together each time, as employed in the conventional method. Hybrid switching enables the converter to operate in a single-stage configuration. As a result, the converter's output response is faster compared to that of the conventional method. However, a large transient may occur during the transition between buck mode and boost mode, leading to overvoltage, overcurrent, and switch failure. Thus, it is necessary to employ a control algorithm to implement a smooth transition between buck mode and boost mode.

3.3. Control Algorithm to Implement Seamless and Autonomous Mode Transition

Figure 8 shows a control algorithm designed to enable a seamless and autonomous mode transition from the buck mode to the boost mode and vice versa. It is composed of two voltage controllers and three current controllers, which achieved average value control using a conventional PI (Proportional–Integral) compensator. Each compensator is saturated or activated, depending on the operation mode of the proposed converter. When the saturated compensator becomes activated, a cumulative error from the saturated integrator may lead to the malfunction of the compensator. In order to prevent malfunction, anti-windup is applied. The parameters of control are listed in Table A1 of Appendix A.

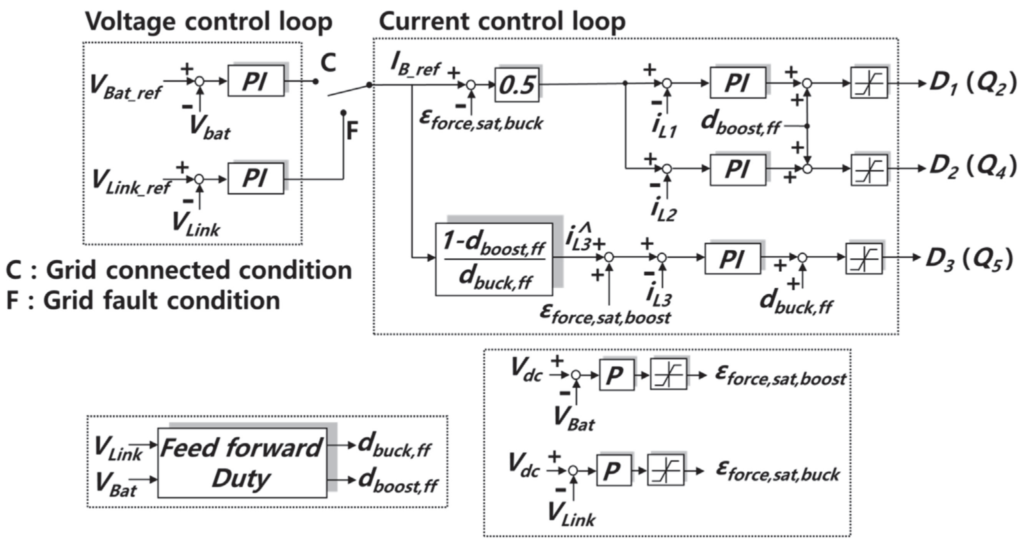

Figure 8. Control algorithm of the proposed converter.

When the grid works properly, the external feedback loop is connected to the battery voltage (V_{Bat}) controller, point (C) in Figure 8. However, in the case of grid failure, the external feedback loop is connected to the DC link voltage (V_{Link}) controller, point (F), in order to execute DC link voltage control. Moreover, the internal feedback loop conducts current control according to the reference value of battery current $I_{\mathrm{B\_ref}}$ required by the external feedback loop. In order to keep each phase current of the interleaved boost converter well balanced, the inductor current of each phase (i_{L1} and i_{L2}) is controlled, through using each current controller. Furthermore, the feed-forward duties $d_{\mathrm{buck,ff}}$ and $d_{\mathrm{boost,ff}}$ are added to the internal feedback loop to improve control performance and disturbance suppression performance. The feed-forward duties $d_{\mathrm{buck,ff}}$ and $d_{\mathrm{boost,ff}}$, which range from 0 to 1, are as described in Equations (3) and (4). This means that when the value of $d_{\mathrm{buck,ff}}$ or $d_{\mathrm{boost,ff}}$ exceeds 1, it is saturated to 1. Furthermore, it is saturated to 0 when the value is below 0.

$$d_{boost,ff} = 1 - \frac{V_{Bat}}{V_{Link}} \ (0 \leq d_{boost,ff} \leq 1) \tag{3}$$

$$d_{buck,ff} = \frac{V_{Link}}{V_{Bat}} \ (0 \leq d_{buck,ff} \leq 1) \tag{4}$$

The inductor current i_{L3} of the buck converter is controlled according to the predicted current $i^{\wedge}_{\mathrm{L3}}$, which is obtained from the combination of Equations (3) and (4). $i^{\wedge}_{\mathrm{L3}}$ is calculated as described in Equation (5).

$$I^{\wedge}_{L3} = \frac{1 - d_{boost,ff}}{d_{buck,ff}} \cdot I_{Bat} \tag{5}$$

In order to assist the saturation or activation of the current control compensator, saturation parameters $\varepsilon_{\text{force,sat,buck}}$ and $\varepsilon_{\text{force,sat,boost}}$ are used in the internal feedback loop.

The parameters $\varepsilon_{\text{force,sat,buck}}$ and $\varepsilon_{\text{force,sat,boost}}$ make the current controller saturated forcibly in the buck mode and boost mode, respectively. The value of parameters is varied from 0 to the value, which is sufficient to saturate the compensator. The $\varepsilon_{\text{force,sat,buck}}$ is in proportion to the difference between V_{dc} and V_{Link}, and the $\varepsilon_{\text{force,sat,boost}}$ is in proportion to the difference between V_{dc} and V_{Bat}. Considering that V_{dc} is equal to V_{Link} in the boost mode and equal to V_{Bat} in the buck mode, the saturation parameter values are as shown in Table 3. During boost mode, i_{L1} and i_{L2} current controllers are activated because $\varepsilon_{\text{force,sat,buck}}$ is 0. Moreover, the i_{L3} current controller is saturated due to the influence of $\varepsilon_{\text{force,sat,boost}}$. As a result, Q_5 remains turned on and Q_6 remains turned off during boost mode, since D_3 is saturated to the value 1. In contrast, the i_{L3} current controller is activated and i_{L1} and i_{L2} current controllers are saturated during buck mode. Likewise, Q_2 and Q_4 remain turned off and Q_1 and Q_3 remain turned on because $\varepsilon_{\text{force,sat,boost}}$ is 0, and $\varepsilon_{\text{force,sat,buck}}$ is sufficient to be saturated.

Table 3. Saturation parameter value according to boost mode and buck mode.

Saturation Parameter	Boost Mode	Buck Mode
$\varepsilon_{force,sat,buck}$	0	α [1]
$\varepsilon_{force,sat,boost}$	α [1]	0

[1] Sufficient value to saturate the compensator.

Figure 9 shows simulated waveforms obtained during the seamless transition between buck and boost mode. As shown in Figure 9, seamless transition between buck and boost modes is possible, because the switchover of the current controller is not required. The simulated power rating of charging or discharging the battery is 20 kW, the DC link voltage is 750 V, and the battery voltage is varied between 225 V and 830 V. The battery current, which is sum of i_{L1} and i_{L2}, is controlled while the battery voltage changes. Figure 9a shows that the battery voltage V_{Bat} increases from 225 V to 830 V, due to charging of the battery. While V_{Bat} increases, mode transition occurs from the boost mode to the buck mode. Contrastively, Figure 9b shows the decrease in the battery voltage due to discharging and also shows the mode transition from the buck mode to the boost mode. In the boost mode, considering that the feed-forward $d_{\text{buck,ff}}$ becomes 1 and the influence of $\varepsilon_{\text{force,sat,boost}}$, D_3 is saturated to 1. Thus, Q_5 remains turned on and Q_6 remains turned off. Meanwhile, switches from Q_1 to Q_4 execute switching operations since the values of D_1 and D_2 fall within the range of the triangle wave, which is a carrier of PWM.

In contrast, during buck mode, Q_5 and Q_6 execute switching operations, because D_3 falls within the range of the carrier for PWM. Furthermore, given that the feed-forward $d_{\text{boost,ff}}$ becomes 0 and the influence of $\varepsilon_{\text{force,sat,buck}}$, D_1 and D_2 are saturated to 0. As a result, Q_1 and Q_3 remain turned on; Q_2 and Q_4 remain turned off. It is found that seamless and autonomous transition between buck and boost modes is achieved because the switchover of the current controller is not required regardless of the step-up or step-down situation. Figure 10 shows simulated waveforms obtained during transition from discharging to charging and vice versa. Figure 10a,b are obtained during boost mode and during buck mode, respectively. Seamless transition between charging and discharging of the battery is possible due to the original characteristic of the bidirectional topology.

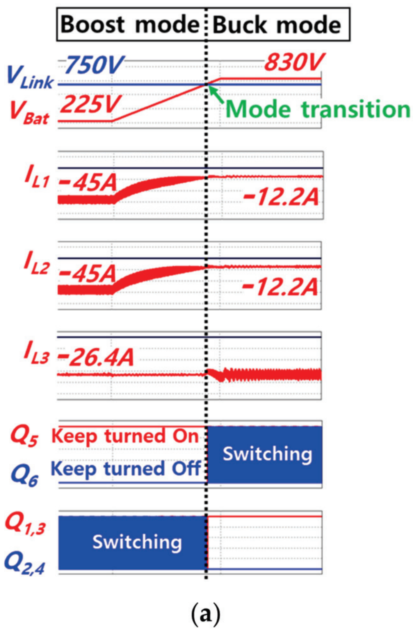

Figure 9. Simulated waveforms for mode transition: (**a**) During charging battery, (**b**) During discharging battery.

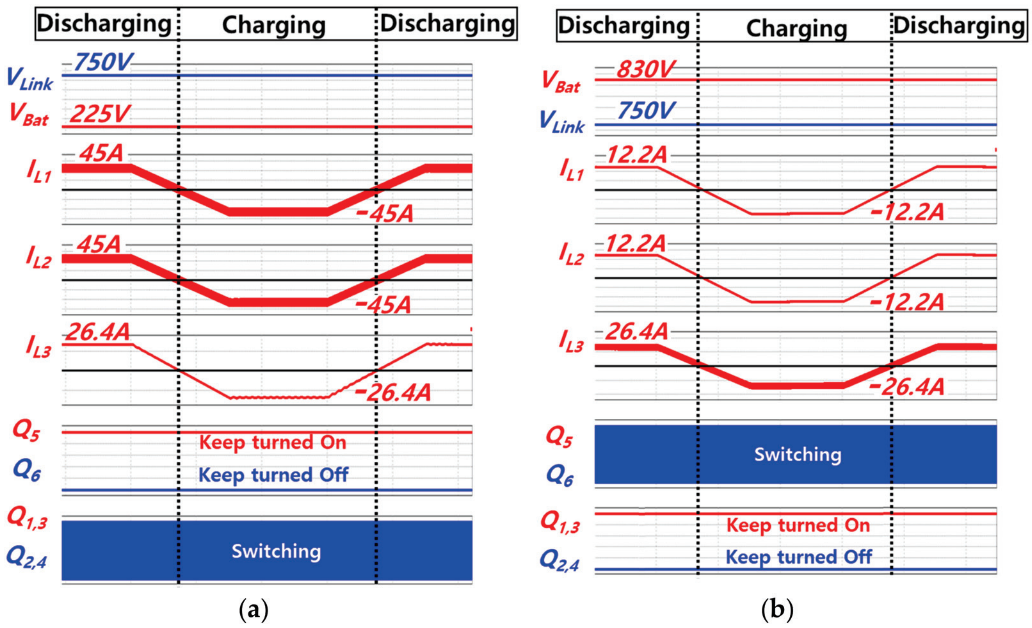

Figure 10. Simulated waveforms for transition from discharging to charging and vice versa: (**a**) During boost mode, (**b**) During buck mode.

4. Parallel Operation Using DC Droop Control

In general, the current sharing performance between modules is degraded due to a difference in line impedance during parallel operation. In order to overcome the degradation, droop control using virtual impedance is applied. Droop control is a distributed parallel operation method, and it is controlled by calculating the reference value of voltage according to the output current of each converter. Moreover, the droop control has an advantage in that it does not require a communication between modules to achieve load sharing. This is because there is a profile between the output current of each converter and the output voltage, using virtual resistance. As a result, it is possible to install it wherever necessary regardless of site conditions.

Figure 11a shows a brief configuration of the parallel connection for circuit modules to analyze droop control. According to the difference between line resistances R_{Line1} and R_{Line2} and also the difference between virtual resistances R_{d1} and R_{d2} of each converter, the output currents i_{o1} and i_{o2} of each converter are unbalanced, as shown in Figure 11b. Furthermore, if virtual resistance is much larger than line resistance, the output currents i_{o1} and i_{o2} are the same because it is possible to neglect the line resistance, in the case of equal virtual resistance. The output voltage V_{o} when droop control is applied can be expressed as shown in Equation (6).

$$V_{\mathrm{o}}^{*} = V_{\mathrm{Link}}^{*} - R_{\mathrm{d}} \cdot i_{\mathrm{oN}} \tag{6}$$

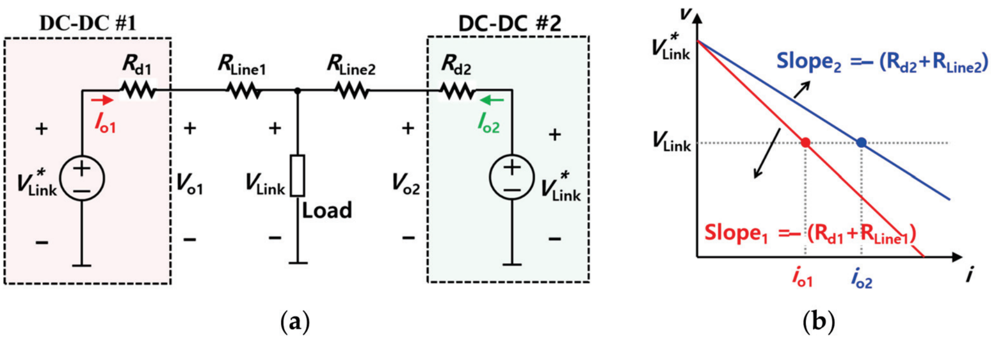

Figure 11. Simplified module for DC droop control: (**a**) Configuration of parallel connection for dc-dc converters, (**b**) DC droop curve.

Equation (6) serves as a profile in droop control. The reference value of V_{o} is a voltage set point $V^{*}{}_{\mathrm{o}}$. The voltage set point is adjusted and controlled according to the output current for load current sharing. However, load sharing between converter modules may be inaccurately conducted due to differences in the line resistance. Thus, it is important to adjust the virtual resistance appropriately.

Figure 12 shows the droop slopes resulting from the difference between the line resistances and the difference between virtual resistances. Figure 12a shows case 1, for which the offset error ΔV_{n} is 0 and the line resistances are different from each other. In contrast, Figure 12b shows case 2, in which the offset error is not 0 and the line resistances are the same. The solid line indicates the case where the virtual resistance R_{d} is smaller, while the dotted line indicates the case where the virtual resistance $R_{\mathrm{d}}{}'$ is larger.

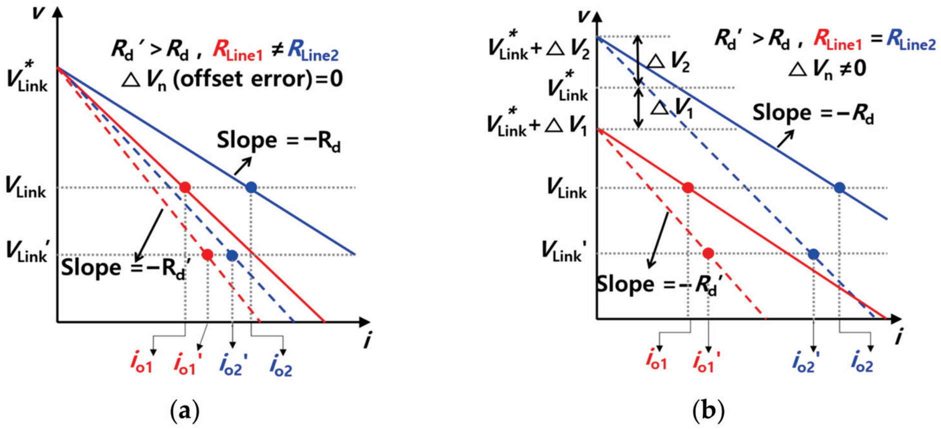

Figure 12. Droop slope with current sharing performance depending on slope gain (R_{d}): (**a**) Case 1 ($R_{\mathrm{Line1}} \neq R_{\mathrm{Line2}}$, $\Delta V_{\mathrm{n}} = 0$), (**b**) Case 2 ($R_{\mathrm{Line1}} = R_{\mathrm{Line2}}$, $\Delta V_{\mathrm{n}} \neq 0$).

The difference between $i_{\mathrm{o1}}{}'$ and $i_{\mathrm{o2}}{}'$ is smaller than the difference between i_{o1} and i_{o2}. In other words, the load sharing performance is better in the case of $R_{\mathrm{d}}{}'$ than in the case of R_{d}. Assuming that the virtual resistance is smaller, the effect of line resistance becomes larger. It should be noted that this leads to a degradation in load sharing performance. In contrast, if the virtual resistance is larger, load sharing performance may be improved, but the amount of the voltage sag increases, as is the case when V_{Link}' is lower than V_{Link}. The trade-off relationship between load sharing performance and voltage sag is affected by a difference in virtual resistance. In order to relieve the trade-off relationship, secondary control is used with droop control. Secondary control is a method used to prevent voltage sag, which occurs when the virtual resistance is large in droop control.

Figure 13 shows the algorithm of DC droop control with secondary control. In secondary control, the central controller controls the DC link voltage, which has been reduced, in order to compensate for the DC link voltage. The central controller transmits the compensation value ΔV_{Link} to each converter's controller, through low-bandwidth network communication. As a result, the value ΔV_{Link} is added to the voltage set point V^{*}_{o}.

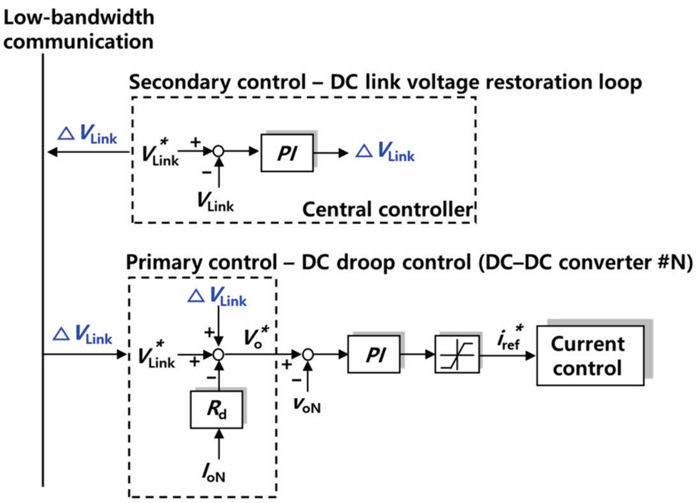

Figure 13. DC droop control with the secondary control algorithm.

Figure 14 shows the droop slope with secondary control. As in Figures 12a,b and 14a shows case 1, for which the offset error ΔV_{n} is 0 and the line resistances are different from each other. Additionally, Figure 14b shows case 2, for which the offset error is not 0 and the line resistances are the same. The solid lines and dotted lines indicate cases before and after the application of secondary control, respectively. As a result, the compensation of the voltage sag is achieved using secondary control with the DC droop control without degradation in the load sharing performance.

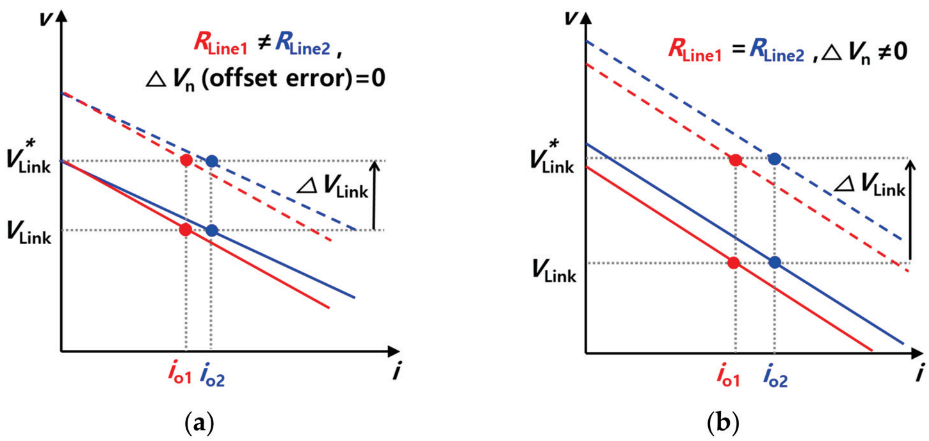

Figure 14. Droop slope with secondary control: (**a**) Case 1 ($R_{\text{Line1}} \neq R_{\text{Line2}}$, $\Delta V_{\text{n}} = 0$), (**b**) Case 2 ($R_{\text{Line1}} = R_{\text{Line2}}$, $\Delta V_{\text{n}} \neq 0$).

5. Experimental Results

In order to verify the performance and feasibility of the proposed bidirectional converter intended for the DC nano-grid system, a set of two 20 kW prototype modules are manufactured and configured, as shown in Figure 15. The overall dimensions of one set are 650 mm × 445 mm × 130 mm (37.6 L). A dual-core DSP TMS320F28377D is used as a digital controller, and each module is controlled by one core.

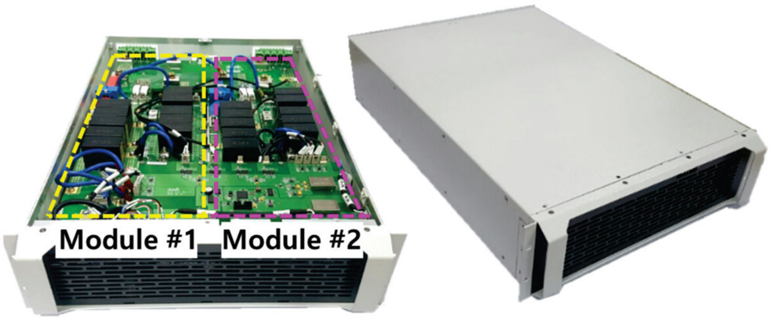

Figure 15. Prototype of proposed converter, which set of two 20 kW modules.

Figure 16 shows experimental waveforms of the proposed converter during the discharging operation. To be more specific, the experimental waveform during boost mode is presented in Figure 16a, and the waveform during buck mode is shown in Figure 16b. The experimental result of Figure 16a confirms that there is no ripple component in the inductor current i_{L3} of the buck converter parts, and ripple components are found in the inductor currents i_{L1} and i_{L2} of the boost converter parts in the boost mode. This is because the hybrid switching control scheme is applied to the proposed converter. In contrast, Figure 16b shows that there is no ripple component in i_{L1} and i_{L2}, and a ripple component is found in i_{L3} during buck mode. Figure 16c shows an experimental waveform of seamless mode transition between boost mode and buck mode, while the battery voltage is varied. During the experiment shown in Figure 16c, the proposed converter maintains the DC link voltage at 750 V. In this case, it should be noted that the proposed converter has seamless mode transition and controls the DC link voltage when a grid failure occurs.

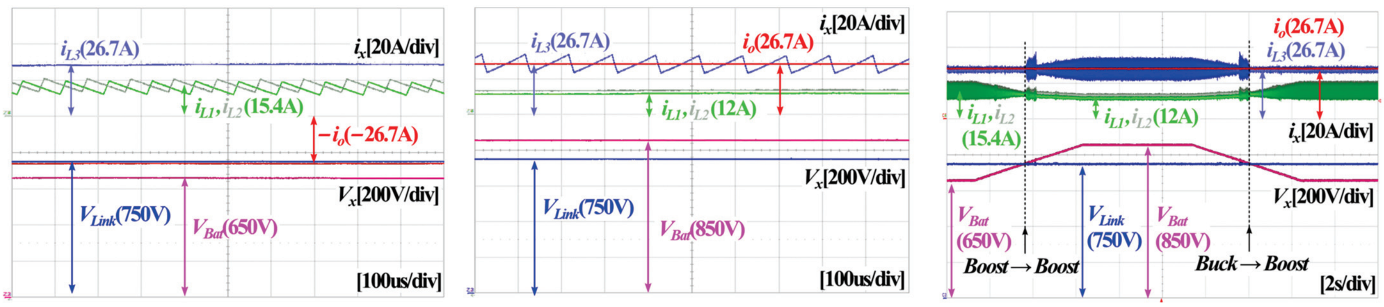

(**a**) (**b**) (**c**)

Figure 16. Experimental waveforms of the proposed converter in discharging operation: (**a**) V_{Link} = 750 V, V_{Bat} = 650 V, P_{out} = 20 kW with boost mode, (**b**) V_{Link} = 750 V, V_{Bat} = 850 V, P_{out} = 20 kW with buck mode, (**c**) V_{Link} = 750 V, V_{Bat} = 650~850 V, P_{out} = 20 kW with mode transition between boost mode and buck mode, during V_{Link} control.

Figure 17 presents waveforms experimentally obtained during droop control according to the virtual resistance R_d. Figure 17a shows cases before and after the application of droop control, when R_d is 0.1 Ω. Furthermore, Figure 17b shows the case when R_d is 3.0 Ω. The more the virtual resistance is increased, the better the load sharing performance is, while the voltage sag is also increased, as shown in Figure 17a,b. A trade-off relationship between the load sharing performance and voltage sag is confirmed while droop control is applied. Furthermore, it is important to adjust the virtual resistance appropriately because the trade-off relationship is sensitive to virtual resistance. It makes parallel operation difficult for each converter module. In order to relieve the difficulty of parallel operation, secondary control is used, which prevents voltage sag.

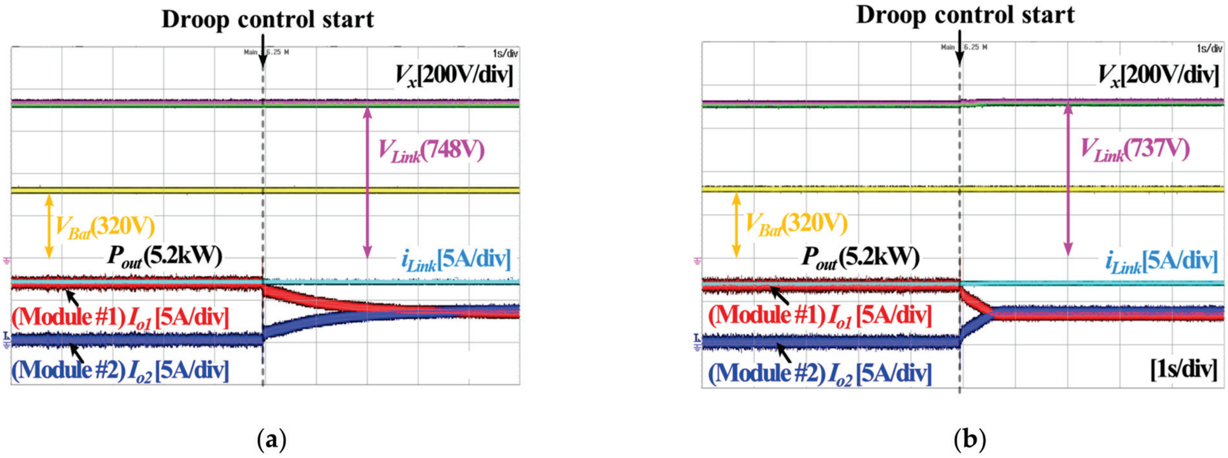

Figure 17. Experimental waveforms of DC droop control according to virtual resistance (R_d): (**a**) R_d = 0.1 Ω, (**b**) R_d = 3.0 Ω.

Figure 18a,b show experimental waveforms before and after the application of secondary control, respectively. Before secondary control is applied, the voltage sag increases as the load increases. This is because the large virtual resistance improves the load sharing performance. However, after secondary control is applied, voltage sag does not occur even though the load increases, and the load sharing performance is improved.

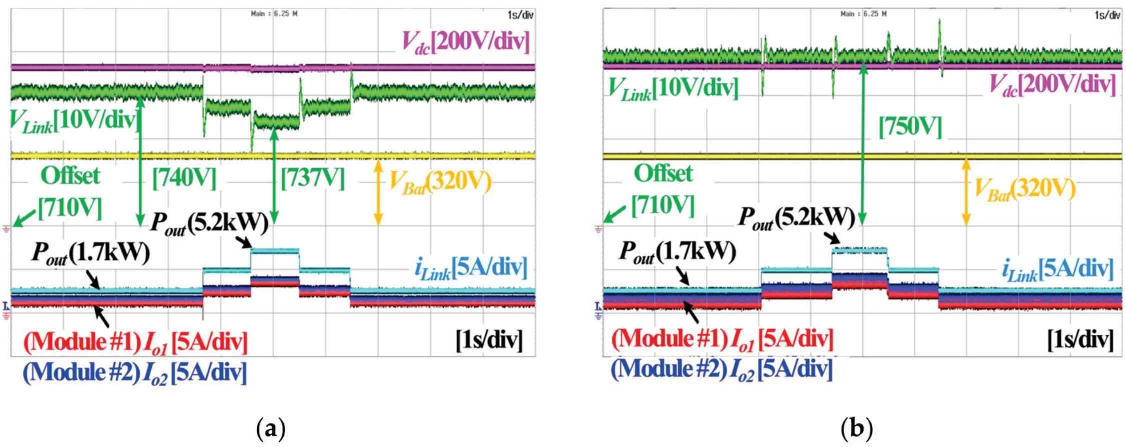

Figure 18. Experimental waveforms of droop control according to application of secondary control: (**a**) Droop control without secondary control, (**b**) Droop control with secondary control.

Figure 19 shows the measured efficiency of the prototype for the proposed converter, which applies a hybrid switching control scheme. The loss of the proposed topology mainly consists of the conduction loss and switching loss of the switch. The conduction loss of the switch is greatly affected by the operating power and is determined by the current according to the battery voltage. Switching losses are determined by battery voltage and current. Thereby, the efficiency is presented according to the operating power and battery voltage. It is measured by a WT3000 (YOKOGAWA). When the efficiency is measured during the battery voltage is 225 V, the efficiency is not measured more than 12 kW. Since operating point of over the 12 kW is exceeds the electrical load equipment specifications.

The measured efficiency during discharging of the battery is shown in Figure 19a. The maximum efficiency is 98.9%, while the rated efficiency is 98.8%. Figure 19b shows the measured efficiency during charging of the battery. The maximum efficiency and the rated efficiency are 99.2% and 98.8%, respectively. The experimental results confirmed that high efficiency is achieved by using the SiC-based six-pack IPM optimally and also by applying the hybrid switching control scheme for the proposed converter.

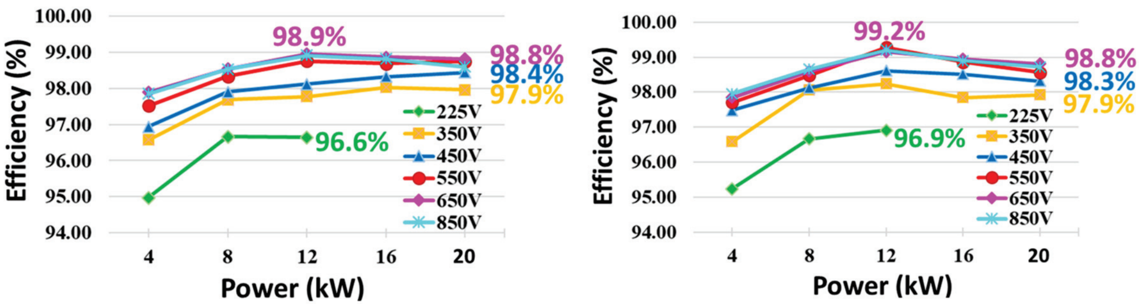

(**a**) (**b**)

Figure 19. Measured efficiency: (**a**) Efficiency of discharge operation, (**b**) Efficiency of charge operation.

6. Conclusions

This paper proposes a bidirectional boost–buck converter employing a six-pack SiC optimally, using droop control with secondary control in DC nano-grid application. The topology is a cascade structure of a two-phase interleaving boost converter and a single-phase buck converter, which has a wide range of battery voltage and the capability to step up and step down in bidirectional power flow. A commercial six-pack SiC-based IPM is optimally used to implement a converter with high efficiency and compact structure. In order to minimize the switching losses, a hybrid switching control scheme, which a particular switch always hold in a turn-off or turn-on state according to the boost mode or buck mode, is applied to the proposed converter. Unlike existing converters in which all switches operate simultaneously, in aspect of the proposed converter, some switches are switching, others hold in a turn-off or turn-on state. Thus, the proposed converter has high efficiency. The maximum efficiency is 99.2%, and the rated efficiency is 98.8%. In addition, there is a smooth transition between buck mode and boost mode, because switchover of the current controller for the converter is not required. Meanwhile, as parallel operation control of the converter modules, DC droop control and secondary control are combined effectively. As a result, not only is current sharing performance improved but so too is the ability of the system to compensate for voltage sag. Experimental results are verified using two modules as laboratory prototypes, of which the power rating is 20 kW. The results from the 20 kW prototype are provided to validate the proposed topology and control schemes, which applied hybrid switching and parallel operation.

Author Contributions: The authors contributed to the paper as follows: Study conception and idea: Y.K. and S.C.; design procedure: Y.K.; experiment and results: Y.K.; draft manuscript preparation: Y.K. and S.C. All authors have read and agreed to the published version of the manuscript.

Funding: This research was funded by a grant of the basic research program from the Korea Institute of Machinery and Materials (grant number: NK246A).

Institutional Review Board Statement: Not applicable.

Informed Consent Statement: Not applicable.

Data Availability Statement: Not applicable.

Acknowledgments: This work was supported by the basic research program grant funded from Korea Institute of Machinery and Materials (KIMM) (grant number: NK246A).

Conflicts of Interest: The authors declare no conflict of interest.

Appendix A

Table A1. Parameter list of the prototype.

Parameter	Meaning
V_{Bat}	Battery voltage
V_{Link}	DC-link voltage
V_{dc}	Voltage of capacitor, which the middle position of the topology
D_1	Duty for Q2 (Switch)
D_2	Duty for Q4 (Switch)
D_3	Duty for Q5 (Switch)
$d_{\mathrm{boost,ff}}$	Feed forward duty for boost mode
$d_{\mathrm{buck,ff}}$	Feed forward duty for buck mode
$i_{\hat{L3}}$	Predicted inductor (L_3) current
$\varepsilon_{\mathrm{force,sat,buck}}$	Parameter for forcing saturation of current controller of i_{L1} and i_{L2} in buck mode
$\varepsilon_{\mathrm{force,sat,boost}}$	Parameter for forcing saturation of controller of i_{L3} in boost mode
R_{d}	Virtual resistance
R_{line}	Line resistance
ΔV_{n}	Offset error for V_{Link} reference

References

1. Dragicevic, T.; Lu, X.; Vasquez, J.C.; Guerrero, J.M. DC Microgrids—Part I: A Review of Control Strategies and Stabilization Techniques. *IEEE Trans. Power Electron.* **2016**, *31*, 4876–4891. [CrossRef]
2. Dragičević, T.; Lu, X.; Vasquez, J.C.; Guerrero, J.M. DC Microgrids—Part II: A Review of Power Architectures, Applications, and Standardization Issues. *IEEE Trans. Power Electron.* **2016**, *31*, 3528–3549. [CrossRef]
3. Zia, M.F.; Benbouzid, M.; Elbouchikhi, E.; Muyeen, S.M.; Techato, K.; Guerrero, J.M. Microgrid Transactive Energy: Review, Architectures, Distributed Ledger Technologies, and Market Analysis. *IEEE Access* **2020**, *8*, 19410–19432. [CrossRef]
4. Peyghami, S.; Palensky, P.; Blaabjerg, F. An Overview on the Reliability of Modern Power Electronic Based Power Systems. *IEEE Open J. Power Electron.* **2020**, *1*, 34–50. [CrossRef]
5. Xu, Q.; Vafamand, N.; Chen, L.; Dragicevic, T.; Xie, L.; Blaabjerg, F. Review on Advanced Control Technologies for Bidirectional DC/DC Converters in DC Microgrids. *IEEE J. Emerg. Sel. Top. Power Electron.* **2021**, *9*, 1205–1221. [CrossRef]
6. Farrokhabadi, M.; Lagos, D.; Wies, R.W.; Paolone, M.; Liserre, M.; Meegahapola, L.; Kabalan, M.; Hajimiragha, A.H.; Peralta, D.; Elizondo, M.A.; et al. Microgrid Stability Definitions, Analysis, and Examples. *IEEE Trans. Power Syst.* **2020**, *35*, 13–29. [CrossRef]
7. Lasseter, R.H.; Chen, Z.; Pattabiraman, D. Grid-Forming Inverters: A Critical Asset for the Power Grid. *IEEE J. Emerg. Sel. Top. Power Electron.* **2020**, *8*, 925–935. [CrossRef]
8. Guerrero, J.; Blaabjerg, F.; Zhelev, T.; Hemmes, K.; Monmasson, E.; Jemeï, S.; Comech, M.P.; Granadino, R.; Frau, J.I. Distributed Generation: Toward a New Energy Paradigm. *IEEE Ind. Electron. Mag.* **2010**, *4*, 52–64. [CrossRef]
9. Vilathgamuwa, D.M.; Gajanayake, C.J.; Loh, P.C. Modulation and Control of Three-Phase Paralleled Z-Source Inverters for Distributed Generation Applications. *IEEE Trans. Energy Convers.* **2009**, *24*, 173–183. [CrossRef]
10. Carrasco, J.M.; Franquelo, L.G.; Bialasiewicz, J.T.; Galván, E.; Portillo Guisado, R.C.; Prats, M.Á.M.; León, J.I.; Moreno-Alfonso, N. Power-Electronic Systems for the Grid Integration of Renewable Energy Sources: A Survey. *IEEE Trans. Ind. Electron.* **2006**, *53*, 1002–1016. [CrossRef]
11. Pindoriya, R.M.; Pindoriya, N.M.; Rajendran, S. Simulation of DC/DC Converter for DC Nano-Grid Integrated with Solar PV Generation. In Proceedings of the 2015 IEEE Innovative Smart Grid Technologies–Asia (ISGT ASIA), Bangkok, Thailand, 3–6 November 2015. [CrossRef]
12. Yoomak, S.; Ngaopitakkul, A. Development of Sustainable Nanogrid Road Lighting Systems. *IEEE Trans. Intell. Transp. Syst.* **2021**, *22*, 6682–6699. [CrossRef]
13. Anita, S.; Sukhi, Y.; Elakkia, E. DC and AC Micro Grid Comparative Analysis. In Proceedings of the International Interdisciplinary Humanitarian Conference for Sustainability(IIHC), Bengaluru, India, 18–19 November 2022; pp. 1156–1160. [CrossRef]
14. Sengarap, S.; Kastha, D.; Bajpai, P. Design and Analysis of A Novel Current-Fed Three Level Three Limb TAB Converter with Auxilary Inductor for DC Micro-Grid Application. In Proceedings of the IEEE Applied Power Electronics Conference and Exposition(APEC) 2023, Orlando, FL, USA, 19–23 March 2023; pp. 2136–2143. [CrossRef]
15. Zhao, B.; Song, Q.; Liu, W.; Sun, Y. Overview of Dual-Active-Bridge Isolated Bidirectional DC–DC Converter for High-Frequency-Link Power-Conversion System. *IEEE Trans. Power Electron.* **2014**, *29*, 4091–4106. [CrossRef]
16. Lee, M.; Choi, D.; Chae, J.; Cheon, S.; Moon, G. Voltage-Balancing Dual-Active-Bridge (VB-DAB) Converter for Bipolar DC Distribution System. *IEEE Trans. Ind. Electron.* **2023**, *70*, 2461–2471. [CrossRef]

17. Qin, D.; Sun, Q.; Wang, R.; Ma, D.; Liu, M. Adaptive bidirectional droop control for electric vehicles parking with vehicle-to-grid service in microgrid. *CSEE J. Power Energy Syst.* **2020**, *6*, 793–805. [CrossRef]
18. Le, T.; Kim, S.; Choi, S. A Four-Phase Current-Fed Push–Pull DAB Converter for Wide-Voltage-Range Applications. *IEEE Trans. Power Electron.* **2021**, *36*, 11383–11396. [CrossRef]
19. Le, T.; Nguyen, M.; Duong, T.; Wang, C.; Choi, S. Open-Circuit Fault-Tolerant Control for a Three-Phase Current-Fed Dual Active Bridge DC–DC Converter. *IEEE Trans. Ind. Electron.* **2023**, *70*, 1586–1596. [CrossRef]
20. Qin, D.; Sun, Q.; Ma, D.; Sun, J. Model Predictive control of dual-active-bridge based fast battery charger for plug-in hybrid electric vehicle in the future grid. In Proceedings of the IEEE Innovative Smart Grid Technologies–Asia (ISGT Asia) 2019, Chengdu, China, 21–24 May 2019. [CrossRef]
21. Paul, A.R.; Bhattacharya, A.; Chatterjee, K. A Single-Phase Grid-Connected Boost/Buck-Boost-Derived Solar PV Micro-Inverter Topology Having Power Decoupling Capability. *IEEE J. Emerg. Sel. Top. Power Electron.* **2023**, *11*, 2340–2349. [CrossRef]
22. Lai, C.-M.; Lin, Y.-C.; Lin, Y.-J. Newly-Constructed Bidirectional DC/DC Converter Topology with High Voltage Conversion Ratio for Vehicle to DC-Microgrid (V2DCG) System. In Proceedings of the IEEE 2nd International Future Energy Electronics Conference (IFEEC), Taipei, Taiwan, 1–4 November 2015. [CrossRef]
23. Lekic, A.; Stipanoviclekic, D.M. Hysteresis Switching Control of the Ćuk Converter Operating in Discontinuous Conduction Modes. *IEEE Trans. Circuits Syst. II Express Briefs* **2017**, *64*, 1077–1081. [CrossRef]
24. Lee, S.W.; Do, H.L. Zero-Ripple Input-Current High-Step-Up Boost-SEPIC DC-DC Converter with Reduced Switch-Voltage Stress. *IEEE Trans. Power Electron.* **2017**, *32*, 6170–6177. [CrossRef]
25. Park, K.B.; Moon, G.W.; Youn, M.J. Nonisolated High Step-up Boost Converter Integrated with Sepic Converter. *IEEE Trans. Power Electron.* **2010**, *25*, 2266–2275. [CrossRef]
26. Rana, N.; Banerjee, S.; Giri, S.K.; Trivedi, A.; Williamson, S.S. Modeling, Analysis and Implementation of an Improved Interleaved Buck-Boost Converter. *IEEE Trans. Circuits Syst. II Express Briefs* **2021**, *68*, 2588–2592. [CrossRef]
27. Ardi, H.; Ajami, A. Study on a High Voltage Gain SEPIC-Based DC-DC Converter with Continuous Input Current for Sustainable Energy Applications. *IEEE Trans. Power Electron.* **2018**, *33*, 10403–10409. [CrossRef]
28. Anand, A.; Singh, B. Modified Dual Output Cuk Converter-Fed Switched Reluctance Motor Drive with Power Factor Correction. *IEEE Trans. Power Electron.* **2019**, *34*, 624–635. [CrossRef]
29. Pandey, R.; Singh, B. A Power-Factor-Corrected LLC Resonant Converter for Electric Vehicle Charger Using Cuk Converter. *IEEE Trans. Ind. Appl.* **2019**, *55*, 6278–6286. [CrossRef]
30. Sathyan, S.; Suryawanshi, H.M.; Shitole, A.B.; Ballal, M.S.; Borghate, V.B. Soft-Switched Interleaved DC/DC Converter as Front-End of Multi-Inverter Structure for Micro Grid Applications. *IEEE Trans. Power Electron.* **2018**, *33*, 7645–7655. [CrossRef]
31. Garg, A.; Tummuru, N.R.; Oruganti, R. Implementation of Energy Management Scenarios in a DC Microgrid Using DC Bus Signaling. *IEEE Trans. Ind. Appl.* **2021**, *57*, 5306–5317. [CrossRef]
32. Braitor, A.C.; Konstantopoulos, G.C.; Kadirkamanathan, V. Current-Limiting Droop Control Design and Stability Analysis for Paralleled Boost Converters in DC Microgrids. *IEEE Trans. Control Syst. Technol.* **2021**, *29*, 385–394. [CrossRef]
33. Bevrani, H.; Shokoohi, S. An Intelligent Droop Control for Simultaneous Voltage and Frequency Regulation in Islanded Microgrids. *IEEE Trans. Smart Grid* **2013**, *4*, 1505–1513. [CrossRef]
34. Chen, Z.; Lasseter, R.H.; Jahns, T.M. Overcurrent Limiting and DC Bus Voltage Ripple Minimization in Grid-Forming PV Sources under Grid Voltage Sags. In Proceedings of the IEEE 10th International Symposium on Power Electronics for Distributed Generation Systems (PEDG), Xi'an, China, 3–6 June 2019. [CrossRef]
35. Fan, B.; Li, Q.; Wang, W.; Yao, G.; Ma, H.; Zeng, X.; Guerrero, J. A Novel Droop Control Strategy of Reactive Power Sharing Based on Adaptive Virtual Impedance in Microgrids. *IEEE Trans. Ind. Electron.* **2022**, *69*, 11335–11347. [CrossRef]
36. Zhao, X.; Meng, L.; Dragicevic, T.; Savaghebi, M.; Guerrero, J.M.; Vasquez, J.C.; Wu, X. Distributed Low Voltage Ride-Through Operation of Power Converter in Grid-Connected Microgrids under Voltage Sags. In Proceedings of the 2015 IEEE Industrial Electronics Society, Annual Conference (IECON), Yokohama, Japan, 9–12 November 2015. [CrossRef]
37. Triki, Y.; Bechouche, A.; Seddiki, H.; Abdeslam, D.O. A Smart Battery Charger Based on a Cascaded Boost-Buck Converter for Photovoltaic Applications. In Proceedings of the IEEE Industrial Electronics Society, Annual Conference (IECON) 2018, Washington, DC, USA, 21–23 October 2018. [CrossRef]
38. Anuraag, B.V.; Mahalakshmi, R.; Likhtih, S.; Bhargavi, P.; Mohanty, A. Design and Comparative Study of DC-DC Quadratic Buck-Boost Converter and Cascaded Buck-Boost Converter. In Proceedings of the 2021 International Conference on Recent Trends on Electronics, Information, Communication & Technology (RTEICT), Bangalore, India, 27–28 August 2021; pp. 642–646. [CrossRef]
39. Duran, E.; Cardona, S.D.; Galan, J.; Andujar, J.M. Comparative analysis of buck-boost converters used to obtain I-V characteristic curves of photovoltaic modules. In Proceedings of the IEEE Power Electronics Specilists Conference (PESC) 2008, Rhodes, Greece, 15–19 June 2008. [CrossRef]
40. Rana, N.; Banerjee, S. Development of an Improved Input-Parallel Output-Series Buck-Boost Converter and Its Closed-Loop Control. *IEEE Trans. Ind. Electron.* **2020**, *67*, 6428–6438. [CrossRef]
41. Chen, Y.Y.; Chang, Y.C.; Wei, C.L. Mixed-Ripple Adaptive On-Time Controlled Non-Inverting Buck-Boost DC-DC Converter with Adaptive-Window-Based Mode Selector. *IEEE Trans. Circuits Syst. II Express Briefs* **2022**, *69*, 2196–2200. [CrossRef]

42. Wang, S.; Gao, M.; Shi, J. A ZVS Buck/Boost Converter with Coupled-Filter-Inductor. In Proceedings of the 2022 International Conference on Power, Energy and Electrical Engineering (CPEEE), Shiga, Japan, 25–27 February 2022; pp. 180–184. [CrossRef]
43. Sozzi, G.; Sapienza, S.; Nipoti, R.; Chiorboli, G. OCVD Measurement of Ambipolar and Minority Carrier Lifetime in 4H-SiC Devices: Relevance of the Measurement Setup. *IEEE Trans. Electron. Devices* **2021**, *68*, 3254–3260. [CrossRef]
44. Chowdhury, S.S.; Arifin, F. The Effects of the Substrate Doping Concentrations on 6H-SiC Nano-Scale GgNMOS ESD Protection Device. In Proceedings of the 2021 International Conference on Robotics, Electrical and Signal Processing Techniques (ICREST), Dhaka, Bangladesh, 5–7 January 2021; pp. 329–333. [CrossRef]
45. Mori, S.; Aketa, M.; Sakaguchi, T.; Asahara, H.; Nakamura, T.; Kimoto, T. Suppression of Punch-Through Current in 3 KV 4H-SiC Reverse-Blocking MOSFET by Using Highly Doped Drift Layer. *IEEE J. Electron. Devices Soc.* **2018**, *6*, 449–453. [CrossRef]
46. Glitz, E.S.; Ordonez, M. MOSFET Power Loss Estimation in LLC Resonant Converters: Time Interval Analysis. *IEEE Trans. Power Electron.* **2019**, *34*, 11964–11980. [CrossRef]
47. Luo, F.L.; Ye, H. Small Signal Analysis of Energy Factor and Mathematical Modeling for Power Dc-Dc Converters. *IEEE Trans. Power Electron.* **2007**, *22*, 69–79. [CrossRef]

sensors

MDPI

Article

Numerical and Experimental Investigation of Time-Domain-Reflectometry-Based Sensors for Foreign Object Detection in Wireless Power Transfer Systems

Martin Helwig *,†, Yun Xu †, Uwe Hentschel, Anja Winkler and Niels Modler

Institut für Leichtbau und Kunststofftechnik, Technische Universität Dresden, 01307 Dresden, Germany; yun.xu@tu-dresden.de (Y.X.); uwe.hentschel@tu-dresden.de (U.H.); anja.winkler@tu-dresden.de (A.W.); niels.modler@tu-dresden.de (N.M.)

* Correspondence: martin.helwig@tu-dresden.de

† These authors contributed equally to this work.

Abstract: Foreign object detection (FOD) is considered a key method for detecting objects in the air gap of a wireless charging system that could pose a risk due to strong inductive heating. This paper describes a novel method for the detection of metallic objects utilizing the principle of electric time domain reflectometry. Through an analytical, numerical and experimental investigation, two key parameters for the design of transmission lines are identified and investigated with respect to the specific constraints of inductive power transfer. For this purpose, a transient electromagnetic simulation model is established to obtain and compare the sensor impedance and reflection coefficients with experimental data. The measurement setup is based on parametrically designed sensors in laboratory scale, using an EUR 2 coin as an exemplary test object. Consequently, the proposed simulation model has been successfully validated in this study, providing a comprehensive quantitative and qualitative analysis of the major transmission line design parameters for such applications.

Keywords: electric time domain reflectometry; wireless power transfer; wireless charging; inductive power transfer; foreign object detection; metal object detection

1. Introduction

Foreign objects are considered a major concern in the safe application of a wireless power transfer system (WPTS). In particular, objects made from electrically or magnetically conductive materials interact strongly with the alternating magnetic when located on the ground assembly (GA). Due to the resulting eddy current and hysteresis losses, objects might heat up strongly. This is a safety hazard as those objects may damage the GA or even cause fire. Moreover, hot objects can lead to burns when touched. In order to mitigate these issues, technical solutions are required to either prevent or limit the exposition of foreign objects to strong magnetic field strengths.

One general approach is the prevention of hazardous strong magnetic field strengths per design; for instance, by either reducing the transfer power or reducing the air gap. An alternative solution is to utilize a monitoring device that can detect foreign objects in the vicinity of strong magnetic field interaction prior to or during power transfer [1].

In the literature, many foreign object detection (FOD) methods are known, which are divided into living object detection (LOD) and metal object detection (MOD) [2–4]. Based on their detection principle, such systems can be categorized into the three groups: system-parameter-based detection, wave-based detection and field-based detection.

System-parameter-based FOD monitors the effect of foreign objects on the electrical, thermal or mechanical parameters of the WPTS. Electrical parameters are usually current [5,6], power loss or efficiency [7], quality factor [8], coil inductance, frequency or phase [9]. Non-electrical parameters are, for example, temperature [10,11], weight or pressure.

Wave-based detection methods rely on imaging or thermal cameras [12–14] and ultrasonic [15] or radar sensors [16], and thus require the use of additional sensing equipment.

Field-based detection methods rely directly on the local interaction between the metallic object and the magnetic field. Such monitoring devices are usually realized as passive inductor loops, which are located below the surface area of the GA coil. Any electrically or magnetically conductive material (i.e., materials with a sufficient deviation in magnetic permeability or electric conductivity relative to air) changes the local magnetic field distribution of the GA coil or of a separate excitation coil, which can be detected as a change in induction voltage of a local sensor loop. Several monitoring device designs based on the field-based detection method have been proposed in the past [17–25]. However, these designs require multiple sensor coils to cover the entire surface area of the GA, which need to be interconnected in pairs to cancel out both the GA induction voltage as well as the external noise and have to be multiplexed to a detection circuit. Furthermore, significant effort is expended on blind spot mitigation [19,20], as neighboring coils also cancel each other out when an object is located precisely in between them and the induction voltage nullifies [17,23,25]. Moreover, such devices are in principle only capable of metal object detection.

In response to these limitations, this study introduces a new FOD technique for a WPTS that utilizes time domain reflectometry (TDR). This approach differs from current field-based detection systems by inherently providing a straightforward, non-overlapping sensor layout without blind spots, while it is able to correlate temporal resolution with spatial resolution to determine object locations. As an active method, it does not depend on an external GA magnetic field, allowing for object detection before initiating power transfer. Additionally, this method is capable of identifying and differentiating between metallic and non-metallic objects due to its fundamental operating mechanism.

To the best of the authors' knowledge, no prior research has been carried out in the field of TDR-based object detection in connection with wireless power transfer (WPT) applications. A partially related study was carried out by Dominauskas et al. [26], employing a "snake"-curved sensor configuration to measure the distributed resin flow during a liquid composite molding process. Another related contribution was made by Kostka et al. [27], wherein TDR was utilized in order to identify touch events during human–machine interactions in robotics. TDR has also found extensive application in moisture sensors. Suchorab et al. [28] presented a surface sensor designed to measure the volumetric water content in concrete samples. A comprehensive review of TDR-based moisture sensing applications in porous media is presented by He et al. [29].

Given the absence of comparable work, the primary aim of this study is to establish a fundamental understanding of the sensor principle and identify specific key design parameters for FOD applications. This is achieved by conducting parametric studies of small-scale laboratory sensor designs, which are introduced in Section 2. Section 3 describes the analytical and numerical methods used for time-dependent impedance calculation, which serve as a reference for measurement data. The experimental setup is then explained in Section 4. Section 5 presents, compares and discusses the simulation and measurement results, followed by a conclusion in Section 6.

2. Proposed TDR Sensor Design

The measurement method of electrical TDR, which is well established in electrical engineering, enables the spatially resolved measurement of the electrical properties of a transmission line (TL) based on propagation times and reflection characteristics of the electrical signals fed in at the beginning of the line. By modifying at least one of the components of the TL, which serves as the sensing element, a physical quantity can be coupled to the electrical properties of the line (resistive coating, inductance coating, leakage coating and capacitance coating).

In the TDR method, a high-frequency signal (pulse signal) is injected into a TL. Reflections occur at inhomogeneities of the TL, which can be detected at the beginning of the line and displayed in a reflectogram in the time domain. Reflections occur as a result of discontinuities in the characteristic impedance along the TL. The impedance at the point of discontinuity differs from the characteristic impedance of the TL.

In principle, a sensor based on a TL is only capable of sensing changes in impedance along its one-dimensional path. Therefore, in order to create a FOD sensor that can be applied on a two-dimensional surface, the TL track must be arranged in the shape of an area-filling curve. Several area-filling curves, such as spiral curves, "snake" curves and fractal curves like the Hilbert curve, have been described in the literature. These curves map the (x,y) coordinates of a two-dimensional surface onto a one-dimensional coordinate along the line.

TLs are commonly used in various practical configurations, such as microstrips, coplanar waveguides, strip lines and coplanar strips (see Figure 1a). However, many of these configurations are unsuitable for the application of FOD sensors under the influence of strong external alternating magnetic fields. For example, coplanar waveguides typically rely on a conductive ground plane covering the entire back face of the substrate. This is disadvantageous for a couple of reasons. Firstly, such a conductive plane would shield the magnetic field of the GA, thereby preventing power transfer. Additionally, induced in-plane eddy currents would lead to a strong heat-up of the conductive sheet. Thus, transmission lines with a continuous ground plane cannot be utilized for this purpose.

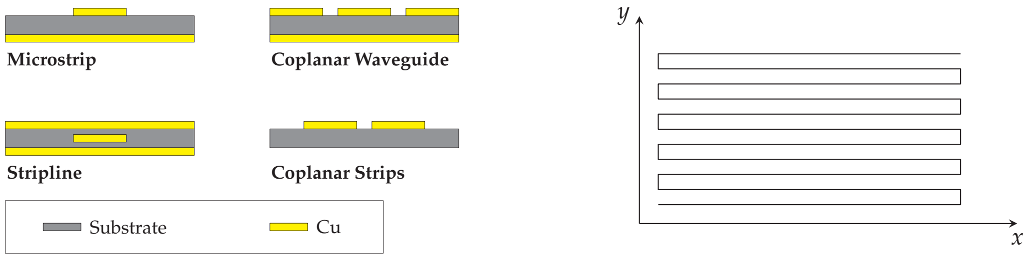

(**a**) (**b**)

Figure 1. (**a**) Examples of commonly used printed circuit board (PCB)-based transmission line designs with and without a conductive ground plane in a cross-sectional view. (**b**) Area-filling, "snake"-curved path design of the sensor transmission line.

In order to detect foreign objects, the TLs' impedance has to change under the influence of the foreign object. In theory, the TL impedance is a function of three material properties: conductivity σ, relative permeability μ_r and relative permittivity ϵ_r. However, for a change in impedance to occur, the electric and magnetic field components of the pulse wave must interact with the foreign object. As a result, the electromagnetic field must not be confined within the substrate, where an interaction with the foreign object is impossible.

However, an "open" designed transmission line is susceptible to electromagnetic interference, primarily to induced voltages, which disturb or even damage the measurement equipment. This needs to be minimized by optimizing and adapting the transmission line and curve design to the specific ground assembly. However, such optimizations or other means of interference suppression are not in the scope of this work and will be addressed in future research.

Unlike most known PCB-based transmission line designs, coplanar strips satisfy these requirements without the need for a solid, conductive ground plane. This is because coplanar strips do not require a conductive ground plane that covers the whole ground assembly, which would shield the magnetic field of the wireless charger and induce in-plane eddy currents. Among area-filling curves, the "snake" curve (see Figure 1b) is a favorable choice as it can be easily implemented, parameterized and optimized to minimize the induction voltage caused by the magnetic field of the GA. Therefore, in this paper, the "snake" curve is utilized for the FOD sensor design.

Note that, in this study, all experiments are conducted without the presence of a magnetic field generated by the GA coil in order to perform measurements in a low-noise environment, serving as a reference for simulation models. Implementing the sensor principle discussed in real-world scenarios would require efficient noise reduction techniques, which are not covered in this study.

The schematic representation of the complete system configuration is presented in Figure 2. The FOD-sensor is connected with a TDR device from Sympuls [30] through a coaxial cable of 50 Ω characteristic impedance. The TDR device generates rectangular pulses at a frequency of 24.4 kHz and a rise time (10 to 90 %) of 80 ps. The sensor is terminated with a 100 Ω resistor, designated as Z_T, which is closer to the expected TL impedances, while also serving as a reference impedance different from the 50 Ω. In order to minimize reflections, the TL is bent with a minimum defined radius r_{min} of three times the copper strand width w [31]. The sensor is positioned on top of a plate of polytetrafluoroethylene (PTFE) with $h_{PTFE} = 7$ mm thickness, which serves as a low-loss dielectric material with a well-defined dielectric constant. The PCB substrate of the sensor is made from RO4350B [32], which has a thickness of $h_{subs} = 0.3$ mm with a copper thickness of 35 μm. It has been chosen because the material properties are well known, it has low dielectric losses and it is easily available through manufacturers. In this work, an EUR 2 coin is utilized as a foreign object for all experiments. It is separated from the sensor surface using a variable thickness PTFE spacer in the shape of the coin. The experimentally measured, time-dependent wave impedance $Z_0(t)$ is finally transferred to a measurement computer via USB.

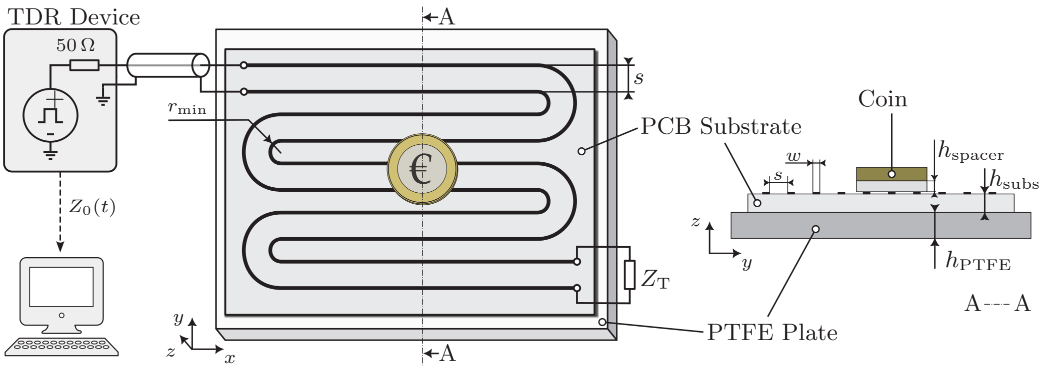

Figure 2. Schematic visualization of the FOD system setup in perspective view (**left**) and in cross-sectional view along the cutting line A (**right**).

Following an initial parameter study of the prototype, two critical parameters that affect the sensitivity of the FOD were identified: the spacing between the two traces and the distance between the detection object and the transmission line. These parameters form the foundation for the parametric investigation presented in this study. The corresponding values for this parametric study were selected within an arbitrary range, derived from the coin size, and are provided in Table 1.

Table 1. Dimensional data of sensors for simulation.

Designation	Description	Unit	Range of Values
s	distance between the two traces	mm	2; 4; 6; 8; 10
h_{spacer}	gap between coin and transmission line	mm	0.5; 1; 2

3. Analytical and Numerical Studies

This section describes the analytical and numerical methods used to obtain the wave impedance Z_0 of the TL. These methods rely on electromagnetic properties of the used materials, such as the relative electric permittivity ϵ_r, the relative magnetic permeability μ_r and the electric conductivity σ. The values for these parameters are provided in Table 2 and serve as the foundation for all the methods used. Note that parameters for conductive materials are not provided in this table because they are neither required for the analytical nor the numerical methods, as can be seen in the subsequent sections. In total, an analytical calculation as well as a two-dimensional and a three-dimensional finite element method (FEM) simulation are conducted. The purpose of the analytic and two-dimensional methods is to determine a reference impedance for the coplanar strips configuration, which is then used to validate the accuracy of the three-dimensional simulation model. In the three-dimensional simulation, the sensor is simulated in the time domain, with and without the presence of foreign objects, to obtain a spatially and temporally resolved impedance. All simulations are conducted in the FEM simulation software COMSOL Multiphysics v6.0.

Table 2. Parameter data for the simulation.

Material	Relative Permittivity ϵ_r [1]	Relative Permeability μ_r [1]	Electrical Conductivity σ [S/m]	Reference
Air	1	1	0	-
PTFE	2.1	1	0	[33]
RO4350B	3.66	1	0	[32]

3.1. Analytical Calculation of Transmission Line Impedance

An analytical solution for the wave impedance of coplanar strips is well known in the literature [34] and can be calculated analytically following Equation (1):

$$Z_0 = \frac{120\pi}{\sqrt{\varepsilon_{\text{eff}}}} \frac{\mathrm{K}(k)}{\mathrm{K}(k')}, \tag{1}$$

where

$$k = \frac{s}{b} \quad \text{and} \quad k' = \sqrt{1.0 - k^2}.$$

Here, K is the elliptic integral of the first kind, the variable s denotes the distance between the copper strands and b is the total width of the transmission line, as shown in Figure 3. The effective permittivity, denoted by ε_{eff}, incorporates the geometric features of the surrounding materials like air as well as a PCB substrate of the thickness h via Equation (2) as follows:

$$\varepsilon_{\text{eff}} = 1 + \frac{\varepsilon_r - 1}{2} \frac{K(k')K(k_1)}{K(k)K(k_1')}, \tag{2}$$

where

$$k_1' = \sqrt{1.0 - k_1^2} \quad \text{and} \quad k_1 = \frac{\sinh(\frac{\pi s}{4h})}{\sinh(\frac{\pi b}{4h})}.$$

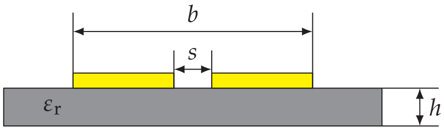

Figure 3. Cross-sectional schematic of coplanar strips on a substrate with a relative permeability of ε_r.

3.2. Two-Dimensional Calculation of Transmission Line Impedance

The wave impedance of a coplanar strip can be determined using the telegrapher's equations, yielding the Equation 3, which relies on the distributed parameters of inductance (L), capacitance (C), resistance (R) and conductance (G). These parameters can be obtained through electrostatic and magnetic simulations conducted within a two-dimensional domain. The angular frequency in Equation (3) is denoted as ω, whereas the imaginary unit is denoted as j.

$$Z_0 = \sqrt{\frac{R + j\omega L}{G + j\omega C}} \tag{3}$$

This work assumes that all dielectric materials exhibit ideal behavior, where neither polarization losses nor conductance losses are accounted for. As a result, the conductance parameter G is zero. The capacity C is derived from an electrostatic simulation according to Figure 4a, where a voltage difference of 1 V is applied between the two conductors. The simulation is governed by Equation (4), where $\boldsymbol{E}$ is the electric field strength, Φ the electric potential, ρ_V the volume charge density and ϵ the absolute electric permittivity.

$$\nabla \cdot \boldsymbol{E} = \frac{\rho_\mathrm{v}}{\epsilon}, \qquad \boldsymbol{E} = -\nabla \Phi \tag{4}$$

The parameters R and L are derived from a magnetic simulation in the frequency domain according to Figure 4b following Equation (5), where $\boldsymbol{H}$ is the magnetic field strength, $\boldsymbol{B}$ the magnetic flux density, $\boldsymbol{A}$ the magnetic vector potential and $\boldsymbol{J}$ the current density, to which $\boldsymbol{J}_\mathbf{e}$ contributes as external current density. The external current density is set by a 1 A external current flowing through the cross section of the right conductor.

$$\nabla \times \boldsymbol{H} = \boldsymbol{J}, \qquad \boldsymbol{B} = \nabla \times \boldsymbol{A}, \qquad \boldsymbol{J} = (\sigma + j\omega\epsilon)\boldsymbol{E} + \boldsymbol{J}_\mathbf{e}, \qquad \boldsymbol{E} = -j\omega \boldsymbol{A} \tag{5}$$

In both simulations, an air domain is modeled around the transmission line and the substrates.

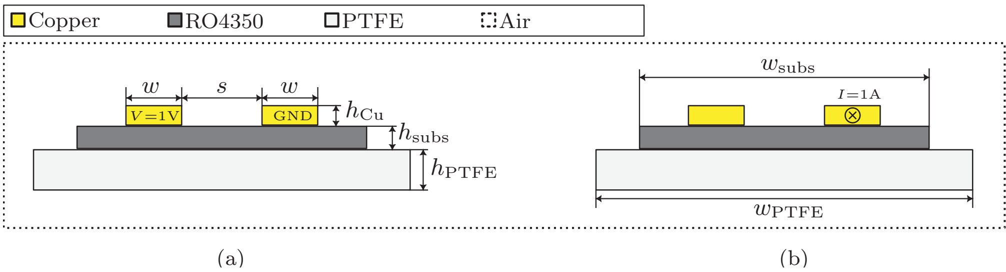

Figure 4. Cross-sectional schematic view of (**a**) the 2D electrostatic simulation model and (**b**) the 2D magnetic simulation in frequency domain.

3.3. Three-Dimensional Simulation of TDR-Based FOD

The 3D simulation model of the FOD sensor consists of five main parts: the air domain, the PTFE plate, the detection object (coin), the PTFE spacer and the sensor, as shown in Figure 5. The sensor for FOD is positioned at the center of a square PTFE plate with a side length of 298 mm each and a thickness of 7 mm. The sensor and the PTFE plate are enclosed by an air domain. The sensor consists of a substrate plate and two parallel meander copper traces. The distance between the sensor surface and coin is set by PTFE spacers of defined thicknesses. Although an EUR 2 coin is composed of two different alloys, in the model, it is only represented as a single cylindrical domain with a perfect electric boundary condition. The diameter of the coin is 25.75 mm and the thickness is 2.2 mm, as shown in Figure 5b,c.

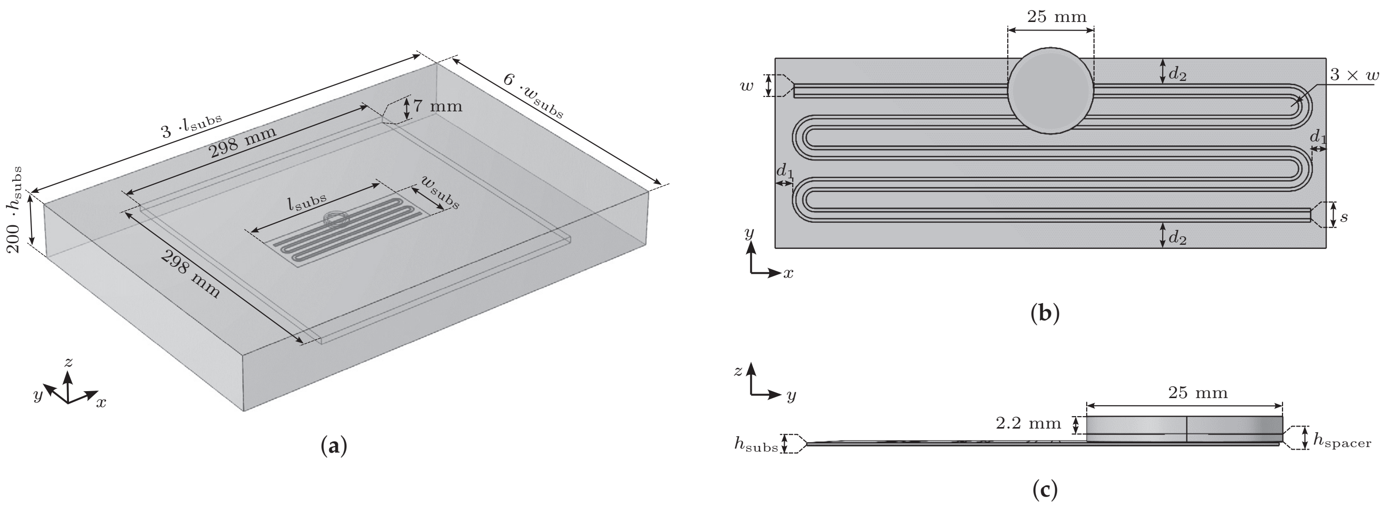

Figure 5. Geometry and dimensions of the model. (**a**) Perspective overview of the geometry. (**b**) Detailed top-down view and (**c**) side view of the sensor PCB with dimensions.

The size of the air domain, the substrate and the position of the coplanar strips on the substrate will change due to the varying trace widths or the varying spacing between them. The size of the air domain is set to at least include the PTFE plate and the sensor. All sensors' copper traces have a defined width of $w = 1\,\text{mm}$ and are centered with respect to the substrate, which is indicated by the distances d_1 and d_2 in Figure 5b. The spacings from $s = 2\,\text{mm}$ to $s = 10\,\text{mm}$ are designated as s2 to s10. The geometric parameters corresponding to the above requirements for s2 to s10 are listed in Table 3.

Table 3. Data of the geometry with different parameters.

Designation	d_1 [mm]	d_2 [mm]	l_{subs} [mm]	w_{subs} [mm]
s2	5	7.5	160	55
s4	5	6.5	160	65
s6	4.5	6	160	75
s8	4.5	6	160	85
s10	4.5	6	160	95

For the computational part of TDR-based FOD in the three-dimensional case, mainly the vector potential formulation for transient electromagnetic waves is applied, following Equation (6):

$$\nabla \times (\frac{1}{\mu_r}(\nabla \times \boldsymbol{A})) + \mu_0\sigma\frac{\partial \boldsymbol{A}}{\partial t} + \mu_0\epsilon_0\epsilon_r\frac{\partial^2 \boldsymbol{A}}{\partial t^2} = 0 \tag{6}$$

The signal is input and terminated by the lumped port surface boundary conditions in COMSOL, which are depicted in Figure 6b as yellow rectangular surfaces bridging the two traces of the coplanar strip line. At the lumped port boundary condition, the characteristic impedance Z is defined as:

$$Z = \frac{V}{I}, \tag{7}$$

where V denotes the voltage at the port and I is the current. In the simulation, the lumped port 1 is designated as the input port, while the lumped port 2 is specified as the terminal port. A step function is used as an input signal to excite the coplanar strip line. The voltage amplitude of the step function is set to 1 V and the rise time is set to 0.2 ns. These values are obtained from the manual of the TDR measuring device [30]. The impedance of lumped port 1 is set to 50 Ω and the impedance of lumped port 2 is set to 100 Ω, according to the experimental setup.

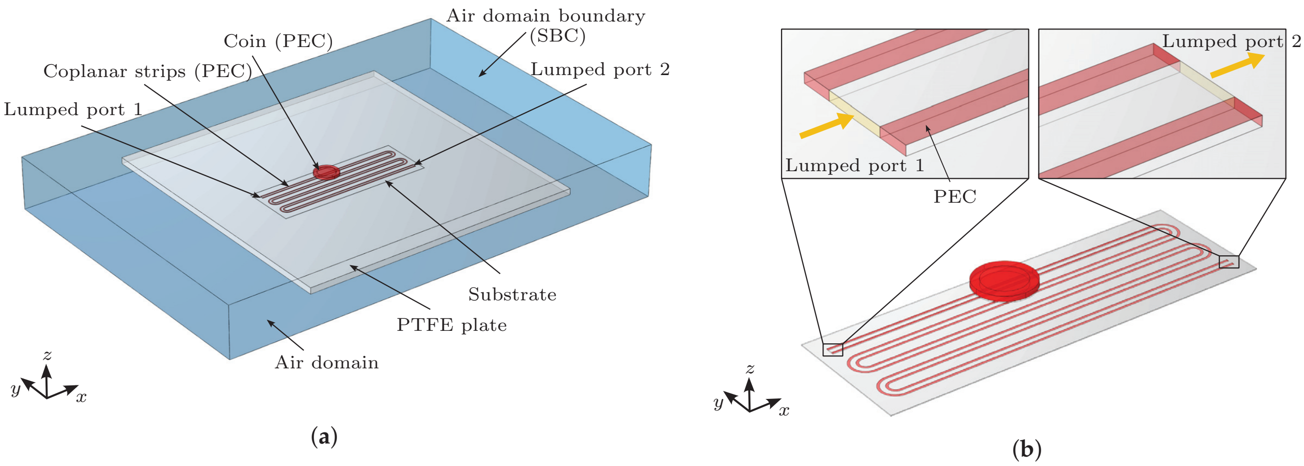

Figure 6. Domain and boundary definitions of the model. (**a**) Perspective overview of the geometry. (**b**) Detailed perspective view of the sensor PCB. For better recognition, the PEC boundary conditions has been colored red and the lumped port boundary conditions has been colored yellow.

In the simulation of electromagnetic waves, the perfect electric conductor (PEC) boundary condition is applied to all metallic parts (depicted as red areas in Figure 6), including the microstrip line and the coin in the three-dimensional simulation model. The PEC boundary condition is set as:

$$\boldsymbol{n} \times \boldsymbol{E} = 0 \tag{8}$$

where $\boldsymbol{n}$ is the unit normal vector of the boundary surface and $\boldsymbol{E}$ is the electric field. The sensor and PTFE plate are surrounded by the air domain. Electromagnetic waves propagate in the air domain and pass through the air domain boundary without reflection. The exterior surfaces of the air domain are set as the scattering boundary condition (SBC), which is an absorbing boundary used to describe an open space. The calculation of the SBC is defined as:

$$\mu_0 \boldsymbol{n} \times \boldsymbol{H} + \frac{\mu_0}{Z_c} \boldsymbol{n} \times (\boldsymbol{E} \times \boldsymbol{n}) - \frac{\sigma Z_c}{2\mu_r} \boldsymbol{n} \times (\boldsymbol{A} \times \boldsymbol{n}) = 0 \tag{9}$$

$$Z_c = \sqrt{\frac{\mu_0 \mu_r}{\epsilon_0 \epsilon_r}} \tag{10}$$

Electromagnetic waves in coplanar strips propagate via a quasi-transverse electromagnetic (quasi-TEM) mode. Since the speed of electromagnetic wave propagation in the substrate differs from that in the air, it is necessary to calculate the phase velocity of the electromagnetic wave in the substrate to obtain the traveling time. The effective dielectric constant required for the computation of the phase velocity of coplanar strips is derived using Equation (2). The phase velocity is then calculated using the expression provided in [34]:

$$v_p = \frac{c}{\sqrt{\epsilon_{eff}}}, \tag{11}$$

where v_p is the phase velocity in the substrate and c is the speed of light. The maximum simulation time is approximated from the traveling time of the wave from lumped port 1 to lumped port 2 and then back to lumped port 1. However, in order to obtain complete simulation results, the approximated maximum simulation time is defined to be at least $12 \cdot l_{subs}/v_p$, which comfortably accounts for twice the TL length plus the corners.

When solving electromagnetic wave problems using the finite element method (FEM), a mesh that is too large can lead to an incorrect resolution of the waves in the signal. Conversely, a mesh that is too small can lead to a longer simulation time, improving the accuracy of the results. The rise time of the signal is 0.2 ns, which leads to a corresponding maximum signal frequency of 5 GHz, designated as f_{max}. Accordingly, the minimum wavelength in the dielectric substrate is set to $\lambda_{min} = v_p/f_{max}$. Following a parameter study of the mesh size, the maximum mesh element size in the dielectric substrate, designated by $e_{\max}$, is set to $0.2{\cdot}\lambda_{\min}$. In the simulation, all domains are meshed with COMSOL's "Finer" mesh size setting, except the air domain, where the "Normal" mesh size setting is applied (as shown in Figure 7).

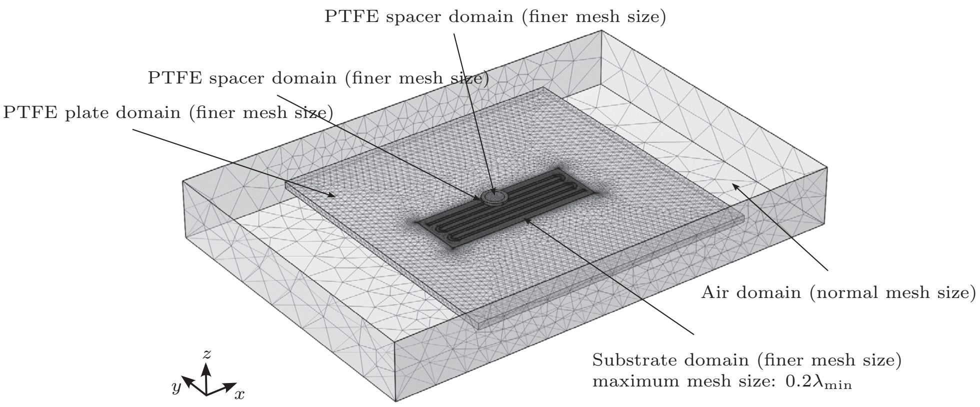

Figure 7. Meshing of the 3D simulation model.

Similar to defining the maximum mesh size in space in solving electromagnetic wave problems, it is also important to define a suitable time step. A too small time step would unnecessarily lead to a longer simulation time, while a too large time step would lead to inaccurate solutions. The maximum time step chosen for the simulation is set to $0.2{\cdot}e_{\max}/v_{\mathrm{p}}$ and has been determined to yield the best results in the simulation.

4. Experimental Setup

As mentioned in the previous sections, two major parameters (spacing s and the distance between object and transmission line h_{spacer}) were determined, which have an impact on the sensitivity of the FOD. The prototypes in the "snake" curvature have been produced on a laboratory scale, and comply with the parameters given in Table 1. Figure 8a shows the prototypes with the trace width of 1 mm and different spacings.

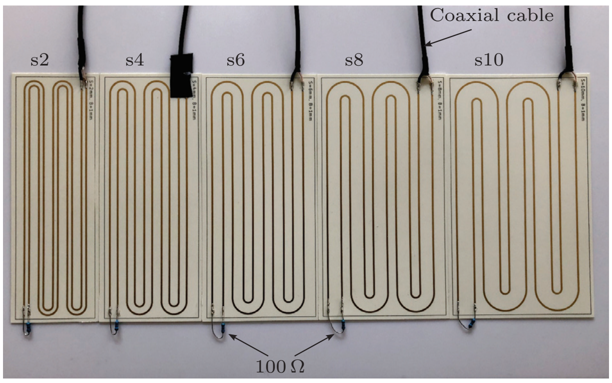

(**a**)

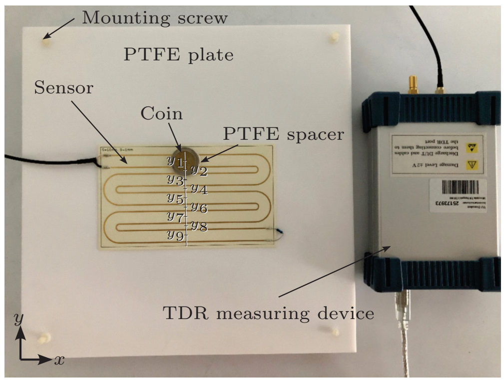

(**b**)

Figure 8. (**a**) Overview of the manufactured parametrically designed sensor samples. (**b**) Overview of the experimental setup.

The prototype for the laboratory experiment consists of three main components: the sensor, an external 100 Ω termination resistor and a 50 Ω coaxial cable. The sensor PCBs are manufactured by Multi Leiterplatten GmbH (Brunntal, Germany) and the substrate material is Rogers 4350, obtained from Rogers Corporation (Chandler, AZ, USA). The FOD experiment device consists of 5 main parts: the PTFE plate, the detection object (coin), the sensor, the PTFE spacer and a TDR measuring device D-TDR 3000 from Sympuls [30].

For the experiments, the coin is placed in nine different locations on the sensor, as shown in Figure 8b. The impedance of each position and three different distances (0.5 mm, 1 mm and 2 mm) between the coin and the sensor are measured. These distances are realized with the coin-shaped PTFE spacers of defined thickness, which also prevent direct electric contact between the coin and the sensor. The purpose of the plastic screws in the PTFE plate is to maintain an air gap between the plate and the table. By doing so, these screws minimize the unknown dielectric influence of the surrounding environment on the impedance measurement results, thus creating a well-defined and specified environment for the purpose of easier simulation validation.

During the measurement, the coaxial cable of the prototype is connected to the TDR measuring device, which, on the other end, is connected to the PC via USB. The corresponding TDR software (v19.1) measures and records the change in sensor impedance. The TDR measuring device creates a 24.4 kHz rectangle function signal with 0.5 V amplitude and a rise time (10 % to 90 %) of 80 ps. In order to reduce noise, the signal is averaged over 256 samples for each impedance measurement. The experimental results are compared with the 2D simulation results and 3D simulation results from chapter 3.

5. Results and Discussion

A comparison between measurement and simulation results of the reference impedance of transmission lines is presented in Figure 9a. The reference impedance Z_{Ref} is the impedance of the sensor without the coin and PTFE spacer measured. The results of the 2D and 3D simulations are obtained using the calculation method and model presented in Sections 3.2 and 3.3, respectively. It can be observed that the reference impedance of the sensor increases with an increase in spacing between the two traces. In general, the results obtained by the three methods are relatively consistent, especially at small spacings, where the results are almost identical. From the consistency of the results, we conclude that the simulation models are valid.

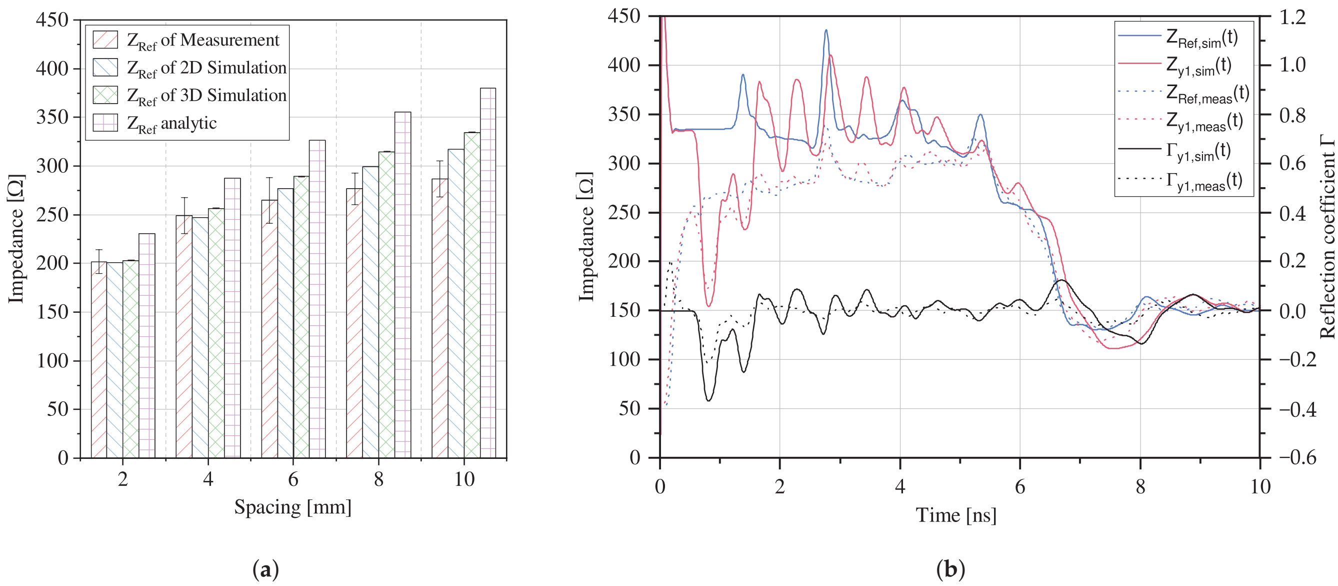

Figure 9. (**a**) Comparison between measurement, simulation and analytical results of the reference impedance of the transmission lines. (**b**) Measurement and simulation results of an exemplary sensor configuration s10 showing the reference impedance and the impedance with the coin on position y1 and distance 0.5 mm, as well as the resulting reflection coefficients.

In this paper, the reflection coefficient Γ determined from the reference impedance signal, designated as $Z_{\mathrm{Ref}}(t)$, and an impedance signal with the object positioned at a specific y-coordinate, designated as $Z_{\mathrm{y}}(t)$, is used to quantify the sensitivity, according to Equation (12). Both signals are time-dependent and obtained either by simulation or measurement.

$$\Gamma_{\mathrm{y}}(t) = \frac{Z_{\mathrm{y}}(t) - Z_{\mathrm{Ref}}(t)}{Z_{\mathrm{y}}(t) + Z_{\mathrm{Ref}}(t)} \tag{12}$$

Figure 9b shows a measurement of a sensor configuration s10 with a coin at position y1 and distance 0.5 mm, where the blue lines are the reference impedances and the red lines are the impedances with the coin. The black lines are the reflection coefficients according to Equation (12). Dotted lines refer to the measurement results, whereas solid lines refer to simulation data.

The impedance signals obtained from the measurement exhibit two consecutive rising slopes, where the first slope rises rapidly from 50 Ω coaxial cable impedance to 260 Ω, followed by a slower rising slope to 320 Ω and then a falling slope ending at 150 Ω. Due to the complex signal shape, it is difficult to determine the effective impedance of the TL directly. To address this, for Figure 9a, the mean value of the slope between 260 Ω and 320 Ω is taken as the effective impedance. The standard deviation is depicted as an error bar, representing the uncertainty associated with determining the effective impedance. The signals are additionally superimposed with impedance variations of higher frequency and small amplitude. However, the impedance changes at coin position y1, which correspond to a time of 0.8 ns, vary significantly compared to the reference measurement. The maximum absolute reflection coefficient observed in this measurement is 0.2.

On the other hand, the simulated impedance signals experience a fast overshoot during the rising transition from 50 Ω to 330 Ω, exceeding the measured impedance by 30 %. The signals are also superimposed with impedance fluctuations of a similar phase and frequency as the measurement, but with higher amplitudes. The falling slopes and final impedances in the simulation are comparable to the measurement data. The simulation result yields an absolute maximum reflection coefficient of 0.38.

5.1. Influence of Position and Spacing

Analogously, the impedance changes caused by the coin at nine different positions (y1 to y9) are investigated. The reflection coefficient of the coin at position 1 with a varying thickness (0.5 mm, 1 mm, 2 mm) of the PTFE spacer can be obtained similarly. Figure 10a shows the maximum absolute reflection coefficients of the coin at nine positions with a 0.5 mm PTFE spacer. From both the simulation and measurement results, it can be seen that the reflection coefficient is highest at position y1, which means that the coin is easiest to detect at position y1. In contrast, the reflection coefficient is smallest at position y9, which means that the coin is most difficult to detect at this position. This phenomenon may be attributed to interference due to reflections at the end of the transmission line, as the termination resistance is not matched to the reference impedance.

Notably, in contrast to the simulations, the measurements did not show a decrease in the reflection coefficient proportional to an increase in the coin position, which is directly related to the sensor length for all sensor configurations. Furthermore, the reflection coefficient observed in the simulations was markedly higher than that observed in the experimental measurements. The authors attribute this discrepancy to the idealized modeling approach employed in the simulations, which does not account for any damping effects resulting from power dissipation mechanisms. However, when comparing the influence of the transmission line spacing in the simulation and experiment at each position, the qualitative characteristics were well captured.

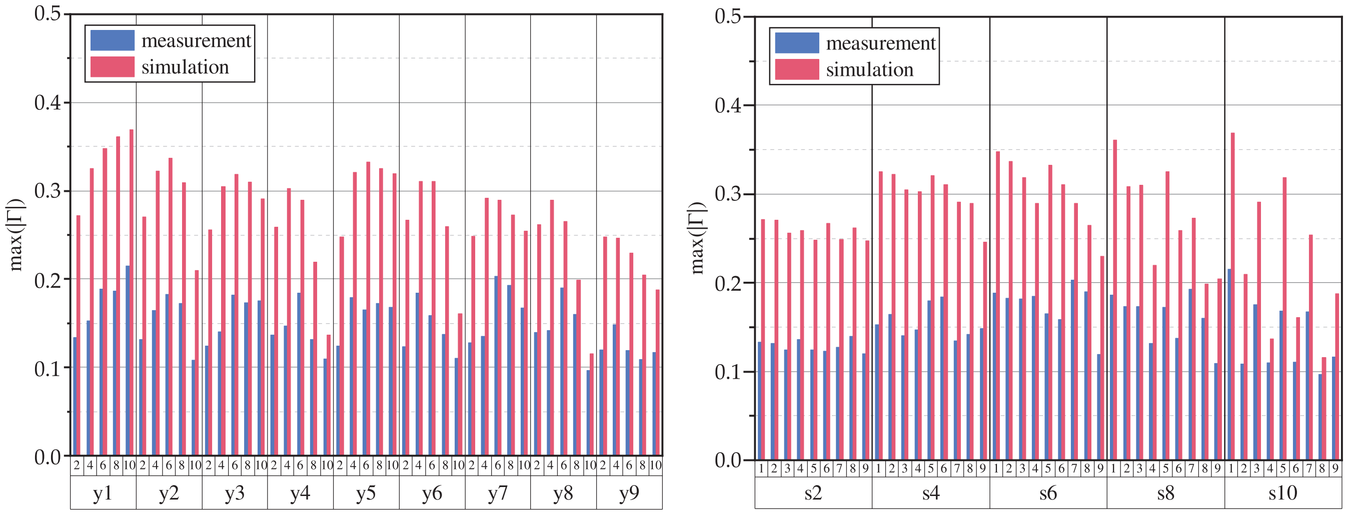

(a)

(b)

Figure 10. Maximum absolute reflection coefficients resulting from nine different coin positions for 5 different sensor configurations: (**a**) grouped by coin positions; (**b**) grouped by spacing.

In Figure 10b, the sorting of spacing and position is reversed with respect to Figure 10a. It can be seen from the results that the difference in the reflection coefficient between the odd positions y1 to y9 and the even positions y2 to y8 is more pronounced with increased spacing. Specifically, the reflection coefficients between the positions are nearly identical for the 2 mm spacing, whereas the reflection coefficients between odd and even positions are considerably different for the 10 mm spacing. This is related to the size of the coin and the spacing of the TL. For a smaller spacing, the coin will always cover at least one TL fully independently from an even or odd position, so there is little difference in the reflection coefficient of each position. In contrast, for a larger spacing, the coin will not cover the transmission line completely in odd positions, resulting in “good” and “bad” detection positions.

Figure 11 illustrates the influence of a coin on the magnetic flux density for different combinations of spacing and position. As a metallic object, the coin interacts with the magnetic field component of the electromagnetic wave propagating through the transmission line. The interaction occurs due to eddy currents induced within the conductive coin, which generates an opposing magnetic field, leading to a perturbation in the source magnetic field; hence, the coin shields the source field. Consequently, this changes the local inductance of the TL and therefore the local impedance. For any configuration, the magnitude of the inductance change is related to the degree of the local coverage of the transmission line.

Similarly, the electric field component of the electromagnetic field also interacts with the coin. When the coin covers the transmission line, most of the electric field lines will propagate through the electrically conductive coin rather than through the air, resulting in a change in the effective capacitance locally. This change in capacitance contributes to the overall change in impedance.

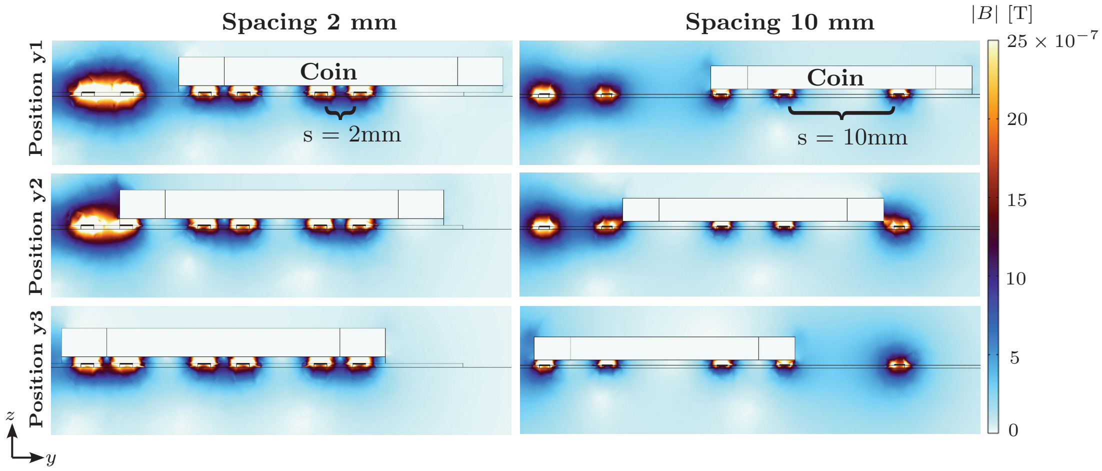

Figure 11. Cross-sectional view of the magnetic flux density norm around the coin and the transmission line of s2 and s10 at position y1, y2 and y3. As the coin is implemented as a surface model only, there is no magnetic field simulated inside the coin.

5.2. Influence of Object Distance

Figure 12 shows the reflection coefficient for different gaps between the coin and transmission line realized with a PTFE spacer. It can be observed that the reflection coefficient becomes larger as the spacing increases for a constant gap, which was already shown and discussed in Figure 10. However, it can also be clearly observed that any further increase in spacing leads to a smaller increase in the reflection coefficient.

Furthermore, it is noticeable that the reflection coefficient increases as the gap between the coin and the transmission line decreases. This is primarily due to the fact that the closer the coin is to the transmission line, the greater the number of magnetic field lines that are deflected by the coin, and the more electric field lines passing through the coin. Therefore, the coin becomes easier to detect.

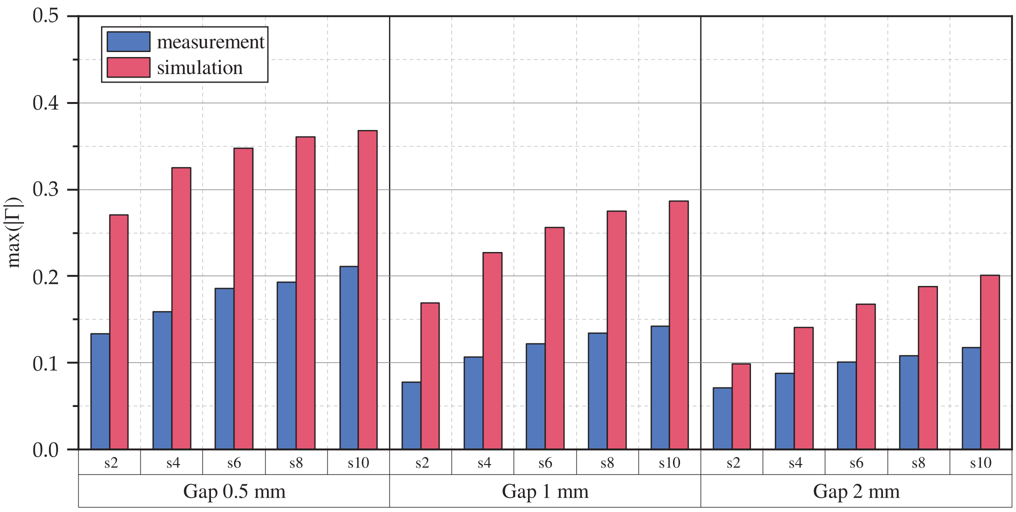

Figure 12. The maximum absolute reflection coefficients for different object distances from 0.5 mm to 2 mm measured for different spacings and at position y1.

5.3. Summary and Limitations

In summary, the measurement results for the coin object indicate that increasing the spacing between the copper tracks of the TL leads to an increase in the maximum absolute reflection coefficient. This suggests that the coin becomes more easily detectable, partially compensating for an increased object distance. However, this effect diminishes as the spacing continues to increase, and eventually, a reversal is expected, resulting in a decrease in the reflection coefficient when the spacing becomes larger than the object itself. Thus, to effectively detect a variety of metallic objects, a careful balance between expected object sizes, distances and transmission line spacings is necessary. Figure 12 shows a rapid decline in the reflection coefficient with an increasing gap. This indicates that objects that are not located in the direct vicinity of the sensor are not detectable. This includes objects that protrude into the air gap between the sending and receiving coil but also metallic parts of the receiver itself. Additionally, based on the observed results, it is unclear whether the effect on the maximum absolute reflection coefficient is predominantly influenced by the electric or magnetic field component. Further investigations are required to gain a better understanding of this aspect.

For practical sensor applications in the real world, it is essential to have a method that effectively filters out the inductive effects of strong external magnetic fields. Fortunately, the nominal operating frequency of the WPTS is 85 kHz [1], while the TDR method operates in the range of megahertz to gigahertz frequencies. This frequency mismatch provides opportunities for the design and implementation of effective high-pass filters.

6. Conclusions

In this study, the influence of varying transmission line parameters on the performance of a novel TDR-based FOD detection system for wireless power transfer applications was investigated on an analytical, numerical and experimental basis. For this purpose, several laboratory-scaled prototypes based on coplanar strips with varying trace spacing were manufactured and tested for different object positions. The measurement results were compared with those obtained from 2D and 3D simulations. Although notable quantitative differences in the simulated and measured impedances were observed, the qualitative comparison of the reflection coefficients shows a very good consistency, indicating that the electromagnetic interaction mechanism is captured well in simulation. In detail, the investigation of both the magnetic flux density and the electric field strength around the coin and the transmission line revealed that the coin interacts with both the magnetic and electric field components of the electromagnetic wave, leading to changes in local inductance and capacitance, respectively. This interaction leads to a distinctive relationship between the spacing of the transmission line's copper tracks and the size and distance of the foreign object, which has been presented in this study.

In conclusion, understanding the impact of varying transmission line parameters is crucial for optimizing FOD detection systems based on time domain reflectometry. As the general detection principle has been proven to work for various distances and without blind spots, this study provides valuable insights into the design considerations of the underlying transmission lines and offers a wide basis for future research in FOD detection system performance. However, a full comparison to conventional FOD systems is currently not feasible, as critical aspects such as electromagnetic compatibility and scalability have yet to be determined. Thus, in the future, the authors will focus on sensor scalability, the extension of the foreign object catalog to comply with the recommended objects in SAE J2954 [1] and on methods for the suppression of electromagnetic interference.

Author Contributions: Conceptualization, methodology, M.H. and Y.X.; software, Y.X.; validation, M.H. and Y.X.; formal analysis, M.H.; investigation, Y.X.; data curation, M.H. and Y.X.; writing—original draft preparation, M.H. and Y.X.; writing—review and editing, U.H. and A.W.; visualization, M.H. and Y.X.; supervision, A.W., U.H. and N.M. All authors have read and agreed to the published version of the manuscript.

Funding: This research project is part of the AI4CSM project that has received funding from the ECSEL Joint Undertaking (JU) under grant agreement No. 101007326. The JU receives support from the European Union's Horizon 2020 research and innovation programme and Germany, Austria, Belgium, Czech Republic, Italy, Netherlands, Lithuania, Latvia, France, Sweden, Norway. The project was also funded by the German Federal Ministry of Education and Research under grant number 16MEE0173. The content of this publication does not reflect the official opinion of the Joint Undertaking ECSEL or the German Federal Ministry of Education and Research. Responsibility for the information and views expressed therein lies entirely with the authors.

Data Availability Statement: Data are contained within the article.

Conflicts of Interest: The authors declare no conflict of interest.

Abbreviations

The following abbreviations are used in this manuscript:

FEM	finite element method
FOD	foreign object detection
GA	ground assembly
LOD	living object detection
MOD	metal object detection
PCB	printed circuit board
PEC	perfect electric conductor
PTFE	polytetrafluoroethylene
SBC	scattering boundary condition
TDR	time domain reflectometry
TL	transmission line
WPT	wireless power transfer
WPTS	wireless power transfer system

References

1. Hybrid—EV Committee. *Wireless Power Transfer for Light-Duty Plug-in/Electric Vehicles and Alignment Methodology*; Technical Report; SAE International: Warrendale, PA, USA, 2022. [CrossRef]
2. Zhang, Y.; Yan, Z.; Zhu, J.; Li, S.; Mi, C. A Review of Foreign Object Detection (FOD) for Inductive Power Transfer Systems. *eTransportation* **2019**, *1*, 100002. [CrossRef]
3. Xia, J.; Yuan, X.; Li, J.; Lu, S.; Cui, X.; Li, S.; Fernández-Ramírez, L.M. Foreign Object Detection for Electric Vehicle Wireless Charging. *Electronics* **2020**, *9*, 805. [CrossRef]
4. Lu, J.; Zhu, G.; Mi, C.C. Foreign Object Detection in Wireless Power Transfer Systems. *IEEE Trans. Ind. Appl.* **2022**, *58*, 1340–1354. [CrossRef]
5. Chu, S.Y.; Zan, X.; Avestruz, A.T. Electromagnetic Model-Based Foreign Object Detection for Wireless Power Transfer. *IEEE Trans. Power Electron.* **2022**, *37*, 100–113. [CrossRef]
6. Deguchi, Y.; Nagai, S.; Fujita, T.; Fujimoto, H.; Hori, Y. Sensorless Metal Object Detection Using Transmission-Side Voltage Pulses in Standby Phase for Dynamic Wireless Power Transfer. In Proceedings of the 2021 IEEE PELS Workshop on Emerging Technologies: Wireless Power Transfer (WoW), San Diego, CA, USA, 1–4 June 2021; pp. 1–5. [CrossRef]
7. Kuyvenhoven, N.; Dean, C.; Melton, J.; Schwannecke, J.; Umenei, A. Development of a Foreign Object Detection and Analysis Method for Wireless Power Systems. In Proceedings of the 2011 IEEE Symposium on Product Compliance Engineering Proceedings, San Diego, CA, USA, 10–12 October 2011; pp. 1–6. [CrossRef]
8. Sun, Y.; Wei, G.; Qian, K.; He, P.; Zhu, C.; Song, K. A Foreign Object Detection Method Based on Variation of Quality Factor of Detection Coil at Multi-frequency. In Proceedings of the 2021 IEEE 12th Energy Conversion Congress & Exposition—Asia (ECCE-Asia), Singapore, 24–27 May 2021; pp. 1578–1582. [CrossRef]
9. Jeong, S.Y.; Thai, V.X.; Park, J.H.; Rim, C.T. Self-Inductance-Based Metal Object Detection With Mistuned Resonant Circuits and Nullifying Induced Voltage for Wireless EV Chargers. *IEEE Trans. Power Electron.* **2019**, *34*, 748–758. [CrossRef]
10. Sun, Y.; Wei, G.; Song, K.; Huang, X.; Zhang, Q.; Zhu, C. Determination Foreign Object Detection Area in Electric Vehicle Wireless Charging System Based on Thermal Temperature Rise Characteristic. In Proceedings of the 2020 IEEE Transportation Electrification Conference & Expo (ITEC), Chicago, IL, USA, 23–26 June 2020; pp. 258–261. [CrossRef]
11. Karanth, A.; Dorairaj, H.H.K.; Kumar, R.B.R. Foreign Object Detection in Inductive Coupled Wireless Power Transfer Environment Using Thermal Sensors. U.S. Patent 20130163635, 27 June 2013.
12. Poguntke, T.; Schumann, P.; Ochs, K. Radar-Based Living Object Protection for Inductive Charging of Electric Vehicles Using Two-Dimensional Signal Processing. *Wirel. Power Transf.* **2017**, *4*, 88–97. [CrossRef]
13. Qi, C.; Wang, W.; Sun, T.; Song, K.; Yang, F.; Duan, H. Research on WPT Foreign Object Detection Method Based on Thermal Infrared Images. In Proceedings of the IECON 2022—8th Annual Conference of the IEEE Industrial Electronics Society, Brussels, Belgium, 17–20 October 2022; pp. 1–6. [CrossRef]
14. Sonnenberg, T.; Stevens, A.; Dayerizadeh, A.; Lukic, S. Combined Foreign Object Detection and Live Object Protection in Wireless Power Transfer Systems via Real-Time Thermal Camera Analysis. In Proceedings of the 2019 IEEE Applied Power Electronics Conference and Exposition (APEC), Anaheim, CA, USA, 17–21 March 2019; pp. 1547–1552. [CrossRef]

15. Bell, D.; Leabman, M.A. Systems and Methods of Controlling Transmission of Wireless Power Based on Object Indentification Using a Video Camera. U.S. Patent 11056929B2, 14 May 2019.
16. Widmer, H.; Sieber, L.; Daetwyler, A.; Bittner, M. Systems, Methods, and Apparatus for Radar-Based Detection of Objects in a Predetermined Space. EP3120463A1, 25 January 2017.
17. Jeong, S.Y.; Kwak, H.G.; Jang, G.C.; Choi, S.Y.; Rim, C.T. Dual-Purpose Nonoverlapping Coil Sets as Metal Object and Vehicle Position Detections for Wireless Stationary EV Chargers. *IEEE Trans. Power Electron.* **2017**, *33*, 7387–7397. [CrossRef]
18. Thai, V.X.; Jang, G.C.; Jeong, S.Y.; Park, J.H.; Kim, Y.S.; Rim, C.T. Symmetric Sensing Coil Design for the Blind-Zone Free Metal Object Detection of a Stationary Wireless Electric Vehicles Charger. *IEEE Trans. Power Electron.* **2019**, *35*, 3466–3477. [CrossRef]
19. Xiang, L.; Zhu, Z.; Tian, J.; Tian, Y. Foreign Object Detection in a Wireless Power Transfer System Using Symmetrical Coil Sets. *IEEE Access* **2019**, *7*, 44622–44631. [CrossRef]
20. Thai, V.X.; Park, J.H.; Jeong, S.Y.; Rim, C.T.; Kim, Y.S. Equivalent-Circuit-Based Design of Symmetric Sensing Coil for Self-Inductance-Based Metal Object Detection. *IEEE Access* **2020**, *8*, 94190–94203. [CrossRef]
21. Song, H.; Huang, X.; Lin, S.; Lin, R.; Huang, J. A Flexible Foreign Object Detection Method Based on Arrayed Vertical-Decoupled Coils for Wireless Power Transfer Systems. In *The Proceedings of 2022 International Conference on Wireless Power Transfer (ICWPT2022)*; Ma, C., Zhang, Y., Li, S., Zhao, L., Liu, M., Zhang, P., Eds.; Springer Nature: Singapore, 2023; Volume 1018, pp. 352–363. [CrossRef]
22. Hentschel, U.; Labitzke, F.; Helwig, M.; Winkler, A.; Modler, N. Aspects of Foreign Object Detection in a Wireless Charging System for Electric Vehicles Using Passive Inductive Sensors. *World Electr. Veh. J.* **2022**, *13*, 241. [CrossRef]
23. Liu, X.; Swaans, L.H.; Chan, K.W.P.; Low, H.K.; Chan, W.K. Methods and Systems for Detecting Foreign Objects in a Wireless Charging System. U.S. Patent 9825486B2, 21 November 2017.
24. Zhang, Y.; Wang, H.; Shen, Z.; Wu, Y.; Mao, X. A Metal Object Detection System for Electric Vehicle Wireless Charging with Quadrupole Detection Coils. *Energy Rep.* **2023**, *9*, 601–607. [CrossRef]
25. Percebon, L.; Kuerschner, D. Hybrid Foreign Object Detection (FOD) Loop Array Board. U.S. Patent 20180072166A1, 15 March 2018.
26. Dominauskas, A.; Heider, D.; Gillespie, J.W. Electric Time-Domain Reflectometry Distributed Flow Sensor. *Compos. Part A Appl. Sci. Manuf.* **2007**, *38*, 138–146. [CrossRef]
27. Kostka, P.; Winkler, A.; Haidar, A.; Khan, M.G.; Jäkel, R.; Winkler, P.; Müller-Pfefferkorn, R. Touch Identification on Sensitive Robot Skin Using Time Domain Reflectometry and Machine Learning Methods. In *Artificial Intelligence for Digitising Industry—Applications*, 1st ed.; River Publishers: New York, NY, USA, 2022; pp. 239–248. [CrossRef]
28. Suchorab, Z.; Malec, A.; Sobczuk, H.; Łagód, G.; Gorgol, I.; Łazuka, E.; Brzyski, P.; Trník, A. Determination of Time Domain Reflectometry Surface Sensors Sensitivity Depending on Geometry and Material Moisture. *Sensors* **2022**, *22*, 735. [CrossRef] [PubMed]
29. He, H.; Aogu, K.; Li, M.; Xu, J.; Sheng, W.; Jones, S.B.; González-Teruel, J.D.; Robinson, D.A.; Horton, R.; Bristow, K.; et al. A Review of Time Domain Reflectometry (TDR) Applications in Porous Media. In *Advances in Agronomy*; Elsevier: Amsterdam, The Netherlands, 2021; Volume 168, pp. 83–155. [CrossRef]
30. SYMPULS Gesellschaft für Pulstechnik und Meßsysteme mbH. Gerätehandbuch: Wellenwiderstandsmessgerät D-TDR 3G-500. 2019.
31. Montrose, M.I. *Printed Circuit Board Design Techniques for EMC Compliance: A Handbook for Designers*, 2nd ed.; IEEE Press: New York, NY, USA, 2000.
32. Rogers Corporation. *Data Sheet: RO4000 Laminates RO4003C and RO4350B*; Rogers Corporation: Chandler, AZ, USA, 2023.
33. Chen, H.; Zhang, J.; Bai, Y.; Luo, Y.; Ran, L.; Jiang, Q.; Kong, J.A. Experimental retrieval of the effective parameters of metamaterials based on a waveguide method. *Opt. Express* **2006**, *14*, 12944–12949. [CrossRef] [PubMed]
34. Wadell, B.C. *Transmission Line Design Handbook*; Artech House: Norwood, MA, USA, 1991.

sensors

MDPI

Review

Review, Properties, and Synthesis of Single-Switch Non-Isolated DC-DC Converters with a Wide Conversion Range

Fernando Lessa Tofoli [1,*], Thaís Martins Jajah Carlos [2] and Aniel Silva Morais [2]

1 Department of Electrical Engineering, Federal University of São João del-Rei, São João del-Rei 36307-352, Brazil
2 Faculty of Electrical Engineering, Federal University of Uberlândia, Uberlândia 38408-100, Brazil; thaisjajah@gmail.com (T.M.J.C.); aniel@ufu.br (A.S.M.)
* Correspondence: fernandolessa@ufsj.edu.br

Abstract: The cascaded connection of power converters extends conversion ranges but requires careful consideration due to high component count and efficiency concerns, as power is processed redundantly. Furthermore, using several active switches that must be turned on simultaneously may introduce significant drive and control complexity. To overcome this limitation, single-switch quadratic DC-DC converters have been proposed in the literature as a prominent choice for various applications, such as light-emitting diode (LED) drivers. Nevertheless, the motivation behind the conception of such topologies, beyond extending the conversion ratio, remains unclear. Another unexplored issue is the possibility of obtaining single-switch versions of cascaded converters consisting of multiple stages. In this context, this work investigates the synthesis of single-switch non-isolated DC-DC converters for achieving high step-down and/or high step-up based on the graft scheme. Key issues such as the voltage gain, additional stresses on the active switches, component count, and behavior of the input current and output stage current are addressed in detail. An in-depth discussion is presented to identify potential advantages and shortcomings of the resulting structures.

Keywords: non-isolated DC-DC converters; graft scheme; quadratic converters; wide conversion range

1. Introduction

DC-DC converters are crucial for modern applications involving electronic equipment. Typical examples include switch-mode power supplies (SMPSs), DC motor drives, renewable energy conversion systems, microgrids, light-emitting diode (LED) drivers in lighting systems, electric vehicles (EVs), uninterruptible power systems (UPSs), and electric aircraft, among others [1]. They play an important role in adapting DC voltage levels between the source and loads, as well as in controlling power flow effectively and maintaining the output voltage constant, particularly when the load power varies [2].

The classical non-isolated DC-DC converters, such as the buck, boost, buck–boost, Ćuk, single-ended primary-inductance converter (SEPIC), and Zeta topologies, are still used in many practical applications nowadays [3]. All of them derive from a basic arrangement referred to as the canonical cell or pulse-width modulation (PWM) switch [4]. They have also led to the conception of numerous derived structures with improved characteristics over the last decades [5]. However, they are limited when dealing with wide voltage conversion ranges, primarily because the ratio between the output voltage and the input voltage depends solely on the duty cycle associated with the active switch [6].

In turn, incorporating high-frequency transformers can extend the voltage conversion ratio of DC-DC converters [7]. The classical isolated topologies, such as the flyback, forward, push–pull, half-bridge, and full-bridge converters, allow for adjusting the output voltage according to not only the duty cycle but also the transformer turns ratio, aiming to achieve high step-up or high step-down [8]. Since high-frequency transformers rely on materials with high magnetic permeability, such as ferrite, unlike their low-frequency counterparts based on silicon–steel, they may be limited in size due to the lack of mechanical robustness and ability to process power levels up to 50 kW; this being a conservative estimate according to [9]. Nevertheless, the utilization of high-frequency transformers can significantly impact power density, especially in high-power applications.

Non-isolated DC-DC converters with a wide conversion range represent a prominent choice for applications in which galvanic isolation is not a mandatory requirement [10]. Perhaps the first work on this subject is [11], which proposed a modular voltage-divider Ćuk converter with multiple active switches connected to a common ground for achieving large voltage step-down ratios. However, the first study to present single-switch DC-DC converters with a wide conversion range seems to be [12], which introduced the so-called quadratic DC-DC buck, boost, and buck–boost converters, as well as other structures based on the combinations of distinct arrangements. In fact, such topologies consist of the cascade association of two conversion stages, yielding redundant power processing and low efficiency. However, the concept that allows for deriving single-switch structures from cascaded converters whose active switches share a common node was only formalized in [13] in terms of the graft scheme.

More recently, non-isolated high step-up DC-DC converters have received significant attention from researchers and experts in the field of power electronics, especially owing to the increasing penetration of grid-connected renewable energy conversion systems [14]. According to [15], one can extend the conversion ratio of the traditional boost converter using switched capacitors, switched inductors, voltage multipliers, voltage lifting techniques, magnetic coupling, and cascaded stages, or even consider a combination of such solutions. A plethora of topologies are available in the recent literature, but discussing them in detail falls outside the scope of this work.

Switched capacitors can achieve high efficiency at low power levels, but the resulting structures may have a limited voltage-boosting capability while requiring the association with other techniques to increase the voltage gain. This inconvenience can be overcome with the use of switched inductors but at the cost of increased dimensions and weight, as well as high electromagnetic interference (EMI) levels. Voltage multipliers are simple solutions for deriving high step-up converters based on a modular approach, although a high component count may be necessary, thus affecting overall power density.

Voltage lifting techniques offer flexibility and adaptability to various input and output configurations, but thermal management becomes a major concern, particularly at high power levels. Magnetic coupling approaches based on built-in transformers and coupled inductors allow for adjusting the voltage gain according to the turns ratio associated with the windings, but this may be a somewhat limited solution at high power levels owing to the increased dimensions of magnetic elements. Cascaded converters can also provide high step-up, but the high component count and sensitivity to parameter variations and mismatches associated with the converter stages may restrict them to low-power applications.

On the other hand, non-isolated high step-down DC-DC converters are available in a much smaller number of publications [16]. Possible strategies for extending the conversion ratio of the conventional buck converter include cascaded stages, coupled inductors, switched capacitors, and switched inductors [17].

Although cascaded and quadratic converters may lead to poor efficiency, as previously mentioned, several topologies with enhanced performance in terms of voltage gain, current/voltage stresses, and efficiency are available in recent works [18]. However, it is reasonable to state that the basic structures introduced in [12] are still an adequate choice for low-power applications involving intermediate voltage gains associated with moderate input voltage and/or output voltage levels, according to [19]. Thus, the authors in [20] formulate a systematic method for the synthesis of power converters based on a specified voltage conversion ratio using the quadratic buck–boost converter as an example. This inverse problem is also addressed in [21], where the conception of the quadratic buck topology is investigated from the forward and reverse perspectives. One can also derive quadratic converters using the fundamental flux balance equation across the inductors [22].

Some modern applications may benefit significantly from the utilization of quadratic converters. For instance, three quadratic DC-DC buck topologies that can be reconfigured in the form of semi-quadratic buck–boost arrangements are proposed in [23] for electrolyzers in DC microgrids. The topology presented in [24] proves to be an adequate choice for the charging and discharging of batteries and supercapacitors. An extendable bidirectional DC-DC converter for vehicle-to-grid (V2G) and grid-to-vehicle (G2V) applications is also proposed in [25].

In this context, this work presents a comprehensive analysis involving the properties and synthesis of single-switch non-isolated DC-DC converters with a wide conversion range derived from the six classical topologies. The main contributions of this study include the following:

- Investigating the modularity of multistage converters aiming at obtaining single-switch structures and extending the concept formerly introduced in [12];
- Applying the graft scheme in the conception of structures with distinct characteristics for high step-down and/or high step-up applications;
- Assessing the properties of derived topologies in terms of the voltage gain, current and voltage stresses, and behavior of the input and output stage currents.

This work is organized as follows. Section 2 addresses the limited capacity of the traditional buck and boost converters in achieving high step-down and high step-up, respectively. Section 3 revisits some basic concepts regarding cascaded converters, while Section 4 discusses the advantages and disadvantages of the graft scheme in generating single-switch topologies. Section 5 shows how one can obtain multistage single-switch topologies based on the six classical non-isolated DC-DC converters. Section 6 summarizes several characteristics desirable for the conception of high step-up and/or high step-down topologies, including some arrangements reported in the literature and their related applications. Section 7 concludes this study and highlights potential future work on the subject.

2. Limitations of Classical Non-Isolated DC-DC Converters

When galvanic isolation is not a must, non-isolated DC-DC converters can be used instead, with the consequent reduction in dimensions and increase in efficiency due to the lack of a high-frequency transformer [26]. The traditional buck and boost converters are the preliminary choices in voltage step-up or step-down, respectively, mainly owing to simplicity and low component count, although some important practical issues must be taken into account. A thorough overview of fundamentals involving basic converter topologies is presented in [27].

First, let us consider the buck converter shown in Figure 1a, where the intrinsic series resistance of the filter inductor represented by R_L is the only parasitic element in the circuit. Thus, one can easily demonstrate that the voltage gain G of the topology in continuous conduction mode (CCM) is given by (1).

$$G = \frac{V_o}{V_i} = \frac{D}{1+\alpha}, \tag{1}$$

where V_o is the average output voltage, V_i is the average input voltage, D is the duty cycle, and α is the ratio between R_L and the load resistance R_o defined as in (2).

$$\alpha = \frac{R_L}{R_o}. \tag{2}$$

Figure 1b shows that the voltage gain is directly influenced by R_L, as it is necessary to impose higher duty ratios on the active switch to obtain a given conversion ratio when compared with the ideal converter in which α = 0, i.e., R_L = 0.

The presence of R_L also affects the converter efficiency, according to Figure 1c, especially in high-power applications, since the losses increase with the square of the root-mean-square (RMS) current through the inductor, which is approximately equal to the average output current I_o in the buck converter. It is also possible to demonstrate that the efficiency η is given by (3).

$$\eta = \frac{1}{1+\alpha}. \tag{3}$$

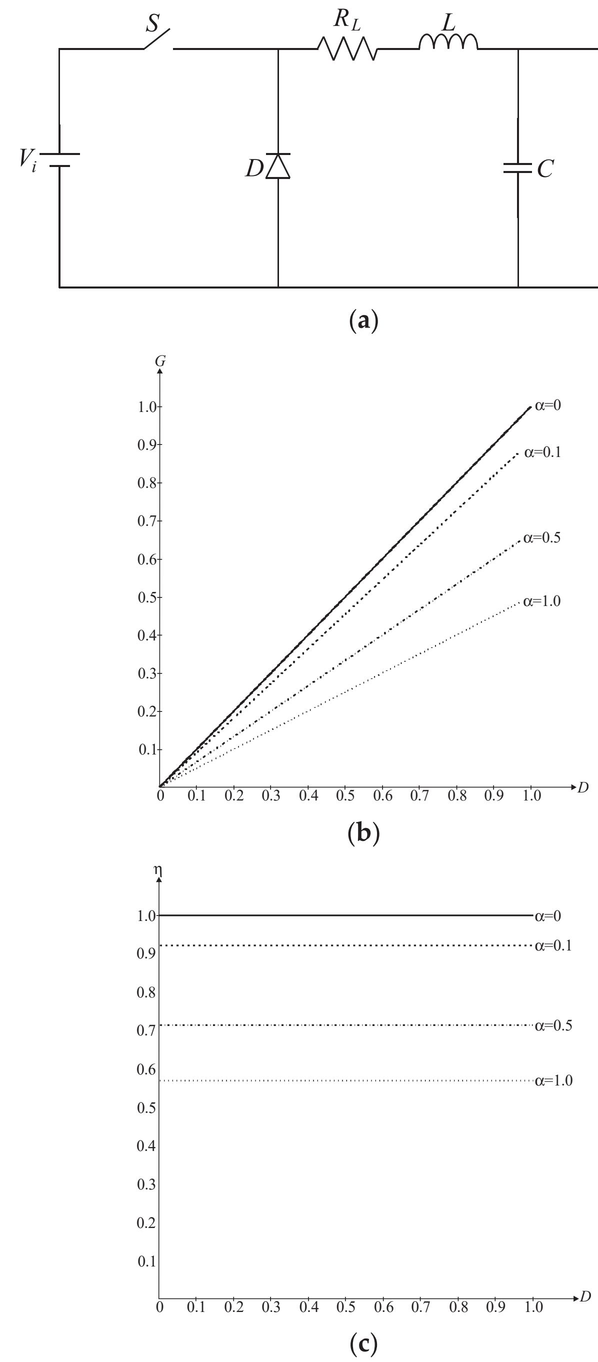

Figure 1. Conventional DC-DC buck converter: (**a**) power stage considering the presence of parasitic elements, (**b**) resulting voltage gain curves as a function of the duty cycle, and (**c**) efficiency curves as a function of the duty cycle.

Another important aspect to be observed in (1) lies in the fact that wide voltage conversion ranges are only possible when dealing with very low duty ratios, which may not be feasible in practical applications. It is worth mentioning that actual gating signals applied to active switches have finite dv/dt rates, while fast semiconductor elements such as metal–oxide–semiconductor field-effect transistors (MOSFETs) have finite turn-on and turn-off times. Moreover, obtaining very low and/or high duty ratios typically requires expensive and complex fast drivers.

Now, let us analyze the classical DC-DC boost topology represented in Figure 2a, where the presence of R_L is also considered. The voltage gain of the converter operating in CCM can then be derived as in (4).

$$G = \frac{V_o}{V_i} = \left(\frac{1}{1-D}\right)\frac{1}{\left[1+\frac{\alpha}{(1-D)^2}\right]}. \tag{4}$$

If the DC-DC boost converter is ideal, that is, α = 0, the output voltage will tend to infinity as the duty cycle tends to unity according to Figure 2b, but it would demand the use of complex and costly drive circuitry. The voltage gain, in practice, is limited to a finite value because high output voltages would demand high duty ratios, thus causing the switch to remain on for long time intervals. If the current through the diode is high, serious drawbacks regarding the reverse recovery phenomenon also exist. Now, considering α = 0.01 in Figure 2b, one can state that the boost converter cannot achieve high step-up, whereas the voltage gain tends to decrease at very high duty ratios owing to the voltage drop on the filter inductor.

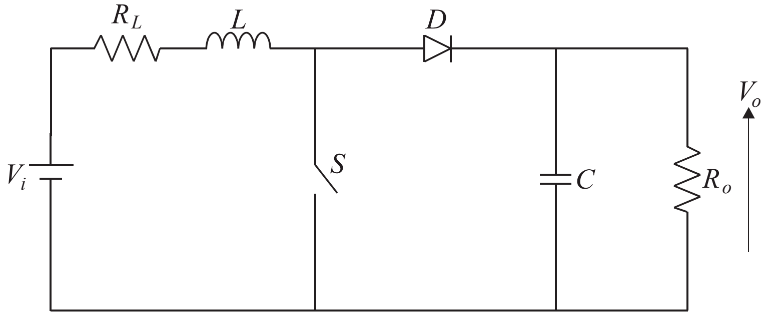

(**a**)

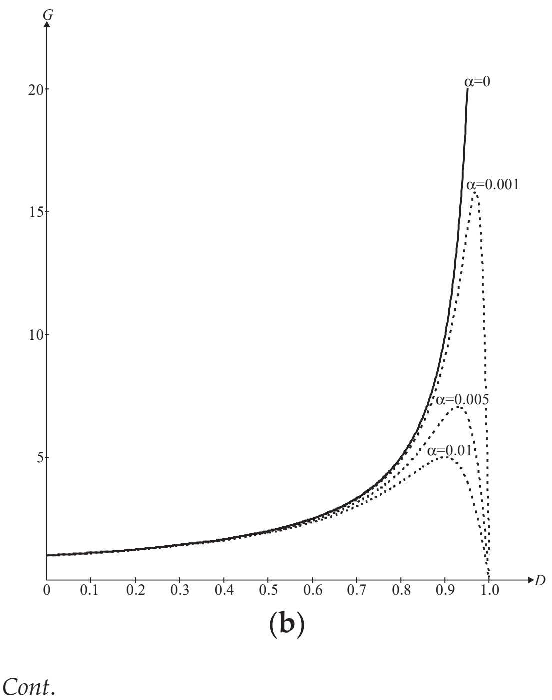

(**b**)

Figure 2. *Cont*.

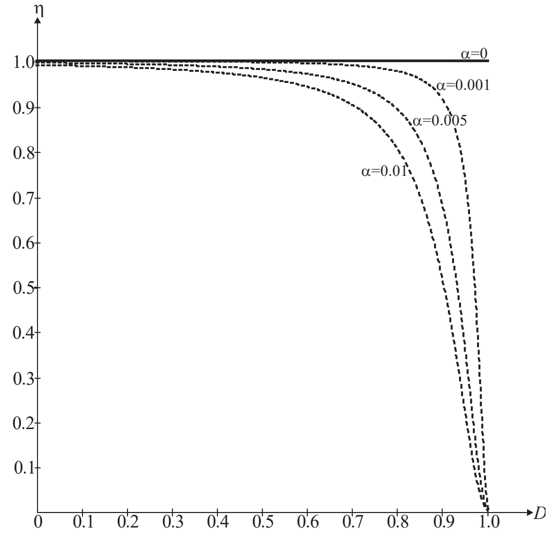

(**c**)

Figure 2. Conventional DC-DC boost converter: (**a**) power stage considering the presence of parasitic elements, (**b**) resulting voltage gain curves as a function of the duty cycle, and (**c**) efficiency curves as a function of the duty cycle.

One can also determine the theoretical efficiency of the boost converter from (5). Figure 2c shows that R_L affects the converter efficiency directly. This issue becomes more evident at high power levels since the inductor losses increase with the square of the RMS input current. Other relevant factors impacting efficiency include the equivalent series resistance (ESR) of the output capacitor, reverse recovery losses, high dv/dt and di/dt rates associated with the diode, and high voltage stresses across the semiconductor elements. Therefore, it is reasonable to state that the conventional boost converter is a simple choice for applications that do not demand high step-up.

$$G = \frac{V_o}{V_i} = \frac{1}{1-D} \cdot \frac{1}{\left(1 + \frac{\alpha}{(1-D)^2}\right)}. \tag{5}$$

3. Cascaded Non-Isolated DC-DC Converters

Cascading power converters is a simple and straightforward approach that yields a wide conversion range, whereas one can virtually extend this concept to any topology [28,29]. To achieve high step-up and/or high step-down, the cascade connection of classical DC-DC non-isolated converters is possible, according to Figure 3. It is worth noting that in buck–boost and Ćuk converters, the output voltage polarity is opposite to that of the input voltage. This requires verifying the placement of the active switch and diode in each cascaded stage to ensure proper circuit operation. As an example, let us consider the total number of stages as N = 2 in Figure 3c. The active switches and diodes of the input stage and its subsequent circuit are positioned to allow current flow through them in opposite directions. This very same reasoning applies to a higher number of power stages.

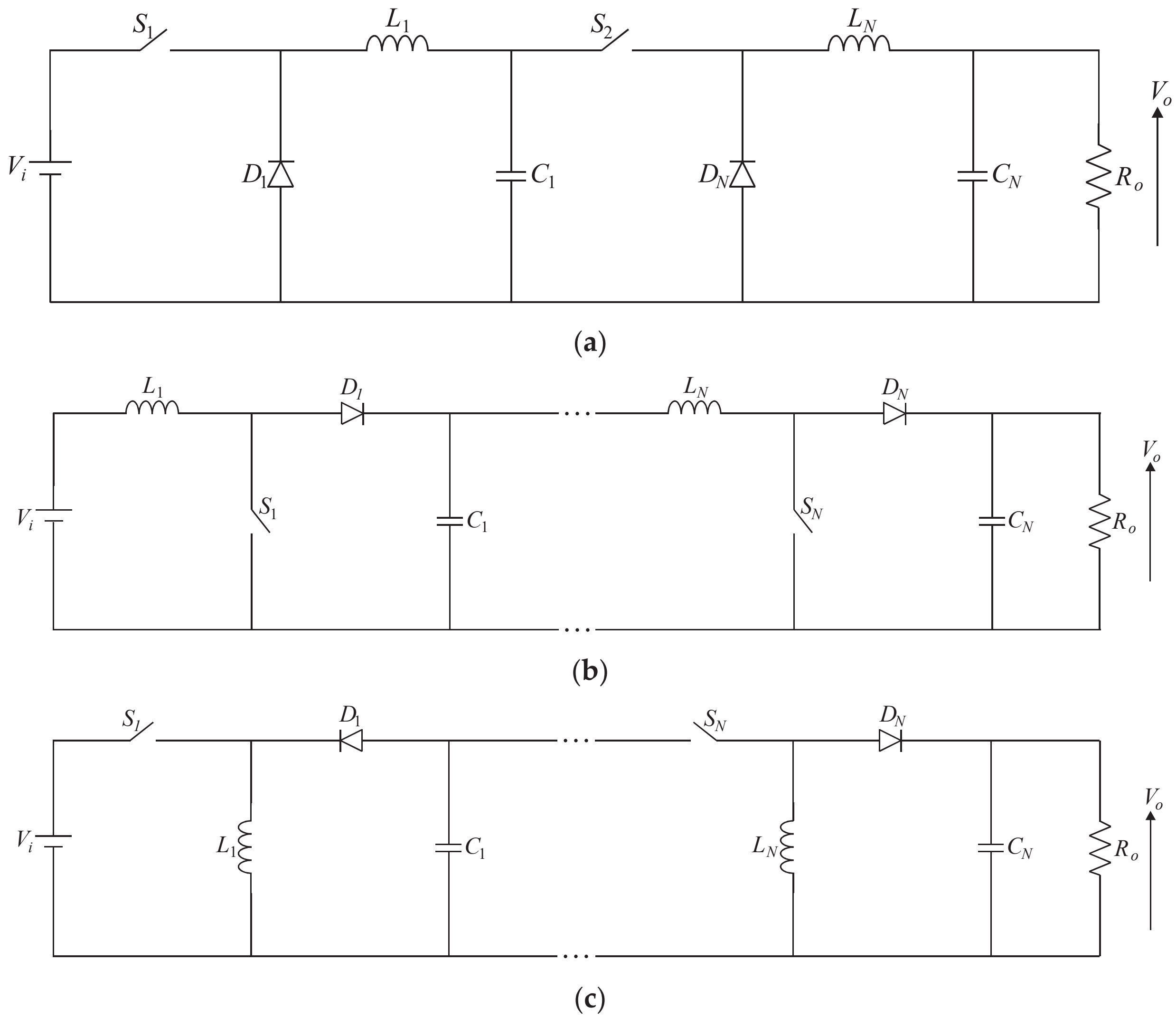

Figure 3. Cascaded DC-DC converters with multiple active switches: (**a**) buck converter, (**b**) boost converter, and (**c**) buck–boost converter.

The following advantages can be attributed to cascaded converters [30]:

- Inherent modularity;
- The voltage gain of the resulting association is equal to the product of the voltage gains associated with the individual stages;
- The active switches can be driven independently with distinct duty ratios;
- Additional degrees of freedom can be incorporated into the control system.
- In turn, significant drawbacks tend to exist:
- High component count, especially when many cascaded converters are used to obtain a wide conversion range;
- All active switches must be turned on simultaneously, as the gating signals must be properly synchronized;
- Reduced robustness due to the presence of several semiconductor elements, while the converter becomes more susceptible to eventual malfunctioning;
- The overall efficiency, determined by the product of the efficiencies of each stage in the cascade configuration, is significantly reduced due to energy flowing through multiple power stages;
- The control system may become significantly complex;

– The current and voltage stresses involving the semiconductor elements in the last stage may be somewhat high, thus limiting the application of cascaded converters to low power levels.

Considering that all converters in Figure 3 operate in CCM, the voltage gains of the N-stage cascaded buck, boost, and buck–boost converters are given by (6)–(8), respectively.

$$G = \frac{V_o}{V_i} = \prod_{n=1}^{N} D_n, \tag{6}$$

$$G = \frac{V_o}{V_i} = \prod_{n=1}^{N} \left(\frac{1}{1 - D_n} \right), \tag{7}$$

$$G = \frac{V_o}{V_i} = \begin{cases} \prod\limits_{n=1}^{N} \left(-\frac{D_n}{1-D_n} \right), \text{ if } n = 1,3,5\ldots \\ \prod\limits_{n=1}^{N} \left(+\frac{D_n}{1-D_n} \right), \text{ if } n = 2,4,6\ldots \end{cases}, \tag{8}$$

where $D_1 \ldots D_N$ are the duty ratios associated with active switches $S_1 \ldots S_N$, respectively; N is the number of cascaded converters; and n = 1, 2, ... N corresponds to a given stage. It is also noteworthy that "+" and "−" in (8) denote that the output voltage is positive or negative, respectively.

This concept can also be applied in the cascade connection of distinct topologies, such as the two-stage association represented in Figure 4, in which a buck converter follows a buck–boost one. If both stages operate in CCM, it is easy to demonstrate that the voltage gain is calculated from (9).

$$G = \frac{V_o}{V_i} = \left(-\frac{D_1}{1 - D_1} \right) D_2, \tag{9}$$

where D_1 and D_2 are the duty cycles of switches S_1 and S_2, respectively. Furthermore, it is observed that the output voltage polarity is opposite to that of the input voltage owing to modifications in the positions of the active switch and the diode in the output stage compared to the traditional buck topology.

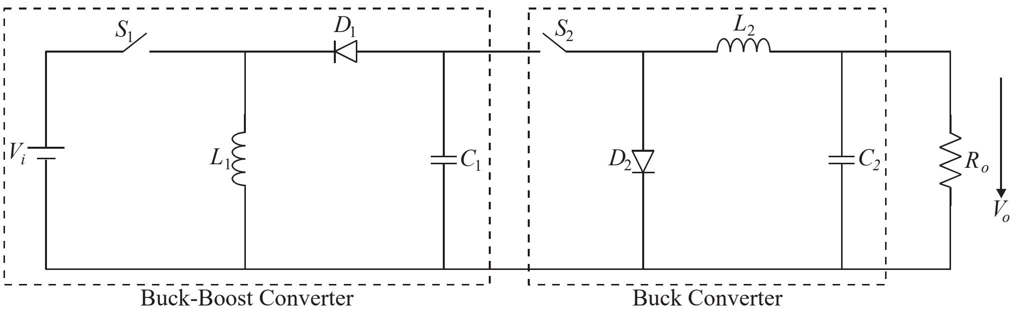

Figure 4. Two-switch cascaded buck–boost/buck converter.

Even though numerous configurations can be obtained in practice, the use of many active switches may lead to increased cost and complexity regarding the control system and/or drive circuitry. It is then desirable to integrate stages so that single-switch topologies can be derived instead using the graft scheme described as follows.

4. Graft Scheme Applied in the Conception of Single-Switch Quadratic DC-DC Converters

One can properly integrate two cascaded converters relying on one active switch each using the so-called graft technique, considering the four possible arrangements described in [13,27] and shown in Figure 5. This concept enables the derivation of small-signal models for single-stage topologies based on basic converter units [31] and assessing their operation in discontinuous conduction mode (DCM) [32].

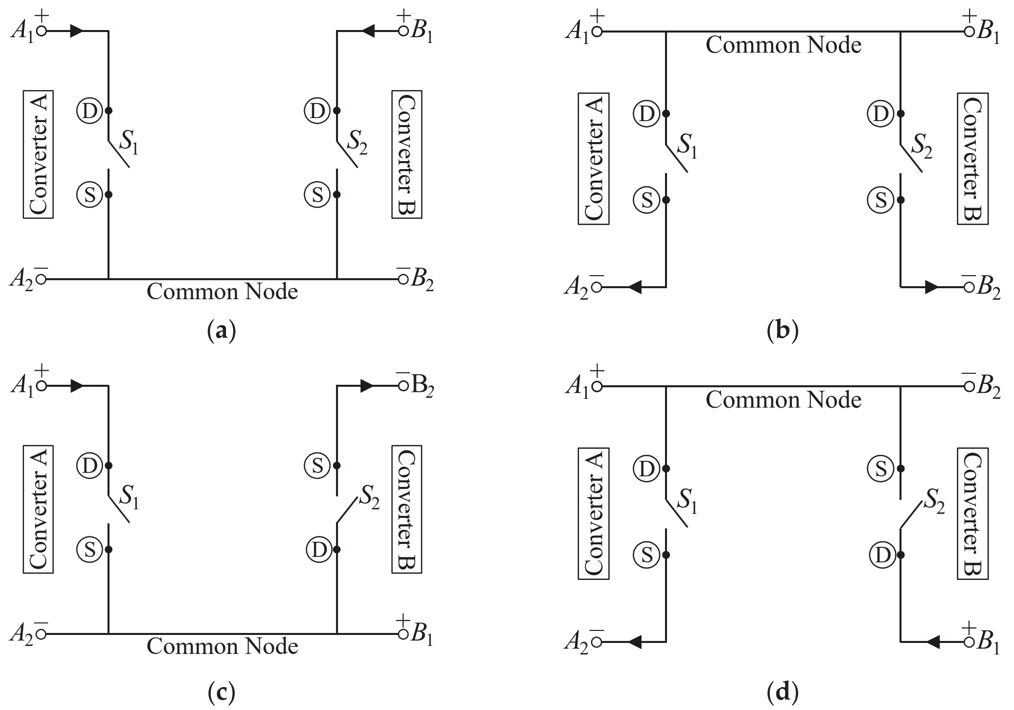

Figure 5. Possible configurations for two active switches connected to a common point: (**a**) configuration I—source–source connection, (**b**) configuration II—drain–drain connection, (**c**) configuration III—source–drain connection, and (**d**) configuration IV—drain–source connection.

Configurations I and II correspond to common source-source and common drain-drain connections, respectively, while configurations III and IV consist of common drain-source and common source-drain connections, respectively. According to [13], the two active switches in each possible combination can be replaced with an arrangement composed of one single active switch and two diodes, yielding the corresponding circuits represented in Figure 6, where "D" and "S" stand for the drain and source terminals of a MOSFET, respectively.

Now, let us consider the cascaded buck–boost/buck converter shown in Figure 4 as an example. Analyzing the circuit, one can identify the existence of configuration III according to Figure 5c. Thus, it is possible to obtain the resulting single-switch converter in Figure 7a from Figure 6c, where two diodes are connected to the active switch. However, since diode D_4 is responsible for ensuring the current flow in a single direction while always remaining forward-biased during the converter operation, one can replace such an element with a short circuit, as shown in Figure 7b. Another topological variation can be derived in Figure 7c, where the position of diode D_2 is modified in the circuit.

Applying the volt-second balance to Figure 7, one can obtain the voltage gain of the converter operating in CCM as in (10).

$$G = \frac{V_o}{V_i} = -\frac{D^2}{1-D}. \tag{10}$$

Despite the reduced cost and increased robustness and reliability associated with single-switch cascaded topologies, there are still some drawbacks [33]. Configurations I and II cause increased current stresses on the switch, while configurations III and IV yield increased voltage stresses on the switch. In configurations I and II, the current stress equals the sum of the currents from both stages. Conversely, in configurations III and IV, it corresponds to the higher of the two currents from the two stages.

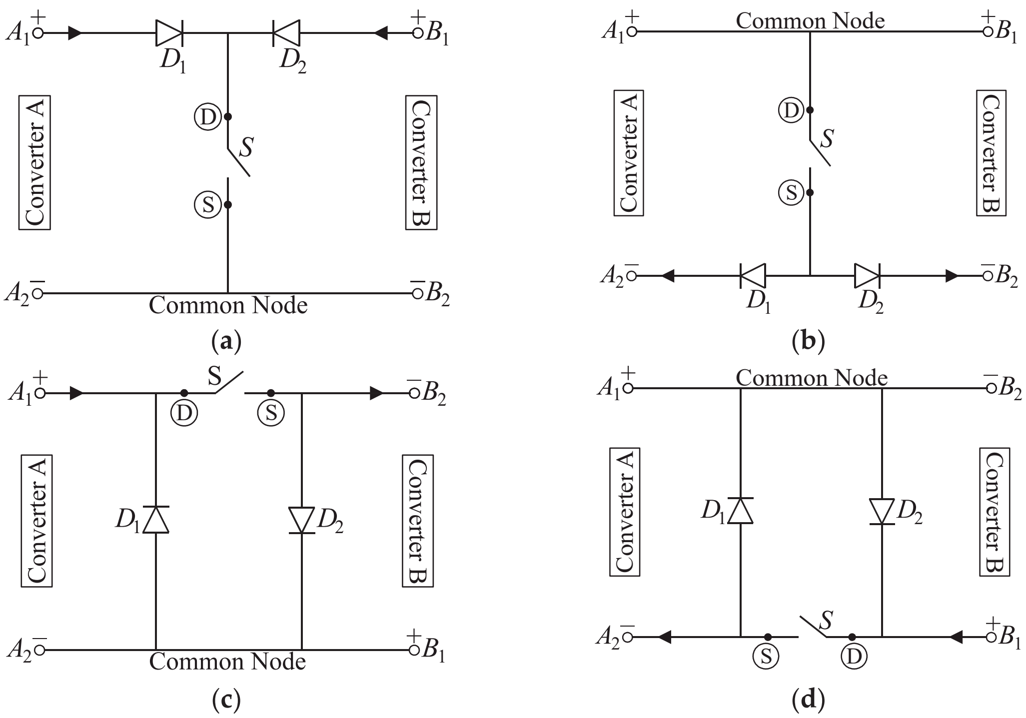

Figure 6. Resulting single-switch configurations for the integration of cascaded converters: (**a**) configuration I, (**b**) configuration II, (**c**) configuration III, and (**d**) configuration IV.

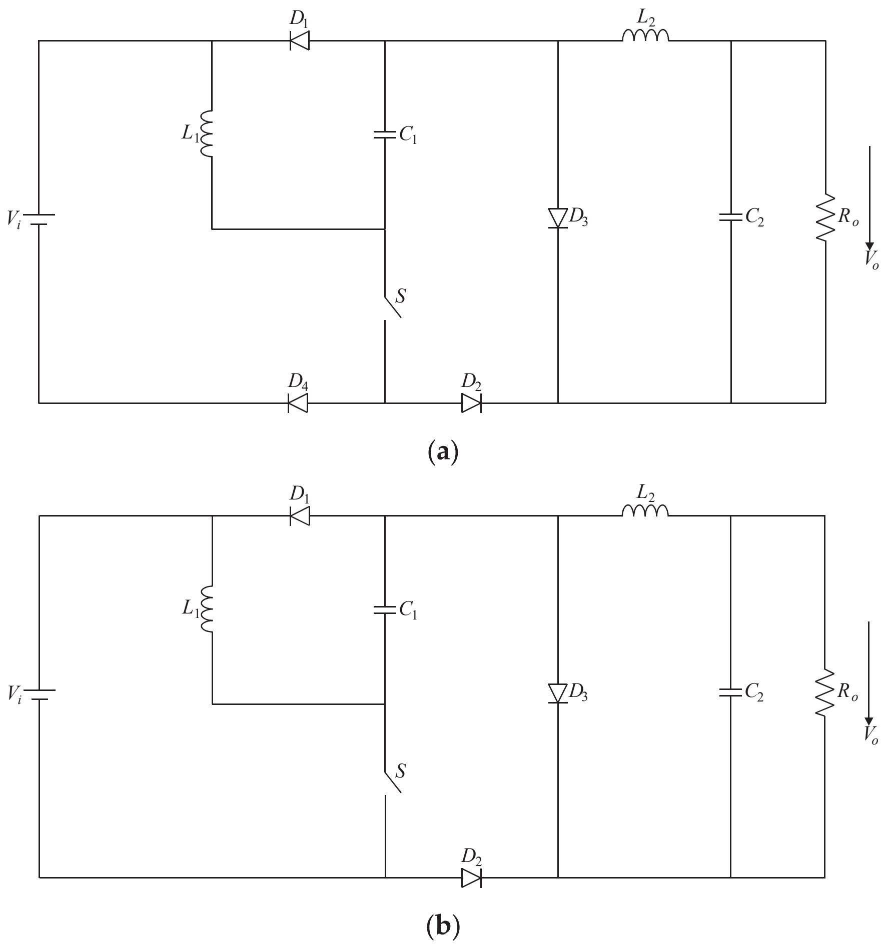

Figure 7. *Cont*.

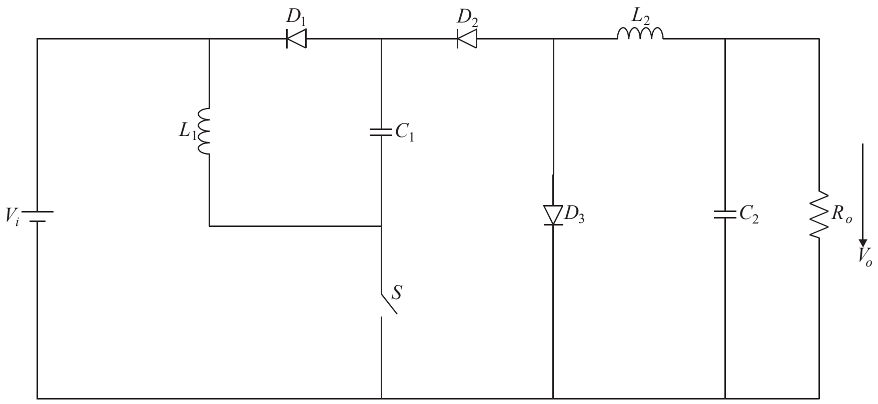

(c)

Figure 7. Single-switch cascaded buck–boost/buck converter: (**a**) configuration with two additional diodes, (**b**) topology with a single diode, and (**c**) resulting modified topology.

5. Deriving Multistage Single-Switch Non-Isolated DC-DC Converters

Alternate topologies with different voltage gain characteristics can be synthesized by cascading basic converters with each other [34]. In addition, it has been demonstrated in [12] that single-switch converters with non-standard conversion ratios, referred to as quadratic converters, can be derived. Even though such structures can achieve wide voltage conversion ratios, they are not widely used for being generally less efficient than other topologies, although they can be useful for some applications [35].

As previously mentioned, the graft scheme proposed in [13] allows for deriving single-switch converters as long as two or more switches share a common connection node. In this sense, it is possible to obtain multistage single-switch non-isolated DC-DC converters based on cascade stages in terms of a modular approach, which has not been presented in the literature before. Let us start with the quadratic buck converter formerly introduced in [12] and shown in Figure 8. Since it consists of the association of two buck stages, one can obtain a single-switch version of the topology by considering the active switches connected to each other in the form of configuration IV, according to Figure 5d. Adopting the resulting arrangement shown in Figure 6d and rearranging the position of power stage elements yields the circuit in Figure 8a, which has a fourth-order characteristic [36]. It is also possible to obtain a modular approach based on a single active switch from the same reasoning, resulting in the multistage converter shown in Figure 8b. This principle was applied in the conception of a cubic buck converter in [37].

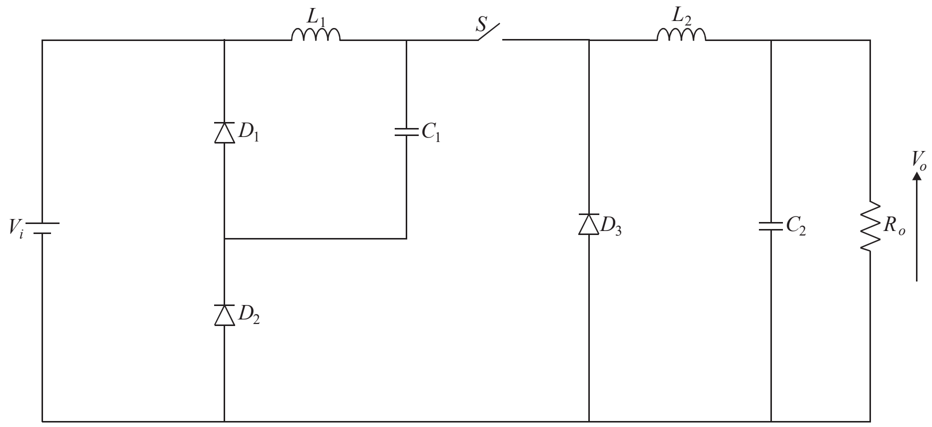

(a)

Figure 8. *Cont.*

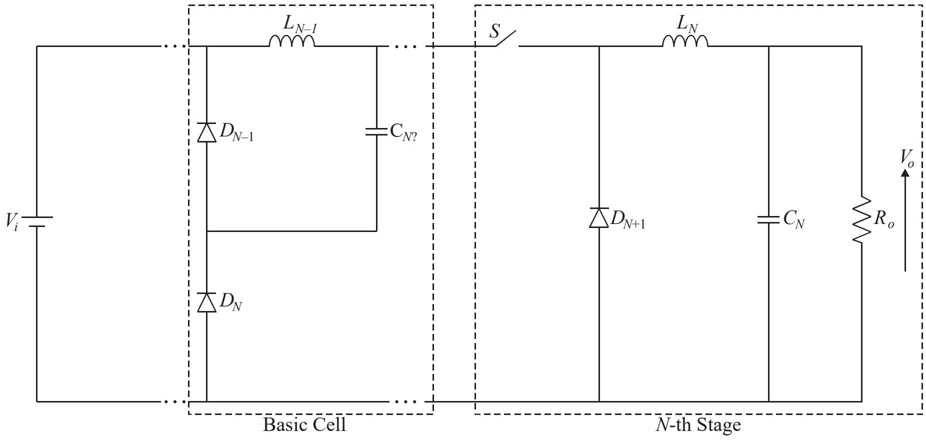

(**b**)

Figure 8. Single-switch quadratic buck converter: (**a**) original topology proposed in [12] and (**b**) converter modularity.

The quadratic boost converter shown in Figure 9a is perhaps one of the first non-isolated high step-up DC-DC converters reported in the literature [12]. Despite the output voltage increasing in a quadratic ratio, the voltage stresses on the active switch S and the output diode D_3 remain equal to the output voltage, as observed in the traditional boost converter. Moreover, since this single-switch topology is obtained from configuration I, as shown in Figures 5a and 6a, the active switch is subjected to a higher RMS current, which leads to higher conduction losses. These two aforementioned issues may restrict the converter to low-power, low-output-voltage applications. It is also worth mentioning that one can derive a multistage single-switch boost converter using the graft scheme in terms of Figure 9b.

The quadratic buck–boost converter shown in Figure 10a was formerly proposed in [12]. The resulting voltage gain in CCM corresponds to the products of the voltage gains of two conventional buck–boost converters. In other words, the topology can provide high step-down and high step-up if $D < 0.5$ and $D > 0.5$. However, if diode D_4 is replaced with a short circuit, as in [12], the converter will only be capable of operating in step-down mode. Incorporating such a diode into the circuit shown in Figure 10b allows for obtaining a multistage structure that can operate in either mode. It is also noteworthy that different basic cells are utilized in deriving such topology, depending on whether the number of cascaded stages is odd or even. An application of the quadratic buck–boost converter operating as an LED driver capable of providing a high input power factor is presented in [38]. The graft scheme was also employed to derive a cubic buck–boost topology with a high step-up capability in [39].

An important issue is that only topologies based on the basic second-order converters were addressed in [12], while the quadratic Ćuk, SEPIC, and Zeta topologies remained unexplored at that time. Let us recall that the Ćuk converter is a fourth-order system in which the boost and buck converters are arranged as the input and output stages, respectively [40]. Another topological variation referred to as the SEPIC converter was introduced in [41], whose input and output stages consist of the boost and buck–boost converters, respectively. The last classical non-isolated DC-DC converter, which is referred to as dual SEPIC or Zeta converter, relies on the association of the buck–boost and buck converters [42].

Other quadratic step-up/step-down DC-DC topologies based on the classical Ćuk, SEPIC, and Zeta converters can be derived using the graft technique. While they can operate over the entire duty cycle range $0 \leq D \leq 1$, their practical application may be restricted owing to the high voltage stress on the active switch, high component count, and significant complexity involved in implementing the control system owing to the high system order. Furthermore, the need for four inductors may lead to increased size, weight, and volume.

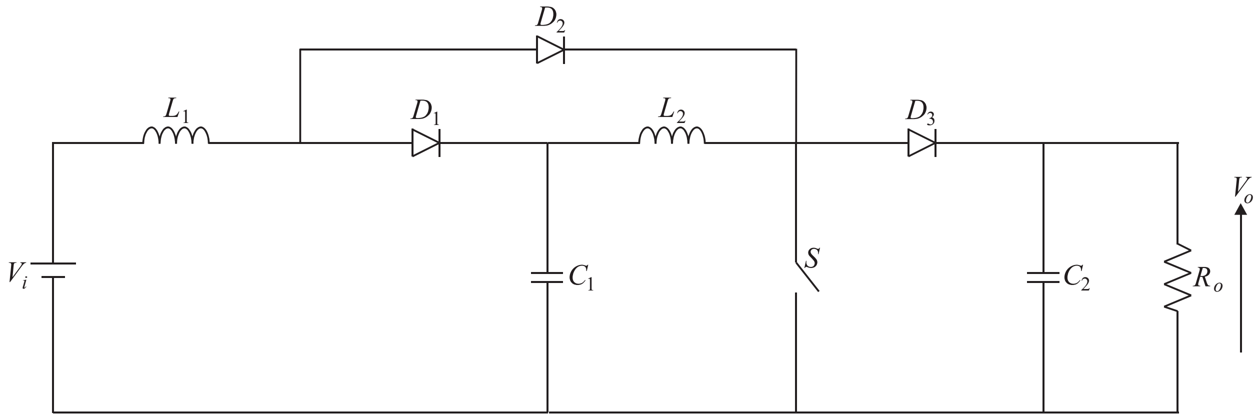

(**a**)

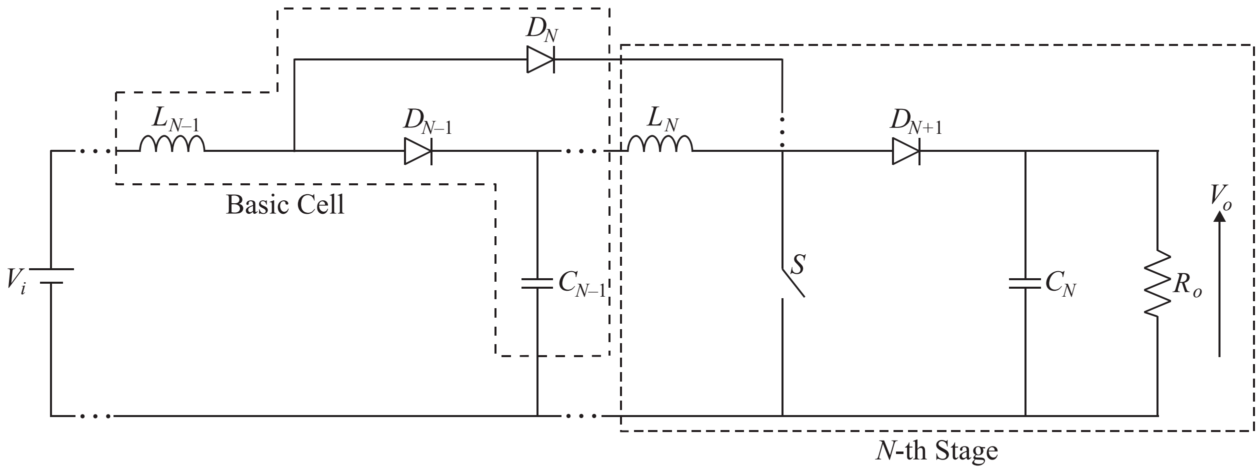

(**b**)

Figure 9. Single-switch quadratic boost converter: (**a**) original topology proposed in [12] and (**b**) converter modularity.

Figure 11 shows the quadratic Ćuk converter, which, like the quadratic buck–boost converter, generates a positive output voltage. Owing to the position of the active switch in the circuit, a priori, it is not possible to arrange it in a single-switch modular form aiming to extend the voltage gain. Even though it presents a high component count, a modified quadratic Ćuk topology based on three inductors and three capacitors was proposed in [43]. In turn, the modular versions of the SEPIC and Zeta converters are presented in Figure 12a,b, respectively. It is necessary to cascade the basic cells represented in the dashed boxes to extend the conversion ratio, as well as to maintain the N-th stage associated with the output stage in any resulting converter. A quadratic AC-DC quadratic SEPIC converter employed as an LED driver was proposed in [44], resulting in a high input power factor and high efficiency over a wide load range while considering a moderate voltage gain. It is also noteworthy that the quadratic Zeta converter shown in Figure 12b remains unexplored thus far.

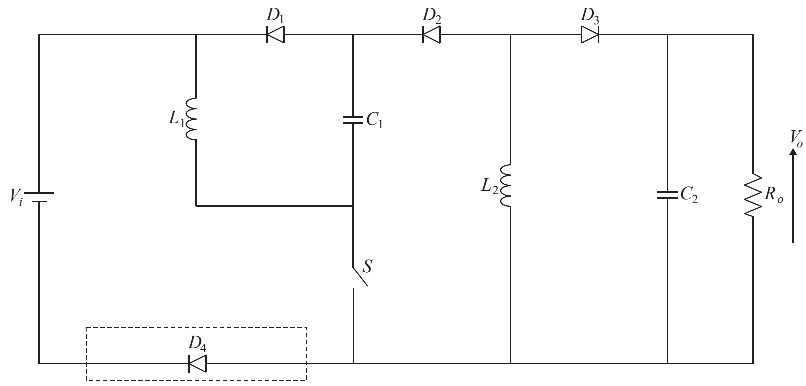

(**a**)

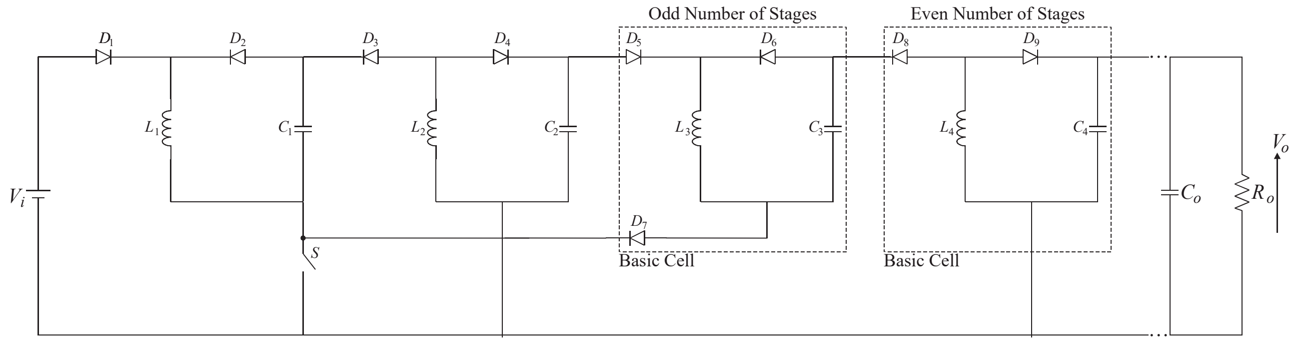

(**b**)

Figure 10. Single-switch quadratic buck–boost converter: (**a**) original topology proposed in [12] and (**b**) converter modularity.

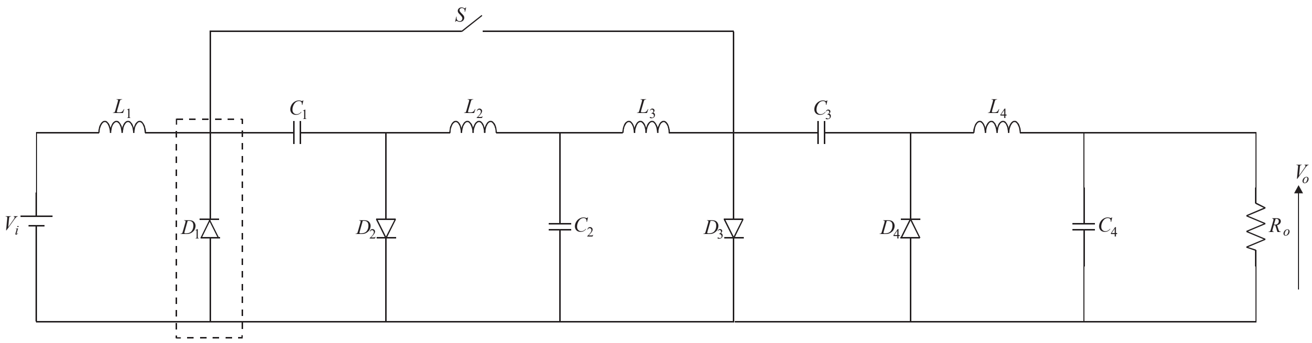

Figure 11. Single-switch quadratic Ćuk converter.

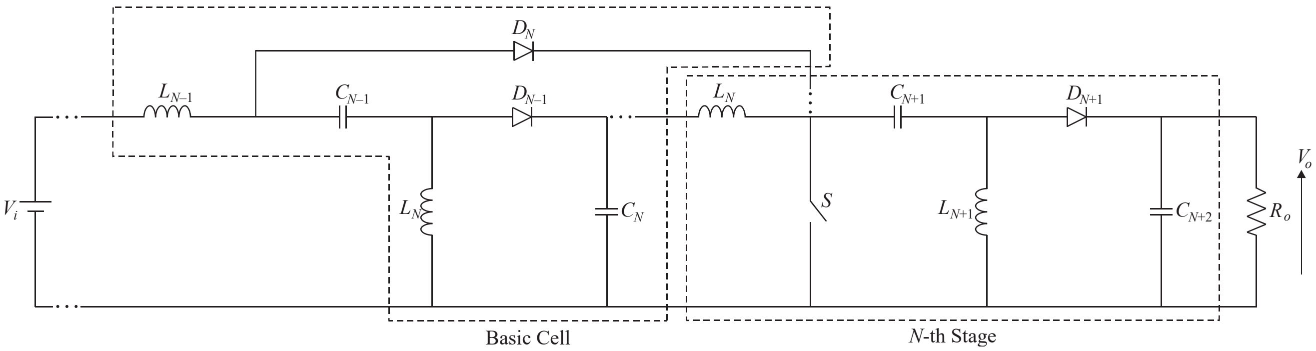

(**a**)

Figure 12. *Cont*.

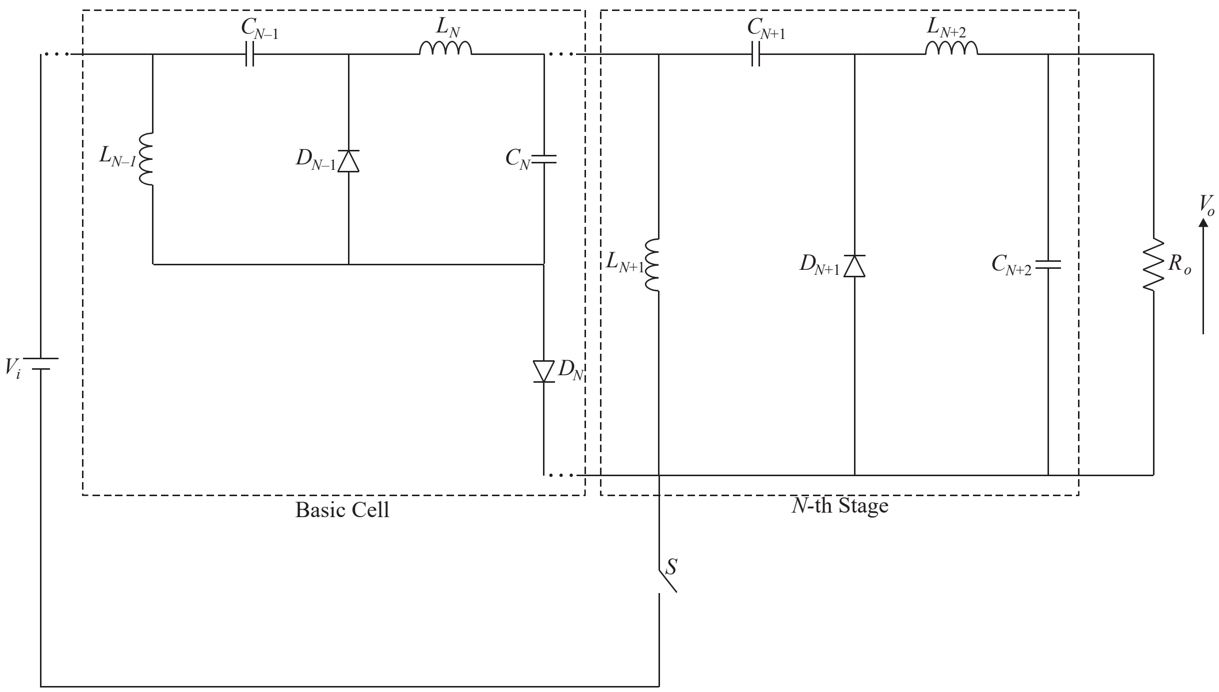

(**b**)

Figure 12. Single-switch multistage DC-DC topologies: (**a**) SEPIC converter and (**b**) Zeta converter.

6. Properties and Synthesis of Two-Stage Single-Switch Non-Isolated DC-DC Converters

The graft scheme is a versatile approach to derive numerous DC-DC converter structures beyond those outlined in [12]. By combining the classical buck, boost, buck–boost, Ćuk, SEPIC, and Zeta converters, it is possible to derive 36 two-stage, single-switch topologies with the most diverse characteristics [45]. In this sense, this section presents a brief discussion of non-isolated DC-DC converters based on the cascaded association of two distinct stages, which can be referred to as hybrid quadratic topologies.

The AC-DC SEPIC/buck–boost converter was proposed in [46] as an offline LED driver that does not rely on electrolytic capacitors. The input stage can operate in DCM and provide power-factor correction (PFC) owing to the voltage follower characteristic of the SEPIC converter. The buck stage operates in CCM as it is responsible for power flow control and LED dimming.

The SEPIC–buck converter is also a compelling option for LED-based lighting applications because the currents through both the input and output stages are non-pulsating, resulting in reduced EMI levels [47]. Similar to [46], the input stage operates in DCM, minimizing the size of the filter inductor and eliminating the need for a control loop for the input current. The output buck stage operates in CCM, aiming to control the current through the LEDs. However, this topology is only adequate for high step-down applications because it only operates in step-up mode for $D > 0.618$. In other words, it means that the circuit is not competitive even when compared with the classical boost converter because it will require a higher duty ratio to provide the same voltage gain.

The SEPIC–Ćuk converter presented in [48] also benefits from non-pulsating currents in both stages. Even though it can achieve high step-up and/or high step-down, a significant drawback lies in high component count, especially because it requires four filter inductors that may drastically impact power density. In turn, even though the boost–Ćuk converter described in [49] relies on three filter inductors instead, it is better recommended for high step-up applications only. This is because the operation in step-down mode occurs only when $D < 0.382$, whereas the converter would require very low duty ratios to provide a high step-down.

Considering that the voltage gain varies as a function of the duty cycle, as shown in Figure 13, it is reasonable to classify the conventional and quadratic single-switch non-isolated DC-DC converters operating into CCM into six types:

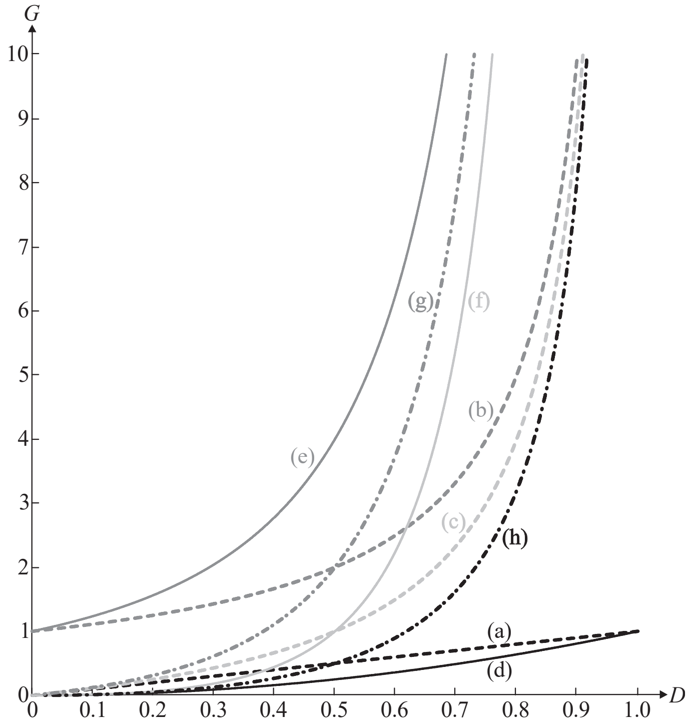

Figure 13. Voltage gains of single-switch conventional and quadratic non-isolated DC-DC converters operating in CCM as a function of the duty cycle: (a) low step-down, (b) low step-up, (c) low step-up/low step-down, (d) high step-down, (e) high step-up, (f) high step-up/high step-down, (g) high step-up/low step-down, and (h) low step-up/high step-down.

(i) Topologies adequate for low step-down (a), low step-up (b), or low step-up/low step-down applications (c), this being the case of the classical buck, boost, and buck–boost converters, respectively;

(ii) Topologies adequate for high step-down applications (d);

(iii) Topologies adequate for high step-up applications (e);

(iv) Topologies adequate for high step-up/high step-down applications (f);

(v) Topologies adequate for high step-up/low step-down applications (g);

(vi) Topologies adequate for low step-up/high step-down applications (h).

While some topologies have been assessed in the literature, many structures remain unexplored thus far. In this sense, Tables 1–6 summarize some important characteristics of all possible combinations, which can be useful for selecting a given topology. For instance, among applications that require a high step-up stage, grid-connected photovoltaic (PV) systems rely on a front-end DC-DC stage for stepping up the low voltage across the modules and supplying a cascaded inverter [50]. The quadratic boost and boost–Ćuk converters could also be adequate choices for this purpose, considering proper tradeoffs among the voltage gain, stresses on semiconductors, and behavior of the currents through the input and output stages. In turn, applications involving battery charging would benefit from the non-pulsating currents of the SEPIC–buck converter operating in CCM, whereas the topology can be connected to the AC grid and achieve input PFC.

Table 1. Single-switch quadratic topologies derived from the buck converter.

Characteristic	Buck/Buck [12]	Buck/Boost	Buck/Buck–Boost	Buck/Ćuk	Buck/SEPIC	Buck/Zeta
Configuration	IV	IV	IV	IV	IV	IV
Voltage gain	D^2 (d)	$\frac{D}{1-D}$ (c)	$-\frac{D^2}{1-D}$ (h)	$-\frac{D^2}{1-D}$ (h)	$\frac{D^2}{1-D}$ (h)	$\frac{D^2}{1-D}$ (h)
Input current	Pulsating	Pulsating	Pulsating	Pulsating	Pulsating	Pulsating
Output stage current	Non-Pulsating	Pulsating	Pulsating	Non-Pulsating	Pulsating	Non-Pulsating
Switch Additional Stresses	Voltage	Voltage	Voltage	Voltage	Voltage	Voltage
Components ($S/D/L/C$)	1/3/2/2	1/3/2/2	1/3/2/2	1/3/3/3	1/3/3/3	1/3/3/3
Applications	High step-down	Low step-up/low step-down	Low step-up/high step-down	Low step-up/high step-down	Low step-up/high step-down	Low step-up/high step-down

Table 2. Single-switch quadratic topologies derived from the boost converter.

Characteristic	Boost/Buck	Boost/Boost [12]	Boost/Buck–Boost	Boost/Ćuk [49]	Boost/SEPIC	Boost/Zeta
Configuration	I	I	I	I	I	I
Voltage gain	$\frac{D}{1-D}$ (c)	$\left(\frac{1}{1-D}\right)^2$ (e)	$-\frac{D}{(1-D)^2}$ (g)	$-\frac{D}{(1-D)^2}$ (g)	$\frac{D}{(1-D)^2}$ (g)	$\frac{D}{(1-D)^2}$ (g)
Input current	Non-Pulsating	Non-Pulsating	Non-Pulsating	Non-Pulsating	Non-Pulsating	Non-Pulsating
Output stage current	Non-Pulsating	Pulsating	Pulsating	Non-Pulsating	Pulsating	Non-Pulsating
Switch Additional Stresses	Current	Current	Current	Current	Current	Current
Components ($S/D/L/C$)	1/3/2/2	1/3/2/2	1/3/2/2	1/3/3/3	1/3/3/3	1/3/3/3
Applications	Low step-up/low step-down	High step-up	High step-up/low step-down	High step-up/low step-down	High step-up/low step-down	High step-up/low step-down

Table 3. Single-switch quadratic topologies derived from the buck–boost converter.

Characteristic	Buck–Boost/Buck	Buck–Boost/Boost	Buck–Boost/Buck–Boost [12]	Buck–Boost/Ćuk	Buck–Boost/SEPIC	Buck–Boost/Zeta
Configuration	III	III	III	III	III	III
Voltage gain	$-\frac{D^2}{1-D}$ (h)	$-\frac{D}{(1-D)^2}$ (g)	$\left(\frac{D}{1-D}\right)^2$ (f)	$\left(\frac{D}{1-D}\right)^2$ (f)	$-\left(\frac{D}{1-D}\right)^2$ (f)	$-\left(\frac{D}{1-D}\right)^2$ (f)
Input current	Pulsating	Pulsating	Pulsating	Pulsating	Pulsating	Pulsating
Output stage current	Non-Pulsating	Pulsating	Pulsating	Non-Pulsating	Pulsating	Non-Pulsating
Switch Additional Stresses	Voltage	Voltage	Voltage	Voltage	Voltage	Voltage
Components ($S/D/L/C$)	1/3/2/2	1/3/2/2	1/4/2/2	1/4/3/3	1/4/3/3	1/4/3/3
Applications	Low step-up/high step-down	High step-up/low step-down	High step-up/high step-down	High step-up/high step-down	High step-up/high step-down	High step-up/high step-down

Table 4. Single-switch quadratic topologies derived from the Ćuk converter.

Characteristic	Ćuk/Buck	Ćuk/Boost	Ćuk/Buck–Boost	Ćuk/Ćuk	Ćuk/SEPIC	Ćuk/Zeta
Configuration	I	I	I	I	I	I
Voltage gain	$-\frac{D^2}{1-D}$ (h)	$-\frac{D}{(1-D)^2}$ (g)	$\left(\frac{D}{1-D}\right)^2$ (f)	$\left(\frac{D}{1-D}\right)^2$ (f)	$-\left(\frac{D}{1-D}\right)^2$ (f)	$-\left(\frac{D}{1-D}\right)^2$ (f)
Input current	Non-Pulsating	Non-Pulsating	Non-Pulsating	Non-Pulsating	Non-Pulsating	Non-Pulsating
Output stage current	Non-Pulsating	Pulsating	Pulsating	Non-Pulsating	Pulsating	Non-Pulsating
Switch Additional Stresses	Current	Current	Current	Current	Current	Current
Components ($S/D/L/C$)	1/3/3/3	1/3/3/3	1/4/3/3	1/4/4/4	1/4/4/4	1/4/4/4
Applications	Low step-up/high step-down	High step-up/low step-down	High step-up/high step-down	High step-up/high step-down	High step-up/high step-down	High step-up/high step-down

Table 5. Single-switch quadratic topologies derived from the SEPIC converter.

Characteristic	SEPIC/Buck [47]	SEPIC/Boost	SEPIC/Buck–Boost[46]	SEPIC/Ćuk [48]	SEPIC/SEPIC	SEPIC/Zeta
Configuration	I	I	I	I	I	I
Voltage gain	$\frac{D^2}{1-D}$ (h)	$\frac{D}{(1-D)^2}$ (g)	$\left(\frac{D}{1-D}\right)^2$ (f)	$\left(\frac{D}{1-D}\right)^2$ (f)	$\left(\frac{D}{1-D}\right)^2$ (f)	$\left(\frac{D}{1-D}\right)^2$ (f)
Input current	Non-Pulsating	Non-Pulsating	Non-Pulsating	Non-Pulsating	Non-Pulsating	Non-Pulsating
Output stage current	Non-Pulsating	Pulsating	Pulsating	Non-Pulsating	Pulsating	Non-Pulsating
Switch Additional Stresses	Current	Current	Current	Current	Current	Current
Components ($S/D/L/C$)	1/3/3/3	1/3/3/3	1/4/3/3	1/4/4/4	1/4/4/4	1/4/4/4
Applications	Low step-up/high step-down	High step-up/low step-down	High step-up/high step-down	High step-up/high step-down	High step-up/high step-down	High step-up/high step-down

Table 6. Single-switch quadratic topologies derived from the Zeta converter.

Characteristic	Zeta/Buck [47]	Zeta/Boost	Zeta/Buck–Boost [46]	Zeta/Ćuk [48]	Zeta/SEPIC	Zeta/Zeta
Configuration	IV	IV	IV	IV	IV	IV
Voltage gain	$\frac{D^2}{1-D}$ (h)	$\frac{D}{(1-D)^2}$ (g)	$\left(\frac{D}{1-D}\right)^2$ (f)	$\left(\frac{D}{1-D}\right)^2$ (f)	$\left(\frac{D}{1-D}\right)^2$ (f)	$\left(\frac{D}{1-D}\right)^2$ (f)
Input current	Pulsating	Pulsating	Pulsating	Pulsating	Pulsating	Pulsating
Output stage current	Non-Pulsating	Pulsating	Pulsating	Non-Pulsating	Pulsating	Non-Pulsating
Switch Additional Stresses	Voltage	Voltage	Voltage	Voltage	Voltage	Voltage
Components ($S/D/L/C$)	1/3/3/3	1/3/3/3	1/4/3/3	1/4/4/4	1/4/4/4	1/4/4/4
Applications	Low step-up/high step-down	High step-up/low step-down	High step-up/high step-down	High step-up/high step-down	High step-up/high step-down	High step-up/high step-down

7. Conclusions

This work has presented the properties and synthesis of single-switch quadratic non-isolated DC-DC converters employing the graft scheme. This principle consists of a useful approach for generating novel power converter topologies while numerous arrangements exist. Combining the six basic non-isolated topologies yields 36 structures with distinct characteristics. Of course, not all of them are feasible for practical applications, whereas it is necessary to consider tradeoffs among the voltage gain, stresses on semiconductors, and component count, among other aspects.

Cascaded converters comprising multiple active switches introduce more flexibility into the control system, whereas the switches can operate independently with distinct duty ratios. In turn, significant drawbacks may include the need for isolated gate drivers and the fact that all switches must be turned on simultaneously, thus requiring complex and costly circuits. In turn, one can derive single-switch counterparts from the graft scheme, but at the cost of additional current or voltage stresses on the switch.

The voltage stress across the semiconductor elements is a key issue in either multiple-switch cascaded or single-switch quadratic DC-DC converters. It is worth mentioning that cost increases significantly as the maximum voltage ratings regarding semiconductors also do, consequently implying increased conduction losses and affecting the converter efficiency.

It is reasonable to state that quadratic converters are suitable for applications with moderately wide conversion ranges, where classical single-stage non-isolated DC-DC converters may be inadequate. Furthermore, such topologies may be restricted to low power levels and low input and/or output voltages so that efficiency is not seriously affected by high losses due to high component count and/or additional current and voltage stresses.

Future work includes investigating proper techniques to reduce voltage stresses across semiconductor elements in single-switch quadratic DC-DC converters, as well as application-specific design considerations for such topologies in particular.

Author Contributions: Conceptualization and methodology, F.L.T. and A.S.M.; formal analysis and investigation, F.L.T.; writing—original draft preparation, F.L.T.; writing—review and editing, F.L.T. and T.M.J.C. All authors have read and agreed to the published version of the manuscript.

Funding: This research was funded by the Coordination for the Improvement of Higher Education Personnel (CAPES). The authors would also like to acknowledge the Brazilian National Council for Scientific and Technological Development (CNPq), the Minas Gerais Research Funding Foundation (FAPEMIG), and the National Institute of Science and Technology in Electric Energy (INERGE) for supporting this work.

Institutional Review Board Statement: Not applicable.

Informed Consent Statement: Not applicable.

Data Availability Statement: Data are available upon request from the authors.

Conflicts of Interest: The authors declare no conflicts of interest.

References

1. Sivakumar, S.; Sathik, M.J.; Manoj, P.S.; Sundararajan, G. An assessment on performance of DC–DC converters for renewable energy applications. *Renew. Sustain. Energy Rev.* **2016**, *58*, 1475–1485. [CrossRef]
2. Farajdadian, S.; Hajizadeh, A.; Soltani, M. Recent developments of multiport DC/DC converter topologies, control strategies, and applications: A comparative review and analysis. *Energy Rep.* **2024**, *11*, 1019–1052. [CrossRef]
3. Li, Z.; Cheng, K.W.E.; Hu, J. Modeling of basic DC-DC converters. In Proceedings of the 2017 7th International Conference on Power Electronics Systems and Applications—Smart Mobility, Power Transfer & Security (PESA), Hong Kong, China, 12–14 December 2017; pp. 1–8.
4. Vorperian, V. Simplified analysis of PWM converters using model of PWM switch. Continuous conduction mode. *IEEE Trans. Aerosp. Electron. Syst.* **1990**, *26*, 490–496. [CrossRef]
5. Gitau, M.N.; Adam, G.P.; Masike, L.; Mbukani, M.W.K. Unified approach for synthesis and analysis of non-isolated DC-DC converters. *IEEE Access* **2021**, *9*, 120088–120109. [CrossRef]
6. Tarzamni, H.; Gohari, H.S.; Sabahi, M.; Kyyrä, J. Nonisolated high step-up dc–dc converters: Comparative review and metrics applicability. *IEEE Trans. Power Electron.* **2024**, *39*, 582–625. [CrossRef]
7. Ragonese, E.; Spina, N.; Parisi, A.; Palmisano, G. An experimental comparison of galvanically isolated DC-DC converters: Isolation technology and integration approach. *Electronics* **2021**, *10*, 1186. [CrossRef]

8. Wang, X.; Luo, C.; Zhao, J.; Luo, Z. Optimal selection of bulk capacitors in flyback converter. *Microelectron. Reliab.* **2024**, *153*, 115306. [CrossRef]
9. Abusara, M.A.; Guerrero, J.M.; Sharkh, S.M. Line-interactive UPS for microgrids. *IEEE Trans. Ind. Electron.* **2014**, *61*, 1292–1300. [CrossRef]
10. Niu, J.; Tang, Y. A family of single-switch wide-gain converters with low voltage stress. *Energy Rep.* **2023**, *9*, 1032–1041. [CrossRef]
11. Middlebrook, R.D. Transformerless DC-to-DC converters with large conversion ratios. *IEEE Trans. Power Electron.* **1988**, *3*, 484–488. [CrossRef]
12. Maksimovic, D.; Cuk, S. Switching converters with wide DC conversion range. *IEEE Trans. Power Electron.* **1991**, *6*, 151–157. [CrossRef]
13. Wu, T.; Yu, T.; Chang, Y. Generation of power converter with graft technique. In Proceedings of the 15th Symposium Electrical Power Engineering, Liège, Belgium, 15 November 1995; pp. 370–376.
14. Espinoza-Trejo, D.R.; Castro, L.M.; Bárcenas, E.; Sánchez, J.P. Data-driven switch fault diagnosis for dc/dc boost converters in photovoltaic applications. *IEEE Trans. Ind. Electron.* **2024**, *71*, 1631–1640. [CrossRef]
15. Forouzesh, M.; Siwakoti, Y.P.; Gorji, S.A.; Blaabjerg, F.; Lehman, B. Step-up dc–dc converters: A comprehensive review of voltage-boosting techniques, topologies, and applications. *IEEE Trans. Power Electron.* **2017**, *32*, 9143–9178. [CrossRef]
16. Liu, Q.; Qian, Q.; Shi, L.; Xu, Q.; Ding, S.; Sun, W. An improved buck converter with high frequency and high step-down ratio for auxiliary power supply applications. *IET Power Electron.* **2023**, *16*, 2638–2649. [CrossRef]
17. Farooq, A.; Malik, Z.; Sun, Z.; Chen, G. A review of non-isolated high step-down DC-DC converters. *Int. J. Smart Home* **2015**, *9*, 133–150. [CrossRef]
18. Izadi, M.; Mosallanejad, A.; Lahooti Eshkevari, A. A non-isolated quadratic boost converter with improved gain, high efficiency, and continuous input current. *IET Power Electron.* **2023**, *16*, 193–208. [CrossRef]
19. Li, G.; Amirabadi, M.; Chen, X.; Lehman, B. The methodology of constructing the quadratic converters. *IEEE J. Emerg. Sel. Top. Power Electron.* **2022**, *10*, 6586–6606. [CrossRef]
20. Panigrahi, R.; Mishra, S.K.; Joshi, A.; Ngo, K.D.T. Synthesis of DC–DC converters from voltage conversion ratio and prescribed requirements. *IEEE Trans. Power Electron.* **2021**, *36*, 13889–13902. [CrossRef]
21. Panigrahi, R.; Mishra, S.K.; Joshi, A.; Ngo, K.D.T. DC-DC converter synthesis: An inverse problem. *IEEE Trans. Power Electron.* **2020**, *35*, 12633–12638. [CrossRef]
22. Nag, S.S.; Panigrahi, R.; Mishra, S.K.; Joshi, A.; Ngo, K.D.T.; Mandal, S. A theory to synthesize nonisolated DC–DC converters using flux balance principle. *IEEE Trans. Power Electron.* **2019**, *34*, 10910–10924. [CrossRef]
23. Gorji, S.A. Reconfigurable quadratic converters for electrolyzers utilized in DC microgrids. *IEEE Access* **2022**, *10*, 109677–109687. [CrossRef]
24. Pires, V.F.; Foito, D.; Cordeiro, A. A DC–DC converter with quadratic gain and bidirectional capability for batteries/supercapacitors. *IEEE Trans. Ind. Appl.* **2018**, *54*, 274–285. [CrossRef]
25. Hosseini, S.H.; Ghazi, R.; Heydari-Doostabad, H. An extendable quadratic bidirectional DC–DC converter for V2G and G2V applications. *IEEE Trans. Ind. Electron.* **2021**, *68*, 4859–4869. [CrossRef]
26. Inoue, S.; Ishigaki, M.; Takahashi, A.; Sugiyama, T. Design of an isolated bidirectional DC–DC converter with built-in filters for high power density. *IEEE Trans. Power Electron.* **2021**, *36*, 739–750. [CrossRef]
27. Wu, T.-F.; Chen, Y.-K. *Origin of Power Converters: Decoding, Synthesizing, and Modeling*; John Wiley & Sons: Hoboken, NJ, USA, 2020.
28. Leal, W.C.; Godinho, M.O.; Bastos, R.F.; Aguiar, C.R.d.; Fuzato, G.H.F.; Machado, R.Q. Cascaded interleaved DC–DC converter for a bidirectional electric vehicle charging station. *IEEE Trans. Ind. Electron.* **2024**, *71*, 3708–3717. [CrossRef]
29. Masike, L.; Gitau, M.N. A modular circuit synthesis oriented modelling approach for non-isolated DC-DC converters in CCM. *Energies* **2023**, *16*, 1047. [CrossRef]
30. Kumari, R.; Pandit, M.; Sherpa, K.S. A comprehensive study on evolution and advancement of DC–DC cascaded converters: A review. *Aust. J. Electr. Electron. Eng.* **2022**, *19*, 40–55. [CrossRef]
31. Tsai-Fu, W.; Yu-Kai, C. A systematic and unified approach to modeling PWM DC/DC converters based on the graft scheme. *IEEE Trans. Ind. Electron.* **1998**, *45*, 88–98. [CrossRef]
32. Tsai-Fu, W.; Yu-Kai, C. An alternative approach to systematically modeling PWM DC/DC converters in DCM based on the graft scheme. In Proceedings of the PESC97. Record 28th Annual IEEE Power Electronics Specialists Conference. Formerly Power Conditioning Specialists Conference 1970–71. Power Processing and Electronic Specialists Conference 1972, St. Louis, MO, USA, 27–27 June 1997; Volume 1, pp. 453–459.
33. Kumar, A.D.; Gupta, J.; Singh, B. A single-stage charger for lev based on quadratic buck-boost AC-DC converter topology. *IEEE Trans. Ind. Appl.* **2023**, *59*, 4252–4263. [CrossRef]
34. Bassan, S.; Moschopoulos, G. Properties and applications of quadratic converters. In Proceedings of the 2007 IEEE Canada Electrical Power Conference, Montreal, QC, Canada, 25–26 October 2007; pp. 123–127.
35. Wijeratne, D.S.; Moschopoulos, G. Quadratic power conversion for power electronics: Principles and circuits. *IEEE Trans. Circuits Syst. I Regul. Pap.* **2012**, *59*, 426–438. [CrossRef]
36. Morales-Saldana, J.A.; Leyva-Ramos, J.; Carbajal-Gutierrez, E.E.; Ortiz-Lopez, M.G. Average current-mode control scheme for a quadratic buck converter with a single switch. *IEEE Trans. Power Electron.* **2008**, *23*, 485–490. [CrossRef]

37. Birca-Galateanu, S. Triple step-down DC-DC converters. In Proceedings of the PESC Record. 27th Annual IEEE Power Electronics Specialists Conference, Baveno, Italy, 23–27 June 1996; Volume 1, pp. 408–413.
38. Alonso, J.M.; Viña, J.; Gacio, D.; Campa, L.; Martínez, G.; Osorio, R. Analysis and design of the quadratic buck-boost converter as a high-power-factor driver for power-LED lamps. In Proceedings of the IECON 2010—36th Annual Conference on IEEE Industrial Electronics Society, Glendale, AZ, USA, 7–10 November 2010; pp. 2541–2546.
39. Botila, D.A.; Pop-Calimanu, I.M.; Lascu, D. Cubic buck-boost converter with high step-up capability. In Proceedings of the 2022 International Symposium on Electronics and Telecommunications (ISETC), Timisoara, Romania, 10–11 November 2022; pp. 1–4.
40. Cuk, S.; Middlebrook, R. A new optimum topology switching DC-to-DC converter. In *Proceedings of the 1977 IEEE Power Electronics Specialists Conference, Palo Alto, CA, USA, 14–16 June 1977*; IEEE: Piscataway, NJ, USA, 1977; pp. 160–179.
41. Massey, R.; Snyder, E. High voltage single-ended DC-DC converter. In *Proceedings of the 1977 IEEE Power Electronics Specialists Conference, Glendale, AZ, USA, 14–16 June 1977*; IEEE: Piscataway, NJ, USA, 1977; pp. 156–159.
42. Jozwik, J.J.; Kazimierczuk, M.K. Dual sepic PWM switching-mode DC/DC power converter. *IEEE Trans. Ind. Electron.* **1989**, *36*, 64–70. [CrossRef]
43. Oliveira, T.M.; Ribeiro, E.R.; de Morais, A.S.; Tofoli, F.L. Non-isolated high step-up/step-down DC–DC quadratic Ćuk converter. *Int. Trans. Electr. Energy Syst.* **2021**, *31*, e13173. [CrossRef]
44. Corrêa, D.R.; de Morais, A.S.; Tofoli, F.L. Non-isolated high step-up/step-down quadratic converter for light-emitting diode driving. *Int. J. Circuit Theory Appl.* **2021**, *49*, 2699–2718. [CrossRef]
45. Chen, Y.K.; Chen, H.Y.; Song, C.C.; Chen, W.Z. Design and implementation of novel single-stage high voltage electrostatic generator for agricultural plant protection machine. In Proceedings of the 2023 International Technical Conference on Circuits/Systems, Computers, and Communications (ITC-CSCC), Jeju, Republic of Korea, 25–28 June 2023; pp. 1–6.
46. Almeida, P.S.; Soares, G.M.; Pinto, D.P.; Braga, H.A. Integrated SEPIC buck-boost converter as an off-line LED driver without electrolytic capacitors. In *Proceedings of the IECON 2012—38th Annual Conference on IEEE Industrial Electronics Society, Montreal, QC, Canada, 25–28 October 2012*; IEEE: Piscataway, NJ, USA, 2012; pp. 4551–4556.
47. Cosetin, M.; Bitencourt, E.; Bolzan, T.; Silva, M.; Alonso, J.; do Prado, R. Comparison of single stage SEPIC and integrated SEPIC-Buck converter as off-line LED drivers. In *Proceedings of the 2013 Brazilian Power Electronics Conference, Gramado, Brazil, 27–31 October 2013*; IEEE: Piscataway, NJ, USA, 2013; pp. 1134–1139.
48. Cosetin, M.; Bolzan, T.; Luz, P.; da Silva, M.; Alonso, J.M.; do Prado, R.N. Dimmable single-stage SEPIC-Ćuk converter for LED lighting with reduced storage capacitor. In *Proceedings of the 2014 IEEE Industry Application Society Annual Meeting, Vancouver, BC, Canada, 5–9 October 2014*; IEEE: Piscataway, NJ, USA, 2014; pp. 1–7.
49. Miranda, L.C.; Sanhueza, R.; López, G.; Fingerhuth, S.; Mussa, S.A.; Ruiz-Caballero, D. High-gain symmetrical hybrid multilevel DC-AC converters—Single phase circuits. In *Proceedings of the 2013 Brazilian Power Electronics Conference, Gramado, Brazil, 27–31 October 2013*; IEEE: Piscataway, NJ, USA, 2013; pp. 161–168.
50. Subhani, N.; May, Z.; Alam, M.K.; Khan, I.; Hossain, M.A.; Mamun, S. An improved non-isolated quadratic DC-DC boost converter with ultra high gain ability. *IEEE Access* **2023**, *11*, 11350–11363. [CrossRef]

energies

MDPI

Review

Wireless Power Transfer for Unmanned Underwater Vehicles: Technologies, Challenges and Applications

Iñigo Martínez de Alegría [1,*], Iñigo Rozas Holgado [1,*], Edorta Ibarra [1], Eider Robles [2] and José Luís Martín [1]

[1] Applied Electronics Research Team (APERT), University of the Basque Country (UPV/EHU), 48013 Bilbao, Spain; edorta.ibarra@ehu.eus (E.I.); joseluis.martin@ehu.eus (J.L.M.)

[2] Tecnalia, Basque Research and Technology Alliance (BRTA), Parque Tecnológico de Bizkaia Astondo Bidea, 48160 Derio, Spain; eider.robles@tecnalia.com

* Correspondence: inigo.martinezdealegria@ehu.eus (I.M.d.A.); inigo.rozas@ehu.eus (I.R.H.)

Abstract: Unmanned underwater vehicles (UUVs) are key technologies to conduct preventive inspection and maintenance tasks in offshore renewable energy plants. Making such vehicles autonomous would lead to benefits such as improved availability, cost reduction and carbon emission minimization. However, some technological aspects, including the powering of these devices, remain with a long way to go. In this context, underwater wireless power transfer (UWPT) solutions have potential to overcome UUV powering drawbacks. Considering the relevance of this topic for offshore renewable plants, this work aims to provide a comprehensive summary of the state of the art regarding UPWT technologies. A technology intelligence study is conducted by means of a bibliographical survey. Regarding underwater wireless power transfer, the main methods are reviewed, and it is concluded that inductive wireless power transfer (IWPT) technologies have the most potential. These inductive systems are described, and their challenges in underwater environments are presented. A review of the underwater IWPT experiments and applications is conducted, and innovative solutions are listed. Achieving efficient and reliable UWPT technologies is not trivial, but significant progress is identified. Generally, the latest solutions exhibit efficiencies between 88% and 93% in laboratory settings, with power ratings reaching up to 1–3 kW. Based on the assessment, a power transfer within the range of 1 kW appears to be feasible and may be sufficient to operate small UUVs. However, work-class UUVs require at least a tenfold power increase. Thus, although UPWT has advanced significantly, further research is required to industrially establish these technologies.

Keywords: autonomous underwater vehicles; inductive wireless power transfer; underwater docking stations; underwater wireless power transfer; unmanned underwater vehicles

1. Introduction

According to the latest data available from the International Energy Agency (IEA), the electricity generation from marine sources increased by 400 GWh (+33%) between 2019 and 2020 [1]. However, these technologies need to be implemented much faster in order to achieve Net Zero emissions by the 2050 scenario [2]. Among them, offshore wind turbines (OWT) are the most mature technology, with many power plants commercially deployed around the world [3–5], while other technologies based on tidal, current or wave energy are promisingly being studied and tested [6–8].

All these marine technologies operate in extremely harsh conditions. In particular, they suffer from corrosion issues generated by salt water. For example, a number of critical elements such as blades, gearboxes, generators, power electronics and towers' mechanical structures are affected by corrosion in OWTs, especially their fixed or floating underwater foundations [9]. Thus, a number of maintenance actions (preventive and corrective) need to be constantly carried out for all the critical elements that make up OWTs [9]. Offshore renewable energy platforms require research in innovative solutions to improve their operation and maintenance to make them cost-effective [10].

Unmanned underwater vehicles (UUVs) such as remotely operated vehicles (ROVs) and autonomous underwater vehicles (AUVs) are very important tools for the visual inspection and maintenance of such offshore infrastructures. UUVs are starting to be broadly deployed in the ocean. They have potential in the operation and maintenance of marine energy plants [11,12] and also in other applications such as marine data collection [13,14], ocean observation [15–17] or aquaculture [18,19]. In general, maneuverability is a key requirement for underwater inspection tasks, and the utilization of drones with multiple propeller configurations, similar to aerial drones, is preferred [20–22]. In contrast, gliders are generally preferred for collecting data over large oceanic areas [23–25].

At the moment, mainly ROV technologies are used for underwater inspection. However, the utilization of AUV platforms is starting to be considered by the maritime industry for a number of reasons [9,26–28]:

(a) ROVs need to be operated on site. Usually, the distances between offshore wind parks and the nearest ports are significantly long. The time required for technicians to reach a given offshore park can be significant.
(b) Many times, the extreme marine weather makes it difficult for the technicians to reach offshore parks.
(c) The on site operation of ROVs is expensive, especially considering the ships and personnel involved.
(d) Operating in offshore power plants can be dangerous for technicians. According to the recent data provided in the scientific literature, work accidents are common in such marine environments. For instance, in year 2019, 865 work accidents were reported in offshore wind farms worldwide.

Due to the future widespread adoption of autonomous solutions, the time frame that technicians will need to expend in offshore parks can be significantly minimized, with all of its associated benefits. In addition to minimizing the aforementioned issues, greenhouse gas emissions can also be reduced, as the number of boat trips is minimized [28]. The first industrial example of an OWT park inspected by AUVs, which was implemented in 2022, can be found in the north coast of the United Kingdom [28].

Although this kind of technology (both remotely operated or autonomous) is very promising for marine infrastructure maintenance duties, there is still a long way to go regarding some technological aspects. For example, and in particular, electrical powering for UUVs is generally delivered via two main techniques:

1. Direct connection to a land-based or ship-based electrical energy source (grid, ship electrical system, batteries, etc.) using submarine cables (tethered systems).
2. Providing UUVs with their own batteries, which must be extracted for recharging.

Both types of powering limit the operative range and operational time of UUVs. Additionally, they require continuous supervision, leading to the aforementioned drawbacks generated when deploying technicians offshore. Thus, UUVs would benefit from the availability of underwater charging, which would increase their autonomy, both in range and in time. There is potential for underwater wireless power transfer (UWPT) to assist in achieving this goal and reduce the drawbacks and costs of UUV operation. This can create new market niches around UWPT technologies, from which marine energy infrastructures can benefit. Considering the potential relevance of charging technologies for future marine-based renewable systems, this article focuses on the state of the art in UWPT.

This manuscript is organized as follows. Section 2 introduces the standard methods for delivering power to UUVs. In Section 3, the main research areas for delivering wireless power to UUVs are described. Section 4 introduces a more detailed insight into inductive wireless power transfer (IWPT) methods, which seem to be the more promising and ready technologies for underwater charging. In Section 5, a comprehensive review of the main IWPT experiments and applications available in the literature is conducted. Section 6 summarizes the main conclusions of the study. Finally, Appendix A describes the study conducted to characterize the main technologies used for UWPT, the existing patents and the corpus of the bibliography used for the study.

2. Conventional UUV Powering Methods

Several methods for powering underwater devices are mentioned in the literature, mainly for powering ROVs and AUVs. Traditional methods such as battery swapping or direct connection using tethers are most commonly used. However, as advanced at the introduction of the manuscript, tethered systems limit the operational range of UUVs, and battery swapping is very time consuming and has very high operational costs [29]. In addition, both systems require a surface vessel, which has very high operational costs.

In recent years, other approaches have been considered, such as the use of devices powered by renewable energies and wireless power transfer in submerged dock facilities, which could reduce the previous shortcomings. These would enable the deployment of low cost AUVs, which would considerably reduce overall operation costs.

2.1. Battery Swapping

Battery swapping is one of the most common methods to supply power to UUVs. By this method, the device is resurfaced and the battery is retired for charging or directly replaced. Each operation is time-consuming and requires a vessel and manpower [30]. Additionally, during the installation and maintenance of OWTs, the vessels emit approximately 28% of the total greenhouse gas and produce significant amounts of pollutants [31].

Some efforts are being carried to try to reduce these drawbacks, such as changing the fuel used by vessels to reduce their emissions [31] or reducing mission duration with innovative battery swapping methods with modular batteries [32]. However, other options may avoid these issues.

2.2. Tether Management Systems

Tether management systems (TMS) are generally used to operate ROVs [33]. In TMS, umbilicals are used to connect the ROV to a control unit, which usually is placed on a vessel. The cable generally provides transmission of bidirectional data in real time and energy to the vehicle and allows the vehicle to be maneuvered in a controlled manner [34]. However, in deep-water applications, the operation is more complex, and tethered systems are very costly [35].

Similar to battery swapping, TMS require a vessel or a sea platform to connect the umbilical and skilled personnel to control the operation of the ROV. To increase the autonomy of these systems, self-managed umbilicals [34] have been recently proposed. Additionally, replacing the vessel with an autonomous surface vehicle connected to the tethered ROV is another interesting proposal [36]. Figure 1a shows an example of the Hercules ROV working while connected to an umbilical cable.

2.3. Renewable Energy Powered UUVs

Renewable energy sources can be harnessed to provide energy to UUVs, thereby increasing their available operational time. The main proposal, which mainly applies to underwater vehicles and buoys, is the use of solar energy. Solar panels are installed in the devices, which have to surface during daytime to harvest and store energy in their batteries [37].

An example of a solar AUV prototype developed by The Autonomous Undersea Systems Institute AUSI, Falmouth Scientific Inc. (FSI), is the SAUV-II (Figure 1c). It is designed for long-term missions that require monitoring, surveillance or station maintenance [38]. The maximum power of the device is 170 W, and the energy is stored in a lithium battery. It can submerge for up to 12 h and reaches a maximum depth of 500 m [39].

Wave energy systems integrated in AUV devices are also a feasible alternative that could allow autonomous operation in some geographic regions that present suitable wave characteristics [40]. In addition to this, other sources such as thermal and salinity gradients have been recently proposed but are still in a very early stage and generate a very limited amount of energy [41].

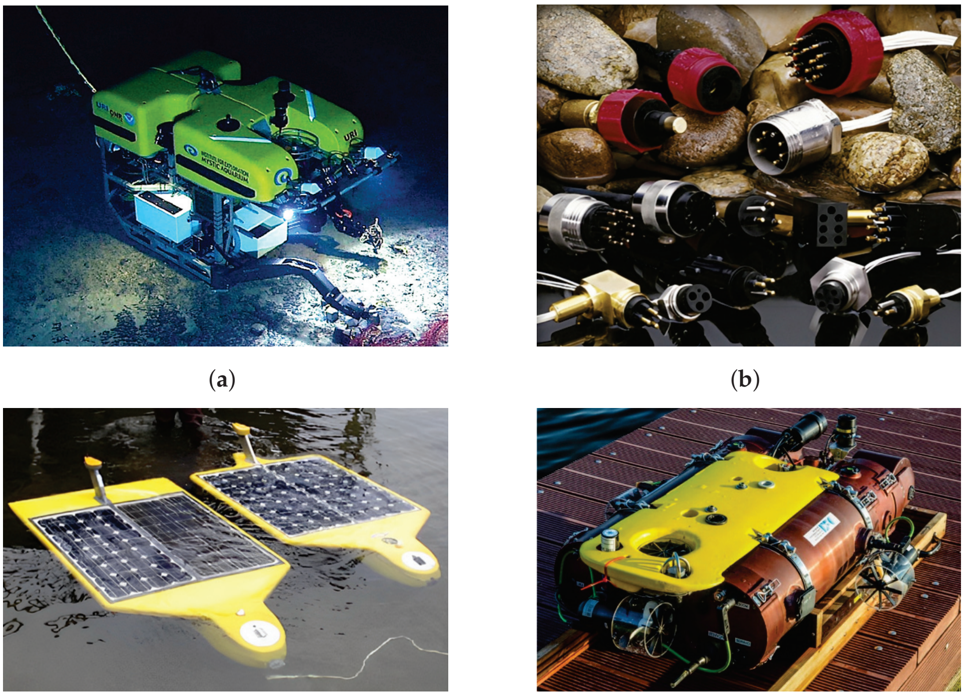

(**a**) (**b**) (**c**) (**d**)

Figure 1. Conventional UUV powering methods. (**a**) Hercules tethered ROV [42]. (**b**) Examples of underwater connectors [43]. (**c**) Solar-powered AUV II (SAUV-II) [44]. (**d**) DAGON hoovering AUV [45].

2.4. Wet-Mate Connectors

Underwater wet-mate connectors (example in Figure 1b) are also used to transfer power to UUVs at underwater docking stations. These connectors are a reliable and efficient method for transferring power to UUVs, and are more established than UWPT. However, these are complex to manufacture and operate, leading to higher costs and maintenance requirements [46], and are susceptible to corrosion [47].

An early example of docking stations that utilize these type of connectors is the Eurodocker docking platform [48]. This station was designed as a funnel-type garage, also providing protection to the AUV, charging the device through wet-mate connectors. A similar concept was developed and tested for the REMUS-100 AUV [49]. The dock was designed to operate with external power or from batteries to charge the AUV through underwater electrical wet-mate connectors. Some successful docking runs were conducted in 2005, with docking connections followed by battery recharges. More recently, the Dagon hovering AUV prototype (Figure 1d) was tested in Germany [50]. In this case, the AUV performed a step-by-step alignment with the docking platform with the help of V-shaped guiding structures. The energy transfer was conducted through an underwater-pluggable connector with a power of 210 W.

3. Underwater Wireless Power Transfer

Securely mating wet-mate connectors is challenging and requires high precision [37]. As an alternative, several wireless power transfer methods have been proposed. One of the earliest underwater "contact-less" experiments that can be found in the literature is presented by Kojiya et al. [51]. The proposed system used electromagnetic induction to transfer power wirelessly to safely charge the AUV. These methods can be classified in the following categories:

(i) Far-field methods: Radio frequency waves, optical link and ultrasonic waves.
(ii) Near-field methods: through-wall acoustic waves, capacitive and inductive wireless power transfer.

All these aforementioned alternatives have a transmitter device (Tx) and a receiver (Rx), and they use different methods to transfer power. This section reviews the main methods found in the bibliographical survey (Figure 2).

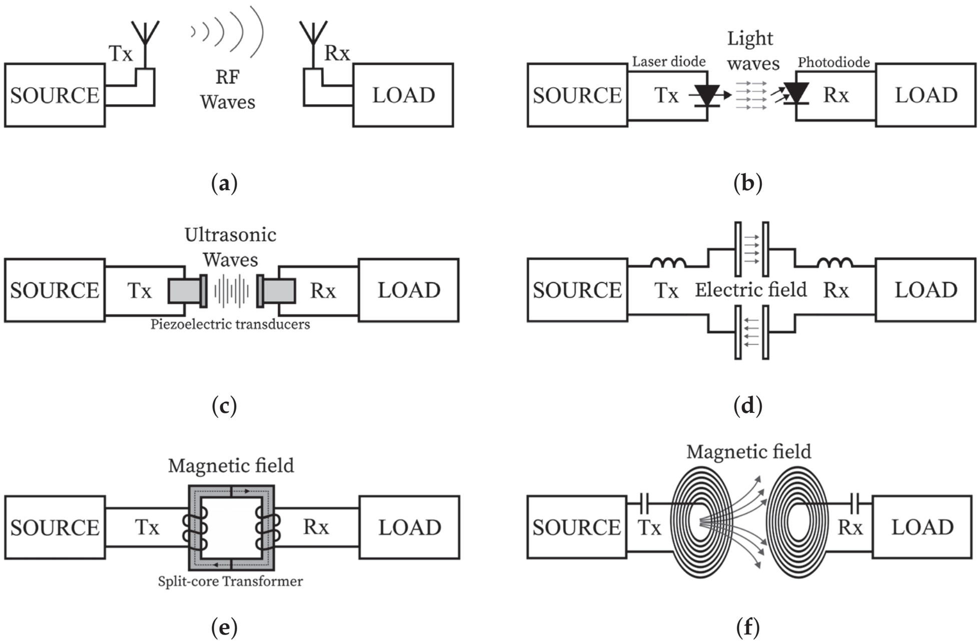

Figure 2. Main wireless power transfer methods [52]. (**a**) Radio-frequency waves. (**b**) Optical link. (**c**) Ultrasonic waves. (**d**) Capacitive. (**e**) Tightly coupled inductive. (**f**) Loosely coupled inductive.

3.1. Radio Frequency Waves

Although radio frequency waves are the most common way to transmit data by air and they have been proposed for contactless long distance power transfer, this is generally not suitable as a charging method. The emitting and receiving antennas operate by the interaction of electromagnetic induction, which is determined by Maxwell's equations [52]. In deep-sea water, radio frequency data communication may have some advantages compared to optical or acoustic transmission, according to [53]. Nonetheless, it is not applicable to submarine electrical power transfer due to an increased attenuation of electromagnetic (EM) waves in seawater. Methods that utilize near-field EM waves are far more suitable.

3.2. Optical Link

Optical links use light to transfer energy between transmitters and receivers. Receivers are light sensitive devices such as solar cells, photo-diodes, or photovoltaic converters, and emitters can be sun or laser powered diodes [52]. These can operate devices and recharge batteries via laser diodes or power remote systems [54]. However, their application is mostly for low power systems that are far from the transmitter. Several applications of this power transfer scheme are reviewed in [55].

Regarding underwater optical link transmission, very few experiments can be found in the literature [56–58]. All of these could achieve power transfers in the mW range, with a power transfer efficiency below 20% for distances over 1 m. Regarding data transfer, in [57], the authors achieved data rates up to 60 Mbps at the receiver side, at a distance of 2.3 m from the emitter. Thus, optical links are not suitable for contactless charging in AUVs due to the low power ratings. However, auxiliary applications such as docking positioning or data transfer could be feasible with this technology.

3.3. Ultrasonic and "Through-Metal Wall" Waves

Acoustic or ultrasonic wireless power transfer technologies use ultrasonic waves that exceed the human hearing limit of 20 kHz to transfer power [52]. It is considered safe, as it uses sound as a propagation medium, making it a suitable option in medical applications. It has been used for low-power data transmission, remote sensing and navigation systems and biomedical implants [59]. A summary of the state of the art for this power transfer method, including data until 2016, can be found in Awal et al. [60].

Regarding underwater applications, very few examples exist in the literature [61–64]. Similarly to optical links, these systems work in the mW range with very low efficiency. For example, in [64] authors tested an experimental prototype applied to the underwater internet of things that had a power transfer efficiency of 4% to 10% for 0.1 W to 1.4 W and 1 m distance. Another experiment yielded results of 20% efficiency at a distance of 10 cm using a modified transducer [63]. These power levels are not enough to charge UUVs.

An alternative that could be suitable for this application is the "through-metal wall" power transfer. It is a near-field application of ultrasonic waves that uses piezoelectric transducers attached to two metal surfaces that are in contact to transfer and receive ultrasonic waves and convert them to electric power [65]. It can be used to transfer power through metal walls such as vehicle armors or sensors within metallic enclosures [66,67]. Most of the applications are in the mW range, as reviewed by Awal et al. [60] and presented in later works such as [68]. However, power transfers in the 1 W range have also been achieved in some studies.

A remarkable example of this technology was presented in 2008 by Sherrit et al. [69] from NASA's Jet Propulsion Laboratory. They designed a 1 kW device that could transfer power with 88% efficiency through a 3.4 mm thick metal wall. Another promising application was also proposed in [70]. The authors were able to simultaneous transfer data and power at 17.37 Mbps and 50 W, respectively, with a power transfer efficiency of 51% through a thicker steel wall of 63.5 mm. Nevertheless, experiments in a seawater environment are required to validate these results.

3.4. Capacitive Wireless Power Transfer

In capacitive wireless power transfer (CWPT), power is transmitted by using a time-varying electric field, using metallic plates on the transmitters and with the receivers working as the two parallel plates of a capacitor. The transfer distance of this system is low and allows the transfer through isolated metal objects.

CWPT has been applied for low-power data transmission in applications such as biomedical implants [71], robots [72] or USB charging [73], among others [74,75]. Higher power applications such as railway applications [76] and the powering of electrical vehicles [77,78] are being recently studied. In the context of railway applications, a 3 kW power transfer system prototype was tested at a distance of 40 mm, yielding an efficiency of 92.5% [76]. The recent designs of large-gap CPT systems intended for EV charging applications are summarized in [79], with distances ranging from 17 mm to 170 mm, power ratings between 0.1 kW and 2.6 kW and efficiencies ranging from 70% up to 92%.

In the field of underwater energy transfer, some CWPT models and prototypes have already been tested in academic studies [80–93]. In most of these works, CWPT systems achieved a power transfer efficiency beneath 70% in seawater environments. However, there are some recent works where this value could be surpassed.

In 2018, Ref. [84] proposed a design method for capacitive couples for fresh water operation. After modeling the system, they constructed a prototype and achieved a power transfer of 400 W with an efficiency of 91.3% for 50 MHz at a transfer distance of 20 mm. Authors also carried out tests for other gaps and frequency values, achieving an efficiency of 80.77% for a 50 mm gap and the same power and frequency values. However, all these tests were conducted in fresh water, and the efficiency in ionized sea water should be tested.

Other works by Tamura et al. [87] present efficiency values up to 91.1% underwater for a CWPT coupler utilizing an electric double layer. By applying this model, they later built a system that could maintain a maximum efficiency of 79% in a seawater environment at 2 MHz [90].

More recently, in a paper by Mahdi et al. [92], authors studied the maximum power capability of a CWPT system by using network theory to then experimentally test it with a prototype in seawater. They were able to achieve an efficiency of 83% for a 100 mm gap and 300 kHz. When the frequency was increased from 300 kHz to 1 MHz, and the separation distance was changed from 100 mm to 300 mm, the power transfer and efficiency decreased.

It is important to remark that CWPT prototypes tested within UUV devices have not been found in the literature. Thus, further research is required to validate its feasibility.

3.5. Inductive Wireless Power Transfer

Inductive wireless power transfer is based on the wireless transfer of power between two coupled coils using a time-varying magnetic field [94]. Depending on the coupling coefficient k between the coils, the system can be loosely or tightly coupled [52]. The system can operate in resonance to achieve higher efficiency. When the distance between coils is constant, the system is considered static, while, if the distance changes, it is considered a dynamic system [95]. IWPT is currently used in consumer electronics, biomedical equipment and vehicle charging. Static IWPT applied to consumer electronics is already a mature technology with commercial standards such as the Alliance for Wireless Power (A4WP) standard, the Qi standard from the Wireless Power Consortium (WPC) and the Power Matter Alliance (PMA) standard [96,97]. The research is underway to improve standardized charging systems [98,99] and design universal charging systems [97,100,101].

In biomedical micro-systems, this technology has been used in endoscopic capsules [102], pacemakers [103], biomedical implants [104] and brain–machine interfaces, among others [105–107]. WPT allows the traditional use of percutaneous cables and implantable batteries to be replaced by rechargeable batteries, reducing the need for surgery and improving system features [105].

For electric vehicles, IWPT is promisingly being studied [108,109], and few commercial products already exist [110]. Two main charging systems are the dominant: the static wireless electric vehicle charging system (S-WEVCS) [111] and the dynamic electric vehicle charging system (D-WEVCS) [112,113]. While static systems function only when the vehicle is stopped and the charger is correctly aligned, dynamic systems are based on a driving path with several coils and a receiver coil in the vehicle [108,114]. In the electric vehicle IWPT charging sector, interoperability and standardization have recently gained significant importance. Standards such as SAE-J2954 [115] have already been published, and certain magnetic couplers have the potential to allow interoperability [116,117]. However, further research is needed in the field of interoperable IWPT systems.

Regarding near-shore applications, IWPT systems have already been tested to be suitable for ship charging. For instance, in [118], the authors were able to conduct laboratory tests with a power transfer of approximately 1 MW for a ship charging application, with its subsequent installation on the Norwegian ferry MS Folgefonn. In the marine environment, many inductive charger prototypes have been tested for underwater recharging of AUVs [119–129] and underwater sensors [130–137]. These charging devices are generally installed in sub-sea docking stations. A sub-sea docking station is a platform that allows underwater power and data transfer for UUVs. It can be directly supported at the seabed, from a ship, or from a buoyed mooring system, or even use their own renewable energy generation.

Apart from transferring power through underwater wet-mate connectors, modern docking stations usually transfer power through wireless power systems, which need to be able to hold the device firmly. These platforms generally have a “landing-type” structure (Figure 3a) or a “funnel-type” structure (Figure 3b). When used for AUV recharging, docking platforms and devices require navigation systems for homing [37] and can use different methods for docking, such as capture, platform or dynamic docking [47].

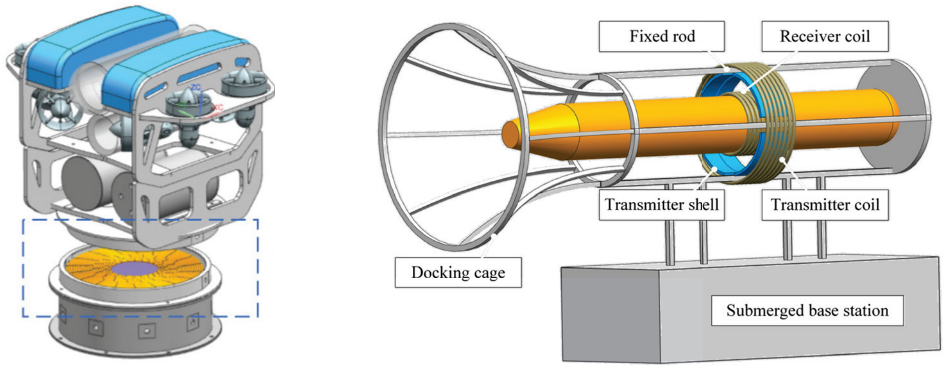

(**a**) (**b**)

Figure 3. Main UUV docking stations. (**a**) Landing-type UWPT station [138]. (**b**) Funnel-type UWPT station [139].

4. Underwater IWPT Technology

As IWPT seems to be the most promising technology for UUV underwater contactless charging, a introductory chapter on this topic is herein presented.

4.1. IWPT System Components

Underwater IWPT systems are generally divided into two separated devices: the docking station and the UUV. The docking station contains the charger, which is formed by the power source, the input power converter, the transmitter resonant tank and the primary side of the coil. On the other side, the UUV contains the secondary coil, the receiver resonant tank, the output power converter and the battery. The block diagram of a two-coil IWPT is depicted in Figure 4. In the following, key aspects about the constituting elements are provided:

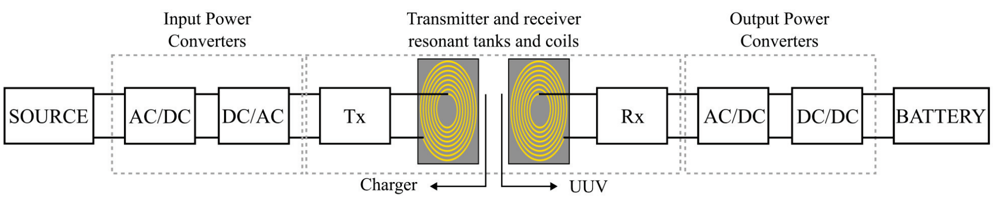

Figure 4. Block diagram of a two-coil IWPT system.

(a) **Input power converters.** Their function is to generate a high frequency AC waveform from the available power source. Depending on the source, power is supplied by an AC/DC or a DC/DC converter to a main DC bus. A full bridge single phase inverter to convert the DC voltage into a high frequency square wave AC voltage waveform is the most extended option [105].

(b) **Transmitter and receiver resonant tanks and coils.** This is the main topic of research and development for IWPT systems. The compensation is essential to cause the coil to resonate at the desired frequency. This is accomplished using different resonant tanks. In order to maximize the efficiency and power capacity of the IWPT system, different coupling structures can be used between the power source and the power receiver or load. The resonant compensation topologies in IWPT can be classified according to the number of compensating capacitors and inductors, their configuration and the type of sources [140]. Generally, four main topologies are used, which, regarding compensating capacitors in the primary and secondary, are series–series (S-S), series–parallel (S-P), parallel–parallel (P-P) and parallel–series (P-S). More complex topologies based on LCC resonant converters such as LCC-S [141,142], LCC-P [143,144], LCC-LCC [145–147] or multi-resonance circuits [147,148] have also been tested in the literature. Using non-resonant (N) IWPT is also possible for low distance and low power transfer with similar efficiency [149]. However, if the transmitting distance and power are increased, resonant IWPT is recommended for optimal power transfer. Thus, resonant IWPT is selected over non-resonant for most applications, including UWPT. The coils consist of various components, usually including copper wire and magnetic cores. These are based on the idea of transformers but with the core split into two parts. These cores are used to shape the path of the magnetic flux and increase inductance, improving the coupling between coils. Metal shields can also be added to reduce electromagnetic interferences and high-frequency magnetic fields [52], which are a source of losses.

(c) **Output power converters.** The function of output converters is to receive and provide stable power to the load or battery. They also can provide feedback information to the transmitter for power regulation according to the load. These are composed of a tuning circuit, power converters and a control unit. The rectifier is the main component in the Rx unit and determines its efficiency. In the output, by connecting batteries or loads to DC/DC converters, stable and regulated power can be provided [105].

(d) **Controller units.** IWPT requires controller units to adjust the output voltage or current in response to load variations during battery charging to maintain efficiency. In electric vehicle charging, three main approaches are employed to manage these variations: transmitter control, receiver control and dual control [108]. Transmitter control and dual control require feedback between the Tx and Rx side, while receiver control utilizes active AC/DC and DC/DC converters to regulate the device from the receiver side. Generally, transmitter control is a more robust option, involving adjustment of the inverter frequency based on feedback from the output. However, in seawater, data sharing between the receiver and transmitter may present challenges, and receiver control or other alternatives may be more suitable [29]. This enables closed-loop control.

4.2. Challenges in Underwater Environments

IWPT has the same structure in water as it has in air. However, it presents some challenges, which are reviewed in this subsection.

4.2.1. Attenuation of Magnetic Fields

The resistance of a coil is the sum of its DC (R_{DC}), AC (R_{AC}) and radiation resistances (R_{RAD}). R_{DC} and R_{AC} depends on its configuration, type of wire and topology. Radiation resistance depends on the permeability and conductivity of the medium and the working frequency of the coils [150]. In air, losses are generally dominated by AC, while R_{RAD} is negligible. However, as seawater is conductive (3–6 S/m), it has to be taken into account.

Several studies have already demonstrated that the radiating losses increase when the operating frequency is increased [151–155], as shown in Figure 5 from [153]. Niu et al. [156], Yan et al. [157] and Zhang et al. [158] also demonstrated that the optimal operating frequency needs to be higher than the resonant one, as seawater causes a detune, and the phenomena of frequency splitting has to be taken into account. Furthermore, as the gap between coils increases, radiation losses also increase, causing an attenuation in the transferred power [29,159].

In addition to radiation losses, eddy current losses (ECL) are a type of AC losses that also depend on conductivity and frequency due to the conductive environment [160]. Eddy currents are loops of induced current that are generated in the surroundings of a conductor, in this case the coils, due to the application of a changing magnetic field. Finding the effect of these losses for different topologies on the system is an important research topic [161–164].

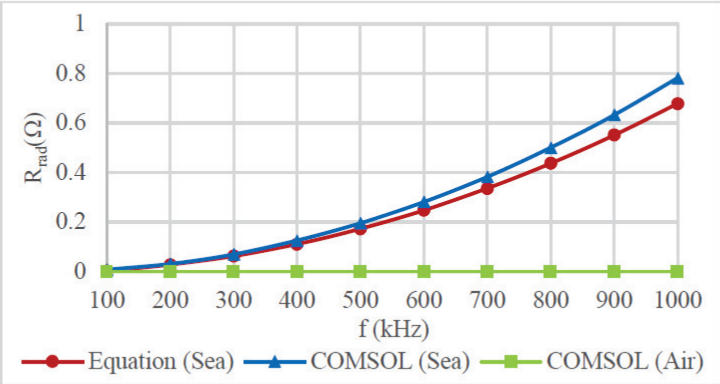

Figure 5. Radiation resistance against frequency, value from equation and from FEM model [153].

As both ECL and radiation losses cause magnetic flux leakage, some possible solutions are being studied to reduce their effects. Using high-permeability materials such as Mn–Zn ferrite as the cores of the coils is the most common approach for frequencies over 100 kHz. However, for frequencies below this value, coreless systems have also been proposed, as AC losses are more prominent than radiation losses, and there is not much difference between seawater and air [153,159]. Higher frequencies allow the construction of more compact devices but increase ECL and R_{RAD}. Therefore, a compromise between compactness and efficiency has to be found in the design of these devices.

4.2.2. Sea Currents and Misalignment

Sea currents are also of significant importance in IWPT losses, as they may cause a misalignment between the transmitter and receiver. When misalignment occur between the coils, coupling is reduced and ECL increase, causing a reduction in efficiency. Several studies have attempted to evaluate these losses [165–167], while others have designed coil topologies that try to address this issue [168–172]. Another possible solution is to achieve this alignment with a mechanical device [143].

The seawater environment makes it difficult to transmit data between Tx and Rx modules due to the attenuation of waves [29]. Therefore, control methods, such as receiver control, that do not require communication between the transmitter and the receiver are highly recommended. In addition to this, its dynamic characteristics cause a variation on the coupling factor Maguer et al. [126]. To solve this problem, control methods based on maximum efficiency tracking have been proposed in the literature [173–175].

4.2.3. Temperature and Biofouling

Regarding temperature, seawater acts as a cooling medium and can increase the thermal limits of coils [176]. However, as temperature dissipates in the coils, a thermal gradient with the environment near the coils can increase marine microbial growth in the coils, causing a phenomena called biofouling.

Biofouling is defined as the accumulation of biotic deposits on a submerged artificial surface [177]. Devices that need to be deployed underwater for a long period of time should consider this issue as it increases the misalignment and gap between coils, which reduces their transfer efficiency [178]. In [178], the authors proposed the use of anti-fouling paint and thermal coating to reduce biofouling. This paper is reviewed with more details in Section 5.4.

4.2.4. High Pressure and Permeability

High pressure in seawater is also an issue for UWPT. As we go deeper in the ocean, pressure is increased approximately by 0.1 MPa per 10 m. Thus, all the equipment needs to be able to stand high pressures, especially in deep sea applications. For a sea depth over a thousand meters, power electronics converters have to be appropriately enclosed with incompressible insulating liquids as a medium [179]. Permeability reduction is also a proven effect of high-pressure environments in ferrite cores. In [180], the authors evaluated permeability as a function of the hydrostatic pressure and presented equations that describe this relation. This reduced permeability leads to a reduction in the magnetic flux shielding, exposing the system to radiation losses.

To evaluate the extension of these losses in IWPT, Li et al. [165] tested a small prototype in a simulated deep water environment of 4000 m by using pressurized salt water. For a frequency of 94.3 kHz and a power transfer of 400 W, efficiency only dropped 2%. This suggests that for low frequency and power values, permeability is not compromised. Another related work is the one by [181], where the authors designed a housing for a wireless charger implemented in an AUV to reduce the effects of the harsh environment and successfully tested it in a hyperbaric chamber at 30 bar (300 m). Their WPT system could reach an efficiency of 75% inside the housing device.

4.2.5. Other Technical Issues

The effects of electromagnetic field emission is an aspect that has not been extensively studied underwater [182]. If the electromagnetic field is contained within the charger and the vehicle and only operates when the vehicle is stationary, it should not pose significant issues for the surrounding marine life. However, its emission could potentially cause interferences in their behavior [182,183]. Regarding its effects in electromagnetic or electronic equipment within the AUV, shielding in AUVs presents a straightforward solution to reduce it [184,185].

Another prevalent topic is interoperability and standardization. These are more challenging for UWPT devices compared to other devices or electric vehicles. This is due to the fact that each application may require a vastly different AUV with varying power ratings, geometries or application ranges. However, for a certain range of applications, it may be possible to design interoperable and standardized devices. Nonetheless, it is a topic that has not been yet addressed in the literature.

5. Review of Underwater IWPT Experiments and Applications

In recent years, the interest in underwater IWPT has increased. Several models and prototypes have been tested. Many are focused on improving efficiency and functionality and reducing the adverse effects of seawater. Some of the main research lines that can be found are related to coupler topologies, compensation schemes, control systems, materials and integration in AUVs and other devices.

5.1. IWPT Prototypes in UUVs and Docking Stations

As previously presented in Section 3.5, IWPT has already been tested for UUV charging in several prototypes. All the IWPT prototypes found in the bibliographical study and other available papers are briefly explained in this subsection. Then, a summary is presented in Table 1, where the power transfer and efficiency of the reviewed AUV charging prototypes are compared.

One of the earliest prototypes of a docking platform found for AUV charging is the homing/docking system for the MIT Sea Grant Program Odyssey AUV [119], which was a "funnel-type" docking station. Another early stage WPT-based docking platform was presented in [120]. It was developed for Marine Bird AUV in Japan and had an underwater docking system based on their "landing-on-Base" concept, where the vehicle was caught by robotic arms and latched to wireless connectors at the docking platform.

In 2007, McGinnis et al. [121] designed an IWPT prototype for the ALOHA-MARS mooring system, a deep-ocean sensor network connected to a sea-floor observatory. They installed it to charge their mooring profiler vehicle, the McLane mooring profiler (MMP). The coupler was loosely coupled and had a ferrite core. The system could transfer power of 250 W with a maximum efficiency of 70% for a 2 mm gap. After an experimental phase, the system was successfully deployed in the ALOHA-MARS mooring system in Puget Sound (USA), in June 2007 and for two months.

Table 1. Comparison of IWPT prototypes tested in AUVs.

Authors	Year	Coupling	P_{out} (W)	η (%)	f_r (kHz)	Gap (mm)
Feezor et al. [119]	1997	Funnel-type	N/A	N/A	N/A	N/A
Fukasawa et al. [120]	2003	Landing-type	N/A	N/A	N/A	N/A
McGinnis et al. [121]	2007	Loosely coupled	250	70	N/A	2
Hobson et al. [122]	2007	Funnel-type	1000	88	N/A	N/A
Pyle et al. [123]	2012	Mothership	450	N/A	N/A	N/A
Yoshida et al. [124]	2016	Funnel-type	1000	75	80-90	70
Yoshida et al. [125]	2016	Landing-type	25	65	200	100
Maguer et al. [126]	2018	Funnel-type	500	90	N/A	N/A
Matsuda et al. [127]	2019	Landing-type	188	70	N/A	N/A
Yang et al. [129]	2020	Funnel-type	680	90	35	N/A

The same year, Hobson et al. [122] developed a docking station for a 54 cm diameter Bluefin AUV. Their system was designed to withstand a 4000 m depth seawater environment. The proposed dock had a funnel-type conic design, as shown in Figure 6a. According to the researchers, the inductive charger was theoretically able to transfer 1 kW while maintaining an efficiency of 88%. However, after conducting some docking trials at the Monterey Inner Shelf Observatory (MISO), they were able to transfer 416 W at a global efficiency of 48%.

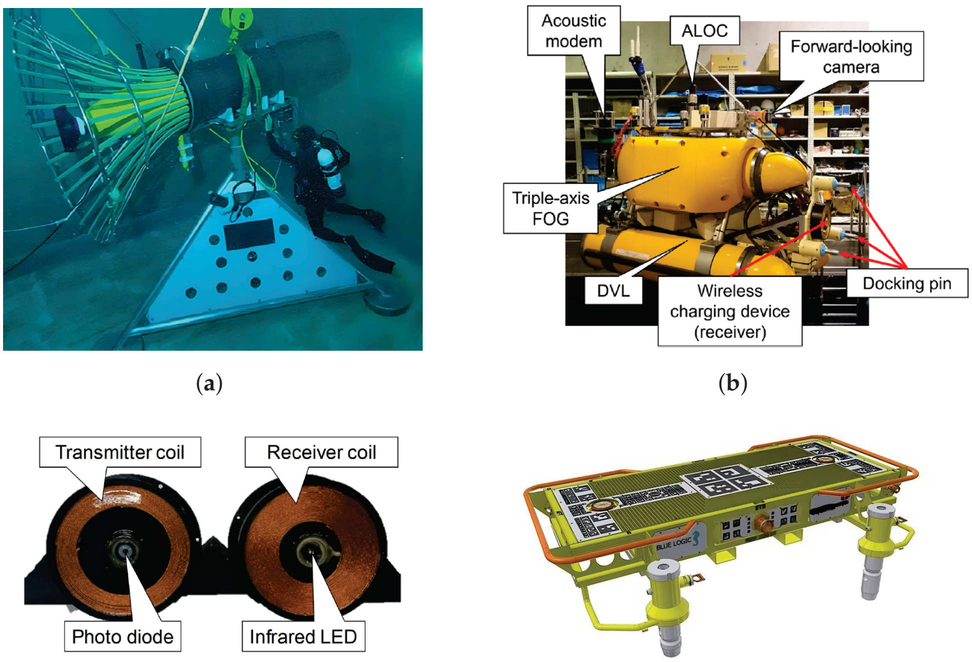

(a) (b) (c) (d)

Figure 6. AUV and docking station prototypes using IWPT. (**a**) Docking station for Bluefin AUV [122]. (**b**) Tri-TON 2 (TT2) AUV and its parts [127]. (**c**) IWPT coils in Tri-TON 2 AUV [127]. (**d**) Blue Logic SDS 3D model [186].

Pyle et al. [123] described, in 2012, the potential use of a larger underwater vehicle as a "mothership". The Battelle-Bluefin Robotics UUV Docking and Recharging Station (UDRS) project developed and tested a concept for a UUV docking station. The UDRS features inductive charging and wireless data transfer in a wet environment to reduce replenishment time and simplify operational employment. They achieved an inductive power transfer in seawater with a power of 450 W.

In 2016, Yoshida et al. [124] proposed an IWPT system for non-fixed and compact UUV charging in the ocean. They built an IWPT system in an UUV with a spiral planar coil. The size of the Tx coil was of 24 cm × 24 cm × 1.5 cm. They tested it in seawater in a floating charging station. They controlled the UUV to reach the floating station, where it transferred 25 W with an efficiency of 65% and a 10 cm gap. In [125], the authors conceptualized a long-term underwater observation system utilizing an AUV, and they built an IWPT prototype for it. Based on this idea, they built a 2200 × 2200 × 1500 mm^3 IWPT prototype and tested it in the sea. For a frequency of approximately 80–90 kHz and a gap of a few millimeters (<70 mm), they were able to transmit 1 kW of power with an efficiency of 75%.

More recently, Maguer et al. [126] presented an IWPT system integrated in a torpedo UUV. Their prototype was composed of a Tx unit in a funnel-type docking platform called AutoLARS and a Rx unit inside their eFolaga torpedo AUV. The couplers are composed of windings, ferrite core and auxiliary feedback control integrated in a "hockey-puck" shaped housing with a size of 78 mm in diameter and 62 mm in height. Their docking platform was modified to ease the eFolaga's entrance and improve clamping and coupling. The system was capable of transferring 500 W with an efficiency of 90% for a 10 mm gap in laboratory tests. Their work ended in November 2017 by conducting a two-week sea experimental campaign with the AUV deployed in the sea.

In [127], another AUV-integrated resonant IWPT sea test was performed. They built the AUV Tri-TON 2 (Figure 6b) for the monitoring of underwater infrastructure and also a seabed station that serves as a positioning reference and as a charging station. The power transfer was made with circular planar coils in a ferrite core. The Tx coil had a photo-diode implemented in the middle of the device and the Rx an infra-red led for positioning (Figure 6c). This way, the charging system can only be activated when both coils are perfectly coupled. They conducted some sea experiments at the Hiratsuka Fishing Port in Japan in January 2018 [128]. The IWPT could transfer 188 W with an efficiency of 70%.

In 2020, Yang et al. [91] proposed a design procedure to select the optimal underwater operating frequency of the IWPT system, taking into account eddy currents. By applying this procedure, they designed a charging system and conducted some sea-trials with an AUV. They tested it in the Leizhou peninsula in China. They placed the docking station at 105 m depth and powered it from a surface vessel. They charged the AUV for 6 min, achieving a wireless charge of 680 W with an efficiency of 90%.

In recent years, few docking stations with wireless power charging are being commercialized. Subsea docking stations (SDS) by Blue Logic [186] are an example of this. Their designs have already been tested for the landing of several commercially available drones. They have produced three universal and open-standard subsea stations with a power rating of 2 kW, 250 W and 50 W. A 3D model of an SDS is provided in Figure 6d.

Other recent papers have also proposed the integration or combination of renewable energies with WPT devices in docking platforms. The Platform for Expanding AUV exploRation to Longer ranges (PEARL), is an example of this. This device was a floating and solar powered platform with batteries that would provide service to AUVs, including docking and power transfer [187]. Another example of the combination of WPT with wave energy was given in [188]. Here, the authors researched the feasibility of the combination of an AUV charging and docking station powered by a wave energy converter and explained the design process of the whole system.

Other devices such as sensors have also been charged using IWPT. For instance, ocean buoys with monitoring sensors can also be used as charging stations by combining IWPT with renewable energies. In these devices, linear coaxial winding transformers (LCWTs) are usually the preferred choice. These transformers are coaxially aligned transformers that are fixed [130]. In these devices, the buoy is connected to the primary, while the sensors are at the secondary winding. The buoys collect energy through the solar panels and the sensors are charged wirelessly. Some examples of these devices can be found in [16,131].

5.2. Laboratory Prototypes with Coaxial and Planar Coils

In the first stages of development, most of the coils were designed with a planar or coaxial topology, as shown in Figure 7. This happened due to the fact that planar coils are most suitable for landing-type docking stations and coaxial coils for the funnel-type ones. The main focus of the laboratory prototypes has been to optimize the power transfer by testing different frequency values, gaps, models or control schemes while trying to overcome the main challenges presented by seawater. The most usual compensation schemes for these systems were series–series and series–parallel. However, in the last five years, there has been an increasing interest in testing LCC compensating schemes.

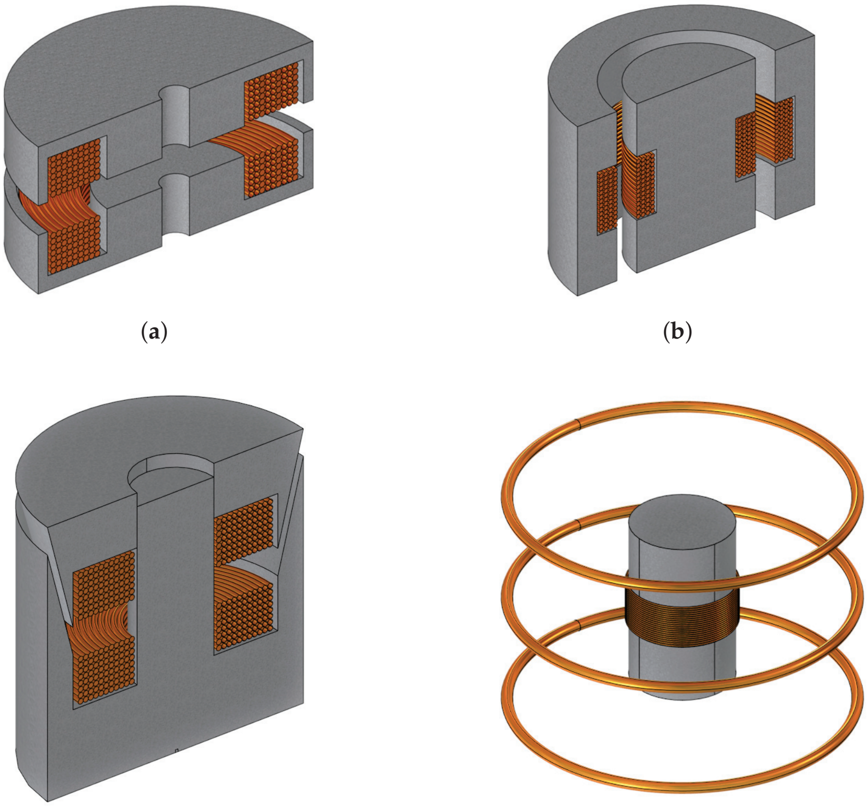

(**a**) (**b**) (**c**) (**d**)

Figure 7. Planar and coaxial coil topologies. (**a**) Planar circular coil with semi-closed core. (**b**) Coaxially coupled coils. (**c**) Self-latching circular coupler model [189]. (**d**) 3 Tx and 1 Rx coaxial IWPT system [190].

In [165], one the earliest laboratory tests for a planar coil was presented. They used planar and semi-closed coils inside of high-pressure (4000 m) salt-water and transferred 400 W. Then, in 2015, a transmission of 10 kW with an efficiency of 92% was achieved by Cheng et al. [151]. In another work by Wu et al. [191], they presented a coreless device that could achieve a maximum load power of 360 W. Yan et al. [157] modeled a coil to obtain its optimal frequency and designed an experimental prototype achieving a 200 W power transfer with 85% efficiency at 504.5 kHz. In [143], the authors achieved a power transfer of 1 kW with an LCC-P compensating circuit. Their peak efficiency was approximately 94%. In [192], the authors constructed a 400 W laboratory prototype with a black-pane ferrite. Liu et al. [193] built a coil mutual inductance model based on an eddy current loss analysis and then tested a 1 kW underwater WPT prototype using an LCC-S compensating method. They achieved an efficiency of 94.05% for a frequency of 100 kHz. In [189], they achieved 92% efficiency on a 3 kW IWPT for a circular resonant coil device. In this case, they designed a self-latching coupling structure that could facilitate AUVs docking and highly reduce misalignment. Their proposal is depicted in Figure 7c.

Regarding coaxial coils, several studies are available in the literature, with efficiency values ranging from 70% up to 90%. Lin et al. [194] designed a coaxially coupled and coreless IWPT system that transferred 300 W. In [195], they proposed a coaxial wireless transfer system for a torpedo-shaped AUV. They designed an impedance matching network that could achieve a 100 W power transfer. In another paper by Guo et al. [196], they designed a coaxial IWPT system with a position adaptive power delivery system to reduce the effect of misalignment with an efficiency of 88% for a 300 W power transfer. In [197], they designed another coaxially aligned IWPT device with high misalignment tolerance and that was compatible with a funnel-type docking station. The authors were able to transfer 2 kW with a 92.7% efficiency. The authors in [167] presented an AUV hull compatible inductive power transfer system with an 80 kW power rating and 93.9% efficiency by using an LCC-S compensation topology, achieving a power transfer of 5180 W in a downscaled prototype. Another coaxially aligned device with a power transfer of 3 kW was presented in [190], which was composed of three Tx devices, as seen in Figure 7d. In the case of the study by Zhang et al. [198], they designed a variable ring-shaped magnetic coupler that improved the transfer efficiency of their coaxial device from 77% to 86.4% for a 800 W power transfer.

In 2023, a coaxial and planar hybrid prototype was proposed by Wen et al. [199]. Here, a solenoid transmitter was tested with a dual planar receiver, achieving an efficiency of 85% for a 401 W power transfer without misalignment. Furthermore, many other planar and coaxial systems that achieved power transfer values below 100 W or did not provide enough information to analyze their parameters can also be found in the literature [159,200–206]. Additionally, some other works present comparisons between planar topologies [207] and planar and coaxial topologies [208].

A summary of the main parameters of the reviewed underwater IWPT system prototypes are collected in Table 2. It is important to note that, in general, the systems operating at higher frequencies have a smaller size than those with lower frequencies.

Table 2. Comparison of resonant IWPT experiments with planar and coaxial topologies.

Authors	Year	Environment	Coil	Core	Comp.	P_{out} (W)	η (%)	f_r (kHz)	Gap (mm)
Li et al. [165]	2010	Salt water	Planar	Semi-closed	S-P	400	90	94.3	2
Cheng et al. [151]	2015	Salt water	Planar	Enclosed	S-P	10340	92.8	38.9	25
Wu et al. [191]	2016	Salt water	Planar	Coreless	S-S	360	90.2	100	1
Yan et al. [157]	2019	Salt water	Planar	Coreless	S-S	200	85	504.5	14
Yan et al. [143]	2019	Air	Planar	Backplane	LLC-P	1000	94	81.6	60
Meşe and Budak [192]	2020	Salt water	Planar	Backplane	S-S	400	86.3	100	50
Liu et al. [193]	2020	Air	Planar	Backplane	LCC-S	1000	94	100	55
Zhou et al. [189]	2021	Salt water	Planar	Self-latch	S-S	3000	92	35.4	5
Lin et al. [194]	2017	Salt water	Coaxial	Coreless	S-P	300	77	52	15
Song et al. [195]	2018	Salt water	Coaxial	Coreless	LCC-S	100	70	214.3	1.6
Guo et al. [196]	2019	Salt water	Coaxial	Enclosed	S-S	300	88	32	5
Liu et al. [197]	2022	Fresh water	Coaxial	Tubular	LCC-S	2000	92.7	200	32
Mostafa et al. [167]	2022	Salt water	Coaxial	Backplane	LCC-S	5180	96.7	200	30
Hasaba et al. [190]	2022	Salt water	Coaxial	Tubular	LCC-LCC	3000	80.7	1.55	770
Zhang et al. [94]	2023	Air	Coaxial	Ring	LCC-S	800	86.4	100	N/A
Wen et al. [199]	2023	Salt water	Hybrid	Coreless	S-S	401	85	100	N/A

5.3. Innovative Topologies and Multi-Coil Systems

In addition to the regular planar and coaxial topologies, in the last five years, there has been a trend towards designing innovative coil topologies to try to improve underwater IWPT characteristics such as integration in AUVs, reduction in size and weight, multiple load charging and misalignment-tolerance. An example of a novel topology is the device presented in 2018 by Cai et al. [209], which used an E-shaped core that followed an arc-shape for AUV applications (Figure 8a). Their design could transmit 605 W with a 91.3% efficiency.

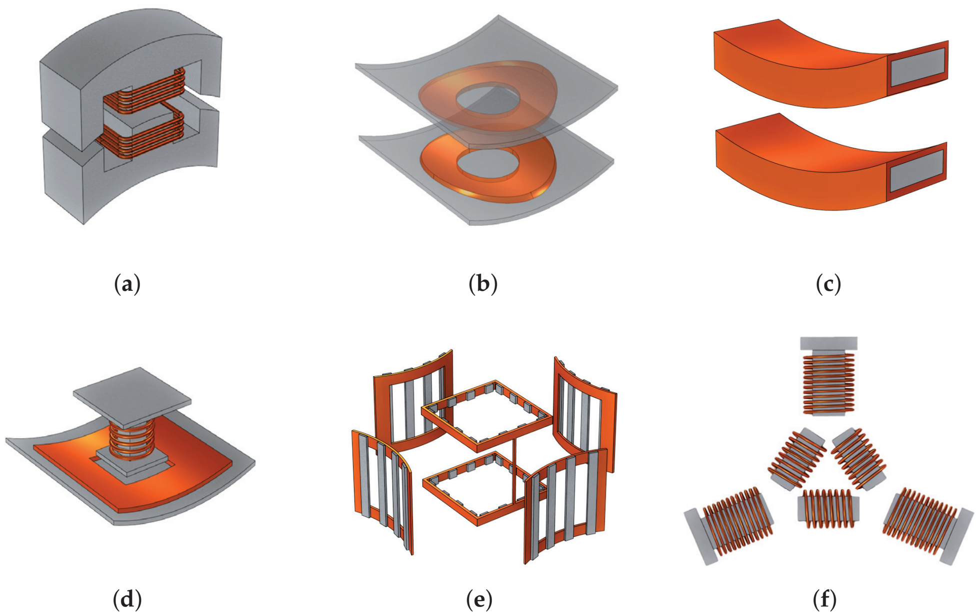

Figure 8. Innovative coil topologies. (**a**) E-shape coil [209]. (**b**) Arc-shaped coil [210]. (**c**) Dipole coil [211]. (**d**) Arc- and H-shaped coil [212]. (**e**) Cuboid and Arc coil [213]. (**f**) Three phase coil [214].

Several other papers have proposed innovative arc-shaped planar topologies that easily adapt to the shape of the AUV and reduce the weight of the IWPT device. In Figure 8b, a general and simplified concept of these topologies is presented. Most of these present an efficiency of approximately 90%. For instance, in [215], the authors designed and tested this coil topology, achieving a power transfer of 1 kW in air. In [141], they integrated the compensation coil and main coil as two unipolar coils on the Tx side for an LCC-S. They achieved power transfer values of around 300 W. In another work by Cai et al. [216], they presented another arc-shaped topology, transferring 1 kW. In [217], they tested a curved coupler with distributed ferrite cores and transferred up to 2.2 kW.

In a similar fashion, Cai et al. [211] proposed an arc-shaped dipole-coil magnetic coupler (Figure 8c). Fe-based nano-crystalline soft magnetic materials were used as coil cores to improve permeability and reduce size and weight. This novel coil topology was constructed and validated in a salt water environment with a 630 W power transfer. Wang et al. [210] proposed the arc-shaped UWPT system from Figure 8b. They also used a a similar alloy material. Their coils could transfer 3 kW of power. In [144], the authors presented an 802.3 W resonant IWPT system with an arc-shaped transmitter and I-shaped receiver (Figure 8d). Xia et al. [218] designed an IWPT device with a coaxial Tx and an arc-shaped Rx that could achieve a stable output power of 575 W. Finally, in [172], they built an arc-shaped transmitter with a pendulum-shaped receiver, transferring up to 3.03 kW when aligned.

Multicoil IWPT systems have also been a dominant topic in the last few years. Most of the works focus on improving the power transfer or reducing misalignment by using more than one coil at the Rx side [213], the Tx side [219–221] or both sides [214,222–224]. Regarding multiple receivers, Zeng et al. [213] proposed a multi-directional magnetic coupler with a cuboid shape as the transmitter for a four arc-shaped receiver system for swarm AUVs (Figure 8e). The system could simultaneously transfer 200 W to four Rx coils.

Regarding multiple Tx devices, Hasaba et al. [219] achieved a 100 W power transfer with a 25.9% efficiency for a distance of up to 10 m. The system was composed of seven bulky Tx coils of 3.4 m in diameter. More recently, in [190], the authors designed an improved coaxial IWPT with three receivers. It allowed a power transfer up to several meters and a maximum efficiency of 80% for a power transfer of 3 kW. The transmitter structure consisted of three circular coils, as shown in Figure 7d, with a diameter of 2000 mm, placed at intervals of 1000 mm. The receiver coil was around a cylindrical aluminum pressure container (emulating an AUV) with a diameter of 460 mm and 1000 mm in length. Finally, in [225], they proposed a free-rotation device with two transmitters and one receiver to reduce misalignment within the system, transferring up to 700 W.

Regarding multiple Rx and Tx devices,Kan et al. [214] proposed the three-phase wireless power transfer system for swarm AUVs in 2017 (Figure 8f), which they constructed and validated for a 1 kW power transfer. Similarly, Yan et al. [222] designed a six-phase prototype where the Tx and Rx devices were inverted. They simultaneously achieved an output power of 500 W for two receivers with a 90% efficiency in air. In addition to these, Sato et al. [224] designed a multiple Tx and two Rx planar circular coupler to improve misalignment and tested a 200 W prototype with success.

Other multi-coil structures that aim to reduce misalignment are the DD and DDQ topologies. These configuration are used to charge only one device and have the advantage of allowing a higher misalignment. Some of the recent studies on these configurations can be found in [226–228]. In [226], they achieved a power transfer of 884 W with a 94.3% efficiency, and in [227], a power transfer of 1.5 kW with an efficiency of 89.8%.

Finally, a comparison between these innovative topologies and some of the most relevant circular and coaxial coils is presented in Table 3.

Table 3. Comparison of resonant IWPT experiments with various topologies.

Authors	Year	Environment	Coil	Core	Comp.	P_{out} (W)	η (%)	f_r (kHz)	Gap (mm)
Li et al. [165]	2010	Salt water	Planar	Semiclosed ferrite	S-P	400	90	94,3	2
Cheng et al. [151]	2015	Salt water	Planar	Enclosed	S-P	10340	92.8	38.9	25
Cai et al. [209]	2018	Air	Circular helical	E-shaped	N/A	606	91.3	50	8
Kan et al. [214]	2017	Air	Three phase	Tx: T-shape Rx: Cuboid	S-S	1000	92.4	465	21
Sato et al. [224]	2019	Salt water	Planar multicoil	Coreless	S-P	200	85	14	10
Yan et al. [215]	2019	Air	Circular arc	Arc	LCC-LCC	1000	95	85	10
Yan et al. [141]	2019	Air	Dual arc	Arc	LCC-S	300	93	85	80
Cai et al. [211]	2020	Salt water	Dipole	Arc	S-S	634	87.9	50	8
Cai et al. [216]	2021	Salt water	Bipolar circular	Arc	LCC-S	1000	95.1	50	8
Zhou et al. [189]	2021	Salt water	Circular planar	Enclosed	S-S	3000	92	35.4	5
Hasaba et al. [190]	2022	Salt water	Coaxial	Backplane	LCC-LCC	3000	80,7	1.55	770
Mostafa et al. [167]	2022	Salt water	Coaxial	Backplane	LCC-S	5180	96.7	200	30
Qiao et al. [144,212]	2022	Salt water	Tx: Arc Rx: H	Tx: Arc Rx: I-shaped	LCC-P	802	91.1	96.2	N/A
Wang et al. [210]	2022	Salt water	Arc	Fe-alloy arc	LCC-LCC	3000	91.9	85	40
Wu et al. [220]	2022	Salt water	Arc	Coaxial multicoil	LCC-LCC	1200	90	85	N/A
Yan et al. [222]	2022	Air	Six-phase	Rx: T-shape Tx: Cuboid	LCC-LCC	2 x 500	90	249	64
Xia et al. [218]	2023	Salt water	Tx: Coax. Rx: Arc	Tx: Coaxial Rx: Arc	S-P	575	92.5	50	8
Zeng et al. [213]	2023	Salt water	Tx: Cage Rx: Arc	Spaced	LCC-S	4 x 200	92.2	249	50
Lin et al. [217]	2023	Salt water	Arc	Distributed	LCC-S	2200	94	35	N/A
Wang et al. [172]	2023	Salt water	Arc Pendulum	Arc Pendulum	LCC-S	3036	95.9	85	50
Yan et al. [225]	2023	Air	Multi Solenoid	Solenoid	LCC-S	700	92	200	N/A
Da et al. [226]	2023	Salt water	DDQ	Backplane	LCC-LCC	884	94.3	85	20
Sun et al. [227]	2023	Salt water	DD-DD	Backplane	S-S	1500	89.9	100	N/A

5.4. Novel Core Materials

The research on new materials for various IWPT system parts has been recently addressed in the scientific literature. The main objectives are reducing size and weight, improving permeability, allowing high pressure applications for deep-sea operation, increasing flexibility for a better AUV integration or reducing biofouling.

Within this context, it is important to consider weight and size reduction strategies. One such strategy involves spacing ferrite cores. One of the strategies involving spacing ferrite cores [213,229,230] is an option that does not require research into new materials. For instance, in [229], they modeled a 6.0 kW underwater IWPT system with several *Rx* core distributions that use less ferrite than usual cores, Figure 9c. However, novel materials seem to be a better option, as spaced ferrite cores reduce the performance of the coils. Within this context, Cai et al. [211] and Wen et al. [146] proposed the use of Fe-based nanocrystalline alloys as core materials. In particular, the size and weight of the IWPT were reduced in [146] up to 41.1% and 42.6%, respectively. According to the researchers, these materials have the following advantages:

(a) Magnetic flux density is up to three times higher than Mn-Zn ferrite materials. For the same volume, twice the ferrite core output power can be reached.
(b) Permeability can be more than 10 times that of the Mn-Zn ferrite material.
(c) Strong deformation ability improves integration in round surfaces.

Few other works have focused on using different materials in the windings to reduce eddy currents or improve their coupling. For instance, Kuroda et al. [231] designed and fabricated some underwater antennas covered by a resin sealing layer. This layer was employed to protect the antenna from high pressure and electrically isolate it to reduce ECL. In [159], the authors also proposed covering the coil winding with a polyurethane sealant, as seen in Figure 9a. Another innovative proposal by Hu et al. [232] consists of using Mu Negative metamaterials for the winding, negative permeability materials that could potentially improve coupling.

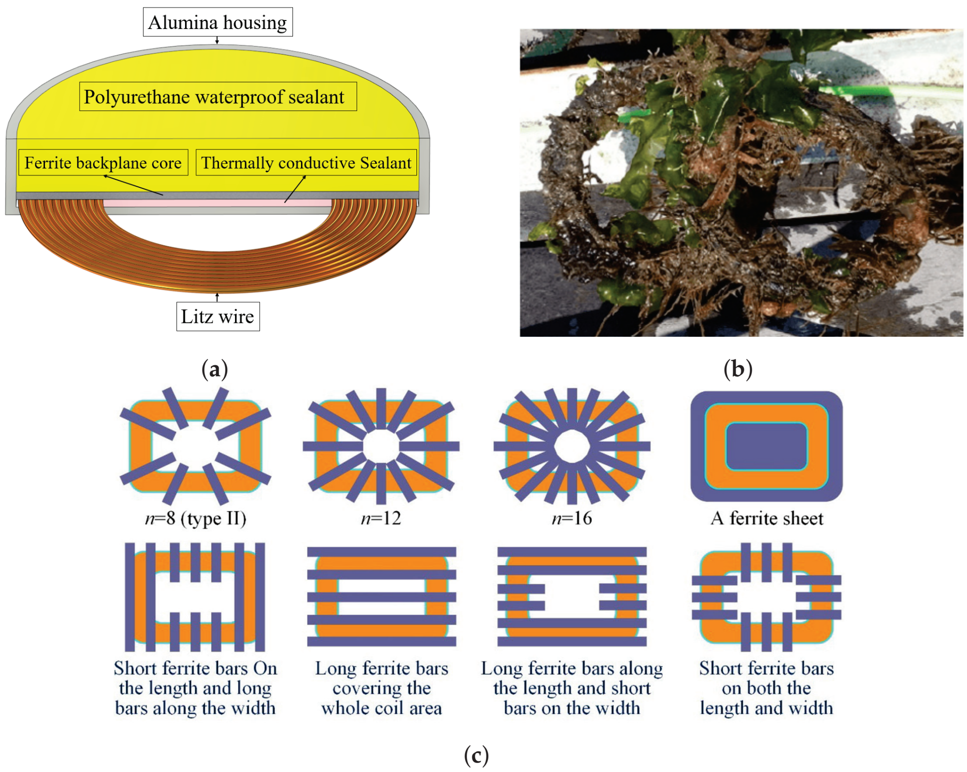

Figure 9. Topologies with novel core materials, distributions and effects of biofouling. (**a**) Planar circular coil with sealant [159]. (**b**) Effect of biofouling in a coil [178]. (**c**) Different ferrite geometries for Rx coils [229].

Some papers have proposed various shielding methods for IWPT devices to reduce the effects of metal hulls in WPT [185]. Regarding AUV hulls, Wen et al. [146] proposed replacing traditional metallic hull materials for silicon–aluminum–oxynitride (SiALON) ceramic ones. According to their research, SiALON could potentially maintain pressure resistance while reducing the interference with the charging system, improve corrosion resistance and avoid structural changes in AUVs, while maintaining the power transfer efficiency. In [184], the authors modeled and tested a prototype that used Nylon6 magnetic shielding to reduce ECL. They could demonstrate that for frequencies over 400 kHz, shielded devices were more efficient than the not shielded ones.

Regarding biofouling resistant materials, Anderson et al. [178] presented a characterization on thermal effects and biofouling in UWPT systems. They prepared eight coils for biofouling tests potted with different materials: two with polyurethane, two with polyurethane and a copper-based anti-foul paint, two with TCE thermal coating and another two with that coating and a copper-based anti-foul paint. They submerged the pots off a pier in San Diego Bay for 45 days. By powering the coils, they generated heat to test the generation of biofouling in each case. One example is shown in Figure 9b. They found out that the anti-fouling paint and thermal coating were effective in reducing coil fouling, and that the combination of both was the optimal option.

5.5. Dual Data and Power Transfer and Innovative Control Systems

The research into innovative control systems and simultaneous power and data transfer is also an increasing trend. As data transfer in seawater can be challenging, control systems that avoid communication between Tx and Rx are being considered to improve overall system feasibility. In addition, the combination of WPT and data transfer could be an effective option to compact the system. Regarding data transfer, some of the previously analyzed AUV prototypes with IWPT systems already incorporated data transfer modules [120,123,124,126]. However, these modules were independent from the power transfer module.

Several hybrid power and data communication systems have been proposed in the literature [15,213,233–237]. In [234], the authors presented a system able to transfer up to 130 W with a 73 mbps full-duplex communication. In [213], a partial Rx coil, a Tx coil and an additional transformer were used to transmit data and power, proving a data transfer rate of 30 kbps at a distance of 5 cm. Wang et al. [235] designed a coaxially aligned underwater IWPT system that could transfer 518 W of power with an efficiency of 92% and 500 kbps/700 kbps full-duplex communication. In [236], they designed a data and power transmission system for a cable-inspecting robot fish with three operating modes: alignment detection, low-speed power transmission and high-speed signal transmission. Cai et al. [238] built a dual prototype with 8.5 kbps data transmission, compact design and a power transfer of 936 W at 94.12% efficiency. Finally, Li et al. [237] achieved a 1-Mbps full-duplex communication link for a 1 kW power transfer.

A number of innovative control approaches have been presented in the literature. Maximum efficiency tracking (MET) control methods are some of the most popular options [29,174,227,239,240], while other papers have proposed different solutions [241–243]. MET control methods focus on finding the variation in the coupling coefficient due to misalignment and adjust the frequency or voltage of one of the sides to maintain an optimal underwater IWPT efficiency. These adjustments are generally achieved by acting on the input or output converters.

Some papers have also developed optimized IWPT models to improve their control [138,244–247]. In [244], a small-signal phasor model was presented, and a control-to-output transfer function was developed, with the output voltage as the regulated variable. In [245], an efficient model for an UWPT system was proposed by using Z-parameters and two port network analysis. Other papers such as [138,246] have very recently presented some mathematical models for underwater IWPT optimization by applying more complex algorithms. In [247], they applied a particle swarm algorithm to adaptively control the output power.

5.6. Bidirectional and Modular IWPT

Another interesting proposal consists of using bidirectional power transfer [248–251]. These type of systems could potentially improve the adaptability of IWPT to any environment [248]. This technology would allow charging an AUV from an underwater power station while also having the ability to charge another device with the same vehicle. In [250], they built a bidirectional IWPT model that could deliver power up to 300 W to a load with an efficiency of 90%, which also could be charged with a power of 51 W and in [251], they achieved a transfer of 519 W with an efficiency of 82.18% and a reverse power of 472 W with 73.63%.

Modularizing IWPT devices is also a recent proposal that very few works like the ones in [252,253] have presented. In [252], the authors designed a small modular vehicle that could be separated into several interchangeable modules, including control and power system. These modules would be provided with data and power through IWPT. On the other hand, Ref. [253] developed a modular housing prototype that sought to adapt the existing IWPT technologies to a marine environment.

6. Conclusions

During recent years, there has been an increasing demand for more efficient and sustainable operation and maintenance UUV devices in the seawater environment. Conventional charging methods are generally more polluting, time-consuming and costly as they require vessels. UWPT devices fed from offshore renewable energy are a great alternative to these. As seen in Appendix A, the interest in UWPT has increased in the last five years, both in academia and in industry, with few commercial devices already available. In this regard, IWPT is the most promising technology, while other near-field technologies such as CWPT or ultrasonic through-wall show potential. On the other hand, far-field technologies have been proven not to be feasible for high power transfer but could be integrated as auxiliary devices and for underwater communication. The combination of renewable energy and UWPT is also a recent proposal that can help to improve the reliability of AUV charging.

In this context, the key conclusions that have been obtained from the comprehensive literature review conducted within this paper can be summarized as follows:

(a) Achieving efficient and reliable underwater UWPT is not a trivial issue. Several challenges such as high-pressures, strong currents or biofouling have to be tackled in subsea docking platforms. In addition to this, the effects of ECL and R_{RAD} need to be reduced to the minimum to maintain efficient IWPT. Regarding these issues, progress has been made in the design of misalignment-tolerant devices and in the characterization of ECL to reduce their effect in the system. Maintaining frequencies below 200 kHz, reducing the gap between the Tx and Rx sides or enclosing the coils are some of the solutions proposed in the literature. On the other hand, very few papers consider the effect of high pressures, biofouling or electromagnetic field emission in underwater wireless technology. These are important issues that warrant attention and should be addressed in the future research.

(b) Due to a lack of standardization, comparing different IWPT systems is difficult. A compromise between size and power often involves low distance, low misalignment, and a frequency range of 50–200 kHz. The latest works have reported efficiency values ranging from 88% up to 93%. However, only a few real-life prototypes have reached up to 90% efficiency. Furthermore, despite sharing the same theoretical background, the experimental results reported in the literature often do not align due to various factors such as different coil shapes, pad designs, ferrite material layouts, shielding techniques, water salinity levels and other factors. This complicates the development of standardized devices, as the optimal configurations may vary depending on the specific application of each AUV. Nonetheless, as the technology matures, there is significant potential to develop general chargers for different types of AUVs.

(c) Power transfer in the range of 1 kW seems already possible, which may suffice for small UUVs, but work-class UUVs require power transfer capabilities with power ratings in the range of 10 kW, which, according to the reviewed literature, seems not to be solved yet today. To meet the power needs of UUVs in industrial applications, further research and improvement of UWPT are essential. One approach is to focus on testing higher power prototypes. By developing and testing prototypes with increased power capabilities, the researchers can assess the feasibility and efficiency of scaling up UWPT technology to meet the demands of work-class UUVs. Furthermore, a collaboration between academia, industry and government agencies can facilitate the exchange of knowledge and resources to accelerate the development and deployment of UWPT technology in real-world settings.

Thus, although significant advances regarding UWPT have been carried out in the last decades, significant research efforts need to be continued to overcome a variety of issues and make UUV charging technologies feasible to, this way, support the autonomous underwater inspection of offshore renewable energy power plants and other offshore and underwater facilities with its added benefits for a more cleaner and sustainable future.

Author Contributions: Conceptualization, I.M.d.A. and I.R.H.; methodology, I.M.d.A. and I.R.H.; validation, I.M.d.A., E.I. and E.R.; investigation, I.M.d.A. and I.R.H.; resources, I.M.d.A. and I.R.H.; data curation, I.R.H.; writing—original draft preparation, I.R.H. and I.M.d.A.; writing—review and editing, E.I. and E.R.; visualization, I.M.d.A., E.I. and E.R.; supervision, I.M.d.A. and J.L.M.; project administration, J.L.M.; funding acquisition, I.M.d.A. and J.L.M. All authors have read and agreed to the published version of the manuscript.

Funding: This work was supported in part by the Government of the Basque Country within the fund for research groups of the Basque University system IT1440-22 and by the CIN/AEI/10.13039/501100011033 within the project PID2020-115126RB-I00. This work was supported in part by "Programa Investigo" within the European Union funding framework of Plan de Recuperación, Transformación y Resilencia—NextGenerationEU.

Acknowledgments: Special thanks to Via Inno university research platform from the University of Bordeaux for giving us the required IPC classifications and keywords to conduct the bibliographical study.

Conflicts of Interest: The authors declare no conflicts of interest.

Abbreviations

AUV	autonomous underwater vehicle
CWPT	capacitive wireless power transfer
D-WEVCS	dynamic electric vehicle charging system
ECL	eddy current losses
EM	electromagnetic
IWPT	inductive wireless power transfer
MET	maximum efficiency tracking
OWT	offshore wind turbine
S-WEVCS	static wireless electric vehicle charging system
SiALON	silicon–aluminum–oxynitride
TMS	tether management system
UUV	unmanned underwater vehicle
UWPT	underwater wireless power transfer
f_r	resonant frequency
k	coupling coefficient
$P-P$	parallel–parallel
$P-S$	parallel-series
R_{AC}	AC resistance

R_{DC}	DC resistance
R_{RAD}	radiation resistance
Rx	receiver
$S-S$	series–series
$S-P$	series–parallel
Tx	transmitter

Appendix A. Bibliographical Study

Appendix A.1. Methodology

In order to characterize the main technologies used in UWPT, a technology intelligence study was conducted by means of a patent and bibliographical search. The existing patents were queried using PATENTSCOPE from WIPO IP in February 2024. The following IPC classification was queried: *H02J-050, Circuit arrangements or systems for wireless supply or distribution of electric power.* Here, multiple sub-fields were included for a more precise decomposition of the corpus:

- H02J 50/05 using capacitive coupling,
- H02J 50/10 using inductive coupling,
- H02J 50/12 of the resonant type,
- H02J 50/15 using ultrasonic waves,
- H02J 50/20 using microwaves or radio frequency waves,
- H02J 50/30 using light, e.g., lasers.

Additionally, *H01F 38/14, inductive couplings* IPC classification and the following keywords were coupled in the search: "underwater", "submarine", "AUV", "autonomous underwater vehicle", "UUV" or "unmanned underwater vehicle" or "marine". This query was conducted in English and repeated in Chinese, Danish, Dutch, French, German, Italian, Japanese, Korean, Polish, Portuguese, Russian, Spanish and Swedish. The search in these languages was carried out after obtaining the translations of English keywords from the cross lingual query search from WIPO PATENTSCOPE.

Regarding scientific publications, the following script was used to query the Scopus database: *(KEY("wireless charging") OR KEY ("wireless power transfer")) AND (TITLE-ABS-KEY(underwater OR subsea OR submarine))*.

Appendix A.2. Patent Corpus

According to the study, a total of 569 patent families have been filed in the field, most of them originating from Asia. The first patent of a wireless underwater transmitter was awarded in 1939 [254]. From that year until 1979, no more patents were found in the study. In the period from 1979 to 2010 few patents were found, with no more than one patent per year on average. Since 2010, the topic has gained increasing interest. The period from 2018 to 2023 has been the most prolific, with an average of 50 patents per year, as seen in Figure A1a.

The increase in patents in the 2016–2023 period is highly due to Chinese applications. The ranking of top applicants is dominated by actors from Asia, though Chinese applicants are mostly academic from Zhejiang university (13 patents), Tianjin university (11 patents) or Harbin engineering university (8 patents), while Japanese patents are from industrial actors such as Panasonic (10 patents), IHI CO (6 patents) or Showa Aircraft ind co LTD (6 patents). On the other hand, western actors mostly come from smaller companies and research organizations, with Finnish company Subsea Energy Oy (6 patents) as one of the most prolific in Europe. Philips is the company with the most patents filed (27) across several patent offices, including the USA, Europe, and China. In the USA, the major patent filers are Panasonic (7 patents) and Philips.

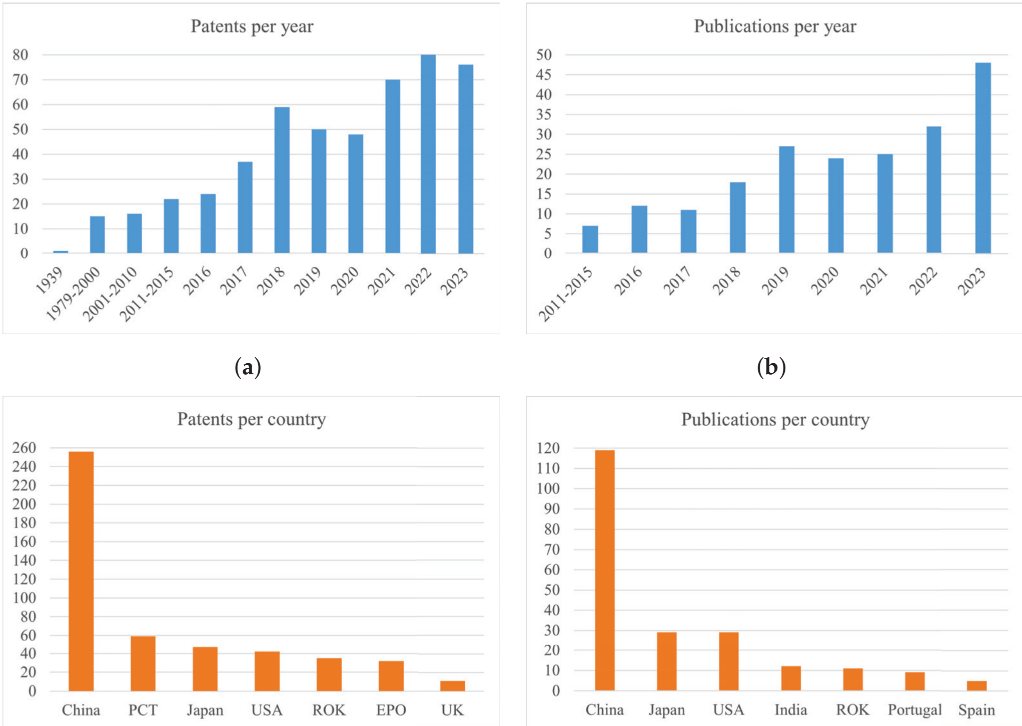

(**a**) (**b**)

(**c**) (**d**)

Figure A1. Derived results from the bibliographical study. (**a**) Patents by year. (**b**) Publications by year. (**c**) Patents by country. (**d**) Publications by country.

Regarding power transfer technologies, the circle chart in Figure A2 shows the percentage of patents in relation to the type of wireless charging technology. This technological decomposition relies on IPC codes, as showcased previously. Inductive coupling technologies are clearly mainstream here, with an approximate 87% of the total, according to the conducted study.

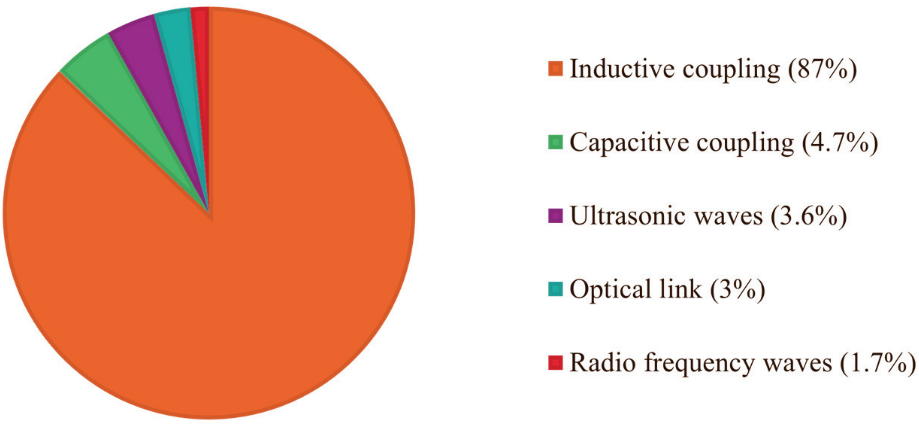

Figure A2. UWPT patents by method.

Appendix A.3. Scientific Publication Overview

In the review carried out for scientific publications, 204 references have been collected on the topic of underwater wireless power transfer since 2011. In a similar fashion to patents, China is the main country of origin, followed by Japan and the United States. In addition to these, India, Portugal and Spain have also shown a significant amount of activity, especially in the last few years (2020–2022), as seen in Figure A1b.

The Northwestern Polytechnical University of Xi'an (China), the Harbin Institute of Technology (China), the San Diego university (United States) and the Toyohashi University of Technology (Japan) appear as the most prolific actors in the field. Additionally, the University of Porto (Portugal) and its Institute for Systems and Computer Engineering, Technology, and Science have also contributed significantly to this topic, along with the Spanish University of Las Palmas, the latter focusing more on publications related to underwater sensor applications [135].

References

1. International Energy Agency (IEA). Ocean Power Generation in the Net Zero Scenario, 2000–2030. 2021. Available online: https://www.iea.org/data-and-statistics/charts/ocean-power-generation-in-the-net-zero-scenario-2000-2030 (accessed on 8 April 2024).
2. International Energy Agency (IEA). Global Energy and Climate Model. 2021. Available online: https://www.iea.org/reports/global-energy-and-climate-model (accessed on 8 April 2024).
3. Hote, K.; Kaushik, R.; Tasnin, W. Global Offshore Wind Scenario: A Review. *ECS Trans.* **2022**, *107*, 11083–11103. [CrossRef]
4. Wang, L.; Kolios, A.; Liu, X.; Venetsanos, D.; Cai, R. Reliability of offshore wind turbine support structures: A state-of-the-art review. *Renew. Sustain. Energy Rev.* **2022**, *161*, 112250. [CrossRef]
5. Li, C.; Mogollón, J.; Tukker, A.; Dong, J.; von Terzi, D.; Zhang, C.; Steubing, B. Future material requirements for global sustainable offshore wind energy development. *Renew. Sustain. Energy Rev.* **2022**, *164*, 1–13. [CrossRef]
6. López, I.; Andreu, J.; Ceballos, S.; Martínez de Alegría, I.; Kortabarria, I. Review of wave energy technologies and the necessary power-equipment. *Renew. Sustain. Energy Rev.* **2013**, *27*, 413–434. [CrossRef]
7. Shetty, C.; Priyam, A. A review on tidal energy technologies. *Mater. Today Proc.* **2022**, *56*, 2774–2779. [CrossRef]
8. Khan, M.; Khan, H.; Aziz, M. Harvesting Energy from Ocean: Technologies and Perspectives. *Energies* **2022**, *15*, 3456. [CrossRef]
9. Ren, Z.; Verma, A.; Li, Y.; Teuwen, J.; Jiang, Z. Offshore wind turbine operations and maintenance: A state-of-the-art review. *Renew. Sustain. Energy Rev.* **2021**, *144*, 110886. [CrossRef]
10. Wang, Z.; Guo, Y.; Wang, H. Review on Monitoring and Operation-Maintenance Technology of Far-Reaching Sea Smart Wind Farms. *J. Mar. Sci. Eng.* **2022**, *10*, 820. [CrossRef]
11. Rémouit, F.; Chatzigiannakou, M.; Bender, A.; Temiz, I.; Sundberg, J.; Engström, J. Deployment and Maintenance of Wave Energy Converters at the Lysekil Research Site: A Comparative Study on the Use of Divers and Remotely-Operated Vehicles. *J. Mar. Sci. Eng.* **2018**, *6*, 39. [CrossRef]
12. Liu, Y.; Hajj, M.; Bao, Y. Review of robot-based damage assessment for offshore wind turbines. *Renew. Sustain. Energy Rev.* **2022**, *158*, 112187. [CrossRef]
13. Wynn, R.; Huvenne, V.; Le Bas, T.; Murton, B.; Connelly, D.; Bett, B.; Ruhl, H.; Morris, K.; Peakall, J.; Parsons, D.; et al. Autonomous Underwater Vehicles (AUVs): Their past, present and future contributions to the advancement of marine geoscience. *Mar. Geol.* **2014**, *352*, 451–468. : 10.1016/j.margeo.2014.03.012 [CrossRef]
14. Wei, X.; Guo, H.; Wang, X.; Wang, X.; Qiu, M. Reliable Data Collection Techniques in Underwater Wireless Sensor Networks: A Survey. *IEEE Commun. Surv. Tutor.* **2022**, *24*, 404–431. [CrossRef]
15. Tibajia, G.; Talampas, M. Development and evaluation of simultaneous wireless transmission of power and data for oceanographic devices. In Proceedings of the SENSORS 2011 Conference, Limerick, Ireland, 28–31 October 2011, pp. 254–257. [CrossRef]
16. Fang, C.; Li, X.; Xie, Z.; Jiayi, X.; Xiao, L. Design and Optimization of an Inductively Coupled Power Transfer System for the Underwater Sensors of Ocean Buoys. *Energies* **2017**, *10*, 84. [CrossRef]
17. Green, R.; Copping, A.; Cavagnaro, R.J.; Rose, D.; Overhus, D.; Jenne, D. Enabling Power at Sea: Opportunities for Expanded Ocean Observations through Marine Renewable Energy Integration. In Proceedings of the OCEANS 2019 MTS/IEEE SEATTLE, Seattle, WA, USA, 27–31 October 2019, pp. 1–7. [CrossRef]
18. Bao, J.; Li, D.; Qiao, X.; Rauschenbach, T. Integrated Navigation for Autonomous Underwater Vehicles in Aquaculture: A Review. *Inf. Process. Agric.* **2019**, *7*, 139–150. [CrossRef]
19. Lee, H.; J.Daehyeonand.; Yu, H.; Ryu, J. Autonomous Underwater Vehicle Control for Fishnet Inspection in Turbid Water Environments. *Int. J. Control. Autom. Syst.* **2022**, *20*, 3383–3392. [CrossRef]
20. Available online: https://www.blueyerobotics.com/products/pro (accessed on 13 April 2023).
21. Available online: https://www.qysea.com/es/products/fifish-v6/ (accessed on 13 April 2023).
22. Available online: https://www.chasing.com/es/chasing-m2.html (accessed on 13 April 2023).
23. Rudnick, D.; Davis, R.; Eriksen, C.; Fratantoni, D.; Perry, M. Underwater Gliders for Ocean Research. *Mar. Technol. Soc. J.* **2004**, *38*, 48–59. [CrossRef]
24. Rudnick, D.; Cole, S. On sampling the ocean using underwater gliders. *J. Geophys. Res.* **2011**, *116*, 1–12. [CrossRef]
25. Waldmann, C.; Kausche, A.; Iversen, M.; Pototzky, A.; Looye, G.; Montenegro, S.; Bachmayer, R.; Wilde, D. MOTH-An underwater glider design study carried out as part of the HGF alliance ROBEX. In Proceedings of the IEEE/OES Autonomous Underwater Vehicles (AUV) Conference, Oxford, MS, USA, 6–9 October 2014; pp. 1–3.
26. Mou, J.; Jia, X.; Chen, P.; Chen, L. Research on operation safety of offshore wind farms. *J. Mar. Sci. Eng.* **2021**, *9*, 881. [CrossRef]
27. Cetin, K.; Suarez Zapico, C.; Tugal, H.; Petillot, Y.; Dunningan, M.; Erden, M. Application of adaptive and switching control for contact maintenance of a robotic vehicle-manipulator system for underwater asset inspection. *Front. Robot. AI* **2021**, *8*, 1–13. [CrossRef]

28. E&T Editorial Staff. Autonomous underwater drones used to maintain offshore wind turbines. *E&T Engineering and Technology*, 23 May 2022.
29. Orekan, T.; Zhang, P.; Shih, C. Analysis, Design, and Maximum Power-Efficiency Tracking for Undersea Wireless Power Transfer. *IEEE J. Emerg. Sel. Top. Power Electron.* **2018**, *6*, 843–854. [CrossRef]
30. Raj, D.; Ko, E.; Yoon, D.; Shin, S.; Park, S.H. Energy Optimization Techniques in Underwater Internet of Things: Issues, State-of-the-Art, and Future Directions. *Water* **2022**, *14*, 3240. [CrossRef]
31. Yang, H.; Lin, C.Y. Promising Strategies for the Reduction of Pollutant Emissions from Working Vessels in Offshore Wind Farms: The Example of Taiwan. *J. Mar. Sci. Eng.* **2022**, *10*, 621. [CrossRef]
32. Chin, C.S.; Jia, J.; Chiew, J.; Toh, W.; Gao, Z.; Zhang, C.; McCann, J. System design of underwater battery power system for marine and offshore industry. *J. Energy Storage* **2019**, *21*, 724–740. [CrossRef]
33. Transeth, A.; Schjølberg, I.; Lekkas, A.M.; Risholm, P.; Mohammed, A.; Skaldebø, M.; Haugaløkken, B.; Bjerkeng, M.; Tsiourva, M.; Py, F. Autonomous subsea intervention (SEAVENTION). *IFAC-PapersOnLine* **2022**, *55*, 387–394. [CrossRef]
34. Viel, C. Self-management of the umbilical of a ROV for underwater exploration. *Ocean Eng.* **2022**, *248*, 110695. [CrossRef]
35. Teague, J.; Allen, M.J.; Scott, T.B. The potential of low-cost ROV for use in deep-sea mineral, ore prospecting and monitoring. *Ocean Eng.* **2018**, *147*, 333–339. [CrossRef]
36. Kapetanović, N.; Krčmar, K.; Mišković, N.; Nad, D. Tether Management System for Autonomous Inspection Missions in Mariculture Using an ASV and an ROV. *IFAC-PapersOnLine* **2022**, *55*, 327–332. [CrossRef]
37. Teeneti, C.R.; Truscott, T.T.; Beal, D.; Pantic, Z. Review of Wireless Charging Systems for Autonomous Underwater Vehicles. *IEEE J. Ocean. Eng.* **2021**, *46*, 68–87. [CrossRef]
38. Jalbert, J.; Baker, J.; Duchesney, J.; Pietryka, P.; Dalton, W.; Blidberg, D.; Chappell, S.; Nitzel, R.; Holappa, K. A solar-powered autonomous underwater vehicle. In Proceedings of the Oceans 2003. Celebrating the Past ... Teaming toward the Future Conference, San Diego, CA, USA, 22–26 September 2003; Volume 2, pp. 1132–1140. [CrossRef]
39. Lu, Z.; Shang, J.; Luo, Z.; Zhu, Y.; Wang, M.; Wang, C. Research on environmental energy-driven intelligent unmanned underwater vehicles and their key technologies. In Proceedings of the 2021 IEEE 4th International Conference on Automation, Electronics and Electrical Engineering (AUTEEE), Shenyang, China, 19–21 November 2021; pp. 564–571. [CrossRef]
40. Driscol, B.P.; Gish, A.; Coe, R.G. Wave-Powered AUV Recharging: A Feasibility Study. In Proceedings of the 2019 International Conference on Offshore Mechanics and Arctic Engineering, Scotland, UK, 9–14 June 2019; pp. 1–8. [CrossRef]
41. Jung, H.; Subban, C.V.; McTigue, J.D.; Martinez, J.J.; Copping, A.E.; Osorio, J.; Liu, J.; Deng, Z.D. Extracting energy from ocean thermal and salinity gradients to power unmanned underwater vehicles: State of the art, current limitations, and future outlook. *Renew. Sustain. Energy Rev.* **2022**, *160*, 1–21. [CrossRef]
42. NOAA/OAR/OER. Mountains in the Sea Expedition 2004. Available online: https://www.flickr.com/photos/noaaphotolib/5424616529/in/photostream/ (accessed on 27 March 2024).
43. Christ, R.D.; Wernli, R.L. Chapter 8—Cables and Connectors. In *The ROV Manual*, 2nd ed.; Christ, R.D., Wernli, R.L., Eds.; Butterworth-Heinemann: Oxford, UK, 2014; pp. 163–220. [CrossRef]
44. Tian, B.; Yu, J. Current status and prospects of marine renewable energy applied in ocean robots. *Int. J. Energy Res.* **2019**, *43*, 2016–2031. [CrossRef]
45. Hildebrandt, M.; Gaudig, C.; Christensen, L.; Natarajan, S.; Carrio, J.H.; Paranhos, P.M.; Kirchner, F. A Validation Process for Underwater Localization Algorithms. *Int. J. Adv. Robot. Syst.* **2014**, *11*, 138. [CrossRef]
46. Song, W.; Cui, W. An Overview of Underwater Connectors. *J. Mar. Sci. Eng.* **2021**, *9*, 813. [CrossRef]
47. Liu, J.; Yu, F.; He, B.; Soares, C.G. A review of underwater docking and charging technology for autonomous vehicles. *Ocean Eng.* **2024**, *297*, 117154. [CrossRef]
48. Brighenti, A.; Zugno, L.; Mattiuzzo, F.; Sperandio, A. EURODOCKER-a universal docking-downloading recharging system for AUVs: Conceptual design results. In Proceedings of the IEEE Oceanic Engineering Society. OCEANS'98. Conference, Nice, France, 28 September–1 October 1998; Volume 3, pp. 1463–1467. [CrossRef]
49. Allen, B.; Austin, T.; Forrester, N.; Goldsborough, R.; Kukulya, A.; Packard, G.; Purcell, M.; Stokey, R. Autonomous Docking Demonstrations with Enhanced REMUS Technology. In Proceedings of the OCEANS 2006 Conference, Boston, MA, USA, 18–21 September 2006; pp. 1–6. [CrossRef]
50. Wirtz, M.; Hildebrandt, M.; Gaudig, C. Design and test of a robust docking system for hovering AUVs. In Proceedings of the 2012 Oceans Conference, Hampton Roads, VA, USA, 14–19 October 2012; pp. 1–6. [CrossRef]
51. Kojiya, T.; Sato, F.; Matsuki, H.; Sato, T. Automatic power supply system to underwater vehicles utilizing non-contacting technology. In Proceedings of the Oceans '04 MTS/IEEE Techno-Ocean '04, Kobe, Japan, 9–12 November 2004; Volume 4, pp. 2341–2345. [CrossRef]
52. Etemadrezaei, M. *22—Wireless Power Transfer*; Butterworth-Heinemann: Oxford, UK, 2018; pp. 711–722. [CrossRef]
53. Saini, P.; Singh, R.P.; Sinha, A. Path loss analysis of RF waves for underwater wireless sensor networks. In Proceedings of the 2017 International Conference on Computing and Communication Technologies for Smart Nation (IC3TSN), Gurgaon, India, 12–14 October 2017; pp. 104–108. [CrossRef]
54. Nguyen, D.H.; Matsushima, T.; Qin, C.; Adachi, C. Toward Thing-to-Thing Optical Wireless Power Transfer: Metal Halide Perovskite Transceiver as an Enabler. *Front. Energy Res.* **2021**, *9*, 1–10. [CrossRef]

55. Ding, J.; Liu, W.; I., C.L.; Zhang, H.; Mei, H. Advanced Progress of Optical Wireless Technologies for Power Industry: An Overview. *Appl. Sci.* **2020**, *10*, 6463. [CrossRef]
56. Kim, S.M.; Choi, J.; Jung, H. Experimental demonstration of underwater optical wireless power transfer using a laser diode. *Chin. Opt. Lett.* **2018**, *16*, 080101. [CrossRef]
57. Kim, S.M.; Kwon, D. Transfer efficiency of underwater optical wireless power transmission depending on the operating wavelength. *Curr. Opt. Photonics* **2020**, *4*, 571–575. [CrossRef]
58. Lin, R.; Liu, X.; Zhou, G.; Qian, Z.; Cui, X.; Tian, P. InGaN Micro-LED Array Enabled Advanced Underwater Wireless Optical Communication and Underwater Charging. *Adv. Opt. Mater.* **2021**, *9*, 2002211. [CrossRef]
59. Basaeri, H.; Christensen, D.B.; Roundy, S. A review of acoustic power transfer for bio-medical implants. *Smart Mater. Struct.* **2016**, *25*, 123001. [CrossRef]
60. Awal, M.R.; Jusoh, M.; Sabapathy, T.; Kamarudin, M.R.; Rahim, R.A. State-of-the-Art Developments of Acoustic Energy Transfer. *Int. J. Antennas Propag.* **2016**, *2016*, 3072528. [CrossRef]
61. Bereketli, A.; Bilgen, S. Remotely Powered Underwater Acoustic Sensor Networks. *IEEE Sens. J.* **2012**, *12*, 3467–3472. [CrossRef]
62. Guida, R.; Demirors, E.; Dave, N.; Rodowicz, J.; Melodia, T. An acoustically powered battery-less internet of underwater things platform. In Proceedings of the 4th Underwater Communications and Networking Conference, UComms 2018, Lerici, Italy, 28–30 August 2018; pp. 1–5. [CrossRef]
63. Zhao, Y.; Du, Y.; Wang, Z.; Wang, J.; Geng, Y. Design of Ultrasonic Transducer Structure for Underwater Wireless Power Transfer System. In Proceedings of the 2021 IEEE Wireless Power Transfer Conference (WPTC), San Diego, CA, USA, 1–4 June 2021; pp. 1–4. [CrossRef]
64. Guida, R.; Demirors, E.; Dave, N.; Melodia, T. Underwater Ultrasonic Wireless Power Transfer: A Battery-Less Platform for the Internet of Underwater Things. *IEEE Trans. Mob. Comput.* **2022**, *21*, 1861–1873. [CrossRef]
65. Yang, H.; Wu, M.; Yu, Z.; Yang, J. An Ultrasonic Through-Metal-Wall Power Transfer System with Regulated DC Output. *Appl. Sci.* **2018**, *8*, 692. [CrossRef]
66. Yang, D.X.; Hu, Z.; Zhao, H.; Hu, H.F.; Sun, Y.Z.; Hou, B.J. Through-Metal-Wall Power Delivery and Data Transmission for Enclosed Sensors: A Review. *Sensors* **2015**, *15*, 31581–31605. [CrossRef]
67. Dai, X.; Li, L.; Li, Y.; Hou, G.; Leung, H.F.; Hu, A.P. Determining the maximum power transfer condition for Ultrasonic Power Transfer system. In Proceedings of the 2016 IEEE 2nd Annual Southern Power Electronics Conference (SPEC), Auckland, New Zealand, 5–8 December 2016; pp. 1–6. [CrossRef]
68. Li, Z.; Zhuang, G.; Wu, Z.; Li, B.; Zhang, X. Modeling of Ultrasonic Wireless Electrical Energy Transfer System. *Huanan Ligong Daxue Xuebao/J. South China Univ. Technol. Nat. Sci.* **2018**, *46*, 72–77. [CrossRef]
69. Sherrit, S.; Bao, X.; Badescu, M.; Aldrich, J.; Bar-Cohen, Y.; Biederman, W.; Chang, Z. KW Power Transmission using Wireless Acoustic-Electric Feed-through (WAEF). In Proceedings of the Earth and Space 2008 Conference, San Diego, CA, USA, 9–11 September 2008; pp. 1–10. [CrossRef]
70. Lawry, T.; Wilt, K.; Ashdown, J.; Scarton, H.; Saulnier, G. A High-Performance Ultrasonic System for the Simultaneous Transmission of Data and Power through Solid Metal Barriers. *IEEE Trans. Ultrason. Ferroelectr. Freq. Control* **2013**, *60*, 194–203. [CrossRef]
71. Jegadeesan, R.; Agarwal, K.; Guo, Y.X.; Yen, S.C.; Thakor, N.V. Wireless Power Delivery to Flexible Subcutaneous Implants Using Capacitive Coupling. *IEEE Trans. Microw. Theory Tech.* **2017**, *65*, 280–292. [CrossRef]
72. Sarin, A.; Abbot, D.; Revzen, S.; Avestruz, A.T. Bidirectional Capacitive Wireless Power Transfer for Energy Balancing in Modular Robots. In Proceedings of the 2020 IEEE Applied Power Electronics Conference and Exposition (APEC), New Orleans, LA, USA, 15–19 March 2020; pp. 852–859. [CrossRef]
73. Wang, K.; Sanders, S. Contactless USB—A capacitive power and bidirectional data transfer system. In Proceedings of the 2014 IEEE Applied Power Electronics Conference and Exposition—APEC 2014, Fort Worth, TX, USA, 16–20 March 2014; pp. 1342–1347. [CrossRef]
74. Lu, F.; Zhang, H.; Mi, C. A Review on Recent Development of Capacitive Wireless Power Transfer Technology. *Energies* **2017**, *10*, 1752. [CrossRef]
75. Lecluyse, C.; Minnaert, B.; Kleemann, M. A Review of the Current State of Technology of Capacitive Wireless Power Transfer. *Energies* **2021**, *14*, 5862. [CrossRef]
76. Liang, J.; Wu, D.; Yu, J. A Design Method of Compensation Circuit for High-Power Dynamic Capacitive Power Transfer System Considering Coupler Voltage Distribution for Railway Applications. *Electronics* **2021**, *10*, 153. [CrossRef]
77. Machura, P.; Li, Q. A critical review on wireless charging for electric vehicles. *Renew. Sustain. Energy Rev.* **2019**, *104*, 209–234. [CrossRef]
78. Cai, C.; Liu, X.; Wu, S.; Chen, X.; Chai, W.; Yang, S. A Misalignment Tolerance and Lightweight Wireless Charging System via Reconfigurable Capacitive Coupling for Unmanned Aerial Vehicle Applications. *IEEE Trans. Power Electron.* **2023**, *38*, 22–26. [CrossRef]
79. Li, C.; Zhao, X.; Liao, C.; Wang, L. A graphical analysis on compensation designs of large-gap CPT systems for EV charging applications. *CES Trans. Electr. Mach. Syst.* **2018**, *2*, 232–242. [CrossRef]
80. Naka, Y.; Yamamoto, K.; Nakata, T.; Tamura, M. Improvement in efficiency of underwater wireless power transfer with electric coupling. *IEICE Trans. Electron.* **2017**, *E100.C*, 850–857. [CrossRef]

81. Naka, Y.; Yamamoto, K.; Nakata, T.; Tamura, M.; Masuda, M. Verification efficiency of electric coupling wireless power transfer in water. In Proceedings of the 2017 IEEE MTT-S International Conference on Microwaves for Intelligent Mobility, ICMIM 2017, Nagoya, Japan, 19–21 March 2017; pp. 83–86. [CrossRef]
82. Urano, M.; Ata, K.; Takahashi, A. Study on underwater wireless power transfer via electric coupling with a submerged electrode. In Proceedings of the IMFEDK 2017—2017 International Meeting for Future of Electron Devices Conference, Kyoto, Japan, 29–30 June 2017; pp. 36–37. [CrossRef]
83. Gao, Z.; Li, Y.; Jing, Q.; Liu, N. Study on the coupling structure of underwater wireless power transmission system via electric coupling. *J. Hohai Univ.* **2018**, *46*, 366–370. [CrossRef]
84. Tamura, M.; Naka, Y.; Murai, K. Design of capacitive coupler in underwater wireless power transfer focusing on kQ product. *IEICE Trans. Electron.* **2018**, *E101C*, 759–766. [CrossRef]
85. Mohamed, A.; Palazzi, V.; Kumar, S.; Alimenti, F.; Mezzanotte, P.; Roselli, L. Towards subsea non-ohmic power transfer via a capacitor-like structure. *Lect. Notes Electr. Eng.* **2019**, *550*, 349–357. [CrossRef]
86. Gao, Z.; Yu, G.; Liu, N. Design of electric-field coupled underwater wireless power transfer system based on class E amplifier. *J. Hohai Univ.* **2019**, *47*, 560–567. [CrossRef]
87. Tamura, M.; Murai, K.; Naka, Y. Capacitive Coupler Utilizing Electric Double Layer for Wireless Power Transfer under Seawater. In Proceedings of the IEEE MTT-S International Microwave Symposium Digest, Boston, MA, USA, 2–7 June 2019; pp. 1415–1418. [CrossRef]
88. Yang, L.; Ju, M.; Zhang, B. Bidirectional Undersea Capacitive Wireless Power Transfer System. *IEEE Access* **2019**, *7*, 121046–121054. [CrossRef]
89. Zhang, H.; Lu, F. Feasibility Study of the High-Power Underwater Capacitive Wireless Power Transfer for the Electric Ship Charging Application. In Proceedings of the 2019 IEEE Electric Ship Technologies Symposium, ESTS 2019, Washington, DC, USA, 14–16 August 2019; pp. 231–235. [CrossRef]
90. Tamura, M.; Murai, K.; Matsumoto, M. Conductive coupler for wireless power transfer under seawater. In Proceedings of the 2020 IEEE MTT-S International Microwave Symposium Digest, Los Angeles, CA, USA, 4–6 August 2020; pp. 1176–1179. [CrossRef]
91. Yang, L.; Ma, L.; Huang, J.; Fu, Y. Characteristics of Undersea Capacitive Wireless Power Transfer System. In Proceedings of the IEEE 9th International Power Electronics and Motion Control Conference, IPEMC 2020 ECCE Asia, Nanjing, China, 29 November–2 December 2020; pp. 2952–2955. [CrossRef]
92. Mahdi, H.; Hoff, B.; Østrem, T. Optimal Solutions for Underwater Capacitive Power Transfer. *Sensors* **2021**, *21*, 8233. [CrossRef]
93. Su, Y.; Qian, L.; Liu, Z.; Deng, R.; Sun, Y. Underwater Electric-Filed Coupled Wireless Power Transfer System with Rotary Coupler and Parameter Optimization Method. *Diangong Jishu Xuebao/Trans. China Electrotech. Soc.* **2022**, *37*, 2399–2410. [CrossRef]
94. Zhang, B.; Chen, J.; Wang, X.; Xu, W.; Lu, C.; Lu, Y. High-Power-Density Wireless Power Transfer System for Autonomous Underwater Vehicle Based on a Variable Ring-Shaped Magnetic Coupler. *IEEE Trans. Transp. Electrif.* **2023**. [CrossRef]
95. Orekan, T.; Zhang, P. *Underwater Wireless Power Transfer: Smart Ocean Energy Converters*; Springer International Publishing: Berlin/Heidelberg, Germany, 2019. [CrossRef]
96. Lu, X.; Niyato, D.; Wang, P.; Kim, D.I.; Han, Z. Wireless Charger Networking for Mobile Devices: Fundamentals, Standards, and Applications. *Wirel. Commun. IEEE* **2014**, *22*, 126–135. [CrossRef]
97. Ahn, D.; Mercier, P.P. Wireless Power Transfer with Concurrent 200-kHz and 6.78-MHz Operation in a Single-Transmitter Device. *IEEE Trans. Power Electron.* **2016**, *31*, 5018–5029. [CrossRef]
98. Berger, A.; Agostinelli, M.; Sandner, C.; Vesti, S.; Huemer, M. High efficient integrated power receiver for a Qi compliant Wireless Power Transfer system. In Proceedings of the 2016 IEEE Wireless Power Transfer Conference (WPTC), Aveiro, Portugal, 5–6 May 2016; pp. 1–4. [CrossRef]
99. Shah, S.A.A.; Khan, D.; Ain, Q.; Basim, M.; Shehzad, K.; Verma, D.; Kumar, P.; Yoo, J.M.; Pu, Y.G.; Jung, Y.; et al. A Design of Wireless Power Receiver with Gate Charge Recycled Dual-Mode Active Rectifier and Step-Down Converter with 88.2% System Efficiency for Power Management IC. *IEEE Trans. Power Electron.* **2023**, *38*, 1348–1360. [CrossRef]
100. Rooij, M.D.; Zhang, Y. A 10 W Multi-Mode Capable Wireless Power Amplifier for Mobile Devices. In Proceedings of the 2016 International Exhibition and Conference for Power Electronics, Intelligent Motion, Renewable Energy and Energy Management, Nuremberg, Germany, 10–12 May 2016; pp. 1–8.
101. Park, Y.J.; Jang, B.; Park, S.M.; Ryu, H.C.; Oh, S.J.; Kim, S.Y.; Pu, Y.; Yoo, S.S.; Hwang, K.C.; Yang, Y.; et al. A Triple-Mode Wireless Power-Receiving Unit with 85.5% System Efficiency for A4WP, WPC, and PMA Applications. *IEEE Trans. Power Electron.* **2018**, *33*, 3141–3156. [CrossRef]
102. Basar, M.R.; Ahmad, M.Y.; Cho, J.; Ibrahim, F. An improved resonant wireless power transfer system with optimum coil configuration for capsule endoscopy. *Sens. Actuators A Phys.* **2016**, *249*, 207–216. [CrossRef]
103. Vulfin, V.; Sayfan-Altman, S.; Ianconescu, R. Wireless power transfer for a pacemaker application. *J. Med. Eng. Technol.* **2017**, *41*, 325–332. [CrossRef]
104. Ahire, D.; Gond, V.J.; Chopade, J.J. Coil material and magnetic shielding methods for efficient wireless power transfer system for biomedical implant application. *Biosens. Bioelectron. X* **2022**, *10*, 100123. [CrossRef]
105. Sun, T.; Xie, X.; Wang, Z. *Wireless Power Transfer for Medical Microsystems*; Springer: New York, NY, USA, 2013; pp. 1–183. [CrossRef]

106. Yilmaz, G.; Dehollain, C. *Wireless Power Transfer and Data Communication for Neural Implants: Case Study*; Springer: Berlin/Heidelberg, Germany, 2017; pp. 1–109.
107. Ahire, D.; Gond, V.J.; Chopade, J.J. Compensation topologies for wireless power transmission system in medical implant applications: A review. *Biosens. Bioelectron. X* **2022**, *11*, 100180. [CrossRef]
108. Sagar, A.; Kashyap, A.; Nasab, M.A.; Padmanaban, S.; Bertoluzzo, M.; Kumar, A.; Blaabjerg, F. A Comprehensive Review of the Recent Development of Wireless Power Transfer Technologies for Electric Vehicle Charging Systems. *IEEE Access* **2023**, *11*, 83703–83751. [CrossRef]
109. Rayan, B.A.; Subramaniam, U.; Balamurugan, S. Wireless Power Transfer in Electric Vehicles: A Review on Compensation Topologies, Coil Structures, and Safety Aspects. *Energies* **2023**, *16*, 3084. [CrossRef]
110. Dankov, D.; Prodanov, P.; Madjarov, N. Application of an Inductive Power Transfer System for Charging Modern Electric Vehicles. In Proceedings of the 17th Conference on Electrical Machines, Drives and Power Systems (ELMA), Sofia, Bulgaria, 1–4 July 2021; pp. 1–6. [CrossRef]
111. Zhang, Z.; Pang, H., WPT for High-power Application – Electric Vehicles. In *Wireless Power Transfer: Principles and Applications*; John Wiley Sons, Inc.: Hoboken, NJ, USA, 2023; pp. 275–325. [CrossRef]
112. Zhang, X.; Yuan, Z.; Yang, Q.; Li, Y.; Zhu, J.; Li, Y. Coil Design and Efficiency Analysis for Dynamic Wireless Charging System for Electric Vehicles. *IEEE Trans. Magn.* **2016**, *52*, 1–4. [CrossRef]
113. Tan, Z.; Liu, F.; Chan, H.K.; Gao, H.O. Transportation systems management considering dynamic wireless charging electric vehicles: Review and prospects. *Transp. Res. Part E Logist. Transp. Rev.* **2022**, *163*, 1–17. [CrossRef]
114. Panchal, C.; Stegen, S.; Lu, J. Review of static and dynamic wireless electric vehicle charging system. *Eng. Sci. Technol. Int. J.* **2018**, *21*, 922–937. [CrossRef]
115. Ramakrishnan, V.; Savio A, D.; C, B.; Rajamanickam, N.; Kotb, H.; Elrashidi, A.; Nureldeen, W. A Comprehensive Review on Efficiency Enhancement of Wireless Charging System for the Electric Vehicles Applications. *IEEE Access* **2024**, *12*, 46967–46994. [CrossRef]
116. Ali, R.A.; Latif, M.H.; Usman, M. Existing Coil Topologies for Inductive Power Transfer in EV Charging: A Review. In Proceedings of the 5th International Conference on Energy Conservation and Efficiency (ICECE), Lahore, Pakistan, 16–17 March 2022; pp. 1–13. [CrossRef]
117. Song, K.; Lan, Y.; Zhang, X.; Jiang, J.; Sun, C.; Yang, G.; Yang, F.; Lan, H. A Review on Interoperability of Wireless Charging Systems for Electric Vehicles. *Energies* **2023**, *16*, 1653. [CrossRef]
118. Guidi, G.; Suul, J.A.; Jenset, F.; Sorfonn, I. Wireless Charging for Ships: High-Power Inductive Charging for Battery Electric and Plug-In Hybrid Vessels. *IEEE Electrif. Mag.* **2017**, *5*, 22–32. [CrossRef]
119. Feezor, M.; Blankinship, P.; Bellingham, J.; Sorrell, F. Autonomous underwater vehicle homing/docking via electromagnetic guidance. In Proceedings of the Oceans '97. MTS/IEEE Conference, Halifax, NS, Canada 6–9 October 1997; Volume 2, pp. 1137–1142. [CrossRef]
120. Fukasawa, T.; Noguchi, T.; Kawasaki, T.; Baino, M. "MARINE BIRD", a new experimental AUV with underwater docking and recharging system. In Proceedings of the Oceans 2003. Celebrating the Past ... Teaming Toward the Future Conference, San Diego, CA, USA, 22–26 September 2003; Volume 4, pp. 2195–2200. [CrossRef]
121. McGinnis, T.; Henze, C.P.; Conroy, K. Inductive Power System for Autonomous Underwater Vehicles. In Proceedings of the OCEANS 2007 Conference, Aberdeen, Scotland, 18–21 June 2007; pp. 1–5. [CrossRef]
122. Hobson, B.W.; McEwen, R.S.; Erickson, J.; Hoover, T.; McBride, L.; Shane, F.; Bellingham, J.G. The Development and Ocean Testing of an AUV Docking Station for a 21" AUV. In Proceedings of the OCEANS 2007 Conference, Aberdeen, Scotland, 18–21 June 2007; pp. 1–6. [CrossRef]
123. Pyle, D.; Granger, R.; Geoghegan, B.; Lindman, R.; Smith, J. Leveraging a large UUV platform with a docking station to enable forward basing and persistence for light weight AUVs. In Proceedings of the 2012 Oceans Conference, Virginia Beach, VA, USA, 14–19 October 2012; pp. 1–8. [CrossRef]
124. Yoshida, S.; Tanomura, M.; Hama, Y.; Hirose, T.; Suzuki, A.; Matsui, Y.; Sogo, N.; Sato, R. Underwater wireless power transfer for non-fixed unmanned underwater vehicle in the ocean. In Proceedings of the Autonomous Underwater Vehicles 2016 Conference, AUV 2016, Tokyo, Japan, 6–9 November 2016; pp. 177–180. [CrossRef]
125. Yoshida, H.; Ishibashi, S.; Yutaka, O.; Sugesawa, M.; Tanaka, K. A concept design of underwater docking robot and development of its fundamental technologies. In Proceedings of the 2016 IEEE Autonomous Underwater Vehicles Conference, Tokyo, Japan, 6–9 November 2016; pp. 408–411. [CrossRef]
126. Maguer, A.; Been, R.; Tesei, A.; Alves, J.; Grandi, V.; Biagini, S. Recent Technological Advances in Underwater Autonomy. In Proceedings of the 2018 OCEANS - MTS/IEEE Kobe Techno-Oceans (OTO) Conference, Kobe, Japan, 28–31 May 2018; pp. 1–8. [CrossRef]
127. Matsuda, T.; Maki, T.; Masuda, K.; Sakamaki, T. Resident autonomous underwater vehicle: Underwater system for prolonged and continuous monitoring based at a seafloor station. *Robot. Auton. Syst.* **2019**, *120*, 103231. [CrossRef]
128. Matsuda, T.; Maki, T.; Masuda, K.; Sakamaki, T.; Ohkuma, K. Port Experiments of the Docking and Charging System Using an AUV and a Seafloor Station: Towards Long-term Seafloor Observation. In Proceedings of the 2018 IEEE/OES Autonomous Underwater Vehicle Workshop, Porto, Portugal, 6–9 November 2018; pp. 1–5. [CrossRef]

129. Yang, C.; Lin, M.; Li, D. Improving Steady and Starting Characteristics of Wireless Charging for an AUV Docking System. *IEEE J. Ocean. Eng.* **2020**, *45*, 430–441. [CrossRef]
130. Heeres, B.; Novotny, D.; Divan, D.; Lorenz, R. Contactless underwater power delivery. In Proceedings of the 1994 Power Electronics Specialist Conference—PESC'94, Taipei, Taiwan, 20–25 June 1994; Volume 1, pp. 418–423. [CrossRef]
131. Huang, Y.; Fang, C.; Li, X. Contactless power and data transmission for underwater sensor nodes. *EURASIP J. Wirel. Commun. Netw.* **2013**, *2013*, 81–87. [CrossRef]
132. Lin, C.; Wang, K.; Chu, Z.; Wang, K.; Deng, J.; Obaidat, M.; Wu, G. Hybrid charging scheduling schemes for three-dimensional underwater wireless rechargeable sensor networks. *J. Syst. Softw.* **2018**, *146*, 42–58. [CrossRef]
133. Hwangbo, S.H.; Jeon, J.H.; Park, S.J. Wireless Underwater Monitoring Systems Based on Energy Harvestings. *Sens. Transducers* **2013**, *18*, 113–119.
134. Santana Sosa, G.; Santana Abril, J.; Sosa, J.; Montiel-Nelson, J.A.; Bautista, T. Design of a Practical Underwater Sensor Network for Offshore Fish Farm Cages. *Sensors* **2020**, *20*, 4459. [CrossRef]
135. Santana Abril, J.; Santana Sosa, G.; Sosa, J.; Bautista, T.; Montiel-Nelson, J. A Novel Charging Method for Underwater Batteryless Sensor Node Networks. *Sensors* **2021**, *21*, 557. [CrossRef]
136. Zhang, S.; Huang, X.; Du, Z. Charging path planning algorithm based on multi-parameters in underwater wireless rechargeable sensor network. *J. Phys. Conf. Ser.* **2021**, *1732*, 012077. [CrossRef]
137. Ahluwalia, U.; Chenevert, G.; Pratik, U.; Pantic, Z. System for Wireless Charging of Battery-Powered Underwater Sensor Networks. In Proceedings of the Oceans Conference Record (IEEE) 2022, Hampton Roads, VA, USA, 17–20 October 2022. [CrossRef]
138. Ma, Y.; Mao, Z.; Zhang, K. Optimization Design of Planar Circle Coil for Limited-Size Wireless Power Transfer System. *Appl. Sci.* **2022**, *12*, 2286. [CrossRef]
139. Zhang, B.; Wang, X.; Lu, C.; Lu, Y.; Xu, W. A wireless power transfer system for an autonomous underwater vehicle based on lightweight universal variable ring-shaped magnetic coupling. *Int. J. Circuit Theory Appl.* **2023**, *51*, 2654–2673. [CrossRef]
140. Sohn, Y.H.; Choi, B.H.; Lee, E.S.; Lim, G.C.; Cho, G.H.; Rim, C.T. General Unified Analyses of Two-Capacitor Inductive Power Transfer Systems: Equivalence of Current-Source SS and SP Compensations. *IEEE Trans. Power Electron.* **2015**, *30*, 6030–6045. [CrossRef]
141. Yan, Z.; Zhang, Y.; Zhang, K.; Song, B.; Li, S.; Kan, T.; Mi, C. Fault-Tolerant Wireless Power Transfer System with a Dual-Coupled LCC-S Topology. *IEEE Trans. Veh. Technol.* **2019**, *68*, 11838–11846. [CrossRef]
142. Kong, F.; Qu, X. Low Eddy Current Loss Constant Voltage Wireless Power Transfer System in Seawater. In Proceedings of the 2022 IEEE International Power Electronics and Application Conference and Exposition, Guangzhou, China, 4–7 November 2022; pp. 1342–1347. [CrossRef]
143. Yan, Z.; Zhang, Y.; Song, B.; Zhang, K.; Kan, T.; Mi, C. An LCC-p compensated wireless power transfer system with a constant current output and reduced receiver size. *Energies* **2019**, *12*, 172. [CrossRef]
144. Qiao, K.; Rong, E.; Sun, P.; Zhang, X.; Sun, J. Design of LCC-P Constant Current Topology Parameters for AUV Wireless Power Transfer. *Energies* **2022**, *15*, 5249. [CrossRef]
145. Yan, Z.; Song, B.; Zhang, Y.; Zhang, K.; Mao, Z.; Hu, Y. A Rotation-Free Wireless Power Transfer System with Stable Output Power and Efficiency for Autonomous Underwater Vehicles. *IEEE Trans. Power Electron.* **2019**, *34*, 4005–4008. [CrossRef]
146. Wen, H.; Li, J.; Yang, L.; Tong, X. Feasibility Study on Wireless Power Transfer for AUV with Novel Pressure-Resistant Ceramic Materials. In Proceedings of the 2022 International Power Electronics Conference (IPEC-Himeji 2022- ECCE Asia), Himeji, Japan, 15–19 May 2022; pp. 182–185. [CrossRef]
147. Zhou, Y.; Wang, Q.; Qiu, M.; Zhang, X. Research on Bilateral LCC Compensation Network of Underwater Wireless Charging System with Multi-resonance Point Switching. In Proceedings of the 2023 International Conference on Wireless Power Transfer (ICWPT2023), Weihai, China, 13–15 October 2023; Cai, C., Qu, X., Mai, R., Zhang, P., Chai, W., Wu, S., Eds.; Springer: Singapore, 2024; pp. 298–319.
148. Goncalves, F.; Duarte, C.; Pessoa, L. A Novel Circuit Topology for Underwater Wireless Power Transfer. In Proceedings of the 2nd International Conference on Systems Informatics, Modelling and Simulation, Okinawa, Japan, 24–26 November 2017; pp. 181–186. [CrossRef]
149. Imura, T. Chapter Comparison between Electromagnetic Induction and Magnetic Resonance Coupling; In *Wireless Power Transfer: Using Magnetic and Electric Resonance Coupling Techniques*; Springer: Singapore, 2020; pp. 113–174. [CrossRef]
150. Jenkins, A.; Bana, V.; Anderson, G. Impedance of a coil in seawater. In Proceedings of the 2014 IEEE Antennas and Propagation Society International Symposium (APSURSI), Memphis, TN, USA, 6–11 July 2014; pp. 625–626. [CrossRef]
151. Cheng, Z.; Lei, Y.; Song, K.; Zhu, C. Design and Loss Analysis of Loosely Coupled Transformer for an Underwater High-Power Inductive Power Transfer System. *IEEE Trans. Magn.* **2015**, *51*, 1–10. [CrossRef]
152. Niu, W.; Gu, W.; Chu, J. Experimental investigation of frequency characteristics of underwater wireless power transfer. In Proceedings of the 2018 IEEE MTT-S International Wireless Symposium, IWS 2018, Chengdu, China, 6–10 May 2018; pp. 1–3. [CrossRef]
153. Rozas Holgado, I.; Martínez de Alegría, I.; Kortabarria, I.; Andreu, J.; Martín, J.L. Wireless Power Transfer: Underwater loss analysis for different topologies and frequency values. In Proceedings of the IECON 2020 Conference, Singapore, 18–21 October 2020; pp. 3942–3947. [CrossRef]

154. Li, J.; Liu, K.; Xie, J.; Zhu, C.; Zhang, X. Frequency Optimization Method for Underwater Wireless Power Transfer Considering Coupling Conditions. In Proceedings of the 2022 IEEE Energy Conversion Congress and Exposition, ECCE 2022, Detroit, MI, USA, 9–13 October 2022; pp. 1–6. [CrossRef]
155. Li, W.; Zhu, J.; Wang, Y.; Liu, B. Modeling and Characteristic Analysis of Magnetic Coupling Mechanism in Seawater Environment. *IEEE Trans. Magn.* **2022**, *58*, 1–6. [CrossRef]
156. Niu, W.; Gu, W.; Chu, J.; Shen, A. Frequency splitting of underwater wireless power transfer. In Proceedings of the 2016 IEEE International Workshop on Electromagnetics, iWEM 2016, Nanjing, China, 16–18 May 2016; pp. 1–3. [CrossRef]
157. Yan, Z.; Zhang, Y.; Kan, T.; Lu, F.; Zhang, K.; Song, B.; Mi, C. Frequency optimization of a loosely coupled underwater wireless power transfer system considering eddy current loss. *IEEE Trans. Ind. Electron.* **2019**, *66*, 3468–3476. [CrossRef]
158. Zhang, K.; Ma, Y.; Yan, Z.; Di, Z.; Song, B.; Hu, A. Eddy Current Loss and Detuning Effect of Seawater on Wireless Power Transfer. *IEEE J. Emerg. Sel. Top. Power Electron.* **2020**, *8*, 909–917. [CrossRef]
159. Bana, V.; Kerber, M.; Anderson, G.; Rockway, J.; Phipps, A. Underwater wireless power transfer for maritime applications. In Proceedings of the 2015 IEEE Wireless Power Transfer Conference, WPTC 2015, Boulder, CO, USA, 13–15 May 2015; pp. 1–4. [CrossRef]
160. Mohsan, S.A.H.; Khan, M.A.; Mazinani, A.; Alsharif, M.H.; Cho, H.S. Enabling Underwater Wireless Power Transfer towards Sixth Generation (6G) Wireless Networks: Opportunities, Recent Advances, and Technical Challenges. *J. Mar. Sci. Eng.* **2022**, *10*, 1282. [CrossRef]
161. Zhang, K.H.; Zhu, Z.B.; Song, B.W.; Xu, D.M. A power distribution model of magnetic resonance WPT system in seawater. In Proceedings of the 2016 IEEE 2nd Annual Southern Power Electronics Conference, SPEC 2016, Auckland, New Zealand, 5–8 December 2016; pp. 1–4. [CrossRef]
162. Hayslett, T.; Orekan, T.; Zhang, P. Underwater wireless power transfer for ocean system applications. In Proceedings of the OCEANS 2016 Conference, Washington, DC, USA, 15–16 September 2016; pp. 1–6. [CrossRef]
163. Niu, W.; Ye, C.; Gu, W. Circuit coupling model containing equivalent eddy current loss impedance for wireless power transfer in seawater. *Int. J. Circuits Syst. Signal Process.* **2021**, *15*, 410–416. [CrossRef]
164. Xu, F.; Huang, H. Frequency selection for underwater wireless power transfer based on the analysis of eddy current loss. *AEU—Int. J. Electron. Commun.* **2023**, *163*, 154618. [CrossRef]
165. Li, Z.; Li, D.; Lin, L.; Chen, Y. Design considerations for electromagnetic couplers in contactless power transmission systems for deep-sea applications. *J. Zhejiang Univ. Sci. C* **2010**, *11*, 824–834. [CrossRef]
166. Yan, Z.; Song, B.; Zhang, K.; Wen, H.; Mao, Z.; Hu, Y. Eddy current loss analysis of underwater wireless power transfer systems with misalignments. *AIP Adv.* **2018**, *8*, 1–6. [CrossRef]
167. Mostafa, A.; Wang, Y.; Zhang, H.; Tangirala, S.; Lu, F. An Ultra-Fast Wireless Charging System with a Hull-Compatible Coil Structure for Autonomous Underwater Vehicles (AUVs). In Proceedings of the 2022 IEEE Transportation Electrification Conference and Expo (ITEC), Anaheim, CA, USA, 15–17 June 2022; pp. 279–284. [CrossRef]
168. Goncalves, F.; Pereira, A.; Morais, A.; Duarte, C.; Gomes, R.; Pessoa, L. An adaptive system for underwater wireless power transfer. In Proceedings of the International Congress on Ultra Modern Telecommunications and Control Systems and Workshops, Lisbon, Portugal, 18–20 October 2016; pp. 101–105. [CrossRef]
169. Lopes, I.F.; Coelho, D.C.; Aguilar Bojorge, E.V.; Andrade de Oliveira, L.R.; Oliveira Almeida, A.; Barbosa, P.G. Underwater Wireless Power Transfer with High Tolerance to Misalignments. In Proceedings of the 2021 Brazilian Power Electronics Conference, João Pessoa, Brazil, 7–10 November 2021; pp. 1–5. [CrossRef]
170. Mototani, S.; Yamamoto, R.; Doki, K.; Torii, A. Effect of Angle Offset of the Power Receiving Coil in Underwater Wireless Power Transfer Using a Cone Spiral Coil. In Proceedings of the 2022 International Power Electronics Conference, IPEC, Himeji, Japan, 15–19 May 2022; pp. 167–174. [CrossRef]
171. Zeng, Y.; Rong, C.; Lu, C.; Tao, X.; Liu, X.; Liu, R.; Liu, M. Misalignment Insensitive Wireless Power Transfer System Using a Hybrid Transmitter for Autonomous Underwater Vehicles. *IEEE Trans. Ind. Appl.* **2022**, *58*, 1298–1306. [CrossRef]
172. Wang, D.; Chen, F.; Zhang, J.; Cui, S.; Bie, Z.; Zhu, C. A Novel Pendulum-Type Magnetic Coupler with High Misalignment Tolerance for AUV Underwater Wireless Power Transfer Systems. *IEEE Trans. Power Electron.* **2023**, *38*, 14861–14871. [CrossRef]
173. Kang, L.; Hu, Y.; Zheng, W. Maximum power efficiency tracking on underwater magnetic resonant wireless power transfer system. *Harbin Gongcheng Daxue Xuebao/J. Harbin Eng. Univ.* **2017**, *38*, 829–835. [CrossRef]
174. Lopes, I.; Lacerda Valle, R.; Azevedo Fogli, G.; Ferreira, A.; Gomes Barbosa, P. Low-Frequency Underwater Wireless Power Transfer: Maximum Efficiency Tracking Strategy. *IEEE Lat. Am. Trans.* **2020**, *18*, 1200–1208. [CrossRef]
175. Zheng, Z.; Wang, N.; Ahmed, S. Maximum efficiency tracking control of underwater wireless power transfer system using artificial neural networks. *Proc. Inst. Mech. Eng. Part I J. Syst. Control Eng.* **2021**, *235*, 1819–1829. [CrossRef]
176. Hassnain Mohsan, S.; Islam, A.; Khan, M.; Mahmood, A.; Rokia, L.; Mazinani, A.; Amjad, H. A review on research challenges, limitations and practical solutions for underwater wireless power transfer. *Int. J. Adv. Comput. Sci. Appl.* **2020**, *11*, 554–562. [CrossRef]
177. Flemming, H.C. *Microbial Biofouling: Unsolved Problems, Insufficient Approaches, and Possible Solutions*; Springer: Berlin/Heidelberg, Germany, 2011; Volume 5, pp. 81–109. [CrossRef]
178. Anderson, G.; Bana, V.; Kerber, M.; Phipps, A.; Rockway, J.D. *Marine Fouling and Thermal Dissipation of Undersea Wireless Power Transfer*; Technical Report; Space and Naval Warfare Systems Center Pacific (SPAWAR): San Diego, CA, USA, 2014.

179. Pittini, R.; Hernes, M.; Petterteig, A. Pressure Tolerant Power Electronics for Deep and Ultra-Deep Water. *Oil Gas Facil.* **2011**, *1*, 47–52. [CrossRef]
180. AG, T.E. *The Impact of Pressure on Ferrites*; Technical Report; TDK Electronics AG (Previously EPCOS): Munich, Germany, 2009.
181. Pereira, P.; Campilho, R.; Pinto, A. Application of a Design for Excellence Methodology for a Wireless Charger Housing in Underwater Environments. *Machines* **2022**, *10*, 232. [CrossRef]
182. Nyqvist, D.; Durif, C.; Johnsen, M.G.; De Jong, K.; Forland, T.N.; Sivle, L.D. Electric and magnetic senses in marine animals, and potential behavioral effects of electromagnetic surveys. *Mar. Environ. Res.* **2020**, *155*, 104888. [CrossRef] [PubMed]
183. Hutchison, Z.L.; Gill, A.B.; Sigray, P.; He, H.; King, J.W. Anthropogenic electromagnetic fields (EMF) influence the behaviour of bottom-dwelling marine species. *Sci. Rep.* **2020**, *10*, 4219. [CrossRef] [PubMed]
184. Wang, Y.; Song, B.; Mao, Z. Application of shielding coils in underwater wireless power transfer systems. *J. Mar. Sci. Eng.* **2019**, *7*, 267. [CrossRef]
185. Yang, L.; Zhang, Y.; Li, X.; Feng, B.; Huang, J.; Zhu, D.; Zhang, A.; Tong, X. The Impact of Metal Hull of AUVs for Underwater Wireless Power Transfer System. In Proceedings of the 2022 International Conference on Wireless Power Transfer (ICWPT2022), Chongqing, China, 28–31 October 2022; pp. 218–228. [CrossRef]
186. Subsea Docking Station (SDS). 2019. Available online: https://www.bluelogic.no/news-and-media/subsea-docking-station-sds (accessed on 13 April 2023).
187. Rolland, E.S.; Haji, M.N.; Weck, O.L. Autonomous Control of a Prototype Solar-powered Offshore AUV Servicing Platform. In Proceedings of the OCEANS 2021 Conference, San Diego, CA, USA, 20–23 September 2021; pp. 1–10. [CrossRef]
188. Sun, X.Y.; Deng, B.; Zhang, J.; Kelly, M.; Alam, R.; Makiharju, S. Reimagining Autonomous Underwater Vehicle Charging Stations with Wave Energy. *Berkeley Sci. J.* **2021**, *25*, 74–78. [CrossRef]
189. Zhou, J.; Yao, P.; Chen, Y.; Guo, K.; Hu, S.; Sun, H. Design Considerations for a Self-Latching Coupling Structure of Inductive Power Transfer for Autonomous Underwater Vehicle. *IEEE Trans. Ind. Appl.* **2021**, *57*, 580–587. [CrossRef]
190. Hasaba, R.; Eguchi, K.; Yamaguchi, S.; Satoh, H.; Yagi, T.; Koyanagi, Y. WPT System in Seawater for AUVs with kW-class Power, High Positional Freedom, and High Efficiency inside the Transfer Coils. In Proceedings of the 2022 Wireless Power Week Conference, Bordeaux, France, 5–8 July 2022; pp. 90–94. [CrossRef]
191. Wu, B.; Liu, J.; Yu, H.; Li, Z.; Chen, Y. Underwater high-power inductive coupling energy transmission system. In Proceedings of the OCEANS 2016 Conference, Washington, DC, USA, 15–16 September 2016; pp. 1–5. [CrossRef]
192. Meşe, H.; Budak, M.A. Efficiency Investigation of a 400W Resonant Inductive Wireless Power Transfer System for Underwater Unmanned Vehicles. In Proceedings of the 2020 IEEE Wireless Power Transfer Conference (WPTC), Seoul, Republic of Korea, 15–19 November 2020; pp. 223–226. [CrossRef]
193. Liu, Z.; Wang, L.; Guo, Y.; Tao, C. Eddy current loss analysis of wireless power transfer system for autonomous underwater vehicles. In Proceedings of the 2020 IEEE PELS Workshop on Emerging Technologies: Wireless Power Transfer, WoW 2020, Seoul, Republic of Korea, 15–19 November 2020; pp. 283–287. [CrossRef]
194. Lin, M.; Li, D.; Yang, C. Design of an ICPT system for battery charging applied to underwater docking systems. *Ocean Eng.* **2017**, *145*, 373–381. [CrossRef]
195. Song, B.; Wang, Y.; Zhang, K.; Mao, Z. Research on wireless power transfer system for Torpedo autonomous underwater vehicles. *Adv. Mech. Eng.* **2018**, *10*, 1–8. [CrossRef]
196. Guo, K.; Zhou, J.; Sun, H.; Yao, P. Design Considerations for a Position-Adaptive Contactless Underwater Power Deliver System. In Proceedings of the 22nd International Conference on Electrical Machines and Systems, ICEMS 2019, Harbin, China, 11–14 August 2019; pp. 1–6. [CrossRef]
197. Liu, P.; Gao, T.; Zhao, R.; Mao, Z. A Novel Conformal Coil Structure Design of Wireless Power Transfer System for Autonomous Underwater Vehicles. *J. Mar. Sci. Eng.* **2022**, *10*, 875. [CrossRef]
198. Zhang, K.; Dai, F.; Li, X.; Yan, Z.; Zhang, F.; Mao, Z.; Hu, A.P. Analysis of Power Transfer Characteristics of IPT System with Near Field Magnetic Coupling. *IEEE Trans. Electromagn. Compat.* **2023**, *65*, 890–899. [CrossRef]
199. Wen, H.; Wang, P.; Li, J.; Yang, J.; Zhang, K.; Yang, L.; Zhao, Y.; Tong, X. Improving the Misalignment Tolerance of Wireless Power Transfer System for AUV with Solenoid-Dual Combined Planar Magnetic Coupler. *J. Mar. Sci. Eng.* **2023**, *11*, 1571. [CrossRef]
200. Shi, J.G.; Li, D.J.; Yang, C.J. Design and analysis of an underwater inductive coupling power transfer system for autonomous underwater vehicle docking applications. *J. Zhejiang Univ.—Sci. C* **2014**, *15*, 51–62. [CrossRef]
201. Shizuno, K.; Yoshida, S.; Tanomura, M.; Hama, Y. Long distance high efficient underwater wireless charging system using dielectric-assist antenna. In Proceedings of the 2014 OCEANS Conference, Washington, DC, USA, 16–17 June 2014; pp. 1–3. [CrossRef]
202. Santos, H.; Pereira, M.; Pessoa, L.; Salgado, H. Design and optimization of air core spiral resonators for magnetic coupling wireless power transfer on seawater. In Proceedings of the 2016 IEEE Wireless Power Transfer Conference, WPTC 2016, Aveiro, Portugal, 5–6 May 2016; pp. 1–4. [CrossRef]
203. Ressurreição, T.; Gonçalves, F.; Duarte, C.; Gonçalves, R.; Gomes, R.; Santos, R.; Esteves, R.; Pinto, P.; Oliveira, I.; Pessoa, L.M. System design for wireless powering of AUVs. In Proceedings of the OCEANS 2017 Conference, New York, NY, USA, 5–9 June 2017; pp. 1–6. [CrossRef]
204. Silva, M.; Duarte, C.; Goncalves, F.; Correia, V.; Pessoa, L. Power Transmitter Design for Underwater WPT. In Proceedings of the OCEANS 2019 Marseille Conference, Marseilles, France, 17–20 June 2019; pp. 1–5. [CrossRef]

205. Dou, Y.; Zhao, D.; Ouyang, Z.; Andersen, M. Investigation and design of wireless power transfer system for autonomous underwater vehicle. In Proceedings of the IEEE Applied Power Electronics Conference and Exposition—APEC, Anaheim, CA, USA, 17–21 March 2019; pp. 3144–3150. [CrossRef]
206. Anyapo, C.; Intani, P. Wireless power transfer for autonomous underwater vehicle. In Proceedings of the 2020 IEEE PELS Workshop on Emerging Technologies: Wireless Power Transfer, WoW 2020, Seoul, Republic of Korea, 15–19 November 2020; pp. 246–249. [CrossRef]
207. Pereira, M.; Santos, H.; Pessoa, L.; Salgado, H. Simulation and experimental evaluation of a resonant magnetic wireless power transfer system for seawater operation. In Proceedings of the OCEANS 2016 Conference, Washington, DC, USA, 15–16 September 2016; pp. 1–5. [CrossRef]
208. Manikandan, J.; Vishwanath, A.; Korulla, M. Design of a 1kW Underwater Wireless Charging Station for Underwater Data Gathering Systems. In Proceedings of the 2018 International Conference on Advances in Computing, Communications and Informatics (ICACCI), Kochi, India, 13–15 September 2018; pp. 211–216. [CrossRef]
209. Cai, C.; Qin, M.; Wu, S.; Yang, Z. A Strong Misalignmentt Tolerance Magnetic Coupler for Autonomous Underwater Vehicle Wireless Power Transfer System. In Proceedings of the 2018 IEEE International Power Electronics and Application Conference and Exposition (PEAC), Shenzhen, China, 4–7 November 2018; pp. 1–5. [CrossRef]
210. Wang, D.; Cui, S.; Zhang, J.; Bie, Z.; Song, K.; Zhu, C. A Novel Arc-Shaped Lightweight Magnetic Coupler for AUV Wireless Power Transfer. *IEEE Trans. Ind. Appl.* **2022**, *58*, 1315–1329. [CrossRef]
211. Cai, C.; Zhang, Y.; Wu, S.; Liu, J.; Zhang, Z.; Jiang, L. A Circumferential Coupled Dipole-Coil Magnetic Coupler for Autonomous Underwater Vehicles Wireless Charging Applications. *IEEE Access* **2020**, *8*, 65432–65442. [CrossRef]
212. Qiao, K.; Sun, P.; Rong, E.; Sun, J.; Zhou, H.; Wu, X. Anti-misalignment and lightweight magnetic coupler with H-shaped receiver structure for AUV wireless power transfer. *IET Power Electron.* **2022**, *15*, 1843–1857. [CrossRef]
213. Zeng, Y.; Lu, C.; Liu, R.; He, X.; Rong, C.; Liu, M. Wireless Power and Data Transfer System Using Multidirectional Magnetic Coupler for Swarm AUVs. *IEEE Trans. Power Electron.* **2023**, *38*, 1440–1444. [CrossRef]
214. Kan, T.; Mai, R.; Mercier, P.P.; Mi, C.C. Design and Analysis of a Three-Phase Wireless Charging System for Lightweight Autonomous Underwater Vehicles. *IEEE Trans. Power Electron.* **2018**, *33*, 6622–6632. [CrossRef]
215. Yan, Z.; Zhang, Y.; Zhang, K.; Song, B.; Mi, C. Underwater wireless power transfer system with a curly coil structure for AUVs. *IET Power Electron.* **2019**, *12*, 2559–2565. [CrossRef]
216. Cai, C.; Wu, S.; Zhang, Z.; Jiang, L.; Yang, S. Development of a Fit-to-Surface and Lightweight Magnetic Coupler for Autonomous Underwater Vehicle Wireless Charging Systems. *IEEE Trans. Power Electron.* **2021**, *36*, 9927–9940. [CrossRef]
217. Lin, M.; Lin, R.; Li, D.; Duan, R. Development of a Radially Coupled Wireless Charging System for Torpedo-Shaped Autonomous Underwater Vehicles. *J. Mar. Sci. Eng.* **2023**, *11*, 1180. [CrossRef]
218. Xia, T.; Li, H.; Yu, H.; Zhang, Y.; Hu, P. A Circular-Arc-Type Magnetic Coupler with Strong Misalignment Tolerance for AUV Wireless Charging System. *J. Mar. Sci. Eng.* **2023**, *11*, 162. [CrossRef]
219. Hasaba, R.; Okamoto, K.; Kawata, S.; Eguchi, K.; Koyanagi, Y. Magnetic resonance wireless power transfer over 10 m with multiple coils immersed in seawater. *IEEE Trans. Microw. Theory Tech.* **2019**, *67*, 4505–4513. [CrossRef]
220. Wu, S.; Cai, C.; Wang, A.; Qin, Z.; Yang, S. Design and Implementation of a Uniform Power and Stable Efficiency Wireless Charging System for Autonomous Underwater Vehicles. *IEEE Trans. Ind. Electron.* **2022**, *70*, 5674–5684. [CrossRef]
221. Zhang, H.; Zhao, Y.; Huang, J.; Zhang, J.; Ji, Y. Propagation Modeling for Underwater Magnetic MISO Wireless Power Transfer. In Proceedings of the 2019 IEEE MTT-S International Wireless Symposium, IWS 2019, Guangzhou, China, 19–22 May 2019; pp 1–3. [CrossRef]
222. Yan, Z.; Zhang, K.; Qiao, L.; Hu, Y.; Song, B. A Multiload Wireless Power Transfer System with Concentrated Magnetic Field for AUV Cluster System. *IEEE Trans. Ind. Appl.* **2022**, *58*, 1307–1314. [CrossRef]
223. Zhang, K.; Zhang, X.; Zhu, Z.; Yan, Z.; Song, B.; Mi, C. A new coil structure to reduce eddy current loss of wpt systems for underwater vehicles. *IEEE Trans. Veh. Technol.* **2019**, *68*, 245–253. [CrossRef]
224. Sato, N.; Kifune, H.; Komeda, S. A coil layout of wireless power transfer systems based on multicoil arrangement for underwater vehicles. *Electr. Eng. Jpn. Engl. Transl. Denki Gakkai Ronbunshi* **2019**, *207*, 38–48. [CrossRef]
225. Yan, Z.; Wu, M.; Zhao, C.; Hu, Q.; Zhu, L.; Qiao, L.; Wang, L. Free-Rotation Wireless Power Transfer System Based on Composite Anti-Misalignment Method for AUVs. *IEEE Trans. Power Electron.* **2023**, *38*, 4262–4266. [CrossRef]
226. Da, C.; Wang, L.; Li, F.; Tao, C.; Zhang, Y. Analysis of Undersea Simultaneous Wireless Power and 1Mbps Data Rate Transfer System Based on DDQ Coil. *IEEE Trans. Power Electron.* **2023**, *38*, 11814–11825. [CrossRef]
227. Sun, A.; Zhu, J.; Wang, F.; Liu, B. Modeling and efficiency optimized control of DD Orthogonal wireless power transfer system. In Proceedings of the 2023 IEEE 6th International Electrical and Energy Conference (CIEEC), Hefei, China, 12–14 May 2023; pp. 2306–2311. [CrossRef]
228. Cai, T.; Lyu, F.; Wang, T.; Huang, F. Design of a Highly Compatible Underwater Wireless Power Transfer Station for Seafloor Observation Equipment. *J. Mar. Sci. Eng.* **2023**, *11*, 1205. [CrossRef]

229. Niu, S.; Zhao, Q.; Chen, H.; Yu, H.; Niu, S.; Jian, L. Underwater Wireless Charging System of Unmanned Surface Vehicles with High Power, Large Misalignment Tolerance and Light Weight: Analysis, Design and Optimization. *Energies* **2022**, *15*, 9529. [CrossRef]
230. Xu, Y.; Yang, J.; Zeng, M.; Dong, L. Wireless Power Transfer System of AUV Based on Improved Coil Structure with Stable Output Power and Efficiency. In Proceedings of the 17th IEEE Conference on Industrial Electronics and Applications ICIEA 2022, Chengdu, China, 16–19 December 2022; pp. 561–565. [CrossRef]
231. Kuroda, J.; Ogawa, M.; Yamaguchi, I.; Sato, R.; Sogo, N.; Matsui, Y. Design of underwater power transfer antenna coverd with resin sealing layer. In Proceedings of the 2018 OCEANS - MTS/IEEE Kobe Techno-Oceans (OTO) Conference, Kobe, Japan, 28–31 May 2018; pp. 1–6. [CrossRef]
232. Hu, Y.; Kang, L.; Zheng, W.; Bai, J. Impedance matching control method for an underwater magnetic resonance-based wireless power transfer system with metamaterials. *J. Electromagn. Waves Appl.* **2016**, *30*, 2003–2019. [CrossRef]
233. Ogihara, M.; Ebihara, T.; Mizutani, K.; Wakatsuki, N. Wireless power and data transfer system for station-based autonomous underwater vehicles. In Proceedings of the OCEANS 2015 Conference, Washington, DC, USA, 5–6 October 2015; pp. 1–5. [CrossRef]
234. Shi, J.; Li, F.; Peng, S.; Cai, W.; Pan, M.; Yu, H. Design and analysis of a noninsert wet mateable connector for underwater power and data transfer. *Mar. Technol. Soc. J.* **2020**, *54*, 65–78. [CrossRef]
235. Wang, Y.; Li, T.; Zeng, M.; Mai, J.; Gu, P.; Xu, D. An Underwater Simultaneous Wireless Power and Data Transfer System for AUV with High-Rate Full-Duplex Communication. *IEEE Trans. Power Electron.* **2023**, *38*, 619–633. [CrossRef]
236. Chen, G.; Sun, Y.; Huang, J.; Zhou, B.; Meng, F.; Tang, C. Wireless Power and Data Transmission System of Submarine Cable-Inspecting Robot Fish and Its Time-Sharing Multiplexing Method. *Electronics* **2019**, *8*, 838. [CrossRef]
237. Li, T.; Sun, Z.; Wang, Y.; Mai, J.; Xu, D. An Underwater Simultaneous Wireless Power and Data Transfer System with 1-Mbps Full-Duplex Communication Link. *IEEE Trans. Ind. Inform.* **2023**, *20*, 2620–2631. [CrossRef]
238. Cai, C.; Li, J.; Wu, S.; Qin, Z.; Chai, W.; Yang, S. A Bipolar and Unipolar Magnetic Channel Multiplexed WPT System with Simultaneous Full-Duplex Communication for Autonomous Underwater Vehicles. *IEEE Trans. Power Electron.* **2023**, *38*, 15086–15090. [CrossRef]
239. Xu, J.; Li, X.; Li, H.; Xie, Z.; Ma, Q. Maximum Efficiency Tracking for Multitransmitter Multireceiver Wireless Power Transfer System on the Submerged Buoy. *IEEE Trans. Ind. Electron.* **2022**, *69*, 1909–1919. [CrossRef]
240. Zheng, Z.; Wang, N.; Ahmed, S. Decoupling Control Scheme Bridging Frequency Tracking and DC Output Stabilizing for Wireless Charging System of Autonomous Underwater Vehicles. *Int. J. Control. Autom. Syst.* **2022**, *20*, 1099–1110. [CrossRef]
241. Yang, L.; Zhang, B.; Ju, M. A fast dynamic response regulation method for undersea wireless power transfer system. In Proceedings of the 14th IEEE Conference on Industrial Electronics and Applications, ICIEA 2019, Xi'an, China, 19–21 June 2019; pp. 1162–1166. [CrossRef]
242. Siroos, A.; Sedighizadeh, M.; Afjei, E.; Fini, A. Comparison of different controllers for wireless charging system in AUVs. In Proceedings of the 13th Power Electronics, Drive Systems, and Technologies Conference, PEDSTC 2022, Tehran, Iran, 1–3 February 2022; pp. 155–160. [CrossRef]
243. Pang, S.; Xu, J.; Li, H.; Ma, Q.; Li, X. Dual-frequency modulation to achieve power independent regulation for dual-load underwater wireless power connector. *IEEE J. Emerg. Sel. Top. Power Electron.* **2022**, *11*, 2377–2389. [CrossRef]
244. Bagchi, A.C.; Wang, H.; Saha, T.; Zane, R. Small-Signal Phasor Modeling of an Underwater IPT System in Constant Current Distribution. In Proceedings of the 2019 IEEE Applied Power Electronics Conference and Exposition (APEC), Anaheim, CA, USA, 17–21 March 2019; pp. 876–883. [CrossRef]
245. Kim, J.; Kim, K.; Kim, H.; Kim, D.; Park, J.; Ahn, S. An Efficient Modeling for Underwater Wireless Power Transfer Using Z-Parameters. *IEEE Trans. Electromagn. Compat.* **2019**, *61*, 2006–2014. [CrossRef]
246. Liang, B.; Mao, Z.; Zhang, K.; Liu, P. Analysis and Optimal Design of a WPT Coupler for Underwater Vehicles Using Non-Dominated Sorting Genetic Algorithm. *Appl. Sci.* **2022**, *12*, 2015. [CrossRef]
247. Xia, T.; Zhang, X.; Zhu, Z.; Yu, H.; Li, H. An Adaptive Control Strategy for Underwater Wireless Charging System Output Power with an Arc-Shaped Magnetic Core Structure. *J. Mar. Sci. Eng.* **2023**, *11*, 294. [CrossRef]
248. Sanborn, G.; Phipps, A. Standards and methods of power control for variable power bidirectional wireless power transfer. In Proceedings of the 2017 IEEE Wireless Power Transfer Conference (WPTC), Taipei, Taiwan, 10–12 May 2017; pp. 1–4. [CrossRef]
249. Kerber, M.; Offord, B.; Phipps, A. Design considerations for an active rectifier circuit for bidirectional wireless power transfer. In Proceedings of the Wireless Power Transfer Conference—WPTC 2017, Taipei, Taiwan, 10–12 May 2017; pp. 1–4. [CrossRef]
250. Lin, M.; Zhang, F.; Yang, C.; Li, D.; Lin, R. Design of bidirectional power converters coupled with coils for wireless charging of AUV docking systems. *J. Mar. Sci. Technol.* **2022**, *27*, 873–886. [CrossRef]
251. Dongye, Z.; Mei, W.; Yuan, J.; Li, T.; Yuan, Q.; Diao, L. Bidirectional Inductive Power Transfer for Unmanned Underwater Vehicles. In Proceedings of the 2023 IEEE 6th International Electrical and Energy Conference (CIEEC), Hefei, China, 12–14 May 2023; pp. 2411–2416. [CrossRef]
252. Tolstonogov, A.Y.; Chemezov, I.A.; Kolomeitsev, A.Y.; Storozhenko, V.A. The Modular Approach for Underwater Vehicle Design. In Proceedings of the Global Oceans 2020 Conference, Singapore, 5–31 October 2020; pp. 1–7. [CrossRef]

253. Agostinho, L.; Ricardo, N.; Silva, R.; Pinto, A. A Modular Inductive Wireless Charging Solution for Autonomous Underwater Vehicles. In Proceedings of the 2021 IEEE International Conference on Autonomous Robot Systems and Competitions, ICARSC 2021, Santa Maria da Feira, Portugal, 28–29 April 2021; pp. 68–73. [CrossRef]
254. Vaughan, C.H. A System for the Transmission of Electrical Energy to or from a Submerged Body. United Kingdom, Patent number: GB499037 1937. Available online: https://patents.google.com/patent/GB499037A/en?oq=GB499037#citedBy (accessed on 8 April 2024).

energies

Article

Array of Active Shielding Coils for Magnetic Field Mitigation in Automotive Wireless Power Transfer Systems

Silvano Cruciani [1], Tommaso Campi [2,*], Francesca Maradei [2] and Mauro Feliziani [3]

[1] Department of Industrial Engineering, Tor Vergata University of Rome, 00133 Rome, Italy; silvano.cruciani@uniroma2.it
[2] Department of Astronautic, Electrical and Energy Engineering, Sapienza University of Rome, 00184 Rome, Italy; francesca.maradei@uniroma1.it
[3] Department of Industrial and Information Engineering, University of L'Aquila, 67100 L'Aquila, Italy; mauro.feliziani@univaq.it
* Correspondence: tommaso.campi@uniroma1.it

Abstract: This paper deals with the mitigation of magnetic field levels produced by a wireless power transfer (WPT) system to recharge the battery of an electric vehicle (EV). In this work, an array of active coils surrounding the WPT coils is proposed as a mitigation technique. The theory and new methodological aspects are the focus of the paper. Magnetic field levels in the environment are calculated numerically without and with the presence of an array of active coils in a stationary WPT system for automotive applications. By the proposed mitigation method, the field levels beside the vehicle are significantly reduced and comply with the reference levels (RLs) of the ICNIRP 2010 guidelines for human exposure to electromagnetic fields and the magnetic flux density limits proposed by ISO 14117 for electromagnetic interference (EMI) in cardiac implantable electronic devices (CIEDs).

Keywords: active coil; cardiac implantable electronic device (CIED); electromagnetic compatibility (EMC); electromagnetic field (EMF) safety; electromagnetic interference (EMI); magnetic field; near field; shielding; wireless power transfer (WPT)

1. Introduction

Electric vehicles (EVs) bring significant advances in transportation technology, promising a green and more sustainable future. For the widespread adoption of electrified transportation on wheels, an efficient and convenient charging infrastructure is necessary. Wireless power transfer (WPT) based on resonant inductive coupling is the most promising technology for its potential and for the elimination of the plug-in physical connections [1–8]. However, the implementation of this technology raises concerns about the strong magnetic fields emitted into the environment from WPT systems, which could pose potential health risks to occupants and nearby people and interfere with sensitive electronic equipment and infrastructures [9–11]. Therefore, WPT systems are critical for the electromagnetic field (EMF) safety of exposed individuals and the electromagnetic compatibility/electromagnetic interference (EMC/EMI) to electric/electronic devices. Such issues can be particularly critical in densely populated urban environments where many electric vehicles may be located. Consequently, there is an urgent need to develop effective mitigation techniques to minimize the magnetic field emitted from automotive WPT systems.

A potential solution for magnetic field mitigation consists in using additional active or passive shielding coils (or loops) that generate a magnetic field opposite to that created by the WPT system. In a passive configuration, the shielding loop is terminated on an impedance, and the current flowing through it is induced by the incident magnetic field produced by the WPT coils according to Faraday's law [11–18]. When the passive loop is properly terminated, typically on a capacitance, the magnetic field produced by the shielding coil can oppose the incident field. However, achieving the desired current (both in magnitude and phase) in the passive shielding coil is not always possible, which can result in suboptimal field mitigations.

Active shielding coils provide a practical and cost-effective solution to the challenges posed by magnetic field emissions from WPT systems [19–28]. Unlike passive ones, active shielding coils have an independent power supply that allows the regulation of the magnitude and phase of the current through appropriate control mechanisms. While the theory behind active shielding coils is well established, this work introduces an innovative approach, using an array of active shielding coils to mitigate the magnetic field in a wireless charging system for EVs. The design of active shielding coils is particularly challenging since a successful field mitigation often negatively impacts the power transfer efficiency. Strategically feeding an array of active shielding coils around the EV WPT charging system helps reduce magnetic field levels while maintaining a high power transfer efficiency and electrical performance [4,13]. The main novelty of the proposed work compared with past works on active shielding lies in the possibility of selecting the optimal power supply for a shielding system composed of N independent coils. This allows for great flexibility and adaptability to any type of WPT system.

The paper is focused on the methodological aspects of an array of active shielding coils and is organized as follows. First, a comprehensive analysis of using an array of active shielding coils for automotive wireless power systems is presented. We begin by providing an overview of the WPT theory and the sources of magnetic field emissions in WPT systems. Next, we discuss the design considerations and optimization techniques for integrating active shielding coils into the WPT infrastructure. Furthermore, we present simulation results to demonstrate the effectiveness of the proposed approach in reducing magnetic field emissions while ensuring high power transfer efficiency. Through a comparative analysis of different array configurations, we highlight the advantages and limitations of the different solutions developed for a WPT system similar to that standardized by SAE J2954 [29].

Additionally, we address practical implementation challenges and considerations, including cost-effectiveness, scalability, and compatibility with existing WPT standards and infrastructure. By providing insights into the performance and feasibility of using an array of active cancellation loops, this paper aims to contribute to the development of robust and environmentally friendly charging solutions for the electric mobility infrastructure.

2. Materials and Methods

A two-coil WPT system with circular coils, as specified by the SAE J2954 standard, is considered and assumed to be the source of the magnetic field [13]. The array of active shielding coils is designed to be placed around and coplanar with the primary WPT coil. This configuration is chosen because the primary coil is considered the main source of magnetic field emissions in the environment, and installing active shielding coils on the ground is straightforward.

One possible configuration of the shielding coils is shown in Figure 1. In this configuration, the shielding structure consists of an array of $N - 2$ active shielding coils. The equivalent circuit can be modeled by N-coupled circuits:

- One primary coil, known in the SAE standard as the ground assembly (GA) coil, represented by the self-inductance L_1 and self-resistance R_1;
- One secondary coil, known as the vehicle assembly (VA) coil, represented by the self-inductance L_2 and self-resistance R_2;
- $N - 2$ active shielding coils. All N coils can be modeled with a self-inductance L_i and self-resistance R_i and are inductively coupled.

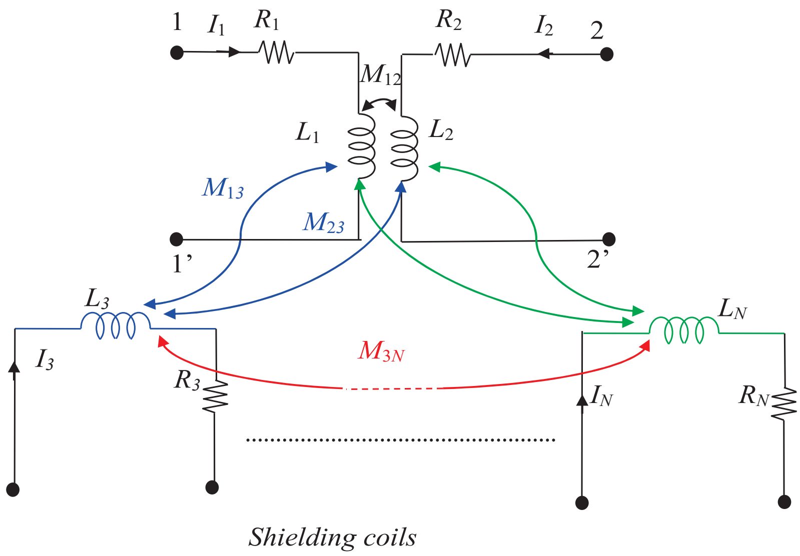

Figure 1. Equivalent circuit of a WPT system in the presence of $N-2$ shielding coils.

The circuit parameters of all N coils can be extracted using an electromagnetic field solver based on the finite element method (FEM). This field solver can also evaluate the magnetic field produced by the coil currents [4]. The numerical approach is employed due to the configuration complexity of the GA and VA coils, which include conductive and magnetic layers, as described in SAE J2954 [29].

The self- and mutual inductances of the N coils can be extracted from the magnetic energy, which is generally numerically calculated in the region under examination [4]. The self-inductance of the i-th coil is calculated as

$$L_i = \frac{2W_i}{I_i^2} \tag{1}$$

where W_i is the magnetic energy produced by the current I_i flowing in the i-th coil, while any other current in the other coils is zero (that is, $I_k = 0$, with $k \neq i$).

The mutual inductance M_{ik} between i-th and k-th coils is calculated by a two-step procedure using the following formula [4]:

$$M_{ik} = \frac{W_{ik}' - W_{ik}''}{2I_iI_k} \tag{2}$$

where

- W_{ik}' is the magnetic field energy obtained, assuming I_i and I_k are flowing in the i-th and k-th coils, respectively, while in the remaining coils, $I_h = 0$, with $h \neq i$ and $h \neq k$;
- W_{ik}'' is the magnetic field energy obtained, assuming the same current, I_i, is flowing in the i-th coil but an opposite current, -I_k, is flowing in the k-th coil, with no current applied to the other coils, $I_h = 0$, with $h \neq i$ and $h \neq k$.

The coil resistance, R_i, of the copper litz wire used for the i-th coil is obtained from the datasheet [30]. The extraction of this parameter through simulation for the litz wire is computationally impracticable or very intensive.

The N-coupled coils are described by an $N \times N$ impedance matrix [Z], whose generic coefficient Z_{ik} is given by

$$Z_{ik} = \begin{cases} R_i + j\omega L_i \ \forall i = k \\ j\omega M_{ik} \ \ \forall i \neq k \end{cases} \tag{3}$$

Double-sided LCC compensation topology is adopted to operate the WPT system under resonant conditions according to the circuit shown in Figure 2, where an equivalent voltage source, V_0, in series with a source resistance, R_S, models the power electronic converters upstream of the transmitting coil, and a load resistor, R_L, models the power electronic converters downstream of the receiving coil [4].

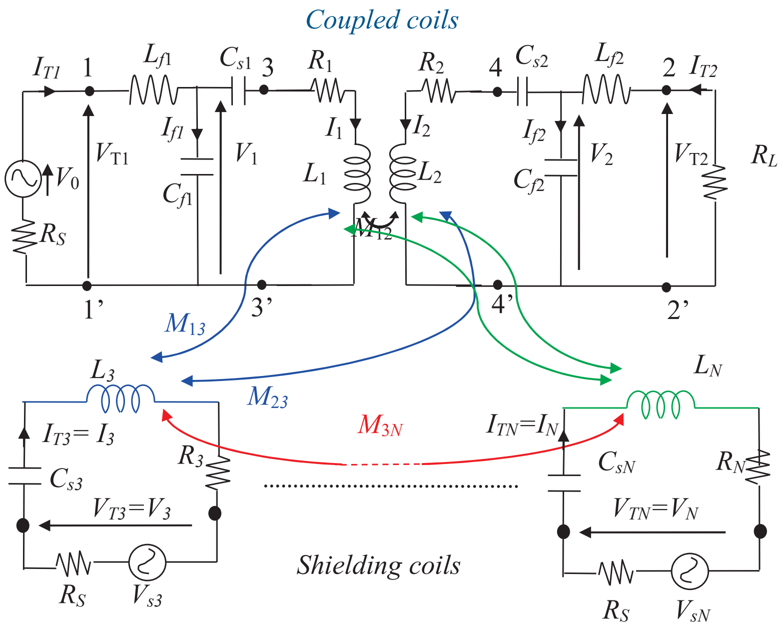

Figure 2. Equivalent simplified circuit of a WPT system LCC compensation and $N-2$ active shielding coils.

The values of the i-th shunt capacitance C_{fi} and series capacitance C_{Si} of the LCC networks are, respectively, given by

$$C_{fi} = 1/\left(\omega_0^2 L_{fi}\right)\ i \in \{1,2\} \tag{4}$$

$$C_{Si} = 1/\left(\omega_0^2\left(L_i - L_{fi}\right)\right)\ i \in \{1,2\} \tag{5}$$

where L_{fi} is the series inductance of the LCC compensation network and ω_0 is the resonant angular frequency.

To improve the efficiency of shielding coils, compensation capacitors $C_{Si} = 1/\left(\omega_0{}^2 L_i\right)$ with $i = 3, N$ are connected in series, and a simplified excitation circuit is adopted for each shielding coil based on the series of a voltage source, V_{sk}, with a source resistance, R_S, assuming that all the sources have the same resistance as the transmitting coil.

For the terminations, the following relation holds:

$$[V_S] = [V_T] + [Z_T][I_T] \tag{6}$$

where $[V_S] = [V_0\ 0\ V_{s3} \ldots V_{sN}]^t$ is the vector of the voltage sources, $[V_T] = [V_{T1}\ V_{T2} \ldots V_{TN}]^t$ is the vector of the terminal voltages, $[I_T]$ is the vector of the N-port terminal currents, and $[Z_T]$ is the $N \times N$ matrix of the terminal impedances given by

$$[Z_T] = \begin{bmatrix} R_S & 0 & \cdots & 0 \\ 0 & R_L & \cdots & 0 \\ \vdots & \vdots & \ddots & \vdots \\ 0 & 0 & \cdots & R_S \end{bmatrix}. \tag{7}$$

Adopting the notation shown in Figure 2, the terminal voltages can also be expressed as

$$\begin{cases} V_{T1} = V_1 + j\omega L_{f1} I_{T1} \\ V_{T2} = V_2 + j\omega L_{f2} I_{T2} \\ V_{T3} = V_3 \\ \vdots \\ V_{TN} = V_N \end{cases} \tag{8}$$

or in compact matrix form as

$$[V_T] = [V] + [Z_f][I_T] \tag{9}$$

where the impedance matrix $[Z_f]$ is diagonal, with non-zero terms only for i = 1, 2 (i.e., WPT coils) given by

$$Z_{fii} = j\omega L_{fi} \; i \in \{1,2\}. \tag{10}$$

The voltage vector $[V]$ in (7) can be expressed as

$$[V] = \{[Z_C] + [Z]\}[I] \tag{11}$$

where the coefficients of matrix $[Z]$ are given by (1), and the matrix $[Z_C]$ is diagonal, with its coefficients given by

$$Z_{Cik} = \begin{cases} -j\frac{1}{\omega C_{Si}} \; \forall i = k \\ 0 \;\; \forall i \neq k \end{cases}. \tag{12}$$

Introducing (11) and (9) into (6) yields

$$[V_S] = \{[Z_C] + [Z]\}[I] + \Big\{[Z_f] + [Z_T]\Big\}[I_T]. \tag{13}$$

According to the Kirchhoff current law applied to the circuit in Figure 2, the following relation between the currents through the terminations and those through the coils can be derived as

$$\begin{cases} I_{T1} = I_1 + j\omega C_{f1} V_1 \\ I_{T2} = I_2 + j\omega C_{f2} V_2 \\ I_{T3} = I_3 \\ \vdots \\ I_{TN} = I_N \end{cases}, \tag{14}$$

which can also be written in compact matrix form as

$$[I_T] = [I] + [Y_f][V] \tag{15}$$

where the shunt admittance matrix $[Y_f]$ is diagonal, with non-zero terms only for i = 1,2 (i.e., WPT coils) given by

$$Y_{fii} = j\omega C_{fi} \; i \in \{1,2\}. \tag{16}$$

Introducing (11) in (15) yields

$$[I_T] = \Big\{[1_N] + [Y_f]\{[Z_C] + [Z]\}\Big\}[I] \tag{17}$$

where $[1_N]$ is the unit matrix of size N.

By introducing (17) into (13), the following relations between the voltage source vector and the coil current vector holds:

$$[V_S] = [Z_{eq}][I] \tag{18}$$

where the transfer impedance matrix $[Z_{eq}]$ is given by

$$\big[Z_{eq}\big] = \big[Y_{eq}\big]^{-1} = \Big\{[Z_C] + [Z] + \Big\{[Z_f] + [Z_T]\Big\}\Big\{[1_N] + [Y_f]\{[Z_C] + [Z]\}\Big\}\Big\}. \tag{19}$$

The currents flowing through the coils, which are the coefficients of vector $[I]$, can be obtained by (18) and are used to calculate the magnetic field. Additionally, the optimal value of the voltage source vector $[V_S]$ can also be derived to minimize the average magnetic field in a given region.

To calculate the magnetic field, the linearity assumption is adopted so that the principle of superposition holds and the number of field simulations is significantly reduced.

Let us indicate $\boldsymbol{b}_i^{(k)}$, the magnetic flux density in a generic k-th point, produced by a unit current I_i = 1 A through the i-th coil, with no currents in other coils (that is, I_k = 0, with $k \neq i$). This function can be expressed in Cartesian coordinates as

$$\boldsymbol{b}_i^{(k)} = \left(\boldsymbol{b}_i^{(k)} \cdot \hat{\mathbf{x}}\right)\hat{\mathbf{x}} + \left(\boldsymbol{b}_i^{(k)} \cdot \hat{\mathbf{y}}\right)\hat{\mathbf{y}} + \left(\boldsymbol{b}_i^{(k)} \cdot \hat{\mathbf{z}}\right)\hat{\mathbf{z}} = b_{i,x}^{(k)}\hat{\mathbf{x}} + b_{i,y}^{(k)}\hat{\mathbf{y}} + b_{i,z}^{(k)}\hat{\mathbf{z}} \tag{20}$$

where $\hat{\mathbf{x}}, \hat{\mathbf{y}}, \hat{\mathbf{z}}$ are the unit vectors along the coordinate axes.

When considering M points with k = 1, 2, . . ., M, we can create 3 column vectors $[b_{i,x}]$, $[b_{i,y}]$, and $[b_{i,z}]$, one for each component, containing the Cartesian components of the field produced by the i-th current in the M selected points.

By applying superposition, the magnetic flux density produced by the coil current vector $[I]$ can be expressed as

$$\begin{bmatrix} [B_x] \\ [B_y] \\ [B_z] \end{bmatrix} = \begin{bmatrix} [b_{1x}] & \cdots & [b_{Nx}] \\ [b_{1y}] & \ddots & [b_{Ny}] \\ [b_{1z}] & \cdots & [b_{Nz}] \end{bmatrix} [I] \tag{21}$$

where $[B_x]$, $[B_y]$, and $[B_z]$ are the Cartesian components vectors of the total magnetic flux density in the M considered points.

The average value of the squared norm of the magnetic flux density in the considered region is given by [17,18]

$$B_{av}{}^2 = \frac{1}{M}\sum_{k=1}^{M}\left\|\mathbf{B}^{(k)}\right\|^2 = \frac{1}{M}\left[[B_x]^* \quad [B_y]^* \quad [B_z]^*\right]\begin{bmatrix} [B_x] \\ [B_y] \\ [B_z] \end{bmatrix} \tag{22}$$

where the star apex represents the conjugate.

Equation (20) can be used in an optimization algorithm to calculate the value of the voltage source vector $[V_S]$ that permits the minimization of the magnetic flux density in the considered region. We start by defining [23,24]

$$\left[[g_1] \quad \cdots \quad [g_N]\right] = \begin{bmatrix} [b_{1x}] & \cdots & [b_{Nx}] \\ [b_{1y}] & \ddots & [b_{Ny}] \\ [b_{1z}] & \cdots & [b_{Nz}] \end{bmatrix} [Y_{eq}]. \tag{23}$$

The voltage source vector $[V_S]$ can be expressed as

$$[V_S] = \begin{bmatrix} 1 \\ 0 \\ [\alpha_{SH}] \end{bmatrix} V_0 \tag{24}$$

where V_0 is the voltage source applied to the primary coil of the WPT system and $[\alpha_{SH}]$ is a $N-2$ column vector containing the gains of the controlled voltage sources applied to the $N-2$ shielding coils, which are assumed to depend on the primary voltage source, V_0 [19,20]. By adopting this notation, (22) can be rewritten as

$$B_{av}{}^2 = \frac{1}{M}\left([g_1] + \left[[g_3] \quad \cdots \quad [g_N]\right][\alpha_{SH}]\right)^*\left([g_1] + \left[[g_3] \quad \cdots \quad [g_N]\right][\alpha_{SH}]\right)|V_0|^2. \tag{25}$$

For an optimization procedure, the objective function can be the minimization of B_{av}. This goal can be achieved by imposing [17,18]

$$[g_1] + \left[[g_3] \quad \cdots \quad [g_N] \right] [\alpha_{SH}] = [0] \tag{26}$$

therefore, making sure that [19,20]

$$[\alpha_{SH}] = -\left[[g_3] \quad \cdots \quad [g_N] \right]^{\dagger} [g_1] \tag{27}$$

where the operator † is the symbol of the pseudoinverse matrix, which is a generalization of the inverse matrix that provides a best-fit solution to linear equation systems.

Equation (25) provides the gains of the controlled voltage sources that need to be applied to the shielding coils in order to minimize the average magnetic field. Finally, the voltage source of the i-th active coil with $i = 3, 4, \ldots, N$ is given by

$$V_{SH,i} = \alpha_{SH,i} V_0. \tag{28}$$

In WPT systems, the power transfer efficiency η is traditionally calculated as the ratio of the real power at the output port, P_2, to the real power at the input port, P_1:

$$\eta = \frac{P_2}{P_1} \tag{29}$$

In the presence of active shielding coils, η is calculated as

$$\eta = \frac{P_1 - \sum_{i=1}^{N} P_{loss,i}}{P_1} \tag{30}$$

where $P_{loss,i}$ represents the power loss in the i-th coil [4].

The described procedure is highly effective for calculating the average magnetic induction value, B_{av}, in a region discretized into a grid of points. If the points are located on a surface, S, it becomes straightforward to compute the magnetic flux as $\boldsymbol{\phi} = B_{av}\, S$. Consequently, the induced electromotive force (*emf*) can be determined in a circuit whose path aligns with the contour of the surface, expressed as $emf = -j\omega\boldsymbol{\phi}$. This capability is crucial for evaluating induced effects on transmission lines and various types of circuits, facilitating the prediction of electromagnetic interference (EMI).

If the surface, S, is relatively small, for instance 100 cm^2, such as that of a magnetic field probe, this method can be employed to predict the maximum (*rms*) magnetic flux density at a specific point. This approach is recommended by SAE J2954 for evaluating compliance with the reference levels specified in ICNIRP 2010 [31] and ISO 14117 [32] for electromagnetic interference (EMI) limits in cardiac implantable electronic devices (CIEDs), which are set at 27 μT and 15 μT at 85 kHz, respectively.

3. Applications

3.1. WPT Systems

The performances and the magnetic field emission are calculated using a demonstrative WPT system. For this test, the worst operational condition is adopted. The maximum ground clearance level, Z3, allowed by the SAE J2954 standard is taken into account, with an air gap between the coils in the range 170–250 mm. A larger air gap is the condition in which the coupling factor is smaller and, therefore, the leakage flux is larger. The GA coil is supposed to be flush mounted in the ground ($z = 0$).

Figure 3 shows the configuration of the GA coil, which consists of a planar spiral coil made of two parallel copper litz wires, each with $N_1 = 8$ turns. The external dimensions of the coil are $w_1 = 500$ mm and $l_1 = 650$ mm. Two planar shields are placed under the coil. A ferrite shield, with the dimensions of $w_{1f} = 500$ mm and $l_{1f} = 650$ mm and a thickness of $t_k = 5$ mm, is used to enhance the magnetic coupling, while an aluminum shield, with the dimensions of w_{1a} = 700 mm and l_{1a} = 900 mm and a thickness of t_k = 2 mm, is used to reduce the magnetic field.

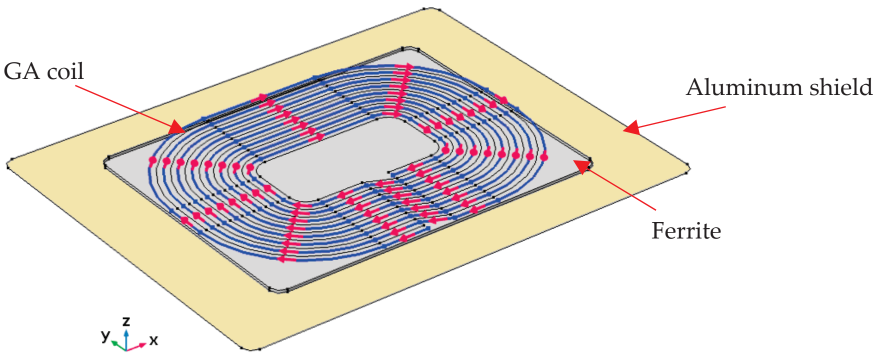

Figure 3. Electro-geometrical configuration of the GA coil.

The VA coil, shown in Figure 4, is mounted under a metal mimic pan that simulates the presence of the conductive bodyshell of the vehicle. The square coil, with sides of s = 380 mm, consists of a planar spiral coil made of a single copper litz wire with N_2 = 8 turns. A square ferrite shield, with sides of s_f = 380 mm and a thickness of t_k = 5 mm, is adopted to enhance magnetic coupling. Additionally, an aluminum shield, with the dimensions of w_{2a} = 700 mm and l_{2a} = 900 mm and a thickness of t_k = 2 mm, is used to reduce the magnetic flux leakage.

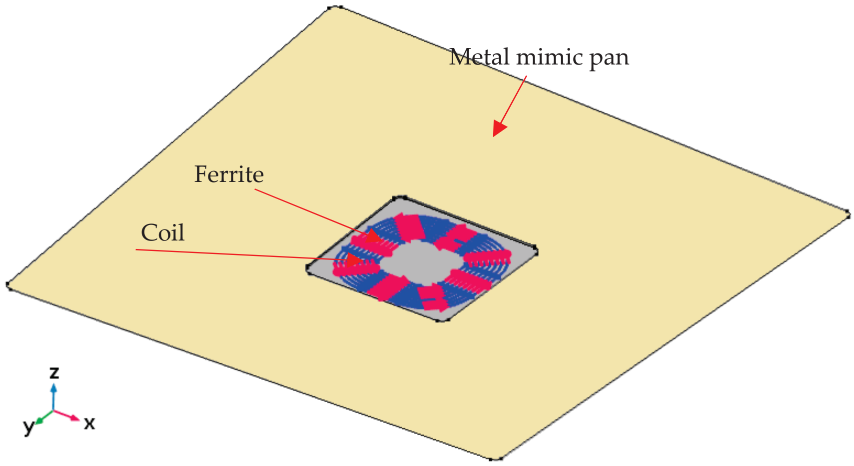

Figure 4. Electro-geometrical configuration of the VA coil.

The operational frequency is f = 85 kHz; the output power is fixed to P_2 = 7.7 kVA (SAE Power Class 2); and the output voltage is fixed to 400 V. The system is terminated on a load resistor, R_L = 10 Ω. For the sake of brevity, only the LCC compensation is considered as it is the most suitable for the coil configuration being considered [29].

The car body is simulated by a square metal mimic pan, with a side length of l_{mp} = 1.5 m. It is made of aluminum, with an electrical conductivity of σ = 37 MS/m and a thickness of t_k = 2 mm. The mimic pan is placed at a distance of d = 2 mm over the VA coil.

The maximum misalignment between the coils is used in this investigation: a front–back offset of Δx = 75 mm; a lateral offset of Δy = 100 mm; and a vertical separation between the GA and the VA coils of Δz = 250 mm. This coil configuration represents the worst-case scenario, according to the SAE standard for the power class considered.

The currents flowing in the GA and VA coils are regarded as being the sources of the magnetic field. Subsequently, three configurations of the active shielding coils are defined, featuring two, four, and six shielding coils positioned around the GA coil, as illustrated in Figure 5. It is assumed that the shielding coils have, in all cases, only one turn. All the coils (WPT and shielding) are constructed from the same litz wire (AWG 38), composed of 1260 insulated strands [30].

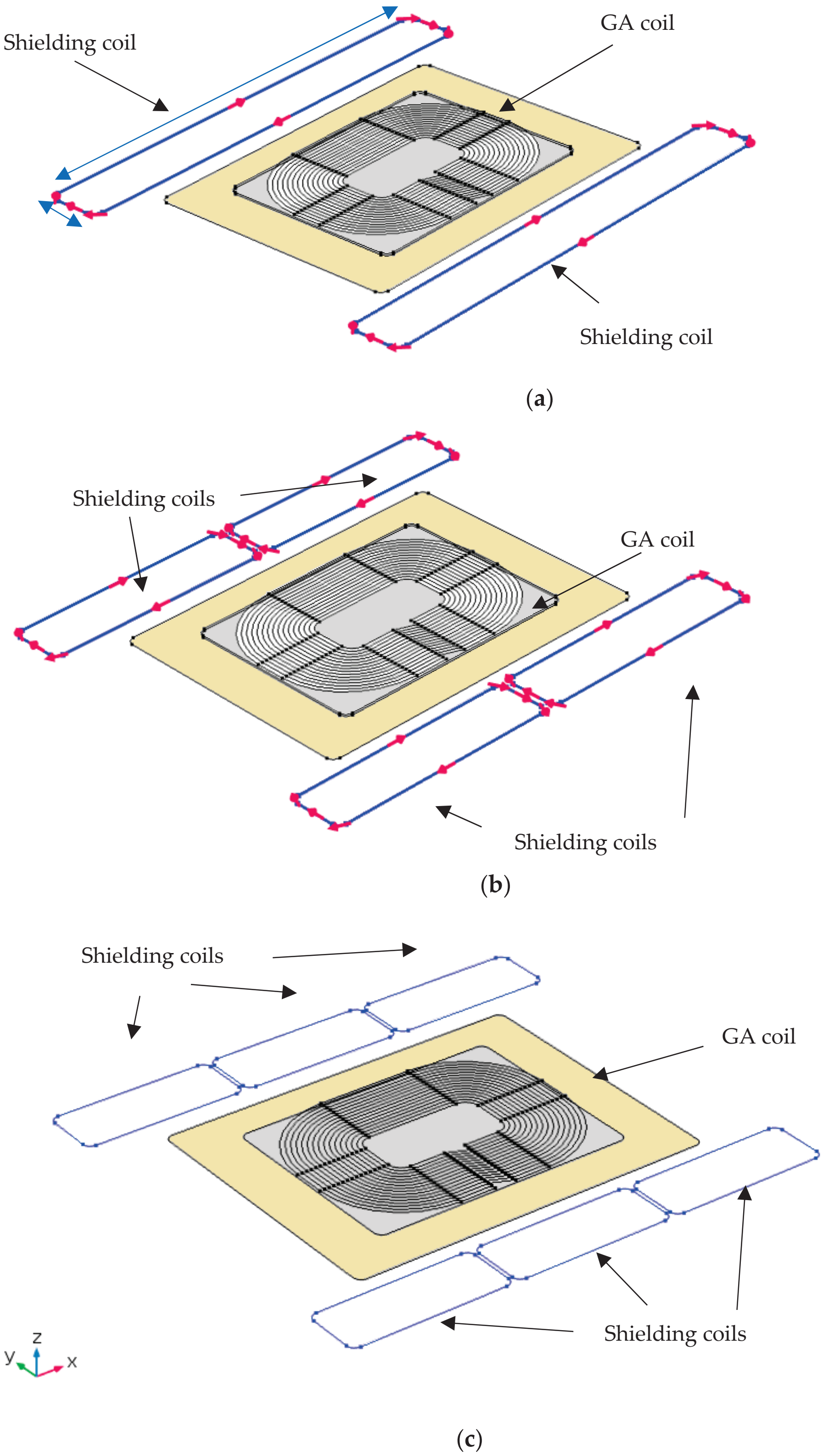

Figure 5. Proposed active shielding coil configuration: 2 coils (**a**), 4 coils (**b**), and 6 coils (**c**).

3.2. Electrical Performances

The self- and mutual inductances of the equivalent circuit are calculated by (1) and (2), respectively, using a 3D numerical simulation software for all configurations considered. The AC resistances of all the coils are taken from the litz wire datasheet at 85 kHz [30]. The obtained circuit parameters for the WPT coils are reported in Table 1.

Table 1. Equivalent circuit parameters without active shielding coils.

L_1 (μH)	L_2 (μH)	M_{12} (μH)	R_1 (mΩ)	R_2 (mΩ)
47.86	39.93	4.00	22.22	31.51

The procedure described in the previous section is then applied to all the shielding coil structures. The grid of points used as an input of the algorithm are taken on surfaces S_1 and S_2 placed on the exterior of the mimic pan, as shown in Figure 6. All the surfaces have a size of 1.5 m along x and 0.8 m along z and are placed at a distance of d_s = 0.8 m from the center of the mimic pan.

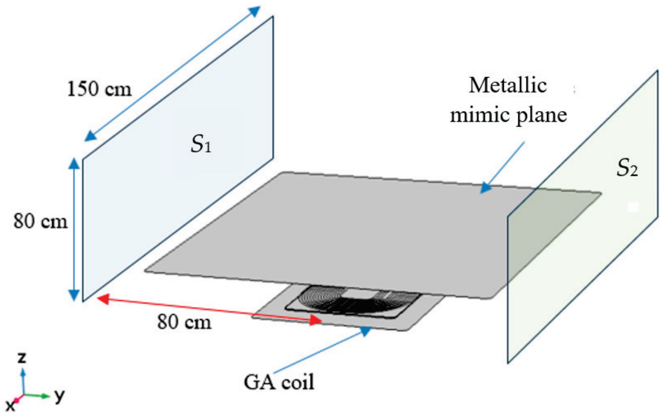

Figure 6. Surfaces S_1 and S_2 beside the WPT coil configuration where the average magnetic flux induction is calculated.

The result of the procedure is the assessment of the vector [α_{sh}] in (25). The obtained coefficients of [α_{sh}] for the three active shielding configurations considered are reported in Table 2. The WPT currents and efficiency obtained with active shielding coils are compared with those without them, and the results are reported in Table 3.

Table 2. Coefficients of [α_{SH}] for the three active shielding coil configurations with maximum misalignment.

	α_{SH}
2 active shielding coils	$-1.9091 \times 10^{-3} + j12.7359 \times 10^{-3}$ $-1.6459 \times 10^{-3} + j1.6536 \times 10^{-3}$
4 active shielding coils	$-1.0114 \times 10^{-3} + j3.0928 \times 10^{-3}$ $-8.0523 \times 10^{-6} + j705.1594 \times 10^{-6}$ $2.8947 \times 10^{-3} + j6.0339 \times 10^{-3}$ $1.7971 \times 10^{-3} + j16.3283 \times 10^{-3}$
6 active shielding coils	$1.2087 \times 10^{-3} + j1.2649 \times 10^{-3}$ $-1.8118 \times 10^{-3} + j5.1854 \times 10^{-3}$ $1.2390 \times 10^{-3} - j1.4751 \times 10^{-3}$ $5.7300 \times 10^{-3} - j4.8383 \times 10^{-3}$ $3.4344 \times 10^{-3} + j22.8283 \times 10^{-3}$ $8.4429 \times 10^{-3} + j7.4163 \times 10^{-3}$

Table 3. System performances with and without active shields.

	$\lvert I_1 \rvert$ (A)	$\lvert I_2 \rvert$ (A)	η (%)
Without active shielding	94.52	55.00	96.3
2 active shielding coils	94.22	55.00	96.1
4 active shielding coils	94.19	55.00	96.0
6 active shielding coils	94.23	55.00	95.8

3.3. Magnetic Field Mitigation

Finally, the obtained coil currents are used for calculating the magnetic field distribution. The field distribution is calculated in two parallelepiped volumes placed at the left and right of the mimic pan, at a distance of d_v = 50 mm from the mimic edge, as shown in Figure 7.

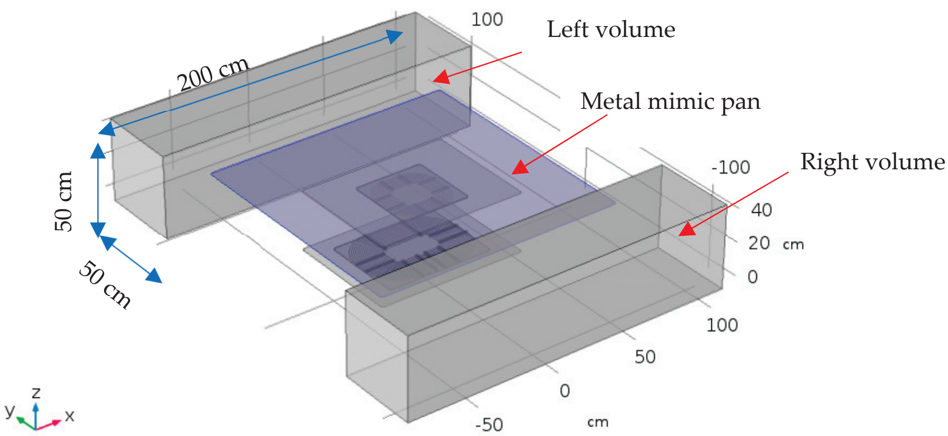

Figure 7. Volumes beside the WPT coil configuration where the magnetic flux induction is calculated.

The magnetic field distributions inside the volumes are depicted in Figure 8 for different active shielding coil configurations, and the maximum and average values of the magnetic flux density are reported in Table 4.

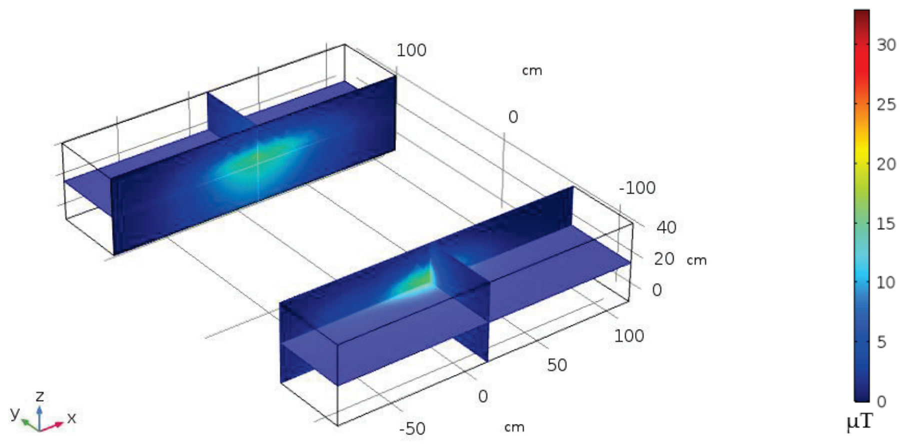

(**a**)

Figure 8. *Cont.*

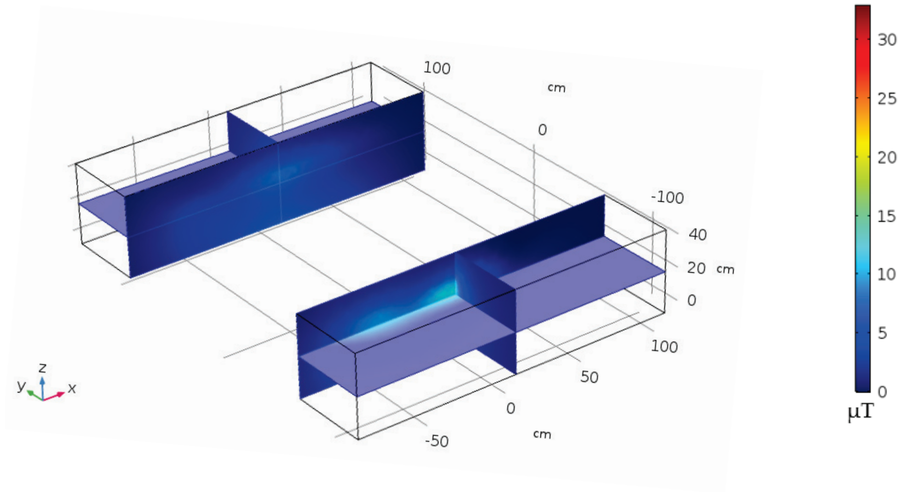

(**b**)

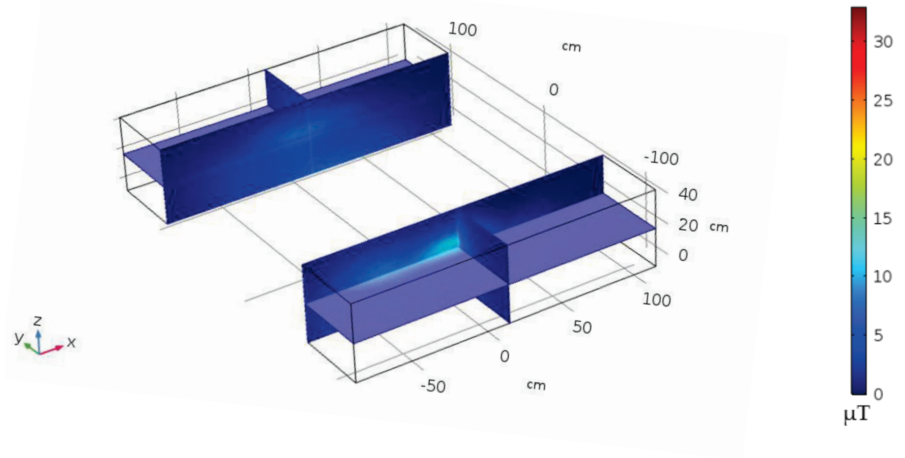

(**c**)

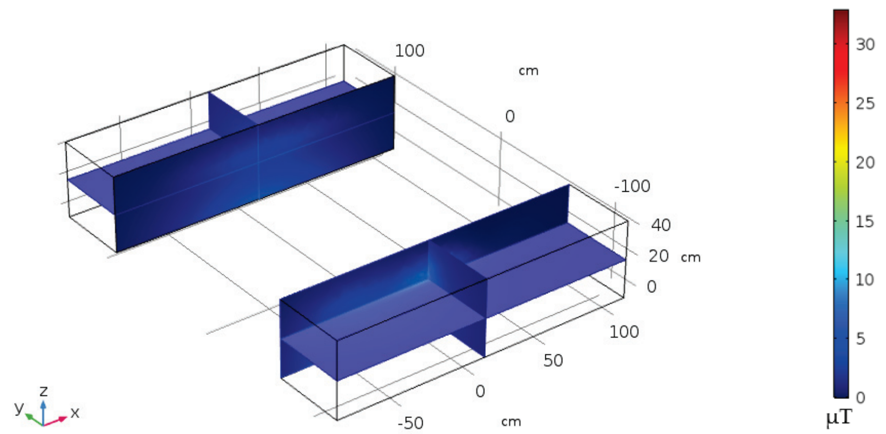

(**d**)

Figure 8. Distribution of the magnetic flux density B (rms) in the volumes without active shielding (**a**), with 2 active shielding coils (**b**), with 4 active shielding coils (**c**), and with 6 active shielding coils (**d**).

Table 4. Maximum and average magnetic flux density (*rms*) in the two volumes.

	Maximum B (μT)		**Average B (μT)**	
	Left Volume	**Right Volume**	**Left Volume**	**Right Volume**
No shielding coil	16.635	17.536	2.286	1.818
2 shielding coils	8.198	12.025	1.673	1.473
4 shielding coils	8.640	12.140	1.571	1.421
6 shielding coils	7.783	9.124	1.467	1.305

The obtained results highlight the significant reduction in the magnetic field achieved by adopting the proposed multicoil shielding configuration. The field in the considered area can be almost halved when six active shielding coils are used. Furthermore, using the six-coil configuration, it is possible to reduce the magnetic field where it is strongest, particularly in the central part of the reference volume (see Figure 8). In this set-up, the two central shielding coils offer superior shielding performance. In contrast, configurations with two or four shielding coils cannot target this specific goal as effectively.

Therefore, using two shielding coils is preferable for achieving a moderate reduction in the magnetic field, while the six-coil configuration allows for a more substantial reduction. In any case, the obtained values are well below the limits fixed by international regulations, such as the reference levels (RL) of the ICNIRP 2010 guidelines [31], and are also below the limit provided by SAE J2594 for people with cardiac implantable electronic devices (CIEDs) [32]. The RL, in terms of the magnetic flux induction at 85 kHz, is 27 μT, while the limit defined by ISO 14117 is set at 15 μT.

4. Conclusions

An innovative shielding solution based on an array of active coils for automotive wireless power systems has been presented. This approach effectively minimizes the magnetic field produced by a wireless charging system designed according to the SAE standard, while avoiding overall efficiency degradation, which is crucial for intentional magnetic field sources, such as WPT coils. The use of multiple shielding coils allows for precise field mitigation across the entire area around the system. The paper provides a detailed description of the theoretical and methodological aspects of an array of active shielding coils applied to a WPT system with double-sided LCC compensation, including the necessary equations, allowing the readers to easily apply the proposed method.

The effectiveness of the proposed procedure has been numerically tested considering the worst-case scenario for the wireless charging of EVs in terms of coil separation and misalignment. The results show that the magnetic field in the most critical areas beside the EV can be significantly reduced with a minimal drop in efficiency, even when accounting for the power needed by the shielding coils. The reduction in the power transfer efficiency was 0.3% when using two or four active coils and 0.5% when using six active coils. Meanwhile, the magnetic field was nearly halved in all tested configurations with the proposed arrays of active coils. Therefore, using four active coils represents the best compromise between maintaining efficiency and reducing the magnetic field. Future work will include the realization of a demonstrator to validate the system in a real scenario.

Finally, the proposed approach can be easily adapted for different configurations of WPT and shielding coils.

Author Contributions: S.C., T.C., F.M. and M.F. conceived and planned the simulations. S.C. and F.M. developed the algorithms. T.C. and M.F. realized the simulations set-up. All authors provided critical feedback, improved the final design, analyzed the data, and wrote the paper. All authors have read and agreed to the published version of the manuscript.

Funding: This research received no external funding.

Data Availability Statement: The original contributions presented in the study are included in the article, further inquiries can be directed to the corresponding author/s.

Conflicts of Interest: The authors declare no conflicts of interest.

References

1. Covic, G.A.; Boys, J.T. Inductive Power Transfer. *Proc. IEEE* **2013**, *101*, 1276–1289. [CrossRef]
2. Wang, C.-S.; Covic, G.A.; Stielau, O.H. Power Transfer Capability and Bifurcation Phenomena of Loosely Coupled Inductive Power Transfer Systems. *Trans. Ind. Electron.* **2004**, *51*, 148–157. [CrossRef]
3. Ahmad, A.; Alam, M.S.; Chabaan, R.A. Comprehensive Review of Wireless Charging Technologies for Electric Vehicles. *Trans. Transport. Electrific.* **2018**, *4*, 38–63. [CrossRef]
4. Feliziani, M.; Campi, T.; Cruciani, S.; Maradei, F. *Wireless Power Transfer for E-Mobility*, 1st ed.; Elsevier-Academic Press: Cambridge, MA, USA, 2023; ISBN 9780323995238.
5. Laporte, S.; Coquery, G.; Deniau, V.; De Bernardinis, A.; Hautière, N. Dynamic wireless power transfer charging infrastructure for future evs: From experimental track to real circulated roads demonstrations. *World Electr. Veh. J.* **2019**, *10*, 84. [CrossRef]
6. Buja, G.; Rim, C.T.; Mi, C.C. Dynamic Charging of Electric Vehicles by Wireless Power Transfer. *IEEE Trans. Ind. Electron.* **2016**, *63*, 6530–6532. [CrossRef]
7. Grazian, F.; Shi, W.; Soeiro, T.B.; Dong, J.; van Duijsen, P.; Bauer, P. Compensation Network for a 7.7 kW Wireless Charging System that Uses Standardized Coils. In Proceedings of the 2020 IEEE International Symposium on Circuits and Systems (ISCAS), Seville, Spain, 12–14 October 2020; pp. 1–5. [CrossRef]
8. Pahlavan, S.; Ashtiani, S.J. Rotation-Tolerant Wireless Power Transmission Scheme with Smart Positioning for Cognitive Research on Moving Animals. *IEEE Trans. Biomed. Circuits Syst.* **2024**, *18*, 123–130. [CrossRef] [PubMed]
9. De Santis, V.; Campi, T.; Cruciani, S.; Laakso, I.; Feliziani, M. Assessment of the Induced Electric Fields in a Carbon-Fiber Electrical Vehicle Equipped with a Wireless Power Transfer System. *Energies* **2018**, *11*, 684. [CrossRef]
10. Ding, P.; Bernard, L.; Pichon, L. Evaluation of Electromagnetic Field in Human Body Exposed to Wireless Inductive Charging System. *IEEE Trans. Magn.* **2014**, *50*, 1037–1040. [CrossRef]
11. Laakso, I.; Hirata, A. Evaluation of the induced electric field and compliance procedure for a wireless power transfer system in an electrical vehicle. *Phys. Med. Biol.* **2013**, *58*, 7583. [CrossRef]
12. Kim, J.; Kong, S.; Kim, H.; Suh, I.-S.; Suh, N.P.; Cho, D.-H.; Kim, J.; Ahn, S. Coil Design and Shielding Methods for a Magnetic Resonant Wireless Power Transfer System. *Proc. IEEE* **2013**, *101*, 1332–1342. [CrossRef]
13. Campi, T.; Cruciani, S.; Feliziani, M. Magnetic Shielding of Wireless Power Transfer Systems. In Proceedings of the 2014 International Symposium on Electromagnetic Compatibility (EMC'14), Tokyo, Japan, 12–16 May 2014; pp. 422–425.
14. Kim, S.; Park, H.-H.; Kim, J.; Kim, J.; Ahn, S. Design and Analysis of a Resonant Reactive Shield for a Wireless Power Electric Vehicle. *IEEE Trans. Microw. Theory Techn.* **2014**, *62*, 1057–1066. [CrossRef]
15. Ishida, M.; Watanabe, T. Magnetic Field Canceling Coil for Wireless Power Transfer System. In Proceedings of the 2015 IEEE Wireless Power Transfer Conference (WPTC), Boulder, CO, USA, 13–15 May 2015; pp. 1–4.
16. Park, J.; Kim, D.; Hwang, K.; Park, H.H.; Kwak, S.I.; Kwon, J.H.; Ahn, S. A Resonant Reactive Shielding for Planar Wireless Power Transfer System in Smartphone Application. *IEEE Trans. Electromagn. Compat.* **2017**, *59*, 695–703. [CrossRef]
17. Zhu, Q.; Zhang, Y.; Guo, Y.; Liao, C.; Wang, L.; Wang, L. Null-Coupled Electromagnetic Field Canceling Coil for Wireless Power Transfer System. *IEEE Trans. Transp. Electrific.* **2017**, *3*, 464–473. [CrossRef]
18. Mohammad, M.; Wodajo, E.T.; Choi, S.; Elbuluk, M.E. Modeling and Design of Passive Shield to Limit EMF Emission and to Minimize Shield Loss in Unipolar Wireless Charging System for EV. *IEEE Trans. Power Electron.* **2019**, *34*, 12235–12245. [CrossRef]
19. Cruciani, S.; Campi, T.; Maradei, F.; Feliziani, M. Active Shielding Design for Wireless Power Transfer Systems. *IEEE Trans. Electromagn. Compat.* **2019**, *61*, 1953–1960. [CrossRef]
20. Campi, T.; Cruciani, S.; Maradei, F.; Feliziani, M. Magnetic Field Mitigation by Multicoil Active Shielding in Electric Vehicles Equipped with Wireless Power Charging System. *IEEE Trans. Electromagn. Compat.* **2020**, *62*, 1398–1405. [CrossRef]
21. Scher, A.D.; Mohammad, M.; Ozpineci, B.; Onar, O. Design and Optimization of Cancellation Coil Topologies for a Ferrite-Less Wireless EV Charging Pad. In Proceedings of the 2021 IEEE Transportation Electrification Conference & Expo (ITEC), Chicago, IL, USA, 21–25 June 2021; pp. 1–7.
22. Qin, R.; Li, J.; Sun, J.; Costinett, D. Shielding Design for High-Frequency Wireless Power Transfer System for EV Charging with Self-Resonant Coils. *IEEE Trans. Power Electron.* **2023**, *38*, 7900–7912. [CrossRef]
23. Cruciani, S.; Campi, T.; Maradei, F.; Feliziani, M. Active Shielding Applied to an Electrified Road in a Dynamic Wireless Power Transfer (WPT) System. *Energies* **2020**, *13*, 2522. [CrossRef]
24. Cruciani, S.; Campi, T.; Maradei, F.; Feliziani, M. Active Shielding Design and Optimization of a Wireless Power Transfer (WPT) System for Automotive. *Energies* **2020**, *13*, 5575. [CrossRef]
25. Kim, H.; Song, C.; Kim, D.H.; Jung, D.H.; Kim, I.M.; Kim, Y.I.; Kim, J.; Ahn, S.; Kim, J. Coil design and measurements of automotive magnetic resonant wireless charging system for high-efficiency and low magnetic field leakage. *IEEE Trans. Microw. Theory Tech.* **2016**, *64*, 383–400. [CrossRef]

26. Li, Y.; Zhang, S.; Cheng, Z. Double-Coil Dynamic Shielding Technology for Wireless Power Transmission in Electric Vehicles. *Energies* **2021**, *14*, 5271. [CrossRef]
27. Tan, L.; Elnail, K.E.I.; Ju, M.; Huang, X. Comparative Analysis and Design of the Shielding Techniques in WPT Systems for Charging EVs. *Energies* **2019**, *12*, 2115. [CrossRef]
28. Choi, S.Y.; Gu, B.W.; Lee, S.W.; Lee, W.Y.; Huh, J.; Rim, C.T. Generalized Active EMF Cancel Methods for Wireless Electric Vehicles. *IEEE Trans. Power Electron.* **2013**, *29*, 5770–5783. [CrossRef]
29. *SAE J2954*; Wireless Power Transfer for Light-Duty Plug-in/Electric Vehicles and Alignment Methodology. Society of Automotive Engineers (SAE): Warrendale, PA, USA, 2022.
30. Available online: https://www.packlitzwire.com/products/litz-wires/rupalit-classic/ (accessed on 4 January 2024).
31. International Commission on Non-Ionizing Radiation Protection. Guidelines for limiting exposure to time-varying electric and magnetic fields for low frequencies (1 Hz–100 kHz). *Health Phys.* **2010**, *99*, 818–836. [CrossRef]
32. *ISO 14117:2019*; Active Implantable Medical Devices—Electromagnetic Compatibility—EMC Test Protocols for Implantable Cardiac Pacemakers, Implantable Cardioverter Defibrillators and Cardiac Resynchronization Devices. ISO: Geneva, Switzerland, 2019.

energies

Article

Hull-Compatible Underwater IPT System with Enhanced Electromagnetic–Thermal Performance for USVs

Qingyu Zhao [1], Songyan Niu [1], Ziyun Shao [2] and Linni Jian [1,*]

[1] Department of Electronic and Electrical Engineering, Southern University of Science and Technology, Shenzhen 518055, China; 12232136@mail.sustech.edu.cn (Q.Z.); 11749179@mail.sustech.edu.cn (S.N.)
[2] School of Electronics and Communication Engineering, Guangzhou University, Guangzhou 510006, China; zyshao@gzhu.edu.cn
* Correspondence: jianln@sustech.edu.cn; Tel.: +86-755-8801-8525

Abstract: With the growing use of unmanned surface vehicles (USVs) for underwater exploration, efficient wireless charging solutions like inductive power transfer (IPT) are crucial for addressing power limitations. This paper presents a novel IPT system for USVs and introduces a systematic design approach for optimizing magnetic couplers. The proposed design addresses three critical challenges: misalignment tolerance, lightweight construction, and thermal safety, which are intricately linked through a magnetic field. In terms of misalignment, this paper demonstrates that the coil length is a key factor in determining misalignment tolerance. For a lightweight design, replacing the ferrite plate with ferrite bars can significantly reduce the weight of the coupler without causing core saturation. The design is further validated through a two-way coupled electromagnetic–thermal simulation. The results reveal that, with proper thermal management, the system avoids thermal risks in underwater environments compared to air. Finally, a 3 kW prototype is constructed and tested in fresh water, achieving 55 V and 50 A wireless charging at an 85.7% full-load dc-to-dc efficiency, thus confirming the practicality and performance of the design.

Keywords: inductive power transfer; magnetic coupler; lightweight design; misalignment tolerance; thermal safety; underwater surface vehicles

1. Introduction

As the exploration of lakes and oceans continues to expand, there is growing demand for underwater detection devices [1]. These battery-powered devices are highly likely to face endurance limitations due to the constraints of battery capacity. To address this challenge, researchers have been exploring various charging solutions, including battery swap, conductive charging, and wireless charging [2]. Among them, inductive power transfer (IPT), a form of wireless charging has emerged as a promising method and has already seen widespread application [3–5]. IPT systems are particularly well-suited for underwater environments, offering a high safety level in a cost-effective manner [6,7].

The aforementioned underwater detection devices are mainly mounted on two types of carriers: autonomous underwater vehicles (AUVs), which operate beneath the water surface [8], and unmanned surface vehicles (USVs) [9], which work on the water's surface at centimeter-level depths. Recently, research on underwater IPT systems has mainly focused on the former, as depicted in Figure 1a. To be specific, misalignments that are both rotational and axial between the transmitter (Tx) and the receiver (Rx) can adversely impact the charging performance of AUVs, which makes the design of a magnetic coupler attractive. Kan et al. [10] employed a configuration comprising three transmitters and a single receiver to maintain a stable mutual inductance despite rotational misalignment. Lin et al. [11] introduced a coaxial design for AUVs with cylindrical hulls, improving misalignment tolerance. Building on these advancements, Zeng et al. [12] developed a hybrid transmitter combining conical and planar spiral sections, with the conical section angled to improve magnetic field uniformity.

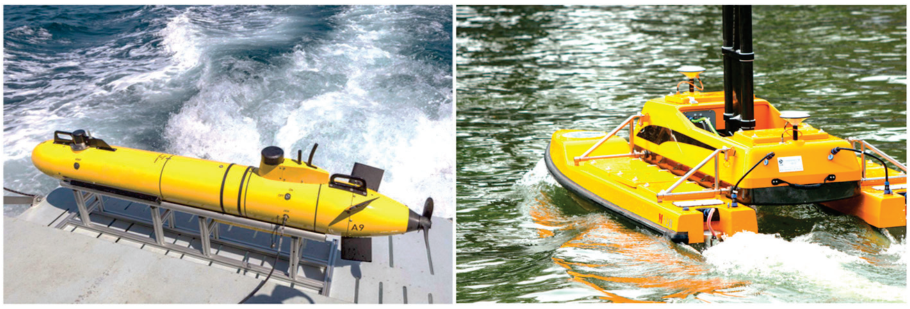

(**a**) (**b**)

Figure 1. Common electric-powered aquatic vehicles. (**a**) AUV. (**b**) USV.

Similar to AUVs, USVs also need to mitigate the impact of misalignment on coupling performance, but their misalignment types are different [13]. USVs typically do not experience rotational misalignment, which will be elaborated upon in Section 2. Additionally, their smaller displacement tonnage imposes strict weight limitations, implying that the mass of the coupler—which directly influences the endurance of USVs—requires careful consideration [14]. Figure 2a illustrates a coupler measuring 500 mm $\times$ 500 mm $\times$ 30 mm, composed of Litz coil, magnetic core, coil mold, shielding, and thermal adhesive. As shown in Figure 2b, the coil mold and magnetic core together account for approximately three-quarters of the total weight, with the magnetic core being significantly heavier than the other components. Lightweight design has become a key focus in IPT research [15,16]. Two common approaches to achieve a lighter coupler are: replacing the traditional Mn-Zn ferrite core with a nanocrystalline ribbon core [17–20], and optimizing the magnetic circuit to reduce ferrite core usage while maintaining performance. For instance, Wang et al. [21] developed an arc-shaped coupler for the REMUS 600 AUV using Fe-based nanocrystalline materials, reducing the receiver's weight by 42.6% while achieving a dc-to-dc efficiency of 91.9%. Although this method reduces the weight, Fe-based nanocrystalline materials are less mature compared to Mn-Zn ferrites in terms of bulk density, volume resistivity, and cost. Another approach fundamentally involves two steps. The first is to obtain the distribution of the magnetic flux using a full core plate, and the second is to remove the sections with low flux density. For instance, Cai et al. [22] utilized magnetic flux density simulations to develop a cross-coupling mode coupler, achieving a dc-to-dc efficiency of 95.1% with a 1 kW prototype while the receiver weighed only 600 g. This paper adopts the second approach, focusing on optimizing the magnetic core configuration to achieve weight reduction.

In addition to lightweight design and misalignment tolerance, thermal safety is another crucial consideration [23,24]. When the coupler is in direct contact with water, it necessitates proper sealing and potting to safeguard the internal components. Once sealed, it is crucial to evaluate the effectiveness of heat dissipation from the magnetic components. While it is acknowledged that underwater environments typically facilitate superior heat dissipation compared to air, the extent to which this advantage translates into more effective heat dissipation in underwater settings remains unexplored.

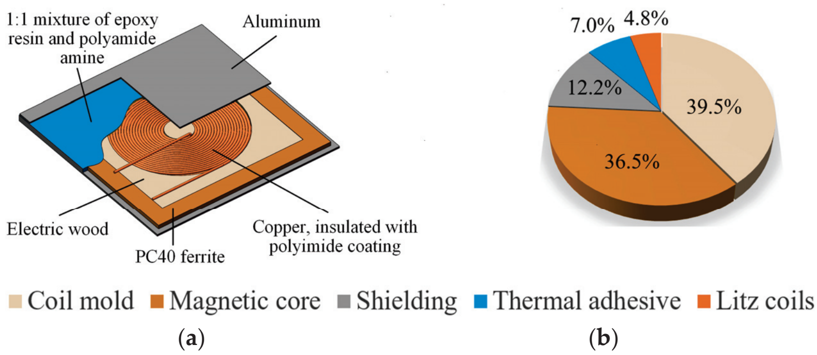

Figure 2. Structure and weight distribution of the IPT magnetic coupler. (**a**) Structural composition and materials. (**b**) Weight distribution.

This paper focuses on underwater IPT for USVs, a field with numerous practical applications but relatively limited research. Furthermore, it not only proposes innovative structures but also introduces a systematic design process for developing a lightweight, misalignment-tolerant, and thermally safe coupler. The main contributions of this work include the following: We propose a dock system to ensure stable coupling conditions between the transmitter and receiver. We comprehensively consider the misalignment tolerance, light weight, and thermal safety in the design objectives, providing a systematic design process. We fabricate a practical IPT system for USVs based on the proposed design process and verify it experimentally.

2. A Systematic Approach to Design Challenges

A practical IPT system requires a comprehensive consideration of electromagnetic and thermal performance while taking into account the weight. Unfortunately, these design considerations often conflict with each other, posing challenges to system design. Specifically, the primary objective is to achieve high misalignment tolerance, which means that the output power of the system still needs to maintain its rated value at the maximum misalignment [25]. This is typically achieved by increasing the number of coils and cores used, but a lightweight design is also an objective—a contradiction. Moreover, since coils are the main heat source in the system, enhancing misalignment tolerance could also lead to increased heat generation—another contradiction. In other words, these three factors—misalignment tolerance, lightweight design, and thermal safety, as depicted in Figure 3—are intricately linked through forms of electrical energy, magnetic field energy, and thermal energy, underscoring the need for a systematic approach in optimizing the coupler design.

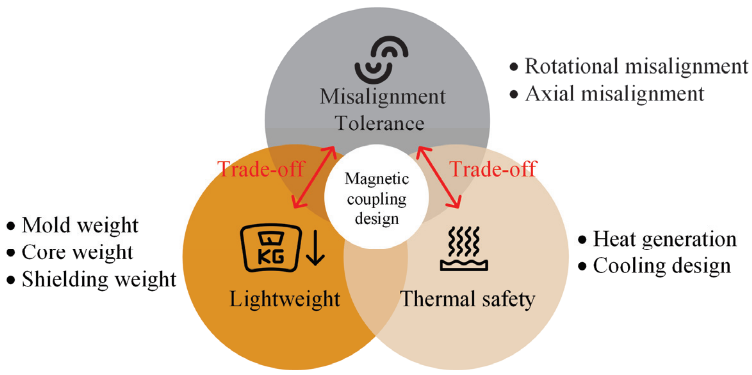

Figure 3. Relationship between misalignment tolerance, lightweight design, and thermal safety.

Figure 4 presents the detailed design process for the coupler. It should be noted that, for the coupler, it was assumed that the main electrical specifications of the IPT system had already been determined, such as the input and output voltages, converter topology, compensation topology, and so on. On this basis, the key electrical parameter for the coupler, viz., the mutual inductance M between the Tx and the Rx, can be discussed. This parameter directly determines the voltage gain of the system, and consequently, the output power of the system. Therefore, this design process began by establishing the minimum M required. Secondly, the range of mutual inductance $[M_{min}, M_{max}]$ and the maximum allowable weight W_{max} were determined based on the misalignment tolerance and weight constraints. It was assumed that the M_{max} occurred when the Tx and Rx were perfectly aligned, while the M_{min} was reached at maximum misalignment. For stable power output, it was ideal to maintain the difference between the M_{max} and M_{min} within 20%. Thirdly, finite element (FE) simulation methods in Maxwell were used to develop the coupler model. To reduce the weight of the coupler, it is recommended to use the hull of the vessel as the base for coils. The model dimensions were dictated by the shape constraints of the USVs or other vessels. Fourthly, the coil dimensions and ferrite core arrangement were adjusted and optimized based on the developed model. For weight reduction, the ferrite core initially covered the entire area but was reduced in regions with low magnetic flux density. Upon completing the coil and ferrite core design, a sweep analysis was performed to ensure that the M remained within the specified range $[M_{min}, M_{max}]$ under various misalignment conditions. The design was also evaluated for its weight and ferrite core saturation. If the design failed to meet these criteria, further adjustments were made. Once all requirements were satisfied, the results were imported into Icepak for a two-way coupled thermal analysis to assess thermal risks. This two-way coupling between Maxwell and Icepak allowed for a more accurate simulation of the temperature distribution within the coupler. For thermal risk assessment, the SAE J2954 standard was referenced, with ignition thresholds set at 90 °C for non-metallic objects and 80 °C for metallic objects [26]. This design process addressed key engineering challenges and facilitated the efficient development of a coupler that meets all specified requirements.

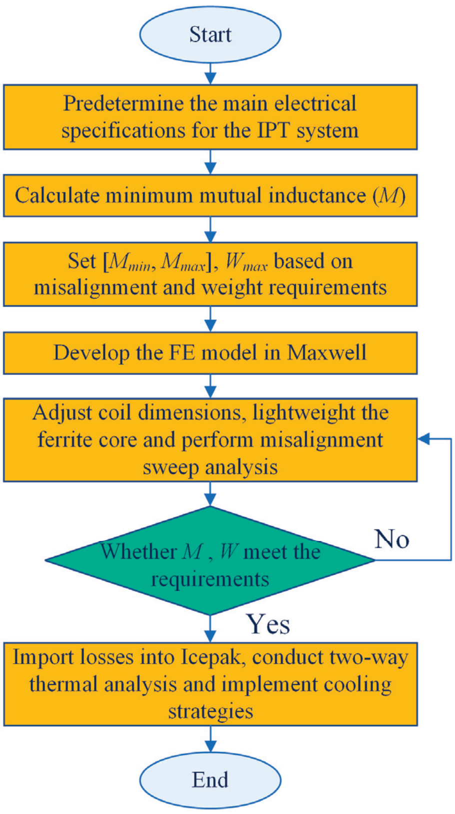

Figure 4. Systematic design process for magnetic coupler.

3. Architecture of Dock System and Charging System

3.1. A Novel Dock System for Underwater IPT

To support safe, stable, and efficient charging operations, an IPT-integrated dock system, which has been implemented in practical applications, is proposed, as shown in Figure 5a. This system is suitable for catamarans consisting of two parallel hulls of equal size, a type of USV. Upon the entry of the USV into the dock, the lifting device, equipped with two transmitters on its upper part, begins to rise and locks into place based on the USV's depth of immersion, ensuring that the vertical distance between the Tx and Rx remains constant during the charging process. The uppermost part of the lifting device is a U-shaped sliding rail with embedded Tx coils, also referred to as the Rx limiter in Figure 5b. Its U-shaped structure perfectly matches the shape of the USV, ensuring no horizontal misalignment occurs between the Tx and Rx, which is conducive to creating stable coupling conditions for IPT. Such conditions do not require precise sensing devices but rely simply on their own gravity, as explained in Figure 5c. In summary, thanks to the dock design, this work can primarily focus on the axial misalignment due to the forward movement of the USV.

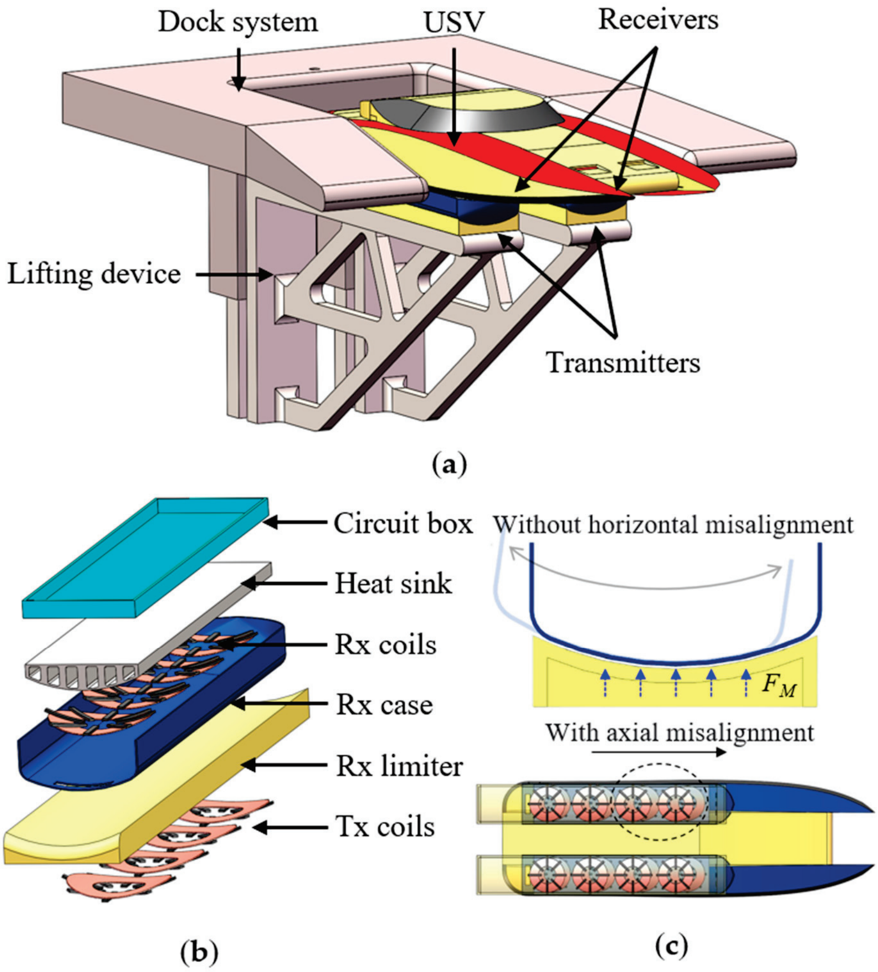

Figure 5. Model of USV IPT system. (**a**) Dock structure. (**b**) Close-up view of Tx and Rx components. (**c**) Working principle of limiter.

3.2. Charging System for Underwater IPT

Defining the electrical parameters is crucial in coupler design. Given that many USVs utilize 48 V lithium iron phosphate (LiFePO4) battery packs, this work focuses on achieving a 3 kW fast charging solution for a 48 V battery pack. To meet the low-voltage, high-current requirements while minimizing heat generation, a configuration consisting of two series-connected Tx coils and two parallel-connected Rx coils was adopted, as illustrated in Figure 6. It was important to ensure that the charging process does not induce excessive temperature rise, as battery temperature fluctuations can negatively affect the accuracy of state-of-charge (SOC) estimation, which is critical for the safe operation of the battery. Inaccurate SOC estimation, especially in varying temperature environments, can lead to thermal runaway and pose significant risks to battery safety and longevity. This is why accurate estimation of both the SOC and temperature is essential to prevent safety hazards in battery charging systems [27].

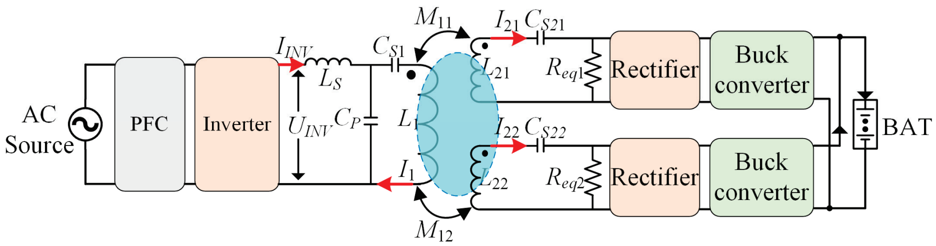

Figure 6. Schematic diagram of IPT circuit with LCC–S topology.

This architecture reduced the cost of the inverter circuit on the Tx side due to the series connection and facilitated closed-loop control. On the Rx side, the parallel connection decreased the current amplitude in the Rx coils, effectively reducing the overall heat generation.

On the Tx side, the input voltage of 110 or 220 V utility power passes through a power factor correction (PFC) stage, converting it into high-voltage dc [28]. This stage converts the ac input to 400 V dc while synchronizing the input current waveform with the input voltage waveform, thereby improving the power factor and reducing harmonic distortion. This dc is then fed into a dc-ac inverter, generating high-frequency ac to power the Tx coil. On the Rx side, two parallel-connected Rx coils each have independent circuits. These circuits consist of a rectifier and buck converter, which convert the received ac into dc and deliver the current in parallel to the USV's battery pack.

As for the compensation circuit, the LCC-S topology was adopted, since it enables straightforward control of the constant current in the Tx coil, independent of variations in load or coupling [29]. As shown in Figure 6, on the Tx side, L_S, C_P, and C_{S1} represent the series inductance, parallel capacitance, and series capacitance of the LCC compensation unit, respectively, while L_1 denotes the self-inductance of the Tx coil. On the Rx side, L_{21} refers to the self-inductance of one of the Rx coils, while C_{S21} represents the series compensation capacitance. R_{eq1} is the equivalent resistances that account for the rectifier, converter, and batteries. Notably, the parameters of the two Rx coils can be considered identical, meaning $L_{21} = L_{22}$ and $C_{S21} = C_{S22}$.

To establish the relationship between the inverter voltage U_{INV} and the currents in the respective coils (I_1, I_{21}, I_{22}), Kirchhoff's voltage law (KVL) was applied within the relevant loops, which is stated as follows:

$$\begin{bmatrix} U_{INV} \\ 0 \\ 0 \\ 0 \end{bmatrix} = \begin{bmatrix} j\omega L_S - j/\omega C_P & j/\omega C_P & j\omega M_{11} & j\omega M_{12} \\ j/\omega C_P & j\omega L_S - j\omega C_{S1} & 0 & 0 \\ 0 & j\omega M_{11} & Z_{21} + R_{eq1} & 0 \\ 0 & 0 & j\omega M_{12} & Z_{22} + R_{eq2} \end{bmatrix} \begin{bmatrix} I_{INV} \\ I_1 \\ I_{21} \\ I_{22} \end{bmatrix}, \quad (1)$$

where M_{11} and M_{12} represent the mutual inductances between the Tx coil and the two sets of Rx coils, respectively. Z_{21} and Z_{22} denote the total impedances of each loop on the Rx side, respectively, which are defined as follows:

$$Z_{2i} = j\omega L_{2i} + 1/j\omega C_{S2i}(i = 1, 2), \tag{2}$$

To achieve resonant operation, the impedance of each component in the LCC topology must be set equivalently, as follows [30]:

$$j\omega L_S = j/\omega C_P = j(\omega L_1 - 1/\omega C_{S1}), \tag{3}$$

Additionally, the Rx coils are designed to operate in full resonance, as follows:

$$j\omega L_{2i} = j/\omega C_{S2i}(i = 1, 2), \tag{4}$$

Under these conditions, the total output power can be readily determined as follows:

$$P_O = U_{INV}^2 \times \left(M_{11}^2/R_{eq1} + M_{12}^2/R_{eq2}\right)/L_S^2, \tag{5}$$

To achieve an output power of over 3 kW for the IPT system, the input voltage was set at 400 V. Based on Equation (5), the minimum mutual inductance M of the coupler was calculated to be approximately 6.7 μH, given that L_S is 40 μH and R_{eq} = 8 × R_{dc}/π^2. To ensure sufficient output capacity, the mutual inductance is typically designed to be higher than this value.

4. Design and Optimization of Magnetic Coupler

4.1. Enhancement of Misalignment Tolerance

As depicted in the design flow of Figure 4, once the minimum values of mutual inductance were established (as described in Section 3.2), the FE model was subsequently developed in Ansys Maxwell, as shown in Figure 7. This model, viz., the initial design, features curved surfaces to match the shape of each side of the catamaran USV. Owing to engineering requirements, four design variables were determined: the transmission distance d_{TR} between the Tx and Rx coils is set at 20 mm, which represents the combined thickness of the adhesive, cover, and U-shaped sliding rail; the curvature θ is 48 degrees to exactly match the curvature of the USV surface; the coil width W is fixed at 165 mm to maximize the use of the assembly space allowed. One of the primary variables affecting misalignment tolerance is the coil length L. Consequently, the primary factors affecting misalignment tolerance are the coil length L and the coil topology.

Figure 7 illustrates the impact of the coil length L, which is the same for both the Tx and Rx coils initially, on the mutual inductance, with axial misalignment d_{mis} incrementally adjusted from 0 to 100 mm in 10 mm steps. Concurrently, L is increased from 200 mm to 1000 mm in 100 mm increments. The vertical axis in Figure 7 represents the mutual inductance ratio R = M_{mis}/M_0, where M_{mis} and M_0 denote the mutual inductance after and before misalignment, respectively. Thus, R can reflect the change in the mutual inductance due to misalignment directly. In general, as the L increases, so does the mutual inductance of the coupler. When the L reaches 400 mm, the minimum mutual inductance requirement has been fulfilled. Nevertheless, considering that further reduction in the weight of the ferrite core might lead to a decrease in the mutual inductance, the L should exceed 400 mm. At L = 700 mm, the variation of R remains within 20% for d_{mis} of up to 100 mm, which successfully satisfies the aforementioned misalignment tolerance requirements.

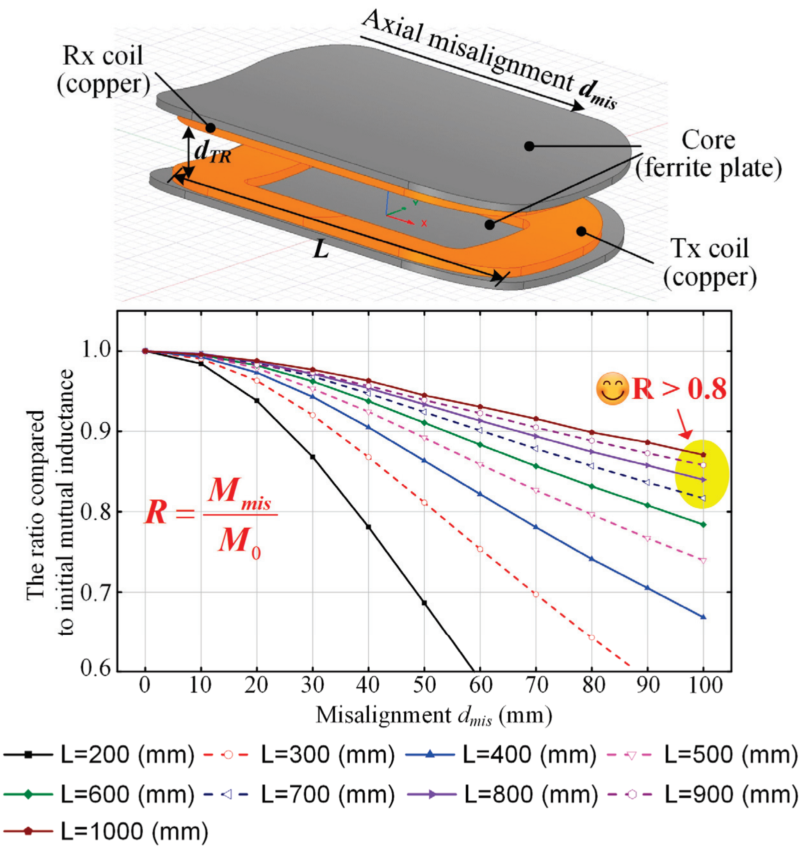

Figure 7. Initial design of coil structure and mutual inductance variation versus misalignment.

4.2. Reduction of Core Weight with Effective EM Shielding

In the FE model, the coil is designed in a running track-shaped configuration to improve the USV's tolerance to axial misalignment. The ferrite plate is shaped to conform to the coil's structure, providing full coverage, as shown in Figure 7. However, in wireless charging scenarios, reducing the ferrite core in areas with lower magnetic flux density can significantly reduce the system's overall weight while minimizing the impact on the coupling performance. As shown in Figure 8a, this work adopted ferrite bars in Rx with dimensions of 60 mm or 80 mm × 15 mm × 5 mm, which are arranged equidistantly along the axial direction of the coil, with the bars oriented toward the center of the coil. In this study, we used Mn-Zn ferrite materials, specifically the PC-40 model, which is widely adopted in high-power wireless charging systems. The initial permeability of the PC-40 ferrite is 2300, and its saturation flux density is 500 mT. These ferrite bars are easily obtainable in practical engineering applications. In addition, as noted by Yang et al. [20], the arrangement of the ferrite bars needs to align with the magnetic flux paths to maximize the coupling efficiency and minimize the loss caused by suboptimal material placement, as illustrated in Figure 8b. Maxwell simulation results indicate that, when the receiver side is not optimized for weight reduction, the magnetic flux density is very low on both sides of the ferrite plate along the *Y*-axis. This suggests that reducing the ferrite material in this region, as in the lightweight design, resulted in minimal changes in the coupling between the transmitting and receiving coils. Compared to the ferrite plate, the use of ferrite bars reduced the ferrite's weight by 80%, while the mutual inductance decreased from 32.17 μH to 23.93 μH, representing only a 25.2% reduction.

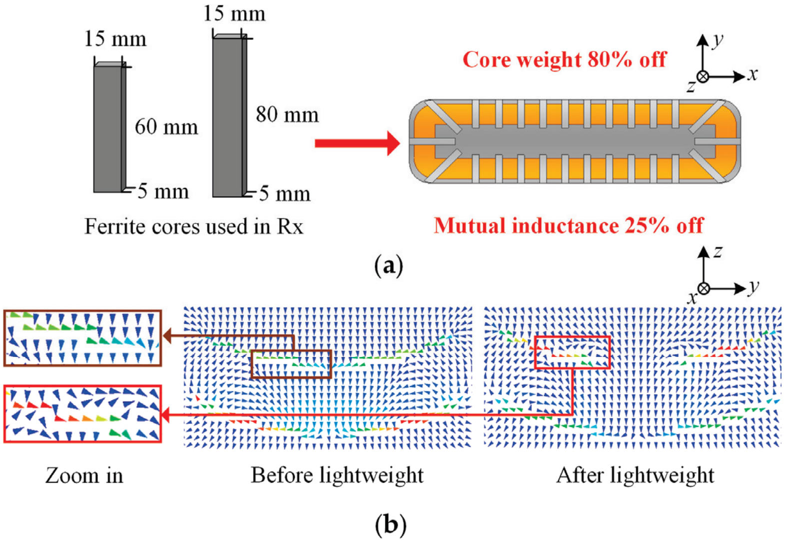

Figure 8. Lightweight design of Rx ferrite core. (**a**) Arrangement of ferrite bars. (**b**) Magnetic flux density distribution.

In addition to using ferrite bars in running track-shaped coil, this work drew inspiration from circular power pads [15]. Based on these findings, the Rx coil is redesigned into four squircle-shaped coils—an intermediate form between a square and a circle—with each coil measuring 175 mm × 165 mm. The squircle-shaped coils are connected in series, ensuring consistent current direction to avoid interference with the induced current generation. This configuration allows for a more compact ferrite bar arrangement, as shown in Figure 9a. Replacing the ferrite plate with ferrite bars in the squircle-shaped coils reduced the mutual inductance from 27.54 µH to 23.54 µH, a reduction of only 14.5%. Compared to the running track-shaped coil, using the same number of ferrite bars in the squircle-shaped configuration improved the magnetic field guidance at the coil's center, as depicted in Figure 9b.

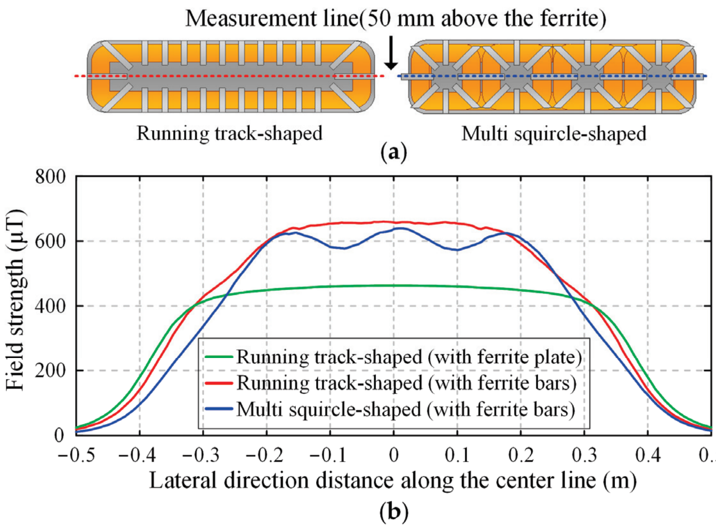

Figure 9. (**a**) Comparison of different coil configurations and ferrite core arrangements. (**b**) Field strength variations along the lateral direction for different configurations.

The use of ferrite bars inevitably increases magnetic field exposure, making electromagnetic (EM) shielding essential. This shielding is typically achieved using aluminum materials. The B field strength measured 50 mm above the Rx coils is shown in Figure 9b. Using a ferrite plate resulted in a maximum B value of 463.01 µT, while using ferrite bars in running track-shaped and multi-squircle-shaped coils produced values of 659.94 µT and 639.17 µT, respectively—both exceeding the SAE J2954 electromagnetic interference limits, which may disrupt circuit function.

Fortunately, this study ingeniously mitigated EM interference by proposing an integrated solution for heat dissipation and shielding. That is to say, the aluminum heat sink traditionally used for dissipating heat from switching devices, typically designed as a small plate, was reconfigured into a closed-layer box, as illustrated in Figure 10. Compared to an aluminum shielding plate placed over the entire Rx coils, this approach significantly reduces the amount of aluminum used. Moreover, the EM interference resistance of the onboard circuits remains unaffected. Interestingly, when the distance from the top surface of the Rx shielding box increased from 10 mm to 50 mm, the intensity of magnetic field exposure counterintuitively increased. However, this is not a concern, as only the electronics within the box are required to be effectively protected.

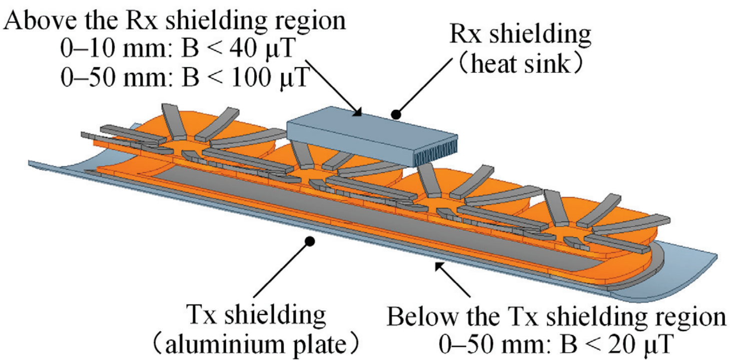

Figure 10. EM shielding solution.

5. Magnetic–Thermal Performance of Magnetic Coupler

5.1. General Description

In an IPT system, the majority of losses occur within the coupler, where they are converted into heat, subsequently leading to temperature rises. Excessive heat can cause problems such as ferrite core fractures and even pose safety hazards. Fortunately, underwater environments can hopefully provide superior heat dissipation compared to air. However, a quantitative analysis of how much more effective underwater environments are at heat dissipation has not been explored. Moreover, to ensure the integrity of the system, proper sealing and potting are required in practice, which adds extra weight and must be factored into the overall design considerations.

5.2. Loss Calculation and Distribution

The primary losses in the coupler are concentrated in the Litz coil, ferrite core, and aluminum plate. A loss analysis of these components was conducted using Maxwell software. Maxwell 2022 R1 provides a simplified Litz coil modeling method, eliminating the need to model each strand individually. Consequently, the model developed in Section 4 was directly applied to this analysis. The losses in the Litz coil were calculated as follows:

$$P_{coil}(T) = \left(F_{skin} + F_{prox}\right) I_{coil}^2 R_{dc}(T), \tag{6}$$

where I_{coil} represents the coil current, R_{dc} is the dc resistance with a temperature correction factor, and F_{skin} and F_{prox} account for the skin and proximity effects, respectively.

Magnetic core losses can be analyzed in Maxwell using three models: electrical steel, power ferrite, and the B-P curve. The first model, which separates losses into hysteresis, eddy currents, and additional losses, was selected, as it integrates well with the eddy-current solver and supports B-P curve input for enhanced precision. When subjected to sinusoidal excitation, the core losses were determined as follows:

$$P_{core} = \int_V \left(k_h f B(T)_m^2 + k_c (f B(T)_m)^2 + k_e (f B(T)_m)^{1.5} \right) dV, \tag{7}$$

where k_h, k_c, and k_e represent the coefficients for hysteresis loss, eddy current loss, and excess loss, respectively. $B(T)_m$ is the magnetic flux density, and f is the frequency of the sinusoidal wave.

Losses in the aluminum plate are primarily caused by eddy currents. For the accurate calculation of these losses in the simulation model, the skin depth must be properly defined, requiring a refined mesh that matches the skin depth, along with the application of impedance boundary conditions [31]. Once the model is solved, the shielding losses can be determined by integrating the current loop using the field calculator.

Based on the loss calculation in Maxwell 2022 R1, Figure 11 illustrates the distribution of losses in the coupler, including both the Tx and Rx sides. The material parameters used for the simulation are listed in Table 1. On the Tx side, the losses in the Litz coil, ferrite core, and aluminum shielding were 24.81 W, 20.27 W, and 4.03 W, respectively. On the Rx side, the losses in the Litz coil and ferrite core were 36.86 W and 12.21 W, respectively. The simulation results show that the coil losses on the Rx side were higher than those on the Tx side, while the ferrite core losses were lower. Note that the aforementioned loss values correspond to the 1.5 kW scenario, representing the transmitted power between a single Tx and a single Rx, as shown in Figure 11. Consequently, the total losses for the 3 kW coupler should be doubled.

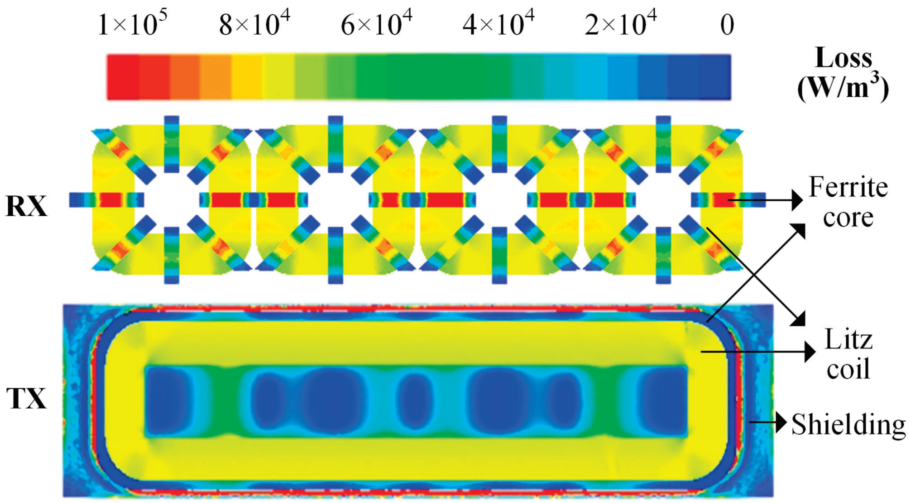

Figure 11. Loss distribution in Litz coil, ferrite core, and shielding.

Table 1. Key material properties of components in a coupler.

Component	Material	Electric Conductivity (S m^{-1})	Relative Permeability	Thermal Conductivity (W m^{-1} K^{-1})
Coil	Copper	58,000,000	0.999991	400
Core	Ferrite	0.01	2300	6
Shielding	Aluminum	38,000,000	1.000021	238
Thermal Adhesive [1]	Epoxy resin	0	1	0.3
	Polyamide amine	0	1	0.25

[1] The thermal conductivity of thermal adhesive can be increased to 2.2 when two components are mixed in a 1:1 ratio.

5.3. Temperature Distribution and Management

The heat generated by the Litz coil, ferrite core, and aluminum plate in the coupler leads to a temperature rise. This heat is dissipated through conduction, convection, and radiation between the coupler and its surroundings, eventually reaching thermal equilibrium. Heat transfer between the coupler and the surrounding air or water occurs primarily through convection, which is governed by Newton's law of cooling, as follows:

$$Q_{conv} = hA\left(T_{surf} - T_{env}\right), \tag{8}$$

where Q_{conv} represents the heat generated, h is the heat transfer coefficient, and A refers to the convective surface area. T_{surf} and T_{env} denote the surface temperature of the coupler material and the ambient air or water, respectively. Regarding heat loss due to radiation, it accounts for a very small fraction of the total and was, therefore, disregarded in the simulation process [28].

In the two-way coupled simulations, Maxwell computed the loss data, which were then imported into Icepak for thermal analysis. Icepak's temperature data were subsequently fed back into Maxwell, allowing for updates to the material properties, such as the temperature coefficient of R_{dc} for the Litz coil:

$$R_{dc}(T) = R_{dc}(T_0)(1 + \alpha_r(T - T_0)), \tag{9}$$

where T_0 is set to 20 °C and a correction factor of α_r = 0.00393, meaning that a 10 °C temperature change results in a 3.93% variation in R_{dc} and an 8.01% change in associated losses [32].

To compare the steady-state thermal distribution of the coupler in air and water environments, the Litz coil, ferrite core, and aluminum plate were sealed in a layer of 50 mm-thick thermal adhesive. The thermal conductivity of each material is listed in Table 1. The water environment featured a convection rate of 3 mm/s, while the air environment experienced natural thermal convection, both at 20 °C. Under the same loss conditions, the thermal distribution of the coupler in air and water is shown in Figure 12. The temperature data reveal that the coupler's maximum temperature in water was much lower than in air, demonstrating that direct contact with water greatly enhanced the heat dissipation. This suggests that proper thermal management—such as increasing the contact area between the coupler and water—can effectively mitigate thermal risks in underwater IPT systems.

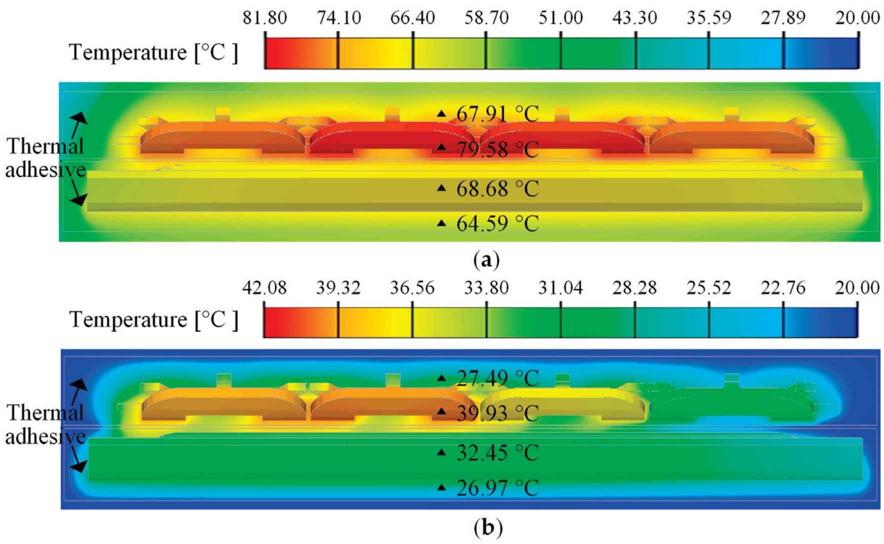

Figure 12. Temperature distribution of coupler in (**a**) air and (**b**) water.

6. Underwater Experimental Validation of 3 kW Prototype

The 3 kW experimental prototype is divided into two parts: the coupler and the circuit components; their specific parameters are shown in Table 2. For the coupler, this work used 3D printing to create the Tx and Rx mold, as shown in Figure 13. The Tx coil follows a running track shape, while the Rx consists of four squircle-shaped coils, both using 1000-strand Litz coils with 6 turns. In practical engineering applications, obtaining a single piece of ferrite plate with the required curvature is challenging due to the material's inherent high hardness and brittleness. To achieve full coverage of the ferrite plate, we used square ferrite cores in Tx with the dimensions of 50 mm × 50 mm × 5 mm, assembling them through a tiling approach, as illustrated in Figure 13. The Tx ferrite plate was placed on a 3 mm thick aluminum shielding plate, which was segmented and bent to minimize the distance between the ferrite plate and the coil. For the Rx ferrite core, we employed the method described in Section 4.

Table 2. Key parameters of experimental prototype.

Parameter	Value	Parameter	Value	Parameter	Value
$W_{Tx\text{-}coil}$ (mm)	165	L_1 (μH)	95.00	Output power (W)	2750
$L_{Tx\text{-}coil}$ (mm)	700	L_{2i}[1] (μH)	43.40	Output dc voltage (V)	54.00
$W_{Rx\text{-}coil}$ (mm)	165	L_S (μH)	40.00	Output dc current (A)	50.93
$L_{Rx\text{-}coil}$ (mm)	175	C_P (nF)	87.00	Operating frequency (kHz)	85
$\theta_{Tx\text{-}Rx}$ (deg)	48	C_{S1} (nF)	66.00	Weight of Rx (kg)	3.57
D_{gap} (mm)	20	C_{S2i}[1] (nF)	90.00	Weight of Tx (kg)	9.42

[1] i = 1, 2. The self-inductance of the two Rx coils differs by 0.2%.

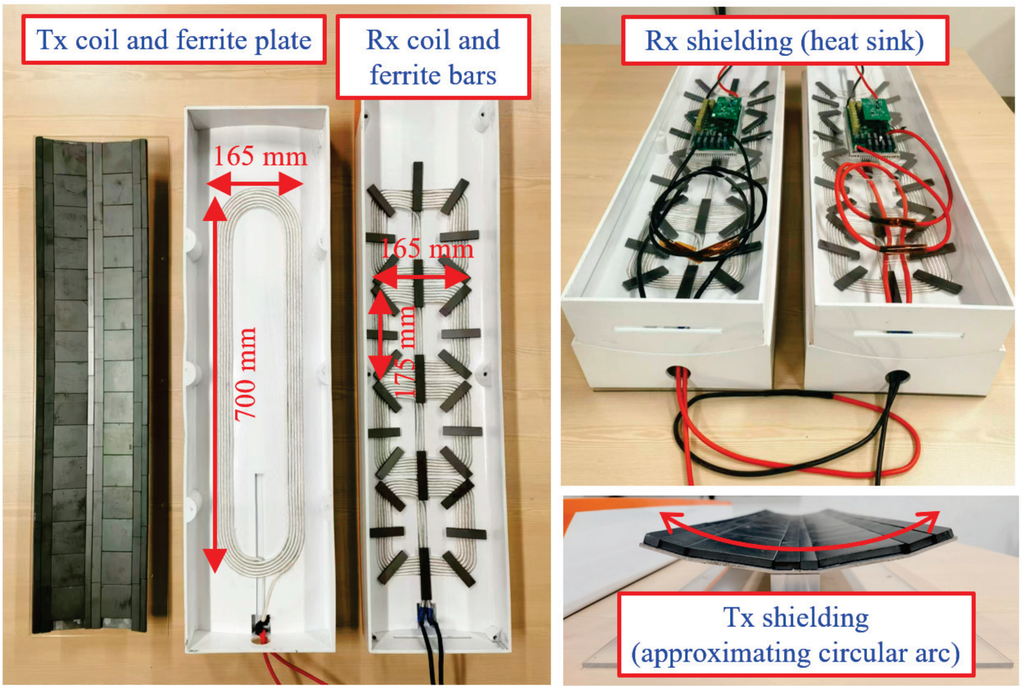

Figure 13. Structural layout of the magnetic coupler prototype: coil, ferrite core, and aluminum shielding.

A lightweight configuration was applied to the Rx side, reducing its weight from 9.66 kg (with an aluminum shielding plate and ferrite plate) to 3.57 kg (with a heat sink and ferrite bars), resulting in a 63% reduction. The mutual inductance of both configurations was measured under various axial misalignment conditions using a Hantek1833C LCR meter (Hantek Electronic Co., Ltd., Qingdao, China) and compared with the simulation results. As shown in Figure 14, the measurements closely match the simulations, with both exhibiting consistent trends across different misalignment scenarios.

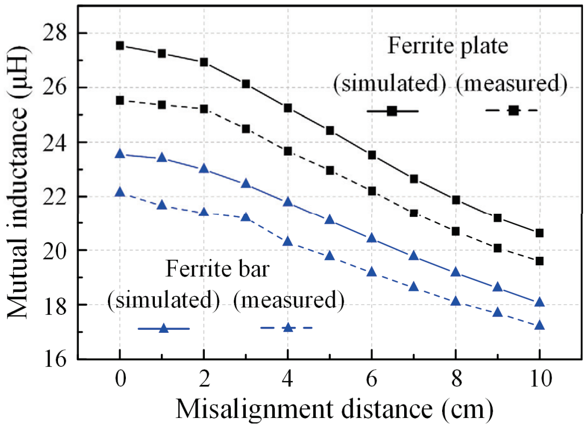

Figure 14. Relationships between mutual inductance and misalignment distance for various Rx ferrite core configurations.

In the circuit section, the front stage of the Tx circuit consisted of a PFC module, providing a 400 V dc output, while the rear stage was a dc-ac inverter unit. The Rx circuit was mounted above the heat sink, which was supported by a slotted acrylic board that acted as waterproof isolation, as shown in Figure 15. The Rx circuit included two parallel ac-dc circuits connected to a 48 V dc electronic load.

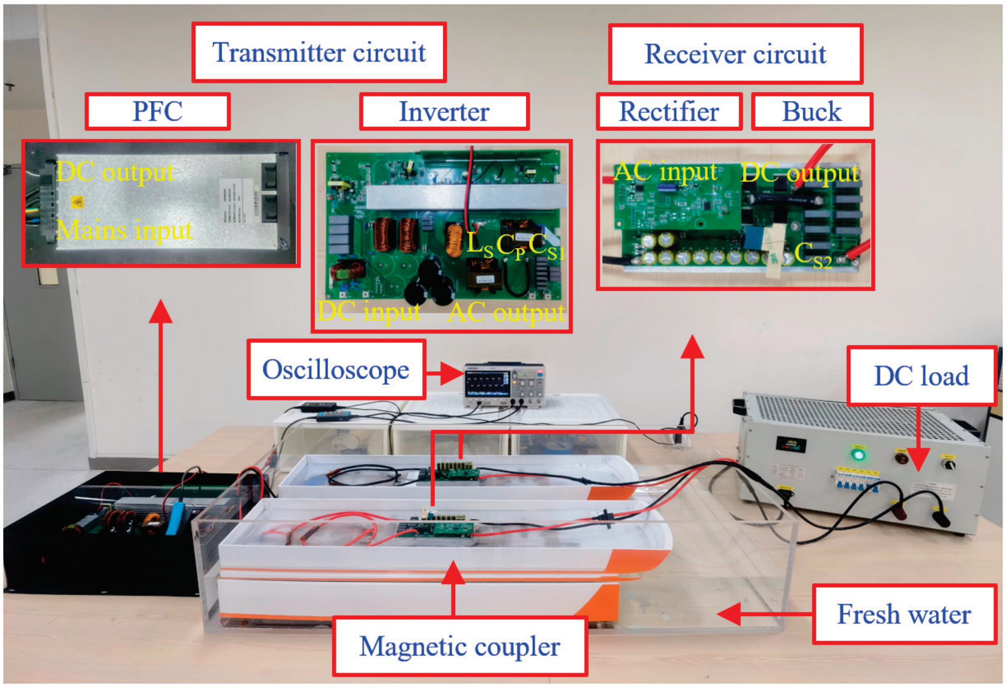

Figure 15. Experimental setup of the 3 kW prototype of the IPT system for USVs.

The coupler was placed in an acrylic water tank filled with fresh water. Using the SIGLENT SDS1104X-U oscilloscope (SIGLENT Technologies Co., Ltd., Shenzhen, China), the waveforms of the inverter output and rectifier input were measured, as shown in Figure 16. Figure 16 illustrates the waveforms measured during full-load operation in the aligned state. The system operated at a frequency of 85 kHz. Channels 1 and 2 displayed the voltage and current waveforms on the inverter output side, specifically at the bridge lags of the inverter. Channels 3 and 4 showed the voltage and current waveforms at the input of the rectifier. Due to the LCC-S resonant circuit, the current phase of the bridge lagged the voltage by 15–20 degrees, achieving ZVS characteristics, which reduced the switching losses. The system's output voltage and current, as well as its link efficiency, were tested under various load and axial misalignment conditions, as shown in Figure 17. The results demonstrate that the system achieved stable output under different load conditions and axial misalignments. Moreover, the results show that the link efficiency, representing the coupler's performance, was at least 96.6% under half-load conditions, which is higher than the 93.2% observed under full-load conditions.

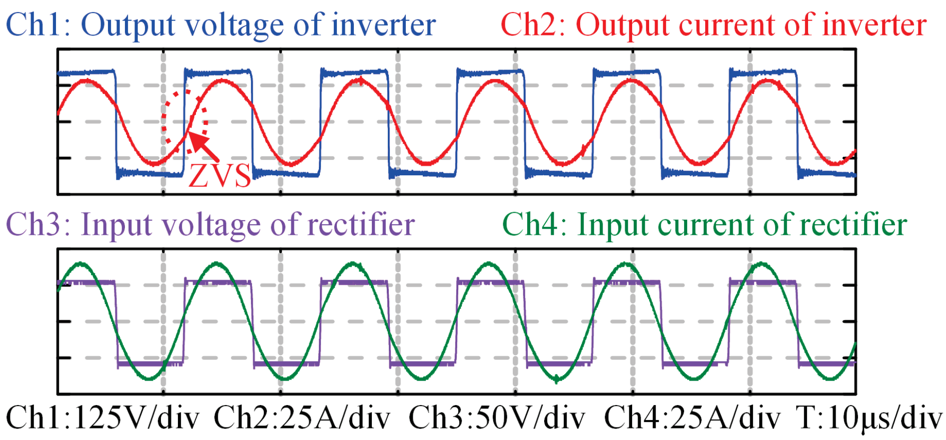

Figure 16. Waveforms of inverter output and rectifier input in fresh water environment.

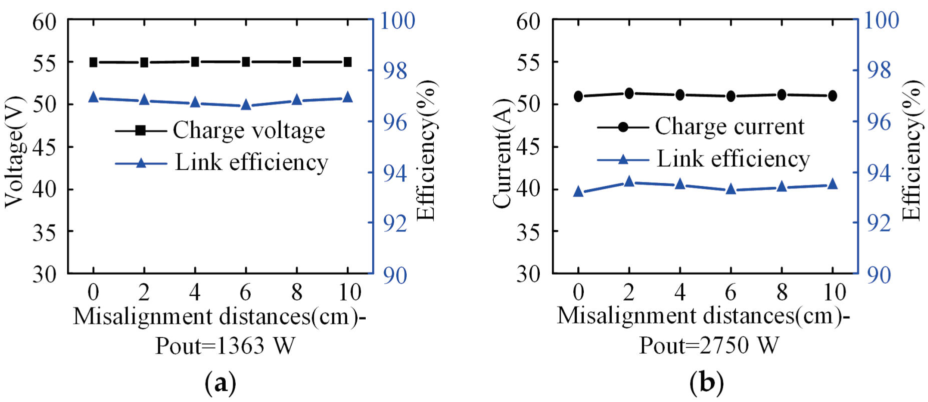

Figure 17. Waveforms of inverter output and rectifier input in fresh water environment. (**a**) Variations of charge voltage and efficiency with axial misalignment distances under half-load operation. (**b**) Variations of charge current and efficiency with axial misalignment distances under full-load operation.

Under full-load conditions, the voltage and current measurements at various circuit terminals reveal the experimental prototype's losses, as shown in Figure 18. The system achieved a dc-to-dc efficiency of 85.7%, with the coupler accounting for the largest loss at 210 W. To manage heat dissipation in the underwater environment, a two-component thermal adhesive was applied for insulation and thermal management. Increasing the contact area between the resin and water, along with enhancing water circulation, effectively dissipated heat. The ambient temperature in the laboratory was 21.4 °C, and the water temperature in the tank was 18.5 °C. When there was no water in the tank, after 30 min of operation, the temperature of the receiver coil reached 43.2 °C, and the ferrite temperature was 31.8 °C. However, when water was added to the tank, the temperature of the receiver coil decreased to 19.2 °C, and the ferrite temperature dropped to 18.8 °C, closely aligning with the surrounding water temperature. This indicates that the underwater environment significantly improved the thermal management of the system, effectively reducing the temperature of the coils and ferrites, ensuring system stability.

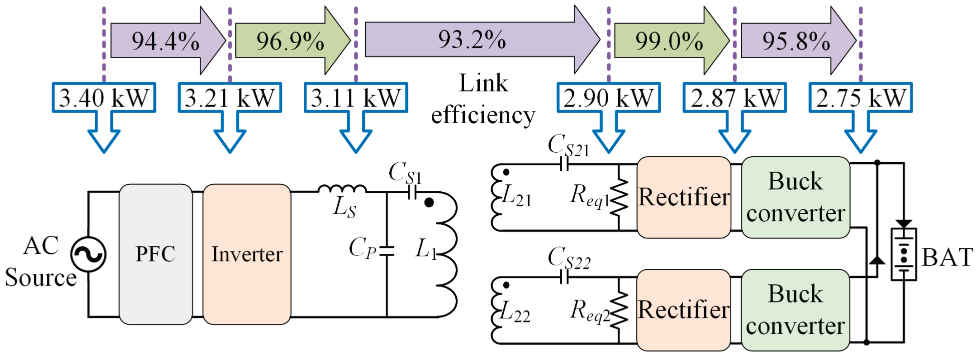

Figure 18. System losses and efficiency analysis.

7. Conclusions

The main challenge of IPT system design lies in the trade-offs among the requirements for misalignment tolerance, lightweight construction, and thermal safety. To effectively address this issue, a systematic design process for the magnetic coupler is proposed. Following this process, a 3 kW IPT system for USVs has been designed with the proposed magnetic coupler for exemplification, which successfully achieved a comprehensive and significant enhancement in both electromagnetic and thermal performance.

First, by optimizing the coil topology and coil length, the system can maintain a mutual inductance variation within 20% under axial misalignment ranging from 0 to 100 mm. Second, the use of ferrite bars instead of ferrite plates reduces the weight of receiver by 63%, ensuring a lightweight design. Third, effective thermal management is achieved through the use of thermal adhesive and by increasing the contact area between the coil and water, preventing thermal risks in fresh water. Fourth, an associated dock system is proposed, which ensures stable coupling conditions by maintaining a constant vertical distance and eliminating horizontal misalignment between the transmitter and receiver. The methodology and engineering techniques demonstrated in this paper can hopefully provide a practical solution for underwater IPT system design, offering a valuable reference for the development of magnetic couplers in similar applications.

Author Contributions: Conceptualization, Q.Z. and L.J.; validation, Q.Z. and S.N.; formal analysis, Q.Z. and S.N.; writing—original draft preparation, Q.Z. and S.N.; writing—review and editing, Z.S. and L.J. All authors have read and agreed to the published version of the manuscript.

Funding: This research was funded by the Jiangyin-SUSTech Innovation Fund, grant number OR2404021.

Data Availability Statement: The original contributions presented in this study are included in the article. Further inquiries can be directed to the corresponding author.

Conflicts of Interest: The authors declare no conflicts of interest.

References

1. De Alegría, I.M.; Rozas Holgado, I.; Ibarra, E.; Robles, E.; Martín, J.L. Wireless Power Transfer for Unmanned Underwater Vehicles: Technologies, Challenges and Applications. *Energies* **2024**, *17*, 2305. [CrossRef]
2. Yan, K.; Dang, R.; Feng, X.; Wang, W. A New Magnetic Coupler with High Misalignment Tolerance and Inherent Constant Current–Constant Voltage for Underground Wireless Charging. *Energies* **2024**, *17*, 5130. [CrossRef]
3. Feng, H.; Tavakoli, R.; Onar, O.C.; Pantic, Z. Advances in High-Power Wireless Charging Systems: Overview and Design Considerations. *IEEE Trans. Transp. Electrif.* **2020**, *6*, 886–919. [CrossRef]

4. Niu, S.; Xu, H.; Sun, Z.; Shao, Z.Y.; Jian, L. The State-of-the-Arts of Wireless Electric Vehicle Charging via Magnetic Resonance: Principles, Standards and Core Technologies. *Renew. Sustain. Energy Rev.* **2019**, *114*, 109302. [CrossRef]
5. Niu, S.; Lyu, R.; Lyu, J.; Chau, K.T.; Liu, W.; Jian, L. Optimal Resonant Condition for Maximum Output Power in Tightly Coupled WPT Systems Considering Harmonics. *IEEE Trans. Power Electron.* **2025**, *40*, 152–156. [CrossRef]
6. Li, K.; Wu, J.; Wang, K.; Yang, Y.; Tang, Y.; Hui, S.Y.R. A Folded Coil Design for Cubic Wireless Charging Space Frames with Even Magnetic Flux Density Distribution. *IEEE Trans. Power Electron.* **2024**, *39*, 9040–9050. [CrossRef]
7. Chen, Z.; Zhang, X.; Xu, F.; Li, M.; Yuan, Z.; Yang, Q. Wide Rotation-Misalignment-Tolerance Design of Magnetic Coupled Structure for AUVs Wireless Charging System. *IEEE Trans. Ind. Electron.* **2024**, *71*, 14086–14096. [CrossRef]
8. Teeneti, C.R.; Truscott, T.T.; Beal, D.N.; Pantic, Z. Review of Wireless Charging Systems for Autonomous Underwater Vehicles. *IEEE J. Ocean. Eng.* **2021**, *46*, 68–87. [CrossRef]
9. Alhattab, Y.A.; Abidin, Z.B.Z.; Faizabadi, A.R.; Zaki, H.F.M.; Ibrahim, A.I. Integration of Stereo Vision and MOOS-IvP for Enhanced Obstacle Detection and Navigation in Unmanned Surface Vehicles. *IEEE Access* **2023**, *11*, 128932–128956. [CrossRef]
10. Kan, T.; Zhang, Y.; Yan, Z.; Mercier, P.P.; Mi, C.C. A Rotation-Resilient Wireless Charging System for Lightweight Autonomous Underwater Vehicles. *IEEE Trans. Veh. Technol.* **2018**, *67*, 6935–6942. [CrossRef]
11. Lin, M.; Li, D.; Yang, C. Design of an ICPT System for Battery Charging Applied to Underwater Docking Systems. *Ocean Eng.* **2017**, *145*, 373–381. [CrossRef]
12. Zeng, Y.; Rong, C.; Lu, C.; Tao, X.; Liu, X.; Liu, R.; Liu, M. Misalignment Insensitive Wireless Power Transfer System Using a Hybrid Transmitter for Autonomous Underwater Vehicles. *IEEE Trans. Ind. Appl.* **2022**, *58*, 1298–1306. [CrossRef]
13. Niu, S.; Zhao, Q.; Chen, H.; Yu, H.; Niu, S.; Jian, L. Underwater Wireless Charging System of Unmanned Surface Vehicles with High Power, Large Misalignment Tolerance and Light Weight: Analysis, Design and Optimization. *Energies* **2022**, *15*, 9529. [CrossRef]
14. Liu, Z.; Zhang, Y.; Yu, X.; Yuan, C. Unmanned Surface Vehicles: An Overview of Developments and Challenges. *Annu. Rev. Control.* **2016**, *41*, 71–93. [CrossRef]
15. Budhia, M.; Covic, G.A.; Boys, J.T. Design and Optimization of Circular Magnetic Structures for Lumped Inductive Power Transfer Systems. *IEEE Trans. Power Electron.* **2011**, *26*, 3096–3108. [CrossRef]
16. Pang, S.; Xu, J.; Xie, Z.; Lu, J.; Li, H.; Li, X. Lightweight UAV's Wireless Power Transfer System for Constant Current Charging without Secondary Feedback Control. *IEEE Trans. Veh. Technol.* **2023**, *72*, 15611–15621. [CrossRef]
17. Wang, Y.; Jiang, C.Q.; Chen, C.; Wang, X.; Li, X.; Long, T. Design and Analysis of Inductive Power Transfer System Using Nanocrystalline Flake Ribbon Core. *IEEE J. Emerg. Sel. Top. Power Electron.* **2024**, *12*, 3334–3347. [CrossRef]
18. Xiong, M.; Wei, X.; Huang, Y.; Luo, Z.; Dai, H. Research on Novel Flexible High-Saturation Nanocrystalline Cores for Wireless Charging Systems of Electric Vehicles. *IEEE Trans. Ind. Electron.* **2021**, *68*, 8310–8320. [CrossRef]
19. Chen, C.; Jiang, C.; Wang, Y.; Fan, Y.; Luo, B.; Cheng, Y. Compact Curved Coupler with Novel Flexible Nanocrystalline Flake Ribbon Core for Autonomous Underwater Vehicles. *IEEE Trans. Power Electron.* **2024**, *39*, 53–57. [CrossRef]
20. Yang, F.; Jiang, J.; Sun, C.; He, A.; Chen, W.; Lan, Y.; Song, K. Efficiency Improvement of Magnetic Coupler with Nanocrystalline Alloy Film for UAV Wireless Charging System with a Carbon Fiber Fuselage. *Energies* **2022**, *15*, 8363. [CrossRef]
21. Wang, D.; Cui, S.; Zhang, J.; Bie, Z.; Song, K.; Zhu, C. A Novel Arc-Shaped Lightweight Magnetic Coupler for AUV Wireless Power Transfer. *IEEE Trans. Ind. Appl.* **2022**, *58*, 1315–1329. [CrossRef]
22. Cai, C.; Wu, S.; Zhang, Z.; Jiang, L.; Yang, S. Development of a Fit-to-Surface and Lightweight Magnetic Coupler for Autonomous Underwater Vehicle Wireless Charging Systems. *IEEE Trans. Power Electron.* **2021**, *36*, 9927–9940. [CrossRef]
23. Wang, Y.; Jiang, C.Q.; Chen, C.; Ma, T.; Li, X.; Long, T. Hybrid Nanocrystalline Ribbon Core and Flake Ribbon For High-Power Inductive Power Transfer Applications. *IEEE Trans. Power Electron.* **2024**, *39*, 1898–1911. [CrossRef]
24. Niu, S.; Zhao, Q.; Niu, S.; Jian, L. A Comprehensive Investigation of Thermal Risks in Wireless EV Chargers Considering Spatial Misalignment from A Dynamic Perspective. *IEEE J. Emerg. Sel. Top. Ind. Electron.* **2024**, *5*, 1560–1571. [CrossRef]
25. Chen, H.; Niu, S.; Shao, Z.; Jian, L. Recognizing Multitype Misalignments in Wireless EV Chargers with Orientation-Sensitive Coils: A Data-Driven Strategy Using Improved ResNet. *IEEE Trans. Ind. Inf.* **2024**, *20*, 280–290. [CrossRef]
26. *J2954_202408*; Wireless Power Transfer for Light-Duty Plug-in/Electric Vehicles and Alignment Methodology. SAE: Warrendale, PA, USA, 2024.
27. Zhang, R.; Li, X.; Sun, C.; Yang, S.; Tian, Y.; Tian, J. State of Charge and Temperature Joint Estimation Based on Ultrasonic Reflection Waves for Lithium-Ion Battery Applications. *Batteries* **2023**, *9*, 335. [CrossRef]
28. Niu, S.; Yu, H.; Niu, S.; Jian, L. Power Loss Analysis and Thermal Assessment on Wireless Electric Vehicle Charging Technology: The over-Temperature Risk of Ground Assembly Needs Attention. *Appl. Energy* **2020**, *275*, 115344. [CrossRef]
29. Bi, Z.; Kan, T.; Mi, C.C.; Zhang, Y.; Zhao, Z.; Keoleian, G.A. A Review of Wireless Power Transfer for Electric Vehicles: Prospects to Enhance Sustainable Mobility. *Appl. Energy* **2016**, *179*, 413–425. [CrossRef]
30. Jiang, C.; Chau, K.T.; Liu, W.; Liu, C.; Han, W.; Lam, W.H. An LCC-Compensated Multiple-Frequency Wireless Motor System. *IEEE Trans. Ind. Inform.* **2019**, *15*, 6023–6034. [CrossRef]

31. Mohammad, M.; Wodajo, E.T.; Choi, S.; Elbuluk, M.E. Modeling and Design of Passive Shield to Limit EMF Emission and to Minimize Shield Loss in Unipolar Wireless Charging System for EV. *IEEE Trans. Power Electron.* **2019**, *34*, 12235–12245. [CrossRef]
32. Resistance Copper Wire Suppliers. Available online: https://www.scottprecisionwire.com/technical-data/alloy-data-sheets/resistance-copper-wire-supplier/ (accessed on 1 December 2024).

energies

MDPI

Article

Topology and Control Strategy of Multi-Port DC Power Electronic Transformer Based on Soft Switching

Jialin Zhang [1,2,3,*], Kunpeng Zha [3], Xiaojun Tang [1], Yuefeng Yang [2,3], Lanfang Li [2,3] and Jiafei Li [2,3]

1 School of Electrical Engineering, Xi'an Jiaotong University, Xi'an 710049, China; xiaojun_tang@xjtu.edu.cn
2 China Power NARI Purui Engineering Co., Ltd., Beijing 102299, China; yangyuefeng@sgepri.sgcc.com.cn (Y.Y.); lilanfang@sgepri.sgcc.com.cn (L.L.); lijiafei@sgepri.sgcc.com.cn (J.L.)
3 NARI Group Corporation, Nanjing 211106, China; zhakunpeng@sgepri.sgcc.com.cn
* Correspondence: jlzhang0324@163.com

Abstract: Multi-port DC power electronic transformer (PET) is a core equipment for achieving transformation of different voltage levels and flexible interconnection of different DC buses in a DC distribution system. It is capable of bidirectional energy flow, flexible regulation of power flow, port fault isolation, and other functions. A new five-port DC transformer topology based on soft switching technology is proposed in this paper. In this topology, different DC voltage levels can be interconnected efficiently, such as 20 kV, 750 V, ±375 V, and 300 to 500 V adjustable. The control of each port is simple and flexible. The output voltage is stable, and they are independent of each other, which can improve the system reliability. The topology of the proposed multi-port DC transformer is introduced in detail. The working principle, control strategy, and parameter design method of the transformer are analyzed. Simulations and experimental results are provided to validate the theoretical analysis.

Keywords: DC distribution network; DC transformer; multi-port converter; soft switching; flexible interconnection

1. Introduction

With the intensification of energy crisis and environmental issues, global energy consumption is gradually shifting from traditional fossil fuels to distributed energy sources such as photovoltaic, wind power, and fuel cells [1,2]. The distributed generation system based on DC distribution network is an important component of the future new power system. Compared with traditional AC distribution networks, there are no reactive power and synchronization issues in the DC distribution systems, and it also has advantages such as low losses and less wire usage.

Nowadays, DC ports with different voltage levels are required in many applications, including hybrid/fuel cell vehicles, renewable energy, water electrolysis, etc. [3–5]. A multi-port DC transformer is an electrical device with multiple ports, which can directly connect distributed power generation systems, energy storage devices, and load. The device integrates multiple single-stage converters, achieves electrical isolation in topology, and can achieve multi-directional energy flow and multi-voltage level outputs in control [6–9].

A typical PET topology is a three-stage structure, including a rectifier circuit, isolated DC/DC circuit, and inverter circuit [10,11]. In [12–14], a three-stage topology based on cascaded H-bridge (CHB) has been proposed, which mainly includes an AC/DC rectifier with cascaded H-bridge modules, an output-parallel DC/DC converter, and a two-level inverter. The three-stage PET based on CHB has three ports, which include a middle-voltage AC (MVAC) port, low-voltage DC (LVDC) port, and LVAC port. The LVDC port can serve as an interface for distributed energy sources such as photovoltaic, energy storage, and DC loads. The medium-voltage port and low-voltage port of the PET is isolated by non-resonant dual active bridge (DAB) converter or a resonant LC, LLC, or CLLC converter [15,16]. In [17–20], a three-stage topology based on modular multilevel converter (MMC) has been proposed, which includes four ports. MMC is used to realize electrical energy conversion between the MVAC port and MVDC port, while isolated DC/DC converters with input-series–output-parallel (ISOP) topology are used to realize electrical energy conversion between the MVDC port and LVDC ports. A low-voltage inverter is used to realize electrical energy conversion between the LVDC port and LVAC port. Under the same voltage and power level, the topology based on CHB uses fewer power modules, while the topology based on MMC is more suitable for applications with MVDC port requirement.

In [21], a multi-port PET with common DC bus has been presented. The common low-voltage DC bus serves as the internal bus to realize energy exchange between the ports. This type of multi-port PET can be considered as a simple combination of converter in each port, which can be designed separately in hardware, and the control strategies between ports can also be independent of each other. However, due to the use of a large number of intermediate energy conversion links, it will increase costs and reduce efficiency.

To reduce the large number of power modules and components used in multi-port PET and avoid redundant intermediate power conversion links, a four-port PET based on multiple active bridges (MAB) converter is proposed in [22,23]. A multi-winding high-frequency transformer is adopted to connect each port, which can significantly reduce the number of electrical energy conversion links. Due to the limitations of insulation and heat dissipation processes of the multi-winding high-frequency transformers, this topology is difficult to apply in high-voltage and high-power applications. In [24], a DC PET topology is proposed, in which the ports are connected through a medium-voltage high-frequency link. The transformation from MVDC port to the medium-voltage high-frequency link is achieved through a four-bridge arm MMC. Multiple two-winding high-frequency transformers are connected in series, and the secondary sides of each high-frequency transformer are rectified by an H-bridge and connected in parallel to form an LVDC port. This type of structure can reduce the number of electrical energy conversion links. However, the locking of the faulty module affects the normal operation of other modules due to the series connection of multiple high-frequency transformers. This will limit the scalability of the structure. In [25,26], a multi-port PET topology with a common low-voltage high-frequency link has been proposed. The topology is easy to expand to the interconnection of any number of high-frequency transformers, which is easier for modular design. However, it requires high consistency in waveform amplitude and phase for each port of the common high-frequency link. The energy collection link between the ports is the high-frequency link. Due to the lack of energy storage capacitors as an energy snubber, there is strong coupling between modules and ports [26]. Therefore, whether from the main circuit hardware or the control strategy of each port, it is necessary to integrate and co-ordinate the design of multi-port PET, which undoubtedly increases the complexity of the design.

In terms of a control strategy for multi-port PET, an adaptive bidirectional droop control is proposed to maintain the DC bus voltage with less communication [27]. A communication-free edge-control strategy for energy routers based on cyber-energy dual modulation is proposed to achieve power balance without the communication network [28]. To realize power balancing, voltage balancing control based on the power decoupling calculations is adopted in [29] and an unbalanced power control strategy for a cascaded dual active bridge (DAB) converter is proposed [30]. Based on the single-phase dq model, a novel voltage and power control strategy is proposed to balance the voltages and power [31]. In [32], a hierarchical management control strategy is applied in a multi-port energy router in smart home. In [33], an isolated three-port bidirectional dc–dc converter is proposed. Duty cycle control and phase-shift control are combined to minimize the overall system losses. In order to improve the reliability of the multi-port PET, a low-voltage ride-through (LVRT) control strategy is proposed in [34].

Based on the analysis above, a topology of five-port DC PET with a common DC bus is proposed. The proposed topology in this paper is simple, efficient, and the ±375 V port can automatically achieve power imbalance output. A conversion circuit based on soft switching technology is connected in series on the 750 V DC bus of the ISOP DC transformer [35] to achieve ±375 V voltage and 300–500 V adjustable voltage port output. Table 1 lists the comparison of different structures in terms of the topological complexity, control complexity, efficiency, scalability, and difficulty of manufacture. Firstly, the working principles of ±375 V and 300–500 V adjustable circuits are analyzed, and the parameter design method and control strategy for the circuit are proposed. Finally, the correctness and effectiveness of the proposed topology and control strategy are verified through simulation and experiments.

Table 1. Basic characteristic comparison of different structures.

	Topological Complexity	Control Complexity	Efficiency	Scalability	Difficulty of Manufacture
Series connected type [10–20]	Low	Medium	Medium	Low	Low
Common DC bus type [21]	High	Low	Medium	High	Low
Common high-frequency link type [22–26]	High	High	Low	Medium	High
The proposed PET	Low	Low	High	High	Low

2. Topology of the Multi-Port DC Transformer

The proposed topology of the multi-port DC PET mainly includes five ports, as shown in Figure 1.

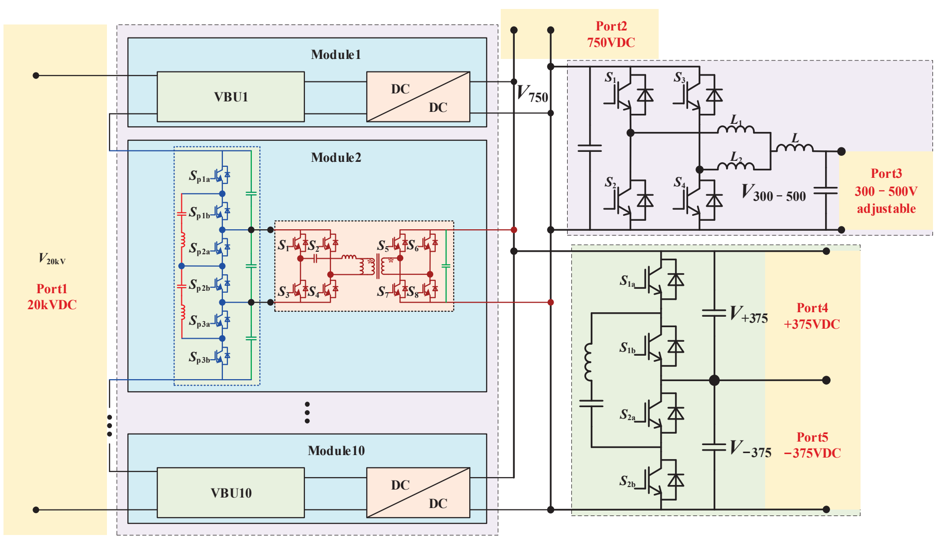

Figure 1. Topology of the proposed five-port DC transformer.

Port 1 (20 kV DC port): generally, 10 kV AC power is converted into 20 kV DC power through the voltage source converter.

Port 2 (750 V DC port): by adopting a voltage balance unit (VBU) and LLC resonant converter, the 20 kV DC power in port 1 is converted into 750 V DC power [27].

Port 3 (300–500 V adjustable port): the 750 V DC power in port 2 is converted into adjustable DC power ranging from 300 to 500 V through a buck converter. The buck converter can achieve high-efficiency conversion by adopting soft switching technology.

Port 4 and port 5 (±375 V DC port): the 750 V DC power in port 2 is converted into ±375 V true bipolar DC power through VBU. The VBU can achieve zero-current turn-on and turn-off by the auxiliary resonant circuit.

3. 300–500 V Adjustable Port

The 300–500 V adjustable port achieves energy exchange with the 750 V port by adopting a buck converter with soft switching. Meanwhile, the voltage and power of the port can be regulated in real time by using closed-loop control to meet the port requirements.

3.1. Working Principle of 300–500 V Adjustable Port

The interleaved buck converter (IBC) is adopted for the 300–500 V adjustable port, as shown in Figure 2. The upper bridge arm switch can achieve zero-current switch (ZCS turn-on), and the lower bridge arm diode can achieve zero-current switch (ZCS turn-off). The current equivalent frequency of the filter inductor L is twice the switching frequency.

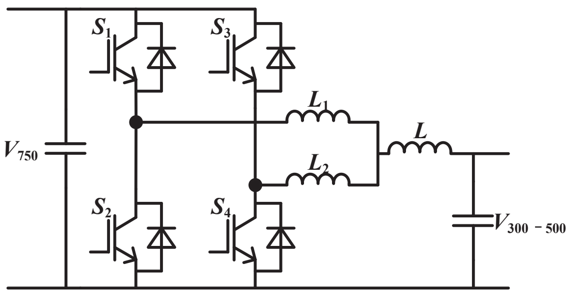

Figure 2. Topology of the proposed IBC.

The working waveform of the IBC is shown in Figure 3. G_1–G_4 are the driving signals of switches S_1–S_4. i_{L1} and i_{L2} are the currents of auxiliary inductors L_1 and L_2, and i_L is the current of filter inductor L. The reference direction of the currents is shown in Figure 2. i_{s1}–i_{s4} are the currents of switches S_1–S_4, and the reference direction of the currents is the current direction flowing through the IGBTs (i_{s1}–i_{s4} > 0 indicates the current flowing through the IGBTs, and i_{s1}–i_{s4} < 0 indicates the current flowing through the anti-parallel diodes).

There are six modes in one working cycle of the IBC.

Mode 1 (t_0–t_1): before t_0, the anti-parallel diode of switch S_3 is in the off state, and the current i_L of filter inductor L flows through the auxiliary inductor L_2 and the anti-parallel diodes of switch S_4. Thus, i_{L2} equals i_L. At t_0, switch S_1 is turned on, and i_{L1} flows from S_1, L_1, and L to the output port. At the same time, a freewheeling circuit of i_{L2} is formed through switch S_4, L_2, L, and the output port. The current commutation from i_{L2} to i_{L1} is completed. The current i_{L2} of auxiliary inductor L_2 drops to zero at the end of the mode. Therefore, the switch S_1 can achieve ZCS turn-on, and the anti-parallel diode of switch S_4 can achieve ZCS turn-off. In this mode, S_2 and S_3 withstand the bus voltage V_{750}. The diagram of this stage is shown in Figure 4a.

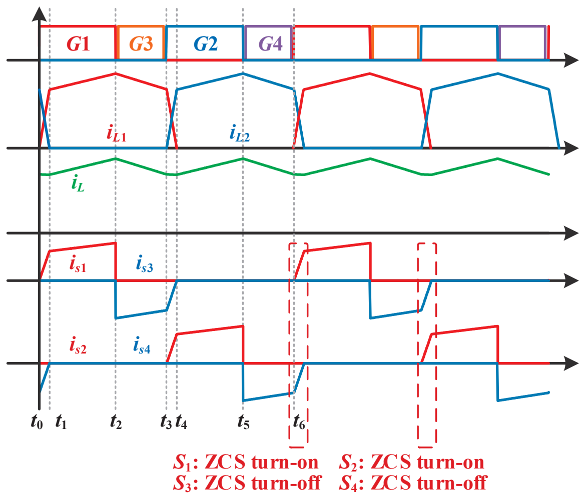

Figure 3. The working waveform of the IBC.

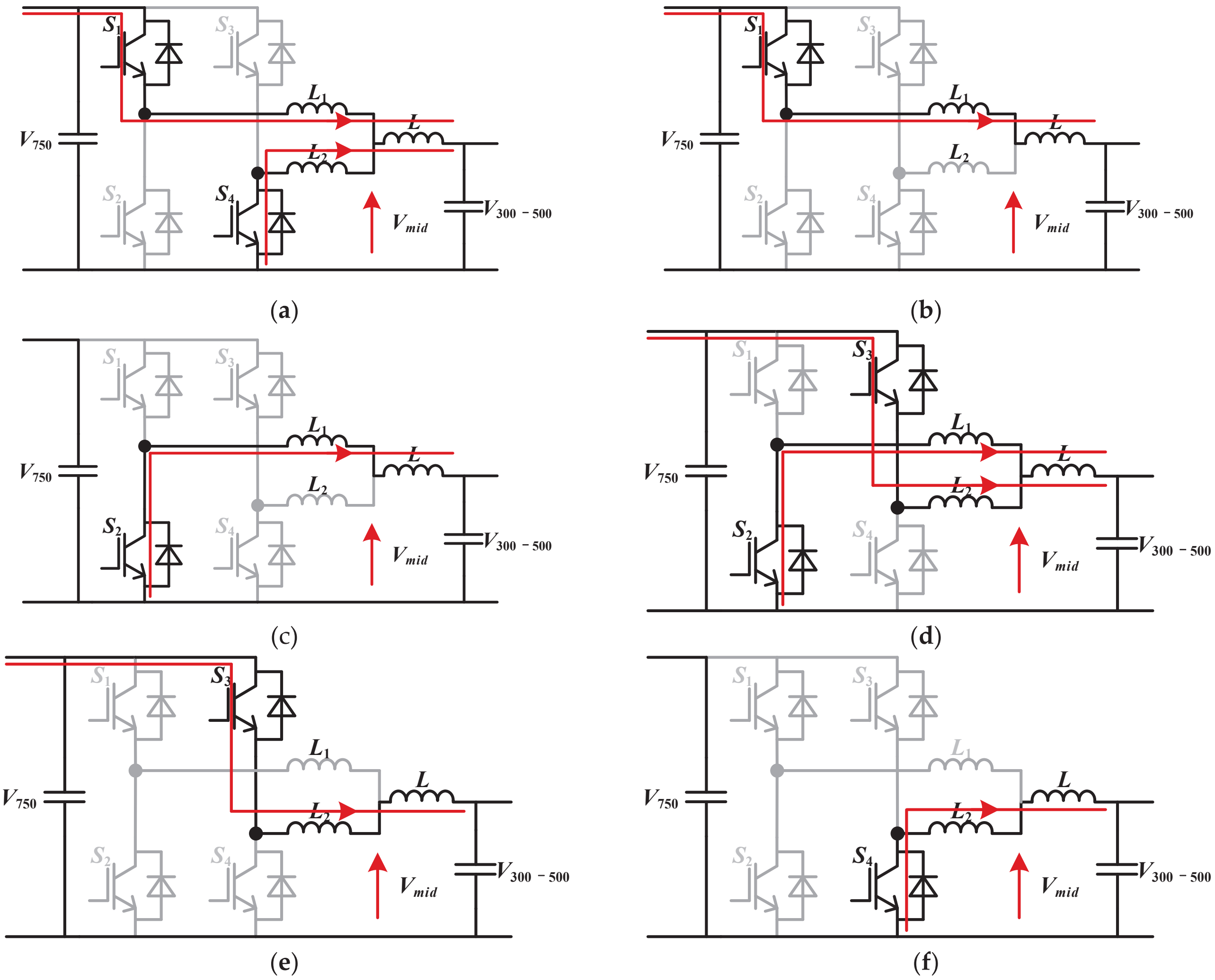

Figure 4. Working modes of IBC: (**a**) Mode 1; (**b**) Mode 2; (**c**) Mode 3; (**d**) Mode 4; (**e**) Mode 5; (**f**) Mode 6. (The direction of the arrow indicates the direction of voltage and current).

Mode 2 (t_1–t_2): the switch S_1 remains on, and the current i_{L1} of auxiliary inductor L_1 flows from the input port, S_1, L_1, and L to the output port. The current i_{L1} of auxiliary inductor L_1 equals the current i_L of filter inductor L at this stage. In this mode, S_2 withstands the bus voltage V_{750}. S_3 and S_4 withstand the bus voltage V_{750} together. The diagram of this stage is shown in Figure 4b.

Mode 3 (t_2–t_3): switch S_1 is turned off at t_2. The freewheeling circuit of i_{L1} includes the anti-parallel diode of switch S_3, L_1, L, and the output port. In this mode, S_1 withstands the bus voltage V_{750}. S_3 and S_4 withstand the bus voltage V_{750} together. The diagram of this stage is shown in Figure 4c.

Mode 4 (t_3–t_4): the switch S_2 is turned on at t_3. The current i_{L2} of auxiliary inductor L_2 flows from S_2, L_2, and L to the output port. At the same time, a freewheeling circuit of i_{L1} is formed through the anti-parallel diode of switch S_3, L_2, L, and the output port. The current commutation from i_{L1} to i_{L2} is completed. The current i_{L1} of auxiliary inductor L_1 drops to zero at the end of the mode. Therefore, the switch S_2 can achieve ZCS turn-on, and the anti-parallel diode of switch S_3 can achieve ZCS turn-off. In this mode, S_1 and S_4 withstand the bus voltage V_{750}. The diagram of this stage is shown in Figure 4d.

Mode 5 (t_4–t_5): the switch S_2 remains on, and the current i_{L2} of auxiliary inductor L_2 flows from the input port, S_2, L_2, and L to the output port. The current i_{L1} of auxiliary inductor L_2 equals the current i_{L} of filter inductor L at this stage. In this mode, S_4 withstands the bus voltage V_{750}. S_1 and S_2 withstand the bus voltage V_{750} together. The diagram of this stage is shown in Figure 4e.

Mode 6 (t_5–t_6): Switch S_2 is turned off at t_5. The freewheeling circuit of i_{L2} includes the anti-parallel diode of switch S_4, L_2, L, and the output port. In this mode, S_3 withstands the bus voltage V_{750}. S_1 and S_2 withstand the bus voltage V_{750} together. The diagram of this stage is shown in Figure 4f.

According to the analysis of the working principle of IBC during one cycle, it can be concluded that the upper arm of the converter can achieve ZCS turn-on and hard turn-off, and the lower arm of the converter can achieve ZCS turn-off. Therefore, the IBC has a higher efficiency due to good soft switching characteristics.

3.2. Parameter Design of 300–500 V Adjustable Port

According to the analysis of the working principle, the current i_{L1} and i_{L2} of the auxiliary inductors during Mode 1 satisfy Equations (1) and (2).

$$\frac{V_{750} - V_{\mathrm{mid}}}{L_1} \cdot (t_1 - t_0) = I_{\mathrm{L1}}, \tag{1}$$

$$\frac{V_{\mathrm{mid}}}{L_2} \cdot (t_1 - t_0) = I_{\mathrm{L0}}, \tag{2}$$

where I_{L0} and I_{L1} are the current i_{L} of the filter inductor L at t_0 and t_1, and V_{mid} is the voltage shown in Figure 4.

Since the inductance of auxiliary inductors L_1 and L_2 are the same, and $I_{\mathrm{L0}} \approx I_{\mathrm{L1}}$, Equation (3) can be derived as follows:

$$\begin{array}{l} V_{750} - V_{\mathrm{mid}} = V_{\mathrm{mid}} \\ \Rightarrow V_{\mathrm{mid}} = 0.5 \times V_{750} \end{array}, \tag{3}$$

Therefore, ZCS turn-on of the switch and ZCS turn-off of the diode can be achieved by designing auxiliary inductors L_1 and L_2 to control the current rise rate of the switch and the current drop rate of the anti-parallel diode.

The current i_{L} of the filter inductor increases linearly in Mode 2 and can be expressed as:

$$\begin{array}{l} I_{\mathrm{L2}} - I_{\mathrm{L1}} = \frac{V_{750} - V_{300-500}}{L + L_1} \times (t_2 - t_1) \\ \Delta I_{\mathrm{Lmax}} \approx \frac{V_{750} - V_{300-500}}{L + L_1} \times DT_{\mathrm{s}} \end{array}, \tag{4}$$

where D is the duty cycle of S_1 and S_2, and T_s is the switching cycle. The relationship between the input and output voltage can be expressed as:

$$\frac{V_{300-500}}{V_{750}} = 2D, \tag{5}$$

Based on the ripple of the filter inductor current, the value of the filter inductor L can be calculated by Equations (4) and (5).

Limiting the current rise rate of the switch and the current drop rate of the diode to below 20 A/μs, the auxiliary inductors L_1 and L_2 can be calculated as 20 μH through Equations (1) and (2). Limiting the current i_L fluctuation below 20%, the inductor can be calculated as 170 μH through Equations (4) and (5).

4. ±375 V Port

The ±375 V port can achieve true bipolar input or output of ±375 V voltage. The energy exchange between ±375 V port and 750 V port can be achieved through two-capacitor VBU (TC-VBU). The open-loop fixed frequency control of VBU is adopted, and the control strategy is simple.

4.1. Working Principle of ±375 V Port

The TC-VBU topology of ±375 V port is shown in Figure 5. The TC-VBU consists of two half-bridges (S_{1a}, S_{1b} and S_{2a}, S_{2b}), which are connected in series. Each half-bridge is connected in parallel with a DC-link capacitor (C_1 and C_2), and an LC resonant branch (L_{p1}, C_{p1}) is connected between the midpoints of each half-bridge to transfer energy between the DC-link capacitors. The TC-VBU can achieve voltage balance between +375 V port and −375 V port under power unbalance condition.

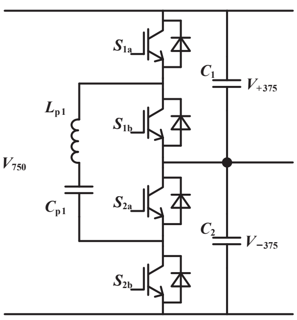

Figure 5. Topology of the TC-VBU.

Before analyzing the working mode and principle, the following assumptions are made:

(1) All components in the circuit are ideal and ignore the influence of parasitic parameters.
(2) The switch signal of the upper and lower switch of the half-bridges are synchronized.
(3) The resonant cycle of the resonant branch (L_{p1}, C_{p1}) is T_r. The switch cycle of the TC-VBU is T_s and the dead time of the switch is T_d. Thus, $T_r = T_s - 2T_d$.

The working mode and principle of the TC-VBU under unbalanced power between ±375 V ports in the forward direction are shown in Figure 6. The working waveform is shown in Figure 7.

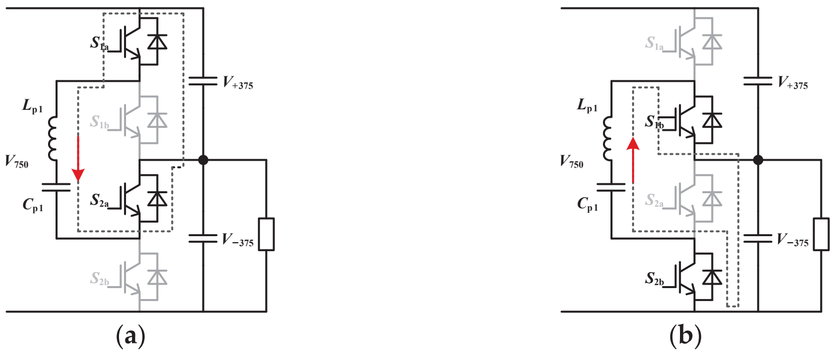

Figure 6. Working modes of TC-VBU: (**a**) Mode 1; (**b**) Mode 2. (The direction of the arrow indicates the direction of current).

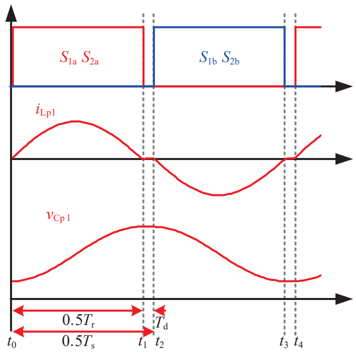

Figure 7. The working waveform of TC-VBU under power-unbalanced condition.

There are four modes in one working cycle.

Mode 1 (t_0–t_1): S_{1a} and S_{2a} are turned on at t_0. The resonant capacitor C_{p1} is charged by DC-link capacitor C_1 through the resonant branch, which is composed of C_1, S_{1a}, L_{p1}, C_{p1}, and the anti-parallel diode of switch S_{2a}. The resonant current i_{Lp1} starts to resonate from zero in the forward direction at time t_0 and, after half of the resonant cycle, it resonates back to 0 at time t_1. S_{1a} and S_{2a} can achieve ZCS turn-on. In this mode, S_{1b} withstands the voltage of DC-link capacitor V_{+375}. S_{2b} withstands the voltage of DC-link capacitor V_{-375}. The diagram of this stage is shown in Figure 6a.

Mode 2 (t_1–t_2): S_{1a} and S_{2a} are turned off at t_1. At this point, the resonant current i_{Lp1} is already zero. Therefore, S_{1a} and S_{2a} can achieve ZCS turn-off. In this stage, only DC capacitor C_2 provides energy to the load. In this mode, S_{1a}, S_{1b}, S_{2a}, and S_{2b} withstand the bus voltage V_{750} together.

Mode 3 (t_2–t_3): S_{1b} and S_{2b} are turned on at t_1. The resonant capacitor C_{p2} is charged by DC-link capacitor C_2 through the resonant branch, which is composed of C_2, S_{1b}, L_{p1}, C_{p1}, and the anti-parallel diode of switch S_{2b}. The resonant current i_{Lp1} starts to resonate from zero in the backward direction at time t_0 and, after half of the resonant cycle, it resonates back to 0 at time t_1. S_{1b} and S_{2b} can achieve ZCS turn-on. In this mode, S_{1a} withstands the voltage of DC-link capacitor V_{+375}. S_{2a} withstands the voltage of DC-link capacitor V_{-375}. The diagram of this stage is shown in Figure 6b.

Mode 4 (t_3–t_4): S_{1b} and S_{2b} are turned off at t_3. At this point, the resonant current i_{Lp1} is already zero. Therefore, S_{1b} and S_{2b} can achieve ZCS turn-off. In this stage, only the DC capacitor C_2 provides energy to the load. In this mode, S_{1a}, S_{1b}, S_{2a}, and S_{2b} withstand the bus voltage V_{750} together.

4.2. Parameter Design of ±375 V Port

According to the working principle of TC-VBU, the current and voltage of the resonant branch in Mode 1 can be calculated as:

$$\begin{cases} i_{\mathrm{Lp1}}(t) = I_{\mathrm{Lp1}} \sin[\omega_{\mathrm{r}}(t - t_0)] \\ V_{\mathrm{Cp1}}(t) = V_1 - Z_{\mathrm{r}} I_{\mathrm{Lp1}} \cos[\omega_{\mathrm{r}}(t - t_0)] \end{cases}, \tag{6}$$

where I_{Lp1} is the peak current of the resonant inductor, Z_{r} is characteristic impedance of the resonant branch, V_1 is the voltage of capacitor C_1, and ω_{r} is the resonant angular frequency. They can be calculated as:

$$\begin{cases} I_{\mathrm{Lp1}} = \pi \frac{V_1}{2R} \cdot \frac{T_{\mathrm{s}}}{T_{\mathrm{s}} - 2T_{\mathrm{d}}} = \pi \frac{I_{\mathrm{o}}}{2} \cdot \frac{T_{\mathrm{s}}}{T_{\mathrm{r}}} = \pi \frac{V_{750}}{4R} \cdot \frac{T_{\mathrm{s}}}{T_{\mathrm{r}}} \\ Z_{\mathrm{r}} = \sqrt{\frac{L_{\mathrm{p1}}}{C_{\mathrm{p1}}}} \\ \omega_{\mathrm{r}} = \frac{1}{\sqrt{L_{\mathrm{p1}} C_{\mathrm{p1}}}} \end{cases}, \tag{7}$$

According to Equations (6) and (7), the peak current of the resonant branch ($I_{\mathrm{Lp\_max}}$) and the peak voltage of the resonant inductor and capacitor ($V_{\mathrm{Lp\_max}}$ and $V_{\mathrm{Cp\_max}}$) can be calculated as:

$$I_{\mathrm{Lp\_max}} = \pi \frac{V_1}{2R} \cdot \frac{T_{\mathrm{s}}}{T_{\mathrm{s}} - 2T_{\mathrm{d}}} = \pi \frac{I_{\mathrm{o}}}{2} \cdot \frac{T_{\mathrm{s}}}{T_{\mathrm{r}}}, \tag{8}$$

$$V_{\mathrm{Lp\_max}} = I_{\mathrm{Lp\_max}} Z_{\mathrm{r}}, \tag{9}$$

$$V_{\mathrm{Cp\_max}} = \frac{1}{2} V_{750} + I_{\mathrm{Lp\_max}} Z_{\mathrm{r}}, \tag{10}$$

From Equations (8) to (10), it can be seen that, when the output voltage and power are determined, the current stress of the resonant inductor is determined and the voltage peak of the resonant inductor and capacitor is affected by the characteristic impedance. If the peak voltage of the resonant capacitor satisfies $V_{\mathrm{Cp\_max}} \geq V_{750}$, it will cause TC-VBU to generate additional operating modes, and the resonant circuit generated by the additional operating modes will affect the normal operation of the converter and the implementation of ZCS. Therefore, in order to avoid additional working modes, the peak voltage of the resonant capacitor must satisfy $V_{\mathrm{Cp\_max}} < V_{750}$. By substituting this constraint into Equation (10), it can obtain:

$$Z_{\mathrm{r}} < \frac{2RT_{\mathrm{r}}}{\pi T_{\mathrm{s}}}, \tag{11}$$

According to the relationship between resonant impedance and resonant inductance $Z_{\mathrm{r}} = L_{\mathrm{p1}}\omega_{\mathrm{r}}$, the maximum value of the resonant inductor can be calculated as:

$$L_{\mathrm{p1}} < \frac{RT_{\mathrm{r}}^2}{\pi^2 T_{\mathrm{s}}}, \tag{12}$$

From the above analysis, it can be concluded that a smaller resonant inductance value can keep the TC-VBU away from additional operating modes and reduce the voltage stress of the resonant inductor and capacitor. However, due to the parasitic resistance of the resonant branch, the value of the resonant inductor cannot be zero. Assuming the parasitic resistance of the resonant branch is R_{p}, the actual resonant frequency of the resonant branch can be calculated as:

$$f_{\mathrm{r}} = \frac{1}{2\pi \sqrt{\frac{1}{L_{\mathrm{p}} C_{\mathrm{p}}} - \left(\frac{R_{\mathrm{p}}}{2L_{\mathrm{p}}}\right)^2}}, \tag{13}$$

To ensure that the resonant frequency of the resonant branch is not affected by parasitic resistance, the resonant parameters need to meet:

$$\frac{1}{L_p C_p} > 100\left(\frac{R_p}{2L_p}\right)^2, \tag{14}$$

Therefore, the minimum value of resonant inductor can be calculated as:

$$L_p > \frac{2.5R_p}{\pi f_r}, \tag{15}$$

From Equations (12) and (15), the value range of the resonant inductor can be obtained as:

$$\frac{2.5R_p}{\pi f_r} < L_p < \frac{RT_r^2}{\pi^2 T_s} \tag{16}$$

The resonant frequency is selected as f_r = 10 kHz and the parasitic resistance of the resonant branch as R_p = 20 mΩ. Considering practical application, the output voltage is selected as V_1 = V_2 = 375 V and the power is selected as 75 kW. By substituting the parameters into (16), the range of resonant inductance values can be obtained as 1.59 μH < L_p < 18.27 μH.

5. Experimental Results

To verify the working principle, parameter design method, and control strategy of the IBC and TC-VBU, an experimental platform is constructed. The corresponding parameters of the IBC and TC-VBU are listed in Tables 2 and 3. The power circulation method between IBC and TC-VBU is adopted. The experimental circuit is shown in Figure 8. IBC adopts a constant power control method, and TC-VBU adopts an open-loop control method.

Table 2. Parameters of IBC.

Parameter	Value
Input voltage	750 V
Output voltage	300–500 V adjustable
Switching frequency	7.5 kHz
Auxiliary inductor L_1/L_2	20 μH
Filter inductor L	170 μH
DC-link capacitor	1 mF

Table 3. Parameters of TC-VBU.

Parameter	Value
Input voltage	750 V
Output voltage	±375 V
Resonant capacitor	100 μF
Resonant inductor	2.55 μH
DC-link capacitor	1 mF
Input voltage	750 V

The experimental platform is shown in Figure 9. The experimental set-up includes a programable DC power, an IBC module, an IBC control board, a TC-VBU module, a TC-VBU control board, a current/voltage sensor, control system, and monitor system. The control system and monitor system are connected via ethernet cable. The monitor system sends the working mode to the control system, while the control system uploads the module's working status to the monitor system for display. The control system and control board are connected through optical fibers. The control system calculates the duty cycle

(D_{IBC}) based on the difference between the reference current (I_{oref}) value and the measured current value (I_{o}) by the current sensor and sends it to the IBC control board. At the same time, the control system sends switch frequency ($f_{\mathrm{sTC\text{-}VBU}}$) and duty cycle ($D_{\mathrm{TC\text{-}VBU}}$) to the TC-VBU control board. The control board and the modules are connected by cables. The control board generates drive signals with dead time and drives the module switches. The closed loop control diagram of IBC is shown in Figure 10a, and the open-loop control diagram of TC-VBU is shown in Figure 10b. The models of key components in IBC and TC-VBU are listed in Table 4.

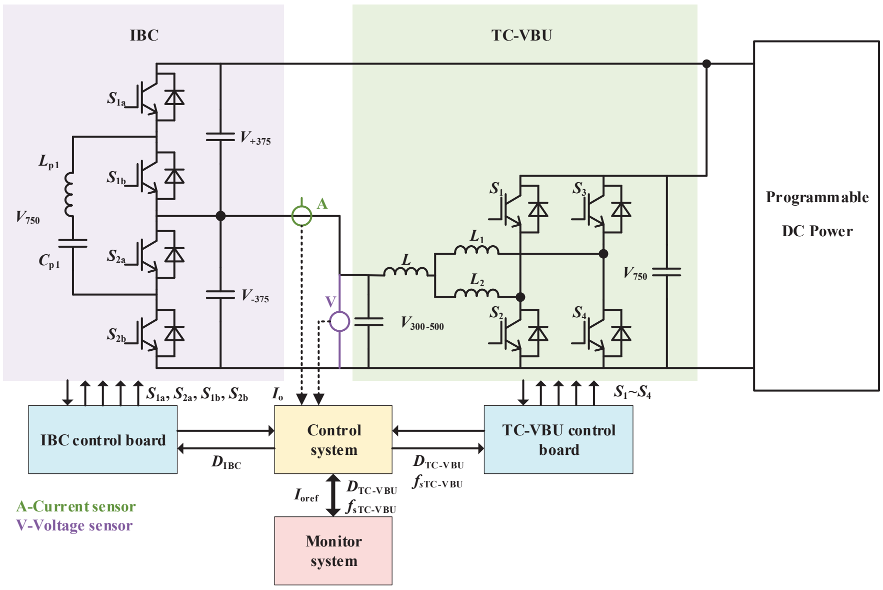

Figure 8. Experimental circuit based on power circulation. (The dashed arrows represent voltage and current sampling).

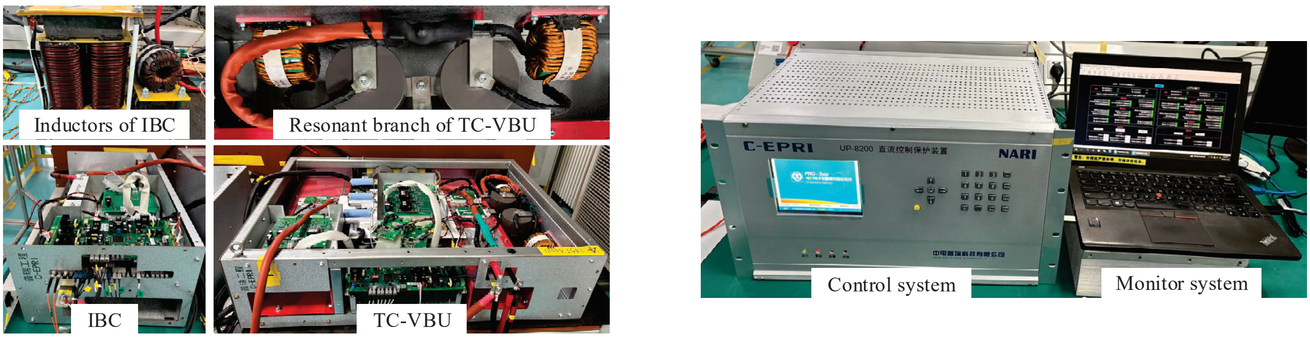

(**a**) (**b**)

Figure 9. The picture of the experimental platform. (**a**) Main circuit; (**b**) Control circuit.

(**a**) (**b**)

Figure 10. The control diagram: (**a**) closed-loop control of IBC; (**b**) open-loop control of TC-VBU.

Before the experiment, all control boards passed an electromagnetic compatibility (EMC) test. The signal line adopts a twisted pair cable and the shorter the better.

The waveforms of IBC output voltage, output current, and filter inductor (L) current both in forward and backward mode are shown in Figure 11. The voltage of −375V port remains stable when the circulating power is 75 kW. The TC-VBU can achieve voltage balance when the output power of the two ports (+375 V port and −375 V port) is extremely unbalanced. It can be seen from the current of the filter inductor L that the frequency of the current is twice the switching frequency.

Table 4. Models of key components in IBC and TC-VBU.

Key Components	Models
Switch of IBC	BSM300D12P2E001 (SiC-Mosfet from ROHM, Kyoto, Japan)
Core material of IBC inductor	Ferrite (Shijiazhuang, China)
Winding of IBC inductor	Copper wire (designed by supplier, Shijiazhuang, China)
Switch of TC-VBU	FF600R12ME4 (IGBT from Infineon, Neubiberg, Germany)
Core material of resonant inductor	Edge (from Magnetics, Pittsburgh, America)
Winding of resonant inductor	Litz wire (Yangzhou, China)

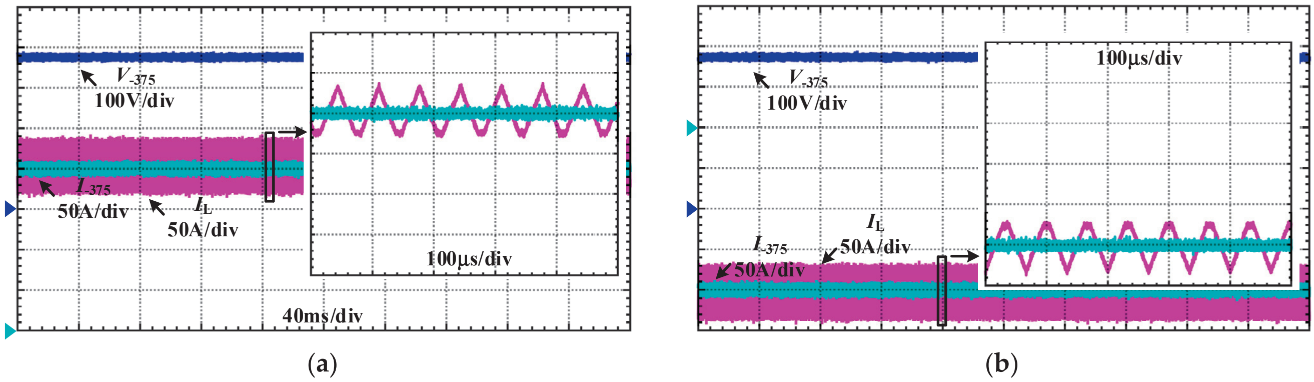

Figure 11. The experimental waveform of IBC output voltage, output current, and inductor (L) current: (**a**) forward mode; (**b**) backward mode. (The triangles represent the coordinate origin).

For IBC, Figure 12 shows the voltage of the switches S_1 and S_3 and the current of the auxiliary inductor. S_1 and S_3 can achieve ZCS turn-on, and the anti-parallel diodes of S_2 and S_4 can achieve ZCS turn-off. IBC has good soft switching characteristics.

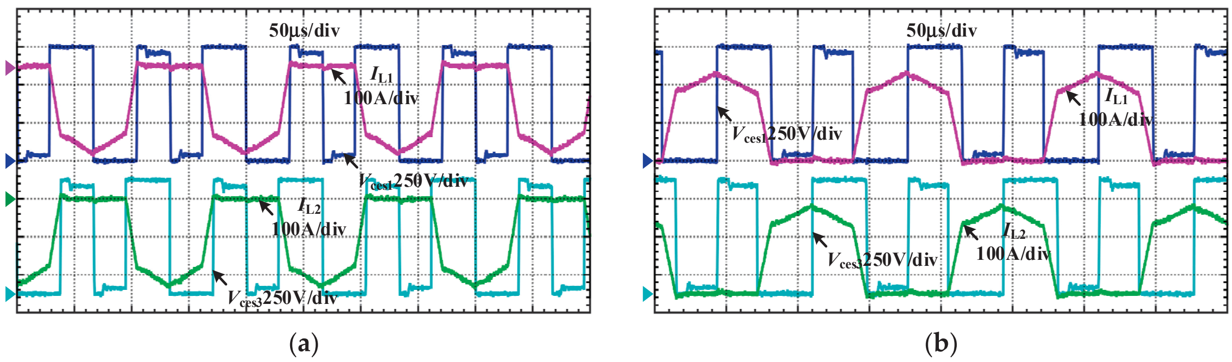

Figure 12. The experimental waveform of switch voltage and auxiliary inductor current of IBC: (**a**) forward mode; (**b**) backward mode. (The triangles represent the coordinate origin).

For the TC-VBU, Figure 13 shows the voltage of the switches S_{1a} and S_{1b} and the resonant current. According to the working principle of TC-VBU, the zero cross-point of both the resonant current and switch current are the same. It can be seen that TC-VBU can achieve ZCS turn-on and turn-off to ensure high efficiency. During the dead time, the resonant current remains zero.

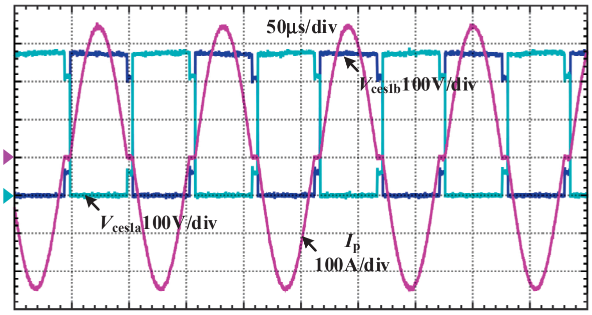

(**a**)

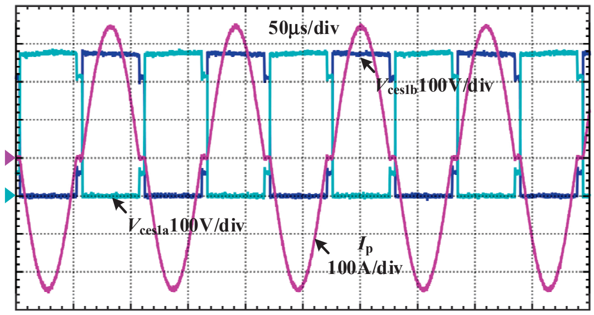

(**b**)

Figure 13. The experimental waveform of switch voltage and resonant current of TC-VBU: (**a**) forward mode; (**b**) backward mode. (The triangles represent the coordinate origin).

Figures 14 and 15 shows the transient waveform of the experiment. In Figure 14, the reference current of IBC in forward mode increases from 100 A to 200 A. It can be seen from Figure 14a that the circulating current reaches 200 A within 10 ms. It can be seen from Figure 14b,c that the soft-switching performance during the transient state in forward mode is consistent with the steady state shown in Figures 12a and 13a. In Figure 15, the input bus voltage V_{750} of IBC and TC-VBU increases from 650 V to 750 V, and the reference current of IBC in backward mode remains 200 A during this process. It can be seen from Figure 15a that V_{-375} increases with V_{750} and remains half of V_{750}. The TC-VBU has good voltage balancing characteristics. The circulating current is controlled to 200 A when V_{750} reaches 750 V. It can also be seen from Figure 15b,c that the soft switching performance during the transient state in backward mode is consistent with the steady state shown in Figures 12b and 13b.

Figure 16 shows the experimental efficiency curves of IBC and TC-VBU under different power points. It can be seen that both IBC and TC-VBU have high efficiency by adopting soft switching technology. The highest efficiency of IBC can reach 98.3%, and the highest efficiency of TC-VBU can reach 99.1%. The loss distribution under 75 kW is shown in Table 5. The loss of switches is calculated by PLECS simulation. The loss of resonant inductors is calculated by the parameter of core and windings. According to Table 5, the efficiency under the rated power is higher than the efficiency in Figure 16. This is due to the fact that the losses of capacitors are not included. Meanwhile, there are some errors due to the calculation method.

Table 5. Loss distribution under 75 kW.

Parameter	Loss Value
Mosfets of IBC	426 W
Inductors of IBC	Unknown (designed by supplier)
IGBTs of TC-VBU	513 W
Resonant inductors of IBC	45 W

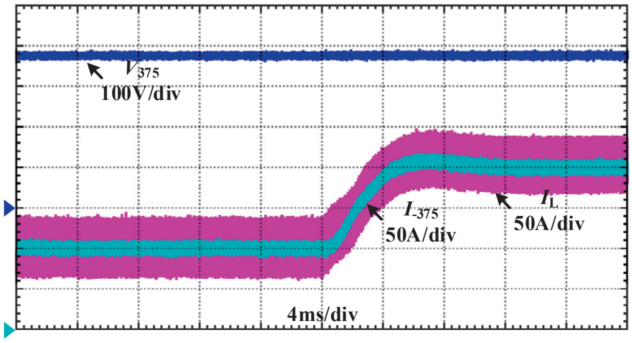

(**a**)

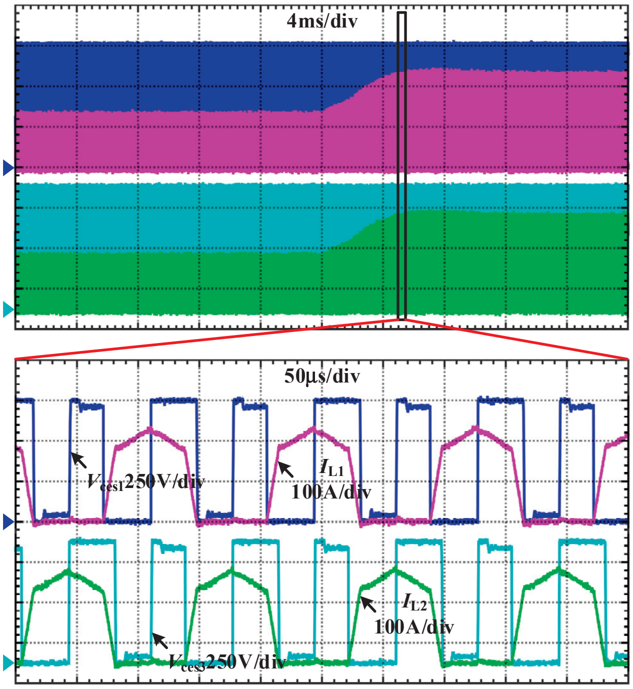

(**b**)

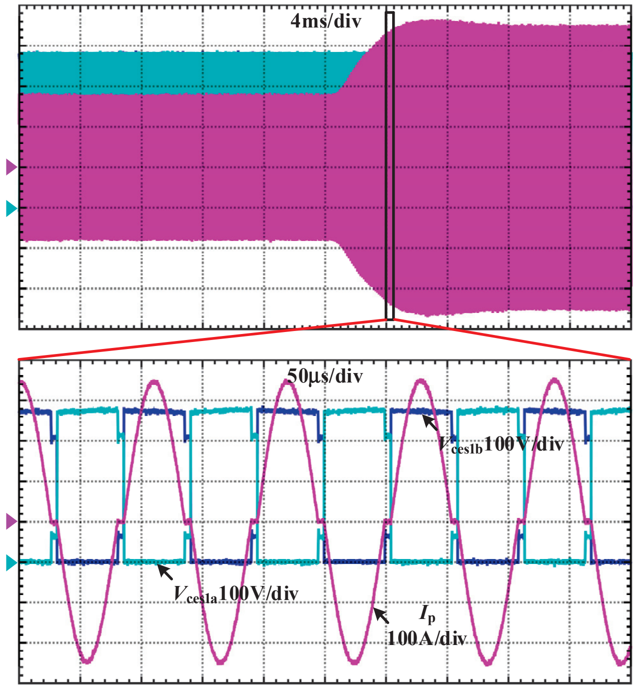

(**c**)

Figure 14. The transient performance of experimental waveform (forward mode): (**a**) IBC output voltage, output current, and inductor (*L*) current; (**b**) switch voltage and auxiliary inductor current of IBC; (**c**) switch voltage and resonant current of TC-VBU. (The triangles represent the coordinate origin).

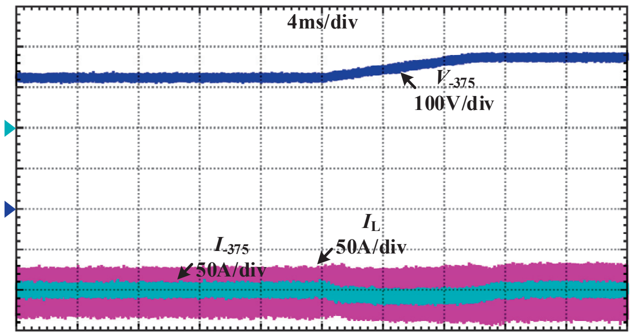

(**a**)

Figure 15. *Cont.*

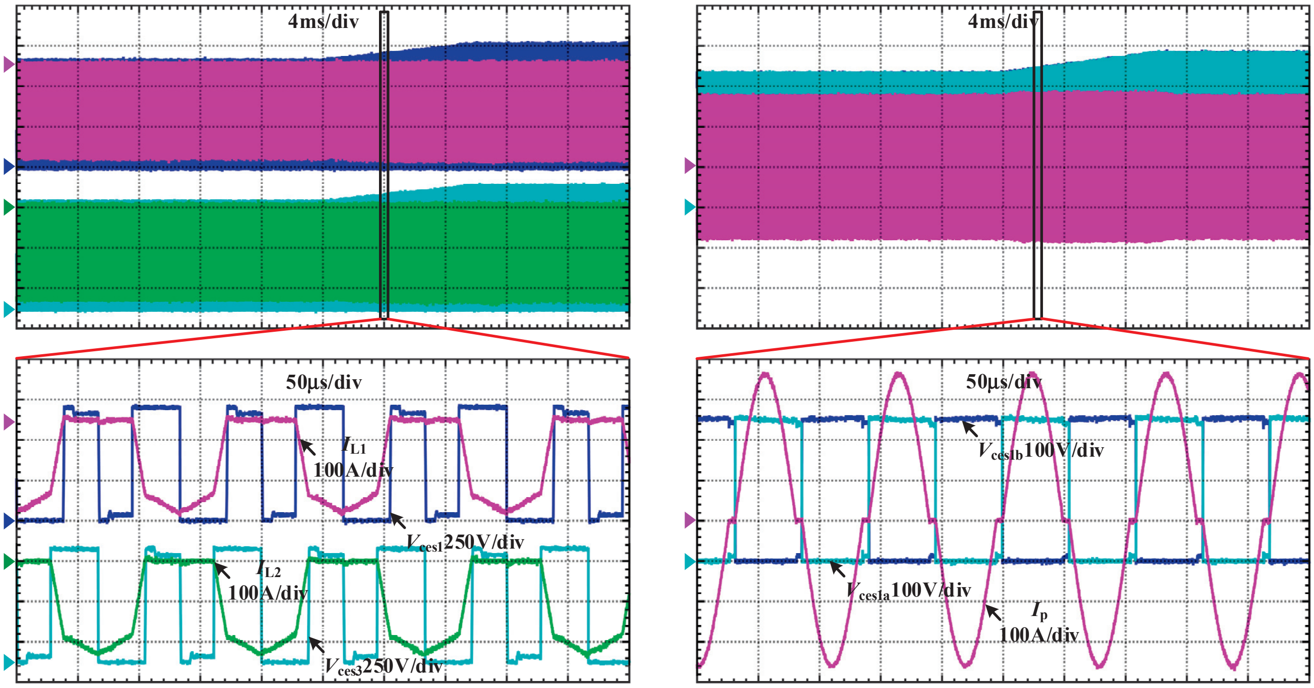

(b) (c)

Figure 15. The transient performance of experimental waveform (backward mode): (**a**) IBC output voltage, output current, and inductor (*L*) current; (**b**) switch voltage and auxiliary inductor current of IBC; (**c**) switch voltage and resonant current of TC-VBU. (The triangles represent the coordinate origin).

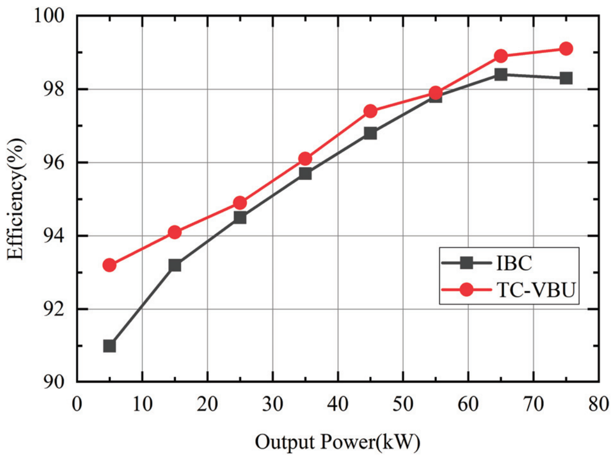

Figure 16. The efficiency curves of IBC and TC-VBU under different power points.

6. Conclusions

This paper proposes an improved multi-port DC transformer based on IBC and TC-VBU to achieve multi-voltage-level output with high efficiency. The working principles of IBC and TC-VBU are analyzed. The mathematical models in different modes are established. The control methods for the two converters are proposed. According to the mathematical models, the IBC and TC-VBU parameters are designed, including auxiliary inductor, filter inductor of IBC, resonant inductor, and resonant capacitor of TC-VBU. Simulation and experimental results verify the excellent performance of the proposed topology and the correctness of the parameter design method. Efficiency above 98% is achieved at extreme power unbalance condition. This will have a good application prospect.

Author Contributions: Conceptualization, J.Z. and K.Z.; methodology, X.T. and L.L.; software, J.L.; writing—original draft preparation, J.Z.; writing—review and editing, J.Z. and Y.Y.; project administration, Y.Y. and K.Z. All authors have read and agreed to the published version of the manuscript.

Funding: This research was funded by National Natural Science Foundation Project of China, grant number U24B2097.

Data Availability Statement: Data are unavailable due to privacy restrictions.

Conflicts of Interest: Authors Jialin Zhang, Yuefeng Yang, Lanfang Li and Jiafei were employed by the company China Power NARI Purui Engineering Co., Ltd. Authors Jialin Zhang, Kunpeng Zha, Yuefeng Yang, Lanfang Li and Jiafei were employed by the company NARI Group Corporation. The remaining authors declare that the research was conducted in the absence of any commercial or financial relationships that could be construed as a potential conflict of interest.

References

1. Bhattacharjee, A.K.; Kutkut, N.; Batarseh, I. Review of multiport converters for solar and energy storage integration. *IEEE Trans. Power Electr.* **2018**, *34*, 1431–1445. [CrossRef]
2. Muhtadi, A.; Pandit, D.; Nguyen, N.; Mitra, J. Distributed energy resources based microgrid: Review of architecture, control, and reliability. *IEEE Trans. Ind. Appl.* **2021**, *57*, 2223–2235. [CrossRef]
3. Nag, S.S.; Satpathi, K.; Ukil, A.; Pou, J.; Zagrodnik, M.A. An isolated bipolar DC-DC converter for energy storage integration in marine vessels. In Proceedings of the IECON 2017-43rd Annual Conference of the IEEE Industrial Electronics Society, Beijing, China, 29 October–1 November 2017.
4. Gu, Y.; Li, W.; He, X. Analysis and control of bipolar LVDC grid with DC symmetrical component method. *IEEE Trans. Power Syst.* **2015**, *31*, 685–694. [CrossRef]
5. Tan, L.; Wu, B.; Yaramasu, V.; Rivera, S.; Guo, X. Effective voltage balance control for bipolar-DC-bus-fed EV charging station with three-level DC–DC fast charger. *IEEE Trans. Ind. Electr.* **2016**, *63*, 4031–4041. [CrossRef]
6. Wang, G.; Wen, H.; Xu, P.; Liu, W.; Zhou, J.; Yang, Y. A Comprehensive Review of Integrated Three-Port DC–DC Converters With Key Performance Indices. *IEEE Trans. Power Electr.* **2024**, *39*, 6391–6408. [CrossRef]
7. Sarnago, H.; Lucia, O.; Perez-Tarragona, M.; Burdio, J.M. Dual-output boost resonant full-bridge topology and its modulation strategies for high-performance induction heating applications. *IEEE Trans. Ind. Electr.* **2016**, *63*, 3554–3561. [CrossRef]
8. Vasiladiotis, M.; Rufer, A. A modular multiport power electronic transformer with integrated split battery energy storage for versatile ultrafast EV charging stations. *IEEE Trans. Ind. Electr.* **2014**, *62*, 3213–3222. [CrossRef]
9. Zhu, H.; Zhang, D.; Athab, H.S.; Wu, B.; Gu, Y. PV isolated three-port converter and energy-balancing control method for PV-battery power supply applications. *IEEE Trans. Ind. Electr.* **2014**, *62*, 3595–3606. [CrossRef]
10. Zhao, C.; Zhang, C.; Jiang, Q. An H-Bridge Time-Sharing Multiplexing-Based Power Electronic Transformer. *IEEE J. Emerg. Sel. Top. Power Electr.* **2023**, *11*, 4831–4840. [CrossRef]
11. Wang, X.; Liu, J.; Ouyang, S.; Xu, T.; Meng, F.; Song, S. Control and experiment of an H-bridge-based three-phase three-stage modular power electronic transformer. *IEEE Trans. Power Electr.* **2015**, *31*, 2002–2011. [CrossRef]
12. Huber, J.E.; Kolar, J.W. Applicability of solid-state transformers in today's and future distribution grids. *IEEE Trans. Smart Grid.* **2017**, *10*, 317–326. [CrossRef]
13. Zhang, J.; Li, H.; Kong, X.; Zhou, J.; Shi, G.; Zang, J.; Wang, J. A Novel Multiple-Medium-AC-Port Power Electronic Transformer. *IEEE Trans. Ind. Electr.* **2023**, *71*, 6568–6578. [CrossRef]
14. Feng, M.; Gao, C.; Ding, J.; Ding, H.; Xu, J.; Zhao, C. Hierarchical modeling scheme for high-speed electromagnetic transient simulations of power electronic transformers. *IEEE Trans. Power Electr.* **2021**, *36*, 9994–10004. [CrossRef]
15. Zhao, B.; Song, Q.; Liu, W.; Sun, Y. Overview of dual-active-bridge isolated bidirectional DC–DC converter for high-frequency-link power-conversion system. *IEEE Trans. Power Electr.* **2013**, *29*, 4091–4106. [CrossRef]
16. Li, X.; Cheng, L.; He, L.; Wang, C.; Zhu, Z. Decoupling control of an LLC-quad-active-bridge cascaded power electronic transformer based on accurate small-signal modeling. *IEEE J. Emerg. Sel. Top. Power Electr.* **2021**, *10*, 4115–4127. [CrossRef]
17. Li, Z.; Pei, Y.; Wang, L.; Zhao, L.; Pei, L.; Cao, W. A comprehensive closed-loop voltage ripple control scheme for modular multilevel converter-based power electronic transformers. *IEEE Trans. Power Electr.* **2023**, *38*, 15225–15241. [CrossRef]
18. Ma, D.; Chen, W.; Shu, L.; Qu, X.; Hou, K. A MMC-based multiport power electronic transformer with shared medium-frequency transformer. *IEEE Trans. Circuits Syst. II Express Briefs* **2020**, *68*, 727–731. [CrossRef]
19. Ma, D.; Chen, W.; Shu, L.; Qu, X.; Zhan, X.; Liu, Z. A multiport power electronic transformer based on modular multilevel converter and mixed-frequency modulation. *IEEE Trans. Circuits Syst. II Express Briefs* **2019**, *67*, 1284–1288. [CrossRef]

20. Lu, S.; Deng, J.; Li, S.; Shao, Y.; Li, K. A Multiport Power Electronic Transformer Based on Three-Phase Four-Arm Full-bridge Modular Multilevel Converter. *IEEE Trans. Power Electr.* **2024**, *39*, 16174–16186. [CrossRef]
21. Jiang, S.; Fan, C.; Huang, N.; Zeng, J. Fault characteristic analysis of DC pole-to-pole fault in power electronic transformer. *Proc. CSEE* **2018**, *38*, 1301–1309.
22. Falcones, S.; Ayyanar, R.; Mao, X. A DC-DC multiport-converter-based solid-state transformer integrating distributed generation and storage. *IEEE Trans. Power Electr.* **2012**, *28*, 2192–2203. [CrossRef]
23. Liu, X.; Gao, F.; Xu, J.; Liu, Y.; Khan, M.M.; Yang, X.; Rogers, D.J.; Liu, D. A compact auxiliary power supply design for a medium frequency solid state transformer. *IEEE Trans. Trans. Electr.* **2022**, *9*, 1443–1457. [CrossRef]
24. Zhao, B.; Song, Q.; Li, J.; Wang, Y.; Liu, W. Modular multilevel high-frequency-link DC transformer based on dual active phase-shift principle for medium-voltage DC power distribution application. *IEEE Trans. Power Electr.* **2016**, *32*, 1779–1791. [CrossRef]
25. Li, K.; Zhao, Z.; Yuan, L.; Zhang, C.; Wen, W.; Sun, J. Synergetic control of high-frequency-link based multi-port solid state transformer. In Proceedings of the 2018 IEEE Energy Conversicongress and Expositi(ECCE), Portland, OR, USA, 23–27 September 2018.
26. Wen, W.; Li, K.; Zhao, Z.; Yuan, L.; Mo, X.; Cai, W. Analysis and control of a four-port megawatt-level high-frequency-bus-based power electronic transformer. *IEEE Trans. Power Electr.* **2021**, *36*, 13080–13095. [CrossRef]
27. Qin, D.; Sun, Q.; Wang, R.; Ma, D.; Liu, M. Adaptive bidirectional droop control for electric vehicles parking with vehicle-to-grid service in microgrid. *CSEE J. Power Energy Syst.* **2020**, *6*, 793–805.
28. Wang, R.; Li, J.; Sun, Q.; Wang, P. Current edge-control strategy for multiple energy routers based on cyber-energy dual modulations. *IEEE Trans. Ind. Electr.* **2023**, *71*, 4079–4088. [CrossRef]
29. Gu, C.; Zheng, Z.; Xu, L.; Wang, K.; Li, Y. Modeling and control of a multiport power electronic transformer (PET) for electric traction applications. *IEEE Trans. Power Electr.* **2015**, *31*, 915–927. [CrossRef]
30. Li, Y.; Sun, Q.; Qin, D.; Cheng, K.; Li, Z. Power control of a modular three-port solid-state transformer with three-phase unbalance regulation capabilities. *IEEE Access* **2020**, *8*, 72859–72869. [CrossRef]
31. Zhao, T.; Wang, G.; Bhattacharya, S.; Huang, A.Q. Voltage and power balance control for a cascaded H-bridge converter-based solid-state transformer. *IEEE Trans. Power Electr.* **2012**, *28*, 1523–1532. [CrossRef]
32. Wang, R.; Jiang, S.; Ma, D.; Sun, Q.; Zhang, H.; Wang, P. The energy management of multiport energy router in smart home. *IEEE Trans. Con. Electr.* **2022**, *68*, 344–353. [CrossRef]
33. Zhao, C.; Round, D.; Kolar, W. An isolated three-port bidirectional DC-DC converter with decoupled power flow management. *IEEE trans. Power Electr.* **2008**, *23*, 2443–2453. [CrossRef]
34. Wen, W.; Zhao, Z.; Ji, S.; Yuan, L. Low-voltage ride through of multi-port power electronic transformer. *iEnergy* **2022**, *1*, 243–256. [CrossRef]
35. Zhang, J.; Zha, K.; Tang, X.; Yang, Y.; Yan, H.; Wen, F.; Shi, M. Topology and start-up strategy for DC–DC transformers based on voltage balancing unit. *J. Power Electr.* **2021**, *21*, 1072–1083. [CrossRef]

sustainability

MDPI

Article

An Analysis of Wireless Power Transfer with a Hybrid Energy Storage System and Its Sustainable Optimization

Changqing Yang, Liwei Zhang * and Sanmu Xiu *

School of Electrical Engineering, Beijing Jiaotong University, Beijing 100044, China; 20117031@bjtu.edu.cn
* Correspondence: lwzhang@bjtu.edu.cn (L.Z.); smxiu@bjtu.edu.cn (S.X.)

Abstract: This study was conducted to achieve simple and feasible secondary-side independent power control for wireless power transfer (WPT) systems with a hybrid energy storage system (HESS) and to minimize the power loss introduced by the added converter. We propose a novel operation mode tailored to a WPT system with a HESS load composed of an *LCC*-compensated WPT system and a Buck/Boost bidirectional converter. Its power control is based on insights into the characteristics of *LCC*–*LCC* compensation. Since this control method requires the cooperation of a DC converter, control of the converter's efficiency is the focus of this paper. Building on this framework, several parasitic parameters such as the equivalent series resistance (ESR) of inductors and switches are taken into account. An improved operation mode is proposed to address the efficiency degradation and control imbalance caused by ESR. By meticulously controlling the behavior of the components of the converter, the devices operate in zero-voltage switching (ZVS) mode, thereby reducing switching losses. Additionally, fuzzy control is utilized in this study to enhance robustness. The analyses are verified through a prototype system. The results of the experiments illustrate that the analytical approach proposed in this study achieves reliable power control and efficient converter operation. The results of this study show that the efficiency of the devices is improved and reached up to 99% with the converter. This study explores the efficiency optimization of the WPT system, which directly supports sustainable practices by reducing resource consumption and minimizing environmental impact. The findings offer valuable insights into sustainable applications and policy implications, aligning with the goals of socio-economic and environmental sustainability.

Keywords: wireless power transfer; hybrid energy storage system; optimization control; efficiency optimization; sustainable energy development; power loss; *LCC*; bidirectional converter; equivalent series resistance

1. Introduction

In recent years, wireless power transfer (WPT) has gained prominence as a secure and convenient method for contactless power delivery [1]. By removing the need for physical connections between the power source and the device, WPT technology proves to be highly suitable for specialized applications such as underwater environments [2,3], high-voltage conditions [4], and electronic medical devices [5,6]. Furthermore, WPT shows great promise in enabling electric-driven devices to efficiently receive power [7–9]. The development of WPT systems for electric vehicle (EV) charging has introduced both stationary and in-motion charging solutions. This technology offers remarkable benefits in terms of convenience, safety, and compactness in energy transfer, positioning it as a highly promising solution to the growing challenge of charging electric vehicles.

Although traditional plug-in charging methods operate reliably, they still present risks such as poor contact, electric sparks, and high voltage issues [10]. In contrast, wireless charging technology offers a contactless solution for electrified transportation [11,12], effectively mitigating the problems associated with contact-based power supply methods and enhancing overall system reliability [13]. Current research on WPT technology predominantly focuses on battery loads [14], with some studies exploring supercapacitor loads, and current charging strategies are tailored to specific load models. In recent studies, power and efficiency have become the key objectives. In WPT systems, their effectiveness directly impacts their interoperability [15,16], which is crucial for meeting the demands of practical applications. The hybrid energy storage system (HESS), which integrates batteries and supercapacitors [17], has garnered attention due to its combined high energy and high-power density benefits [18–20]. However, a noticeable gap exists in the research regarding WPT system control for HESS loads. Consequently, this study aims to develop a method to address the challenge of output regulation in WPT systems with HESS loads.

In WPT systems, energy is transferred using coupling inductors [7]. The physical separation between these inductors results in low mutual inductance and significant leakage inductance. Although leakage inductance does not directly facilitate energy transfer, it can reduce the power factor during transmission, leading to decreased efficiency. To address this issue, various compensation circuits have been proposed [21–23]. These circuits, developed with different compensation topologies, aim to achieve optimal output characteristics and are suitable for diverse application scenarios [23]. Initially, resonant circuits consisted of single elements and were categorized based on their connection within the circuit, resulting in topologies such as the series–series (SS), series–parallel (SP), parallel–series (PS), and parallel–parallel (PP) topologies [21]. At the resonant frequency, these compensation circuits can absorb the reactive power generated by leakage inductance during energy transfer, thereby enhancing efficiency. For improved performance, more advanced topologies like *LCL* and *LCC* configurations have been introduced [23,24]. Both of these structures are capable of providing a constant current output. The *LCC* compensation network, in particular, reduces the size of the compensation inductor by incorporating a capacitor in series with the primary coil, which can operate under zero current switching (ZCS) conditions [24–26]. Due to its symmetrical design, the *LCC* configuration offers superior performance, including higher power levels and enhanced anti-offset capabilities, making it a favored compensation topology in current research.

To fulfill the transmission requirements for system efficiency and load energy demand, a method for tracking maximum energy efficiency was proposed by Zhong and Hui [27]. Their method involves the DC converter controlling the voltage output from the rectifier to be constant, while the input-side inverter adjusts the input power to track the system's maximum efficiency. Wu et al. [28] presented a bilateral control scheme utilizing *LCL* compensation to improve system efficiency for battery charging. Achieving system efficiency and meeting load energy demand are two primary control objectives, necessitating two control loops, typically involving the primary-side inverter and the secondary-side DC converter. Hence, these methods require control adjustments on both the primary and secondary sides.

For the application of a HESS in WPT systems, Wang et al. [29] configured the capacity of the hybrid energy storage system based on multiple wireless charges and practical application scenarios, with the supercapacitor directly connected to the battery via a DC converter. Hata et al. [30] proposed a hybrid energy storage charging scheme for electric vehicles and a power control method for constant current charging of the main battery, where the supercapacitor is similarly connected to the battery through a DC converter. Additionally, Geng et al. [31] provided an in-depth analysis of the SWPT system for modern trams with hybrid energy storage and, using the *LCC*-S topology, proposed a HESS power distribution strategy based on optimal power indicators [31]. This strategy uses the output power parameters during optimal transmission efficiency as the control target for the total charging power of the HESS. In this setup, the supercapacitor operates in constant current charging mode while the battery compensates for the difference between the supercapacitor charging power and the system's optimal power to achieve optimal efficiency tracking. However, the aforementioned studies do not address control for optimized converter efficiency. As a complex topology widely used in WPT systems, the optimization control of converter efficiency in such systems remains a challenging task. To address this issue, fuzzy control can be introduced as an effective solution. Fuzzy control, based on fuzzy set theory, fuzzy logic, and fuzzy inference, is particularly suitable for handling complex nonlinear systems and uncertainties. By incorporating fuzzy control into the *LCC* topology of a HESS in WPT applications, we can significantly enhance the overall system performance and efficiency. The adaptive and robust nature of fuzzy control makes it an ideal choice for managing the complexities and uncertainties inherent in such systems.

This study introduces a control strategy for hybrid energy storage loads within an *LCC*–*LCC*-compensated WPT system. Initially, an equivalent circuit incorporating the HESS load is presented within the system model. A symmetric *LCC*-compensated WPT system model is then developed based on the mutual inductance model. By analyzing this precise model, the system's output characteristics, particularly the relationship between power and output port voltage, are identified. From this analysis, a method for controlling output power is designed. The power control method based on output voltage offers a straightforward approach, in contrast to impedance matching control methods [14], which require an accurate impedance model. Furthermore, this study examines the control strategy for the independent control converter on the secondary side. After detailing the operating modes of the DC converter, the working mode with a twice-reversed inductor current is introduced, allowing the device to function in the ZVS state. This soft-switching method reduces operational losses in the converter, thereby improving efficiency and minimizing the impact of additional control stages on the system's overall efficiency. Subsequently, a power control strategy for the bidirectional Buck/Boost converter is proposed based on actual circuit resistance parameters, achieving stable power control without the need for an inner current loop. To address the large time constant issue introduced by the supercapacitor group, fuzzy control is employed, providing a simple and effective means of controlling the converter and enhancing system robustness.

The structure of this paper is organized as follows: Section 2 presents a mathematical model for the *LCC*–*LCC*-compensated WPT system and details its output characteristics. Section 3 introduces a detailed analysis of the secondary-side DC converter, covering its operating modes and control strategies. Section 4 presents the prototype system used to validate the preceding analysis and the proposed control method. Finally, Section 5 provides the conclusions of this study.

2. Working Principle of the Wireless Power Transfer System

The configuration of the *LCC*–*LCC* compensation network and its associated power electronics components are depicted in Figure 1. On the primary side, Q_1–Q_4 represent four power switches. They form a full-bridge inverter to provide AC excitation for the compensation network from the DC bus U_{in}. The self-inductance of the loosely coupled transformer is denoted as L_1 and L_2. The primary-side compensation comprises the inductor L_{f1} and capacitors C_{f1} and C_1, while the secondary-side compensation includes the inductor L_{f2} and capacitors C_{f2} and C_2. The mutual inductance between the two coils is represented by M. The secondary-side rectifier diodes are indicated as D_1–D_4. Of note, the system model includes a HESS load, which consists of supercapacitors and batteries. A DC converter is employed to control the energy flow within the system.

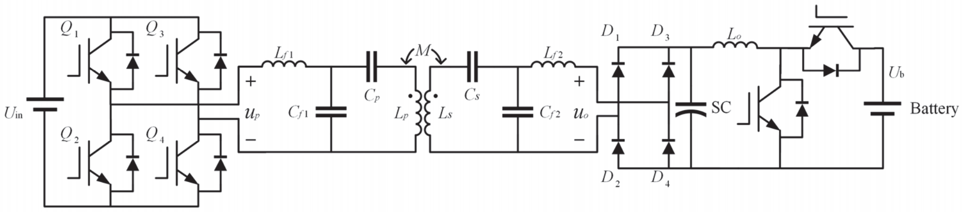

Figure 1. Schematic diagram of a WPT system with a HESS load.

By neglecting the losses in the circuit and treating the circuit after the rectifier as an integrated load, R_{eq}, we can derive a simplified WPT system, illustrated in Figure 2. The input voltage is referred to as u_p, and the output voltage before the rectifier is denoted as u_o. The currents flowing through L_1, L_2, L_{f1}, and L_{f2} are indicated by i_1, i_2, i_{Lf1}, and i_{Lf2}, respectively. Similarly, the voltages across C_1, C_2, C_{f1}, and C_{f2} are indicated by u_{C1}, u_{C2}, u_{Cf1} and u_{Cf2}.

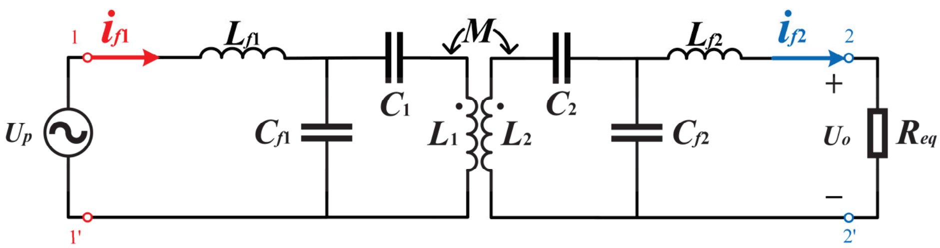

Figure 2. Equivalent circuit of an *LCC*–*LCC*-compensated WPT system.

The frequency characteristics of the *LCC*–*LCC* network can be represented by state–space equations. By choosing capacitor voltages and inductor currents as state variables, a unified form of the state–space representation is derived:

$$\begin{cases} \frac{dx(t)}{dt} = \boldsymbol{A}\boldsymbol{x}(t) + \boldsymbol{B}\boldsymbol{u_p}(t) \\ \boldsymbol{i}_{\boldsymbol{L_{f2}}}(t) = \boldsymbol{C}\boldsymbol{x}(t) \end{cases} \tag{1}$$

where $\boldsymbol{x}(t)$ denotes the state vector, input voltage $\boldsymbol{u_p}(t)$ is defined as the system input variable, the output current $\boldsymbol{i_{Lf2}}(t)$ is defined as the system output variable, and the state variables and the parameter matrices are defined as follows:

$$\boldsymbol{x} = \begin{bmatrix} i_{Lf1} & u_{Cf1} & u_{C1} & i_{L1} & i_{L2} & u_{C2} & u_{Cf2} & i_{Lf2} \end{bmatrix}^T \tag{2}$$

$$\boldsymbol{A} = \begin{bmatrix} & \frac{1}{L_{f1}} & & & & & & \\ \frac{1}{C_{f1}} & & & -\frac{1}{C_{f1}} & & & & \\ & & & \frac{1}{C_1} & & & & \\ & \frac{L_2}{L_k} & -\frac{L_2}{L_k} & & & -\frac{M}{L_k} & -\frac{M}{L_k} & \\ & \frac{M}{L_k} & -\frac{M}{L_k} & & & -\frac{L_1}{L_k} & -\frac{L_1}{L_k} & \\ & & & & \frac{1}{C_2} & & & \\ & & & & \frac{1}{C_{f2}} & & & -\frac{1}{C_{f2}} \\ & & & & & \frac{1}{L_{f2}} & -\frac{R_{eq}}{L_{f2}} & \end{bmatrix} \tag{3}$$

$$\boldsymbol{B} = \begin{bmatrix} \frac{1}{L_{f1}} & 0 & 0 & 0 & 0 & 0 & 0 & 0 \end{bmatrix}^T \tag{4}$$

$$\boldsymbol{C} = \begin{bmatrix} 0 & 0 & 0 & 0 & 0 & 0 & 0 & 1 \end{bmatrix} \tag{5}$$

where L_k is defined as follows:

$$L_k = L_1 L_2 - M^2 \tag{6}$$

The characteristic equation of the system can thus be deduced as follows:

$$|s\boldsymbol{E}_8 - \boldsymbol{A}| = 0 \tag{7}$$

where $\boldsymbol{E}_8$ denotes the eight-order identity matrix. The Laplace form of Equation (1) can be derived as follows:

$$\begin{cases} \boldsymbol{i}_{Lf2}(s) = \boldsymbol{Y}(s)\boldsymbol{u}_p(s) \\ \boldsymbol{Y}(s) = \boldsymbol{C}(s\boldsymbol{E}_8 - \boldsymbol{A})^{-1}\boldsymbol{B} \end{cases} \tag{8}$$

Herein, $\boldsymbol{Y}(s)$ epitomizes the steady-state relationship between output $\boldsymbol{i}_{Lf2}$ and input $\boldsymbol{u}_p$.

As depicted in Figure 3, there are multiple resonant frequencies ω_0, ω_1, and ω_2. However, in this study, we do not focus on the overall frequency-domain characteristics. The constant resonant frequency ω_0 is determined under the following conditions:

$$\begin{cases} L_{f1} \cdot C_{f1} = \frac{1}{\omega_0^2} \\ L_{f2} \cdot C_{f2} = \frac{1}{\omega_0^2} \\ L_1 - L_{f1} = \frac{1}{\omega_0^2 C_1} \\ L_2 - L_{f2} = \frac{1}{\omega_0^2 C_2} \end{cases} \tag{9}$$

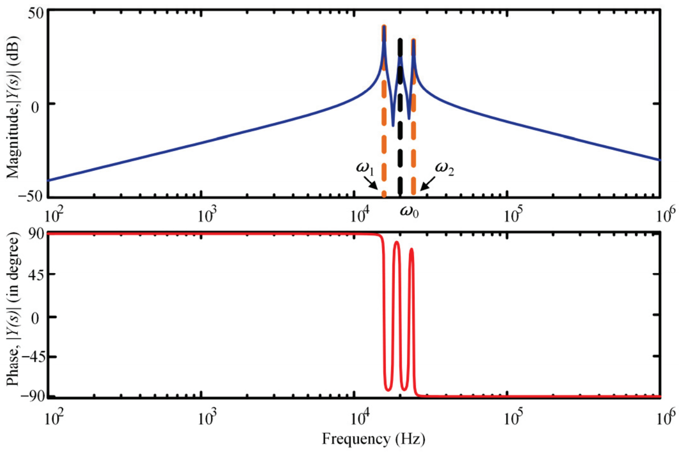

Figure 3. Frequency characteristics of the *LCC–LCC* network.

The inverter generates a square voltage, u_p, across its output. At a constant resonant frequency, ω_0, the fundamental voltage component can be considered approximately. Consequently, a phasor analysis of the WPT system is appropriate. In the subsequent analysis, the phasor forms of the system variables are represented by $\mathbf{U}_p$, $\mathbf{U}_o$, $\mathbf{I}_1$, $\mathbf{I}_2$, $\mathbf{I}_{Lf1}$, and $\mathbf{I}_{Lf2}$. Taking the input voltage $\mathbf{U}_p$ as the reference, we can proceed with the analysis as follows:

$$\mathbf{U}_p = U_p \angle 0^\circ \tag{10}$$

$$\mathbf{I}_1 = \frac{\mathbf{U}_p}{j\omega_0 L_{f1}} \tag{11}$$

Based on mutual inductance coupling, the voltage induced in the secondary coil can be determined as follows:

$$\mathbf{U}_{trans} = \boldsymbol{j}\omega_0 M_1 = \frac{MU_p}{L_{f1}}\angle 0^{\circ} \quad (12)$$

When $\mathbf{U}_{trans}$ is applied in the secondary *LCC* circuit, the analysis is similar to that when $\mathbf{U}_p$ is applied to the primary side. As a result, the output current can be determined using similar principles:

$$\mathbf{I}_{Lf2} = \frac{\mathbf{U}_{trans}}{\boldsymbol{j}\omega_0 L_2 + \frac{1}{\boldsymbol{j}\omega_0 C_2}} \quad (13)$$

After substituting Equations (9) and (12) into (13), the output current $\mathbf{I}_{Lf2}$ can be obtained as follows:

$$\mathbf{I}_{Lf2} = \frac{\mathbf{U}_{trans}}{\boldsymbol{j}\omega_0 L_{f2}} = \frac{MU_p}{\omega_0 L_{f1} L_{f2}}\angle -90^{\circ} = I_{Lf2}\angle -90^{\circ} \quad (14)$$

Since the terminal voltage of the rectifier, $\mathbf{U}_o$, must be in phase with $\mathbf{I}_{Lf2}$, $\mathbf{U}_o$ is a passive voltage generated based on the load condition, as shown in Figure 4.

$$\mathbf{U}_o = U_o\angle -90^{\circ} \quad (15)$$

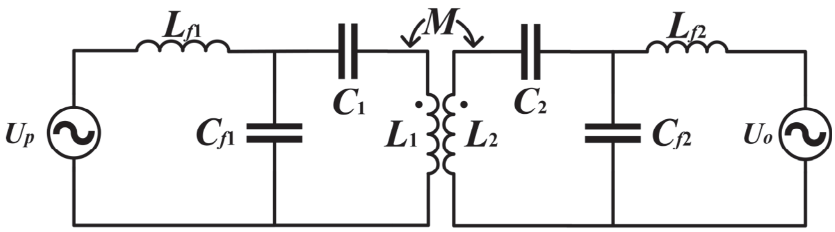

Figure 4. Equivalent circuit of *LCC–LCC* topology.

Based on Equations (13) and (14), the output power can be derived as follows:

$$P_o = U_o I_{Lf2} = \frac{MU_p U_o}{\omega_0 L_{f1} L_{f2}} \quad (16)$$

According to Equation (16), the output power of the WPT system is related to the terminal voltage U_o. Moreover, Equation (14) shows that the *LCC–LCC* compensation structure enables the system to operate in a constant current mode. Therefore, by adjusting U_o, the output power P_o can be regulated effectively.

3. Analysis of the DC Converter

3.1. Operation of the DC Converter

As depicted in Figure 1, a DC converter between the supercapacitor and the battery can regulate $\mathbf{U}_o$, thereby indirectly managing the system's output power. Nevertheless, the inclusion of the converter adds an additional stage in the system, which diminishes the overall efficiency. To counteract this reduction in efficiency, this study proposes an efficient Buck/Boost converter operation mode to enhance efficiency. Figure 5 shows the Buck/Boost converter topology. In this configuration, U_{SC} denotes the port voltage across the supercapacitor, U_b denotes the battery port voltage, Q_1 and Q_2 are the switching devices, D_1 and D_2 are the anti-parallel diodes, L is the inductor, and C_{oss1} and C_{oss2} represent the drain-source capacitances of the switching devices. Lying on the low-voltage side, the supercapacitor enhances voltage utilization, reduces the voltage stress, and improves economic efficiency.

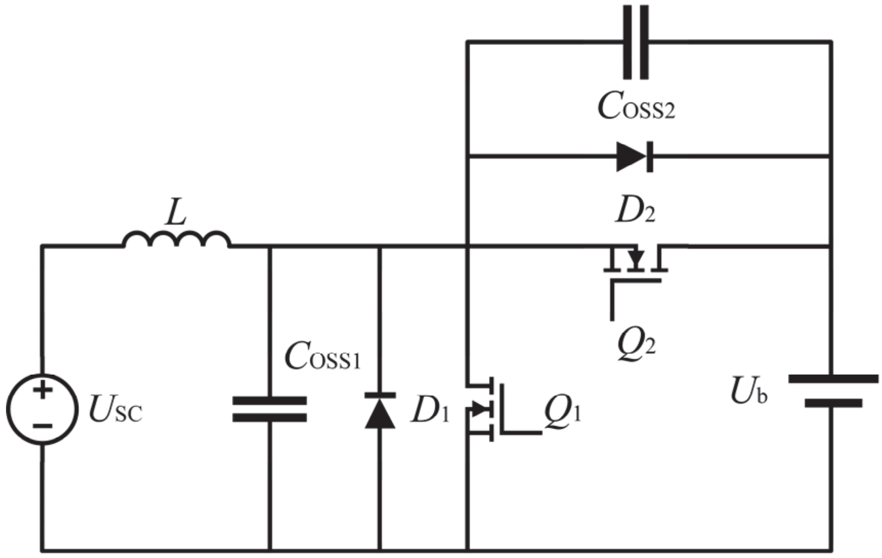

Figure 5. Equivalent circuit of Buck/Boost converter.

The conventional control strategy for the Buck/Boost bidirectional converter employs an independent PWM control strategy where switching devices Q_1/D_1 and Q_2/D_2 do not operate concurrently. Under this strategy, the circuit functions as a back-to-back configuration of Buck and Boost circuits. To maintain bidirectional power flow, a logic unit is essential for switching between operating states, typically utilizing hysteresis logic for smooth transitions. Conversely, in the complementary PWM control strategy, Q_1/D_1 and Q_2/D_2 operate concurrently, a method referred to as synchronous rectification. This mode allows the Buck/Boost bidirectional converter to achieve soft switching. Moreover, without a logic control unit, the system response is quick. In terms of rapid energy storage, the supercapacitor frequently absorbs and releases power, making it well suited for complementary PWM control.

In continuous current mode (CCM), diode conduction loss is significant, and the devices can only perform hard switching. In contrast, discontinuous current mode (DCM) allows for soft switching but still incurs diode conduction losses. The inductor current continues through the anti-parallel diode. When this current is substantial, conduction losses increase in the diode. In CCM, moreover, reverse recovery currents of the diode lead to additional losses.

To minimize working losses and achieve soft switching for the switching devices, the converter operates in synchronous PWM mode. The alternating conduction of Q_1/D_1 and Q_2/D_2 replaces the anti-parallel diode for current commutating. Since the MOSFET's conduction loss is lower than that of the diode, the conduction losses are reduced. Moreover, by controlling the switching devices, the inductor current can flow bidirectionally in each cycle, forming an asymmetric bidirectional conduction mode. In this mode, the switching devices turn off while the current is still flowing, enabling the drain-source capacitance to charge and discharge effectively, thus achieving zero-voltage switching (ZVS) turn-off. Additionally, commutating by switching devices eliminates oscillations caused by the diode. By configuring the dead time, the switching devices perform brief conductance during the transition. This enables ZVS turn-on of the MOSFET after the dead time ends.

The operating states of the converter are illustrated in Figure 6. The circuit waveforms are depicted in Figure 7.

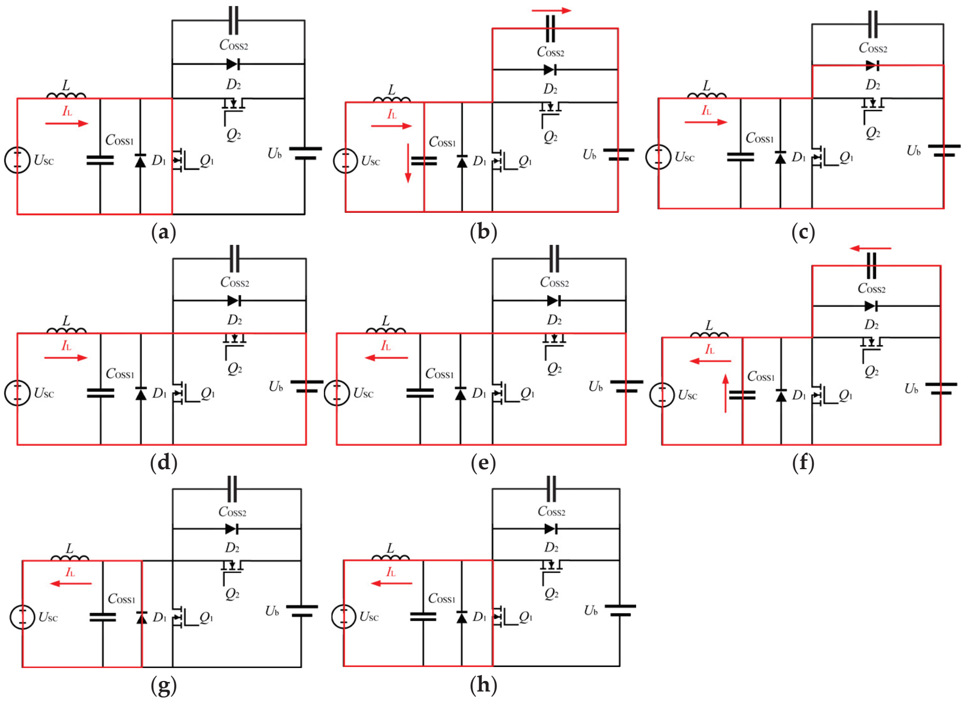

Figure 6. The operating states of the Buck/Boost converter during the time intervals (**a**) T_1, (**b**) T_2, (**c**) T_3, (**d**) T_4, (**e**) T_5, (**f**) T_6, (**g**) T_7 and (**h**) T_8.

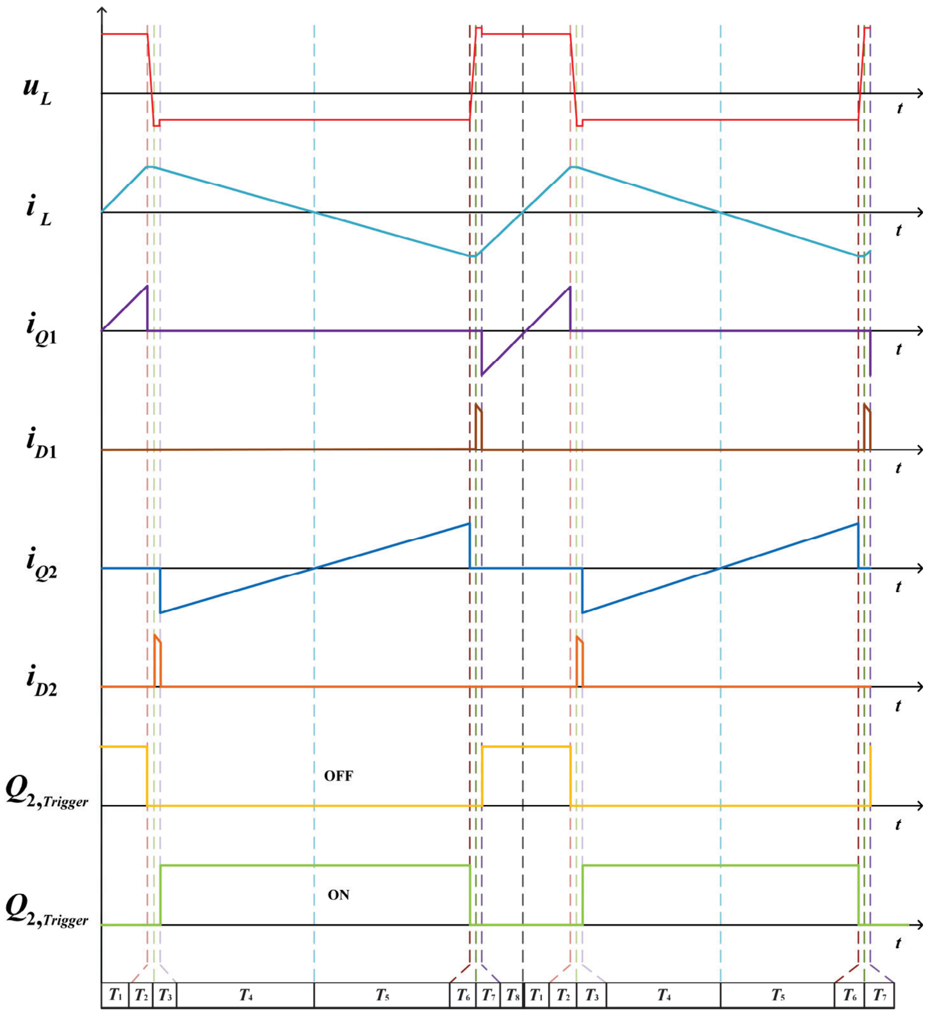

Figure 7. The waveforms of Buck/Boost converter.

In a steady state, the initial condition is that Q_1 is turned on while Q_2 is off. At this moment, the circuit operates in Boost mode. Inductor L holds a positive voltage, and inductor current i_L increases, as shown in Figure 6a. The waveform corresponds to time interval T_1 in Figure 7. Next, Q_1 is turned off, and i_L continues to flow through D_1, charging C_{oss1} and discharging C_{oss2}. The circuit transitions into T_2, as shown in Figure 6b. Due to the small drain-source capacitance and large inductance of L, T_2 lasts for a very short duration with almost no change in the i_L. After the dead time ends, Q_2 is turned on, transitioning the circuit into T_4, as shown in Figure 6d. Since D_2 conducts first, no voltage crosses Q_2 before it turns on, thus achieving ZVS. Consequently, the circuit operates in Buck mode.

In Buck mode, the current decreases as it passes through L until it reaches zero; then, it starts increasing in the opposite direction. The circuit transitions into T_5, as illustrated in Figure 6e. Subsequently, Q_2 turns off, and the circuit experiences a second dead time within the cycle. The circuit transitions into T_6, as shown in Figure 6f. Until the voltage passing through Q_1 drops to zero, Q_1 naturally turns on. Due to the dead time, Q_1 cannot turn on immediately. Period T_7 is shown in Figure 6g. When Q_1 turns on after the dead time, its anti-parallel diode, D_1, conducts first, achieving ZVS, and the circuit transitions into Boost mode again. T_8 is shown in Figure 6h. During operation, the circuit continuously cycles through these eight modes to achieve efficient operation.

3.2. Circuit Analysis and Controller

Based on the above analysis, when the Buck/Boost converter is in a steady state, the average inductor current over a period must satisfy the volt-second balance principle. Consequently, the duty cycle D_{ref} can be derived as follows:

$$D_{ref} = 1 - \frac{U_{SC}}{U_b} \tag{17}$$

In control theory, it is necessary to change the reference value and wait for the converter to return to a steady state. This control strategy relies on the current loop, which demands high precision and fast response in current sampling and often neglects the equivalent series resistance (ESR) in the circuit. In practical circuits, the inductor possesses ESR, and the switching devices have conduction resistance, which should be considered in the control strategy. Additionally, under the complementary PWM control strategy, the conduction time of the diodes and the charging and discharging times of C_{oss1} and C_{oss2} are relatively short and can be neglected. Consequently, the Buck/Boost bidirectional converter circuit topology considering the resistance parameters is shown in Figure 8.

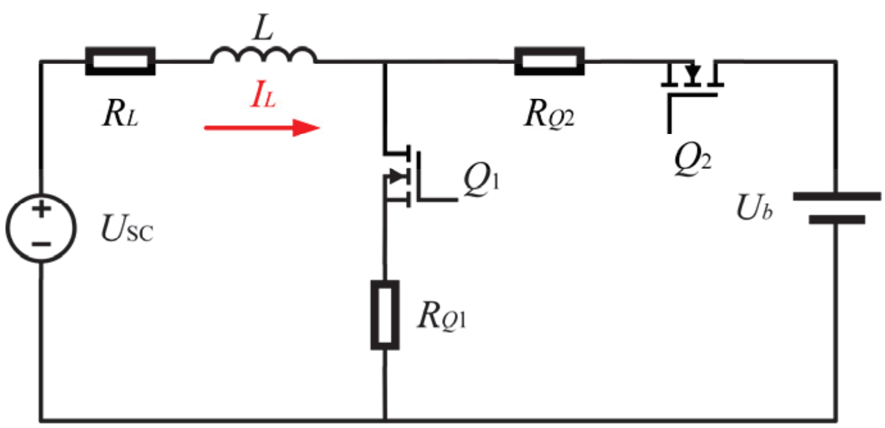

Figure 8. Equivalent circuit of Buck/Boost converter with resistance parameters.

The following analysis is conducted on the circuit model in Figure 8. As the converter switches between the Boost and Buck modes, the positive direction is defined as shown in Figure 8. The expressions for i_L can be derived as shown in Equations (18) and (19).

$$L\frac{di_L(t)_{\text{Boost}}}{dt} = U_{\text{SC}} - (R_L + R_{Q1})i_L(t)_{\text{Boost}} \tag{18}$$

$$L\frac{di_L(t)_{\text{Buck}}}{dt} = U_{\text{SC}} - U_b - (R_L + R_{Q2})i_L(t)_{\text{Buck}} \tag{19}$$

Assuming that the on-state resistances of Q_1 and Q_2 are equal, we can obtain that $R_Q = R_{Q1} = R_{Q2}$. Thus, Equation (20) can be derived, where D represents the duty cycle of Q_1.

$$\begin{aligned}\int_T^{T+DT} L\frac{di_L(t)}{dt}dt &= \int_T^{T+DT} L\frac{di_L(t)_{\text{Boost}}}{dt}dt + \int_{T+DT}^{2T} L\frac{di_L(t)_{\text{Buck}}}{dt}dt \\ &= U_{\text{SC}}T - U_b(T-DT) - (R_L + R_Q)\int_T^{2T} i_L(t)dt = 0\end{aligned} \tag{20}$$

Thus, steady-state duty cycle D is as follows:

$$D = \frac{(R_L + R_Q)}{U_b}\frac{1}{T}\int_T^{2T} i_L(t)dt + 1 - \frac{U_{\text{SC}}}{U_b} = \frac{(R_L + R_Q)}{U_b}I_{L,\text{avg}} + 1 - \frac{U_{\text{SC}}}{U_b} \tag{21}$$

Considering resistance in the circuit, duty cycle D is no longer solely dependent on U_{SC} and U_b. It is also influenced by the periodic average value of the inductor current $I_{L,avg}$. From Equation (21), the following can be derived:

$$I_{L,\text{avg}} = \frac{U_bD - U_b + U_{\text{SC}}}{R_L + R_Q} \tag{22}$$

Thus, the output power of the converter can be obtained as follows:

$$P_{conv} = U_{\text{SC}}I_{L,\text{avg}} = U_{\text{SC}}\frac{U_bD - U_b + U_{\text{SC}}}{R_L + R_Q} \tag{23}$$

where R_{ref} represents the sum of R_L and R_Q, and R_t represents the actual value of the sum of R_L and R_Q. Since R_{ref} is a reference and R_t is difficult to measure accurately, any discrepancy between them will inevitably affect the operation of the converter. According to Equation (22), when R_{ref} is given, the expected average inductor current I_{ref} can be determined. $I_{L,AVG}$ represents the average inductor current based on a real circuit. The relationship between them is shown in Equation (24), which leads to Equation (25), where P_{conv} denotes the actual transmitted power, and P_{ref} denotes the reference:

$$\frac{I_{L,AVG}}{I_{ref}} = \frac{\frac{U_bD - U_b + U_{\text{SC}}}{R_t}}{\frac{U_bD - U_b + U_{\text{SC}}}{R_{ref}}} = \frac{R_{ref}}{R_t} \tag{24}$$

$$\frac{P_{conv}}{P_{ref}} = \frac{U_{\text{SC}}I_{L,AVG}}{U_{\text{SC}}I_{ref}} = \frac{R_{ref}}{R_t} \tag{25}$$

Taking R_{ref} as the control variable, the transmission power of the converter can be controlled. Based on this, a power control strategy for a bidirectional Buck/Boost converter using resistance parameters is proposed. According to Equations (22)–(25), we obtained the following:

$$D = \frac{2LU_b - 2LU_{\text{SC}}}{2LU_b - R_{ref}TU_{\text{SC}}} \quad \left(-R_t < R_{ref} < R_t\right) \tag{26}$$

$$P_{conv} = \frac{R_{ref} T U_{SC}^2 (U_b - U_{SC})}{R_t (2LU_b - R_{ref} T U_{SC})} \quad \left(-R_t < R_{ref} < R_t\right) \tag{27}$$

Based on the analysis of the bidirectional Buck/Boost converter, a control strategy is proposed. In a HESS, the presence of supercapacitors introduces a large time constant to the system. This characteristic poses significant challenges for traditional control methods, as determining precise control parameters for such plants becomes difficult. Conventional control strategies often struggle with the high-order system modeling accuracy required for effective control, leading to suboptimal performance. Fuzzy control, on the other hand, offers a robust solution by converting system uncertainties and fuzziness into fuzzy sets and utilizing fuzzy rules for inference and decision-making. This approach enables effective control of the system without the need for precise mathematical modeling, which is particularly advantageous for high-order systems where traditional methods fall short. By integrating fuzzy control into the *LCC* topology of a HESS in WPT applications, we can significantly enhance the overall system performance and converter efficiency. Fuzzy control's ability to handle nonlinearities and uncertainties makes it an ideal choice for managing the complex dynamics of HESS systems. The fuzzy controller can dynamically adjust control parameters based on real-time system conditions, ensuring optimal performance even in the presence of variations and disturbances. The implementation of fuzzy control in the *LCC* topology provides a promising solution to optimize converter efficiency and improve system performance. It effectively addresses the control challenges posed by the large time constants and high-order dynamics inherent in HESS systems. In summary, the necessity of fuzzy control in HESS systems lies in its ability to transform uncertainties into manageable control actions, thereby overcoming the limitations of traditional control methods. This integration not only optimizes converter efficiency but also enhances the robustness and adaptability of the overall system, making it a crucial component for advanced WPT applications. The corresponding control flow diagram is shown in Figure 9. Finally, considering the instability and uncertainty of the WPT system, an intelligent control method, a fuzzy controller, is selected.

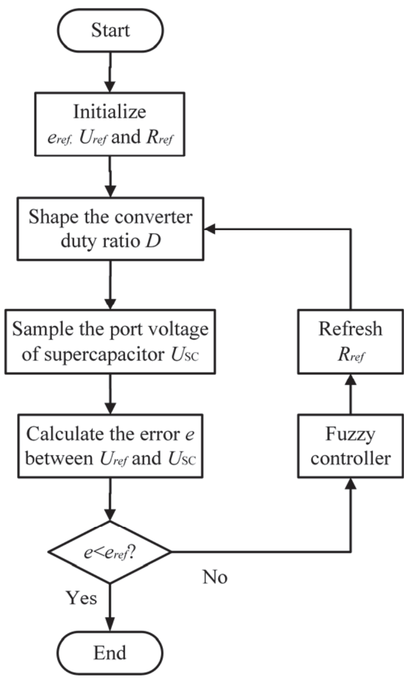

Figure 9. Control flow diagram of the Buck/Boost converter.

The fuzzy control rules used in this paper are shown in Figure 10. Here, *e* represents the error with respect to the reference value; *de* represents the rate of change in the error; and the output is the variation in R_{ref}, ΔR. The fuzzy inference is based on the Mamdani method, and the defuzzification is based on the centroid method. The fuzzy rules are listed in Table 1.

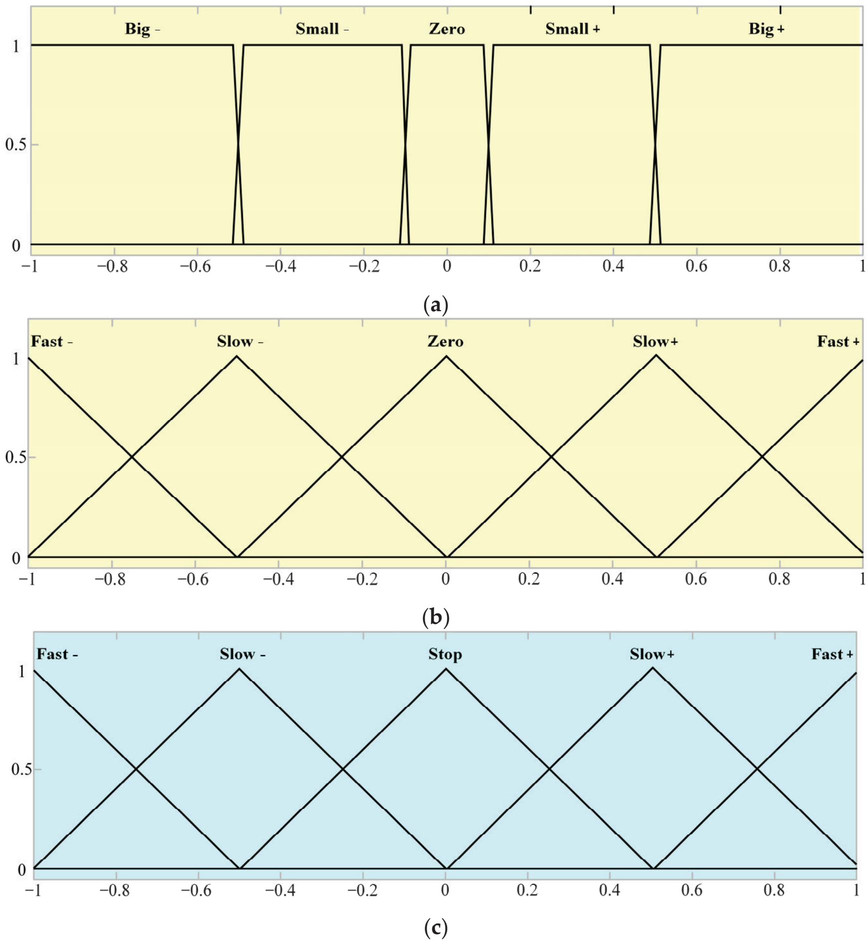

Figure 10. The fuzzy control rules of (**a**) *e*, (**b**) *de*, and (**c**) ΔR.

Table 1. Fuzzy control rules.

e	Big−	Small−	Zero	Small+	Big+
ΔR	Fast+	Slow+	Stop	Slow−	Big−

4. Experiments

A prototype of the *LCC*–*LCC*-compensated WPT system with a HESS load has been implemented in this experiment. As shown in Figure 11, the experiment platform comprises a host computer, a programmable DC power supply, a high-frequency inverter, *LCC*–*LCC* compensation circuits, a magnetic coupler, a rectifier bridge, a Buck/Boost converter, and a DC electronic load acting as a battery. The programmable DC power supply and the full-bridge inverter generate a fixed-magnitude square wave at the resonant frequency to power the entire system. Control signals are generated by a TI-TMS320F28335 core control chip. This experiment utilizes the MATLAB ver. R2021a Embedded Coder for Hardware-in-the-Loop (HIL) experiments. To achieve better performance, the parameter configuration of the double-sided *LCC* compensation network follows the methodology outlined in [32]. The experimental parameters are shown in Table 2, where L represents the DC inductance, and C_{SC} represents the total capacitance of the supercapacitor bank.

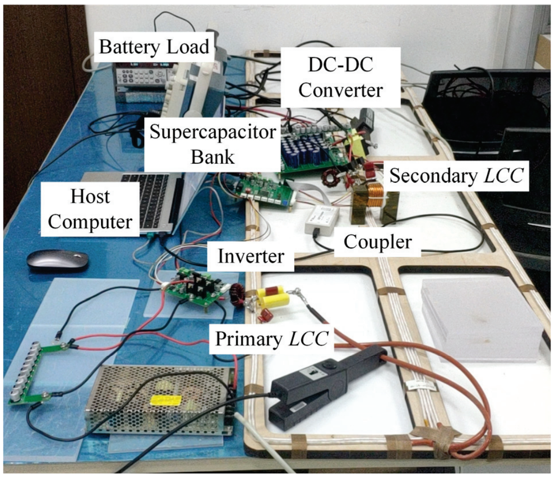

Figure 11. Experimental platform.

Table 2. Parameters of the experiment platform.

Parameter	Value	Parameter	Value
U_{in}/V	15	U_b/V	24
L_{f1}/μH	35	C_{SC}/F	3
C_{f1}/μF	7.2	L/μH	60
C_1/μF	50.7	C_2/μF	5.1
L_1/μH	40.07	C_{f2}/μF	16.9
L_2/μH	65.22	L_{f2}/μH	15
U_{in}/V	15	U_b/V	24

First, the voltage of the supercapacitor bank was charged to 12 V through the soft-start circuit. The waveforms of U_L and I_L once the steady state was reached are shown in Figure 12. The inductor current I_L reached zero twice within a cycle, indicating that the Buck/Boost bidirectional converter operated in the designed mode. The DC converter steadily transferred power to the DC bus. When the port voltage was stabilized at 12 V, the output current was approximately 2.34 A, and the power output to the Buck/Boost bidirectional converter was 28.1 W. For the battery load, the electronic load received a current of 1.16 A and obtained a power of 27.8 W. Thus, the power transmission efficiency in the DC/DC stage was 98.9%.

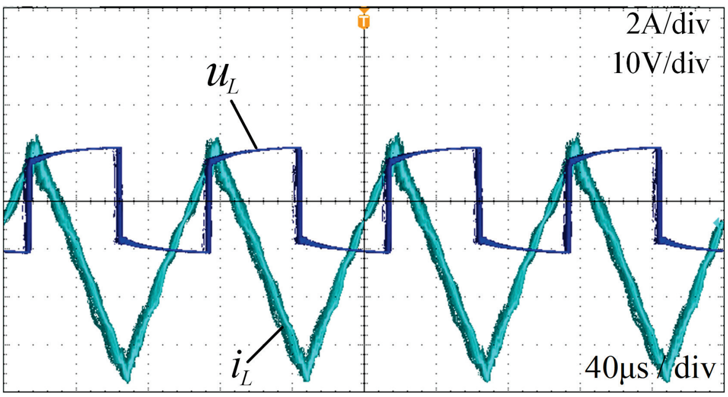

Figure 12. Waveforms of U_L and I_L when U_{SC} is 12 V and the air gap is small.

Subsequently, the air gap of the electromagnetic coupler increased, resulting in a reduction in coupling inductance. The waveforms of U_L and I_L after the adjustment are shown in Figure 13. As seen from the waveform of I_L, the Buck/Boost bidirectional converter consistently maintained operation in the critical mode. The supercapacitor bank charged the battery with maximum power. The output current was 1.62 A; the port voltage of the supercapacitor is 19 V; the supercapacitor bank provides an input power of 30.8 W to the converter; the battery load receives a current of 1.27 A from the converter; and the output power of converter is 30.5 W, resulting in a transmission efficiency of 99.0%.

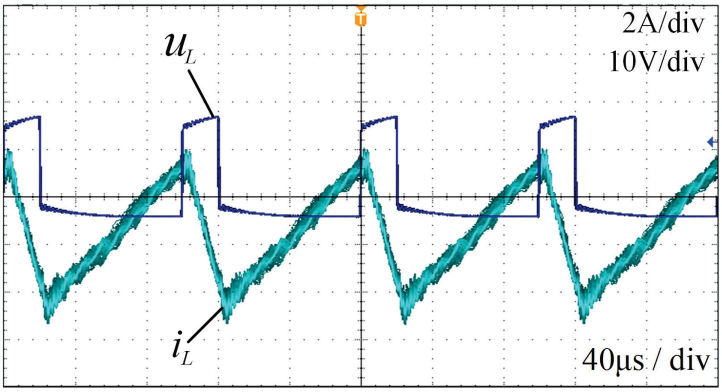

Figure 13. Waveforms of U_L and I_L when U_{SC} is 19 V and the air gap is large.

Finally, the air gap decreased. The waveforms of U_L and I_L are shown in Figure 14. The output current decreased to 2.15 A, and the converter consistently operated in critical mode. At this time, the supercapacitor bank provided an output power of 40.9 W to the converter. The current flowing into the battery load was 1.69 A, with a charging power of 40.6 W. The transmission efficiency in a DC/DC stage was 99.3%.

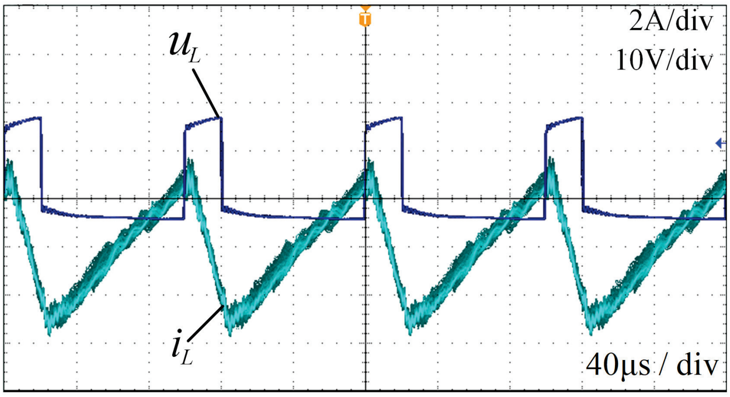

Figure 14. Waveforms of U_L and I_L when U_{SC} is 19 V and the air gap decreased.

5. Conclusions

This paper has investigated the suitability of HESS loads for WPT systems. A topology for the HESS load is derived, and the compensation performance is analyzed. It has been shown that the output characteristics of the *LCC*–*LCC* topology built-in view of the HESS load are flexible. With the aid of supercapacitors and a DC converter, the output power of the WPT system can be easily controlled. We expect the total efficiency to remain largely unaffected by the converter. Additionally, the control of the converter needs to meet the system's requirements. Therefore, an efficient operation mode for the converter is proposed, which generally exhibits lower switching losses and conduction losses. Consequently, the overall system efficiency is improved as the influence of the converter decreases. Besides, the operation principle of the converter is studied, and a fuzzy controller is implemented to achieve high robustness and handle the large time constant of the supercapacitor bank. Analysis and experimental results show that the proposed system can easily control the output power while maintaining high efficiency. While the results are promising, several specific challenges need to be addressed to fully realize the potential of this system in practical EV applications. One significant challenge is the real-time implementation of fuzzy control algorithms in hardware, ensuring that they can operate efficiently under varying conditions. Furthermore, the development of standardized protocols for communication and control in large-scale WPT networks is essential to ensure interoperability and seamless operation.

Author Contributions: Conceptualization, C.Y.; methodology, C.Y.; validation, C.Y., L.Z. and S.X.; formal analysis, C.Y.; resources, C.Y.; writing—original draft preparation, C.Y.; writing—review and editing, C.Y.; visualization, C.Y.; supervision, S.X. and L.Z.; project administration, L.Z. All authors have read and agreed to the published version of the manuscript.

Funding: This research received no external funding.

Institutional Review Board Statement: Not applicable.

Data Availability Statement: The original contributions presented in this study are included in the article. Further inquiries can be directed to the corresponding author.

Conflicts of Interest: The authors declare no conflicts of interest.

References

1. Zhu, L.; Wang, L.; Wu, M.; Zhao, C.; Yu, L. Precise Modeling and Design of Self-Resonant for High-Efficiency Mid-Range Wireless Power Transfer System. *IEEE Trans. Power Electr.* **2023**, *38*, 7848–7862. [CrossRef]
2. Chen, Y.; Niu, W.; Yang, Y.; Amirat, Y. Experimental Results and Analysis of Midrange Underwater Asymmetric Wireless Power Transfer. *J. Mar. Sci. Eng.* **2024**, *12*, 567. [CrossRef]
3. Ma, Y.; Liang, B.; Wang, J.; Cheng, B.; Yan, Z.; Dong, M.; Mao, Z. A Novel Hill Climbing-Golden Section Search Maximum Energy Efficiency Tracking Method for Wireless Power Transfer Systems in Unmanned Underwater Vehicles. *J. Mar. Sci. Eng.* **2024**, *12*, 1336. [CrossRef]
4. Feng, H.; Tavakoli, R.; Onar, O.C.; Pantic, Z. Advances in High-Power Wireless Charging Systems: Overview and Design Considerations. *IEEE Trans. Transp. Electr.* **2020**, *6*, 886–919. [CrossRef]
5. Liu, C.; Jiang, C.; Song, J.; Chau, K.T. An Effective Sandwiched Wireless Power Transfer System for Charging Implantable Cardiac Pacemaker. *IEEE Trans. Ind. Electron.* **2019**, *66*, 4108–4117. [CrossRef]
6. Moore, J.; Castellanos, S.; Xu, S.; Wood, B.; Ren, H.; Tse, Z.T.H. Applications of Wireless Power Transfer in Medicine: State-of-the-Art Reviews. *Ann. Biomed. Eng.* **2019**, *47*, 22–38. [CrossRef]
7. Patil, D.; McDonough, M.K.; Miller, J.M.; Fahimi, B.; Balsara, P.T. Wireless Power Transfer for Vehicular Applications: Overview and Challenges. *IEEE Trans. Transp. Electr.* **2018**, *4*, 3–37. [CrossRef]
8. Li, K.; Liu, Y.; Sun, X.; Tian, X.; Lei, G. Applications of Wireless Power Transfer System in Motors: A Review. *IEEE Access* **2024**, *12*, 80590–80606. [CrossRef]
9. Sun, L.; Ma, D.; Tang, H. A review of recent trends in wireless power transfer technology and its applications in electric vehicle wireless charging. *Renew. Sustain. Energy Rev.* **2018**, *91*, 490–503. [CrossRef]
10. Fan, M.; Shi, L.; Yin, Z.; Jiang, L.; Zhang, F. Improved Pulse Density Modulation for Semi-bridgeless Active Rectifier in Inductive Power Transfer System. *IEEE Trans. Power Electr.* **2019**, *34*, 5893–5902. [CrossRef]
11. Chen, S.; Zeng, J.; Tang, Y. A Super-Resonant Frequency Control for Handshaking of an Inductive Power Transfer System with Adjacent Units. *IEEE Trans. Ind. Electron.* **2024**, *71*, 1073–1076. [CrossRef]
12. Huang, J.; He, X.; Huo, P.; Xu, R. A Hybrid Modulation Strategy for *LCC–LCC* Compensated Bidirectional Wireless Power Transfer System to Achieve High Efficiency in the Whole Operating Range. *IEEE Trans. Ind. Electron.* **2024**, *71*, 327–337. [CrossRef]
13. Luo, B.; Long, T.; Guo, L.; Dai, R.; Mai, R.; He, Z. Analysis and Design of Inductive and Capacitive Hybrid Wireless Power Transfer System for Railway Application. *IEEE Trans. Ind. Appl.* **2020**, *56*, 3034–3042. [CrossRef]
14. Tan, T.; Chen, K.; Lin, Q.; Jiang, Y.; Yuan, L.; Zhao, Z. Impedance Shaping Control Strategy for Wireless Power Transfer System Based on Dynamic Small-Signal Analysis. *IEEE Trans. Circuits Syst. I Regul. Pap.* **2021**, *68*, 1354–1365. [CrossRef]

15. Song, K.; Lan, Y.; Zhang, X.; Jiang, J.; Sun, C.; Yang, G.; Yang, F.; Lan, H. A Review on Interoperability of Wireless Charging Systems for Electric Vehicles. *Energies* **2023**, *16*, 1653. [CrossRef]
16. Lan, Y.; Jiang, J.; Yang, F.; Song, K.; Fan, F.; Sun, C.; Yang, G.; Zhang, B.; Lan, H. Research on Impedance Boundary and Tolerance Zone for Improving Wireless Charging Interoperability Evaluation of Electric Vehicles. *IEEE Trans. Power Electr.* **2024**, *39*, 12035–12040. [CrossRef]
17. Chang, X.; Huang, L.; Zhang, X.; Yang, J.; Liu, H. Study on the Dynamic Optimal Control Strategy of an Electric-Hydrogen Hybrid Energy Storage System for a Direct Drive Wave Power Generation System. *J. Mar. Sci. Eng.* **2023**, *11*, 1347. [CrossRef]
18. Saeed, M.; Briz, F.; Guerrero, J.M.; Larrazabal, I.; Ortega, D.; Lopez, V.; Valera, J.J. Onboard Energy Storage Systems for Railway: Present and Trends. *IEEE Open J. Ind. Appl.* **2023**, *4*, 238–259. [CrossRef]
19. Zhao, J.; Li, L.; Wu, H.; Luo, B.; Li, H.; Zhang, Y.; Liu, S.; Zhao, L. An Optimized Multi-Level Control Method for Wireless Power Transfer System Using the Particle Swarm Optimization Algorithm. *Electronics* **2024**, *13*, 4341. [CrossRef]
20. Gao, P.; Li, Y.; Yao, W.; Zheng, X.; Zhang, C. Optimization of Hybrid Energy Storage System Sizing with Considering Energy Management Strategy for High-Power Pulsed Load in Aircraft. *IEEE Trans. Veh. Technol.* **2023**, *72*, 4525–4537. [CrossRef]
21. Shevchenko, V.; Husev, O.; Strzelecki, R.; Pakhaliuk, B.; Poliakov, N.; Strzelecka, N. Compensation Topologies in IPT Systems: Standards, Requirements, Classification, Analysis, Comparison and Application. *IEEE Access* **2019**, *7*, 120559–120580. [CrossRef]
22. Iam, I.; Choi, C.; Lam, C.; Mak, P.; Martins, R.P. A Constant-Power and Optimal-Transfer-Efficiency Wireless Inductive Power Transfer Converter for Battery Charger. *IEEE Trans. Ind. Electron.* **2024**, *71*, 450–461. [CrossRef]
23. Lu, Y.; Ge, D.; Meng, L.; Sun, C.; Tang, Q.; Gao, Y.; Chen, M.; Xia, C. A Novel Optimization Method of Compensation Network Parameters for *LCC* Topology Wireless Power Transfer System with Anti-Offset Characteristics. *IEEE Access* **2024**, *12*, 5960–5972. [CrossRef]
24. Xiong, M.; Dai, H.; Li, Q.; Jiang, Z.; Luo, Z.; Wei, X. Design of the*LCC* -SP Topology with a Current Doubler for 11-kW Wireless Charging System of Electric Vehicles. *IEEE Trans. Transp. Electr.* **2021**, *7*, 2128–2142. [CrossRef]
25. Hou, X.; Hu, H.; Su, Y.; Liu, Z.; Deng, Z.; Deng, R. A Multirelay Wireless Power Transfer System with Double-Sided *LCC* Compensation Network for Online Monitoring Equipment. *IEEE J. Emerg. Sel. Top. Power Electron.* **2023**, *11*, 1262–1271. [CrossRef]
26. Wang, F.; Zhang, W.; Ye, L.; Guo, J.; Liu, K.; Do, H.T. A Design Method to Implement ZVS for Electric Vehicle Wireless Charging System with Double-Side *LCC* Compensation. *IEEE J. Emerg. Sel. Top. Power Electron.* **2021**, *9*, 3791–3801. [CrossRef]
27. Zhong, W.X.; Hui, S.Y.R. Maximum Energy Efficiency Tracking for Wireless Power Transfer Systems. *IEEE Trans. Power Electr.* **2015**, *30*, 4025–4034. [CrossRef]
28. Wu, H.H.; Gilchrist, A.; Sealy, K.D.; Bronson, D. A High Efficiency 5 kW Inductive Charger for EVs Using Dual Side Control. *IEEE Trans. Ind. Inf. Inform.* **2012**, *8*, 585–595. [CrossRef]
29. Wang, L.J.; Gonder, J.; Burton, E.; Brooker, A.; Meintz, A.; Konan, A. IEEE A Cost Effectiveness Analysis of Quasi-Static Wireless Power Transfer for Plug-In Hybrid Electric Transit Buses. In Proceedings of the 2015 12th IEEE Vehicle Power and Propulsion Conference (VPPC), Montreal, QC, Canada, 19–22 October 2015.
30. Hata, K.; Huang, X.L.; Hori, Y. IEEE Power Flow Control of Magnetic Resonance Wireless Charing for Hybrid Energy Storage System of Electric Vehicles Application. In Proceedings of the 2015 54th Annual Conference of the Society of Instrument and Control Engineers of Japan (SICE), Hangzhou, China, 28–30 July 2015; pp. 1459–1462.
31. Geng, Y.Y.; Li, B.; Yang, Z.P.; Lin, F.; Sun, H. A High Efficiency Charging Strategy for a Supercapacitor Using a Wireless Power Transfer System Based on Inductor/Capacitor/Capacitor (*LCC*) Compensation Topology. *Energies* **2017**, *10*, 135. [CrossRef]
32. Nguyen, V.; Vu, V.; Gohil, G.; Fahimi, B. Coil-to-Coil Efficiency Optimization of Double-Sided *LCC* Topology for Electric Vehicle Inductive Chargers. *IEEE Trans. Ind. Electron.* **2022**, *69*, 11242–11252. [CrossRef]

MDPI AG
Grosspeteranlage 5
4052 Basel
Switzerland
Tel.: +41 61 683 77 34

MDPI Books Editorial Office
E-mail: books@mdpi.com
www.mdpi.com/books

Academic Open
Access Publishing

mdpi.com

ISBN 978-3-7258-4212-4